

Crystal Growth Technology

K. Byrappa
T. Ohachi

William Andrew
publishing



Springer

Springer Series in
MATERIALS PROCESSING

Springer

Berlin

Heidelberg

New York

Hong Kong

London

Milan

Paris

Tokyo

Physics and Astronomy



ONLINE LIBRARY

<http://www.springer.de/phys/>

Springer Series in
MATERIALS PROCESSING

Series Editors: W. Michaeli H. Warlimont E. Weber

This series is focused on the science and application of materials processing as an essential part of progress in the materials field. It addresses researchers and process engineers alike. The scope of the series includes all classes of materials – metals, inorganic non-metallic materials, polymers and composites – in the form of bulk materials, thin films and layered structures as well as micro- and nanostructured forms. All aspects of materials processing from fundamental understanding to innovative strategies and methods of practical process implementation and control are covered. It is the aim of the series to provide comprehensive information on the science and application of leading-edge and well-established processing technologies.

Low-Pressure Synthetic Diamond. Manufacturing and Applications

Editors: B. Dischler and C. Wild

Purification Process and Characterization of Ultra High Purity Metals

Application of Basic Science to Metallurgical Processing

Editors: Y. Waseda and M. Isshiki

Supercritical Fluid Science and Technology

Editors: Y. Arai, T. Sako, and Y. Takebayashi

Epitaxy. Physical Foundation and Technical Implementation

By M.A. Herman and W. Richter

Crystal Growth Technology

Editors: K. Byrappa and T. Ohachi

K. Byrappa T. Ohachi (Eds.)

Crystal Growth Technology

With 309 Figures and 45 Tables

William Andrew
publishing



Springer

Professor Kullaiah Byrappa
University of Mysore
P.B. No. 21, Manasagangotri
Mysore – 570 006, India
E-mail: kbyrappa@rediffmail.com

Professor Tadashi Ohachi
Doshisha University
Department of Electrical Engineering
Kyoto, Japan
E-mail: tohachi@eml.doshisha.ac.jp

Series Editors:

Professor Dr. Walter Michaeli
Institut für Kunststoffverarbeitung, Pontstrasse 49
52062 Aachen, Germany

Professor Dr. Hans Warlimont
Institut für Festkörper- und Werkstoffforschung e.V., Helmholtzstrasse 20
01069 Dresden, Germany

Professor Dr. Eicke Weber
University of California, Materials Science and Mineral Engineering
587 Evans Hall, Berkeley, CA 94720-1760, USA

ISSN 1434-9795

ISBN 0-8155-1453-0 William Andrew Inc., Norwich, New York
ISBN 3-540-00367-3 Springer-Verlag Berlin Heidelberg New York

Cataloging-in-Publication Data applied for
Bibliographic information published by Die Deutsche Bibliothek
Die Deutsche Bibliothek lists this publication in the Deutsche
Nationalbibliografie; detailed bibliographic data is available in the
Internet at <<http://dnb.ddb.de>>.

This work is subject to copyright. All rights are reserved, whether the whole or part of the material is concerned, specifically the rights of translation, reprinting, reuse of illustrations, recitation, broadcasting, reproduction on microfilm or in other ways, and storage in data banks. Duplication of this publication or parts thereof is permitted only under the provisions of the German Copyright Law of September 9, 1965, in its current version, and permission for use must always be obtained from Springer-Verlag. Violations are liable for prosecution act under German Copyright Law.

Springer-Verlag Berlin Heidelberg New York
a member of BertelsmannSpringer Science+Business Media GmbH
<http://www.springer.de>

© William Andrew Inc., Norwich, New York
Printed in USA

The use of general descriptive names, registered names, trademarks, etc. in this publication does not imply, even in the absence of a specific statement, that such names are exempt from the relevant protective laws and regulations and therefore free for general use.

Cover-concept: eStudio Calamar Steinen
Cover production: *design & production* GmbH, Heidelberg

DEDICATION

This book has been dedicated to:

Professor C.N.R. Rao, FRS
President, JNCASR
Bangalore, India

FOREWORD

Approximately fourteen years ago I was privileged to attend a conference in Japan whose title now escapes me, but whose scope covered a broad spectrum of modern technology. One lecturer has stood out in my memory over the years. He was Dr. Sekimoto, a Japanese businessman and eminent scientist whose specialty was in the field of communications. In his career at NEC he became President and finally Chairman of the Board. At the Conference I was particularly impressed by the content of one of his slides on which the following prophetic handwritten phrase occurred, "Who dominates materials dominates technology." The message was true and unambiguous then and history has simply emphasized its significance.

The ability to dominate materials requires an in-depth knowledge of the science and technology of crystal growth since crystals, especially single crystals have increasingly become a vital necessity in modern technology. How this domination is achieved is what this book is about. Crystal Growth is a universal phenomenon in the field of materials. It has a long history but a significant impetus, which accelerated its evolution from "a substance potting art" to a science in its own right, was the invention of the transistor in 1948, and the subsequent need for high purity semiconductor single crystals. As a result crystal growth has developed into a core discipline in materials science.

The evolution of our knowledge of crystal growth requires not only scientific understanding, but the driving force of applied technology which so often provides a significant influence in highlighting our lack of scientific knowledge and the need for a more refined science and indeed the development of new concepts. It is the knowledge of this balanced scientific evolution which Professor Byrappa and Professor Ohachi, the editors have achieved in the selection of critically important materials and technologies.

Both editors have international reputations in crystal growth. Professor Byrappa is an expert in the field of hydrothermal growth and is well-known for his work on the growth of complex coordination compounds especially in the field of phosphates, silicates, germinates and vanadates. He has carried out extensive pioneering work in the scientific application of physical chemistry and thermodynamics to the role of solution media, and the elucidation of the mechanisms of crystal growth in this difficult field. Such work has been at the forefront of knowledge, which has transformed the growth of many very difficult crystals from an empirical art to a controlled engineering science.

Professor Ohachi has extensive experience in the study of crystal growth mechanisms especially in the field of semiconductors and has been a leading fig-

ure in unraveling the mechanisms involved in the growth of GaAs by MBE. He is an expert in the field of ionic conduction in solids and has pioneered many fundamental studies in this more exotic field of crystal growth including the crystal growth of silver from silver chalcogenides using solid-state ionics. His work for the crystal growth community is also extensive. He has just been appointed President of the Japanese Association of Crystal Growth and held a pivotal position as Secretary of the recent combined International Conferences on Crystal Growth and Vapor Growth and Epitaxy (ICCG-13/ICVGE-11) held at Doshisha University, his Alma Mater. In this connection one must mention the role of Professor Nishinaga, one of the authors, who was Co-Chair of the ICCG-13/ICVGE-11 Conference. He was President of the International Organization of Crystal growth for the last six years and has just been appointed President of Toyohashi University of Technology.

Crystal growth now embraces an immense field of materials and technologies, which could not be covered in-depth by any one book. Nevertheless the present selection of chapters does provide a comprehensive coverage, which has succeeded in advancing our knowledge of the latest developments in crystal growth. For this purpose the editors have commissioned a fine selection of authors who are leading authorities in their respective fields of crystal growth. In broad terms the coverage deals with electronic materials and optical materials.

The basic science involved in vapor and solution growth provides an excellent initial introduction for advancing the role of fundamental science in our understanding of crystal growth. Also fundamental to our scientific understanding of hydrothermal growth is the need for detailed modeling with intelligent engineering. This is now possible thanks to advances in our knowledge of solution chemistry, phase equilibria and applied thermodynamics.

One must not miss the significance of the morphology of crystals, which is well reviewed in connection with mineral crystals. The observation of growth spirals on the surface of crystals was important evidence used by the late Professor Sir Charles Frank in his discovery the role dislocations can play in crystal growth.

The electronic materials discussed involve the III-Vs, the Zn chalcogenides, diamond and SiC as well as essential thermal modeling that is needed for achieving the effective growth of this difficult material. The oxides include families of materials related to lead zirconate titanate (PZT), the perovskites, the vanadates, bismuth germanate, and lithium niobate. Also, quartz and a range of high temperature non-linear optical materials including the borates as well as BiSrCaCu and related superconducting compounds are discussed in depth. A very welcome addition is that of the hydroxyapatite materials involved in biocrystallisation, which are important in bone development. Also, recent ideas on the growth of nano crystals are highlighted. A chapter on gemstones enhances the variety of materials and their compelling interest.

In order to achieve the successful crystal growth of these materials a whole range of different technologies are needed, they include vertical crystal pulling, CVD, sublimation and epitaxial growth for MOCVD and MBE. The oxides illustrate the full extent of the difficulties that can be encountered in crystal growth and the wide range of technologies needed to overcome them. In addition to the

growth technologies mentioned above laser assisted vapor deposition, hydrothermal growth solution, as well as flux and Verneuil growth are discussed.

The value of this interesting book lies not just in the increased scientific understanding of crystal growth, which one gains but in the extensive knowledge which is presented on the wide variety of technologies required to achieve application-quality crystal properties of an ever increasing range of crystals for modern technology. The reader is cordially invited to explore and assess the crucial role and significance of crystal growth in the various technologies for him or herself.

J.B. Mullin
U.K.

PREFACE

Crystals are the unacknowledged pillars of modern technology. Crystal growth can be regarded as an ancient subject, owing to the fact that the crystallization of salt and sugar was known to the ancient Indian and Chinese civilizations. The subject of crystal growth was treated as part of crystallography and never had an independent identity until the last century. The fundamentals of crystal growth were entirely bestowed upon the morphological studies of the naturally occurring crystals. Thus began the scientific approach for this subject during the 17th century by Kepler, followed by quite a few others like Nicolous Steno, Descartes, Bartholinus, etc. This type of morphological study slowly led to the understanding of the atomistic process of crystal growth. Recent bursting research on nanostructured materials depends on the crystal growth theory and technology.

In the early 20th century, crystal growth evolved as a separate branch of science and several theories from Kossel, Donnay-Harker, Volmer and Burton, Cabrera and Frank (BCF), etc., were proposed. Although the science of crystal growth originated through the explanations of Nicolous Steno in 1669, the actual impetus to this field began after the BCF theory was formulated and also when there was a great demand for crystals during World War II. Professor H. Scheel has dealt with the subject of historical development of crystal growth remarkably in the first volume of *Hydrothermal Crystal Growth*, edited by D.T.J. Hurlle. Since there are other books dealing with similar topics, the present book omits the historical aspects and basic techniques of crystal growth and focuses extensively on the techniques of current importance.

The editors conceived the idea of publishing a volume that covers both theory and practice together, containing all the latest developments in the area of crystal growth. The book deals mainly with the crystals of commercial value with an emphasis on the science of their growth.

There are 17 chapters in this book, beginning with a chapter by Professor Ichiro Sunagawa dealing with the growth history of mineral crystals as seen from their morphological features as a key to the understanding of essential points of fundamental growth. The editors are lucky to have contributions from the most eminent crystal growers like Professors T. Nishinaga, S. Naritsuka, T. Inoue, H. Komatsu, I. Sunagawa, M. Hosaka, V. Lantto, and a host of others in spite of their busy schedules. The topics have been selected based on their current significance in this frontier area of technology and thus there is a wide range of topics including modeling of crystal growth and thermochemical calculations which in turn lead to the intelligent engineering of the crystal growth processes. We have a perfect blend of

senior crystal growers with the upcoming talents of the recent generation. The range of crystals included in this book varies from electronic, electro-optic, piezoelectric, ferroelectric, jewelry, to bioelectric fields. Furthermore, techniques like MOCVD, hydrothermal, laser assisted, CVD, flux, melt, etc., dealing with the actual process of crystal growth are discussed.

We hope that this book will be highly valuable to the entire crystal growth community and remain as an important source for crystal growers, beginners and specialists alike. The editors greatly acknowledge the help and cooperation extended by each and every author in this book. Our special thanks go to Professor Brian Mullin for penning the foreword for this book. Also, thanks to our esteemed friends like Prof. Masahiro Yoshimura of Tokyo Institute of Technology, Japan; Prof. Richard E. Riman of Rutgers University, NJ, USA; Prof. Jan Bart of DSM, The Netherlands; Prof. H. Klapper, Germany; Prof. J.N. Sherwood, UK; Prof. D.T.J. Hurle, UK; Prof. H. Scheel, Switzerland; Prof. T. Nishinaga, Japan; Prof. H. Komatsu, Japan; Dr. R. Fornari, Italy; Prof. M. Dudley, USA; Dr. David Bliss, USA; Prof. K. Sato, Japan; Prof. T. Duffar, France; Prof. Derek Palmer, UK; Prof. Keshra Sangwal, Poland; Prof. Rafael Rodriguez Clemente, Spain; Prof. Salvador Gali, Spain, and many others who have helped us directly or indirectly for the successful completion of this useful volume. Also, our indebted thanks to our family members Dr. K.T. Sunitha Byrappa, Mr. Shayan M. Byrappa, Mr. Nayan M. Byrappa, Mrs. Michiko Ohachi, Mr. Shinobu Ohachi, and daughters Kyoko and Keiko for their patience and cooperation.

Lastly, our thanks to all those from William Andrew and Springer publications associated with the production of this book, especially to Kathy Breed, Keith Stein, Brent Beckley, Jim Willis, and Nanette Anderson.

June 2002
Editors
K. Byrappa
T. Ohachi

Contents

1 Growth Histories of Mineral Crystals as Seen from Their Morphological Features

Ichiro Sunagawa	1
1.1 Introduction	1
1.2 Morphology of Crystals	3
1.3 Diamond	7
1.4 Beryl	13
1.5 Trapiche Ruby	18
1.6 Summary	22
References	22

2 Theory of Crystal Growth from Vapor and Solution

Toshiharu Irisawa	25
2.1 Various Crystal Growth Processes	25
2.1.1 Driving force	25
2.1.2 Rate-determining process	27
2.2 Vapor Growth	28
2.2.1 Step velocity	31
2.2.2 Mechanism of two-dimensional nucleation growth	35
2.2.3 Mechanism of spiral growth	39
2.3 Growth of a Crystal in a Solution	42
2.3.1 Solvation effects and growth rates	42
2.3.2 Handling of polyhedral finite crystals	49
References	54

3 Epitaxial Growth of III-V Compounds

T. Nishinaga and S. Naritsuka	55
3.1 Introduction	55
3.2 MBE of III-V Compounds	56
3.2.1 MBE system	56
3.2.2 RHEED intensity oscillation	57
3.2.3 Surface diffusion and stepped surface	59
3.2.4 2D-nucleation and step flow modes	61

3.2.5 Critical temperature and growth conditions.....	64
3.2.6 Incorporation diffusion length.....	66
3.2.7 Intersurface diffusion.....	68
3.2.8 Elementary growth processes.....	70
3.3 MOCVD of III-V Compounds	71
3.3.1 Growth of high-purity materials by MOCVD	71
3.3.2 <i>In situ</i> monitoring and study of growth kinetics in MOCVD	75
3.3.3 Nanostructure fabrication by MOCVD.....	80
3.3.4 Highly-mismatched heteroepitaxy and microchannel epitaxy with MOCVD.....	84
3.4 Summary	89
References	90

4 CVD Diamond Growth

C. Chang, Y. Liao, G.Z. Wang, Y.R. Ma, and R.C. Fang	93
4.1 Introduction.....	93
4.2 Preparation and Application of CVD Diamond Film.....	94
4.2.1 Preparation methods	94
4.2.2 Applications of diamond film.....	98
4.3 Nucleation and Growth of Diamond Films	102
4.3.1 Homoepitaxy of diamond film	102
4.3.2 Heteroepitaxy of diamond film	103
4.4 Phase Diagram and Gas-Phase Species in CVD Diamond Growth Processes.....	111
4.4.1 Phase diagram	112
4.4.2 Gas phase species.....	113
4.5 <i>In Situ</i> Diagnostic Techniques for Diamond Growth.....	116
4.5.1 Molecular beam mass spectroscopy.....	117
4.5.2 Laser-induced fluorescence.....	120
4.5.3 Optical emission spectroscopy	123
4.6 Summary	131
References	132

5 Laser-Assisted Growth and Characterization of Multicomponent Lead-Zirconate-Titanate Films

Jyrki Lappalainen, Johannes Frantti, and Vilho Lantto	143
5.1 Introduction.....	143
5.1.1 Laser-assisted growth of thin films.....	143
5.1.2 Ferroelectric PZT thin films	144
5.2 Film Deposition Process.....	145
5.2.1 Principles of pulsed-laser-deposition technique	145
5.2.2 Growth and structure of thin films	147
5.3 Case Study: Nd-Modified PZT Films.....	149
5.4 Results from XRD and EDS Measurements.....	151
5.5 Compositional and Structural Changes in the Target.....	154

5.6 Raman Spectroscopy Studies of PZT Films	158
5.6.1 Basic concepts of the Raman effect	158
5.6.2 Raman active modes	160
5.6.3 Raman spectra of ceramics	160
5.6.4 Raman active phonons of PZT ceramics.....	161
5.6.5 Characteristic features of the Raman scattering from the structural point of view	162
5.6.6 Raman spectra of PZT thin films.....	163
5.7 Electrical Properties of PNZT Films.....	166
5.7.1 Permittivity and spontaneous polarization.....	166
5.7.2 Electronic conduction	168
5.7.3 Role of macroscopic residual stresses.....	171
5.8 Summary	174
References	176

6 Silicon Carbide Crystals — Part I: Growth and Characterization

G. Dhanaraj, X.R. Huang, M. Dudley, V. Prasad, and R.-H. Ma.....	181
6.1 Introduction	181
6.1.1 Applications of SiC.....	183
6.1.2 Historical development of SiC crystal growth.....	185
6.2 Vapor Growth	186
6.2.1 Acheson method.....	186
6.2.2 Lely method.....	187
6.2.3 Modified Lely method	189
6.2.4 Sublimation sandwich method.....	190
6.2.5 Chemical vapor deposition	191
6.3 High Temperature Solution Growth.....	193
6.3.1 Bulk growth.....	193
6.3.2 Liquid phase epitaxy	193
6.4 Bulk Growth by Seeded Sublimation: The Industrial Process.....	194
6.4.1 Growth system	195
6.4.2 Seeding and growth process	197
6.5 Doping in Bulk and Epitaxial Growth	200
6.5.1 Doping in modified Lely method	200
6.5.2 Doping in epitaxial films	200
6.6 Growth Defects	201
6.6.1 Growth spirals and micropipes	201
6.6.2 Polytypism.....	202
6.6.3 Graphitization.....	203
6.7 Defect Analysis.....	204
6.7.1 Micropipes and closed core screw dislocations	204
6.7.2 Basal plane dislocations.....	221
6.7.3 Small angle boundaries	221
6.7.4 Hexagonal voids.....	222
6.8 Summary	223

References	225
7 Silicon Carbide Crystals — Part II: Process Physics and Modeling	
Q.-S. Chen, V. Prasad, H. Zhang, and M. Dudley	233
7.1 Introduction.....	235
7.2 Modeling of Heat and Mass Transfer and Growth Rate	236
7.2.1 Growth process	236
7.2.2 Flow and heat transfer parameters	237
7.2.3 One-dimensional network model.....	240
7.2.4 Thermal transport model	241
7.2.5 Mass transport model.....	244
7.2.6 Numerical method.....	249
7.3 Growth Simulation.....	251
7.3.1 Electromagnetic field and heat generation.....	251
7.3.2 Temperature field.....	253
7.3.3 Growth rate calculations.....	257
7.3.4 Thermally induced stress.....	263
7.4 Summary	265
References	266
8 Thermodynamics of Multicomponent Perovskite Synthesis in Hydrothermal Solution	
Malgorzata M. Lencka and Richard E. Riman	271
8.1 Introduction.....	271
8.2 Thermodynamic Model	272
8.2.1 Computational method	274
8.2.2 Standard-state properties	276
8.2.3 Stability and yield diagrams	277
8.2.4 Stability and yield diagrams for the stoichiometric ratio of precursors ($A/B = 1$).....	279
8.2.5 Stability and yield diagrams for the nonstoichiometric ratio of precursors ($A/B > 1$)	286
8.2.6 Carbon dioxide contamination	289
8.3 Validation and Applications of Thermodynamic Modeling	292
8.4 Summary	294
References	294
9 Growth of Multicomponent Perovskite Oxide Crystals: Synthesis Conditions for the Hydrothermal Growth of Ferroelectric Powders	
Bonnie L. Gersten.....	299
9.1 Introduction.....	299
9.2 General Overview	299
9.2.1 Description	299
9.2.2 Perovskite ferroelectrics	300

9.2.3 History	301
9.3 Synthesis Conditions for Controlled Chemical and Phase Purity	305
9.3.1 Thermodynamic conditions	305
9.3.2 Mineralizers and additives	309
9.3.3 Homogeneity	310
9.3.4 Reaction time and temperature	311
9.3.5 Hydroxyl groups	311
9.3.6 Summary	312
9.4 Kinetics and Rate Controlling Mechanisms	312
9.4.1 Rate determining step in the mechanisms	312
9.4.2 Precipitation	314
9.4.3 Reaction rate.....	314
9.4.4 Variables affecting the reaction rate.....	318
9.5 Synthesis Conditions for Controlled Morphology.....	319
9.5.1 Precursor.....	319
9.5.2 Temperature	321
9.5.3 Reagent concentration.....	322
9.5.4 Additives	322
9.5.5 Mineralizer type and concentration.....	322
9.5.6 Summary	324
9.6 Synthesis Conditions for Controlled Particle Size.....	324
9.6.1 Precursor.....	324
9.6.2 Concentration and molar ratio.....	325
9.6.3 Mineralizer type and concentration.....	325
9.6.4 Reaction time	326
9.6.5 Temperature	326
9.6.6 Summary	326
9.7 Summary	327
References	327

10 Crystal Growth, Size, and Morphology Control of Nd:RVO₄ Under Hydrothermal Conditions

K. Byrappa, B. Nirmala, K.M. Lokanatha Rai, and M. Yoshimura	335
10.1 Introduction.....	335
10.2 Technologically Important Vanadates	336
10.3 Phase Equilibria	336
10.4 Structure of Nd:RVO ₄	338
10.5 Synthesis and Growth of Rare Earth Vanadates.....	339
10.5.1 Zone melting	339
10.5.2 Czochralski technique.....	340
10.5.3 Flux growth	341
10.5.4 Top seeded solution growth (TSSG).....	342
10.6 Solubility Study	343
10.7 Crystal Growth.....	347
10.8 Morphology.....	351

10.8.1 Surface morphology.....	355
10.9 Characterization.....	358
10.9.1 XRD and IR studies.....	358
10.9.2 Laser spectroscopy.....	358
10.9.3 Absorption measurements.....	361
10.10 Summary.....	362
References.....	363

11 Hydrothermal Growth of Quartz Under Specific Conditions and the Raman Spectra of Ion Species in a Hydrothermal Growth Solution

M. Hosaka.....	365
11.1 Introduction.....	365
11.1.1 Growth of quartz with small content of Al^{3+}	367
11.1.2 Synthesis of micro α -quartz crystals by hydrothermal hot-pressing method.....	368
11.1.3 Growth of quartz crystals above transition temperature and morphology of synthetic crystals.....	368
11.1.4 Raman spectral studies of SiO_2 - $NaOH$ - H_2O and SiO_2 - Na_2CO_3 - H_2O system solutions under hydrothermal conditions.....	369
11.2 Growth of Quartz with Poor Al^{3+} Content.....	370
11.2.1 Experimental method.....	370
11.2.2 Experimental results.....	371
11.3 Synthesis of Micro α -Quartz Crystals by Hydrothermal Hot-Press Method.....	372
11.3.1 Experimental method.....	372
11.3.2 Experimental results.....	373
11.4 Growth and Morphology of Quartz Crystals Synthesized Above Transition Temperature.....	374
11.4.1 Experimental method.....	374
11.4.2 Experimental results.....	376
11.5 Raman Spectral Studies of the Solution Chemistry of SiO_2 - $NaOH$ - H_2O and SiO_2 - Na_2CO_3 - H_2O Systems Under Hydrothermal Conditions.....	379
11.5.1 Experimental method.....	379
11.5.2 Experimental results.....	381
11.5.3 Discussion.....	383
11.5.4 Summary.....	384
References.....	384

12 Growth and Characterization of Technologically Important Oxide Single Crystals

Krishan Lal, R.V. Anantha Murthy, Ashutosh Choubey, and Niranjana Goswami.....	387
12.1 Introduction.....	387

12.2 Crystallographic Structure.....	388
12.3 Growth of Lithium Niobate Crystals: Earlier Work.....	389
12.4 Growth of Bismuth Germanate Crystals: Earlier Work	390
12.5 A Crystal Growth System for Cz Growth of Nearly Perfect Crystals	392
12.5.1 A crystal growth system for low thermal gradient Czochralski (LTG Cz) technique.....	393
12.6 High Resolution X-ray Diffractometers.....	395
12.6.1 Double crystal X-ray diffractometer	395
12.6.2 Five crystal X-ray diffractometer	397
12.7 Synthesis of Lithium Niobate and Bismuth Germanate Powders.....	398
12.8 Growth of Nearly perfect Crystals of LiNbO ₃ and BGO	400
12.8.1 LiNbO ₃ single crystals	400
12.8.2 Bismuth germanate single crystals	402
12.9 Evaluation of Perfection of Lithium Niobate and Bismuth Germanate Single Crystals by High Resolution X-ray Diffractometry and Topography.....	404
12.9.1 Characterization of lithium niobate crystals	405
12.9.2 Characterization of bismuth germanate single crystals	407
12.10 Summary	412
References	413

13 Growth and Development of Nonlinear Optical Borate Crystals for Generation of Visible and UV Light

Takatomo Sasaki, Yusuke Mori, Masahi Yoshimura, and Yoke Khin Yap	419
13.1 Introduction.....	419
13.1.1 Coherent solid-state light source in the visible and UV regions by nonlinear optical crystals	419
13.1.2 NLO borate crystals	420
13.2 CLBO Crystals for High-Power Generation of Deep-UV Light	422
13.2.1 The search for CsLiB ₆ O ₁₀ (CLBO)	422
13.2.2 Growth of CLBO	425
13.2.3 Structural and optical properties of CLBO	426
13.2.4 Degradation of CLBO crystallinity and solution.....	427
13.2.5 Performance of CLBO for generation of deep-UV light.....	432
13.2.6 Relation between crystal quality and resistance to bulk laser-induced damage	433
13.3 GdYCOB Crystal for Noncritical Phase-Matching (NCPM) of Visible and UV Light	434
13.3.1 The search for Gd _x Y _{1-x} Ca ₄ O(BO ₃) ₃ (GdYCBO).....	434
13.3.2 Noncritically phase-matched THG for Nd:YAG lasers by GdYCOB	436
13.3.3 Noncritically phase-matched SHG for Nd:YAG lasers by GdYCOB	438

13.3.4 Noncritically phase-matched SHG for Ti:sapphire lasers by GdYCOB	439
13.3.5 Optical damage of GdYCOB and its solution	440
13.4 KAB Crystal: Difficulty of Growing Borate Crystal with Layered Structure.....	443
13.4.1 The search for $K_2Al_2B_2O_7$ (KAB)	443
13.4.2 Growth of KAB.....	445
13.4.3 Optical properties of KAB.....	447
13.5 Summary and Perspective	447
References	448
14 Growth of High T_C Crystals	
T. Inoue, S. Miyashita, Y. Nishimura, J. Takemoto, Y. Suzuki, S. Hayashi, and H. Komatsu	453
14.1 Introduction.....	453
14.2 Growth of the High T_C Phase of BSCCO	453
14.2.1 Synthesis of the high T_C phase by sintering the powder of Bi-Sr-Ca-Cu	454
14.2.2 Preparation of single crystals containing the high T_C phase of a Bi-Sr-Ca-Cu-O superconductor.....	458
14.2.3 Conversion of superconducting Bi-system single crystals from 2212 to 2223 by the annealing method	462
14.3 Liquid Phase Epitaxial Growth of Low T_C Phase of BSCCO.....	467
14.3.1 $SrTiO_3$ (100) substrate	469
14.3.2 $LaAlO_3$ (100) substrate.....	471
14.3.3 $NdGaO_3$ (001) substrate.....	472
14.4 Construction of Phase Diagrams by <i>In Situ</i> Observation and Their Application to Crystal Growth of Oxide Superconductors	474
14.4.1 Apparatus	475
14.4.2 Phase diagram of $SmBa_2Cu_3O_{7-\delta}$ and its application.....	478
14.4.3 Phase diagram of Bi-based oxide superconductors	483
14.4.4 Primary crystallization field of Bi-based oxide superconductors and its application	491
References	493
15 Growth of Zinc Chalcogenides	
Robert Triboulet	497
15.1 Introduction.....	497
15.2 Zn Chalcogenide Growth	498
15.2.1 ZnTe	498
15.2.2 ZnSe	502
15.2.3 ZnS	509
15.2.4 ZnO.....	510
15.3 Properties and Defects of the Crystals.....	512

15.4 Purity, Contamination and Doping..... 513
 15.5 Applications and Perspectives..... 513
 References 514

16 Growth of Hydroxyapatite Crystals

Atsuo Ito and Kazuo Onuma..... 525

16.1 Introduction..... 525
 16.2 Calcium Orthophosphates..... 526
 16.3 *In Vivo* Calcification of Biomaterials..... 528
 16.3.1 Calcification of biomaterials used in contact with bone..... 528
 16.3.2 Calcification of biomaterials used in contact with blood 529
 16.4 Apatite Deposition on Biomaterials as Surface Modification..... 532
 16.5 Calcium Phosphate Cements 536
 16.6 Hydroxyapatite Ceramics 537
 16.7 Hydrothermal Growth of Hydroxyapatite..... 538
 16.8 Factors Influencing Apatite Formation in Hard Tissues 540
 16.9 Ectopic Calcifications..... 542
 16.10 Kinetics of Hydroxyapatite Crystal Growth in Solution 544
 References 548

17 Crystal Growth of Gemstones

Shuji Oishi..... 561

17.1 Introduction..... 561
 17.2 Growth Methods of Gemstones..... 563
 17.2.1 Verneuil method..... 564
 17.2.2 Czochralski method 566
 17.2.3 Hydrothermal method 567
 17.2.4 Flux method..... 567
 17.3 Emerald 569
 17.3.1 Growth of emerald crystals..... 569
 17.3.2 A simple method of growing emerald crystals 570
 17.4 Summary 578
 References 579

Index..... 581

1 Growth Histories of Mineral Crystals as Seen from Their Morphological Features

Ichiro Sunagawa

Yamanashi Institute of Gemology and Jewelry Arts, Toukoji-machi 1955-1, Kofu, 400-0808, Japan

1.1 Introduction

The late Sir Charles Frank once said, “If one could understand enough about the morphology of crystals, he understood essential points of the fundamentals of crystal growth.” This sentence captures the importance of morphology of crystals in understanding how crystals nucleate and grow. He also answered in the following haiku to a haiku by Ukichiro Nakaya “A snow flake is a letter to us from the sky.”

“Diamonds are letters
Still better worth the reading;
We can reach the sky.”

Interest in the morphology of crystals started in the 17th century when Kepler observed elaborately varied dendritic snow crystals in 1611, and Steno was fascinated by the variety of polyhedral forms that rock crystals from Alpine mineral fissures exhibited. Kepler considered that the building unit of snow crystals, in spite of their varied forms, was spheres of equal size. Steno gave an explanation in terms of growth rate anisotropy for his observations that the same mineral, rock crystal, could take a variety of polyhedral forms in his treatise published in 1669. Kepler’s idea was the origin of structural crystallography, and Steno’s explanation was the starting point of the science of crystal growth.

Interest and understanding of the morphology of crystals which started in the 17th century, independently one of dendritic forms and the other of polyhedral forms bounded by flat faces, have now advanced to a state to be understood from a unique viewpoint, the atomistic process of crystal growth. This is due to the development of the science of crystal growth in the 20th century, particularly after the 1950s. For simple and pure model systems, it is now possible to explain at the atomistic level why and how the same crystal can take a variety of forms, from dendritic, hopper, to polyhedral forms, and why different crystal species exhibit different characteristic forms or Habitus. How our understanding of morphology

and growth mechanism of crystals has developed since the time of Kepler and Steno has recently been summarized by Sunagawa [1].

Both snow crystals and rock crystals are naturally formed crystals under uncontrolled, fluctuating, and often sharply changing growth conditions. Any mineral crystals constituting the solid earth and planetary bodies were formed under such conditions and in impure, complicated, and complex systems. Also inorganic and organic crystals are formed in various organs and cells of animate bodies, through biological processes necessary to sustain life or to eliminate unnecessary waste compounds. How crystals nucleate and grow, and how their forms are controlled in such complicated and complex systems are problems still waiting for proper answers at the atomistic level.

The temperature and pressure conditions of mineral formation have been estimated based on equilibrium thermodynamics and phase relations. Information about conditions of mineral formation may be obtainable assuming that any geological systems have already reached the equilibrium state. However, crystals can neither nucleate nor grow under equilibrium condition. Driving forces, namely conditions deviating from the equilibrium state, are necessary to realize nucleation and growth of crystals. In natural crystallization, growth rates may fluctuate or abruptly change during their growth processes, and morphology and element partitioning are influenced accordingly. Crystals may be partially dissolved during the process of formation, or experience transformation in their post growth histories.

We are unable to observe *in situ* the growth or post growth process of mineral formation, but we can investigate samples that experienced these processes, provided that these processes are recorded in the samples in some form and can be visualized by appropriate methods. In nearly perfect single crystals, these are recorded in the form of various physical imperfections and chemical heterogeneities, preserving the records of morphological evolution during the growth or post growth processes. Information obtainable from such samples is equally important and informative in understanding the formation of solid earth and planetary materials, provided that such information can be evaluated properly.

Since the morphology of a crystal appears through growth or dissolution processes, and is controlled by both internal (structural) and external (growth or dissolution parameters) factors, morphological features of crystals are the most useful information in deciding the growth or post growth history that a crystal experienced, since both growth and dissolution uniquely take place on the solid-liquid interface, that is, crystal surfaces and surface microtopographs of crystal faces offer useful information on how the crystal grew or partially dissolved at an atomistic level. Various optical microscopy and interferometry techniques, such as phase contrast microscopy (PCM), differential interference contrast microscopy (DISM) and interferometries, atomic force microscopy (AFM), and scanning tunneling microscopy (STM) can visualize and measure growth steps of nanometer height. External morphology (crystal habit or *Habitus* and *Tracht*) is a result and reflection of crystal growth. Depending on growth conditions, the same crystal species may show different external forms. Morphological changes and accompanied variation in element partitioning are recorded in single crystals in the form of

growth banding, growth sectors, and sector boundaries. Generation and spatial distribution of dislocations and other lattice defects in single crystals are also records of what happened during the growth process. Inclusions serve as informative indicators of growth and environmental conditions. At present we have various sophisticated methods to visualize and analyze these physical imperfections and chemical inhomogeneities, such as X-ray topography, laser-beam tomography, cathodoluminescence tomography, electron-probe microanalyzer, micro-focused X-ray fluorescence, and so forth.

It is the purpose of this chapter to demonstrate how one can decode letters sent from the deep interior of the earth, based on the analyses of morphological features recorded in mineral crystals. For this purpose, the author has selected diamond crystals as a representative example of crystal growth taking place in deep-seated magma and in the subduction zone, beryl crystals occurring in pegmatites which represent crystallization in super-critical liquid phase at the latest stage of magmatic solidification, and trapiche ruby formed by contact metasomatism due to intrusion of a granitic magma into carbonate rocks. The author has deliberately selected gem minerals in this chapter, since they occur as nearly perfect single crystals, and information obtained on such crystals serves as very useful diagnostic features in distinguishing natural from synthetic gemstones.

Following this introduction, the present understanding of morphological aspects of crystals will be briefly summarized in Section 1.2. Then discussions on diamond, beryl, and trapiche ruby will be presented in their respective sections. In this chapter, descriptions and discussions on mineral crystals formed by regional metamorphism and sedimentogenesis are excluded, since these were treated in [2,3].

1.2 Morphology of Crystals

Growth and dissolution of crystals uniquely take place on the surfaces of a crystal, that is on the solid-liquid (ambient phase) interface. Depending on the structure of an interface (rough or smooth), the growth mechanism, and thus the relations between the driving force and growth rate are different. The growth mechanisms can be classified into three types depending on interface roughness: adhesive type for rough interface, two-dimensional nucleation growth, and spiral growth for smooth interface. The interface roughness (smooth or how rough) is different depending on crystallographic directions, which are related to the crystal structure. The interface structure transforms from smooth to rough with increasing growth temperature (thermodynamic roughening transition) and driving force (kinetic roughening transition). Under the conditions where a smooth interface is assumed, growth proceeds tangentially parallel to the interface, and the crystal will take a polyhedral or hopper (skeletal) morphology bounded by crystallographic flat faces. Under conditions where a rough interface is assumed, the crystal is bounded by rounded noncrystallographic interfaces. If morphological instability occurs on such a rough interface, the crystal takes dendritic form. By further increasing the

driving force, spherulitic and fractal patterns will appear through aggregation of polycrystals. Summarizing these, the relations among polyhedral, hopper, dendritic, spherulitic, and fractal morphologies may be represented as schematically shown in Fig. 1.1, which represents only one section of events. Positions of * and ** indicate where growth mechanism and morphology changes are different depending on crystallographic directions, ambient phases, solute-solvent interaction energies, and other factors. The analysis and discussion of these problems are given in [1–4].

In mineral formation, crystals nucleate and grow in impure, complicated, and complex systems, and the growth conditions are not controlled, but variable. There may be abrupt changes or gentle fluctuations in growth parameters during the growth or post growth process. External forms, perfections, and element partitioning change accordingly, and the changes are recorded in various forms of physical imperfection and chemical inhomogeneity in single crystals.

When a crystal grows in a closed system, the driving force diminishes monotonously as growth proceeds. As a result, starting from dendritic morphology appearing at the earlier stage and under higher driving force conditions, the morphology transforms to a polyhedral one. Within a polyhedral single crystal, record of dendritic growth may be discernible surrounded by straight growth banding (Fig. 1.2a), if a bisected sample is investigated by appropriate methods to reveal

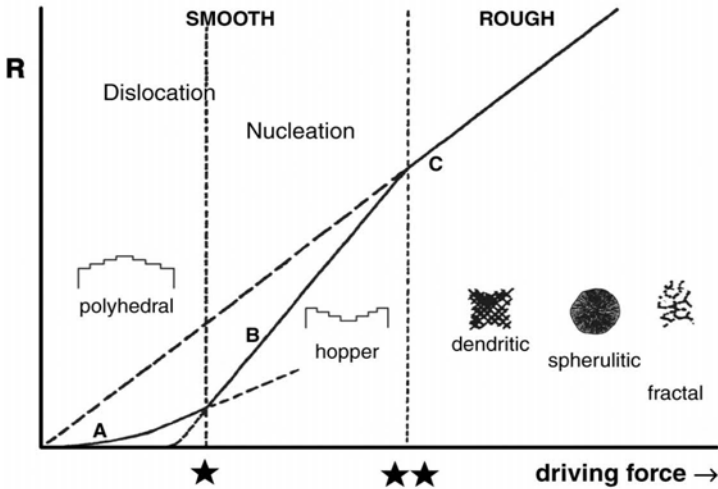


Fig. 1.1. Morphologies of single crystals (polyhedral, hopper, dendritic) and polycrystalline aggregates (spherulitic and fractal) in relation to growth rate R , driving force, interface roughness (smooth and rough) and growth mechanisms. Curve a represents the spiral growth, curve b the two-dimensional nucleation growth, and curve c adhesive-type growth mechanisms. The critical points * and ** are the points where the predominant growth mechanism changes [4]

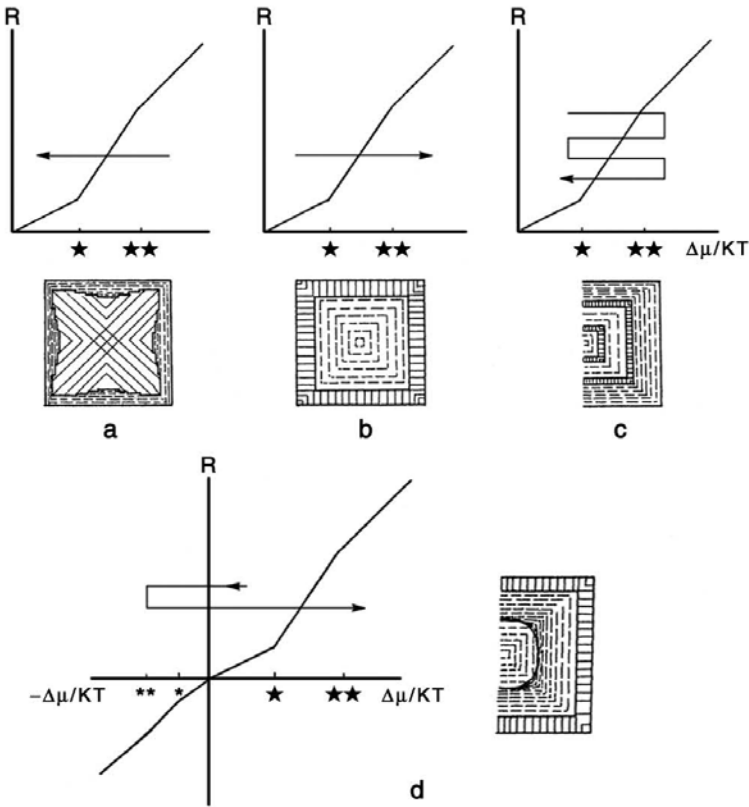


Fig. 1.2. Expected internal morphologies in single crystals due to the change of growth parameters during the formation of a single crystal. Arrows in respective R vs. $\Delta\mu/KT$ diagrams indicate the route of change of driving force conditions during the growth process. Broken lines represent growth banding formed by smooth interface growth, and solid lines dendritic or fibrous textures which appeared by rough interface growth [4]

faint heterogeneity and imperfection. If a magma containing polyhedral crystal is uplifted, the growth condition changes abruptly to another condition under which dendritic growth or partial dissolution will take place. Surrounding a clear single crystalline core, a mantle portion with fibrous texture will be formed (Fig. 1.2b), or a rounded discontinuous outline will be recorded in a single crystal (Fig. 1.2d). Various internal morphologies may be expected to be seen depending on the changes of parameters. Figure 1.2 schematically illustrates some of these internal morphologies.

Similarly, since interface roughness and growth kinetics are different in different crystallographic directions, growth sectors appear in a single crystal. Depending on relative growth rates in neighboring sectors, various forms of growth sector boundaries appear, some examples of which are schematically shown in Fig. 1.3.

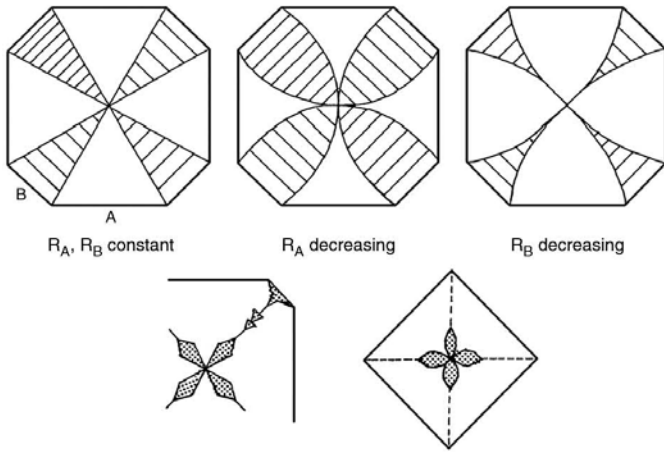


Fig. 1.3. Various growth sector boundaries: Upper three figures show expected growth sector boundaries in relation to relative growth rates R_A and R_B . Lower two figures show actually observed growth sector boundaries [4]

Growth rates within one growth sector, and also among crystallographically equivalent growth sectors are neither constant nor uniform, which results in the formation of growth banding. Since both thermodynamic and kinetic parameters contribute to growth banding, growth sectors which control element partitioning may be visualized by various techniques, including X-ray topography, cathodoluminescence tomography, element mapping techniques using EPMA, XFA, and other spectroscopies.

Polyhedral crystals appear principally by a spiral growth mechanism under conditions shown below * in Fig. 1.1. Spiral step patterns of molecular height are observable on as-grown low index crystal faces. The morphology of growth spirals varies depending on different crystallographic faces, and on growth parameters. They offer useful information to evaluate how and under what condition the crystal grew. Similarly, surface microtopographs of crystal faces, such as dissolution steps and etch figures, tell us information relating to the dissolution process.

In terms of morphological features of crystals, the following are included in this chapter, which demonstrate how growth, dissolution, or transformation of natural crystals proceeded:

1. External morphology (polyhedral, hopper, and dendritic forms of single crystals, or spherulitic and fractal forms of polycrystalline aggregates)
2. Morphology of polyhedral crystals (crystal habit, Habitus and Tracht [4])
3. Surface microtopography of crystal faces (spiral step patterns, dissolution steps, etch figures [4])
4. Growth sectors, sector boundaries
5. Growth banding
6. Element partitioning associated with the above

1.3 Diamond

The origin of natural diamonds has been an enduring subject of interest and controversy. Some believe that they were formed in magmas in the mantle, others argue mantle metasomatic origin. There are also some who argue that carbonados (polycrystalline aggregate of diamonds) were formed near the earth's surface by radiogenetic energy, and some even assume cosmic dust origin for carbonados. Some believe the mantle originated inorganic carbon as the carbon source for diamond formation, and others suggest organic carbon origin derived from subducted oceanic sediments.

Natural diamonds occur in a variety of forms, to which different variety names have been given. The names include, in addition to single crystalline diamond, ballas, coated stone, bort, shot bort, hailstone bort, framesite, stewartite, and carbonado. Only single crystalline stones and coated stones have been used for gem purpose, others have been used for industrial purposes. Orlov [5] classified natural diamonds into ten types on the morphological basis, whereas Sunagawa [6] classified them into three major types, based on the relation between morphology and driving force as shown in Fig. 1.1. According to Sunagawa's classification, diamonds of single crystalline type are formed under small driving force conditions, below ** in Fig. 1.1, polycrystalline type are formed under much higher driving force conditions, above **, and coated stone and cuboid are those that experienced two different driving force conditions. The three types are schematically illustrated in Fig. 1.4.

Extensive X-ray topographic and cathodoluminescence tomographic investigations have been made principally on gem quality single crystalline diamonds, and secondarily on cuboid and polycrystalline diamonds [7,8]. Commonly observed dislocation distributions in single crystalline diamonds are those originating from the center of a crystal, and radiating nearly perpendicular to $\{111\}$, with dislocation direction $\langle 110 \rangle$. Growth banding in such crystals is in most cases straight and parallel to $\{111\}$. These suggest that natural diamond crystals of single crystalline type grew freely in a fluid phase, that is in magma, by the spiral growth mechanism. In fact, the spiral growth was proved on an octahedral crystal from Siberia, by correlating the growth step pattern on as-grown $\{111\}$ faces and outcrops of dislocations which were identified as screw type [8].

In contrast to single crystalline type, most polycrystalline type diamonds except for carbonado show a spherulitic radiating texture consisting of fibrous thin diamond needles and other interstitial minerals. Such textural characteristics represent formation under high driving force conditions. The mantle portion of coated stones and cuboids show basically the same texture as those of polycrystalline aggregate, surrounding a clear central single crystalline core. Thus, it is considered that the central clear single crystalline core portion and fibrous mantle portion were formed under different driving force conditions. Namely, the core portion grew in magma under small driving force conditions, then the magma containing the diamond crystals was uplifted, and on the core fibrous growth of diamond took

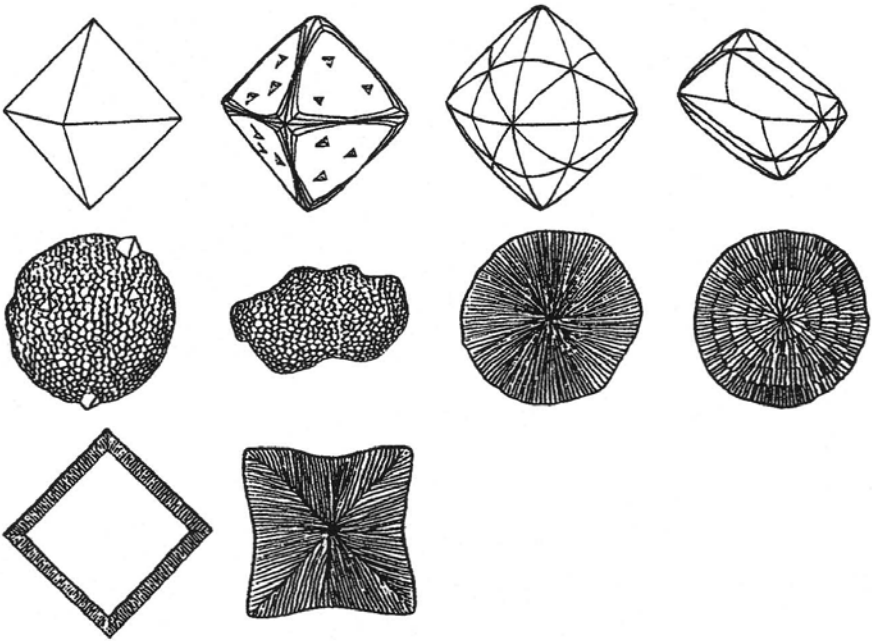


Fig. 1.4. Three types of morphologies encountered among natural diamonds. Top four figures show morphologies of single crystalline type, middle four those of polycrystalline type, and the bottom two those of diamond crystals which experienced two different growth parameters

place under higher driving force conditions. Similar textures are commonly observed on phenocrysts of various rock-forming minerals in volcanic rocks, which experienced similar magmatic solidification history, and diamond of this type is no exception. For the origin of carbonado, a randomly oriented polycrystalline type, arguments are still not settled.

Tiny diamond crystals, less than a few tens of microns across, were reported to occur in crystals of garnet and zircon in ultra-high-pressure metamorphic rocks formed in a subduction zone [9]. Similar occurrences of micro-diamonds have been reported at many localities. Ultra-high-pressure metamorphic rocks are the third type of environment where diamonds were formed, in addition to the previously known two types, ultramafic suite (kimberlite and lamproite) and eclogitic suite.

These micro-diamonds occur sporadically in the grains of silicate minerals formed by metamorphism, and in very high content (much higher than in kimberlite or lamproite). Although simple octahedral crystals are found among these micro-diamonds, many of them take cuboid form or forms of polycrystalline aggregates. Their cuboid faces are rugged and not crystallographic $\{100\}$ faces, unlike $\{111\}$ faces, which are smooth. Thus a term 'cuboid' and not cubic is given here.

When diamond crystals grow in nature, only the $\{111\}$ faces behave as a smooth interface on which spiral growth can take place, and the $\{100\}$ faces behave as rough interfaces [6]. Namely, under the conditions of natural diamond formation, the position of $**$ in Fig. 1.1 for $\{100\}$ is much closer to the origin than for $\{111\}$. This implies that under high driving force conditions, rough cuboid faces appear first, followed by the appearance of smooth $\{111\}$ faces on which spiral growth takes place. It is reasonable to expect a higher proportion of cuboid or spherulites, and higher concentration of diamond in ultra-high-pressure metamorphic rocks due to subduction as judged from the following. The original source for ultra-high-pressure metamorphic rocks are subducted slabs, consisting of oceanic crust and sediments, which contain organic carbon. Since the melting temperature of silicate-carbon eutectic is lowered, liquid droplets are formed sporadically in solid silicate mineral grains. If diamond crystallization takes place within such liquid droplets, a higher content of source carbon and higher driving force conditions can be assumed for diamond formation than in a larger scale magma. It is natural to expect a higher content of diamond and higher proportion of cuboid or spherulitic forms than simple octahedral crystals in ultra-high-pressure metamorphic rocks than in ultramafic magmas.

When solvent components are different, the morphology of crystals can be different, since the difference in solute-solvent interaction energies modifies the morphology. In the case of synthetic diamond under high pressure and temperature conditions using metals or alloys as solvent, both $\{111\}$ and $\{100\}$ behave as smooth interfaces. Growth spirals have been observed on both faces. In the case of natural diamond, only the $\{111\}$ faces behave as smooth interfaces on which growth spirals are expected, whereas $\{100\}$ faces behave as rough interfaces. The difference in growth mechanism and morphological characteristics between natural and synthetic diamonds serve as diagnostic features, since their morphologies are recorded in the form of internal morphologies, which remain unchanged by later cutting and polishing processes and can be visualized by cathodoluminescence (CL) tomography [10].

Recently, evidence to prove the presence of seed crystal in gem quality single crystalline diamond has been reported [11]. The presence of seed crystal was proven on the basis of X-ray topographic and cathodoluminescence tomographic investigations of three brilliant cut stones. One round brilliant stone shows the ordinary spatial distribution of dislocations, which originate from a point center and radiate in bundles perpendicular to the $\{111\}$ surface. The dislocation directions are parallel to $\langle 110 \rangle$. A pair of round and pear-shaped brilliants, which proved to have been cut from the same rough, show entirely different dislocation distributions. The core portion with cuboid form is detected in the two brilliants as a square discontinuity line on X-ray topographs. Dislocations mostly generate from the boundary between the core and major portion, and radiate in bundles in $\langle 100 \rangle$ directions in the major portion of the brilliants. The concentration of CL emitting centers is high and uniformly surrounds the core-major portion boundary. Figure 1.5a,b show X-ray topographs and Fig. 1.5c shows a CL tomograph around the core portion. This type of dislocation generation and element partitioning is universally observed when a seed crystal is used in growing larger single crystals.

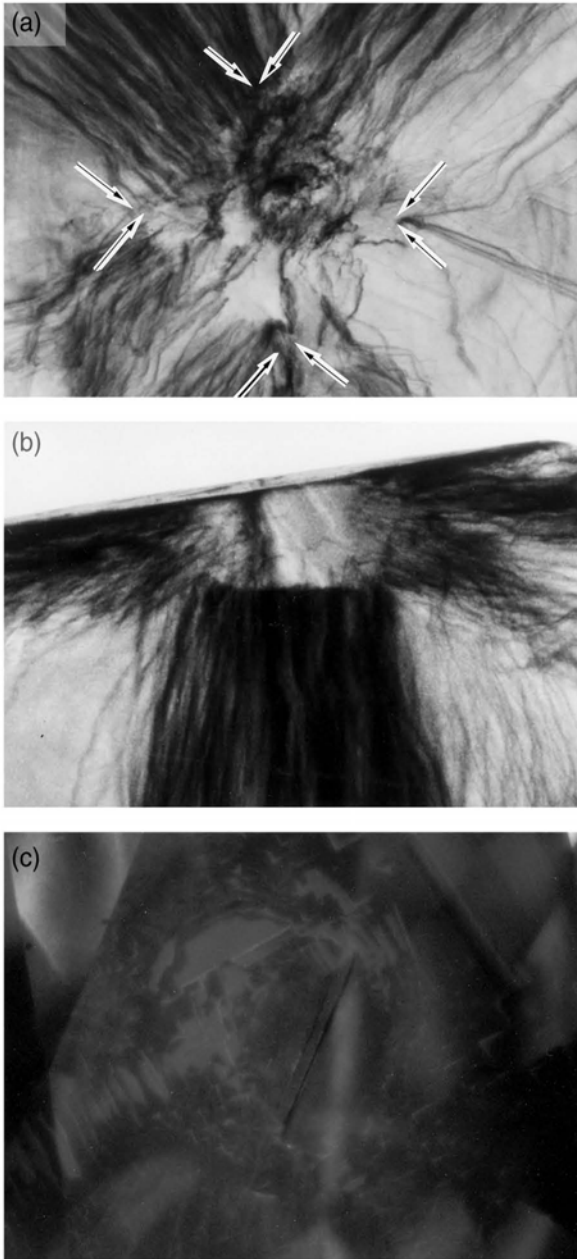


Fig. 1.5. X-ray topographs (a and b) and cathodoluminescence tomograph (c) of core portion of a round (a) and pear-shaped (b and c) brilliant cut diamonds. (a) and (b) are plan and profile views, respectively, (c) is a plan view. White arrows in (a) indicate the boundary of the core portion [10]

The observations described above indicate that the core portion was formed elsewhere and later transported into a new growth environment where the core acted as a seed for further growth under lower driving force conditions. This was the first evidence to verify the presence of seed crystal in the formation of natural diamond crystals.

The most likely place where the core portion was formed is in subducted ultra-high-pressure metamorphic rocks. Assuming that ultra-high-pressure metamorphic rock containing micro-diamond crystals of cuboid form was subducted further and eventually trapped into a magma, where further growth of diamond took place, the presence of a seed crystal in the natural diamond formation can be understood reasonably. It is impressive to see the whole circulation history taking place in plate, subduction, and mantle convection, within a small cut stone of diamond.

Natural diamond crystals were formed at a depth greater than 100–120 km, then rapidly uplifted to the Earth's surface by kimberlite or lamproite magma, and quenched metastably by adiabatic expansion due to volcanic eruption of the magma. During uplifting, they passed through the thermodynamic conditions unfavorable for diamond; also they received severe stress. All these processes are recorded in the form of surface microtopographs, external forms of crystals, dislocation nature, precipitation textures, and so forth. Most natural diamond crystals

Table 1.1. Morphological Features Observed on Natural Diamond Crystals Indicating Dissolution Process

(I) External Forms	(II) {111} Surfaces	(III) Dodecahedral Surfaces
Rounded corners and edges Curved surfaces Curved hexaoctahedral forms Curved dodecahedral forms	Trigons (mostly negatively oriented to the trainage of (111) face) are universally observed on {111} surface. Both point bottomed (P type) and flat bottomed (F type) are seen corresponding to etch pits at surface outcrops of dislocations and point defect, respectively. Deep and shallow trigons are present in both P and F types; respectively name PD, PS, FD and FS types. Depending on etching condition, trigons may show change their orientations and forms from truncated negative trigons, hexagons, truncated positive trigons to positive trigons.	Scaly surface Network ditches Superimposed ring or circular patterns

show morphological characteristics as summarized in Table 1.1, which are due to partial dissolution during the uplifting process. However, there are rare cases in which crystals received only a very little dissolution, preserving their as-grown surfaces. On such crystals, triangular growth hillocks can be observed, as the example shown in Fig. 1.6. The summits of these hillocks correspond to the outcrops of dislocations, where we see tiny trigons (triangular etch pits with opposite orientation to the triangle of the $\{111\}$ face). Dissolution proceeded very weakly, attacking only the outcrops of dislocations. In this particular case, dissolution features are observed together with growth features. But, on most natural diamond crystals, dissolution proceeded more severely, and as-grown surface microtopographs are entirely erased out. Figure 1.7 shows an example of such surface microtopographs.

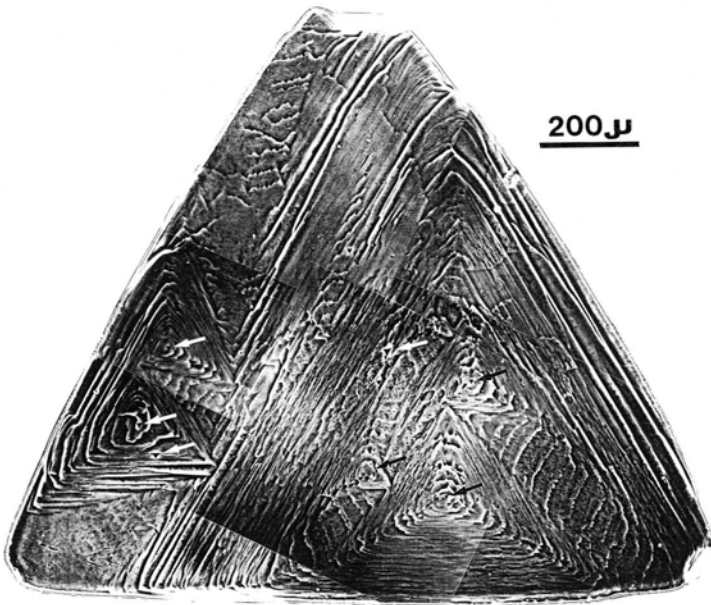


Fig. 1.6. Mosaic phase contrast photomicrograph of a (111) face of an octahedral diamond crystal from Siberia, which received only a slight dissolution. Note triangular growth hillocks with the same orientation as the triangle of the (111) face, and a tiny triangular pit (opposite orientation; trigon) at the respective summit of the former growth hillocks. The thinnest growth layers, which consist of growth hillocks, have a step height of less than 0.5 nm. Bar = 200 μm

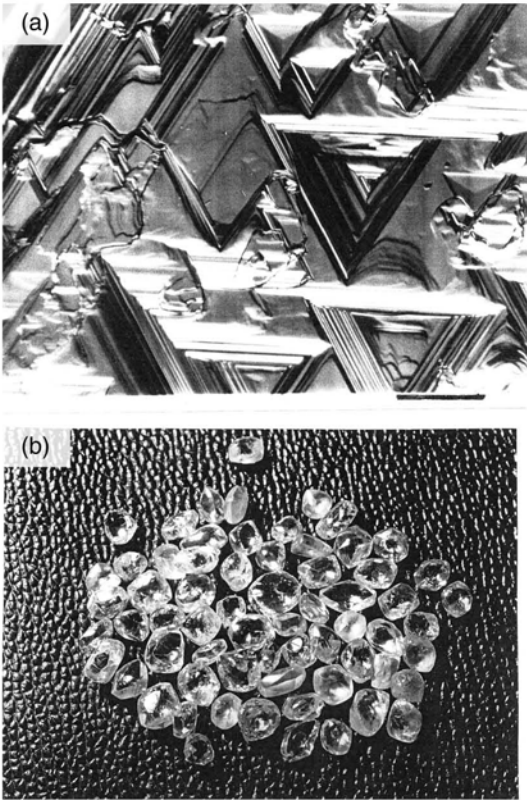


Fig. 1.7. DICM photomicrograph of triangular etch pits (trigons) on a (111) face (a). Bar = 0.1 mm. (b) Rounded morphology of natural diamond crystals. Both features are due to dissolution

1.4 Beryl

Pegmatite is a lenticular or vein form of discordant igneous rock mass or cutting in the surrounding strata, and produces much larger and more perfect crystals than those in mother rocks. It is also a treasure box of unusual mineral species containing large cations. Crystals grow in a void in solidifying magma due to the concentration of volatile components and large cations, which cannot find the sites in the structure of rock-forming minerals. Various gem quality crystals and radioactive or rare earth minerals occur in pegmatite. As a representative example to investigate how crystals grow in pegmatites, the author has selected beryl ($\text{Be}_3\text{Al}_2\text{Si}_6\text{O}_{18}$) crystals from several pegmatite localities, and investigated their surface microtopographs, spatial distribution of dislocations, inclusions, and growth banding [12]. Beryl is the most persistent mineral among 8 beryllium-

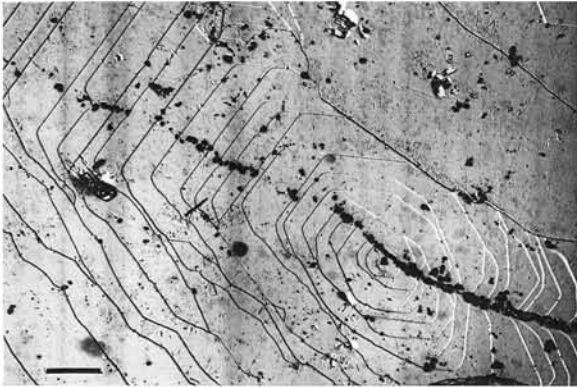


Fig. 1.8. DICM photomicrograph of elemental growth spirals on (0001) face of a beryl crystal from Minas Gerais, Brazil. Bar = 500 μm . Small dots are etch pits selectively formed at dislocation outcrops [12]

containing minerals of 18 minerals belonging to the $\text{BeO-Al}_2\text{O}_3\text{-SiO}_2\text{-H}_2\text{O}$ (BASH) system [13], and its stability field ranges from about 320° to 680°C in temperature and up to 10 kbar in pressure. It is therefore assumed that beryl represents the conditions covering the major range of pegmatite formation.

Many beryl crystals show partially dissolved morphological features, rounded corners and edges or pencil-like tapered prismatic forms, but some crystals preserve their as-grown crystal faces. On such as-grown $\{0001\}$ and $\{1010\}$ faces, one observes elemental growth spirals with unit cell height, originating either from an isolated or group of dislocations. These growth spirals are essentially polygonal in form following the symmetry of respective faces, and the values of step separation versus step height are in the range of 10^4 to 10^6 . This means that the spirals have profiles of 10,000 m to 1,000,000 m flat terrace and 1 m cliff. This also indicates conditions of very small driving force, and diluted ambient phase, probably a supercritical vapor phase [14].

Figure 1.8 is a representative growth spiral on a $\{0001\}$ face. Small dots are etch pits formed selectively at the outcrops of dislocations, both active and inactive for the spiral growth.

Figure 1.9 shows an X-ray topograph (a), a photomicrograph under crossed polarizers before (b) and after etching (c) of a section cut parallel to the (0001) face of a beryl crystal from Arasuai, Minas Gerais, Brazil. From this set of photographs, we obtain information relevant to the growth process of the beryl crystal, which is summarized below.

1. There are three types of dislocations: one parallel to (labeled A), the second perpendicular to (labeled B), and the third inclined to (labeled C) the (0001) face. Dislocations A originate from inclusions trapped at the discontinuity boundary in contrast on the X-ray topograph. Dislocations B give strain birefringence under crossed polarizers (Fig. 1.9b), and dislocations C form etched

tunnels with pits on the terminations. Most of these dislocations are considered to have acted as growth centers to produce elemental growth spirals on the (0001) (B and less probably C) and $(10\bar{1}0)$ faces (A).

2. At least three stages of intermission and associated changes of morphology are discernible during the growth process of this particular crystal. Two discontinuities in contrast are discernible on the X-ray topograph of Fig. 1.9a, the outlines, that is the morphology of this beryl crystal change at these discontinuities. Partial dissolution is also discerned from the rounded outline of the second discontinuity line, where inclusion entrapment is seen, and from which dislocations A generates.
3. Growth rates are markedly different among crystallographically equivalent directions, as judged from the width between the successive discontinuity lines. For example, the growth rates in $+a_1$ and $-a_2$ directions are nearly twice those in $-a_1$ and $+a_2$ directions, respectively. This indicates that there was a directional flow of the fluid phase, and the direction changed during the growth process.

Figure 1.10 shows a mosaic photograph (a) of a prismatic crystal immersed in *n*-methylaniline solution with $RI = 1.5702$, taken under crossed polarizers, and the corresponding sketch (b), as well as an X-ray topograph of another similar prismatic crystal (c). From Fig. 1.10, one can see the following growth history for beryl crystals.

4. There were at least five stages of partial dissolution followed by regrowth during the growth process of the crystal shown in Fig. 10a and b, indicated by labels A to E. Rounded corners of hexagonal prismatic outline, truncating the straight growth banding, show the presence of a partial dissolution period. The subsequent regrowth period is witnessed by transformation from the rounded outline to the straight banding parallel to the hexagonal dipyramidal faces, which eventually disappear from the crystal. The crystal takes on a hexagonal prismatic habit bounded by the $\{0001\}$ and $\{10\bar{1}0\}$ faces alone, when the condition is stabilized.
5. From Fig. 1.10c, it is seen that many bundles of dislocations generate on the surface of prismatic crystal where discontinuities are seen in the contrast image of the X-ray topograph. The dislocations run nearly perpendicular to the prism faces. The outcrops of these dislocations on the $\{10\bar{1}0\}$ faces are considered to have acted as sources for growth spirals on the prism faces.
6. In Fig. 1.10a, tube-like inclusions and dislocations are seen running parallel to the *c*-axis. They originate from solid inclusions present on the boundary surface between partial dissolution and regrowth periods.

Figure 1.11a and b are the polarization photomicrographs of the tube-like two-phase inclusions and negative crystals running parallel to the *c*-axis. It is seen that the two-phase inclusions are formed behind solid inclusions of platy form, probably mica flakes, adhered on the surface when regrowth started after partial dissolution. The negative crystal in Fig. 1.11b appeared by growth on the wall of an inclusion from the entrapped mother liquid. An interesting point is that dislocations parallel to the *c*-axis are generated at the tip of tube-like inclusions, when enclosure failed.

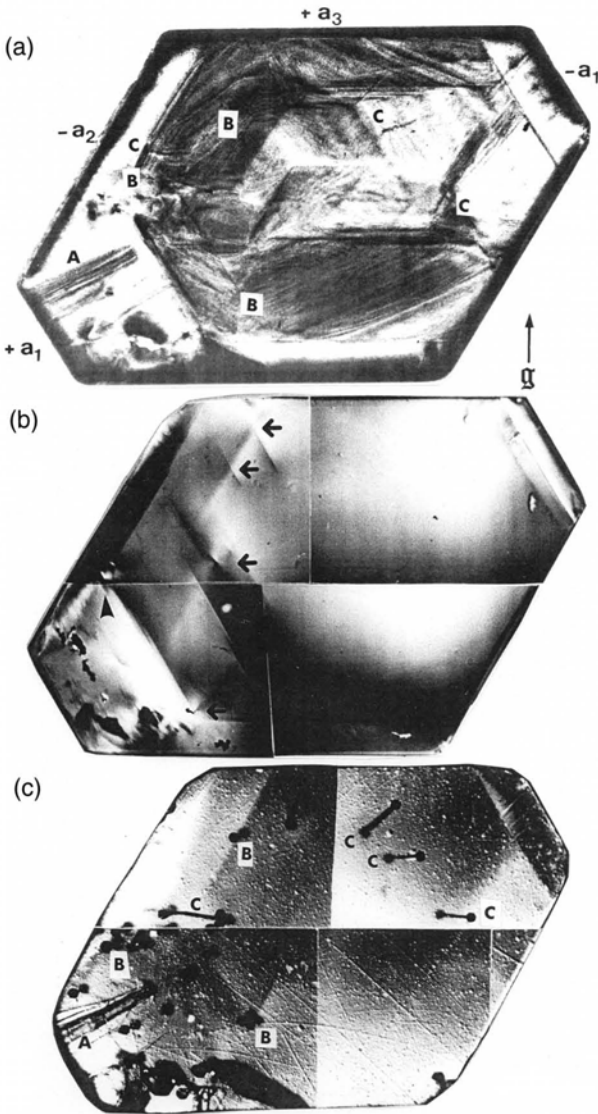


Fig. 1.9. X-ray topograph (a) and photomicrographs taken under crossed polarizers before (b) and after (c) etching of a section parallel to the (0001) face of a beryl crystal from Arasuai, Minas Gerais, Brazil. Bar = 1 mm. Arrow with label of g indicates g -vector [12]

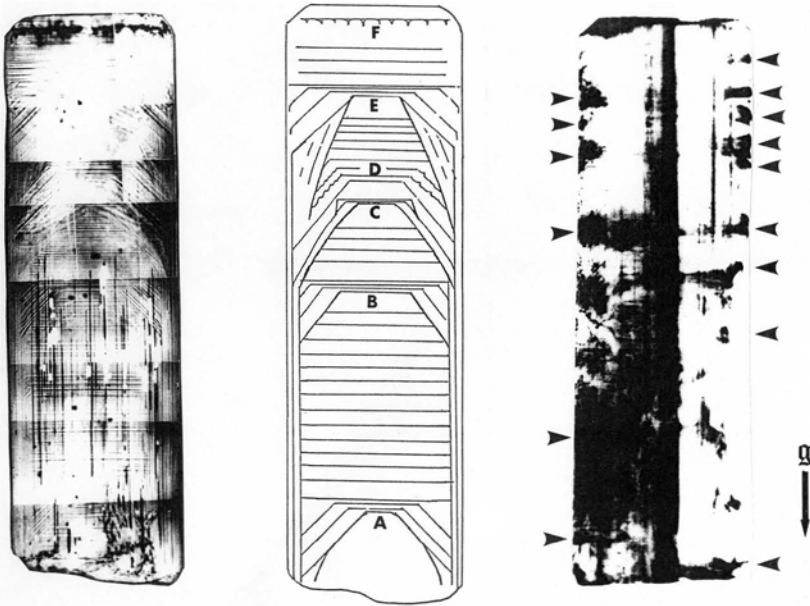


Fig. 1.10. (a) Mosaic photomicrograph under crossed polarizers, (left) and the corresponding sketch (middle) showing the internal texture of a hexagonal prismatic beryl crystal from Hefferman’s mine, Australia. Labels A to F indicate the stages where partial dissolution or change of conditions took place. (Right) X-ray topograph of another prismatic beryl crystal from the same locality. Arrows indicate the positions of generation of dislocations running perpendicular to the prism faces. Arrow *g* indicates *g* vector. Bar = 1 mm [12]

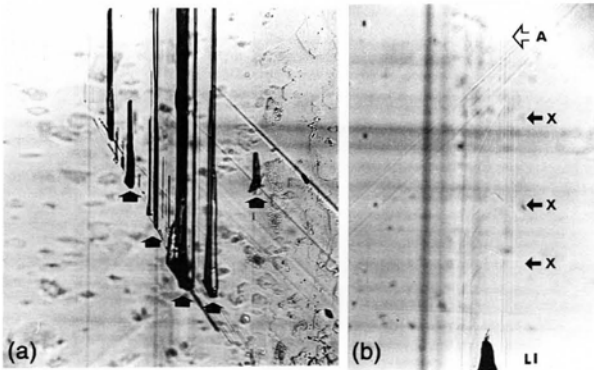


Fig. 1.11. (a) Photomicrograph of tube-like two-phase inclusions formed behind solid inclusions indicated by arrows. (b) Strain field (arrow A) around a dislocation generated from a misfit in the incorporation of the inclusion and negative growth banding (arrows X). LI is a two-phase inclusion [12]

From the preceding explanation, we may consider the growth process of beryl crystals in pegmatitic conditions in the following manner. Crystallization of minerals in pegmatite does not take place in a closed system under static conditions. Directional inflows of nutrients into a void formed in a solidifying magma took place many times, resulting in partial dissolution and regrowth of crystals. At the onset of regrowth, solid inclusions were trapped on the surface, which formed tube-like two-phase inclusions and generated dislocations. Dislocations thus generated acted as self-perpetuating step sources of spiral growth on both the $\{0001\}$ and $\{10\bar{1}0\}$ faces. Hexagonal dipyrarnidal faces appeared only during the regrowth period, and are taken as transient faces.

1.5 Trapiche Ruby

When a magma intrudes into pre-existing strata, contact metamorphism takes place and mineral crystals are newly formed, which are stable phases for the new pressure and temperature conditions. Since magma intrusions supply higher temperature and additional compositions, such processes are customarily called *contact metasomatism*. How nucleation and growth of newly formed crystals take place in the pre-existing solid rocks under such conditions has not been thoroughly understood. It has been a subject of controversy whether the crystallization should be regarded as solid-state crystallization or a solution growth dissolution-precipitation process.

Trapiche ruby is an unusual type of ruby crystal showing unique textures, which resemble a sugar cane crushing gear. *Trapiche* is a Spanish word for such gears, and was originally applied to emerald crystals from Chivor and Muzo, Columbia showing similar texture. Trapiche emerald occurs in hydrothermally metasomatized country slates around calcite-emerald veins cutting into the slate strata [15]. Trapiche ruby occurs in contact metasomatized carbonate strata in the Mong Hsu mining area, Myanmar [16].

In Fig. 1.12, schematic diagrams of textures seen in both trapiche emerald and ruby are compared [17]. Different terms have been used to describe the textures seen in Fig. 1.12, but we adopt the terminology given for trapiche ruby in this figure.

Trapiche ruby occurs in the form of barrel-shaped prisms, with internal texture characterized by a core, six arms extending along the $\langle 10\bar{1}0 \rangle$ direction, and branches there from running parallel to the z axes, with six clear ruby growth sectors. The barrel-shaped crystal is bounded by basal $\{0001\}$ and tapered prism $\{11\bar{2}0\}$ faces, although for the latter faces very high indexed scalenohedral faces, like $\{14\ 14\ 2\bar{8}\ 3\}$ were assigned in [16].

The arms and branches are yellow, white, or black in color and translucent to opaque. Through EPMA analysis, it was confirmed that these portions consist of several mineral phases, corundum, carbonate, and tiny unidentified K-Al-Fe-Ti

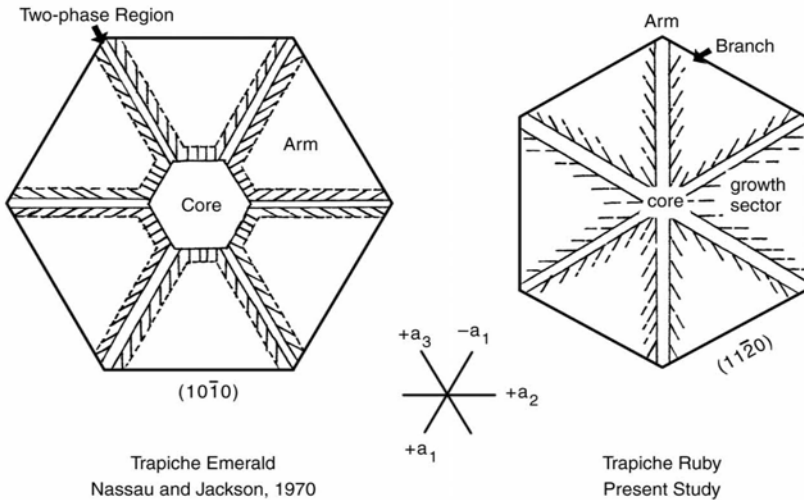


Fig. 1.12. Schematic illustration of textures and terms used to denote respective portions in trapiche emerald (a) [15] and trapiche ruby [16]. From [17]

silicate mineral grains [16]. The pattern shown by the arms and branches is typical for dendritic growth, such as snow dendrites. The six growth sectors are triangular or trapezohedral in form, and transparent to translucent red in color, and consist of pure ruby single phase. The growth sectors appear filling the interstices of arms and branches. The core portion is in most cases black and opaque and mineralogically and texturally the same as the arms and branches, but in rare cases a hexagonal prismatic clear ruby core portion is present.

The problems we intend to understand here are how such textures were formed, how element partitioning was governed, and how long it took to form the present size in the contact metasomatic condition.

The arms run from a central point or from six corners of a central hexagonal core to the six corners of a hexagonal prism, nearly parallel to the $\{0001\}$ face, with about 5° bending toward the center. The arms and branches extend from the core with similar texture as the arms in most samples, but the arms start from the corners of the core hexagon and branches from the core-growth sector boundaries when a clear ruby core is present. The boundary of the hexagonal core and the six growth sectors are thus rugged and splintered. The branches show similar appearance in color, transparency, and mineral compositions as the arms. Six growth sectors consist of corundum single phase, but color-zoning parallel to tapered prism faces is also observed.

It has been well established that a dendritic pattern appears due to morphological instability [18] of the growing rough interface, where an adhesive type growth mechanism operates. The arms and branches can be taken as representing such rough interface growth. In contrast to this, a layer-by-layer growth mechanism on the $\{0001\}$ and $\{11\bar{2}0\}$ faces form growth sectors. Namely these two faces be-

haved as smooth interfaces during their formation. Therefore, it can be assumed that both interfacial roughness and growth mechanisms were different in the formation of portions of arms and branches and of growth sectors.

By means of X-ray microfluorescence analysis (XRMF) and electron microprobe analysis (EPMA), elemental mapping was performed on slices cut perpendicular to the *c*-axis. The results clearly indicated a marked difference in chemistry and mineralogy between arms and branches, and growth sectors. Important differences between the two portions noticed in the element mappings are:

1. The arms and branches are composed of polyphases; corundum, carbonate, and silicate. But the corundum in these parts is chemically homogeneous, showing no chemical zoning from the root to the tip of an arm or a branch. The Chromium (Cr) content in corundum in these parts is constant and much lower than in the corundum in the growth sectors. The Cr content in corundum is nearly the same or at the most two times higher than that in carbonate or silicate grains coexisting in the arms and branches.
2. The growth sectors consist of single phase ruby, but distinct chemical zoning in Cr content, and less distinct Ti content are seen parallel to the tapered prism faces. The Cr content in the growth sectors is much higher than in the arms and branches, and ranges from 0.60 to 1.70%. The Cr content in the growth sectors sharply increases more than 8 times at the boundary between the central core and growth sectors. It gradually decreases going outward, namely as growth proceeded and increases slightly again followed by sharp decrease at latest stage.
3. The black and opaque core portion shows the same character as that of the arms and branches, whereas the clear hexagonal core resembles that of the growth sectors except for Cr zoning.

Figure 1.13 shows plots of EPMA point analyses along the A-A, B-B lines and section 2 in Fig. 1.13a. All analyses were performed with beam diameter 1 μm ; A and B, point separation, 20 μm , 1.5–1.6 mm extension; section 2, point separation 3 μm , extension 300 μm . Figure 1.13 clearly indicates the above summaries.

From the textural and chemical characteristics described above, the author concludes the following:

- a. The arms and branches are formed by dendritic growth by an adhesive-type growth mechanism on the rough interface, during which eutectic-type multi-phase precipitation took place.
- b. The growth sectors are formed by a layer-by-layer growth mechanism on the smooth interface, principally the $\{0001\}$ and $\{11\bar{2}0\}$ faces, and a later or concurrent filling-in process of interstices of earlier formed dendrite arms and branches.
- c. Elemental partitioning was governed by thermodynamic parameters during the dendritic growth stage on rough interfaces, and by kinetics (growth rates) during the formation of growth sectors.
- d. Dendritic growth took place under higher driving force conditions, followed by a filling-in process of the interstices of arms and branches through a layer-by-

layer growth mechanism. The filling-in process took place either concurrently with dendritic growth or slightly later, since the concentration at the root of the dendrites is depleted.

- e. Depending on the conditions, layer-by-layer growth may sometimes precede dendritic growth, forming a hexagonal core of single phase ruby, on which dendritic growth followed by layer-by-layer growth takes place.
- f. The present size of the trapiche ruby was formed during the dendritic growth stage, and thus in a very short time.

In Fig. 1.14, superimposing the routes and textural changes of trapiche rubies on Fig. 1.1 illustrates the above discussions.

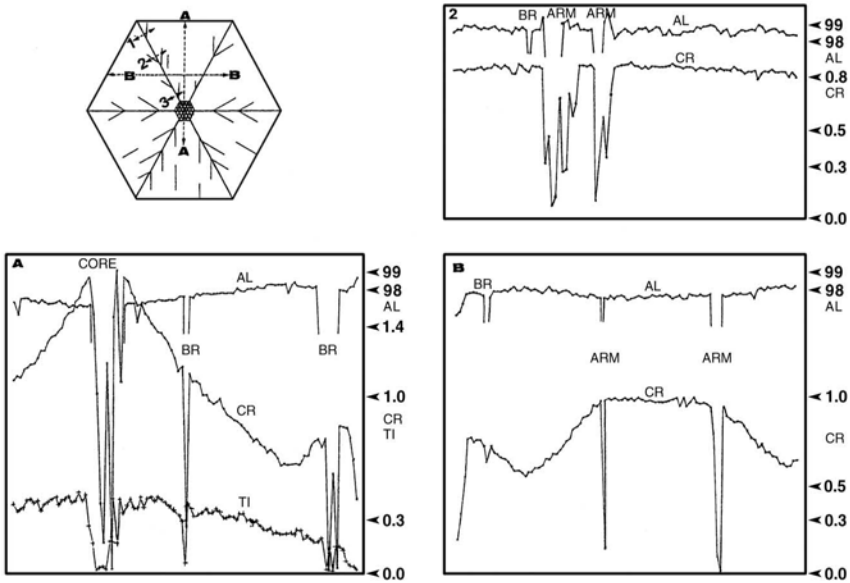


Fig. 1.13. Positions of scans A, B, and 1–3 (a), and corresponding plots of microprobe analyses of Al_2O_3 (AL), Cr_2O_3 (CR) and TiO_2 (TI). Core indicates opaque core portion, arm and br indicate, respectively, arms and branches [17]

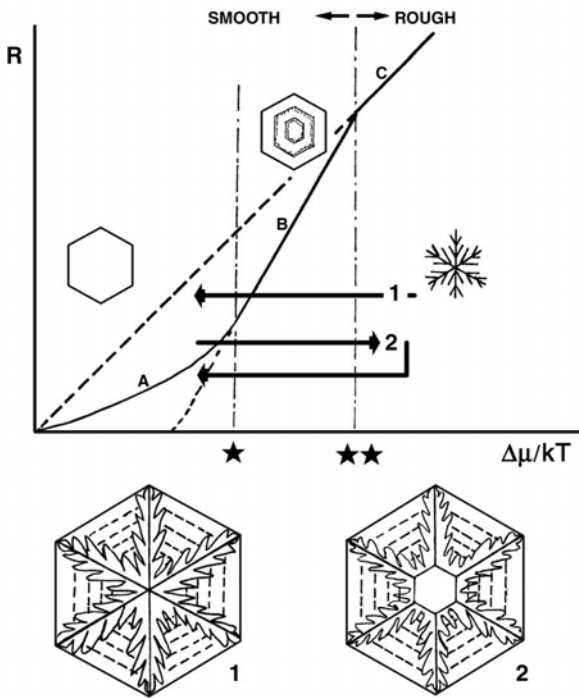


Fig. 1.14. Schematic diagram showing two routes 1 and 2 for trapiche ruby without (route 1) and with clear ruby core (route 2), superimposed on Fig. 1.1 [17]

1.6 Summary

Diamond, beryl, and trapiche ruby are used to demonstrate how the present understanding of growth, morphology, and perfection of crystals can be used to decode the letters sent from the depths of the earth. The same concept is applicable to other earth and planetary processes, as well as to organic and inorganic crystal formation in animate bodies.

References

1. Sunagawa I (1999) Growth and morphology of crystals. *Forma* 14:147–166
2. Sunagawa I (1994) Investigations of crystal growth in earth and planetary sciences. In: Hurle DTJ (ed) *Handbook of Crystal Growth*, Elsevier Science BV, Amsterdam, pp 1–49
3. Sunagawa I (1994) Nucleation, growth and dissolution of crystals during sedimentogenesis and diagenesis. In: Wolf KH, Chilingarian GV (eds) *Diagenesis IV. Development of Sedimentology* 51, Elsevier Science BV, Amsterdam, pp 19–47

5. Sunagawa I (1987) Morphology of minerals. In: Sunagawa I (ed) *Morphology of Crystals, Part B*, Terra Science Publishers, Tokyo/ D Reidel, Dordrecht, pp 509–587
6. I. Sunagawa (1984) Morphology of natural and synthetic diamond crystals. In: Sunagawa I (ed) *Materials Science of the Earth's Interior*, Terra Science Publications, Tokyo/ D Reidel, Dordrecht, pp 303–330
7. Lang AR (1978) Internal structure. In: Field JE (ed) *The Properties of Diamond*, Academic Press, London, pp 425–469
8. Sunagawa I, Tsukamoto K, Yasuda T (1984) Surface microtopographic and X-ray topographic study of octahedral crystals of natural diamond from Siberia. In: Sunagawa I (ed) *Materials Science of the Earth's Interior*, Terra Science Publications, Tokyo/ D Reidel, Dordrecht, pp 331–349
9. Sobolev NV, Shatsky VS (1990) Diamond inclusions in garnets from metamorphic rocks; A new environment for diamond formation. *Nature* 343:742–746
10. Sunagawa I (1995) The distinction of natural from synthetic diamonds. *J Gemmol* 24:485–499
11. Sunagawa I, Yasuda T, Fukushima H (1998) Fingerprinting of two diamonds cut from the same rough. *Gem & Gemol* 34:270–280
12. Sunagawa I, Yokogi A (1999) Beryl crystals from pegmatites: Morphology and mechanism of crystal growth. *J Gemmol* 26:521–533
13. Barton MD (1986) Phase equilibria and thermodynamic properties of minerals in the BeO-Al₂O₃-SiO₂-H₂O system with petrologic applications. *Amer Mineral* 71:277–300
14. Sunagawa I (1978) Vapor growth and epitaxy of minerals and synthetic crystals. *J Crystal Growth* 45:3–12
15. Nassau K, Jackson KA (1970) Trapiche emeralds from Chivor and Muzo, Colombia. *Amer Mineral* 55:416–427
16. Schmetzer K, Hänni HA, Berhardt H-J, Schwarz D (1996) Trapiche rubies. *Gem & Gemol* 32:242–250. Schmetzer K, Beili Z, Yan G, Berndhardt H-J, Hänni HA (1999) Element mapping of trapiche rubies. *J Gemmol* 26:289–301
17. Sunagawa I, Berhardt H-J, Schmetzer K (1999) Texture formation and element partitioning in trapiche ruby. *J Crystal Growth* 206:322–330
18. Mullins WW, Sekerka RF (1963) Morphological stability of a particle growing by diffusion or heat flow. *J Appl Phys* 34:323–329

2 Theory of Crystal Growth from Vapor and Solution

Toshiharu Irisawa

Computer Center, Gakushuin University, Mejiro 1-5-1, Toshima-ku, Tokyo, 171-8588, Japan

2.1 Various Crystal Growth Processes

For a crystal to grow, a seed crystal capable of maintaining a stable condition in a melt, solution, or vapor phase must first be produced. In vapor deposition, the substrate serves as the seed crystal. The process by which a seed crystal is born and grows into a nucleus is called the nucleation process, which plays an important role in the process of crystal growth. The seed requires the formation of a three-dimensional nucleus, but because the workings of three-dimensional nucleation are analogous to those for two-dimensional nucleation, only the latter is treated here. In this part of the book, we will discuss what happens after a nucleus has formed and the crystal has grown in size, specifically, how crystals grow and at what speeds [1,2,5].

2.1.1 Driving force

For crystals to grow, some driving force is required. We first define this driving force. The conditions in any given system change according to the laws of thermodynamics in such a manner that the free energy in the whole of the system decreases. This means that any decrease in free energy associated with the crystallization process works to promote the growth of crystals. Namely, the difference $\Delta\mu = \mu_m - \mu_c$ between the chemical potential μ_m of a melt, solution, or vapor phase (*the growth medium*) and the chemical potential μ_c of the crystalline phase becomes a driving force towards crystal growth. In the nucleation process, the number of atoms that form a surface or interface is as important as the number of atoms that form crystals because those forming a surface supply the energy needed to grow the crystals. After a nucleus forms and the crystal grows to a sufficient extent, the contribution of the interface energies can be ignored and the difference in bulk free energy in each phase becomes the difference in chemical potential. Therefore, a difference in chemical potential in various growth environments can be associated with measurable, physical quantities as shown below.

When the growth medium is a melt, the molten and crystalline phases coexist in a stable state if the system is at the melting point T_m . If the temperature falls below T_m , crystals grow. That is, the level of supercooling $\Delta T = T_m - T$ becomes the driving force for crystal growth. The relationship between the level of supercooling ΔT and $\Delta\mu$ can be expressed as follows:

$$\Delta\mu = L\Delta T/T_m \quad (2.1)$$

Here, L is the latent heat of melting.

In the case where the growth medium is a vapor, crystals will grow when the vapor pressure p is higher than the equilibrium or saturated vapor pressure p_e , and then the level of supersaturation $\sigma = (p - p_e)/p_e$ becomes the driving force. A difference in chemical potential between the vapor phase and the crystal phase based on vapor pressure can be expressed as follows:

$$\Delta\mu = k_B T \log(p/p_e) \quad (2.2)$$

Therefore, the relationship between $\Delta\mu$ and the level of supersaturation σ can be expressed as follows:

$$\Delta\mu = k_B T \log(1 + \sigma) \approx k_B T \sigma \quad (2.3)$$

Here, k_B is Boltzmann's constant.

If the growth medium is a solution, the threshold concentration of solutes that can be dissolved into the liquid (i.e., the concentration C_e of a saturated solution) is used as the criterion. The level of supersaturation $\sigma = (C - C_e)/C_e$, which can be calculated from C_e and the actual solute concentration C , can be defined as the driving force. The relationships of the chemical potential differences between the solution phase and the crystal phase can be expressed as follows:

$$\Delta\mu = k_B T \log(C/C_e) \quad (2.4)$$

$$\Delta\mu = k_B T \log(1 + \sigma) \approx k_B T \sigma \quad (2.5)$$

In a typical crystal growth experiment, the supersaturation σ becomes positive by lowering the system temperature to decrease the concentration C_e of the saturated solution instead of increasing the concentration C .

There is also a mechanism for solid-phase growth that occurs when a polycrystal that formed through the agglomeration of small crystal grains is then subjected to heat and pressure, and then grows into a large single crystal. In this case, the growth driving force can be expressed as the distortion or intergranular energy in crystal grains. However, this chapter focuses on the growth of crystals that are surrounded by vapor or other fluid growth media: we do not deal with solid-phase growth.

Although a growth unit can be an atom, molecule, or a larger cluster, we will routinely use an atom as the unit of growth in this book.

2.1.2 Rate-determining process

The next question to address is the actual growth mechanism, or how crystals grow when put under certain driving forces. In general, crystals grow in three different processes as shown below:

1. Atoms and molecules are introduced into the crystal phase through an interface between the crystals and the growth medium. This is called the interface, or surface, kinetic process.
2. Atoms and molecules in the growth medium are supplied to the growth interface, or crystal surface. This stage is called the volume diffusion process.
3. Latent heat generated at the growth interface during crystallization is removed.

The growth rate is determined by the rate at which the crystals pass through each of these processes. The process that has the largest impact on the overall rate of growth is clearly the process in which the rate of growth is the slowest. This particular process is therefore known as the *rate-determining process*. Exactly which of the processes becomes the rate-determining process depends on the growth environment and the growth conditions. To accurately identify the rate-determining process, the points described below must be considered.

If the environment is a melt, the number density of atoms in the melt and the analogous density of atoms in the crystal are considered to be approximately the same (known as a *dense environment phase*). Therefore, process (2) is not the rate-determining process. Also, because the growth interfaces of almost all substances grown in a melt are not flat if viewed on an atomic scale, the orientation time during which the atoms are contained in the crystals is not a factor that affects the rate. Thus, process (1) can be ignored and process (3) is the rate-determining process.

If the growth medium is vapor or solution, many of the crystals in it will grow as polyhedrons. Although this will be described later in greater detail, in this case the growth interface is flat on an atomic scale. Therefore, the rate-determining step is the interface kinetic process (1) because the orientation time for this particular process is sufficiently long compared with both the atom-supply process (2) and the heat removal process (3). Process (2) can be ignored if a crystal grows in vapor because the concentration in the growth medium is sufficiently low, and thus volume diffusion can take place easily. If the crystals grow in a solution, the concentration of solute atoms in the growth medium is lower than that in the crystals, but the density of the solution itself is almost equal to that of the crystal. Therefore, the volume diffusion coefficient is estimated to be smaller by two orders of magnitude than that of the mixed gas phase, so it is not necessarily appropriate in this case to ignore process (2). This point will be discussed in greater detail in the section that describes growth in a solution.

Because the density of solute atoms in a vapor or solution phase is sufficiently low compared to that in crystals, vapor and solution phases are called *thin* growth media. However, the density of atoms in the environment surrounding the crystals is significantly different from that of the atoms in the crystals, so one phase can be clearly distinguished from the other at a boundary (surface). In this chapter, we

will restrict our discussion to the mechanism of crystal growth seen in relation to a thin growth medium.

2.2 Vapor Growth

Atoms that leave the vapor phase and enter the surfaces of crystals give up almost all of their energy to the crystals in the form of kinetic energy. Therefore, they are captured on the surface as adatoms. There are also some atoms that jump back into the vapor phase. This raises the question of how we can identify the atoms that have been included within the crystal phase from those that have not. It is presumed that a sufficiently large number of atoms, which is defined as N , coalesce to form a bulky crystal. The decrease in ΔE per atom in potential energy resulting from interatomic binding can be calculated using the following formula:

$$\frac{\Delta E}{N} = \frac{1}{2} \sum n_i \phi_i = \phi_{1/2} \quad (2.6)$$

Here, ϕ_i is the binding energy of the nearest neighbor atoms with position labeled by i . n_i is the number of nearest neighbor atoms for the atom at position i . The factor $1/2$ means that two atoms bound to each other share the energy gain produced by their interatomic bond. Therefore, if there is an energy gain larger than $\phi_{1/2}$ when the atoms enter the surfaces of the crystals, we can consider that these atoms have been included within the crystals. If we observe the actual surfaces of the crystals, an energy gain of $\phi_{1/2}$ is seen when an atom enters the bent portion K, a kink site, which has a size of one atom and exists along the step S-T. This has a thickness of one atomic layer on the surface, as shown in Fig. 2.1. Figure 2.1 shows the (001) plane of a simple cubic lattice. This energy gain principle also applies to a plane that has a different orientation or any plane in the other crystal lattices. Table 2.1 shows a list of some values of $\phi_{1/2}$ for various crystal lattices with particular consideration given to the second nearest neighbor. The kink does not disappear when atoms are added to it; it only slides along a step [3, 4]. This point is important because we cannot observe the same phenomenon at other surface positions. For example, consider the lattice point H (surface vacancy) shown in Fig. 2.1. If atoms enter this point H, they can have an energy gain greater than when they enter at a kink position. The point H (surface vacancy) disappears the instant they enter it. Therefore, their chance to contribute to the growth of the crystal is lost. The kink position is also called the half-crystal position, which means that the binding energy of atoms at the kink position is half that of the internal atoms in the bulk crystal. Supposing that the surface shown in Fig. 2.1 is made by cutting a bulk crystal into two parts, then the surface of one cut crystal has the same number of steps and kinks as that of the other cut crystal surface.

The number of atoms that leave the vapor phase and enter the surface of a crystal per unit time per unit area is $p/\sqrt{2\pi mk_B T}$. Here, p is the vapor pressure, m

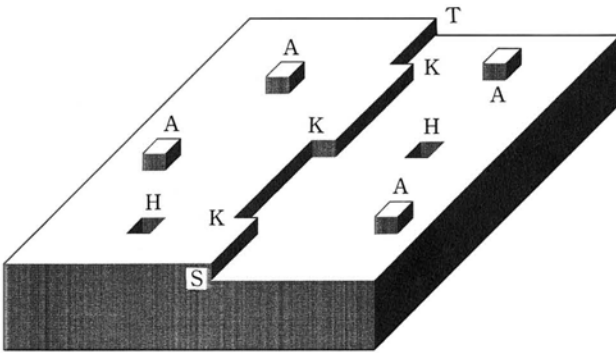


Fig. 2.1. Surface structure of Kossel model

Table 2.1. Binding Energies for Various Crystal Lattices

Lattice	$\phi_{1/2}$
Simple cubic	$3\phi_1 + 6\phi_2$
Face center cubic	$6\phi_1 + 3\phi_2$
Body center cubic	$4\phi_1 + 3\phi_2$
Diamond lattice	$2\phi_1 + 6\phi_2$
Hexagonal	$6\phi_1 + 3\phi_2$

is the mass of an atom, k_B is Boltzmann’s constant, and T is temperature. The greatest growth rate occurs if all of the incident atoms condense into the crystal. It must be kept in mind, however, that atoms on the surfaces of crystals can jump out into the vapor phase if heat fluctuations cause them to acquire energy larger than the adsorption energy. Therefore, the growth rate can be estimated based on the difference between the number of atoms entering the surfaces of the crystals and that of atoms jumping back out into the vapor phase. Because the growth rate is zero in an equilibrium, or saturated, state, the number of atoms jumping out of the surfaces is equal to that of the atoms entering the surfaces. Therefore, the number of atoms jumping out of the surfaces of the crystals is $p_e / \sqrt{2\pi mk_B T}$ per unit time per unit area under the equilibrium vapor pressure p_e .

Because the number of atoms that jump out is not dependent on vapor pressure, the maximum growth rate at any given vapor pressure p can be calculated using the following formula:

$$R_{\max} = \frac{\Omega(p - p_e)}{2\pi mk_B T} = C\sigma \quad ; \quad C = \frac{\Omega p_e}{2\pi mk_B T} \tag{2.7}$$

Here, Ω is the atomic volume. This formula is called the Hertz-Knudsen formula. It must be noted that the maximum growth rate calculated with this formula is proportional to the supersaturation, $\sigma = (p - p_e) / p_e$, which is the growth driving force in the vapor phase.

The maximum growth rate quoted above is obtained under the condition where all atoms leaving the vapor phase and entering the surfaces of the crystals are then included within the crystalline phase. This total containment can occur if the surfaces of the crystals are uneven and rough, or if all of the lattice points are at kink positions (or at positions where an even greater energy gain can be obtained through crystallization). This growth pattern is called *adhesive growth*. The different types of roughness relating to crystal surfaces can be classified into geometrical roughness and the roughness caused by a roughening transition. The geometrical roughness is the type seen on the (111) plane of a simple cubic lattice or other high-index plane. Specifically, a lattice plane exposed after a crystal is cut in half is rough and uneven if viewed from the point of view of geometry. The roughness caused by a roughening transition is the sort of unevenness seen on a plane that initially had a smooth surface at low temperature, but which developed a rough surface after it was exposed to its critical temperature T_R or higher, and then transformed into a different phase.

Rough, uneven planes grow at the maximum growth rate R_{\max} , but they disappear as the crystals grow large. As they disappear, the crystals retain only flat, smooth surfaces, and their external form becomes a polyhedron enclosed by such smooth planes. These planes are called *singular surfaces*; the interatomic binding in these planes is strong, and they have a high roughening temperature. They are usually low-index planes, such as those of simple cubic lattices (001). Considering the observations above, a key factor in the growth of crystals in the vapor phase is whether flat, smooth singular surfaces can develop or not. (See Fig. 2.2.)

A singular surface does not have kinks where atoms are contained in a crystalline phase. Hence, for a singular surface to grow, steps that contain kinks must appear. The two-dimensional nucleus formation and screw dislocation methods are both used as a means of providing a singular surface with steps. These will be described in more detail later in this book.

Once a step is provided on a singular surface, atoms enter the kinks and crystallization begins. Atoms that enter a flat plane (terrace) are first adsorbed onto the surface of the plane as explained earlier. These adatoms reside on the surface until they acquire the required adsorption energy E_a , which is created through heat fluctuations. The average residence time τ_s can be expressed using E_a as follows:

$$\tau_s = \nu^{-1} \exp(E_a / k_B T) \quad (2.8)$$

Here, ν is a frequency term of the adatoms. During the residence time τ_s , the adatoms do not stay fixed in the same position; they diffuse over the surface. If these adatoms on the terrace diffuse sufficiently and reach a kink before they desorb into the vapor phase, they can then be acquired by the crystal phase. Assuming that the activation energy for the adatoms diffusing on the surface is E_{sd} , which is the energy needed to move adatoms to an adjacent lattice point, the surface diffusion coefficient D_s can be defined as follows:

$$D_s = a^2 \nu \exp(-E_{sd} / k_B T) \quad (2.9)$$

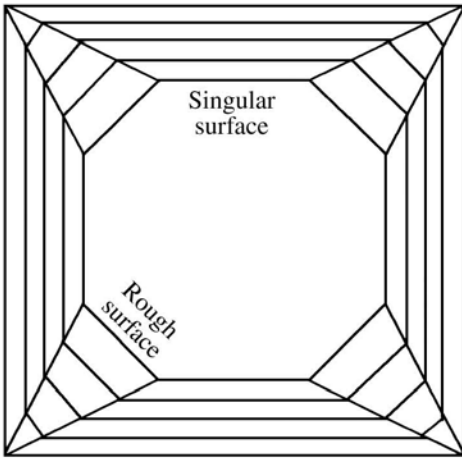


Fig. 2.2. Disappearance of rough surface

Here, a is the lattice constant. The average distance λ_s that the adatoms diffuse during the residence time τ_s can be calculated using Einstein's expression $D_s \tau_s = \lambda_s^2$ as follows:

$$\lambda_s = a \exp[(E_a - E_{sd}) / 2k_B T] \quad (2.10)$$

E_{sd} is smaller than E_a and has a typical magnitude such that $\lambda_s \sim 10^2 a$ if the crystals are growing in the vapor phase. This means that atoms entering a position at a distance of λ_s , or less from a kink can contribute to the growth, indicating that surface diffusion plays an important role in growth in the vapor phase.

As described above, atoms entering a terrace near to a step provided on a singular surface can diffuse across the surface, reach a kink and become included in the crystal. This growth mechanism is called the Kossel mechanism [3].

Once the adatoms attach at a kink, the kink moves forward a step. As this movement of the kink takes place repeatedly, the step moves forward across the surface and this is the way that the crystal growth process proceeds. This growth pattern is called *lateral growth* and differs from the adhesive growth mentioned previously. To determine the growth rate of this growth mechanism, it is necessary to identify the forward speed of a step, also called the step velocity.

2.2.1 Step velocity

Velocity of advance of a single step

A straight step that does not contain a kink has an advantage in terms of energy; however, this is a disadvantage in terms of entropy. Therefore, a step will contain a certain number of kinks at finite temperatures. We find that the average distance

between neighboring kinks is far smaller than the average surface diffusion distance λ_s of the adatoms. Thus, if the kink density is sufficiently high, a step functions as a sort of hole through which adatoms can be drawn in an unbroken flow.

To determine the step velocity, the quantity of atoms drawn onto the growth front must be calculated. Interactions between the vapor phase and the surface should first be examined. Based on the difference between the number of atoms entering kink sites after leaving the vapor and the number of atoms leaving the surface, the net flow j_v per unit time per unit area crossing from the vapor phase to the surface can be expressed as follows (Fig. 2.3):

$$j_v = \frac{p}{\sqrt{2\pi mk_B T}} = \frac{n_s}{\tau_s} \quad (2.11)$$

Here, n_s is the density of adatoms adsorbed onto the surface. On the other hand, the surface diffusion flow of adatoms per unit time per unit area j_s can be calculated based on the two-dimensional gradient of density n_s as follows:

$$j_s = -D_s \text{grad } n_s \quad (2.12)$$

Using the above equation, the following continuity equation can be calculated regarding the density of atoms adsorbed onto the surface:

$$\frac{\partial n_s}{\partial t} = -\text{div } j_s + j_v \quad (2.13)$$

Here, divergence is two-dimensional. Because the step velocity calculated in this way is much slower than the surface diffusion speed of adatoms, the movement of a step can be ignored.

If we can obtain a solution for the steady state ($\partial n_s / \partial t = 0$) of this continuity equation, the density distribution n_s of the adatoms can be determined. Because a step is effectively a hole through which atoms are drawn in one unbroken flow, n_s is uniform in the direction parallel to the step and is dependent only on its distance x from the step.

In an equilibrium state, there is no surface diffusion flow and the number of atoms arriving and the number of atoms leaving are balanced; thus $j_v = 0$. Therefore, from Eq. (2.11), the equilibrium density of adatoms n_{se} is

$$n_{se} = \frac{p_e}{\sqrt{2\pi mk_B T}} \tau_s \quad (2.14)$$

At a point far from the step ($x = \infty \gg \lambda_s$), the quantity of atoms entering and the number that are leaving is also balanced, even in a state of supersaturation, which results in $j_v = 0$. If we define the level of supersaturation of the adatoms as $\sigma_s(x) = (n_s(x) - n_{se}) / n_{se}$, then $\sigma_s(\infty)$ is equal to the level of supersaturation of the vapor phase $\sigma = (p - p_e) / p_e$. On the other hand, the density of adatoms $n_s(0)$ at the step position ($x = 0$) can be considered to be equal to the equilibrium density n_{se} . This is because there are no energy barriers when the atoms are contained in the kink position, and the atoms in the crystal can interact fully with the adatoms.

In summary, assuming that the density of adatoms is $\phi(x) = \sigma - \sigma_s(x)$, we should calculate the following equation using the boundary conditions in (2.16) below.

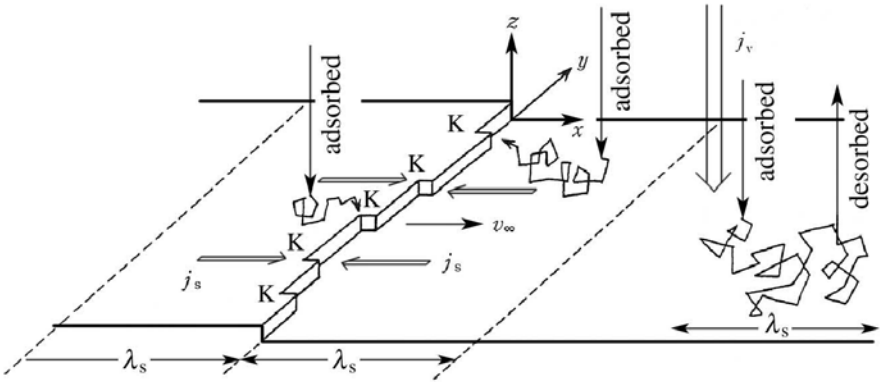


Fig. 2.3. Motion of a step and adatoms

$$\lambda_s^2 d^2 \phi / dx^2 = \phi \tag{2.15}$$

The boundary conditions are:

$$\begin{aligned} \phi(0) &= \sigma \\ \phi(\infty) &= 0 \end{aligned} \tag{2.16}$$

The solution that we derive is $\phi(x) = \sigma \exp(-x / \lambda_s)$. Therefore, the density of adatoms can be calculated as follows:

$$n_s(x) = n_{se} + (n_s - n_{se})[1 - \exp(-x / \lambda_s)] \tag{2.17}$$

Here, n_s is the density of adatoms that matches the vapor pressure p . The step velocity v_∞ can be obtained from the gradient at that step position as follows:

$$v_\infty = \frac{2D_s}{n_0} \frac{dn_s}{dx} \Big|_{x=0} = \frac{2\lambda_s}{n_0} \frac{p_e}{2\pi mk_B T} \sigma \tag{2.18}$$

Here, $n_0 (= 1 / a^2)$ is the density of lattice points on the surfaces of the crystals. The factor of 2 appears here because we assume there are flows running from both sides of a step. We should also note here that the step velocity v_∞ is proportional to both supersaturation σ , which is the driving force for growth, and is proportional to $2\lambda_s$. The step velocity can then be obtained from the simple assumption that all atoms entering a point which is a distance of λ_s or less away from a step (i.e., an area $2\lambda_s$ wide) diffuse over the surface, reach a step and are included in the crystal, but atoms entering a point farther away than λ_s cannot reach a step and hence do not contribute to the growth. The step velocity obtained based on this simple assumption is consistent with the results described above. Therefore, we can refer to areas of λ_s in width on both sides of a step as the capture areas.

Velocity of advance of parallel steps at regular intervals

We can observe that many steps caused by screw-dislocations (to be explained later in this book) are formed nearly parallel to each other at regular intervals on the actual surfaces of the crystals. By applying the above assumption, we can estimate that the forward speed of these steps is slower than that of a single step because the capture areas of each step will overlap if the interval λ between neighboring steps is smaller than $2\lambda_s$. Assuming that $n_s(x)$ equals the equilibrium density n_{se} at $x = 0, \lambda$, we can obtain n_s using the following equation:

$$n_s(x) = n_s + (n_{se} - n_s) \frac{\cosh[(x - \lambda/2)/\lambda_s]}{\cosh[\lambda/2/\lambda_s]} \quad (2.19)$$

Therefore, the step velocity can be expressed based on the above equation as follows:

$$v(\lambda) = v_\infty \tanh\left(\frac{\lambda}{2\lambda_s}\right) \quad (2.20)$$

If $\lambda \gg 2\lambda_s$, the step velocity $v(\lambda)$ of parallel steps at regular intervals λ are equal to that of a single step v_∞ . On the contrary, if $\lambda \ll 2\lambda_s$, we obtain $v(\lambda) = v_\infty \lambda / 2\lambda_s$ and we can assume that the capture area of each step has become equal to the interval λ between steps.

Parallel steps at regular intervals can move forward by a specified step interval λ during a set time period τ , which can be calculated using $\tau = \lambda/v(\lambda)$. Because the surface of the crystal grows by one layer during this time period, the growth rate R can be calculated as follows, providing that the thickness of one layer is d :

$$R(\lambda) = \frac{d}{\tau} = \frac{(p - p_e)\Omega}{\sqrt{2\pi m k_B T}} \frac{2\lambda_s}{\lambda} \tanh\left(\frac{\lambda}{2\lambda_s}\right) \quad (2.21)$$

Here, $\Omega = d/n_0$ is the atomic volume. This growth rate $R(\lambda)$ increases in proportion as the step interval λ decreases. At the point where $\lambda \ll 2\lambda_s$, $R(\lambda)$ becomes equal to the maximum growth rate R_{max} , which can be calculated using the Hertz-Knudsen formula (2.7). If the capture area spreads all over the surface, the growth rate becomes a maximum, even if the surface is not uneven or does not have many kinks.

Velocity of a curved step

So far we have assumed that a step is straight (the width is partly uneven since a step contains many kinks). An actual step, however, is curved. In the case of a step on the surface of a crystal, a loss in the step energy per unit length γ can occur because a chain of atomic binding is terminated on the edges of a step.

If a step curves or bends, the step energy per unit length becomes large compared to that of a straight step. As a result, the equilibrium vapor pressure $p_e(\rho)$ for a step with a curvature of radius ρ becomes larger than the equilibrium vapor pressure p_e of a straight step. Providing that the level of supersaturation is $\sigma_e(\rho) = (p_e(\rho) - p_e)/p_e$ [5]:

$$\sigma_e(\rho) = \exp\left(\frac{\gamma}{\rho n_0 k_B T}\right) - 1 \quad (2.22)$$

The equilibrium density of adatoms at the step position is consistent with the result obtained using the above equation. To obtain the forward speed $v(\rho)$ of a step with a curvature of radius ρ , Eq. (2.15) is converted to a polar form to calculate the density distribution of adatoms under the above boundary condition, and the result is substituted into Eq. (2.18):

$$v(\rho) = \frac{\lambda_s [1 - \sigma(\rho)/\sigma]}{2\rho I_0(\rho/\lambda_s) K_0(\rho/\lambda_s)} \quad (2.23)$$

Here, I_0 and K_0 are class-1 and class-2 deformation Bessel functions, respectively. In the range where the conditions $\rho \ll \lambda_s$ and $\sigma \gg 1$ can be satisfied, $v(\rho)$ can be approximated as follows:

$$v(\rho) = v_\infty \left(1 - \frac{\rho_c}{\rho}\right) \quad (2.24)$$

Here, ρ_c is the radius of curvature of a step that neither advances nor retracts when exposed to a supersaturation of level σ . ρ_c is called the critical radius of curvature.

$$\rho_c = \frac{\gamma}{n_0 k_B T \log(1 + \sigma)} \quad (2.25)$$

If the density of kinks on a step is low and the step cannot then be regarded as a hole through which atoms are drawn in one continuous flow, or if a resistance exists when adatoms are contained in kinks, thereby making it difficult to consider the density of adatoms to be an equilibrium value, it then becomes necessary to make some modifications to this derivation [5].

As described previously, the formation of a two-dimensional nucleus or of a screw dislocation are two mechanisms that can provide the surface of a crystal with a step. In the following section, we explain how a crystal grows after it has acquired a step.

2.2.2 Mechanism of two-dimensional nucleation growth

Frequency of two-dimensional nucleus formation

As explained in the section that describes how the step velocity can be calculated, atoms that enter the surface and those that leave the surface are in equilibrium; adatoms exist in a certain density and they are moving about on the surface. Therefore, they can collide and attach to each other. As these collisions and attachments take place repeatedly, many adatoms congregate and form a two-dimensional cluster. A small cluster might lose atoms and disappear, but if a cluster is exposed to fluctuations and increases in size, the probability that it will survive becomes higher. If the probability that a certain nucleus could increase in size

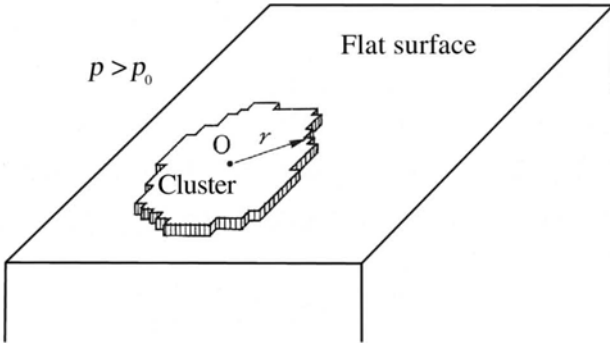


Fig. 2.4. Cluster on the flat surface (two-dimensional nucleus)

is equal to the probability that it could decrease, then such a nucleus is called a critical nucleus. To understand the size of such a cluster more clearly, we will attempt to estimate its size by assuming that the shape of a two-dimensional cluster is circular (Fig. 2.4).

We must keep a watch on the whole system, including the crystal and the growth medium. When a cluster forms on a flat crystal face, all of the atoms can be considered to be in crystalline form except those along the fringe of the cluster. The free energy decreases by the difference between the chemical potential of the growth medium and that of the crystal phase, $-\Delta\mu$ per atom. Atoms along the fringe of a cluster are exposed to external turbulence, and they behave in such a manner that they disturb the process of cluster formation. The loss in the step energy per unit length needed to form this edge is defined as γ , and the radius of the cluster is defined as r . The number of atoms that comprise a cluster is approximately $\pi r^2 n_0$, and the circumference is $2\pi r$. Therefore, the increase of $\Delta G(r)$ in free energy in the whole system can be expressed as follows:

$$\Delta G(r) = -\pi r^2 n_0 \Delta\mu + 2\pi r\gamma \tag{2.26}$$

Here, the Boltzmann factor $\exp[-\Delta G(r)/k_B T]$ is proportional to the probability of survival of a cluster with a radius of r . When a cluster has a radius of ρ^* or larger, which will serve to maximize $\Delta G(r)$, the probability of its survival increases. A cluster having a radius of ρ^* or smaller will decrease in size. This radius ρ^* is known as the two-dimensional radius of a critical nucleus. The two-dimensional radius of a critical nucleus ρ^* , and the maximum value ΔG^* of the free energy can be expressed based on maximum value conditions as follows (Fig. 2.5):

$$\rho^* = \frac{\gamma}{n_0 \Delta\mu} = \frac{\gamma}{n_0 k_B T \log(1 + \sigma)} \tag{2.27}$$

$$\Delta G^* = \frac{\pi\gamma^2}{n_0 k_B T \log(1 + \sigma)} \tag{2.28}$$

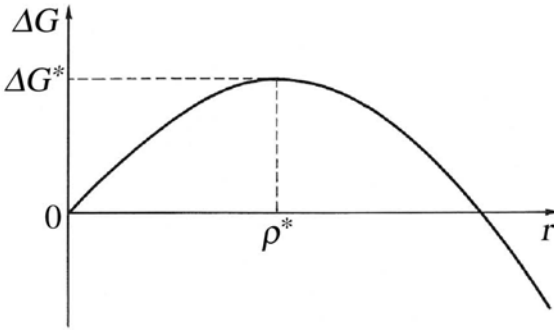


Fig. 2.5. Change of the free energy with cleating the disk cluster

Although the system is in a nonequilibrium state, nucleus formation seldom occurs. Assuming that the process proceeds according to the theory of equilibrium distribution, the density N^* of a critical nucleus can be calculated as follows, where the density of a single atom is defined as n_s :

$$N^* = n_s \exp(-\Delta G^*/k_B T) \quad (2.29)$$

Assuming that a nucleus becomes stable when one extra atom is added to it, as assumed by Volmer and Weber [6], one adatom moves to an adjacent lattice point with a frequency of D_s/a^2 . Taking this into consideration, the frequency ν^+ can be calculated using the following equation:

$$\nu^+ = 2\pi\rho^* D_s / a n_0 \quad (2.30)$$

Therefore J , the frequency of nucleus formation, can be calculated as follows:

$$J = \nu^+ N^* = 2\pi\rho^* (D_s/a) n_0^2 \exp(-\Delta G^*/k_B T) \quad (2.31)$$

This approach assumes that the process proceeds according to the theory of equilibrium distribution. Becker, Doring [7] and Zeldvich [8] demonstrated that the density of a critical nucleus in a stable state is lower than that in a state of equilibrium distribution. The value presented by them is smaller by Z (the Zeldvich factor, shown below) than J in the above equation. The Zeldvich factor Z can be calculated as follows:

$$Z = \{\Delta G(i^*) / 4\pi k_B T \cdot i^*\}^{1/2}$$

Here, i^* is the number of atoms that comprise a critical nucleus. Therefore,

$$J(\sigma) = D_s n_s^2 \{\log(1 + \sigma)\}^{1/2} \exp\left[-\pi \left(\frac{\gamma}{k_B T}\right)^2 / \log(1 + \sigma)\right] \quad (2.32)$$

As is apparent from Eq. (2.32), the frequency of two-dimensional nucleus formation J is extremely low if the level of supersaturation is low, but it quickly increases as the level of supersaturation rises. The formation of two-dimensional nu-

clei and the frequency of nucleus formation is observable if the level of supersaturation is over 10% [5].

Two-dimensional nucleus formation and growth rate

As a two-dimensional nucleus that forms with a frequency J spreads with a step velocity v , layers are formed and a plane is completed. Therefore, J and v are factors that determine the growth pattern of crystals [1].

Providing that the area of the surface of a crystal is S , the waiting time t_w during which a two-dimensional nucleus forms on the surface is $t_w = 1/J$. On the other hand, the approximate time t_s during which the fringe of an already formed two-dimensional nucleus spreads with a step velocity v and covers the whole surface of a crystal can be estimated as $t_s = \sqrt{S}/v$. Growth patterns of two-dimensional nuclei can be classified into two different mechanisms as follows, depending on the relationship between t_w and t_s .

If $t_w \gg t_s$:

Because a nucleus that has been formed after a long waiting time quickly spreads over the whole surface, one two-dimensional nucleus alone contributes to the growth of one layer. This growth pattern is known as single nucleation growth. The growth rate R_{sn} [6] is:

$$R_{sn} = dJS \quad (2.33)$$

In this growth mechanism, it should be noted that the growth rate is proportional to the area of the surface of the crystal S .

If $t_w \ll t_s$, many two-dimensional nuclei form one after another, all over the surface. They spread and couple with each other and develop layers. This growth pattern is known as multinucleation growth. Two-dimensional nuclei can also form on existing nuclei that are already spreading; this particular growth pattern is called *multinucleation multilayer growth*.

If the average distance that a nucleus travels before it couples with an adjacent nucleus during the multinuclear growth process is A , the time τ that it takes for this nucleus to travel this average distance is $\tau = \sqrt{A}/v$. On the other hand, two-dimensional nuclei form in an area A with the waiting time defined as τ , and thus steady, consistent growth can be achieved. Therefore, $\tau = 1/JA$ becomes true. From this equation, we can obtain the following:

$$\tau = \left(\frac{1}{Jv^2} \right)^{1/3}$$

Because the formation of one layer takes place in time τ , the growth rate R_{mn} can be expressed as follows:

$$R_{mn} = d/\tau = dJ^{1/3} v^{2/3} \quad (2.34)$$

We should note that the growth rate is not dependent on the area S . Area A is called the territory of influence per stable nucleus.

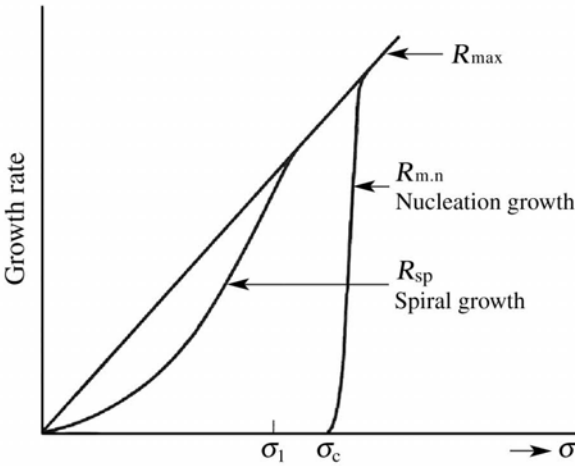


Fig. 2.6. Supersaturation dependence of the growth rate

In the case of multinuclear multilayer growth, the waiting time τ' from when the first nucleus forms to when the next nucleus forms on top of the first one can be estimated using the following equation:

$$\int_0^{\tau'} \pi J (v t)^{1/2} dt = 1 \tag{2.35}$$

The rate obtained using this equation is the same as that obtained for multinuclear growth [9].

The level of supersaturation is low under the particular condition $t_w \gg t_s$, under which single nucleus growth occurs. The growth rate is so slow that it is not observable. Therefore, any two-dimensional growth that is observable is either multinuclear growth or multinuclear multilayer growth. Fig. 2.6 shows how the level of supersaturation affects the growth rate. When the level of supersaturation is low, the rate is almost zero. As it increases, the rate quickly increases. If the level of supersaturation is low, an accurate value can be obtained using the above equation. If the level is high, an overestimated value will be obtained. (See section 2.3.1 d.)

2.2.3 Mechanism of spiral growth

In the majority of cases however, the growth of two-dimensional nuclei is observable at a low level of supersaturation, even if we hardly expected the growth to happen. This is because many crystals grow according to a spiral growth mechanism, which is closely associated with the screw dislocation.

Real crystals are not perfect crystals, and they contain defects in varying degrees. If the end of screw dislocation, which is a line defect, is exposed on the surface of a crystal, a step extending from this exposed end to the edge of the crystal

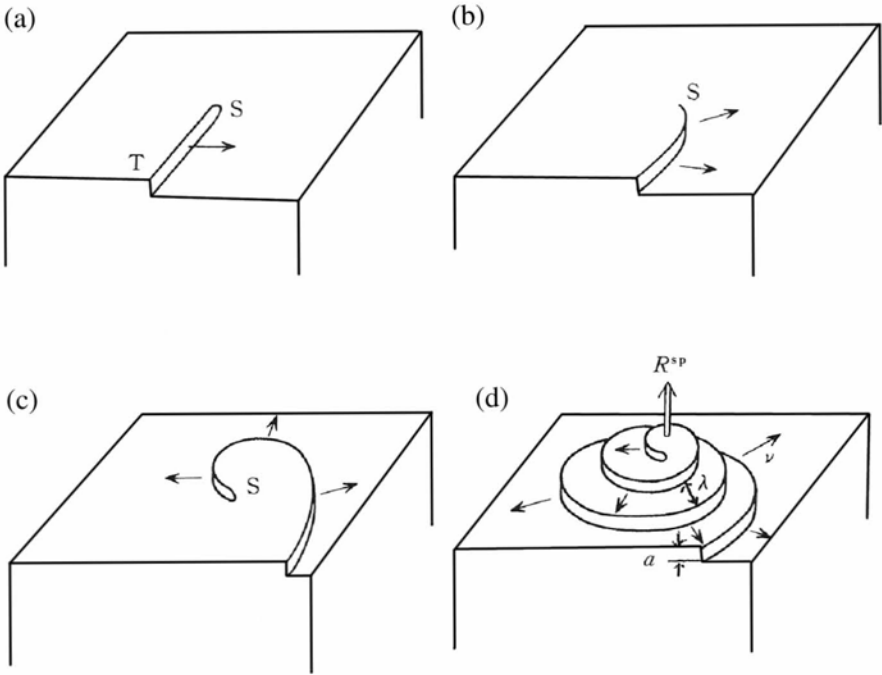


Fig. 2.7. Spiral growth by screw dislocation

surface is formed, as shown in Fig. 2.7. Although this step continues to move forward, it never disappears. Therefore, steps do not need to be supplied to allow two-dimensional nucleus formation. Growth will continue at a low level of supersaturation without any additional supply of steps. This growth mechanism is called the Frank mechanism, after F. C. Frank who first developed this theory [10].

As the step created by the screw dislocation continues to move forward, it reaches out from the point where it intersects with the surface and soon forms a spiral pattern. This is because the point where it emerges is fixed. Because the forward speed at which a curved step travels in the direction normal to the line can be calculated using Eq. (2.24), the shape of a step can be determined. On a curved coordinate system (r, θ) with the center of the spiral as the origin, an approximate stationary solution can be calculated as follows [5]:

$$\log\left(1 + \frac{r}{3\rho_c}\right) = 2\left(1 + \frac{1}{3}\right)\theta + \left[2\rho_c\left(1 + \frac{1}{3}\right)\right] \quad (2.36)$$

According to this equation, the movement of the step can be represented as being very close to an Archimedean spiral under the condition where $r \propto \theta$. Far from the

center of this spiral, the steps are aligned nearly parallel to each other with step interval λ :

$$\lambda = 4\pi(1 + 1/\sqrt{3})\rho_c \approx 20\rho_c \quad (2.37)$$

(The value $20\rho_c$ was later corrected to $19\rho_c$ by Cabrera and others [14].) The step interval λ is proportional to the critical radius of curvature, ρ_c . This is because the spiral movement continues until the radius of curvature ρ_c of a step in the center becomes ρ_c . If the step interval λ in a parallel step line is determined, the growth rate can be obtained, as previously explained, and the growth rate R_{sp} of a step moving according to the spiral growth mechanism can be calculated as follows:

$$R_{sp} = \frac{(p - p_e)\Omega}{\sqrt{2\pi m k_B T}} \frac{\sigma^2}{\sigma_1} \tanh\left(\frac{\sigma_1}{\sigma}\right) \quad (2.38)$$

Here, the level of supersaturation σ_1 is introduced as a parameter, which can be defined as follows:

$$\sigma_1 = \frac{\lambda}{2\lambda_s} \sigma \cong \frac{10\gamma}{n_0 k_B T \lambda_s} \quad (2.39)$$

If we examine the dependence of growth rates on the level of supersaturation with reference to the results obtained using Eq. (2.38), we note that R_{sp} is proportional to σ^2 if the level of supersaturation is low ($\sigma \ll \sigma_1$), and R_{sp} is proportional to σ and equal to R_{max} if the level of supersaturation is high ($\sigma \gg \sigma_1$), as shown in Fig. 2.6. If the level of supersaturation is high, we should note the following point: If the level of supersaturation becomes high, the step interval becomes smaller and many adatoms in the center of the spiral are assimilated into the surrounding steps.

This causes the actual level of supersaturation to decrease below σ , the radius of curvature of a step in the center becomes large, and the step interval λ increases. Therefore, the growth rate drops below the estimated value. Any steps generated by a step itself cause the density to decrease, and eventually the growth rate to increase, which is called the back-force or back-stress effect. This phenomenon was pointed out by Cabrera and others [11], and was analyzed by Van der Erden and others [12] in greater detail.

To obtain a reliable, approximate value, the center radius ρ_c of a spiral should not be estimated from the level of supersaturation σ in the vapor phase. Instead, we should estimate it from the level of surface supersaturation $\sigma(\rho_c, 0)$ in the center, assuming that there is a circular step with a radius ρ_c . We will not discuss this in detail here.

So far we have only dealt with the type of step that is created from one screw dislocation, and which has a height equal to that of a single atom. However, mention must be made of the fact that in the actual crystal formation process, complex steps can be created through a combination of screw dislocations of the same or of different types, and a step which is several atoms in height can be created through screw dislocations with a Burgers vector of one or greater. The points discussed here have already been analyzed in great detail by Burton, Cabrera, and Frank. The theory developed by them is called the BCF theory.

2.3 Growth of a Crystal in a Solution

In this section we discuss the mechanism of the growth of a crystal in solution. Although the density of a solution phase is higher than that of a vapor phase, the density of each growth unit (dissolved atom) in a solution phase is low. Therefore, the theory that each individual growth unit is *contained in a crystal phase* still holds true [1]. For a crystal to grow in a solution, the principle that soluble atoms can be easily dissolved into a solvate (solvation) must be used. Therefore, desolvation must take place when dissolved atoms are included into a crystal. This applies to the growth of a crystal in the vapor phase in which a strong interaction with the vapor occurs, as is the case in the chemical vapor deposition (CVD) process. In the case of growth in the vapor phase, the process where atoms are supplied from the growth medium could be ignored. In the case of growth in a solution, the diffusion coefficient of the atoms dissolved in the solution is far smaller than that in the vapor phase. Therefore, the density of atoms varies greatly in solution, so the process by which the dissolved atoms are supplied from the growth medium cannot be ignored, and the process of diffusion of dissolved atoms in a solution must be examined.

2.3.1 Solvation effects and growth rates

Diffusion in a solution [2]

Although the diffusion of dissolved atoms in a solution is taken into consideration, it is almost impossible to apply the BCF theory strictly from the analytical viewpoint. Therefore, two different approaches were taken. First, we conceived the volume diffusion model, which assumes a condition where the surface diffusion is totally ignored and the dissolved atoms are taken out of solution and placed directly onto kink positions. The second model is the surface diffusion model, which assumes that the condition for the BCF theory is applied to the neighborhood of an interface, through simplification of the volume diffusion. There is also the coupled bulk-surface diffusion model of Gilmer, Ghez, and Cabrera [13].

The first approach is based on the assumption that the volume diffusion coefficient D , is larger than the surface diffusion coefficient D_s , in the case of growth in a solution, whereas the second approach maintains that desolvation should not take place with all atoms simultaneously. Instead, the atoms should first be adsorbed onto the surface of a crystal to allow them to diffuse over the surface, and then they should migrate into kink positions, which is effectively step-by-step desolvation. When designing an experiment to observe the growth of a crystal in a solution, the solution is often stirred and therefore the level of supersaturation σ (namely, density C) in an area remote from the surface of the crystal by a distance of δ or more, is defined as a constant value that is controlled for the duration of the experiment.

In an attempt to develop a volume diffusion model, Chernov [15] inferred a diffusion field through analysis using the conformal transformation method, on the

assumption that linear steps are formed at a regular interval λ on the surface of the crystal. The boundary condition was defined as follows:

The volume diffusion flow $D (\partial C / \partial r)_{r=a}$ that arrives into a radius $r = a$ (approximately equal to the lattice constant) with a step as its origin is equal to the atomic flow $\beta_{st}[C(a) - C_e]$ entering a crystal phase from any point where there is a step. Namely,

$$D \left(\frac{\partial C}{\partial r} \right)_{r=a} = \beta_{st} [C(a) - C_e] \quad (2.40)$$

Here, C_e is the equilibrium density and β_{st} is the rate constant. These are termed the kinetic coefficients of a step. Fig. 2.8 shows the diffusion field qualitatively: the dotted line is the isosbestic line. Using Eq. (2.40), the rate of step movement v can be calculated. Also, using Eq. (2.37), the step interval λ can be calculated. Therefore, the following equation can be established, based on the spiral growth rate $R_{v,d}^{sp} = av/\lambda$, which was obtained using the volume diffusion model:

$$R_{v,d}^{sp} = \beta_{st} \frac{a^2 k_B T C_e}{4\gamma} \frac{\sigma_\delta^2}{1 + (\beta_{st} a / D) \log \left[\frac{\delta\sigma_0}{a} \sigma_\delta \sinh \left(\frac{\sigma_\delta}{\sigma_0} \right) \right]} \quad (2.41)$$

Here, γ is the step energy, a is the lattice constant, and σ_δ is the level of supersaturation in the solution. Because there are only a few cases in which this approach can be applied, it is recommended that you refer to the original work for greater detail. Here we should only mention that the square law $R_{v,d}^{sp} \propto \sigma^2$ applies if $\sigma \ll \sigma_0$ and the linearity law $R_{v,d}^{sp} \propto \sigma$ applies if $\sigma \gg \sigma_0$, which is characteristic of spiral growth.

On the other hand, we also have the surface diffusion model, as created by Bennema and others [16,17]. As shown in Fig. 2.9, this model assumes that the isosbestic point in a solution is parallel to an interface, and that the diffusion field is one-dimensional. The reasoning behind this assumption can be explained as follows: For the dissolved atoms to diffuse in a solution towards kink positions and then become included in the crystalline phase, layers of solvates on atoms must be removed. The activation energy ΔG_k^{vd} needed for desolvation is far larger than the ΔG_d needed for volume diffusion (see Fig. 2.10). Therefore, it is inconceivable to think of a flow running from a solution directly to a step from the standpoint of kinetics. On the other hand, if the dissolved atoms first adsorb onto the surface of the crystal, diffuse over the surface, and then enter kinks, the activation energy needed for desolvation can be divided into the energy for adsorbing onto the surface ΔG_{desolv} and the energy for leaving the surface and entering the kinks ΔG_k^{ad} .

Therefore, the atoms can move more smoothly by traveling this route rather than taking the route of entering kinks directly. The relaxation time $\tau_{desolv} = v^{-1} \exp(\Delta G_{desolv}/kT)$ needed for atoms to adsorb onto the surface is sufficiently longer than $\tau_d = v^{-1} \exp(\Delta G_{desolv}/kT)$, which is needed for atoms to diffuse in a solution. Therefore, the dissolved atoms become stagnant on the surface of the crystal, and

the solute density becomes uniform along its surface; that is the isobestic surface is parallel to the surface of the crystal.

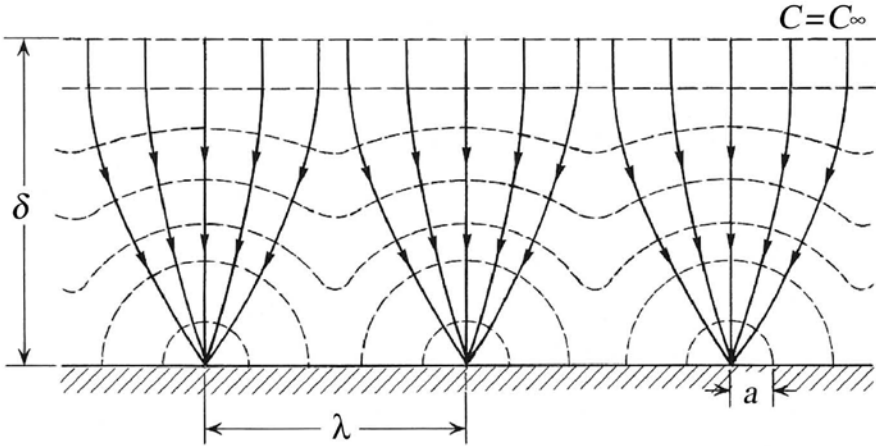


Fig. 2.8. Distribution of concentration for the volume diffusion model. The dotted line is the isobestic line.

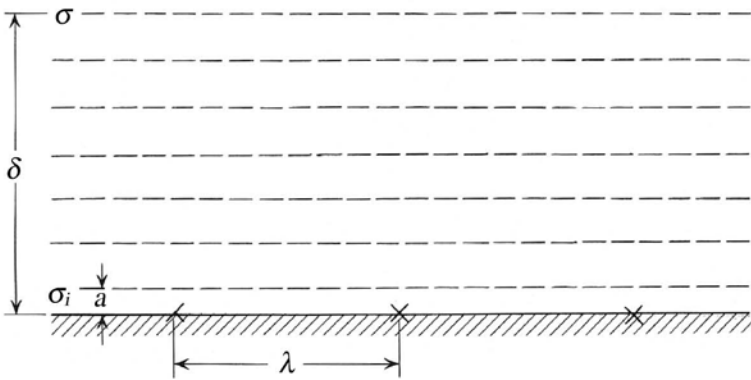


Fig. 2.9. Distribution of supersaturation for the surface diffusion model by Bennema. There are steps at the cross point.

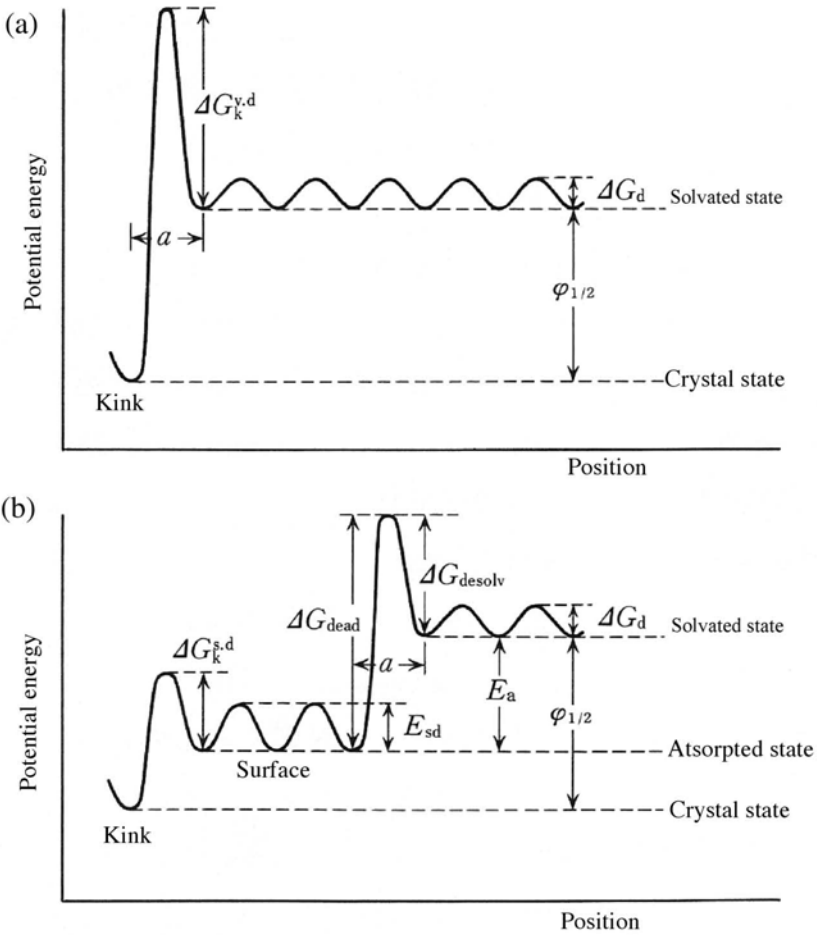


Fig. 2.10. Potential energy of desolvation

Modifying the BCF theory

The level of supersaturation at a point δ away from an interface is defined as σ , and a point which is one lattice constant a away from an interface is defined by σ_r . The excitation energy needed to allow atoms to enter kinks is $\Delta G_k^{s,d}$. Therefore, it can be assumed that a kink position, which can be considered as identical to a step because a step has many kinks, has a supersaturation σ_k . If we use the same approach as that used for growth in the vapor phase, the net flow J_v from the solution to the surface of the crystal can be calculated as follows. Assuming that the solute density directly above the surface is C_i and the equilibrium density of the surface is C_e :

$$J_v = a(C - C_e)v \exp(-\Delta G_{desolv}/k_B T) = aC_e v \exp(-\Delta G_{desolv}/k_B T)(\sigma_i - \sigma_k) \quad (2.42)$$

Therefore, a counterpart equation to Eq. (2.21) for the growth in a vapor phase is

$$R_{BCF} = \frac{a}{\tau_{desolv}} C_e \Omega \left[\frac{2\lambda_s}{\lambda} \tanh\left(\frac{\lambda}{2\lambda_s}\right) \right] (\sigma_i - \sigma_k) \quad (2.43)$$

However, the surface diffusion distance λ_s is not controlled by the adsorption energy E_a , but depends on the excitation energy ΔG_{dead} needed for desolvation. According to the result obtained from $\Delta G_{dead} \gg E_a$, the value of λ_s is nearly as long as the length that we found in the case of growth in the vapor phase.

The growth rate R_{diff} that is determined from the volume diffusion in a solution can be calculated using the volume diffusion coefficient D , as follows:

$$R_{diff} = DC_e \Omega \frac{\sigma - \sigma_i}{\delta} \quad (2.44)$$

Lastly, the rate R_{kink} , which is determined by the speed that atoms enter the kink positions, can be calculated using the flow of atoms into kinks per unit length of step J_s as follows:

$$R_{kink} = 2\Omega / \lambda J_s = \frac{2an_e \Omega}{\lambda \tau_k} \sigma_k \quad (2.45)$$

Here, n_e is the equilibrium density at the kink position, and τ_k is the relaxation time that atoms require before they enter kinks.

$$\tau_k = v^{-1} \exp(\Delta G_k^{s,d}/k_B T)$$

Because these three growth rates must be equal in a steady state, we have the following equation:

$$R_{diff}(\sigma - \sigma_i) = R_{BCF}(\sigma_i - \sigma_k) = R_{kink}(\sigma_k) \quad (2.46)$$

The growth rate R can be calculated using the following equation, which takes the results from $\sigma = (\sigma - \sigma_i) + (\sigma_i - \sigma_k) + \sigma_k$ into account:

$$R = \frac{C_e \Omega a}{\tau_{desolv}} \sigma \left[\frac{\delta a}{\tau_{desolv} D} + \frac{\lambda}{2\lambda_s} \coth\left(\frac{\lambda}{2\lambda_s}\right) + \frac{\tau_k}{\tau_{dead}} \frac{\lambda}{2a} \right]^{-1} \quad (2.47)$$

The first term is the resistance resulting from the volume diffusion, the second term is the resistance resulting from the surface diffusion mechanism, and the third term is the kink resistance. Although the second term is always greater than unity, the first and second terms are considered to be $\ll 1$ in a system in which the solvation effects are significant. Therefore, the assumptions of $\sigma - \sigma_i \approx \sigma$, $\sigma_k = 0$ are valid, and we can approximate as follows:

$$R \equiv \frac{C_e \Omega a}{\tau_{desolv}} \sigma \frac{2\lambda_s}{\lambda} \tanh\left(\frac{\lambda}{2\lambda_s}\right) \quad (2.48)$$

Because the step interval λ in spiral growth is $20\rho_c$, which was calculated for growth in the vapor phase, the growth rate can be calculated as follows:

$$R_s = C \frac{\sigma^2}{\sigma_1} \tanh\left(\frac{\sigma_1}{\sigma}\right) \quad (2.49)$$

$$\sigma_1 = 10 \frac{\gamma}{k_B T} \frac{a}{\lambda_s}$$

$$C = C_e \Omega a / \tau_{desolv}$$

In the region where the level of supersaturation is low, that is, where $\sigma \ll \sigma_1$, the growth rate is proportional to the supersaturation squared. In the region where the level of supersaturation is high, that is, where $\sigma \gg \sigma_1$, growth rate is proportional to the supersaturation. If an interface has many steps and the surface is rough, the growth rate can be calculated using the following equation, which is called the *Wilson-Frenkel Formula*:

$$R_{max} = av \exp(-\Delta G_{desolv}/k_B T) C_e \Omega \sigma \quad (2.50)$$

Two-dimensional nucleation growth

As far as the basic concept of the growth mechanism from a two-dimensional nucleation is concerned, growth in a solution is the same as growth in the vapor phase. However, for growth in a solution, the following equation is used, which contains the solution density C and the equilibrium density C_e to obtain the driving force $\Delta\mu$:

$$\Delta\mu = k_B T \log(1 + \sigma), \quad \sigma = (C - C_e)/C_e \quad (2.51)$$

Including desolvation effects, the frequency ν^+ at which one adatom is included into a critical nucleus can be expressed as follows:

$$\nu^+ = 2\pi\rho^* \frac{D_s}{a} \exp(-\Delta G_{k_b}^{s,d}/k_B T) \quad (2.52)$$

The growth speed of multinuclear multilayer growth $(\pi/3)^{1/3} \nu^{2/3} J^{1/3}$ can be calculated using the above equation in combination with the following:

$$R_n = A \sigma^{5/6} \exp[-\Delta G^*/3k_B T] \quad (2.53)$$

$$A = \left(\frac{2\pi c_0}{3}\right)^{1/3} \frac{2\lambda_s}{a} C$$

Here it is assumed that $\sigma \ll 1$, so $\log(1 + \sigma) \sim \sigma$, and c_0 results from the desolvation effects [17].

The energy needed to form a critical nucleus ΔG^* governs the frequency of two-dimensional nucleus formation, and it is greatly influenced by a reduction in step energy of a two-dimensional nucleus γ . Because atoms in a step can interact with the solutes when growing in a solution, it is expected that the step energy γ is smaller by one order of magnitude than that for growth in the vapor phase. Solvation effects work to inhibit growth if a crystal undergoes the spiral growth process,

whereas they work to promote growth if a crystal undergoes two-dimensional nucleus growth.

Figure 2.11 illustrates the spiral growth formula (2.49) based on the step energy $\gamma/(n_0 k_B T) = 0.2$, $\lambda_s = 100a$, the rate constant $C = 10^{-3}$ mm/sec, $c_0 = 10^{-2}$, and the two-dimensional nucleus growth formula (2.53). The two-dimensional nucleus growth formula does not include the effects of the slowdown of migration speeds that result from a decrease in the level of supersaturation on a terrace when the interval λ between steps becomes smaller than λ_s . Neither does it include the decreased frequency of two-dimensional nucleus formation (back-force effects), which results from a decrease in the level of supersaturation on a two-dimensional nucleus when a two-dimensional nucleus is growing. Therefore, the result given by this formula may exceed the maximum growth rate given by the Wilson-Frenkel formula. However, at a level of supersaturation of 0.7% or lower, it is estimated that the growth rate can be measured correctly. Unlike growth in the vapor phase, realistic growth rates can be obtained at such low supersaturations.

Back-force effects

If the level of supersaturation becomes high and nucleus formation occurs frequently, the intervals between the creation of steps becomes small. If multinuclear multilayer growth is taking place, the crystal should be growing while straight steps are forming at an interval λ if this is taking place at a location remote from where the nucleus forms. For a crystal to grow in a steady state, the growth rate $R(\lambda)$, which is determined by λ , must be equal to the rate of nucleus formation, R_n . In Eq. (2.53), R_n is the migration speed of steps at the fringe of the nucleus v_∞ . The migration rate v_∞ should be slower than the migration rate $v(\lambda)$ of steps being formed at an interval λ . Therefore, a minor modification must be made by replacing v_∞ with $v(\lambda)$. If this modification is made, the growth rate of two-dimensional nucleus formation does not exceed the maximum growth rate given by the Wilson-Frenkel formula. However, calculations must be done using specific numerical values. Besides this, the presence of steps was ignored in our estimation of the frequency of nucleus formation; therefore, the supersaturation is overestimated. In the case of steps near a nucleus, their speed of movement is slower than $v(\lambda)$ and the step interval is less than λ because the curvature cannot be ignored, that is after a nucleus forms, the next nucleus will form on a cluster that has a radius smaller than λ . Assuming that the cluster is circular and that its radius is ρ , the level of supersaturation $\sigma_s(0)$ in the center of the cluster can be expressed using the level of supersaturation of an interface σ_i as follows:

$$\sigma_s(0, \rho) = \sigma_i - (\sigma - \sigma_{eq}(\rho)) / I_0(\rho/\lambda_s) \quad (2.54)$$

Here, $\sigma_{eq}(\rho)$ is the equilibrium level of supersaturation of a circular step that has a radius of curvature of ρ and I_0 is a class-1 Bessel function.

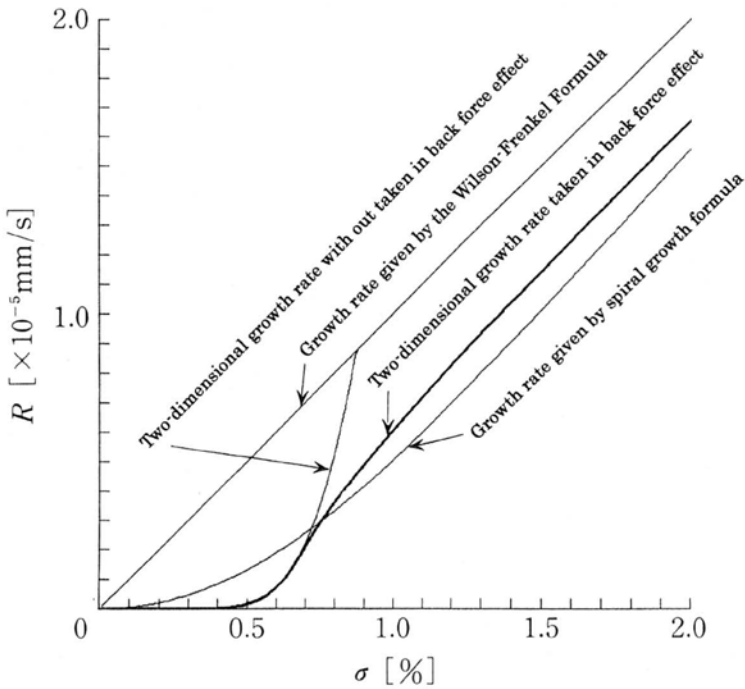


Fig. 2.11. Growth rate for a solution growth

Therefore, to estimate the frequency of nucleus formation, the level of supersaturation $\sigma(0, \lambda)$ at the center of a disk with a radius of curvature of at least λ must be used. In Fig. 2.11, the thick line shows the growth rates obtained by making these modifications and performing numerical calculations. This indicates that the result obtained using the back-force effects deviates from that obtained using the formula (2.53) if the supersaturation is low. Also, these growth rates exceed the rates of spiral growth. This is because the introduction of the back-force effect was insufficient. For further details, refer to Reference 18.

2.3.2 Handling of polyhedral finite crystals [2,19]

When a crystal is still small and growing slowly at a moderate supersaturation in solution or in the vapor phase, its form is a clear-cut polyhedron. If the level of supersaturation is increased as the crystal grows in size, we can observe an osseous crystal or a dendriform crystal, which looks like a snow crystal. Using the conventional approach, where the surface of the crystal is infinitely large, we cannot explain this phenomenon. We should note that there is a limit to the size of a polyhedral crystal, and we will discuss here the stability of such a crystal. Although growth in a solution is taken as an example, the observations presented here can also be applied to growth from a gas mixture in the vapor phase.

Berg effects

It is well known that a crystal extracted from a lean or rarefied growth medium will be a polyhedral crystal. This means that the crystal is undergoing epitaxial growth, with the growth rate determined at the interfaces. Berg [20] examined a crystal undergoing epitaxial growth to verify the density, or supersaturation, distribution in a solution using the light interference technique. He found that the density distribution is not uniform at the interface of a crystal, and that the density is high at the edges and smallest in the center, as shown in Fig. 2.12. This is called the Berg effect. If the migration speed of each point at an interface is proportional to the local supersaturation, then the edges grow more than the other regions, and therefore a polyhedron cannot be maintained.

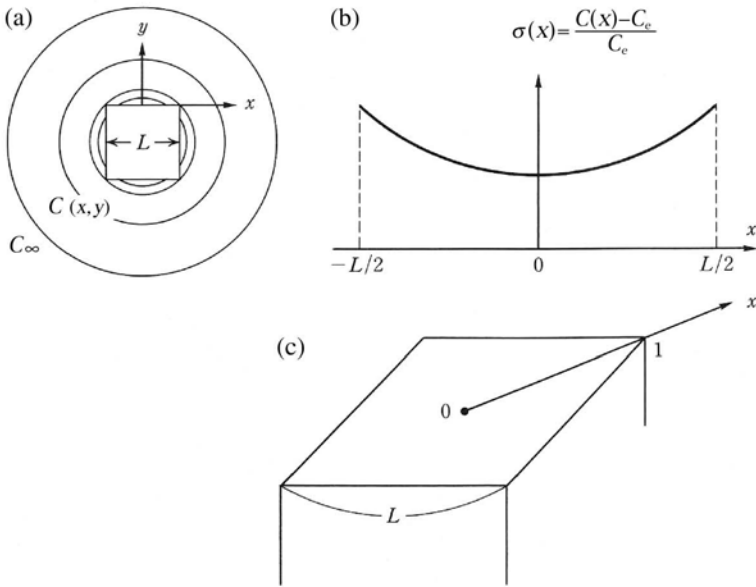


Fig. 2.12. Solute density distribution in a solution

Stable growth

Here we assume that a crystal is a cube with side of length L . Because the growth rate is very slow, the distribution, C , of solute density in a solution is considered to be in a quasistationary state (stationary distribution), that is:

$$\Delta C = 0 \tag{2.55}$$

Boundary conditions include the density C_∞ specified at a sufficiently remote point (the solution is not stirred), as well as the uniform density gradient $(\partial C / \partial n)$ in the

direction of a normal line on the surface, which can be calculated with the following equation:

$$\left(\frac{\partial C}{\partial n} \right)_{\text{surface}} = q \quad (2.56)$$

Eq. (2.56) means that the growth rate to be determined by the volume diffusion flow must be uniform at any point on the surface when a polyhedral crystal grows. The growth rate can be expressed as follows:

$$R_D(x) = \Omega D q \quad (2.57)$$

Here, Ω is the volume of a dissolved atom and D is the volume diffusion coefficient. If space is two-dimensional, this equation can be solved holomorphically using the conformal transformation method [21]. If space is three-dimensional, it must be solved numerically. If the solutions of the equation $f(x, y, z)$ are obtained in advance under each condition of $L = 1$, $q = 1$, $C_\infty = 0$, then solutions for L , q , and C_∞ can be calculated based on the linearity of the Laplace formula by using the following equation:

$$C(x, y, z) = C_\infty + q L f(x/L, y/L, z/L) \quad (2.58)$$

Here, although f is negative, the f -coefficient is equal to a value obtained by multiplying the growth speed q by the crystal size L . The greater the magnitude of qL , the larger the difference between the density in the center and that at the edges.

Focusing on the surface kinetics, the growth rate at each point of an interface is

$$R(x) = av(x)/\lambda(x) = p(x) \cdot v(x) \quad (2.59)$$

Here, v is the migration rate of a step, λ is the interval between steps, a is the lattice constant, and $p(x) = a/\lambda(x)$ is the tilt of an interface from the low-index plane. Hereafter, the center of the plane is defined as $x = 0$ and an edge is defined as $x = 1$. $v(x)$, $\lambda(x)$, and $p(x)$ are not uniform on an interface. According to Eq. (2.59), a polyhedron cannot be maintained unless these parameters are uniform across each face. If fluctuations in the migration rate $v(x)$ of a step can be compensated by the local tilt $p(x)$ of an interface, it becomes possible to maintain a polyhedron [22]. Because $v(x)$ actually becomes higher at the edges and slower in the center due to the nonuniformity in the supersaturation (Fig. 2.13), an interface should be tilted more toward the center of the plane.

A step-source that produces a step must then be determined. To create a step source, two mechanisms are conceivable: the formation of a two-dimensional nucleus and the activation of a screw dislocation. If a step source is created by a screw dislocation, the crystal seed is exposed around the center of an interface in the majority of cases. In this case, the growth rate near the step source is governed by the level of supersaturation $\sigma(0)$ in the center of the plane, and Eq. (2.49) is used with σ replaced by $\sigma(0)$. If the formation of a two-dimensional nucleus is the step source, the growth rate is governed by the level of supersaturation at the edges $\sigma(1)$, where the level of supersaturation is highest. To obtain the growth rate at the edges, Eq. (2.53) is used, with σ replaced by $\sigma(1)$.

R_s and R_n are generally not equal. Therefore, a plane must be covered by steps that are generated by higher-value step sources. That is,

$$R_k = \max \{R_s, R_n\} \tag{2.60}$$

In this equation, R_k must be equal to the growth rate R_D , which is determined by the diffusion flow. It is evident that $R_D(\sigma_\infty, L, q)$ is a function of the supersaturation at a remote point σ_∞ , the size of the crystal L , and the density gradient q . Additionally, $R_k(\sigma_\infty, L, q)$ is a function of σ_∞, L , and q in terms of the supersaturation

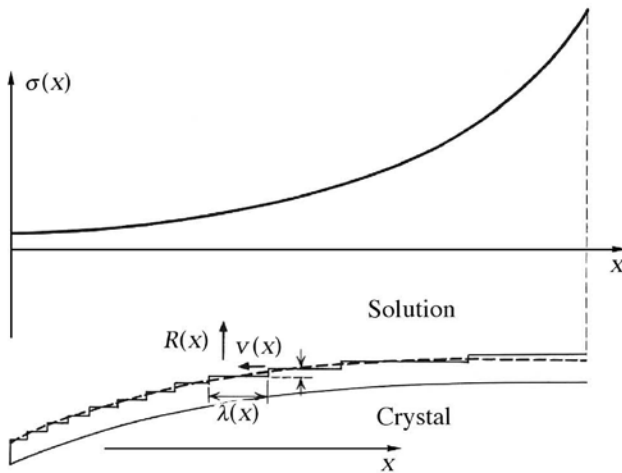


Fig. 2.13. Distribution of supersaturation and a surface morphology

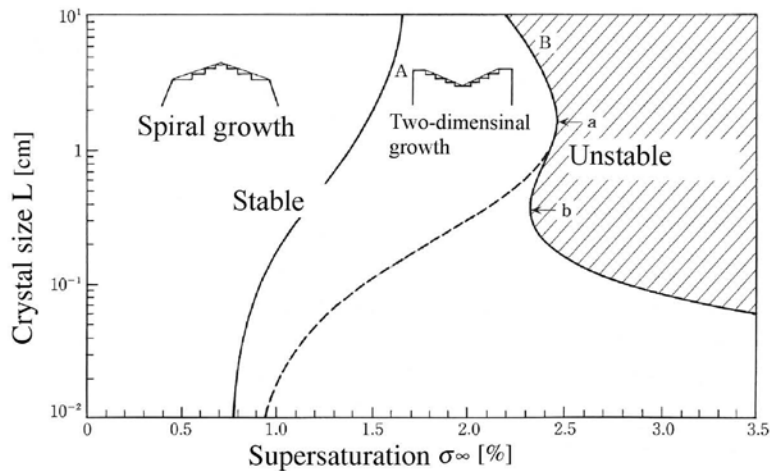


Fig. 2.14. Critical line for stable growth condition

at the interface. Therefore, if the values of σ_∞ and L are known, the growth rate q can be determined. At the same time, the step source can be identified as well as its external form.

Therefore, the criticality condition that determines the step source can be expressed as follows:

$$R_s \{ \sigma(0; \sigma_\infty^*, L^*) \} = R_n \{ \sigma(1; \sigma_\infty^*, L^*) \} \quad (2.61)$$

Figure 2.14 shows the supersaturation at remote points σ^∞ along the abscissa and the crystal size along the ordinate. The base values in the diffusion field are approximately $f(0) = -0.9$ and $f(1) = -0.7$. The curved line A shows the critical levels of supersaturation that may transform step sources in the stable growth region. Because it is difficult for the formation of a two-dimensional nucleus to take place where the supersaturation is low, the screw dislocation governed by the supersaturation $\sigma(0)$ on the surface center becomes the step source, and the external form of the crystal becomes convex. A screw dislocation can produce a concave surface too (see Fig. 2.9a of Nelson and Knight). On the other hand, if the level of supersaturation at a remote point is increased, the level of supersaturation at the edges becomes high, and the formation of a two-dimensional nucleus governed by $\sigma(1)$ becomes the step source. In this case, the external form of the crystal surfaces becomes concave.

Occurrence of unstable conditions

As Eq. (2.58) suggests, the nonuniformity in the supersaturation increases if the size of a crystal becomes large, or if the growth rate q becomes too high.

$$R(x) = p(x) \cdot v(x) = R_D = \text{constant} \quad (2.62)$$

At the point where the above conditional expression holds true, the crystal is unable to maintain its polyhedral form and consequently cannot grow with uniform flux across the face. This is because, technically, this is *not* a growth instability; it is a uniform-flux impossibility. The cause of this is that the migration rate of a step becomes dependent on not only the supersaturation σ , but also the step interval λ ; thus, the growth rates of local interfaces reach a maximum, even if the tilt of the plane around the center is increased. Therefore, the criticality condition for stable (or “uniform”) growth can be expressed as follows:

$$R_{\max}(0) \equiv C \sigma(0; \sigma_\infty^{**}, L^{**}) = R_n \left[\sigma(1; \sigma_\infty^{**}, L^{**}) \right] \quad (2.63)$$

The dotted line of the criticality curve B in Fig. 2.14 shows stable growth without including the back-force effects (Eq. 2.53), whereas the thick solid line includes the back-force effects. As is apparent from this figure, we could postulate that the back-force effects are a key factor responsible for allowing a small crystal to grow in a stable way while still maintaining a polyhedral form. At point *a* of the criticality curve, the supersaturation at the edge of the crystal surface is about 0.64% and at point *b* it is around 0.84%. This level of supersaturation at the interface is much lower than the value of 2.3% at a remote point. Although λ_s was de-

fined as being equal to $100a$ in this calculation, the growth rate becomes slow if the surface diffusion distance becomes short. Therefore, the stable region moves off to the side, where the level of supersaturation is high.

In the course of studying growth in an unstable region, an equation was introduced for verifying how the external form of a crystal develops over time. This is a new topic that has many applications to the formation of crystal forms [24–26].

References

1. Hartman P (ed) *Crystal growth: An introduction*, North-Holland, Amsterdam (1972)
2. Chernov AA (1984) *Modern Crystallography III*, Springer-Verlag, Berlin; New York
3. Kossel W (1927) *Nachr Ges Wiss Gottingen* 135 (in German)
4. Stranski IN (1928) *Z Phys Chem* 136:259 (in German)
5. Burton WK, Cabrera N, Frank FC (1951) *Phil Trans Roy Soc A* 243:299
6. Volmer M, Weber A (1926) *Z Phys Chem A* 119:277
7. Becker R, Doring W (1935) *Ann Phy* [5]24:719
8. Zeldvich J (1942) *J Exp Theor Phys* 12:525
9. Hillig WB (1966) *Acta Met* 14:1868
10. Frank FC (1949) *Disc Faraday Soc* 5:48
11. Cabrera N, Coleman RV (1963) *The Art and Science of Growing Crystals*, Gilman JJ (ed) 3, Wiley, New York
12. van der Eerden JP (1981) *J Crystal Growth* 53:305
13. Gilmer GH, Ghez R, Cabrera N (1971) *J Crystal Growth* 8:79
14. Cabrera N, Levine MM (1956) *Phil Mag* 1:450
15. Chernov AA (1961) *Sov Phys Uspeki* 4:116
16. Bennema P (1969) *J Crystal Growth* 5:29
17. Bennema P, Gilmer GH, *Crystal Growth*, Hartman P (ed) North Holland, Amsterdam, p 263
18. Arima Y, Irisawa T (1990) *J Crystal Growth* 104:297
19. Kuroda T, Irisawa T, Ookawa A (1977) *J Crystal Growth* 42:11
20. Berg WF (1938) *Proc Roy Soc A* 164:79
21. Seeger A (1953) *Phil Mag* 44:1
22. Chernov AA (1974) *J Crystal Growth* 24/25:11
23. Nelson, Knight (1998) *J Atmospheric Sciences* 55:1452–1465
24. Yokoyama E, Kuroda T (1990) *Phys Rev A* 41:2038
25. Wood SE, Baker MB, Calhoun D (2001) *J Geophys Res* 106:4845–4870
26. Nelson J (2001) *Phil Mag A* 81(9)

3 Epitaxial Growth of III-V Compounds

T. Nishinaga and S. Naritsuka

Department of Materials Science and Engineering, Meijo University 1-501,
Shiogama-guchi, Tempaku, Nagoya, 468-8502, Japan

3.1 Introduction

The first event that showed the importance of III-V epitaxy was the success of Alferov in 1969 in fabricating a cw laser diode that operated at room temperature by liquid phase epitaxy (LPE). For this, he received the Nobel Prize in physics in 2000 with two other scientists. LPE, which was proposed by Nelson [1], makes high quality, thin-film semiconductors. In III-V LPE, the compounds are grown from group-III metal solution on a substrate, which gives highly stoichiometric, thin, pure, and perfect films.

The next important event in the history of III-V epitaxy is the invention of a high electron mobility transistor (HEMT) by Mimura et al. [2], which was made by molecular beam epitaxy (MBE). They used the idea of modulation doping, which was originally proposed by Dingle et al. [3].

The growth technology of high quality and ultra-thin III-V films of about 10 nm thickness was required for the fabrication of HEMT. At that time, such films could be grown only by MBE. Almost at the same time, the technology of metal organic chemical vapor deposition (MOCVD) was developed and employed for growing high quality thin films. Without MBE and MOCVD, neither HEMT nor high performance laser diodes such as quantum well (QW) and multi-quantum well (MQW) lasers could be made.

Recent success in growing high quality GaN and related compounds was made by Amano et al. [4] by using a low temperature buffer layer on sapphire in MOCVD. The huge improvement in crystal quality thus realized made it possible to get p-type GaN. The success of p-GaN was a real breakthrough for making blue-ultraviolet lasers and light emitting diodes.

In this chapter, we focus on MBE and MOCVD as examples of epitaxy because they are the major technologies in III-V epitaxy.

3.2 MBE of III-V Compounds

In molecular beam epitaxy (MBE), the growth is conducted under an ultra-high vacuum of up to $10^{-8} \sim 10^{-9}$ Pa. Under such a high vacuum, O_2 , CO_2 , H_2O , and N_2 contamination on the growing surface can be negligible. This makes it possible to reduce the growth rate down to nm/sec, so that precise control of the growth thickness is possible.

As described in the next section, MBE uses a Knudsen cell (or effusion cell) from which growth elements are evaporated. By opening and closing the shutter in front of the Knudsen cell, the operator can abruptly switch on or off the fluxes; hence, sharp interfaces between successively grown layers are possible.

Another important advantage of MBE is that *in situ* monitoring of the growing surface is possible. Reflection high-energy electron diffraction (RHEED) is one of the most powerful tools used to see the flatness and atomic structure of the surface during growth. Furthermore, intensity oscillation of the RHEED signal accurately measures the growth rate in $\text{\AA}/\text{sec}$.

3.2.1 MBE system

Figure 3.1 shows a schematic of a conventional MBE machine. An ion-sputtering pump evacuates the growth chamber to a high vacuum, typically. To keep the chamber at high vacuum during the growth, a liquid N_2 shroud like that shown in the figure is employed. An electron beam is aimed at the substrate, then the diffracted beam strikes a fluorescent screen. In the case of GaAs MBE, at first the substrate is heated at high temperature under arsenic pressure to remove the oxide layer. Because the oxide evaporation happens at around 580°C and this event can be monitored by RHEED, the oxide removal can be used to calibrate the temperature of the substrate. Then, after setting the substrate temperature at the required value, the Ga shutter is opened to start the growth. To grow (Ga, Al)As, one opens the shutters of both Ga and Al cells. Choosing Ga and Al cell temperatures varies the composition of the alloy. An n-type and p-type GaAs layer can be grown by opening the shutter of the Si cell and Be cell, respectively.

Sample exchange should be carried out keeping the growth chamber at high vacuum. This can be done employing either a two-chamber or a three-chamber system. Figure 3.1 shows a two-chamber system, which is composed of a growth chamber and a preparation chamber. The preparation chamber is also evacuated at high vacuum and the second sample is already installed inside. After the experiment, without breaking the vacuum, the grown sample is transferred through the gate valve to the preparation chamber, and the next sample is transferred to the growth chamber by a transfer rod. Thus, a high vacuum is kept for a long time until a problem occurs in the chamber. In such a case, the chamber should be opened to the air during the repair. When source materials such as Ga, As, Al are finished, the growth chamber should be opened and new sources recharged.

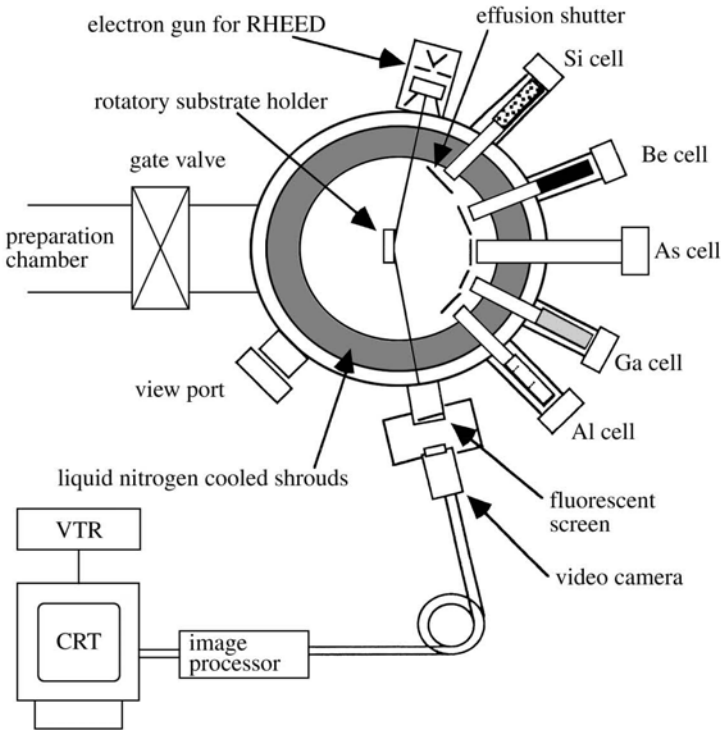


Fig. 3.1. Schematic illustration of the conventional two-chamber MBE

3.2.2 RHEED intensity oscillation

RHEED intensity oscillations (hereafter, RHEED oscillations) provide extremely important information about the growth in real time. Already in 1980, it was reported that an AES (Auger Electron Spectroscopy) signal shows oscillation as the growth thickness of a thin film is increased [5]. Just after this work, Harris et al. reported that the RHEED intensity oscillates as the film thickness is increased in GaAs MBE, and they showed that the period coincides with the time for monolayer growth [6]. One year later, Gronwald and Henzlan observed intensity oscillations of the low energy electron diffraction (LEED) signal during the MBE of Si on a (111) substrate, and confirmed that the period coincides with the growth time of (111) double layers [7].

In 1983, Neave et al. studied RHEED oscillations of GaAs in more detail, and concluded that this oscillation is caused by the birth and spread of 2D-nuclei that happen repeatedly during growth [8].

Schematics of this process from Neave et al. are given in Fig. 3.2 and 3.3. As shown in Fig. 3.2, just after the shutter of a Ga cell is opened, the intensity drops sharply while it recovers to a value slightly below the previous peak. Figure 3.3

shows what happens during one period of the oscillation. Here, θ is the coverage of the surface. Before growth, the surface of the substrate, in this case (001), is very flat as shown in (a). This can be realized by preparing the surface of the substrate exactly ($< 0.01^\circ$) oriented to (001). Then, the steps supplied from misoriented substrate can be nearly eliminated. As the growth starts, 2D-nuclei are generated on the substrate as shown in (b). The electron beam is partly scattered by the 2D nuclei and lost resulting in the decrease of the RHEED intensity. As growth proceeds, many 2D nuclei are generated (c), and the intensity is further decreased. However, those 2D nuclei start to coalesce to form a continuous layer (d) and as the flatness is recovered the intensity begins to increase. When the coalescence is completed the intensity increases to the initial value. In the experiment, as we see in Fig. 3.2, the recovery of the intensity is not complete. This happens because 2D-nucleation of the second layer starts on the surface like that in Fig. 3.3 (d). Due to this, this growing surface becomes rough as growth proceeds. However, the surface flatness is recovered when the Ga shutter is closed and the growth is stopped as shown in Fig. 3.2.

RHEED oscillations can be used to control the growth thickness on the order of a monolayer and actually is a very powerful tool used to fabricate sophisticated electronic and optical devices with complicated structures. RHEED oscillations are also a very powerful tool for studying the elementary growth process of MBE because it can detect the birth and spread of 2D-nuclei under various growth conditions.

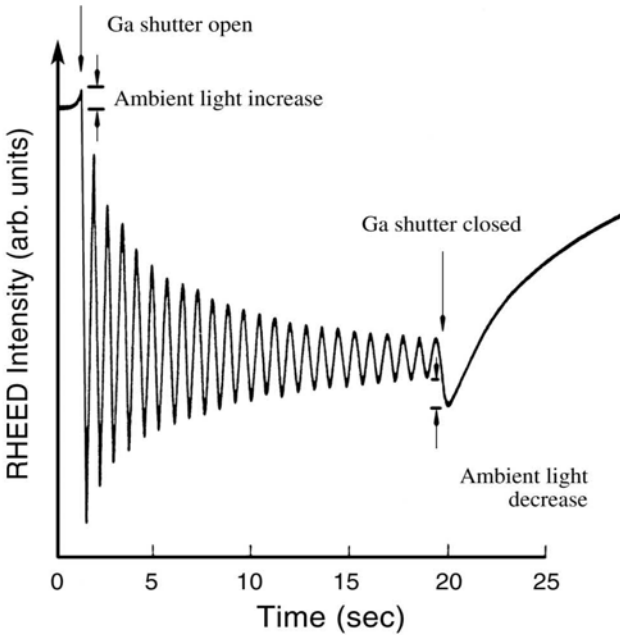


Fig. 3.2. RHEED intensity oscillation observed in MBE of GaAs [8]

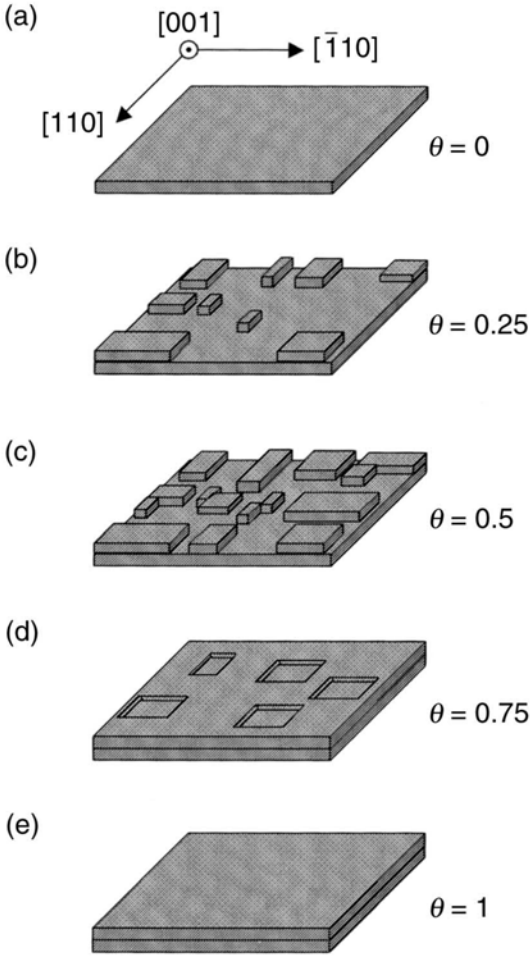


Fig. 3.3. Illustrations of the surface during MBE in 2D-nucleation growth mode. θ denotes the surface coverage [8].

3.2.3 Surface diffusion and stepped surface

According to BCF theory [9], the adatom concentration $n_s(y)$ on a vicinal (stepped) surface shown in Fig. 3.4 is given by

$$n_s(y) = J\tau_s + (n_{\text{step}} - J\tau_s)\cosh(y/\lambda_o)/\cosh(\lambda_o/2\lambda_s) \quad (3.1)$$

where J , τ_s , λ_s , n_{step} and λ_o are respectively the incident flux of growing atoms, the re-evaporation time, the diffusion length for re-evaporation, the adatom concentration near the step edge, and the interstep distance.

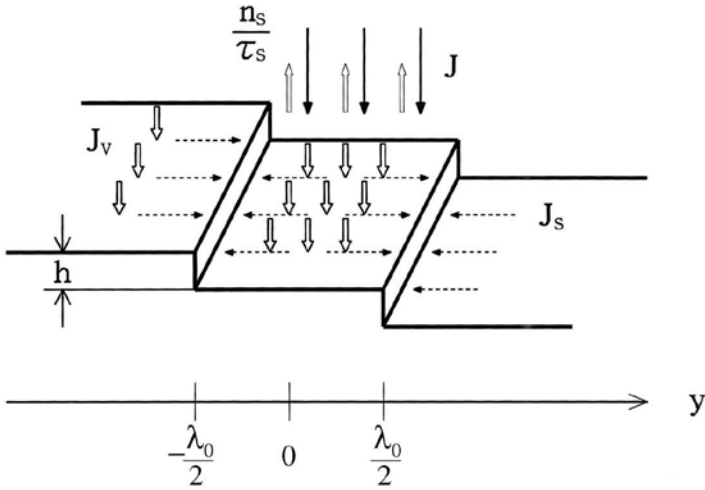


Fig. 3.4. Vicinal (stepped) surface

$n_s(y)$ is schematically shown in Figs. 3.5 and 3.6 respectively for $\lambda_o \gg \lambda_s$ and $\lambda_o \ll \lambda_s$. If λ_o is much larger than λ_s , $n_s(y)$ increases as a function of distance from a step edge and saturates at a constant value after a certain distance, as shown in Fig. 3.5. On the other hand if $\lambda_o \ll \lambda_s$, one can neglect the evaporation of adatoms from the surface and $n_s(y)$ is given by

$$n_s(y) = n_{step} + (J\lambda_o^2/8D_s)[1 - (2y/\lambda_o)^2] \tag{3.2}$$

In this case, $n_s(y)$ is parabolic as shown in Fig. 3.6. In III-V MBE, the vapor pressure of a group III element is very low at the growth temperature and $\lambda_o \ll \lambda_s$ is usually established.

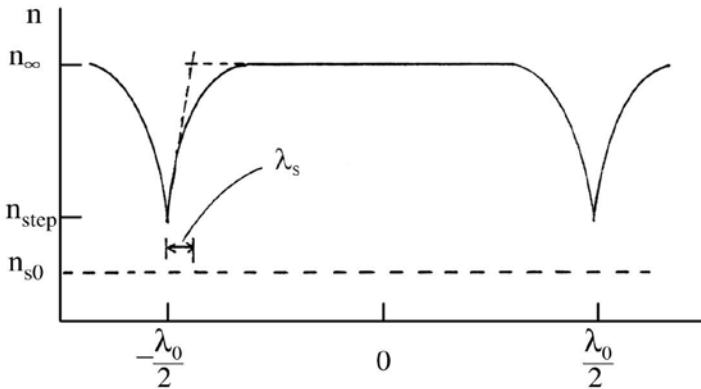


Fig. 3.5. $n_s(y)$ as a function of the position between steps for $\lambda_o \gg \lambda_s$

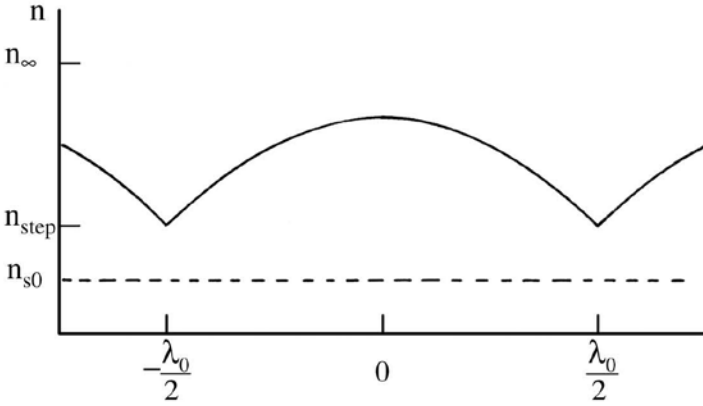


Fig. 3.6. $n_s(y)$ for $\lambda_0 \ll \lambda_s$.

3.2.4 2D-nucleation and step flow modes

In 1985, Neave et al. did an important experiment [10]. They used a slightly misoriented (001) GaAs as a substrate and observed the surface by RHEED during MBE growth of GaAs. The result is shown in Fig. 3.7. They found that as the growth temperature increased, RHEED oscillations vanished at a certain temperature. They explained the reason for the vanishing oscillations as follows. When the temperature is low and the adatom migration velocity is slow, it takes time for the adatom to reach the step edge and thus the adatoms can instead cluster to form 2D-nuclei. This causes the RHEED oscillation as shown in the bottom figure of Fig. 3.7 (a). On the other hand, when the growth temperature is high, adatoms can move very fast to easily reach the step edge before contacting other adatoms. In this case, all adatoms go to the step edges without forming the 2D-nuclei as shown in the top figure of Fig. 3.7 (a). Under their growth condition, the critical temperature for the mode transition T_c is 590°C . Above this temperature, all steps advance in one direction and this mode of the growth is called step flow. On the other hand, below this temperature, 2D-nuclei are generated between steps and as growth proceeds, they coalesce to each other to form a new layer. This growth mode is called the 2D-nucleation growth mode.

From this experiment, Neave et al. calculated the surface diffusion length as a function of temperature as follows. They assumed at the critical temperature for the mode transition the diffusion length becomes equal to the step distance, λ_0 . This assumption gives

$$\lambda_0 = \sqrt{D_s \tau}, \quad (3.3)$$

where τ is some kind of relaxation time and D_s is the surface diffusion coefficient. For the numerical value of τ , they used the monolayer growth time.

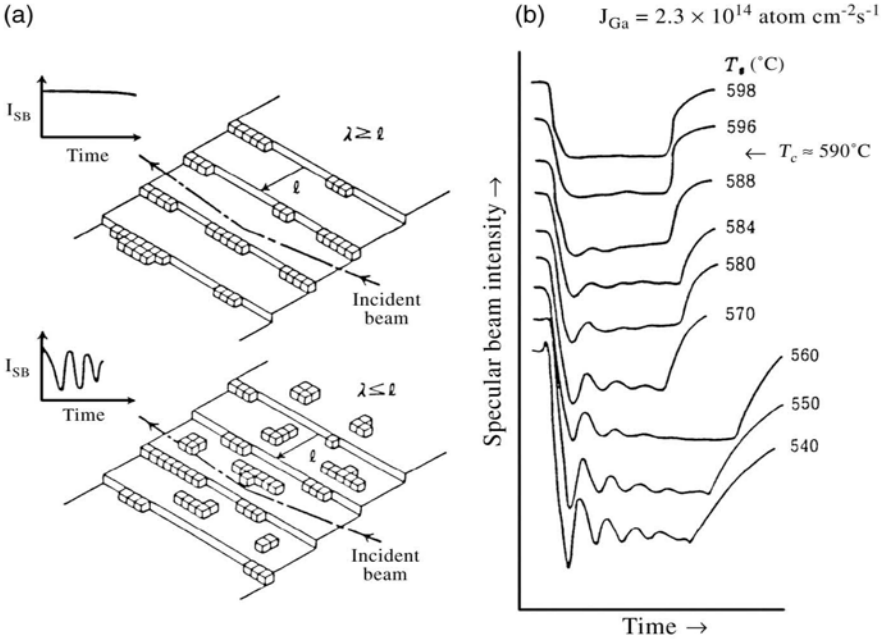


Fig. 3.7. Change of growth modes between 2D-nucleation and step flow. (a) Illustrations of the surface for the two modes, (b) RHEED oscillations and growth temperature [10]

With Eq. 3.3, they calculated D_s as a function of growth temperature. However, there is no physical meaning of the diffusion length for monolayer growth. Instead, τ should be used as an average nucleation time. Namely, if adatoms can diffuse in a longer distance than λ_o , the adatoms can reach the step edge before generating nuclei and the growth occurs in step flow mode. Hence, the critical condition for the mode transition should be

$$\lambda_o = \sqrt{D_s \tau_{nuc}}, \quad (3.4)$$

where τ_{nuc} is an average time for one adatom to form a nucleus. If the size of the critical nucleus is two atoms, τ_{nuc} becomes identical with a collision time τ_{coll} . However, this assumption may not be true for all cases so we have to derive a more reliable equation.

Before doing this, we will estimate D_s . If we employ the equation given by Neave et al., we get $D_s \sim 10^{-12} \text{ cm}^2/\text{sec}$ with $\lambda_o = 10 \text{ nm}$ and $\tau = 1 \text{ s}$. On the other hand, a typical value of τ_{nuc} is 1 msec, which gives $D_s \sim 10^{-9} \text{ cm}^2/\text{sec}$. This value is 10^3 larger than Neave's value. Hence, we have to study this problem more carefully.

Figure 3.8 shows the distribution of interface supersaturation between two steps. In this figure, we assumed that a thermal equilibrium is established at the step edges and we defined supersaturation ratio as

$$\alpha = n_s/n_{so}, \quad (3.5)$$

where n_{s0} means the equilibrium surface concentration of adatoms. This ratio is unity at the step edges. However, once 2D-nuclei are generated the supersaturation drops around them so that profile of supersaturation given in Fig. 3.8 no longer exists.

At the critical temperature, the top of the parabola touches the line of critical supersaturation ratio α shown in Fig. 3.8. The critical supersaturation for 2D nucleation is given by [11]

$$\alpha_c = \exp\left\{\Omega\pi h\sigma^2\left[(65 - \ln 10^{12})K^2T^2\right]^{-1}\right\} \quad (3.6)$$

where Ω , h , and σ are, respectively, the solid atomic volume, the step height, and the free energy of the side surface surrounding a 2D-nucleus. Because the supersaturation is maximum in the center of the step terrace, one can calculate the value with Eq. (3.1) as

$$\alpha_{\max} = 1 + J\lambda_0^2/8D_s n_{s0} \quad (3.7)$$

At the critical temperature,

$$\alpha_c = \alpha_{\max} \quad (3.8)$$

should hold. The values for T , J , and λ_0 can be obtained if the growth conditions are known. σ can be given if an approximation such as a bond breaking model is employed. However, n_{s0} includes the unknown re-evaporation time of the group III element. If we can know this value, we can determine D_s from the experiment, but so far this has not been possible.

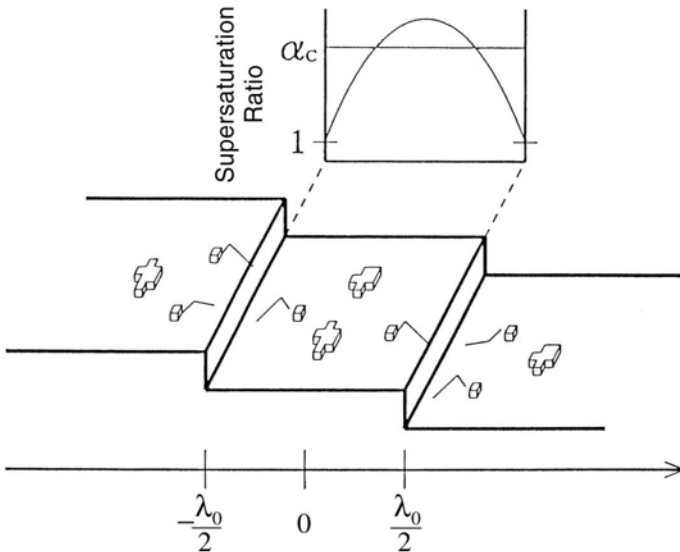


Fig. 3.8. Distribution of supersaturation between two steps

3.2.5 Critical temperature and growth conditions

Figure 3.9 shows T_c as a function of growth rate for two different misorientations. As seen in the figure, T_c increases as the growth rate increases. This means that as the growth rate increases, 2D nucleation occurs more easily. The schematic for the Ga adatom distribution between steps is given in Fig. 3.10, where α_{step} denotes α at the step edge. If the re-evaporation rate of Ga is negligibly small, as in the case of GaAs MBE, n_s follows a parabolic curve [12] and takes the maximum and the minimum, respectively, at the center between steps and at their edges. Now, at low growth rates, the number of Ga atoms arriving on the terrace is small so that the maximum supersaturation cannot reach α_c and the growth occurs in step flow mode. However, if the growth velocity is increased, the maximum increases and above a critical growth velocity α exceeds α_c and the mode change occurs from the step flow to the 2D nucleation.

Figure 3.11 shows T_c as a function of the interstep distance under a constant growth rate. As seen in the figure, T_c increases with increasing step distance. This means that a larger step distance makes 2D nucleation easier. Schematics of the Ga adatom distributions for two different interstep distances are given in Fig. 3.12. When the step distance is short, the total number of Ga atoms arriving on the step terrace becomes small so that the gradient of n_s at the step edge becomes small. This makes the maximum at the center also small, leading to step flow growth.

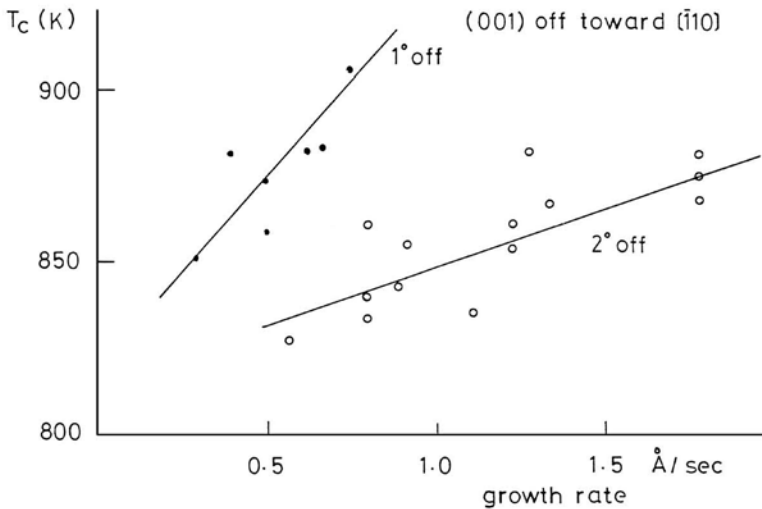


Fig. 3.9. Critical growth temperature for the mode transition vs. growth rate

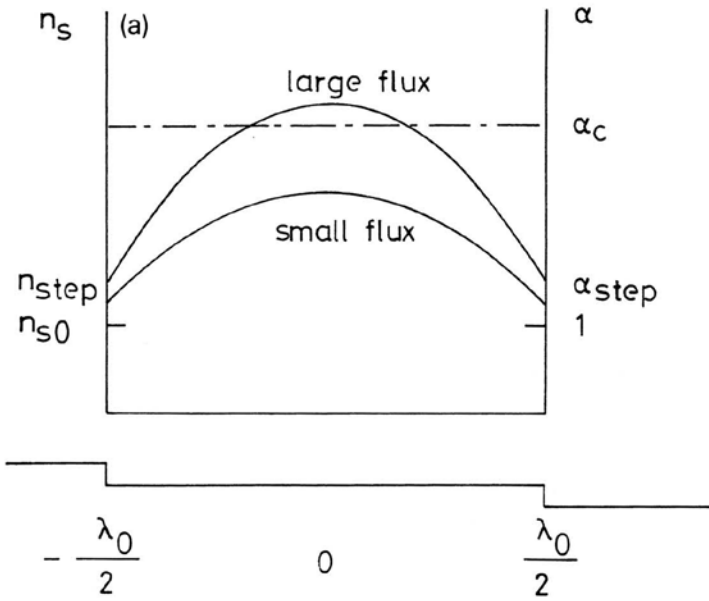


Fig. 3.10. Distribution of the adatom concentration between steps for different Ga fluxes

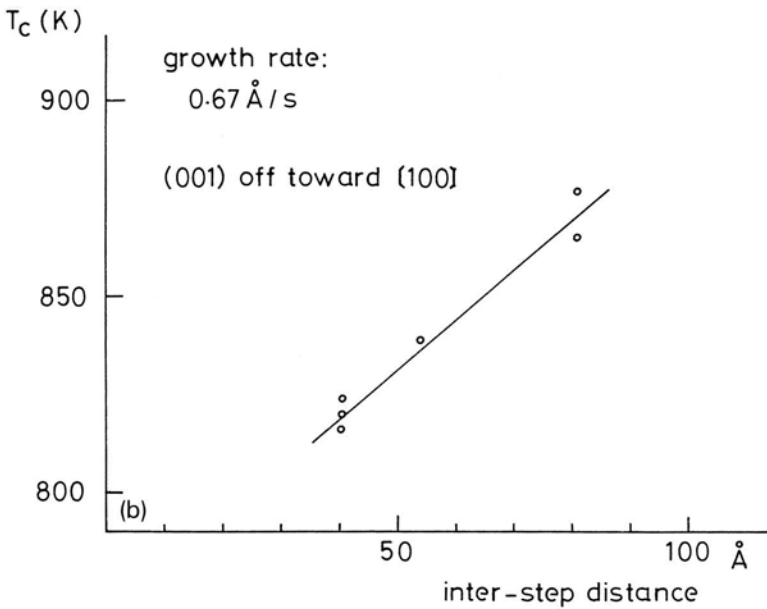


Fig. 3.11. Critical growth temperatures for the mode transition vs. step distance

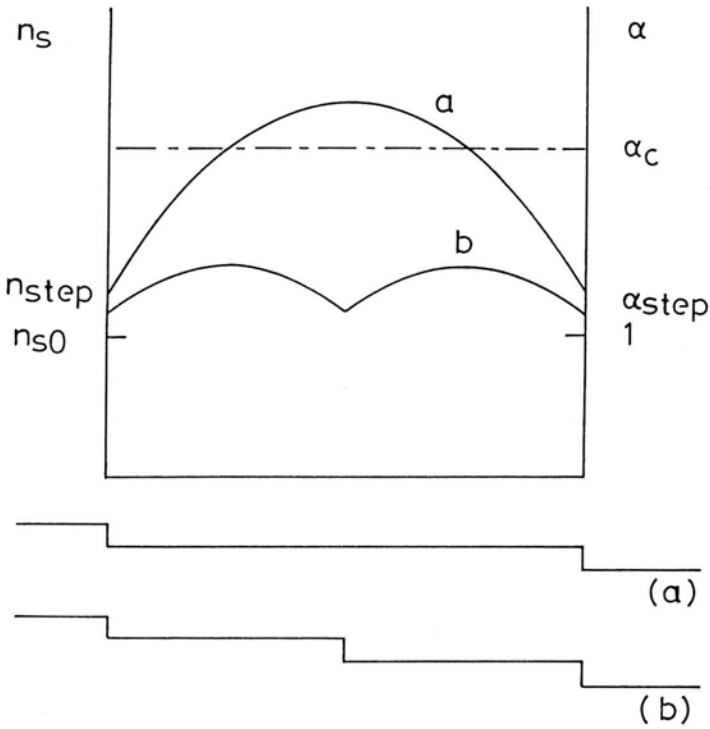


Fig. 3.12. Distribution of the adatom concentration between steps for different step distances

3.2.6 Incorporation diffusion length

There are two kinds of diffusion lengths employed in the theory of crystal growth. One is the average distance of an adatom between arrival and evaporating points. However, in MBE of GaAs, Ga atoms are difficult to evaporate at typical growth temperatures and stay until they are incorporated into the crystal. The other is the incorporation diffusion length λ_{inc} that is defined as the distance between arrival and incorporating points. The concept of the incorporation diffusion length is not clear compared with the evaporation diffusion length because the former depends on the step density and the arsenic pressure in the case of GaAs MBE, whereas the latter is defined on an ideal surface where no step exists and hence is a simple function of the temperature, and also depends on the adsorption and desorption energies. However, the incorporation diffusion length is a key parameter that characterizes the growth in nanostructure fabrication.

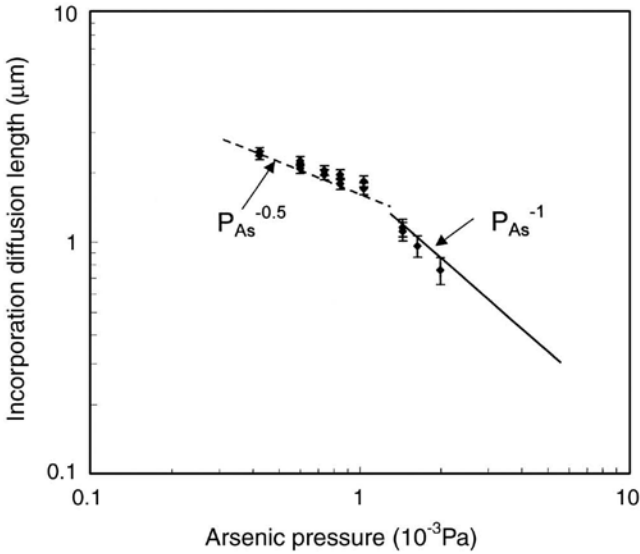


Fig. 3.13. Arsenic pressure dependence of the incorporation diffusion length of Ga on the (001) surface. The growth temperature and the side surface were respectively 580°C and (110).

The incorporation diffusion length can be determined experimentally by measuring the distribution of growth rate on a facet where the growth atoms diffuse laterally from or to the next facet. During MBE of GaAs, Ga adatoms can diffuse about 1–10 μm before incorporation. It has been shown that on (001) surfaces, the incorporation diffusion length of Ga depends on the arsenic pressure [13,14]. In our previous report, we showed the diffusion length is inversely proportional to the As_4 pressure. However, we found that when the arsenic pressure is low, the diffusion length is inversely proportional to the square root of the As_4 pressure. The dependence of λ_{inc} on arsenic pressure on (001) surface is given in Fig. 3.13. For this figure, the arsenic pressure has been recalculated so that the arsenic flux impinges normal to the (001) surface.

λ_{inc} is given by the well-known formula

$$\lambda_{\text{inc}} = \sqrt{D_s \tau_{\text{inc}}} \quad (3.9)$$

where D_s and τ_{inc} denote the diffusion coefficient and the incorporation lifetime of Ga adatoms, respectively. Because the GaAs growth rate R_{GaAs} is proportional to the inverse of τ_{inc} ,

$$R_{\text{GaAs}} = A_1 / \tau_{\text{inc}} \quad (3.10)$$

where A_1 is a constant. From Fig. 3.13,

$$\lambda_{\text{inc}} = A_2 P_{\text{As}_4}^{-n} \quad (3.11)$$

where A_2 is a constant and n takes the values of 0.5 and 1 when P_{As_4} is lower than 8×10^{-4} Pa and higher than this value, respectively. With the Eqs. from (3.9) to (3.11) we get,

$$R_{GaAs} = A_3 P_{As_4} \quad (P_{As_4} \leq 8 \times 10^{-4} \text{ Pa}) \quad (3.12)$$

$$= A_3 P_{As_4}^2 \quad (P_{As_4} \geq 8 \times 10^{-4} \text{ Pa}) \quad (3.13)$$

respectively, for lower and higher As_4 pressures. Eq. (3.12) shows that at lower As_4 pressure R_{GaAs} is proportional to P_{As_4} , which means one As_4 molecule decomposes and gives active arsenic atoms or molecules for the growth. On the other hand, at high arsenic pressure, Eq. (3.13) shows that two As_4 molecules react to give the active arsenic atoms or molecules. There is no information to determine the kind of the active arsenic atoms or molecules, but As_2 is the most probable candidate [15–17].

3.2.7 Intersurface diffusion

When two facets are generated side by side during the growth, Ga atoms diffuse from one facet to the other depending on the growth conditions. We call this intersurface diffusion. If there is a difference in adatom concentration, surface diffusion occurs assuming there is no potential difference and no barrier exists between the facets. Once intersurface diffusion occurs, one facet grows faster than the other, and the facet growing fast will disappear quickly [18,19]. Thus, during growth many facets appear and disappear and only a few facets remain in the final stage of growth. For the fabrication of nanostructures, the relative growth rate among various facets during the growth is important. However, the growth rate of facets depends on the growth conditions, and hence one should understand what the factor is that determines the growth rate.

By measuring the growth rate distribution on one facet near the boundary, one can know the direction of the intersurface diffusion [20,21]. Figure 3.14 shows the principle. In this figure, $x = 0$ is the position of the boundary between two facets. The growth rate distribution can be obtained by microprobe-RHEED by measuring the intensity oscillation. As shown in the figure, if the growth rate decreases as the distance is increased, one knows the lateral flux occurs from the adjacent facet ($x < 0$) to the facet ($x > 0$) on which the growth rate distribution is measured. Whereas, if the growth rate increases as the distance is increased, the intersurface diffusion is in the opposite direction.

We measured the distribution of the growth velocity on the (001) surface of GaAs. As the side facet, we have chosen the (111)B surface. Instead of measuring the whole distribution, we measured the growth rate at two points. One is on the facet and close to the boundary and the other is the point on the facet very far from the boundary. We define each growth rate as R_{corner} and R_{planar} , respectively. Figure 3.15 shows the results for a combination of (111)B–(001) facets. In the figure,

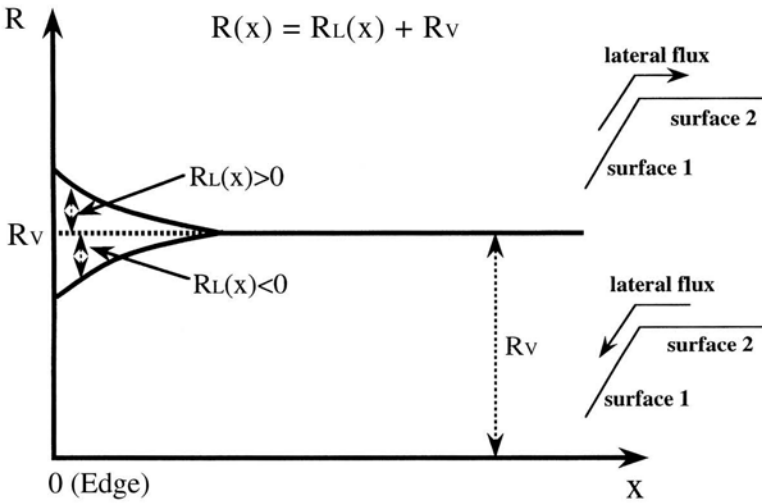


Fig. 3.14. Schematic of the growth rate $R(x)$ as a function of position x from the boundary between two facets. R_L is the growth rate caused by lateral flux, and R_V is the growth rate caused by the direct flux. R_V equals the growth rate far from the boundary.

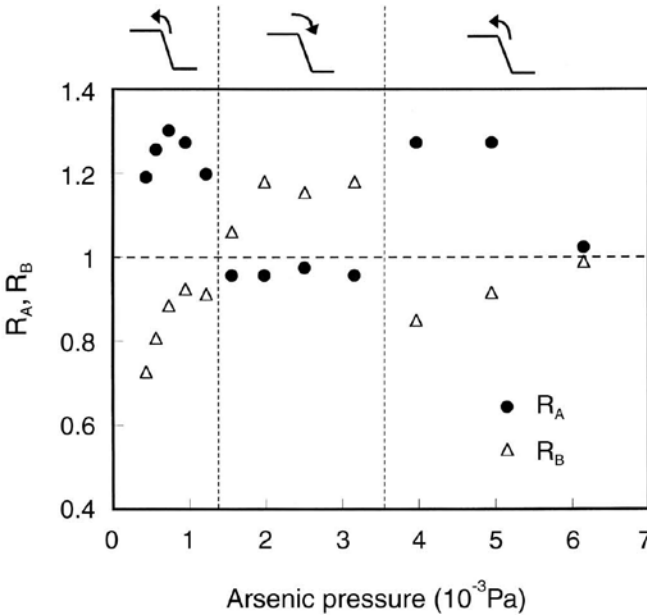


Fig. 3.15. Normalized growth rate on (001) near the boundary and that on (111)B vs. arsenic pressure. $R_A = R_{\text{corner}}^{(001)} / R_{\text{corner}}^{(001)}$ and $R_B = R_{\text{corner}}^{(111)B} / R_{\text{planar}}^{(111)B}$

closed circles and open triangles denote $R_{\text{corner}}^{(001)} / R_{\text{planar}}^{(001)}$ and $R_{\text{corner}}^{(111)\text{B}} / R_{\text{planar}}^{(111)\text{B}}$, respectively. Here, we define these normalized growth rates as R_A and R_B , respectively. When the arsenic pressure is low, R_A is larger than unity. As easily understood with Fig. 3.14, this indicates that Ga adatoms diffuse from (111)B to (001). On the other hand, R_B is lower than unity which indicates that Ga adatoms diffuse from (111)B to (001); this is consistent with the direction given by R_A . As the arsenic pressure increases, R_A decreases and crosses the line of unity at the arsenic pressure of 1.4×10^{-3} Pa, which means the direction of the lateral flow is reversed, namely, from (001) to (111)B. At the same arsenic pressure, R_B also crosses the line of unity from the lower side to the higher side. This is very important because if this does not happen, one cannot assume a pure two-face inter-surface diffusion [20]. As the arsenic pressure is increased, both R_A and R_B keep almost constant values, but as the arsenic pressure is further increased, they again cross the line of unity which means the direction of the diffusion has reversed again. The direction of the diffusion for each arsenic pressure range is given at the top of the figure.

3.2.8 Elementary growth processes

Based on the above experimental results, we discuss the elementary growth processes involved in the MBE growth of GaAs.

Growth mode

In section 3.2.7, we showed that Ga adatoms diffuse from one facet to the other. With the measured growth rate distribution on a facet, such as that drawn in Fig. 3.14, one can deduce the diffusion length of incorporation. This is how we obtained the arsenic pressure dependence of the incorporation diffusion length in Fig. 3.13. Here, the experimental growth rate was measured by RHEED intensity oscillations so that the growth can be understood as being conducted in 2D nucleation mode. This means that the birth and spread of 2D nuclei are continually happening during growth and Ga adatoms diffuse between and over the 2D nuclei. The incorporation lifetime of Ga, τ_{inc} that was defined in section 3.2.6, should be the function of the available number of incorporation sites. Hence, in this situation, the number changes periodically with the same periodicity but in opposite phase of RHEED intensity oscillations. Nevertheless, we can define the time average of τ_{inc} and λ_{inc} that was described in section 3.2.6.

The average distance of the adatom incorporation is about 1 μm ; therefore, under arsenic pressure, Ga adatoms can cross over many steps formed by 2D nucleation. Hence, the sticking coefficient of Ga adatoms at the step edges is much less than unity.

Change in the direction of intersurface diffusion

Intersurface diffusion occurs if there is a difference in Ga adatom concentrations between two facets. Here, we assume there is no potential difference and no barrier between these faces. But, there is no evidence for these assumptions.

The adatom concentration of Ga, n_{Ga} , is proportional to the incident flux of Ga, J_{Ga} , and τ_{inc} as

$$n_{\text{Ga}} = J_{\text{Ga}} \tau_{\text{inc}} \quad (3.14)$$

As we have discussed, τ_{inc} is inversely proportional to the available number of Ga sites, in other words, to the step density. The step density depends on the number of 2D nuclei and their sizes. Hence, τ_{inc} depends on the nucleation rate and the energy barrier for Ga adatoms to enter and to leave the kink site on a step. There is almost no information on their energies, so that we should be satisfied at this moment with qualitative discussions.

In section 3.2.7, we showed the experimental observation for the change in the diffusion direction. These experimental findings also give us information of elementary growth processes. Figure 3.15 showed that the direction of the intersurface diffusion changes twice as the arsenic pressure increases. At the reversal with the highest arsenic pressure, the reconstruction of (111)B changes from $(\sqrt{19} \times \sqrt{19})$ to (2×2) as arsenic pressure increases, while the reconstruction of (001) remains at (2×4) . It is known that the (2×2) reconstruction consists of an arsenic trimer that is difficult to decompose. Hence, once the (2×2) reconstruction is formed, 2D nucleation might be more difficult, and this causes the increase of τ_{inc} and hence increases the Ga adatom concentration.

The direction reversal with the lower As pressure of 1.4×10^{-3} Pa was explained in terms of the difference in arsenic pressure dependence of τ_{inc} on (001) and (111)B facets. In our previous paper, we extrapolated the $P_{\text{As}_4}^{-4}$ dependency of τ_{inc} on (111)B, but as described in section 3.3, we recently found that there is a region in the lower arsenic pressure side where τ_{inc} depends on $P_{\text{As}_4}^{-2}$. So that up to now, our previous conclusion for the $P_{\text{As}_4}^{-4}$ dependency of τ_{inc} that is responsible for the direction reversal probably should be changed to a $P_{\text{As}_4}^{-2}$ dependency. If this is the case, we should assume a $P_{\text{As}_4}^{-1}$ dependency for the (001) surface and a $P_{\text{As}_4}^{-2}$ dependency for the (111)B surface that allows the crossing of τ_{inc} on (111)B and τ_{inc} on (001) at the arsenic pressure of around 1.4×10^{-3} Pa.

3.3 MOCVD of III-V Compounds

3.3.1 Growth of high-purity materials by MOCVD

It has been said that the materials grown by MOCVD have inferior purity compared to those grown by other growth techniques such as MBE and LPE. But it is time to correct this inaccurate description about MOCVD. State-of-the-art data

shows that the purity of materials grown by MOCVD already have become a strong competitor to MBE-grown materials. In this section, we describe the present status and the origins of the residual impurities in GaAs and AlGaAs grown by MOCVD.

Hata et al. reported on an extensive study of the origin of residual impurities in GaAs and AlGaAs grown by MOCVD [23]. In their experiments, epitaxial layers of GaAs and AlGaAs were grown using two lots of TMG, two lots of TMA, and six lots of AsH₃ to examine the effects of source materials on their properties. The analytical data for TMG and TMA are listed in Table 3.1, and the electrical properties of undoped GaAs obtained from Hall measurement at 77 K are summarized in Table 3.2. Though the analytical data of TMG #1 and TMG #2 show a noticeable difference, the electrical properties of GaAs layers are nearly identical. The properties of the layers seem to depend more on the choice of the AsH₃ cylinder. Germanium (S8, S9, S10, and S15) and silicon (S11) were detected as main donors in each layer. From these results, they concluded that most of the residual impurities of donors, Ge or Si, were carried into the system by AsH₃ because the same TMG were used throughout the series of experiments.

On the other hand, carbon acceptors were detected by the photoluminescence measurement in all samples [23]. The residual C, probably coming from TMG, decreases as the AsH₃/TMG ratio increases. The highest mobility at 77 K of 153,000 cm²/V s with an electron concentration of 3.4×10^{13} cm⁻³ was obtained by optimizing the conditions. This value is nearly comparable to those from MBE-grown GaAs layers. In addition to this measurement, Hanna et al. also reported a high purity GaAs layer with an excellent mobility of 162,000 at 77 K with an electron concentration of 8.7×10^{13} cm⁻³ [23].

The electrical properties of undoped AlGaAs were reported to largely depend on the purity of the source materials [22]. Figure 3.16 shows the electrical properties of undoped Al_{0.2}Ga_{0.8}As obtained from Hall measurements at RT. When AsH₃ was used without purification, the layers grown at 700°C showed a p-n conversion depending on the AsH₃/(TMG+TMA) ratio, which is similar to the case of GaAs. However, the layers grown at 650°C had a high resistance for a wide range of AsH₃/(TMG+TMA) ratios, and had no near-band emission in the PL measurement. This indicates that a large amount of deep centers associated with oxygen in AsH₃ are included in these layers. When AsH₃ was passed through a ternary (Al:In:Ga = 1:10:100) melt, the quality of the AlGaAs layers grown at 650°C was

Table 3.1. Analytical Data for TMG and TMA by Atomic Absorption [22]

Lot No.	Si [ppm]	Fe [ppm]	Zn [ppm]	Cu [ppm]	Sn [ppm]
TMG #1	0.3	<0.2	0.6	0.2	0.2
TMG #2	0.2	<0.1	0.1	<0.1	<0.1
TMA #1	0.1	<0.1	<0.1	0.3	<0.1
TMA #2	<0.1	0.1	<0.1	<0.1	<0.1

Table 3.2. Electrical Properties of GaAs that were Obtained from Hall Measurements [22]

Sample No.	Source lot		Growth conditions		Electronic properties	
	TMG	AsH ₃	AsH ₃ /TMG	Temp. [°C]	n at 77 K [cm ⁻³]	μ at 77 K [cm ² /V • s]
S1	#1	#A	50	650	2.2×10^{14}	80,200
S2	#1	#D	50	650	High resistivity	
S3	#1	#D	70	650	3.6×10^{13}	152,000
S4	#2	#D	30	650	High resistivity	
S5	#2	#D	40	650	High resistivity	
S6	#2	#D	50	650	High resistivity	
S7	#2	#D	60	650	High resistivity	
S8	#2	#D	70	650	3.4×10^{13}	153,000
S9	#2	#D	80	650	4.2×10^{13}	139,000
S10	#2	#A	50	650	3.2×10^{14}	89,000
S11	#2	#B	50	650	6.1×10^{13}	135,000
S12	#2	#C	50	650	8.1×10^{14}	63,300
S13	#2	#E	50	650	1.3×10^{15}	57,400
S14	#2	#F	50	650	3.8×10^{15}	32,000
S15	#2	#F	200	700	5.1×10^{16}	9,280

improved to equal that of layers grown at 700°C. The purity of TMA is also very important to obtain high-quality AlGaAs layers. The oxygen impurities in TMA, such as methoxide (-OMe), was reported to be the origin of oxygen impurities in AlGaAs layers [24]. The oxygen concentration increases when the AlAs mole fraction increases, but decreases when either the AsH₃/(TMG + TMA) ratio or the growth temperature increases [24]. Oxygen is thought to form deep electron traps that compensate carriers and act as nonradiative centers. Similarly, Yamanaka et al. reported that oxygen-related deep levels also exist in MBE-grown AlGaAs layers. The concentration of these levels increases with increasing AlAs mole fraction and decreases with increasing growth temperature. But, on the contrary to the former report, these levels increase with increasing As/Ga flux ratio [25,26]. The incorporation behavior is similar, and these oxygen-related deep levels were known to act both as electron traps and nonradiative centers [26]. Naritsuka et al. reported that the deep levels originate from arsenic oxide, usually from a surface oxide of arsenic source in the MBE [27]. They also reported that oxygen becomes a deep donor in InAlAs grown by MOCVD and that the oxygen incorporation dependence on the growth conditions is quite similar to that of AlGaAs [28,29], which strongly suggests that the origin of the oxygen impurities is almost the same.

As described above, O, Si, Ge, and C are major impurities in MOCVD. Numerous studies have found ways to decrease these residual impurities and, as a result, the quality of epitaxial layers has significantly improved. Various kinds of

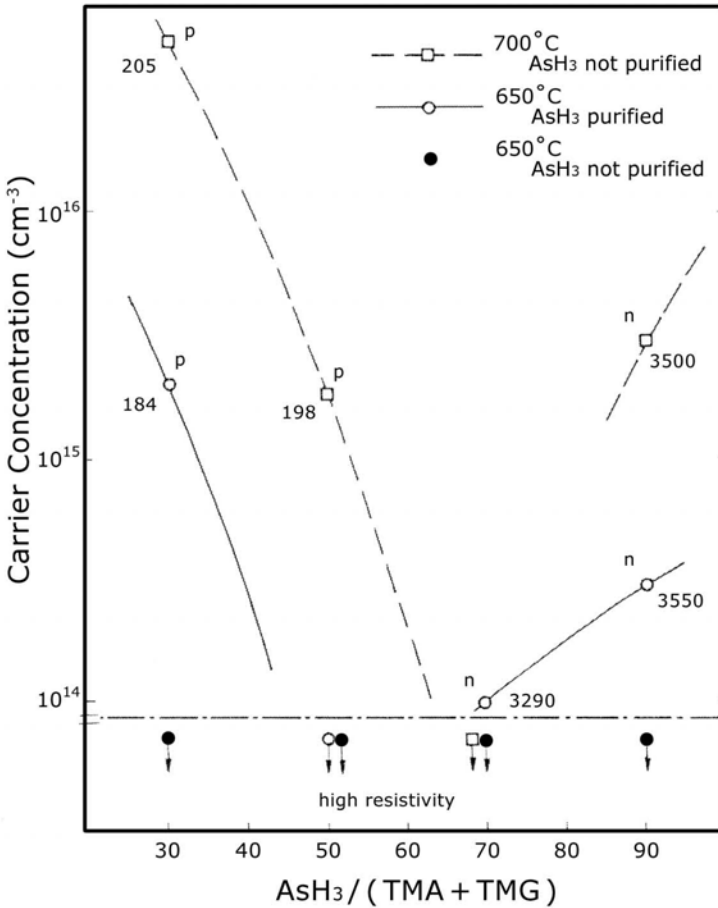


Fig. 3.16. Electrical properties of AlGaAs ($X_{Al} = 0.2$) obtained from Hall measurements at RT: (Y) AsH₃ was purified ($T_g = 650^\circ\text{C}$), (λ) AsH₃ was not purified ($T_g = 650^\circ\text{C}$), (\blacklozenge) AsH₃ was not purified ($T_g = 700^\circ\text{C}$). The same AsH₃ cylinder and TMA (#1) were used throughout [22].

devices are commercially available, including ones made from materials that contain phosphorous, made using MOCVD. In addition, by fabricating a low-threshold current MQW laser, Naritsuka et al. found that epitaxial layers grown at high growth temperature of about 800°C by MOCVD had superior optical properties to those grown by MBE. Finally, submilliampere lasing of AlGaAs/GaAs MQW laser at 77 K has been achieved for the first time using the wafers [30].

The incorporation of residual impurity is usually a difficulty in MOCVD, but it sometimes has a wonderful outcome. Carbon, which comes from the methyl groups of TMG and TMA or actively from halomethanes, such as CH_yX_{4-y}, where X = Cl, Br, or I, is a very promising dopant for p-type because C has a very low

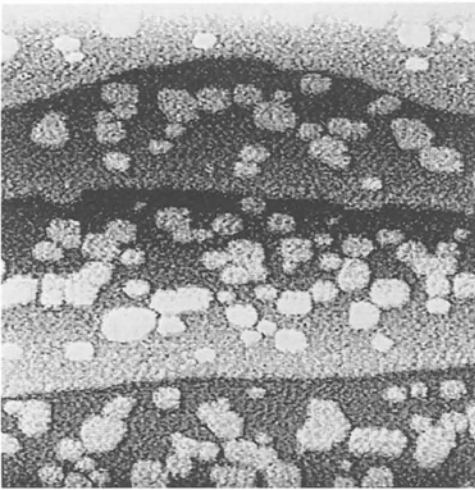
acceptor binding energy and a low diffusion constant even at a very high doping level [31]. Therefore, C doping by MOCVD is widely and commercially used, and a variety of kinds of devices including HBT or lasers are produced.

It is appropriate to add the hydrogen passivation of dopants in MOCVD, here. Hydrogen, which comes from ambient H_2 or the products of decomposing reaction of source materials, is easily incorporated into a growing crystal at interstitial sites and makes complexes with the dopant that can passivate either type of doping. These hydrogen atoms are very mobile and are easily annealed out from the crystals for activating dopants.

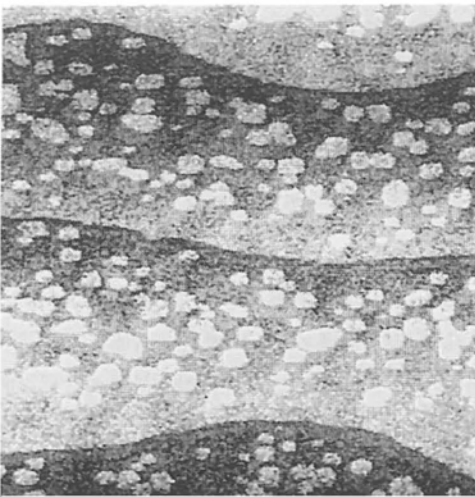
Low toxicity in MOCVD is another important issue. This has been attained by the development of new precursors, for example, TBAs, TMAs, or TBP, as alternatives to the toxic hydride of AsH_3 or PH_3 . Further study of new precursors is also useful to decrease unintentional doping. TMAA is a promising substitute for TMA to decrease the oxygen incorporation. Besides this, TBAs are useful not only to decrease toxicity, but also to decrease the oxygen incorporation. For example, Leu et al. reported that $Al_{0.3}Ga_{0.7}As$ with an excellent low O-concentration of $2.5 \times 10^{16} \text{ cm}^{-3}$ was able to be grown using TBAs [32]. The value is much less than the critical O-concentration of $1.0 \times 10^{17} \text{ cm}^{-3}$ as required for low threshold current density (AlGa)As/GaAs MQW lasers [33].

3.3.2 *In situ* monitoring and study of growth kinetics in MOCVD

In situ monitoring is essential for the study of growth mechanisms. A considerable part of the MOCVD growth mechanism has been understood using newly developed *in situ* monitors. For example, using high-vacuum scanning tunneling microscopy (STM), Kasu et al. observed 2D nuclei on the surface of a GaAs layer grown by MOCVD [34,35]. They also studied surface diffusion kinetics of GaAs and AlAs in MOCVD [36]. Figure 3.17 shows STM images of 2D nuclei and denuded zones of GaAs (a) and AlAs (b) formed at 630°C . From the figure, the following was found. 2D nucleation occurs on each terrace during growth, which is similar to that with MBE. The AlAs 2D nucleus density is about two times larger than that of GaAs. The 2D nucleus sizes in the $\langle 110 \rangle$ direction are about twice as large as those in the $\langle -110 \rangle$ direction. They attributed the anisotropy to the difference in the lateral sticking probability (P_s). The lateral sticking probability at steps along $\langle 110 \rangle$ directions (B steps) is more than three times greater than that at $\langle -110 \rangle$ (A steps). The elongation direction on 2D nuclei in MOCVD is different to that in MBE. They thought that this is due to the difference in reconstructions: $c(4 \times 4)$ in MOCVD and (2×4) in MBE. The denuded zone widths on the upper terraces are about two times wider than those of lower terraces and they ascribed this to the difference in P_s . The P_s at descending steps was 10 to 300 times larger than that at ascending steps. Using Monte Carlo simulations, they also estimated the surface diffusion coefficient of GaAs and AlAs to be 2×10^{-6} and $1.5 \times 10^{-7} \text{ cm}^2/\text{s}$ at 530°C , and the energy barriers for migration to be 0.62 and 0.8 eV, respectively.



(a) $\downarrow [\bar{1}10]$ $\overline{200 \text{ nm}}$ \downarrow Down



(b) $\downarrow [\bar{1}10]$ $\overline{200 \text{ nm}}$ \downarrow Down

Fig. 3.17. STM images showing the denuded zones near steps and the 2D nuclei of (a) GaAs and (b) AlAs. About a 1/6 ML of GaAs or AlAs was deposited on a very flat (001) GaAs surface at 630°C [36].

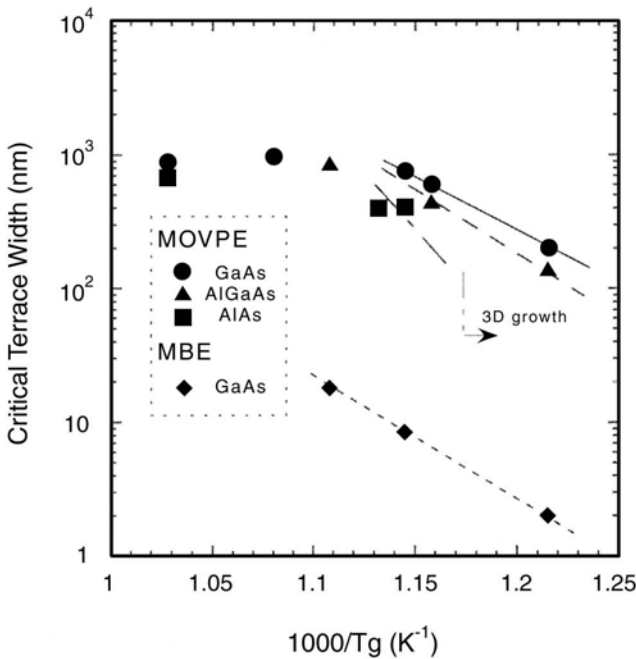


Fig. 3.18. Dependence of the critical terrace width for 2D nuclei generation on the growth temperature [37]

On the other hand, Shinohara et al. studied the enhancement of surface diffusion of column-III species in MOCVD. From AFM observations of GaAs surfaces after growth, they found that the critical terrace width for MOCVD was much larger than that of MBE, as shown in Fig. 3.18 [37]. They attributed this to the enhancement of surface diffusion of column-III species on H-terminated As atoms. Hydrogen radicals are produced by the decomposition of arsine and terminate on the top layer of As atoms during growth. The H-terminated As surface enhances the surface diffusion and, consequently, the critical terrace width increases.

In situ monitoring is effective not only for the study of growth mechanisms but also for process control. Though electron-based analytical tools under UHV cannot be used in H₂ ambient MOCVD, X-ray or light-based tools can be used in MOCVD. *In situ* and real-time monitoring of growth using grazing incidence scattering of X-ray (GIXS) was reported [38]. Synchrotron-based X-ray sources were used in GIXS because the source of X-rays must be bright for real-time measurements. First, surface reconstructions of (001) GaAs surfaces were studied. After heating in ambient hydrogen for 10 min at 580°C, a (4 × 2) reconstruction was observed, but it was not consistent with the typical (4 × 2) reconstruction in MBE that is modeled with missing rows. On the other hand, after annealing in TBAs, the GIXS indicated that the surface had the c(4 × 4) reconstruction, which was very similar to that in MBE. After a dose of TMG (2 × 10⁻³ Torr) for 2 s, this

changed to the (4×2) Ga-based reconstruction, which is the same as the former (4×2) reconstruction. In a typical growth condition of MOCVD, the $c(4 \times 4)$ reconstruction is maintained during growth. Therefore, the $c(4 \times 4)$ reconstruction should be destroyed for continuing growth. Monte Carlo simulation indicates that the existence of Ga dimers on the surface increases the exchange of surface As atoms for Ga atoms, which helps Ga atoms to come into the correct crystal sites by preserving the $c(4 \times 4)$ reconstruction during growth [39]. This phenomena is called the self-surfactant effect [40].

As the crystal truncation rod (CTR) is extremely sensitive to surface roughness, its intensity oscillates when GaAs nuclei form, grow, and finally coalesce. The cyclic behavior is the evidence of layer-by-layer growth and can be used as a direct, *in situ* monitor of growth. Figure 3.19 shows the GaAs growth performed for 15 s at 40 Torr and 540°C . The dashed line in the figure shows the calculated TMG concentration in the reactor. From the figure, it is found that the oscillation shows very good correlation to the flow of TMG. Figure 3.20 shows the results at several temperatures from 520 to 625°C . The inset in the figure shows the growth rate change. It can be seen that the growth rate is reduced at the lowest temperatures because of the limited decomposition of the sources. At higher temperature, the growth rate becomes constant, as expected for the mass transport limited regime. Moreover, the oscillation is gone at 625°C , which indicates the presence of the step-flow mode in MOCVD as it does in MBE. This is expected because the column III species are very mobile on the H-terminated As surface, and thus they can reach the step sites.

Using reflectance difference spectroscopy (RDS), the layer-by-layer growth can also be monitored in real time in MOCVD [41]. Figure 3.21 shows the RDS response of a (110) GaAs surface when TEG is supplied to an AsH_3 -stabilized

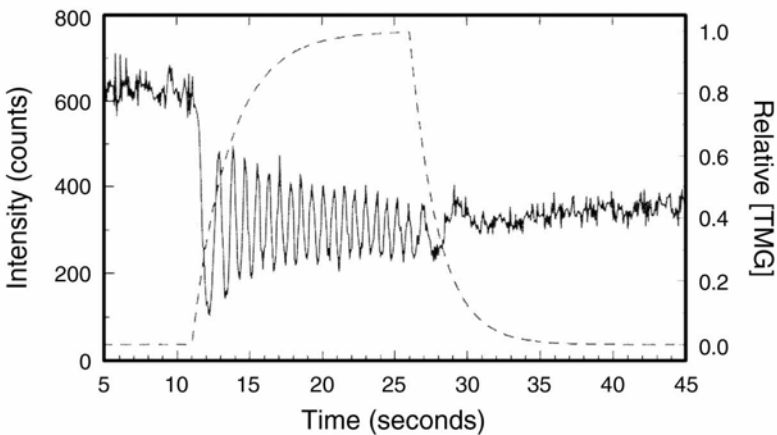


Fig. 3.19. CTR intensity during growth. Solid line: intensity of 110 CTR as layer-by-layer growth occurs. Dashed line: Calculated TMG concentration [38]

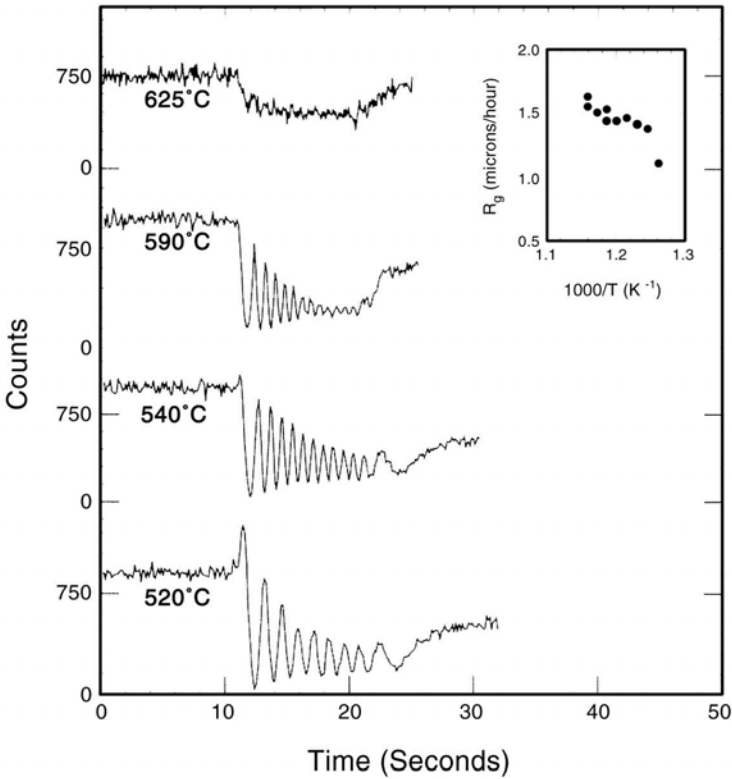


Fig. 3.20. Effect of temperature on layer-by-layer growth. Inset: Arrhenius plot of the temperature-dependent growth rate [38]

surface at (a) 430°C and (b) 550°C. The arrows indicate the event when TEG starts to be supplied. Each period of the oscillation corresponds to the growth of a monolayer of GaAs in MOCVD. The oscillation, and hence, layer-by-layer growth was maintained a long time at 550°C, whereas the oscillation immediately disappeared at 430°C. This means that the surface became rough immediately at 430°C because the migration length of surface species is very short at such a low temperature. RDS is also sensitive to the chemical nature of the surface dimers. Therefore, it can be useful to control precisely the formation of heterointerfaces, which will likely be necessary to fabricate novel, sophisticated devices. Other useful techniques to monitor growth in real time are ellipsometry and photoreflectance (PR). Although *in situ* monitoring in MOCVD began only recently, such techniques have revealed a lot about the elemental processes in MOCVD.

3.3.3 Nanostructure fabrication by MOCVD

MOCVD, similar to MBE, is very good for fabricating nanostructures. Some kinds of growth mechanisms are effectively used to fabricate nanostructures. These types of fabrication methods are very promising because they require no damage-introducing processes such as lithography and dry etching, and nanostructure sizes can be controlled simply by changing the crystal growth conditions. The typical example is quantum well wires (QWWs), which uses the step bunching mechanism. Another example is the “self-assembled” quantum dot, which requires the Stranski-Krastanow (S-K) growth mode.

The QWWs technique was first proposed by Fukui et al. [42]. At first, a GaAs buffer layer is grown. Then, the wafer is annealed under an AsH_3 atmosphere to obtain straight multiatomic steps. Then, the GaAs/AlGaAs QWW structure is grown on the multiatomic steps. The GaAs active layer becomes thicker at the corners of the multiatomic steps and, consequently, quantum wire structures are formed as shown in Fig. 3.22. In QWWs, (001) vicinal GaAs substrates misoriented by a few degrees towards the $\langle -110 \rangle$ direction are usually used to supply the surface steps. Because the bunched steps are very straight, as seen in the AFM image in

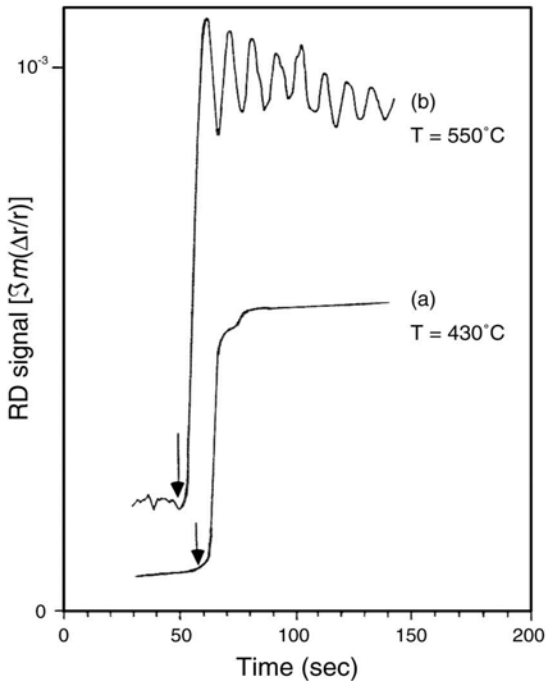


Fig. 3.21. RDS response of a (001) GaAs surface when TEG is supplied to an AsH_3 -stabilized surface at (a) 430°C and (b) 550°C . The arrows indicate the event when TEG was injected into the growth chamber [41].

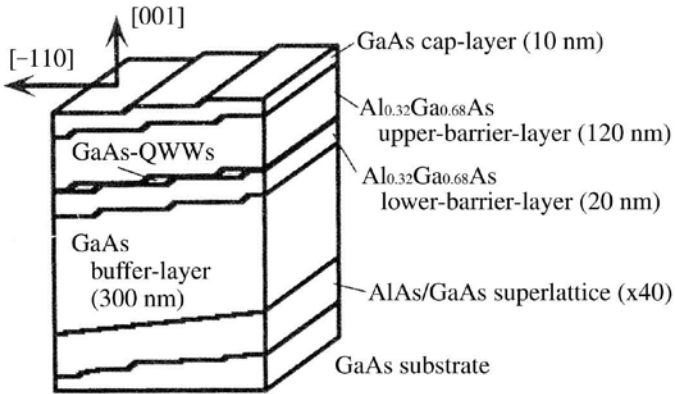


Fig. 3.22. Schematic illustration of a QWW structure on a GaAs vicinal substrate [43]

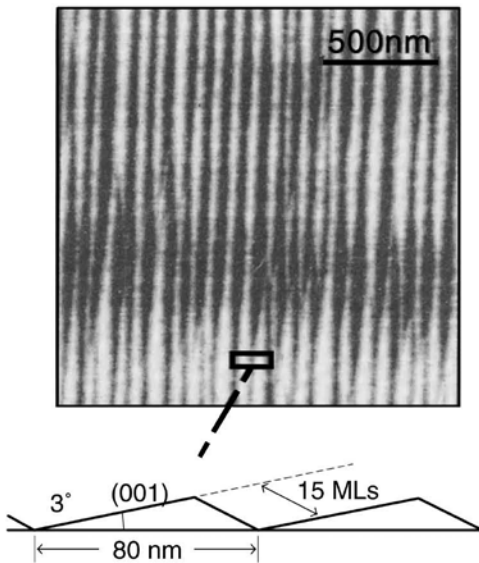


Fig. 3.23. AFM images and cross-section of a thick GaAs buffer layer surface on a vicinal substrate. Observed area is $1700 \text{ nm} \times 1700 \text{ nm}$ [43]

Fig. 3.23 [43], the fabricated QWWs have superior optical characteristics. Figure 3.24 shows the photoluminescence spectra of QWW structures on 5° misoriented substrates and on 3° misoriented substrates and single quantum well on exactly oriented substrates. The PL peak energy of the QWW structures grown on 5° misoriented substrate was 23 meV smaller than that of QW on the exactly oriented substrate. This indicates that the quantum well wire structures were successfully formed at the corners of multiatomic steps, as schematically shown in Fig. 3.22.

In SK mode, 2D layer-by-layer growth changes to 3D island growth at a certain critical thickness [44]. No dislocations are introduced as long as the island sizes are small. Moreover, the residual stress will limit their size, which is quite useful for the fabrication of quantum dots (QDs). The high uniformity of QDs leads to a narrow luminescence linewidth, which increases the gain in optical devices. Therefore, a lot of reports have been published about QD fabrication that used the SK mode. Here, we show one example of the early stage of the research. Figure 3.25 shows AFM images of InGaAs surfaces grown on GaAs [45]. The deposition times were (a) 0.5 s, (b) 1.0 s, (c) 1.5 s, (d) 2.0 s, (e) 2.5 s, (f) 3.0 s, (g) 3.5 s, and (h) 3.7 s. The scan size of the images was $1 \mu\text{m} \times 1 \mu\text{m}$. Below 2.5 s of InGaAs deposition time, the growth mode was 2D. On the other hand, once the thickness reached the critical thickness of 3 ML, which required a deposition time of 3 s (Fig. 3.25 (f)), the QDs started to form on terraces. As seen from the figure, the increase in the deposition time above 3 s only leads to an increase in the density of the QDs. Figure 3.26 shows the PL spectrum from the sample grown for 3.7 s. The excitation intensities were 2.25 and 6350 W/cm². The PL spectrum of 1136 nm at low excitation intensity in Fig. 3.26 (a) is thought to originate from the QDs. On the other hand, the PL spectrum at high excitation intensity in Fig. 3.26 (b) has another three peaks that are caused by higher energy subbands at 980 nm and 1060 nm and from a 2D InGaAs layer of 4 ML at 915 nm. In this way, nanostructures can be fabricated in MOCVD using special growth modes. Furthermore, intersurface diffusion of column III species or material transport in the gas phase is also important in the fabrication of nanostructures.

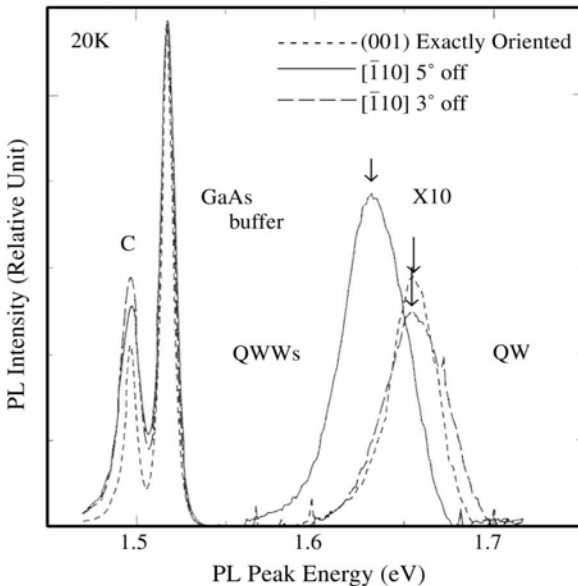


Fig. 3.24. Photoluminescence spectra of QWW structures [43]

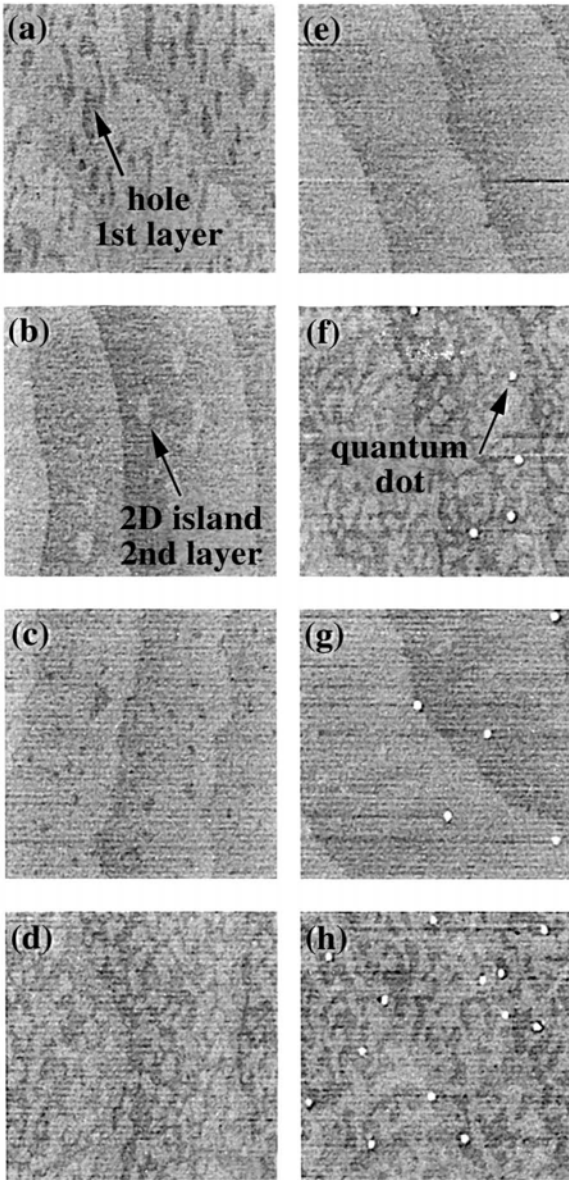


Fig. 3.25. AFM images of InGaAs surface grown on GaAs. The deposition times were (a) 0.5 s, (b) 1.0 s, (c) 1.5 s, (d) 2.0 s, (e) 2.5 s, (f) 3.0 s, (g) 3.5 s, and (h) 3.7 s. The scan size of the images was $1 \mu\text{m} \times 1 \mu\text{m}$ [45].

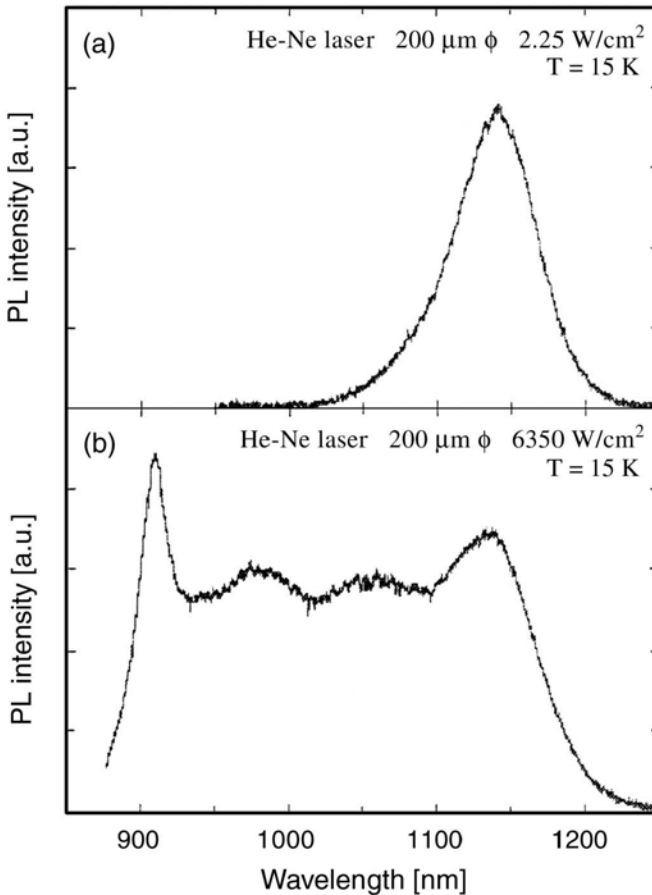


Fig. 3.26. PL spectrum from a dot sample that was grown with a deposition time of 3.7 s. The excitation intensities are (a) 2.25 W/cm^2 , (b) 6350 W/cm^2 [45]

3.3.4 Highly-mismatched heteroepitaxy and microchannel epitaxy with MOCVD

Highly-mismatched (HM^2) heteroepitaxy is another important issue in the growth of III-V compounds. Using low temperature buffer layers [46–48], Akiyama et al. succeeded in growing antiphase domain-free (APD-free) GaAs layers on Si substrates [49,50]. Subsequent studies achieved a decrease in the dislocation density to about $1 \times 10^6 \text{ cm}^{-2}$ by using superlattice buffer layers or thermal cyclic annealing or both. But it is not sufficient for the fabrication of devices with excellent characteristics. The subject of dislocation reduction is extensive; in this subsection, we add only some special issues concerning the elimination of defects.

The residual stress in HM^2 heteroepitaxial layers is one of the most important properties; it can even produce dislocations in the cooling stage after growth. Narituska et al. reported a particular example of a good use for the residual stress to eliminate twins in a GaAs layer on (001) Si [51]. They used nominally-just (001) Si, within 0.5° misorientation, as a substrate. Usually, use of just (001) Si substrates only leads to the formation of APDs. On the contrary, they obtained an extremely smooth surface of GaAs layers without APDs using a particular thermal treatment on a low temperature GaAs buffer layer. As shown in Fig. 3.27, this included the crystal growth of a buffer layer at low temperature, annealing for 10 min at 700°C , cooling to room temperature, and second annealing at 700°C . The process was named the thermal cycle treatment to buffer layer (TCTBL). The TCTBL brought not only APD-free smooth GaAs surfaces, but also the truncation of twins in the buffer layer. The detailed process was investigated using TEM and SEM observations [52]. Figure 3.28 shows the (011) lattice image of GaAs layer grown on (001) Si substrate with TCTBL. The figure shows that twins generate at the Si substrate surface, and propagate into the buffer layer. However, they disappear at the interface between the buffer and overgrown GaAs layer. The strain on the surface of the buffer layer induced by TCBL might introduce dislocations for destroying the twins. As a result, the upper layer became twin-free. This is an example of stress-assisted epitaxy, which might open up a new field of epitaxy in the near future.

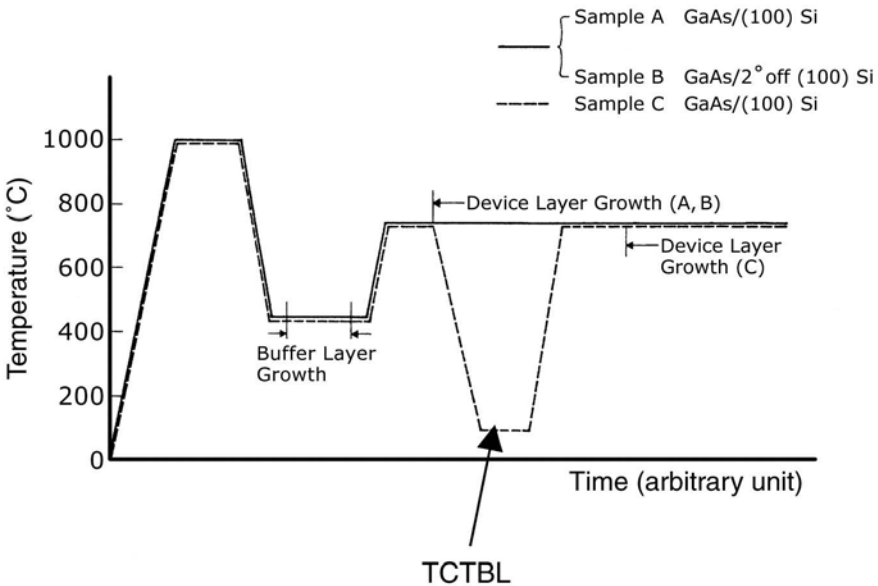


Fig. 3.27. Temperature diagrams [52]

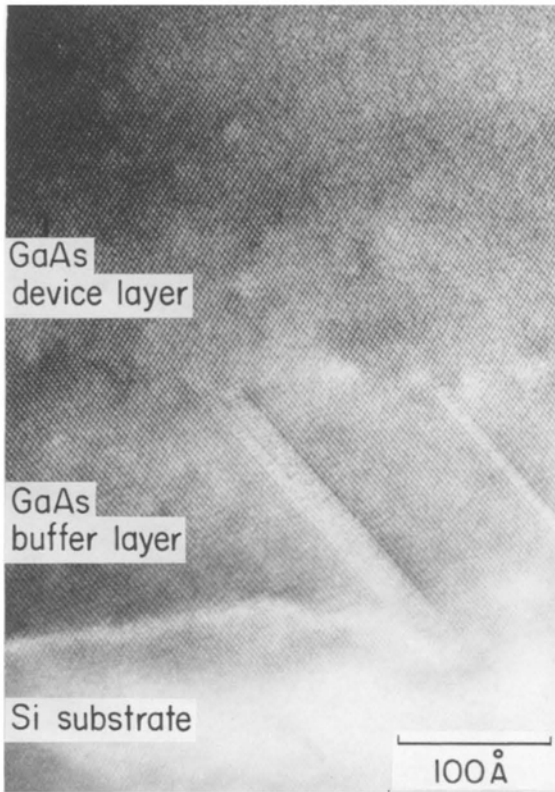


Fig. 3.28. The (011) lattice image of GaAs layer grown on a (001) Si substrate using TCTBL [52]

As shown above, the generation of a high dislocation density and large residual stress are the main problems in HM^2 heteroepitaxy. To reduce both dislocations and residual stress, a successful method was proposed by Nishinaga et al. called microchannel epitaxy (MCE) [53,54]. In MCE, a narrow channel is used to transfer only crystal information but not defect information from the substrate. Figure 3.29 shows an illustration of MCE. An opening in a mask acts as a microchannel that transfers crystal information to the overgrown layer, whereas the mask prevents dislocations from transferring to the overgrown layer. Hence, the overgrown layer becomes dislocation free. The 3D structure of MCE also gives it another advantage in stress release. The residual stress can be released effectively because the overgrown layer easily deforms. We have demonstrated these advantages in various kinds of materials including homoepitaxies of Si [55,56], GaP [57], GaAs [53,58], InP [59,60], and heteroepitaxies of GaAs on Si [61–63], and InP on Si [64–67] by employing the MCE technique. These advantages are definitely important for device fabrication because devices with superior characteristics cannot be produced unless the number of dislocations is reduced.

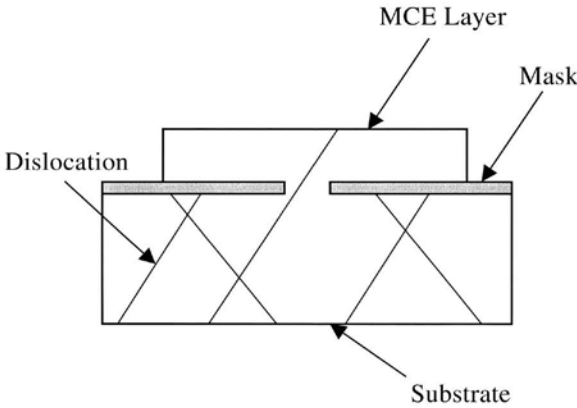


Fig. 3.29. Schematic illustration of MCE

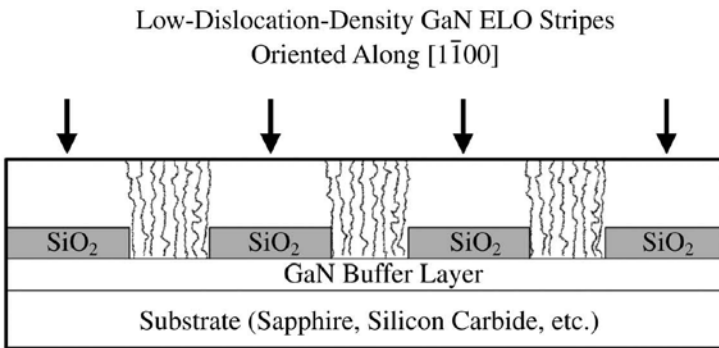


Fig. 3.30. Schematic illustration of the MCE process for GaN. The GaN emerging from the window regions has a high density of threading dislocations, whereas the GaN overgrowth on the SiO₂ masks has a drastic reduction in dislocation density [68].

The MCE technique was also applied to GaN growth in MOCVD. Figure 3.30 shows an MCE structure of a GaN layer on an Al₂O₃ substrate, in which a GaN buffer layer is used to improve the crystallinity. Each stripe of overgrown layer coalesces together, thus forming a flat and uniform surface of MCE [68]. A CL image of the MCE layer is shown in Fig. 3.31 that indicates dislocation-free regions in the overgrown areas [68]. The vertical cross-sectional TEM image in Fig. 3.32 shows that single crystal GaN with low dislocation density ($<10^6 \text{ cm}^{-2}$) was obtained in the region above the SiO₂ mask, whereas columnar, high-dislocation-density ($\sim 10^{10} \text{ cm}^{-2}$) GaN existed in the window region. These GaN layers with low dislocation are quite beneficial for making devices with excellent characteristics. Using MCE, Nakamura et al. has produced laser diodes having very long CW

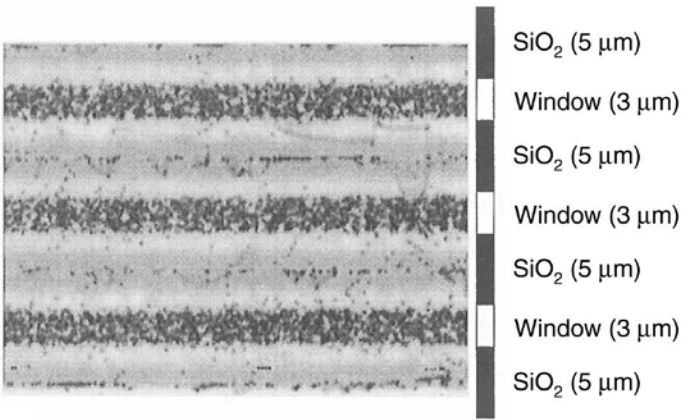


Fig. 3.31. CL image of a GaN MCE layer for which coalescence at the centers of the SiO₂ masks is completed [68]

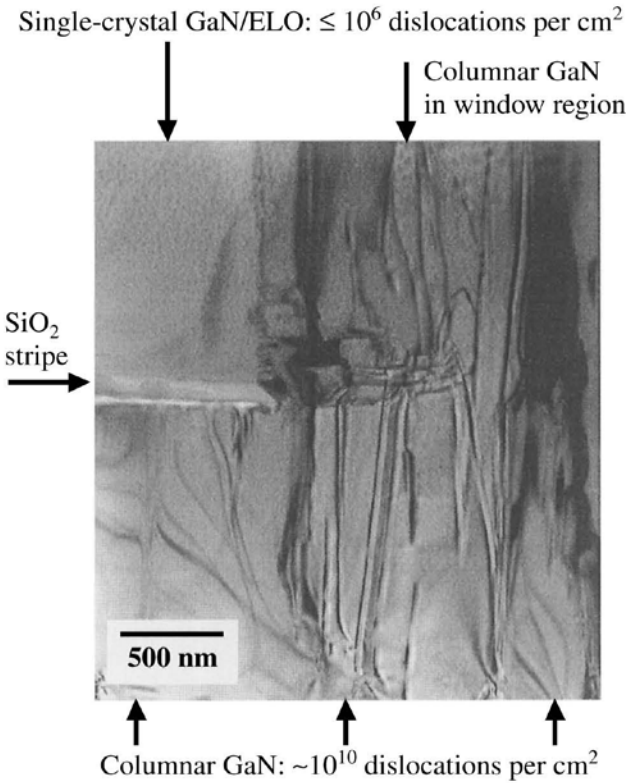


Fig. 3.32. Vertical-cross-section TEM image ($g = (0001)$) [68]

lifetime of more than 10,000 hours [69]. Furthermore, MCE has another advantage for selective growth: devices can be fabricated at any point one wants. For this reason, MCE is very suitable to fabricate future 3D ICs including opto-electronic integrated circuits (OEIC).

If the size of the microchannel is decreased to the nanoscale, a completely new phenomenon will occur where no dislocation is produced at a heterointerface. That is to say, when the width of the MCE is narrower than a certain value, the stress in the layer does not exceed the critical one, above which dislocations start to form. The MCE can be grown heteroepitaxially without the formation of misfit dislocations even when the lattice mismatch is fairly large; this includes pseudomorphic epitaxial growth. Naritsuka estimated the critical width (L_c) of the MCE layer in HM^2 heteroepitaxy [70]. From his estimation, L_c for GaAs on Si was found to be 440 Å. Namely, we can grow HM^2 heteroepitaxial material systems as if they have no lattice mismatches.

3.4 Summary

Epitaxial growth of III-V compounds was described using molecular beam epitaxy (MBE) and metal-organic chemical vapor deposition (MOCVD) as examples. MBE was described first. Elementary growth processes involved in MBE were described using GaAs as a model material. The origin of the mode transition that is observed experimentally in MBE on a vicinal substrate was discussed. This model assumes that 2D nucleation occurs on the terrace between steps at supersaturations above a critical value. With this model, the growth rate and the inter-step distance dependencies of the mode transition temperature were explained.

The elementary growth processes were discussed based on measurements of the incorporation diffusion length. The experiments show that the arsenic pressure dependence of the incorporation diffusion length is different in different ranges of the arsenic pressure. From the dependencies, it was concluded that on (001) surfaces As_4 molecules decompose to give active arsenic elements for the growth at lower arsenic pressure, while at high arsenic pressure two As_4 molecules react to give active arsenic elements, which agrees with the model given by Foxon and Joyce. Intersurface diffusion was studied and it was concluded that the factor governing the direction of the intersurface diffusion is the incorporation lifetime of Ga, which depends on the available number of growth sites and the arsenic pressure. The former depends on the step density and hence on the nucleation rate, which is influenced by the type of surface reconstruction.

In the second part, a short review of up-to-date MOCVD technologies was described. For the growth of high-purity materials by MOCVD, understanding the incorporation mechanism of impurities is extremely important. For this purpose, *in situ* monitoring becomes very useful. The elementary growth process of MOCVD was discussed, and we pointed out some similarities between elementary processes in MOCVD and MBE. Understanding of the growth mechanism often gives rise to new growth technologies. As examples of such newly-born technologies in

epitaxial growth, nanostructure fabrication and highly-mismatched (HM^2) heteroepitaxy were described. By understanding basic growth phenomena such as step-bunching or nucleation in SK mode, fabrication of nanodot and wire structures became possible. MCE in HM^2 heteroepitaxy is a very promising technique for both decreasing the dislocation density and reducing the residual stress. MCE will open new fields of epitaxy, which should enable the growth of novel materials that have not yet been studied in detail. We conclude that thin-film growth technologies such as MBE and MOCVD will open a new era that will realize the potential of devices such as OEICs.

References

1. Nelson H (1963) *PCA Rev* 24:603
2. Mimura T, Hiyamizu S, Fujii T, Nanbu K (1980) *Jpn J Appl Phys* 19:L 255
3. Dingle R, Stormer HL, Gossard AC, Wiegmann W (1978) *Appl Phys Lett* 33:655
4. Amano H, Sawaki N, Akasaki I, Toyoda Y (1986) *Appl Lett* 48:353
5. Gillet E, Gruzza B (1980) *Surf Sci* 79:553; Gruzza BE (1980) *Thin Solid Films* 68:345
6. Harris JJ, Joyce BA, Dobson PJ (1981) *Surf Sci* 103:L90
7. Gronwald KD, Henzlar M (1982) *Surf Sci* 117:180
8. Neave JH, Joyce BA, Dobson PJ, Norton N (1983) *Appl Phys* A31:1
9. Burton WK, Cabrera N, Frank FC (1951) *Phil Trans Roy Soc A* 243:299
10. Neave JH, Dobson PJ, Joyce BA, Zhang J (1985) *Appl Phys Lett* 47:100
11. Hirth JP, Pound GM (1963) In: *Condensation and Evaporation, Nucleation and Growth Kinetics*, Pergamon, Oxford
12. Nishinaga T, Cho KI (1988) *Jpn J Appl Phys* 27:L12
13. Shen XQ, Kishimoto D, Nishinaga T (1994) *Jpn J Appl Phys* 33:11
14. Nishinaga T, Shen XQ, Kishimoto D (1996) *J Crystal Growth* 163:66
15. Foxon CT, Joyce BA (1974) *Surf Sci* 44:69
16. Foxon CT, Joyce BA, *Surf Sci* 50:434 (1975)
17. Foxon CT, Joyce BA, *Surf Sci* 64:293 (1977)
18. Shen XQ, Ren HW, Tanaka M, Nishinaga T (1996) *J Crystal Growth* 169:607
19. Shen XQ, Ren HW, Nishinaga T (1997) *J Crystal Growth* 177:175
20. Yamashiki A, Nishinaga T (1997) *Cryst Res Technol* 32:1049
21. Nishinaga T, Yamashiki A, Shen XQ (1997) *Thin Solid Films* 306:187
22. Hata M, Fukuhara N, Zempo Y, Isemura M, Yako T, Maeda T (1988) *J Crystal Growth* 93:543
23. Hanna MC, Lu ZH, Oh EG, Mao E, Majerfeld A (1992) *J Crystal Growth* 124:443
24. Hata M, Tanaka H, Yako T, Fukuhara N, Maeda T, Uemura Y (1992) *J Crystal Growth* 124:427
25. Yamanaka K, Naritsuka S, Kanamoto K, Mihara M, Ishii M (1987) *J Appl Phys* 61:5062
26. Yamanaka K, Naritsuka S, Mannoh M, Yuasa T, Nomura Y, Mihara M, Ishii M (1984) *J Vac Sci Technol B* 2:229–232
27. Naritsuka S, Yamanaka K, Mannoh M, Mihara M, Ishii M (1985) *Jpn J Appl Phys* 24:1324
28. Naritsuka S, Noda T, Wagai A, Fujita S, Ashizawa Y (1993) *J Crystal Growth* 131:186

29. Naritsuka S, Noda T, Wagai A, Fujita S, Ashizawa Y (1993) *Jpn J Appl Phys* 32:L925
30. Kurobe A, Furuyama H, Naritsuka S, Kokubun Y, Nakamura M (1986) *Electron Lett* 22:1117
31. Kuech TF, Redwing JM (1994) *J Crystal Growth* 145:382
32. Leu S, Hohnsdorf F, Stolz W, Becker R, Salzman A, Greiling A (1998) *J Crystal Growth* 195:98
33. Mihashi Y, Miyasguta M, Kaneko N, Tshugami M, Fujii N, Takamiya S, Mitsui S (1994) *J Crystal Growth* 141:22
34. Kasu M, Kobayashi N (1994) *J Crystal Growth* 145:120
35. Kasu M, Kobayashi N (1995) *J Appl Phys* 78:3026
36. Kasu M, Kobayashi N (1997) *J Crystal Growth* 170:246
37. Shinohara M, Tanimoto M, Yokoyama H, Inoue N (1994) *J Crystal Growth* 145:113
38. Kisker DW, Stephenson GB, Fouss PH, Lamelas FJ, Bernnan S, Imperatori P (1992) *J Crystal Growth* 124:1
39. Ito M, Bell GR, Avery AR, Jones TS, Joyce BA, Vedensky DD (1998) *Phys Rev Lett* 81:663
40. Shiraishi K, Ito T (1998) *Phys Rev* B57:6301
41. Jonsson J, Deppert K, Jeppesen S, Paulsson G, Samuelson L, Schmidt P (1990) *Appl Phys Lett* 56:2414
42. Fukui T, Saito H (1990) *Jpn J Appl Phys* 29:L483
43. Hara S, Ishizaki J, Motohisa J, Fukui T, Hasegawa H (1994) *J Crystal Growth* 145:692
44. Stranski IN, von Kratanow L (1939) *Akad Wiss Lit Mainz Math Naturw Kl* 146:797
45. Kitamura M, Nishioka M, Schur R, Arakawa Y (1997) *J Crystal Growth* 170:563
46. Ohnishi S, Hirokawa Y, Shiosaki T, Kawabata A (1978) *Jpn J Appl Phys* 17:773
47. Nishino S, Hazuki Y, Matunami H, Tanaka T (1980) *J Electrochem Soc* 127:2674
48. Ishida M, Ohyama H, Sasaki S, Yasuda Y, Nishinaga T, Nakamura T (1981) *Jpn J Appl Phys* 20:L541
49. Akiyama M, Kawarada Y, Kaminishi K (1984) *Jpn J Appl Phys* 23:L843
50. Nishi S, Inomata H, Akiyama M, Kaminishi K (1985) *Jpn J Appl Phys* 24:L391
51. Naritsuka S, Nozaki C, Sugiyama N, Nishikawa Y, Yasuami S, Kokubun Y, Extended Abstract of 19th Conference of Solid State Devices and Materials, Tokyo, 1987, p 143
52. Nozaki C, Naritsuka S, Kokubun Y, Yasuami S (1988) *Jpn J Appl Phys* 27:L293
53. Nishinaga T, Nakano T, Zhang S (1988) *Jpn J Appl Phys* 27:1964
54. Nishinaga T, Scheel HJ (1996) *Advances in Superconductivity VIII*, Hayakawa H, Enomoto Y (eds) Springer-Verlag, Tokyo p 33
55. Suzuki Y, Nishinaga T (1989) *Jpn J Appl Phys* 28:440
56. Suzuki Y, Nishinaga T, Sanada T (1990) *J Crystal Growth* 99:229
57. Zhang S, Nishinaga T (1990) *Jpn J Appl Phys* 29:545
58. Zhang S, Nishinaga T (1990) *J Crystal Growth* 99:292
59. Narituska S, Nishinaga T (1995) *J Crystal Growth* 146:314
60. Yan Z, Naritsuka S, Nishinaga T (1998) *J Crystal Growth* 192:11
61. Ujii Y, Nishinaga T (1989) *Jpn J Appl Phys* 28:L337
62. Sakawa S, Nishinaga T (1992) *Jpn J Appl Phys* 31:L359
63. Chang YS, Naritsuka S, Nishinaga T (1998) *J Crystal Growth* 192:18
64. Naritsuka S, Nishinaga T, Tachikawa M, Mori H (1995) *Jpn J Appl Phys* 34:L1432
65. Naritsuka S, Nishinaga T (1997) *J Crystal Growth* 174:622
66. Naritsuka S, Nishinaga T (1998) *Jpn J Appl Phys* 37:5885
67. Naritsuka S, Nishinaga T, Tachikawa M, Mori H (2000) *J Crystal Growth* 211:395

68. Yu Z, Johnson MAL, Brown JD, El-Masry NA, Cook Jr JW Schetzina JF (1998) *J Crystal Growth* 195:333
69. Nakamura S, Senoh M, Nagahama S, Iwasa N, Yamada T, Matusshita T, Kiyoku H, Sugimoto Y, Kozaki T, Umemoto H, Sano M, Chocho K (1998) *J Crystal Growth* 189/190:820
70. Naritsuka S (1993) Ph. D. dissertation, University of Tokyo

4 CVD Diamond Growth

C. Chang, Y. Liao, G.Z. Wang, Y.R. Ma, and R.C. Fang

Structure Research Laboratory, Department of Physics, University of Science and Technology of China, Hefei, 230026 Anhui, China

4.1 Introduction

Diamond is becoming an increasingly important material in the recent decades. The unique predominance of diamond that brings together both excellent physical and chemical properties shows its promise for applications in many areas. However, the rarity and the high cost of natural diamond have severely limited its applications and thus has stimulated scientists to search for methods to synthesize diamonds.

The first successful synthesis of diamond was reported by Bundy and co-workers (1962) [1]. They used the high pressure and high temperature (HPHT) technique in which diamond was prepared at 8 GPa pressure and 1500 °K, and graphite was the source of carbon and Fe, Ni, and Co were used as catalyzers. After that the HPHT technique was developed by many researchers. Until now diamond for industrial consumption has been produced mainly from the HPHT synthesis method.

Other synthesis methods of diamond were also found. It's known that the hydrothermal process may be responsible for most natural diamonds. Using this idea, diamond from metal-carbon solution was reported in 1990 and there is now a revival of interest in synthesizing diamonds hydrothermally in the laboratory [2].

Owing to the cost of production and the small size, applications of diamond prepared by the above techniques were always limited, unlike those of natural diamond. Diamond film formation under relatively low pressure and temperature has always been a dream of researchers. Fortunately, Russian researchers reported the successful growth of diamond from a gas phase under metastable conditions in the 1960s. The major breakthrough in diamond growth using the chemical vapor deposition (CVD) method was reported by Spitsyn et al. [3], and after that the hydrocarbon and hydrogen gas mixture has been widely used as a basic gas source in diamond growth systems.

Many CVD techniques have been used to prepare diamond. The growth rates of polycrystalline diamond from different methods vary from several microns to several hundreds of microns per hour. Although the techniques are different, the growth conditions are very similar, that is 10 to 100 Torr pressure, 700 to 1100°C

substrate temperature, and about 1% C/H ratio. The results show that the properties of polycrystalline diamond films are close to that of single crystal diamond. With the development of CVD techniques diamond films have the commercial potential to surpass the HPHT diamond technique.

Although diamond can be routinely produced using a myriad of techniques, our understanding of the deposition mechanism of metastable diamond is far from complete. It is known that the saturated atomic hydrogen must be present in the growth process of diamond film, but there is no satisfactory model available to explain it until now. Therefore, scientific interest in diamond CVD processes stems not only from the potential applications, but also from the need to understand the formation processes of diamond under apparently metastable conditions.

4.2 Preparation and Application of CVD Diamond Film

4.2.1 Preparation methods

Numerous chemical vapor deposition techniques are used to produce diamond films, since diamond can be successfully synthesized from the gas-phase activation condition. These techniques are grouped into four categories: thermal activation, plasma activation, laser ablation, and combustion flames. Beside CVD, most of the physical vapor deposition (PVD) techniques have also attempted to synthesize diamond at low temperature recently. Here, the authors will introduce three kinds of CVD technique for diamond film preparation.

Hot-filament CVD (HFCVD)

The schematic diagram of a hot-filament CVD apparatus is shown in Fig. 4.1. This technique was first reported by Matsumoto et al. (1982) [4]. One or multiple filaments, such as W, Ta, and Re, are mounted near the substrate and electrically heated to over 2000°C, where the simultaneous production of atomic hydrogen during the hydrocarbon pyrolysis will promote the growth of diamond film. Therefore, the filament temperature plays an important role in the diamond deposition process in HFCVD. The substrate temperature is measured by a thermocouple placed under the substrate and controlled to between 700 and 1100°C. The gas source usually is the mixture of 99% hydrogen and 1% methane. Diamond films are formed at chamber pressures between 10 and 100 Torr. Depending on the deposition conditions, such as the properties of the substrate surface, methane concentration, filament or substrate temperature, the growth rate of diamond films is from 0.5 $\mu\text{m/hr}$ to several $\mu\text{m/hr}$ and the surface morphology and the quality of diamond films also vary.

In the case of HFCVD design, a modification has been developed. A moderately positive voltage and negative voltage are put to the substrate and to the filament, respectively. This is the so-called electron-enhanced HFCVD technique.

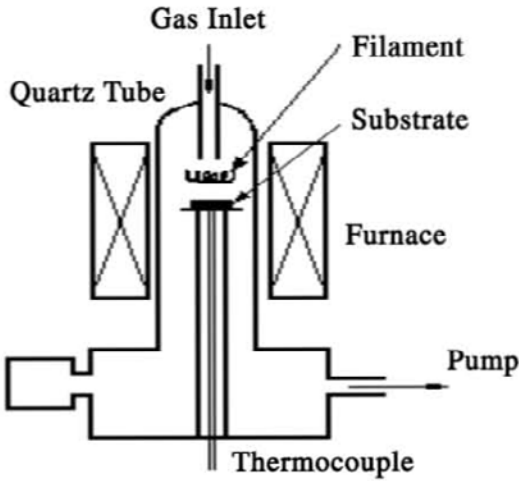


Fig. 4.1. Schematic diagram of the hot-filament CVD apparatus

The application of DC bias results in electron or ion bombardment to gas species that promote the decomposing reaction of the gas species. In addition, electron or ion bombardment to the substrate also enhances the desorption of the surface hydrogen and the diffusion of carbon-containing species on the substrate surface.

HFCVD technique is a simple method compared to others used in the growth of diamond film under low pressures. Large areas of deposition of diamond films (~30 cm in diameter) and highly-oriented diamond films have been realized by this technique. Therefore, it is also the most popular method for the growth of CVD diamond film. However, a series of problems including carbonization and distortion of the filament at high temperature and contamination of the metal filament onto the deposited diamond film were discovered. Hence, the carbide-forming pretreatment of refractory metal filaments is necessary for the deposition of diamond film.

Microwave plasma-assisted CVD

A schematic diagram of microwave plasma-assisted CVD (MPCVD) is shown in Fig. 4.2. It was first applied to the diamond film area by Kamo and colleagues at NIRIM in 1983 [5]. Like hot-filament CVD technique, microwave plasma-assisted CVD technique is also thought to be potentially applied in the industrial production of diamond films.

First, a gas mixture of hydrogen and methane or hydrocarbon is provided into a reaction chamber that contains the substrate to be coated. Then microwave power with a typical excitation frequency of 2.45 GHz is coupled into the chamber in order to create a discharge. High ionization fractions are generated as oscillating electrons collide with gas molecules and form the so-called microwave plasma.

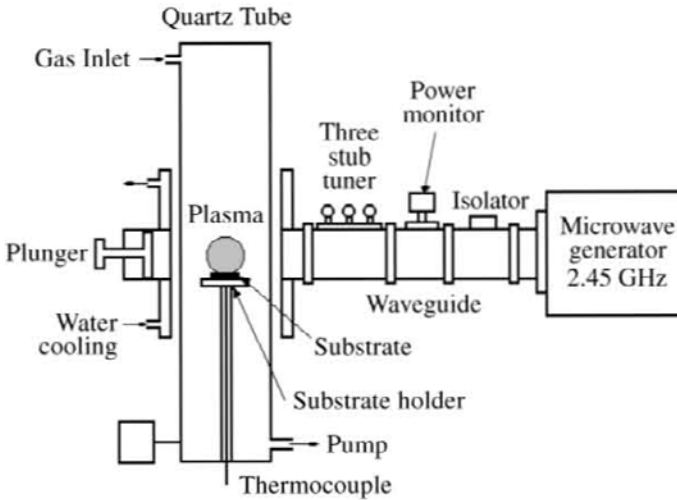


Fig. 4.2. Schematic diagram of the microwave plasma-assisted CVD apparatus

The ions formed do not destroy the substrate surface and the deposited diamond film due to their low kinetic energy. Generally, the growth rate of diamond film with the MPCVD technique is in the range of several micrometers per hour.

The technique has found a lot of success because of its simplicity, flexibility, and the early commercial availability of reactors from New Japan Radio Corporation based on the work at NIRIM. The first successful deposition of highly-oriented diamond film was reported using this technique in 1993 [6,7]. The quality of diamond films produced with this apparatus is outstanding as judged by their optical transparency and thermal conductivity [8].

However, it is very difficult to prepare a large area of diamond film due to the size limitation of the standing wave cavity. In addition, the plasma stability and shape during the process of creating diamond film is another problem to be improved upon. These problems can be partially overcome by using a larger plasma with higher microwave power. A new reactor with 915 MHz has been designed to produce the diamond film. At this frequency magnetron tubes are available at power levels of up to 100 kW continuous power. A manufacturer, AsteX, has finished such a prototype, and with this apparatus diamond films 20 cm in diameter having uniformity of 15% have already been obtained [9]. The deposition rate of diamond film is also increased from 0.5 mg/h to 1 g/h. Recently, Fünér et al. (1998) have used a rotational ellipsoid as a reactor cavity instead of the conventional cylindrical shape [10]. The position of this new design is very stable and independent of gas pressure and microwave power. With these ellipsoid reactors, diamond films of 15 cm diameter have been produced.

DC arc plasma jet CVD

DC arc plasma jet CVD is a modified DC plasma-assisted CVD. DC plasma CVD is another effective technique used to activate a gas source (a mixture of hydrogen and hydrocarbon) for diamond film deposition. Under conditions of high voltage (~ 1 kV) and current density (~ 4 A/cm²) the substrate temperature is controlled at about 1100 °K by a water-cooling adjusting system. DC plasma-assisted CVD possesses the ability to produce large areas of diamond films, but are limited by the electrodes and DC power supply.

A schematic diagram of DC arc plasma jet CVD is shown in Fig. 4.3 and is being applied popularly in the deposition of diamond film by researchers in Japan [11]. The advantage of DC arc plasma jet CVD is the significant increase in the growth rate of diamond film. The typical growth rate is several tens of micrometers per hour. Recently, diamond films with a high growth rate of 930 $\mu\text{m/h}$ and higher quality have been obtained using DC arc plasma jet CVD and supply the need for a tool-cutting coat and heat sink in electronic devices. However, the thickness uniformity of diamond films is expected to be enhanced.

In addition, other methods, including electron cyclotron resonance (ECR) microwave plasma-assisted CVD [12,13,14], combustion flame CVD [15,16,17], and laser ablation CVD [18] were reported in the recent decade. Among these, the most popular method is the combination of DC-plasma or MW-plasma with HFCVD [19,20,21]. Therefore, the success of CVD diamond films enables the wider application of diamond films to be likely. Similarly, the study of preparation methods of diamond films also promotes the development of CVD techniques.

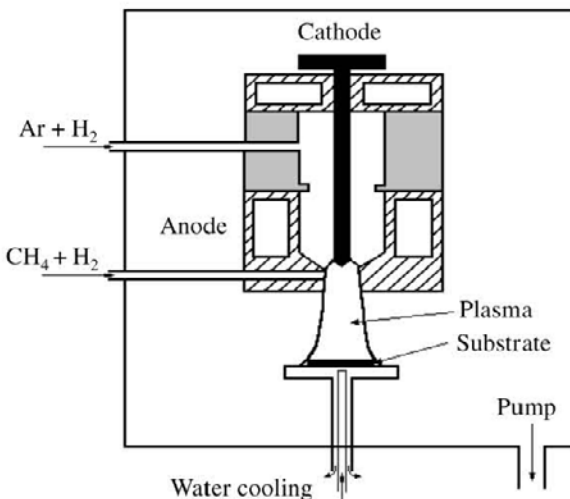


Fig. 4.3. Schematic diagram of the DC arc plasma jet CVD apparatus

4.2.2 Applications of diamond film

Interest in CVD diamond film, which is deposited from the gas phase, is replacing natural or HPHT diamond in the market. CVD diamond film inherits part of the outstanding properties of single crystalline diamond and is finding applications where bulk diamond is usually used. With the development of CVD diamond film, one can see a tremendous range of possibilities, the most exciting of which seem to be in active electronics, and the most immediate as abrasive or cutting tool coatings and heat sinks or other passive substrates for electronic circuitry.

Properties and general applications

In the diamond structure, each carbon atom is covalently bonded to four other atoms with sp^3 tetragonal bonds. The stable sp^3 structure enables diamond to possess many excellent properties as shown in Table 4.1 [22,23].

Table 4.1. Some of the Outstanding Properties of Diamond [22,23]

	Properties	Diamond
Mechanical properties	Density	3.51 g/cm ³
	Hardness	10 ³ kg/mm ²
	Young's modulus	1200 Gpa
	Bulk modulus	1040 Gpa
	Compressibility	4.0 Gpa
	Friction coefficient	0.05–0.1
	Poisson's ratio	0.2
Thermal properties	Thermal impact coefficient	10 ⁷ W/m
	Thermal conductivity	20 W/cm·K
Optical properties	Thermal expansion coefficient	2.3 × 10 ⁻⁶ /K
	Light transmission	225 nm – far IR
	Light absorption	5 μm
Electronic properties	Refractive index	2.41 (590 nm)
	Band gap	5.5 eV
	Dielectric constant	5.5
	Breakdown voltage	3.5 × 10 ⁶ V/cm
	Electrical resistivity	10 ¹⁶ Ω.cm
	Electron mobility	2200 cm ² /V.s
	Hole mobility	1800 cm ² /V.s
Saturated electron drift velocity	2.5 × 10 ⁷ cm/s	
Acoustic property	Longitudinal sound velocity	18.2 km/s
Chemical property		Inertness

It is known that diamond is the hardest material in the world, and obviously diamond has a great application as a coating on abrasive and cutting tools to prolong their application life. In addition, diamond has the highest bulk modulus ($\sim 1.2 \times 10^{12} \text{ Nm}^{-2}$) and the lowest compressibility ($\sim 8.3 \times 10^{-13} \text{ m}^2\text{N}^{-1}$) compared with other known materials. Diamond is known as the most suitable material for acoustic products, such as speaker diaphragms, due to its large longitudinal sound velocity (18.2 km/s). At room temperature, the dynamic friction coefficient of diamond is only 0.05, as low as that of teflon and the lowest among the materials of interest.

Diamond also has the highest thermal conductivity, which is about 20 W/cm·K at room temperature, roughly four times higher than that of copper. Thermally conducting substrates or “heat sinks” are one of the most imminent of the potential applications of CVD diamond films whose thermal conductivity is close to that of bulk diamond [24]. In fact diamond heat sinks have already been sold in the market now. In general, the diamond films with thickness of about 250 μm are needed. Compared with that of bulk diamond, diamond film heat sinks are likely to make an impact on much larger substrates, such as semiconductor laser repeater assemblies, and subsequently on smaller devices through the advantages of CVD technology.

Diamond is an ideal candidate for optical windows or lenses, especially in extreme conditions since it is optically transparent from the ultraviolet (UV) to the far infrared (IR). The use of polycrystalline CVD diamond film in optics depends mainly on the surface morphology, grain size, impurities, and quality of the film, which determine the transparency and the spectral range of transparency of optical components. At present, the best CVD diamond films with a transparency in the visible spectrum were prepared in the MWCVD chamber [25]. Generally, CVD diamond films are transparent in the range of infrared at least, which seems to be an imminent application of this window material. At the other end of the spectral range CVD diamond film supports are in use for X-ray lithography.

As to its chemical resistance, diamond will oxidize at high temperatures, and dissolve in carbide forming metals, but it is not attacked by other reactions. Diamond coatings could replace platinum in many laboratory applications having an extreme environment.

Application in electronics. The electronic properties of diamond, such as wide band gap, high dielectric constant, and electron and hole mobility are prominent in semiconductor materials. Coupled with its excellent thermal properties, diamond would be a promising material for high-power and high-temperature electronic devices. In addition to its other useful electrical properties, diamond has a stable, intrinsic negative electron affinity.

Doping of diamond. The realization of *n*-type and *p*-type doping is the key step for diamond application in electronics. The ideal doping is expected to form the substitution solid solution and no other defects are electrically active. This type of doping will not influence the energetic characteristics of the host diamond lattice. To date, boron has been successfully demonstrated to be the only dopant which

exists with the substitution incorporation in the diamond lattice. It makes diamond *p*-type with an activation energy of 0.37 eV [26].

The boron incorporation in CVD diamond film can be achieved by *in situ* doping during the growth process. Toxic diborane, which is the only gaseous form of boron, was widely used during the growth process of CVD diamond film [27,28,29]. Nontoxic and more easy to handle sources in solid form, like boron powder [30] and boron trioxide [31], or liquid form, such as trimethylborate [32], have been successfully introduced. The nongaseous boron sources are usually heated or dissolved in a high-pressure liquid in order to enhance their vapor pressure sufficiently. It was also found that the addition of boron can act as a catalyst to promote the diamond film growth and control the surface morphology of diamond film [33].

The other doping technique for diamond is ion implantation. During the ion implantation process, the temperature is maintained either at room temperature or at 1200°C, but the subsequent annealing is performed at 1400°C. The graphitization of the damaged diamond is its main problem and limits the amount of dopant in the diamond [34]. Using the low diffusivity of point defects created in the implantation, doping of diamond with boron was successfully obtained by combining low-temperature (at 77 °K) ion implantation into the samples that were predamaged by carbon implantation [35].

Recently, it was noted that the *p*-type diamond layer has been produced in polycrystalline diamond by means of rapid thermal diffusion of boron where the deposited boron on thin film is the source and the temperature is near 1600°C [36]. The average sheet resistance of the conducting layer formed is about 356 Ω.cm and the diffused-layer thickness is about 0.6 μm. The advantages of this approach are that a low contact resistance can be obtained and only one high-temperature step is involved.

Unfortunately, the *n*-type doping of diamond has not been completely achieved until now. The potential dopants are nitrogen, phosphorus, lithium, and sodium. However, the low thermal diffusivity of these in diamond matrix does not fit the need of *n*-type semiconductor enough. Most of the attempts on *n*-type diamond have been focused on nitrogen that was introduced into the gas phase with N₂ or NH₃ during the preparation process of diamond film. It was shown that nitrogen couldn't form the ideal substitution doping. Theoretical calculation also shows that nitrogen forms a deep energy level of 1.2 eV below the bottom of the conduction band [37]. Like in the case of boron, the growth rate of diamond film in the nitrogen-containing environment can be increased and smooth diamond films are obtained.

The attempt of phosphorus doping into diamond film has also been reported [38]. Okano et al. (1990) have used phosphorus doping to fabricate a *p-n* junction in CVD diamond film [39]. However, it was dubious whether the *n*-type conductivity was due to phosphorus incorporation into the diamond lattice or to lattice damage due to its extremely low electron mobility. Recently, Koizumi et al. (1997) produced *n*-type diamond films with activation energy of 0.43 eV when phosphorous was introduced during the CVD process [40]. Further studies are required to confirm the success of this work.

Field-electron emission of diamond. Diamond has been considered as a cold cathode material due to its negative electron affinity (NEA). Electrons from the conduction band can easily escape from a diamond surface into a vacuum, provided that as they leave they are replaced from another source. Expelling electrons from most materials requires temperatures between 1000 and 3000°C, or electric fields greater than 10 MV per centimeter. Semiconductors such as silicon and gallium arsenide can be given a negative electron affinity by coating them with a thin layer of cesium, but extremely small amounts of water or oxygen can react with the coating and destroy its effect. Once free of the diamond surface, these electrons can be accelerated by an electric field, formed into a beam to strike a target (perhaps a phosphor, which will glow in proportion to the current impinging on it) or modulated by an external signal. Due to the electrons that can easily emit from diamond, vacuum tubes fabricated with diamond cathodes should not be subjected to the factors that limit the life of conventional cathodes. Hence, the cold diamond cathodes could be used in small gas discharge lamps, panel computer and television displays, and perhaps even submicron triodes that would out-perform conventional semiconductors.

The early work on field-electron emission from diamond was done in the beginning of 1990. Geis et al. (1991) fabricated such cathodes of *p*-type single crystalline diamond where a current density of about 10 A/cm² was observed [41]. Givargizov et al. (1995) also obtained a high current density from microcrystalline diamond particles on the tips of silicon [42]. Although single crystalline diamond is not applied widely in flat-panel displays due to its high preparation cost, such studies are beneficial to our understanding of the diamond electron emission process.

The field-electron emission of diamond film has been currently of much interest in the development of CVD diamond [43,44]. As far as such field emission applications of diamond film are concerned, considerable technological progress has been achieved recently with emission thresholds as low as 1 V/μm [45]. In fact, CVD diamond films are polycrystalline and contain nondiamond components. Besides the negative electron affinity of diamond, these factors also determine the electron emission from CVD diamond films. Emission results for carbon-based emitters strongly depend upon the materials phase purity, dopants, and surface treatment.

By comparison of the different doped diamond samples, Geis et al. (1995) found that the best emission was obtained from nitrogen-doped diamond samples, followed by carbonized polymer, the lithium-doped, polycrystalline phosphorus-doped diamond films, and boron-doped diamonds [46]. All samples had enhanced emissions compared with undoped diamond, except for boron-doped samples. This was proven by Sowers and colleagues (1999) [47]. Sub-bands or defects formed by N and Li impurities are believed to be responsible for this enhanced emission. Although *p*-type semiconducting diamond is readily available by doping with boron, it is not helpful for achieving low-field electron emission due to the Fermi level of 5.0 eV below the vacuum level. Therefore, a reliable shallow *n*-type dopant for diamond is needed for the low-field and efficient electron emission of CVD diamond films.

The effect of defects on electron emission of diamond films was studied by Zhu et al. (1995) [48]. They have found that the threshold electric field required to generate sufficient emission current densities for panel display applications (>10 mA/cm²) can be reduced when the diamond is grown so as to contain a substantial number of structural defects. The succeeding works of these authors have further confirmed the role of defects by reporting the effects of ion bombardment on the field emission characteristics of CVD diamond films [49]. They believed that the defects create additional energy bands within the band gap of diamond and thus contribute electrons for emission at low electric fields.

Surface states below the conduction band of 1 eV are supposed to be attributed to the electron emission of diamond [50]. In fact, surface states do exist in the band gap on reconstructed diamond surfaces [51]. However, this viewpoint does not explain that the non-surface-reconstructed or H-terminated diamond films, where there exist no surface states, also can emit electrons. In addition, it is also not known how the electrons are transported to these surface states to sustain the emission from the undoped or *p*-type-doped diamonds.

As mentioned above, the carbon phase also influences the electron emission. Recently, a few other carbon materials, such as nanodiamond [52], diamond-like carbon [53], carbon nanotubes [54] and nanostructured carbon films [55] can also emit electrons. However, the emission mechanism of these materials is not completely understood but seems to be related to a substantial geometric enhancement factor or perhaps an electrical field enhancement created by highly nonuniform electronic properties over short (nanometer) distances.

Indeed, the electron emission of diamond cathode is limited for practical purposes by three factors, which include the large area heteroepitaxy of diamond film, the resistance of the conducting substrate that supplies it with electrons, and the mechanism of electron emission of CVD diamond films. However, with the development of CVD diamond film the application of field electron emission has never been seen as uncertain. Recently, the success of the 1" \times 1" diode display of diamond was reported by American Si-Diamond Company. It reveals the application potentials of CVD diamond films.

4.3 Nucleation and Growth of Diamond Films

4.3.1 Homoepitaxy of diamond film

For electronic applications of diamond films there is great interest in the growth of high-quality single-crystal diamond film. Early in 1990s the diamond deposition on natural or high-pressure-synthesized diamond substrate was successfully achieved by many research groups [56,57,58]. This kind of diamond growth mode is called homoepitaxy. Although the diamond application with the homoepitaxial method is greatly limited by the cost of natural diamond and the small size (<0.5 mm) of high-pressure-synthesized diamond crystals, homoepitaxial growth studies

promise to be extremely useful in advancing our understanding of the growth mechanism.

An understanding of the growth mechanism of diamond film is necessary to explain the variation in growth rate and surface morphology observed for deposition on the low-index faces of diamond. Investigation of homoepitaxial growth shows that the diamond growth rate decreased in the order (110), (111), and (100) [59,60]. Doping with boron during deposition can change the growth rates of diamond crystalline faces. Growth rates of (110) and (100) faces were significantly increased to 14 and 6.6 $\mu\text{m/hr}$, respectively, whereas a decreasing growth rate was observed on the (111) face [61].

Flat films were observed only on the (100) face, while (110)- and (111)-oriented diamond film surfaces have been rough on the μm scale. Sutcu et al. (1992) have studied the surface morphology on the nanometer to micrometer scale of homoepitaxy diamond films using atomic force microscopy [62]. Their observations showed that (100) epitaxial films displayed a growth-condition-dependent morphology: rough on the μm scale with pyramidal features and penetration twin at a low substrate temperature and CH_4 flow; and nearly atomically smooth at higher temperature and hydrocarbon flow rate. The facts imply that the growth predominantly at steps, ledges, or kinks occurs much faster than nucleation of a new layer when the hydrocarbon mole fraction and the substrate temperature are increased. However, the (110) surface of diamond film is found to be extremely smooth on the nm scale, which suggests that the gross morphology is built up from one- or few-atom-high steps and kinks and that growth occurs preferentially at these low-coordination sites.

The films on (111) face of diamond with a high degree of defects and cracks have been observed by many authors [59,61,63]. It is believed that the cracking is a consequence of tensile stress, which is caused by unequal thermal expansion coefficients of the substrate and diamond film. The cause of the increased thermal expansion coefficient in the (111) film is still unclear, but Raman spectra study shows some incorporation of amorphous carbon into the film. In addition, several authors have also reported that stacking-fault formation and twinning are ubiquitous in (111)-oriented growth, and either of these cracks may be responsible [64,65]. A high degree of defects and twins were also usually found in the boron-doped (111)-oriented diamond films.

4.3.2 Heteroepitaxy of diamond film

Nucleation process

It is known that the initial nucleation step of thin film is an area of importance that has bearing on adhesion, film properties, and the type of substrates that can be successfully deposited. Unlike homoepitaxy, the biggest problem of diamond film deposited on mirror polished nondiamond substrate is that it is more difficult for diamond nucleation due to its higher surface free energy (6–9 J/m^2 for low-index faces) than for heterosubstrates and also the relatively low sticking probability of

the precursor of diamond nucleation. Without surface pretreatment, the diamond nucleation density only reaches $10^5/\text{cm}^2$ which isn't high enough for heteroepitaxial growth of diamond film. Therefore, the low diamond nucleation density on nondiamond substrates has been an obstacle for heteroepitaxy and the wide application of diamond film.

In order to enhance the diamond nucleation density on heterosubstrates, many pretreatment methods have been developed. They may be grouped into four major categories: (1) diamond powder scratching of the substrate surface [66,67]; (2) predepositing the buffer layer on the substrate surface [68,69]; (3) electrochemical etching [70,71]; and (4) bias-enhanced nucleation method [72,73]. Of these methods, the bias-enhanced nucleation method is reported to be the best way to increase the diamond nucleation density on nondiamond substrates and to better realize the heteroepitaxial growth of diamond films, followed by diamond powder scratching.

Diamond powder scratching of the substrate surface using mechanical and ultrasonic techniques is usually done before the deposition of diamond films. The common density of diamond nucleation is about $10^8/\text{cm}^2$, three orders of magnitude higher than that of the substrate without pretreatment. The nucleation enhancement by diamond powder scratching is first attributed to the presence of defects and sharp edges on the substrate surface. It was known that the large density of defects and sharp edges can provide the high-energy nucleation sites (unsaturated bonds) which can capture carbon atoms rapidly enough to directly form the critical diamond nuclei. It has also been proposed that surface defects or pseudomorphic lattice matching reduce the free energy of diamond, compared with graphite, and thus stabilize the diamond nucleation. This view can also explain the nucleation enhancement by the electrochemical etching method, where it was found that almost all the diamond nuclei grow at the edge of the etched pores on porous silicon substrate [70].

It is thought that the seeding effect also promotes the increase of diamond nucleation density by diamond powder scratching. Iijima et al. (1990) found a diamond residue of ~ 100 nm on the diamond-abraded substrate surface [74]. This observation strongly implies that presetting is indeed responsible for nucleation enhancement by promoting diamond-on-diamond growth.

In 1991, Yugo et al. reported that the nucleation density of diamond was greatly increased to over $10^{10}/\text{cm}^2$ when the negative bias at the substrate was used [75]. Thereafter, the bias-enhanced nucleation is usually applied in the CVD diamond film process. The first successful growth of high textured (100) diamond film was reported by Stoner and Jiang et al. using the MW CVD technique in 1993 [6,7]. It was also reported in the hot-filament CVD system in 1995 [76]. The bias-enhanced nucleation method allows for control of the nucleation density and film morphology and offers a better potential for heteroepitaxial diamond film growth. However, the mechanism remains unclear so far.

It is known that the bombardment of an active gas species to the substrate surface is very important for the deposition of thin film in physical vapor deposition. The bombardment effect not only provides the large active sites on the substrate surface for the precursor, but also promotes the diffusion of adsorptive species on

the substrate surface. The effect also exists in the CVD process. It is out of question that the negative bias application at the substrate enhances the bombardment effect, where the impact of the positive gas species hastens the movement of the diamond precursors on substrate surface and gets them together regularly to form the orientation nuclei of diamond. Tomelini et al. (1991) also found that the ion impact could increase the defect density (such as point defects, steps) on the substrate surface that were like the high-energy sites for diamond nucleation [77]. It was proven by Wang et al. (1997) who directly observed the micro-pit caused by ion impact, with the atomic force microscope technique [78]. In the bias-enhanced nucleation process, Sattel et al. (1996) found that peak values of the nucleation density always correspond to ion energies in the range of 70 to 90 eV, independent of the methane concentration used [79]. Further studies by these authors have shown that the range of ion energy is close to the optimum energy for ion subplantation, responsible for sp^3 bonding in diamond-like carbon. They thought that it was the key process for diamond nucleation. The diamond crystallites only along the $\langle 001 \rangle$ axes in the flow direction of the bombarding ions are usually obtained, but no proper explanation is available.

Although the explanation of ion bombardment for negative bias enhanced nucleation is widely accepted [80], it also encounters a series of problems. It is found that using the positive or AC bias can also enhance the nucleation density of diamond on mirror-polished substrate surface [81,82]. This phenomenon can't be completely explained by the ion bombardment effect. Hence, Chen et al. (1995) suggested that the electron emission from diamond surface is the key to nucleation enhancement [83]. The high electron emission accelerates the dissolution of hydrogen molecules and other gas species and increases the concentrations of atomic hydrogen and hydrocarbon species near the substrate surface, thereby enhancing the nucleation density of diamond. It is deduced that the growth of diamond (111) facet is suppressed or etched due to its low work function compared with the (100) facet and therefore displays the (100) orientation of diamond nuclei. Shigeato et al. (1993) also suggested that the impact of accelerated ions or electrons on gas species changes the chemistry near the substrate surface [84,85]. However, the study of *in situ* optical emission spectra shows that the variety of atomic hydrogen and hydrocarbon species is not as great as the nucleation density of diamond.

Stoner and Glass (1992) found that biasing pretreatment creates a layer of non-crystalline carbon, however, increasing substrate temperature promotes the formation of a sublayer of SiC by reaction with the Si substrate [86]. The formation of a SiC buffer layer was also observed by other researchers [87,88,89]. Hence, the SiC buffer layer possibly plays an important role in promoting diamond nucleation. Also the SiC interface prepared by microwave-assisted growth has been identified as crystalline β -SiC, while an amorphous SiC layer was found in the case of biased hot-filament CVD process. However, the SiC buffer layer may be a competitive carbon reaction channel and not a necessary condition for the diamond growth, because the final formation of the SiC layer is achieved in only ~ 2 min, long before diamond nucleation occurs. The results of Williams et al. (1990) indicated that a deposited SiC layer on silicon substrate didn't promote diamond

nucleation [64]. Therefore, the formation of a SiC intermediate layer along with seems to be an inadequate explanation for the nucleation enhancement.

Recently, our group used a novel bias method that is applied parallel to the substrate surface [90,91,92]. The typical features of this new method are: (1) the substrate is not biased to avoid the ion or electron bombardment of the silicon surface; and (2) the pretreatment process of the silicon substrate is isolated from the growth process. Using this method a significant increase in diamond nucleation density was also found. The nucleation density on silicon substrates pretreated by the discharge at room temperature is similar to that treated at high temperature. Due to no obvious impact of charged particles, it was suggested that the increase in hydrocarbon concentration leads to the formation of a thin amorphous layer and thus promotes the diamond nucleation on the substrate surface. In the conventional substrate bias process, the formation of amorphous carbon was also found and is obviously beneficial for the nucleation of diamond [93]. The results of Chiang et al. (2000) also showed that surface pretreatment would introduce a substantial amount of carbon species on the substrate surface and that was the primary reason for the enhancement of diamond nucleation [94]. As mentioned above, the diamond nucleation density could be enhanced by amorphous carbon deposited on the silicon surface. The amorphous carbon layer can offer the nucleation sites and saturated carbon for diamond nucleation. On the other hand, amorphous carbon contains sp^2 and sp^3 components and the application of high temperature for normal diamond growth dissolves the sp^2 bonded carbon faster than sp^3 structures, and eventually there are more sp^3 clusters on which the diamond can grow. Additionally, Geyber et al. (1994) observed that diamond crystals 5 nm in size were embedded in the amorphous carbon after bias pretreatment [95]. A similar result was also reported by Zarrabian et al. (1997) using the electron cyclotron resonance technique at room temperature [96]. Therefore, another possibility for amorphous carbon enhanced nucleation might be that the diamond nucleates on the nanodiamond particles embedded in the amorphous carbon.

Growth process. Single crystal silicon has been used as the most common substrate for diamond film due to its low cost and compatibility in electrical device applications. In addition, it is one of the substrates on which the heteroepitaxial growth of diamond film was first achieved. Therefore, much of the understanding of CVD diamond film, including nucleation and growth process, is based on this kind of substrate. To date, the heteroepitaxial growth of diamond films on silicon have only been observed either in MWCVD chamber or in HFCVD chamber. And as stated above, the application of the negative electrical potential to the substrate plays an important role in the nucleation process.

In the initial stage of CVD diamond film deposition an amorphous carbon layer or SiC layer was usually found to form on the silicon surface. The role of the intermediate layer in CVD diamond deposition is still a controversy, because it has also been shown by using cross-sectional transmission electron microscopy that diamond could be grown directly on silicon substrate without any intermediate buffer layer [97]. A recent study by Lee et al. (2000) implied that the diamond nucleation site is important to the epitaxial growth of diamond [98]. Cross-section

HRTEM in Fig. 4.4 shows a grooved Si morphology onto which a predominantly amorphous carbon is deposited and no SiC crystallites were found. Some diamond crystallites have grown directly on Si, and some are embedded in the α -C matrix. Two nucleation sites in Fig. 4.4 for the diamond crystallite directly grown on Si contribute to the epitaxial growth of diamond. Therefore, a mechanism for the heteroepitaxial growth of diamond is suggested, in which etching of the nondiamond carbon binder exposes and removes nonadherent nanodiamond nuclei, leaving intact only those directly nucleated on the silicon substrate.

An understanding of diamond film growth under CVD conditions is attributed to the role of atomic hydrogen. Figure 4.5 shows the possible reaction process. Atomic hydrogen and methyl radicals, which come into being by thermal or electronic methods, are the important growth precursors for diamond. Generally, the dangling bonds of carbon atoms on the growing surfaces of diamond film were terminated by atomic hydrogen to prevent the surfaces from reconstructing to the graphite-like surface. Due to the stronger H-H bond in molecular hydrogen than the C-H bond, the surface-bonded atomic hydrogen can be abstracted by a gas-phase atomic hydrogen with the formation of a stable molecular hydrogen and lead to activating a vacant site. This process is called the abstraction effect of atomic hydrogen. Then a methyl radical occupies this vacant site to form a new C-C bond, therefore providing a possible extension of the diamond lattice. In addition, atomic hydrogen can etch both diamond and graphite, and the etching rate of atomic hydrogen to the former exceeds that to the later. Thus, the diamond film can be synthesized under the CVD conditions. These processes indicate that the abstraction of atomic hydrogen and the etching of atomic hydrogen to diamond and graphite on the diamond growth surface influence the growth, growth rate, and the quality of the diamond film.

The growth modes of diamond films were studied by many researchers. Kreutz et al. (1995) reported that screw dislocations in the middle of spirals serve as continuous sources of steps for layer growth producing (111) facets of high crystal perfection on boron-doping CVD diamond using the scanning tunneling microscopy (STM) technique [99]. Godbole et al. (1997) indicated that the basic mechanisms for growth in the (100) and (111) directions could be of a different kind according to the investigations on the hot filament CVD diamond using STM technique [100,101]. A large number of nanofacets exhibit a layer structure which commensurates with the underlying micron-sized parent (100) crystallites, and this is in contrast to their earlier STM studies on (111) diamond crystallites where they frequently observed the presence of screw dislocations. Zhu et al. (1992) reported the observation of a two-dimensional step growth mechanism on (110) faces of diamond films made by an oxyacetylene combustion flame technique [102]. Furthermore, these are some reports available on the step flow growth on (001) diamond substrates [103,104,105,106].

Recently, Han et al. (1999) reported the presence of terraces on (111) facets, and fairly convincing evidence for two kinds of growth mechanisms on (111) diamond facets of the same crystallite by scanning electron microscopy (SEM) is that shown in Fig. 4.6 [107]. Both left- and right-handed spirals were obtained

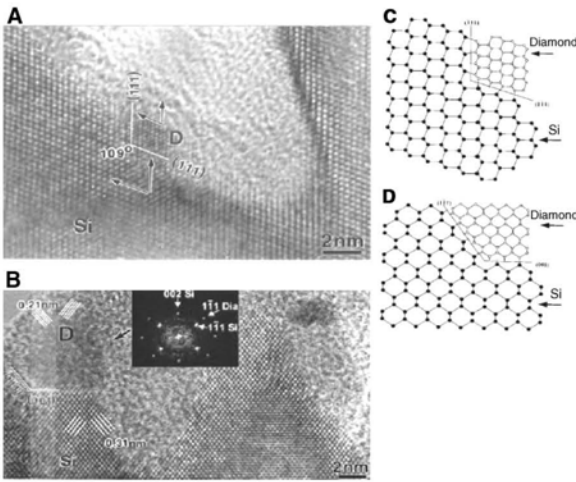


Fig. 4.4. (A) HRTEM image of a diamond crystallite (diameter ~2 nm) grown directly on a Si step with an epitaxial alignment. (B) HRTEM image of a diamond crystallite (diameter ~6 nm) grown directly on a Si (001) surface with an epitaxial alignment. (C) and (D) Ball-and-stick diagrams illustrate the interfaces between the diamond crystallites and the Si substrate in (A) and (B) [98].

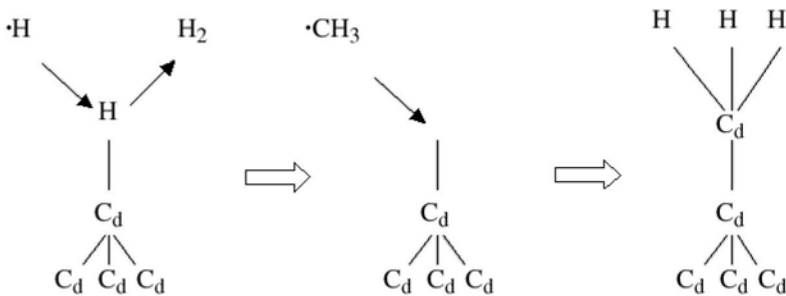


Fig. 4.5. A possible reaction schemes for the growth of CVD diamond film

on a five-fold multiply twinned particle. According to the classical crystal growth theory of Burton-Cabrera-Frank (BCF), the growth mechanism on singular surfaces can be either a two-dimensional (2D) nucleation or spiral growth. The steps intrinsically connected to a screw dislocation on the original surface, which act as continuous sources of growth steps, winds up to a spiral. Crystals grown that way are of high perfection. On the other hand, 2D nucleation and step flow are used to elucidate those features of facets A and D in Fig. 4.3(b). When the facet is free of screw dislocations, some impurities segregated onto the underlying diamond substrate surface might act as nucleation sites in the initial growth stage, resulting

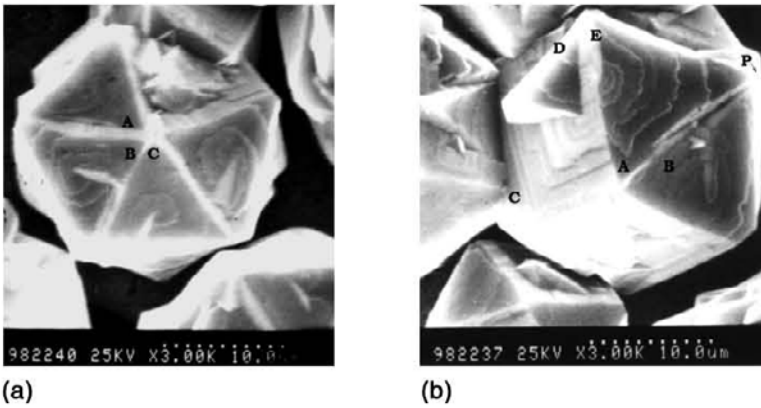


Fig. 4.6. Scanning electron micrographs of diamond film. (a) A five-fold twin particle. Facets B and C show right- and left-handed spirals, respectively. (b) A multiply twinned particle. Facet A shows some terraces by step flow growth mode; facet B shows a spiral growth [107].

in 2D nucleation on the edge or apex of terraces, which have a lower nucleation barrier than the center. Then, those precursors for diamond growth reach the substrates and migrate onto the surfaces, before being incorporated into macrosteps. These steps adsorb carbon atoms with sp^3 hybridization from the gas phase and flow forward continually until they cover the crystal face completely.

Substrate materials. Besides Si, heteroepitaxial or textured growth of diamond has been reported on c-BN [108,109], Ni [110,111], Cu [112], β -SiC [113,114], and BeO [115], in which c-BN showed the most promise as a heteroepitaxial substrate due to its similar structure to diamond, close lattice match ($\sim 1.3\%$) and relatively high surface energy. However, the growth of large single-crystal c-BN is probably as difficult as growing large diamond single crystals. There were some reports on the local epitaxial growth of diamond on Ni or Cu substrate due to their close lattice match with diamond. The large thermal mismatch to diamond makes them unsuitable as substrates for epitaxial growth of diamond film. As mentioned earlier, higher nucleation density and local epitaxial growth on silicon were found through a buffer layer of silicon carbide. It is known that the lattice mismatch between β -SiC and diamond is rather large; the following epitaxial relationship $(100)_{\text{diamond}} // (100)_{\beta\text{-SiC}}$ and $[110]_{\text{diamond}} // [110]_{\beta\text{-SiC}}$ found by Stoner et al. (1992) probably indicates such a lattice mismatch couldn't prohibit heteroepitaxy. The theoretical studies of the interfaces between diamond and c-BN or BeO show that BeO is, like c-BN, a potentially suitable substrate for heteroepitaxial growth of diamond film [116,117,118]. The BeO/diamond adhesion energy was estimated to be 4.6 J/m^2 , slightly smaller than that of c-BN/diamond (5.4 J/m^2). The success of diamond epitaxial growth on BeO substrate and the easy synthesis of high-quality large BeO crystals seem to bring us the hope of heteroepitaxial growth of CVD diamond film. However, attention must be paid to the fact that BeO is a toxic ma-

terial, which complicates processing. Here, the authors emphasize some other substrates recently reported as having some novel possibilities.

Recently, a new kind of material, LaAlO_3 , was attempted as a possible substrate for diamond film [119]. It was noticed that at about 460°C , LaAlO_3 single crystal undergoes a phase transition from perovskite-like at room temperature to simple cubic structure. Its crystalline direction of (012) changes into (100), and its lattice constant is about 3.82 \AA at temperatures above 800°C , which is close to that of diamond. The lattice mismatch of 7.2% to diamond at high temperature is much smaller than the lattice mismatch between silicon and diamond ($\sim 52\%$). As an insulating substrate, a nucleation density of more than 10^8 cm^{-2} was achieved on ultrasonically cleaned wafers. The epitaxial relationship between them was found to be $(110)_{\text{diamond}}/(100)_{\text{LaAlO}_3}$ [120]. The high quality and no stains found in diamond films are attributed to the better lattice match. X-ray photoelectron spectroscopy (XPS) analysis shows that the diamond film is formed directly on the LaAlO_3 substrate without a buffer layer. Hence, it may be a good heteroepitaxial substrate for diamond film.

AlN ceramic, a dielectric and passivation material for compound semiconductors, is routinely used as a heat sink for integrated circuits and photoelectric devices [121]. Godbole et al. (1995) have studied nucleation and growth characterization of diamond film on nickel with an AlN buffer layer. It was found that the AlN layer plays a crucial role in limiting carbon diffusion and inhibiting the formation of graphitic carbon, while simultaneously enhancing the nucleation and adhesion of diamond film [122]. The similar results of Chen et al. (1996) have supported this effect [123]. Recently, the (100)- and (110)-textured diamond films directly grown on AlN ceramics were reported by Shang et al. (1998) in a hot-filament CVD system [124,125]. Our group has studied the thermal properties of the diamond film/ AlN ceramic composite by the photothermal deflection (PTD) technique [126,127]. We have found that the thermal conductivity of AlN ceramic could be greatly improved when diamond film is deposited on it. The unusual stability and very good adhesion of the diamond film on AlN ceramic substrate are attributed to the formation of carbide, and the small thermal mismatch between them make it satisfactory for the application as a heat sink for high-power integrated circuits and electronic devices. So, considering the cost and realistic aspects, the diamond film/ AlN ceramic composite may be a more suitable heat sink material than thick diamond film.

It may prove interesting to deposit the diamond film on polycrystalline diamond substrate. It has been found that using homogeneous material as a buffer layer can markedly improve the quality of GaN films due to the exact lattice and thermal expansion match between them [128,129]. It would seem more logical to use a diamond buffer layer in the growth of diamond film. This approach has been successfully employed to obtain high quality diamond films by Liao et al. (1999) [130]. First, a diamond film grown for 4 hours was cleaned using an *in situ* method (such as hydrogen plasma etching) or *ex situ* method (such as strong oxidants), then the sequential growth of diamond film was carried out on this buffer

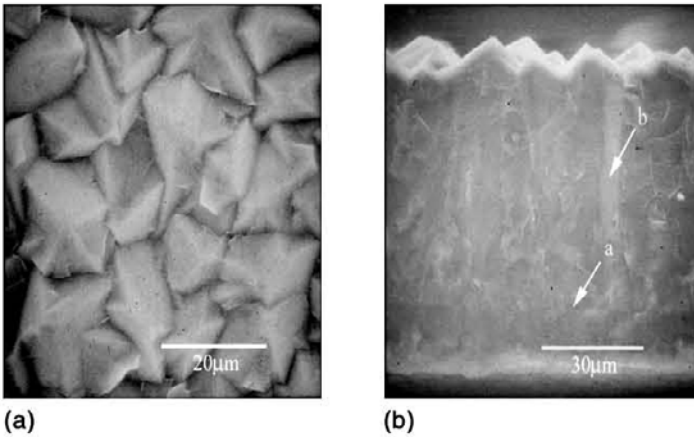


Fig. 4.7. SEM photographs of diamond film with the two-step growth method. (a) (110)-orientation diamond film and (b) the cross section of diamond film [130]

layer for 6 hours. This is called the two-step growth method. By this method two-layer structure, high-quality diamond film with high growth rate was obtained, and is shown in Fig. 4.7. Significant improvement in surface resistivity was also found. The authors believe that the improvement is attributed to the decreasing activated carbon concentration and increasing second nucleation density of diamond on the first diamond layer [130]. The same lattice and thermal stability of the buffer layer is also beneficial to the deposition of high quality diamond film. The buffer layer approach will perhaps enable the evaluation of electronic devices fabricated with this material to commence in the future.

4.4 Phase Diagram and Gas-Phase Species in CVD Diamond Growth Processes

The growth of diamond films on nondiamond substrate by chemical vapor deposition (CVD) was first reported by Spitsyn et al. in the 1970s [3]. This technique was later implemented by Matsumoto et al. (1982) [4]. They used a CH_4 and H_2 mixture as input gases. These pioneering experiments opened new perspectives in diamond applications and were shortly followed by a large number of researchers. To date, different input gas mixtures, such as $\text{CH}_4/\text{H}_2/\text{O}_2$, CO/H_2 , $\text{C}_2\text{H}_2/\text{O}_2$, and $\text{N}_2/\text{CH}_4/\text{H}_2$, different deposition techniques, such as hot-filament CVD, microwave CVD, and combustion flame CVD, have been successfully utilized for diamond film growth. CVD is now a highly reproducible growth process for synthetic diamond films. Although the diamond quality obtained is comparable to single-crystalline natural diamond to some extent, the possibility of including another carbon phase, the polycrystalline nature of CVD diamond films, and their conse-

quent high surface roughness still limit its practical application. Many experimental and theoretical works have been produced to better understand the diamond growth mechanism, in the attempt to find the answer to why diamond films can be deposited from these different gas sources by different synthesis techniques.

4.4.1 Phase diagram

Bachmann et al. (1991) have analyzed a number of experiments on diamond growth, and obtained a very important realization regarding understanding the effects of the gas mixtures used in the growth of films [131]. In the ternary C-H-O phase diagram only a restricted region (named the “diamond domain”) leads to the growth of diamond. This diamond domain seems to have the shape of a triangle, nearly centered on the H-CO tie line, with one angle roughly coincident with the H vertex. If the gas composition lies outside this triangle, either no growth occurs (in the region towards the O vertex), or nondiamond carbon phases are obtained (in the region towards the C vertex). Bachmann proposed that if the experimental point is located in the diamond domain, diamond growth should occur irrespective of the gas composition.

From this diagram, we can see that only the overall content of C, H, and O in the gas mixture determines the final outcome of the growth process. By using various kinds of input gases at a given C, H, and O atomic ratio, the same gas-phase environment and diamond precursor should form. Although this scheme is now accepted, there are practical problems in the direct use of this diagram for choosing a gas composition suitable for diamond growth, because careful flow meter calibration is needed, and other experimental parameters, such as substrate temperature and gas pressure, also have strong influences on diamond growth. Even in this region, the growth rate, quality, and morphology of the diamond films grown may be very different. Furthermore, the exact limits of the diamond domain region are still under discussion, so that a new mixture cannot be made to induce diamond growth by just finding the corresponding position in the C-H-O diagram.

Marinelli et al. (1994) have verified this diamond domain by “spanning” the C-H-O ternary phase diagram using several gas mixtures, each consisting of two gases, such as $\text{CH}_4\text{-CO}_2$, $\text{C}_2\text{H}_6\text{-CO}_2$, $\text{C}_2\text{H}_4\text{-CO}_2$, and $\text{C}_2\text{H}_2\text{-CO}_2$ [133]. By varying the relative concentrations of two gases, a line was obtained in the C-H-O diagram for each gas mixture. The lines have been made to cross the diamond domain, and properties of the films obtained by different mixtures also were compared. They found that the borders of the diamond domain deduced from these experiments considerably differ from the ones originally indicated by Bachmann et al. (1991). A very sharp border between the no-growth zone and the diamond domain occurs for higher C concentrations, and coincides with the H-CO tie line. The width of the diamond domain is much narrower, and shrinks while moving away from the H vertex. These results are shown in Fig. 4.8, which compares the triangular C-H-O diagram of the diamond domain proposed by Bachmann et al. (1991) and the

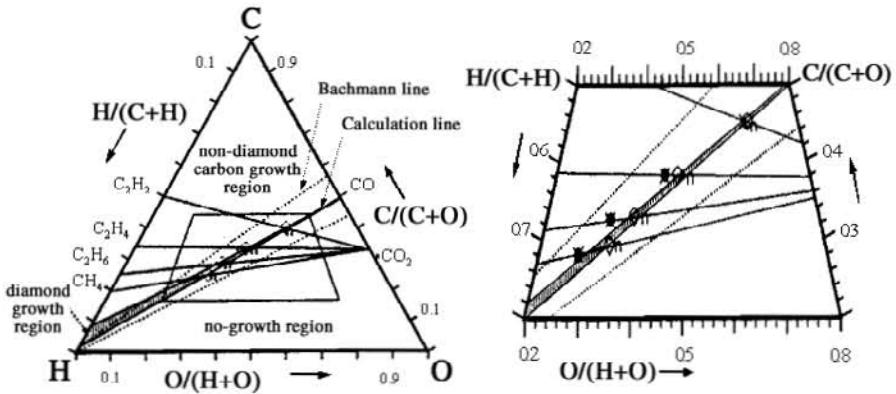


Fig. 4.8. Triangular C-H-O diagram for comparison of the diamond domain proposed by Bachmann and the experimental points investigated by Marinelli et al. [132]. The right graph is an enlarged view of the diamond domain region.

experimental points investigated by Marinelli et al. (1994). The right graph is an enlarged view of the diamond domain region. In this figure, the open triangles correspond to the onset of diamond growth; open squares mark the texturing conditions, and filled stars correspond to heavy graphite contamination.

In the C-H-O system, the phase equilibria are dominated by the very stable species H_2 and CO. As a consequence, only compositions lying above the H-CO line can produce carbon atoms that are “free” from the CO ties, and therefore available for the growth of any carbon phase [134]. It should be noted that the substrate temperature and the gas pressure could play an important role, affecting the total extension of the diamond domain. Actually, the Bachmann et al. (1991) phase diagram is a projective diagram in some range of temperature and pressure, which is formed by overlapping of many different phase diagrams, each one having a certain temperature and pressure. So the Bachmann et al. (1991) diamond domain may include nondiamond growth and nongrowth experimental points. Hwang et al. (1993) employed thermodynamics to calculate the theoretical diamond domain [134], and the results are consistent with the experimental points of Marinelli et al. (1994).

4.4.2 Gas phase species

Many ideas have been proposed over the past decade to rationalize the experimental results that diamond can be prepared by chemical vapor deposition. Most of them demand the presence of atomic hydrogen as a primary reactant and assign it to one or more roles, depending on one’s point of view. A popular suggestion was that atomic hydrogen acted as a means of etching graphite rather than diamond and therefore prevented the nucleation and growth of graphite or graphitic

carbons; diamond is kinetically stable relative to graphite in the presence of atomic hydrogen [135]. The vapor phase growth of diamond films can be thought of as the result of two processes. The first one involves reactions in a gas-phase environment to produce the precursor of diamond growth (dissociation); the second one is the process of adding material to the growing solid by the reactions between the precursor and growth surface, and then relaxation of this material to a lower free energy configuration or accommodation to the underlying lattice structure (deposition). These processes have been widely investigated in many experimental and theoretical works. Although the diamond film growth should be a non-equilibrium thermodynamical process, the equilibrium composition calculation can also give general information about the situation in the gas-phase chemical environment.

An established method for evaluating chemical equilibrium is the element-potential method. This is done by assuming that the gas-phase is a mixture of ideal gases and selecting atomic populations by the identity of initial species and their fraction in the mixture, as well as by state parameters [136]. The state parameters can be specified in a number of different ways, including a) temperature and pressure; b) pressure and entropy; c) enthalpy and pressure; and d) volume and entropy.

The basic theory for the element-potential method of determining equilibrium is based on the minimization of Gibbs free energy. The Gibbs function of a system is:

$$G = \sum_{k=1}^K \overline{g}_k N_k, \quad (4.1)$$

Where \overline{g}_k is the partial molal Gibbs function and N_k is the number of moles of each species k in the system. K is the total number of species. For ideal-gas mixtures or ideal solutions, the partial molal Gibbs functions are given by:

$$\overline{g}_k = g_k(T, P) + RT \ln X_k, \quad (4.2)$$

where $g_k(T, P)$ is the Gibbs function for the pure species k , evaluated at the system temperature and pressure; R is the universal gas constant; and X_k is the mole fraction of the k th species. The equilibrium solution at a given temperature and pressure is the distribution of N_k that minimizes the system Gibbs function.

We have calculated the gas-phase chemical equilibrium with an initial gas mixture of $N_2/CH_4/H_2$ of 0.1/1/100 mole ratios under constant temperature and pressure. By changing gas temperature in the range of 500 to 3500 K and keeping gas pressure at 10 kPa, we got the equilibrium concentrations of main species versus gas temperature, which include H, H_2 , C^+ , CH, CH^+ , CH_3 , CH_4 , C_2 , C_2H_2 , C_2H_4 , N, NH, NH_3 , N_2 , CN, and HCN, as shown in Fig. 4.9. The shadow region is the range of substrate temperature for successful diamond growth. The right vertical dot line at 2500 K is the highest temperature that filament can approach in a hot-filament CVD diamond environment. The region between these lines can be taken into account as the virtual gas-phase environment for diamond growth.

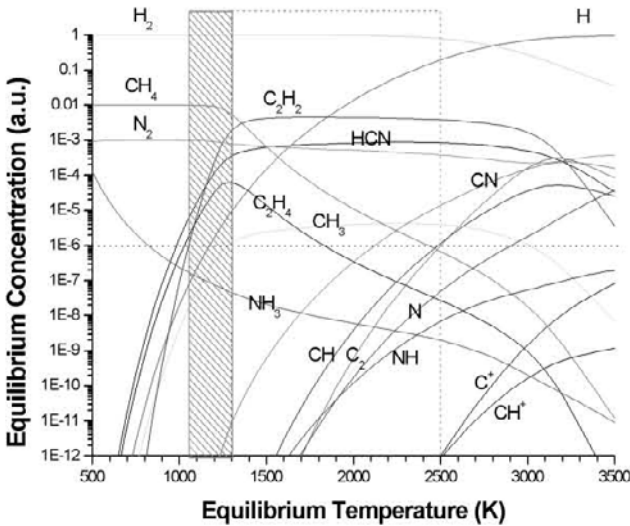


Fig. 4.9. Equilibrium concentrations of main species in $N_2/CH_4/H_2$ mixture versus temperature [137]

But the surface chemical reactions and the transportation of gas-phase species were not included in our calculations. In practice, the concentrations of the precursor and active species for diamond growth should decrease in the vicinity of the substrate, and depending on its diffusion coefficient or gas flow velocity, the species created near the filament would still have an opportunity to be diffused or convected to the substrate position. For the homogeneous recombination of atomic hydrogen: $H + H + M \rightarrow H_2 + M$, the characteristic reaction time is of the order 1 s at 20 Torr [138] (M is the third body for carrying the excess heat of recombination). The diffusion distance of an atom at time t is of the order \sqrt{Dt} , where D is the diffusion coefficient. For H in H_2 at 20 Torr, $D = 0.12 \text{ m}^2/\text{s}$. This implies a diffusion distance of 35 cm in 1 s. When we take into account another reaction path in the presence of hydrocarbon, for example, $H + CH_4 \rightarrow CH_3 + H_2$, the reaction time is deduced to be about 50 ms for a gas composition of 0.5% CH_4 in H_2 [138]. The diffusion distance is shortened to about 8 cm. The typical distance between the filament and substrate is about 1 cm, so H atoms in an H_2 background are able to freely diffuse to the substrate. In the DC arc jet CVD diamond reactor, the high speed reactive gas plume strikes the boundary layer above the substrate, and because the gas speed mostly exceeds the speed of sound, the reactive species haven't enough time to completely recombine in this convection process, and the spatial distribution of the species are influenced by both chemistry and fluid mechanics [139].

Although temperature gradients and finite residence time prevent the gas from attaining chemical equilibrium, the equilibrium composition provides a rough first

approximation to the actual composition [140]. The magnitude of real species concentration should be consistent with the result of the equilibrium calculation.

As shown in Fig. 4.9, the dominant hydrocarbon is methane below about 1500 K, while above this temperature it is acetylene. The reason for this becomes apparent if we consider the reaction: $2\text{CH}_4 \leftrightarrow \text{C}_2\text{H}_2 + 3\text{H}_2$. With the equilibrium temperature, the atomic H concentration rapidly increases. Besides C_2H_2 , CH_3 is also one of the most predominant hydrocarbon species; both these two species have already been proposed as the diamond precursor by many researchers. For the N-containing species, HCN has the highest concentration compared to that of the others because it has the highest chemical stability. Many investigations have suggested that the magical influences on diamond growth observed with the addition of nitrogen to the conventional methane/hydrogen mixture are related to the presence of CN radicals. We can see that the atomic N concentration is very low, and in the high temperature region, the concentration of CN is also high, and it shows a trend to exceed that of HCN.

Species whose concentration is below the 1 ppm horizontal line it hardly have notable influence in the typical thermal environment for diamond growth. But in DC arc jet CVD and microwave CVD diamond reactor, both C^+ and C_2 have been proposed as the diamond precursor, and in the electron-enhanced hot-filament CVD diamond reactor, CH^+ also has been suggested as the active species for diamond growth, because if there are a lot of electrons existing in the gas phase or the gas temperature is very high, both of them strongly change the distribution of gas-phase species.

4.5 *In Situ* Diagnostic Techniques for Diamond Growth

Despite the progress made in the past decades, the mechanism of the CVD diamond growth process has remained somewhat a mystery. Considering the two growth techniques just mentioned, the hot-filament system is a thermal system, while the microwave plasma involves processes such as excitation, ionization, dissociation, and ion-neutral reactions. It has always been perplexing that these two techniques, being so different in nature, require nearly identical conditions for diamond growth and produce fairly similar results. When using a microwave source (800 W), with the process pressure at ~ 20 Torr, a feed gas with methane/hydrogen $\sim 0.5\%$, and a substrate temperature of 1073°K , high quality polycrystalline diamond films can be produced like in hot-filament (2600°K) operated under the same conditions. The only significant difference being that the growth rate is approximately a factor higher in the microwave plasma [141]. However, that the two techniques would produce nearly identical results appears to suggest that under the conditions necessary for diamond deposition the gas phase kinetics existing in a microwave plasma system are not that dissimilar to those in a hot-filament system. This implies that there must be a uniform dominating mechanism for diamond growth.

The physical properties of diamond films grown using CVD techniques have been shown to be sensitive to the changes in the growth environment. As a result, most studies of diamond CVD attempt to optimize film growth properties by either probing different regions of the reactor parameter space or by changing the identity of the carbon source in the reactor feed. For example, film growth rate and morphology have been shown to be affected by changes in both the surface temperature T_s , and the carbon mole fraction in the reactor feed X_C [142]. Although these types of studies identify reaction conditions that promote diamond film formation, they provide relatively little insight into the reaction mechanisms that govern diamond CVD.

In order to understand the relationship between the reactor parameters and the properties of diamond film, and also obtain information about the uniform dominating mechanistic pathways for diamond film growth, many *in situ* diagnostic techniques have been employed for growth environment evaluation. These techniques can provide direct, quantitative or semi-quantitative information for a large number of stable and radical gas species about their energy and spatial distribution. With fast, *in situ* diagnostics, we can efficiently correlate gas phase conditions with film properties such as growth rate, texture, morphology, and uniformity. Experience gained with CVD diamond can hopefully be exploited with similar materials and, ultimately, the results and techniques will be applied during deposition for *in situ* process control.

4.5.1 Molecular beam mass spectroscopy

The most useful technique for characterizing the complex diamond CVD gas phase process is molecular beam mass spectroscopy (MBMS), because in the CVD diamond environment (especially for hot-filament system) a large number of neutral species or radicals exist or both neutral and ion forms exist (especially for microwave system). It has the versatility to quantitatively determine the composition of the gas in the immediate vicinity of the growth surface [143], it can detect stable and free radical species, and can be applied to a thermal [144] as well as a plasma environment [145]. The former feature is particularly important since it is the principal species in this region that interact with the surface and directly influence film growth properties.

The molecular beam mass spectroscopy (MBMS) measurements on CVD diamond growth were pioneered by Hsu et al. during the early 1990s [143,144,145,146,147], and then were extended by Rego et al. (1996) and Tsang et al. (1996, 1997) [148,149,150] to cover many important aspects of diamond growth using hydrocarbon, both with and without the presence of chlorine, nitrogen, or phosphorus-containing gases.

Typical mole fractions of species at the substrate under low-pressure diamond CVD conditions in a microwave system are shown in Fig. 4.10, as a function of the carbon content of the feed gas. These results were obtained by McMaster et al. (1995) using molecular beam mass spectrometry, extracting gas through a small

pinhole in the substrate [147]. The microwave power, reactor pressure, and surface temperature were held constant at 850 W, 20 Torr and 825°C, respectively.

We can see that these two figures are very similar, and the species mole fractions are almost independent of whether carbon is introduced into the reactor as methane or acetylene. These results indicate that the identity of the molecular species fed to the MPCVD reactor is lost and the gas phase composition depends only on the C/H ratio of the inlet gas stream. And, in either case, both methane (CH_4) and acetylene (C_2H_2) are found at the substrate, and these two species account for the majority of the gas-phase carbon. Ethylene (C_2H_4) is present at much lower levels, and ethane (C_2H_6) is not detected. Only two radical species, atomic H and methyl radical CH_3 , are detected under these conditions. The atomic hydrogen mole fraction seems to be nearly independent of the carbon content in the gas, at a level slightly below 10^{-3} . The methyl radical mole fraction rises with increasing carbon content, and is typically about an order of magnitude lower than methane.

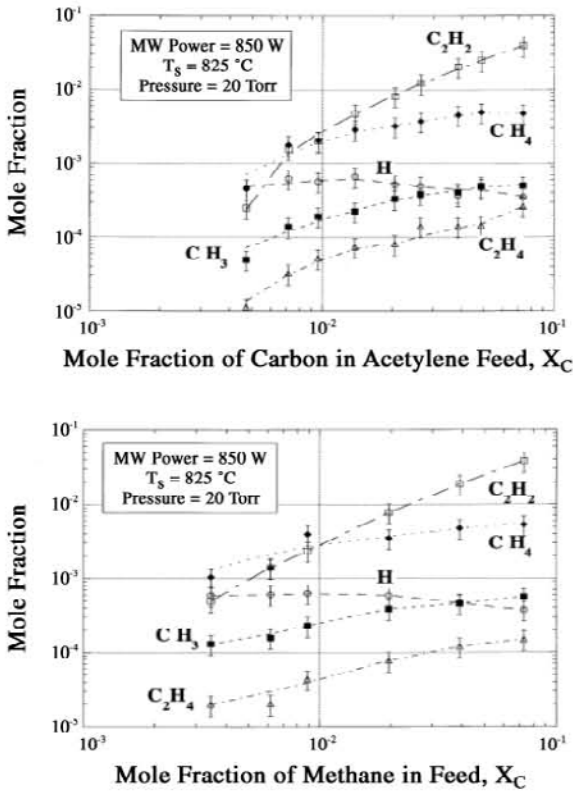


Fig. 4.10. Mole fractions measured at the substrate in a microwave plasma reactor as a function of carbon mole fraction in the feed gas X_C . (a), the carbon is introduced as acetylene, (b) the carbon is introduced as methane [147].

The mole fractions of the microwave system shown in Fig. 4.10 are very similar to those found in the hot-filament system [151,152], the main difference being that there is a sharp decrease in atomic H concentration by about an order of magnitude with the carbon mole fraction increasing in the hot-filament system. Sommer and Smith (1990) attributed this effect to the catalytic poisoning of atomic H production due to hydrocarbon decomposition on the hot-filament surface [153]. And the numerical simulations of the reaction environment predict that the gas-phase reactions will produce only a slight reduction in the atomic H concentration as the hydrocarbon concentration in the feed increases [154]. This prediction is consistent with the results shown in Fig. 4.10.

Nitrogen addition to the conventional hydrocarbon/H₂ mixture has shown significant influences on diamond growth, such as increasing growth rate, inducing (100) texture [155], and decreasing field emission voltage threshold [45]. But the amount of nitrogen incorporation into the diamond films has been found to be very low [155]. Besides N₂ gas, many other nitrogen-containing source gases have been used to investigate the mechanism. To date, the precise reaction kinetics attributed to these observations have not been studied in detail. But these experiments have provided valuable information about the natural processes.

Figure 4.11 shows product distribution of the major stable gas-phase species as a function of filament temperature measured 4 mm from the filament [150], reported by Tsang et al. (1997), and they utilized 0.5% CH₄/0.5% N₂ in H₂ as the input gas mixture. The methane and nitrogen concentrations decrease steadily with filament temperature, accompanied by a rise in HCN, C₂H₂, CH₃NH₂, and NH₃

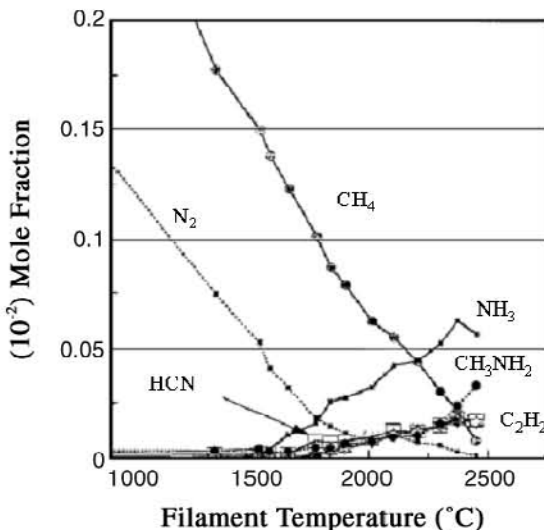


Fig. 4.11. Product distribution of major stable gas-phase species as a function of filament temperature measured 4 mm from the filament [150], using 0.5% CH₄/0.5% N₂ in H₂ as the input gas mixture

concentrations at $\sim 1700^\circ\text{C}$. Furthermore, in order to investigate the behavior of nitrogen in hot-filament CVD diamond in terms of the changes in the gas-phase chemistry when nitrogen is present, they used different nitrogen-containing sources as input gases, and found the differences in entire gas-phase species concentrations. In these experiments, C_2H_2 radicals were detected, which have been proposed by many researchers as precursors for diamond growth [188]. Comparison of the relative concentrations of these major stable species in different nitrogen-containing sources indicates that for a CH_4/N_2 gas mixture, HCN concentration decreases to just 1/4 of the original value, with most of the nitrogen-containing species in the gas-phase being NH_3 , not HCN, but the acetylene concentration is around an order of magnitude greater than that of other nitrogen-containing gases. It is consistent with the film growth result that the CH_4/N_2 gas mixture leads to a higher growth rate than that of the others [150]. Atakan et al. (1999) also reported similar results [156]. They investigated diamond CVD in atmospheric acetylene-oxygen flames doped with N-containing species, such as N_2 , N_2O , NH_3 , $\text{N}(\text{CH}_3)_3$, and found the growth-effective amount of N-additive decreases by more than an order of magnitude in the sequence $\text{N}_2 > \text{N}(\text{CH}_3)_3 \cong \text{N}_2\text{O} > \text{NH}_3$. These results imply that besides the gas-surface reaction, the gas-phase chemistry in the N-doping environment is a more dominant factor for the growth mechanism than the conventional hydrocarbon/ H_2 mixture system.

4.5.2 Laser-induced fluorescence

LIF is an optical technique capable of detecting species with good spatial and temporal resolution. Ground-state atoms and molecules can also be observed by laser-induced fluorescence (LIF). In a LIF measurement, the ground-state atoms or species are excited to a selected upper state by absorption of tunable pulsed dye laser energy. This absorption is followed by spontaneous emission of the excited state to lower energy levels. In this situation, emission can also be said to be fluorescence. One of these wavelengths is picked up by an interference filter or spectrometer, then used to record the LIF signal intensity. From measured fluorescence intensities, species or atom concentrations can be determined by calculating the ground-state population.

Several mechanisms have been proposed for the role of hydrogen atoms in CVD diamond film growth. It's generally believed that hydrogen atoms incident on the surface abstract hydrogen to produce vacant sites, where growth species can then stick to the diamond layer, and that atomic hydrogen etches surface graphite [157]. Gas phase hydrogen atoms may also produce condensable carbon radicals by reactions with hydrocarbons [158], and, impinging on the surface, they may create surface radicals and refill vacant sites by absorption [140]. Once absorbed, atomic hydrogen may also stabilize the diamond surface structure [159]. Several multiphoton excitation LIF schemes have been used to measure atomic H concentration in CVD diamond environments. Lucht et al. (1983) measured H-atom concentration in low-pressure flames using 205 nm laser radiation to excite the $n = 3$ level in a two-photon absorption process [160]. Alden et al. (1984) re-

ported using 308 nm light to excite the $n = 3$ level or using 292 nm light to excite the $n = 4$ level in three-photon-excitation LIF experiments [161]. Goldsmith (1985) described a multistep process where two photons at 243 nm excite atomic hydrogen from the $n = 1$ to $n = 2$ level followed by absorption of a third photon at 656 nm to excite the atom to the $n = 3$ level [162]. Bertagnolli et al. (1998) recently reviewed the energy level schematic for these multiphoton-excitation LIF techniques for measuring atomic H concentration [163], as shown in Fig. 4.12.

Bertagnolli et al. (1998) have used a three-photon-excitation LIF instrument [163] to measure the atomic hydrogen atom concentration in a stagnation-flow diamond-forming flame apparatus; the results are shown in Fig. 4.13. One can clearly see that the atomic hydrogen concentration decreases sharply near the substrate, because of the heterogeneous recombination of atomic hydrogen with the diamond surface. In thermal plasma and combustion systems, H is nearly in chemical equilibrium outside the boundary layer. In these systems, homogeneous recombination is only of concern within the boundary layer. Numerical simulations have shown that it is usually unimportant in high-speed arc jet or combustion systems [164], although it is predicted to become significant at pressures above about 2 atm [165]. Since homogeneous recombination of H atoms is usually negligible, the loss of H atoms must occur primarily on reactor walls and on the diamond surface itself. Measurements of the H concentration profile near a diamond substrate clearly show that diamond is a sink for H at typical substrate temperatures because of the atomic hydrogen absorption reaction or abstraction reaction ($H + H \rightarrow H_2$). In diamond surface chemistry, the most important aspect is the reaction between atomic hydrogen and the diamond surface. Because of the continual bombardment of the diamond surface with reactive atomic hydrogen during growth, most of the diamond surface is hydrogenated, and is therefore unreactive with incoming hydrocarbon species. In ultra-high vacuum, hydrogen desorbs from diamond as H_2 above about 800°C (ca. 75 kcal/mol activation energy). However, for diamond CVD conditions, this process does not appreciably contribute to creating the vacant site, since the desorption rate only becomes comparable to atomic hydrogen absorption or abstraction reactions at significantly higher temperatures ($\gg 1100^\circ\text{C}$) [166].

In order to determine the mechanism of the magical influences of nitrogen on diamond growth, many experiments have been undertaken to reveal the relationship between gas-phase chemistry and diamond growth [168]. Klein-Douwel et al. (1995) have applied a two-dimensional laser-induced fluorescence (2D-LIF) instrument to the chemical vapor deposition (CVD) of diamond by an oxyacetylene flame to visualize the distribution of CN in the gas phase during the diamond growth process [167]. Clear relations were observed between the distribution of CN and the local variation of the growth rate, the morphology, and the nitrogen incorporation. Figure 4.14 shows horizontal profiles of the CN LIF signal close to the substrate during diamond growth by an oxyacetylene flame (solid and dashed lines, right-hand ordinate) and the deposition rate v_d of the corresponding diamond layer along the path of the laser beam (diamonds, left-hand ordinate). d is the distance between the flame front and substrate, z is the height above the substrate at

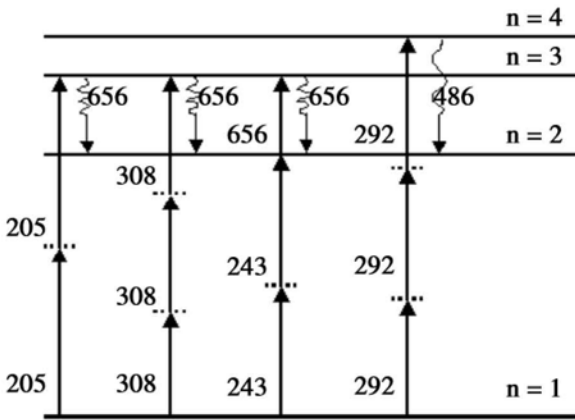


Fig. 4.12. Energy level schematic for various multiphoton-excitation LIF techniques for the measurement of atomic hydrogen concentration [163]

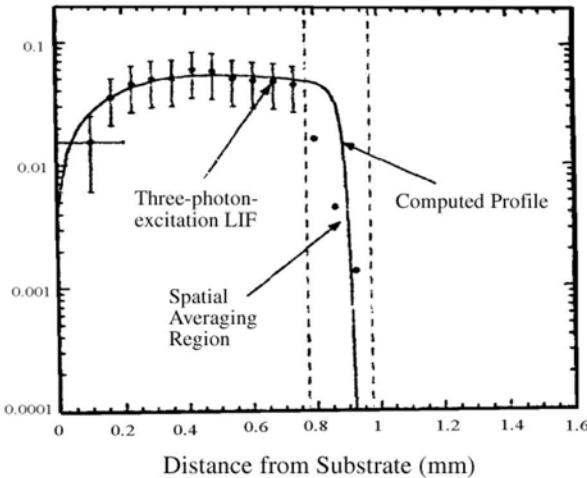


Fig. 4.13. Atomic hydrogen atom concentration profile measured using three-photon-excitation LIF in stagnation-flow diamond-forming flame apparatus [163]

which the profiles are taken. One can see that the CN LIF signal spatially resolved curves were very similar to that of the diamond growth rate. The fact that the maxima in the horizontal CN profiles coincide with the enhanced growth indicates that CN or a closely related species (only one or two reaction steps away) may be important in determining the local growth rate. In addition, the comparison of CN LIF signal variation with the distance from substrate shows that a low concentration of CN species exist in the vicinity of substrate, which may be due to the CN

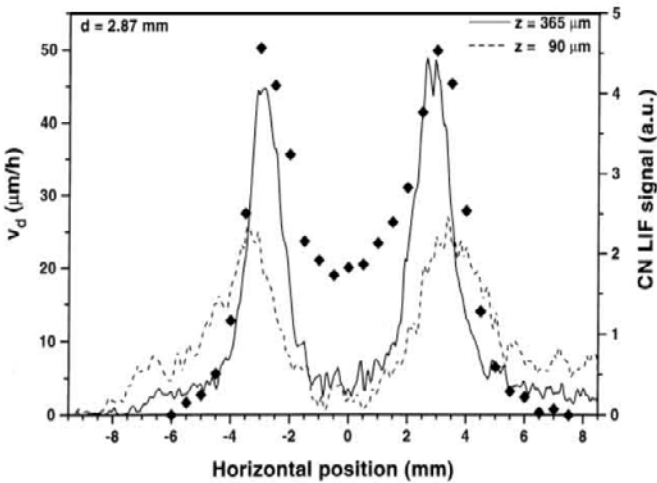


Fig. 4.14. Horizontal profiles of the CN LIF signal close to the substrate during diamond growth by an oxyacetylene flame (solid and dashed lines, right-hand ordinate) and the deposition rate v_d of the corresponding diamond layer along the path of the laser beam (diamonds, left-hand ordinate) [167], d is the distance between the flame front and substrate, z is the height above the substrate at which the profiles are taken.

species that were consumed in the diamond surface chemical reaction processes. This agrees with the possibility that CN and HCN abstract adsorbed hydrogen from the growing diamond surface [169,170], which creates free growth sites, and with the observed positive effects on the growth rate of nitrogen addition to diamond-growing CVD systems.

4.5.3 Optical emission spectroscopy

Optical emission spectroscopy (OES) measurement is another very popular *in situ* diagnostic method, which offers a powerful tool for both monitoring and investigating the process of CVD diamond film growth without disturbing the growth process, and spatially resolved information can be obtained. By comparison with molecular beam mass spectroscopy (MBMS) and laser-induced fluorescence (LIF), optical emission spectroscopy (OES) does not have the potential risk of distorting the gas composition (MBMS) or causing gas composition dissociation or ionization in the photochemical process (LIF). In plasma processing, it has been widely used for real-time monitoring.

The diamond film quality varies with deposition method and conditions, and numerous researches have been undertaken to develop a simple relationship between OES and the quality of deposited diamond film. Klein-Douwel et al. (1998) found a correlation between C_2 emission and the diamond film quality in an oxy-

cetylene flame [171]. Lang et al. (1996) found the diamond film quality to correspond to H atom actinometry measurements [172]. Gruen et al. (1995) found OES signals from C_2 emission in a microwave plasma correlate with the growth rate, but not the emission from either H or CH [173]. Cui et al. (1997) observed emission from H and CH^+ relate to high quality diamond, and CH emission indicates the presence of nondiamond carbon [174]. Shang et al. (1998) suggested that the transverse bias-enhanced nucleation of diamond in hot filament chemical vapor deposition is due to the production of many more atomic hydrogen and CH radicals [175]. Luque et al. (1998) reported the quantitative optical emission of H, C, C_2 , and CH, and found all the excited species to be present in concentrations two or more orders of magnitude smaller than the corresponding ground states measured in the same reactor and conditions [176]. Raiche et al. (1993) reported emission from CH, C_2 , C_3 , in a DC arc jet system [177]. Reeve and Weimer (1995) observed CH(A-X) and C_2 (d-a) emission [178], and found quite different vibrational and rotational temperatures in CH(A) and C_2 (d) by analyzing the spatial distributions of the emission intensities, and it was suggested that the excited C_2 (d) was formed by chemical reactions and CH(A) by electron impact.

Emission lines of various plasma species originate from electrically excited states of these species. The emission intensities are proportional to the densities of electrically excited species and the electron energy distribution function of the plasma. The emission intensity I_x of species x is given by [179],

$$I_x = C_x k_x n_e N_x g(\lambda), \quad (4.3)$$

where C_x is a constant, k_x the excitation rate constant of species x by electron collision that is a function of the electron energy and collision cross section, n_e is the concentration of electrons in the plasma, N_x is the concentration of the species x , and $g(\lambda)$ is the counting ratio of λ photons collected to the total. It can be seen as a constant in a certain experiment, while n_e , $k_{x,j}$, and N_x are determined by the reaction conditions. It can be seen that the emission intensity I_x is proportional to the concentration of species x , and to the excitation rate constant, that is to the concentration and energy of electrons in the plasma. Therefore, through the OES measurements, one can get information about the species concentration and the electron density and its temperature in the plasma.

Nitrogen is one of the most common impurities encountered both in natural and synthetic diamond. It is either concentrated in small aggregates (type Ia) or incorporated as a single substitutional species (ESP P1-defect) to act as a deep donor. As mentioned above, nitrogen-containing gas addition to conventional methane/hydrogen mixture has many positive effects on diamond film growth. But the mechanism of nitrogen incorporation in chemical vapor deposition diamond is still an open question. This is mainly due to the complexity of the N-incorporation process involved, depending not only on experimental parameters, but also on the diamond crystal orientation and its surface termination. Figure 4.15 shows a diagram of the type of films produced on Si substrates after CVD as a function of different substrate temperatures and methane/ammonia ratios [180]. At substrate temperatures lower than about 800°C only amorphous carbon films were produced,

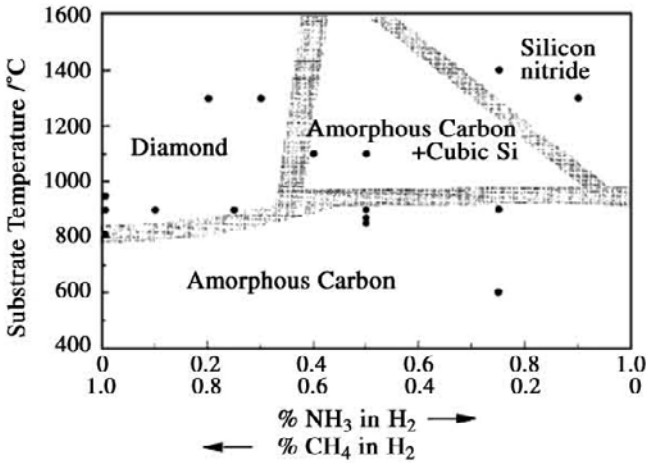


Fig. 4.15. Diagram showing the type of films produced on Si substrates after CVD as a function of different substrate temperatures and methane/ammonia ratios. Approximate phase boundaries are included to guide the eye [180]

with little or no N content. At higher temperatures, the film composition depended strongly on the ammonia-to-methane ratio. With methane-rich gas mixtures, diamond was grown, the morphology of which was similar to that seen in standard CVD process, although as the fraction of ammonia increased, the films became more nanocrystalline and the growth rate decreased. With ammonia-rich gas mixtures, the Si substrate preferentially reacted with the ammonia to produce a Si₃N₄ coating, with no carbon content.

Figure 4.16 shows a schematic diagram of a computerized hot-filament CVD diamond film system for 2-dimensional spatially resolved optical emission spectroscopy measurements [181]. The optical system includes a 2D-SROES detector, a monochromator, and photon counter. The emission light through an optical window is collected at the entrance of the optical system that is driven automatically in two dimensions by a controller connected to the computer. A special design of the optical collection system ensures the spatial resolution of the 2D-SROES system to be better than 0.1 mm. The collection light is decomposed by a monochromator and recorded by a photon counter. The spectral resolution of the monochromator is 0.1 nm. Beside the *in situ* spatially resolved OES, the optical system can be used for wavelength and temporally resolved spectroscopy as well.

In order to understand the mechanism of the diamond growth with nitrogen-containing gas addition to conventional methane/hydrogen mixture, Chang et al. (1999) employed *in situ* OES to do systematical investigating about the influences of system parameters on gas phase species [182]. A typical optical emission spectroscopy during diamond growth within a (N₂+CH₄+H₂) mixture in the above hot-filament chemical vapor deposition diamond apparatus is shown in Fig. 4.17.

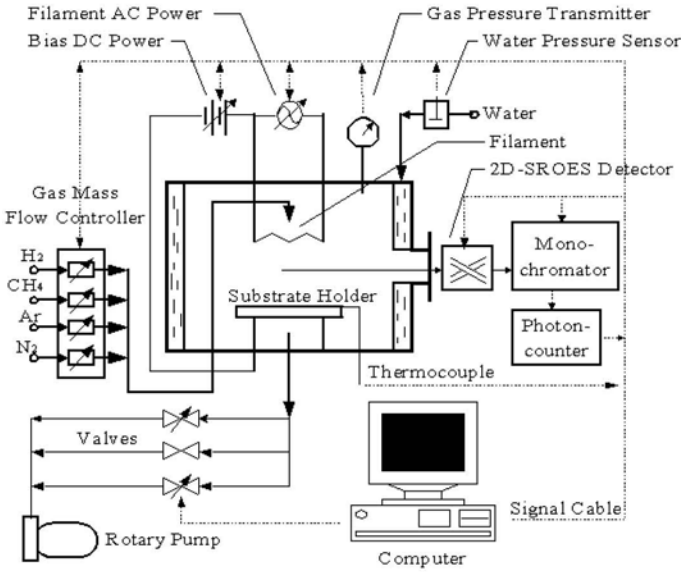


Fig. 4.16. Schematic diagram of experimental apparatus useful for spatially resolved optical emission spectroscopy [181]

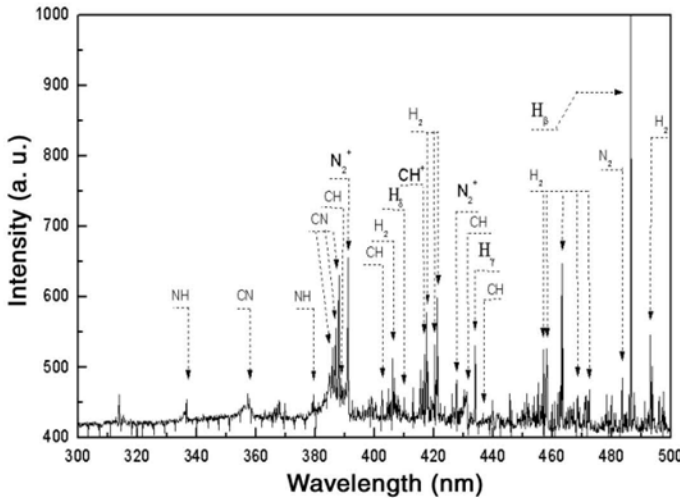


Fig. 4.17. Typical optical emission spectroscopy during diamond growth within a ($N_2 + CH_4 + H_2$) mixture in the above Hot-Filament Chemical Vapor Deposition diamond apparatus [182]

Table 4.2. Observed Optical Emission Lines During Diamond Growth Within a ($N_2 + CH_4 + H_2$) Mixture [183]

Species	Transition	Peak positions [nm]
H_α	$n = 3 \rightarrow n = 2$	656.2
H_β	$n = 4 \rightarrow n = 2$	486.2
H_γ	$n = 5 \rightarrow n = 2$	434.1
H_δ	$n = 6 \rightarrow n = 2$	410.1
H_2		406.7, 417.7, 420.5, 421.2, 457.2, 458.2, 463.2, 468.4, 472.3, 493.4
N_2	$A^3\Sigma^+U \rightarrow X^1\Sigma^+G$	483.7
N_2^+	$B^2\Sigma^+U \rightarrow X^2\Sigma^+G$	391.4, 427.8
CH	$A^2\Delta \rightarrow X^2\Pi$ $B^2\Sigma \rightarrow X^2\Pi$	431.4, 438.5 387.1, 388.9, 402.5
CH^+	$A^1\Pi \rightarrow X^1\Sigma$	417.1, 422.5
CN	$B^2\Sigma \rightarrow X^2\Sigma$	359.0, 385.5, 386.2, 387.1, 388.3
NH	$A^3\Pi \rightarrow X^3\Sigma$	336.0, 379.5

For this example we have chosen a gas mixture of $0.5N_2/2CH_4/100H_2$ gas flow ratio. In conventional OES measurement of hot-filament CVD, the filament radiation background decreases the signal-to-noise ratio and makes analysis difficult. In Fig. 4.17, it has been avoided by carefully adjusting the optical route and filament fabrication. The negative peaks in the baseline were due to the electromagnetic pulses in the external environment. The emission lines of atomic hydrogen, molecular hydrogen, CH, CH^+ , CN, NH, N_2 , and N_2^+ were observed. The detailed peak positions are listed in Table 4.2.

Figure 4.18 shows the intensity ratios of CN, H_2 , N_2^+ , N_2 , H_α , CH, and CH^+ to H_β as a function of the filament temperature. The most remarkable information in this figure is that the CN radical concentration was sharply increased at $\sim 1700^\circ\text{C}$, which is close to the conventional filament temperature zone of diamond growth, $\sim 2000^\circ\text{C}$ to 2200°C . As shown in Fig. 4.11, the nitrogen containing species HCN, NH_3 , and CH_3NH_2 concentrations started obviously increasing at $\sim 1700^\circ\text{C}$ by MBMS measurements; this temperature also was pointed out by OES measurements. Below this temperature, because the dissociation of the strong $N\equiv N$ bonds requires much more energy (bond strength: $N\equiv N$, 945.4 kJmol^{-1} ; $H-CH_3$, 435.0 kJmol^{-1} ; $H-H$, 435.9 kJmol^{-1}), besides CN radicals, few nitrogen-containing radicals are formed. Thus, at lower temperatures, N_2 is seen as being virtually a spectator to the CVD process. At higher temperatures, CN radicals can be rapidly

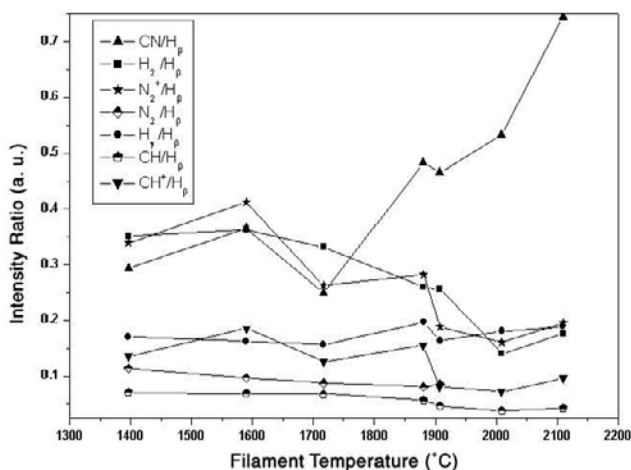


Fig. 4.18. Effect of filament temperature on the relative emission intensities [182]

converted to HCN by the reaction: $\text{CN} + \text{H}_2 \rightarrow \text{HCN} + \text{H}$, which has very low activation energy [184] (only 9.4 kJmol^{-1}). And HCN is a very stable species in the typical diamond growth environment. So CN performs the task of transferring N atoms from nitrogen to HCN. Other nitrogen-containing species may be influenced by CN through several reaction steps. The CN radical seems to act as a very important factor in controlling the production of stable species such as HCN, CH_3NH_2 , etc. It affects the processes of both gas-phase chemistry and surface reactions.

In Fig. 4.18, decrease of the reactants H_2 , N_2 , and N_2^+ with filament temperature clearly shows that the reaction was accelerated by increasing filament temperature, and that the reactants were consumed in the chemical processes. Accompanying these reactions, CH and CH^+ species decrease because of the following reaction: $\text{CH} + \text{N} \rightarrow \text{H} + \text{CN}$, $\text{CH} + \text{N}_2 \rightarrow \text{HCN} + \text{N}$. Such reactions have been considered in mechanisms occurring within the discharge and in afterglows of microwave plasma [185]. In addition, the ratio of H_γ to H_β remains unchanged as the filament temperature increases, that is to say electron temperature was maintained constant.

Nitrogen concentration is a critical parameter for the growth of diamond when nitrogen gas is added to a conventional methane/hydrogen mixture. The growth habit was found to change from (111) to (100) with an increase of nitrogen in the gas phase from $\text{N/C} = 0.1\%$ to 10% , so also the growth rate of diamond films increases and diamond Raman peak sharpens with the amount of nitrogen [155]. In the microwave system, nitrogen addition even in ppm magnitude has led to significant changes in diamond growth [186]. Figure 4.19 shows the effect of nitrogen concentration on the relative emission intensities. With the concentration of nitrogen, CH^+ species steadily decrease, accompanied by a rapid increase in the

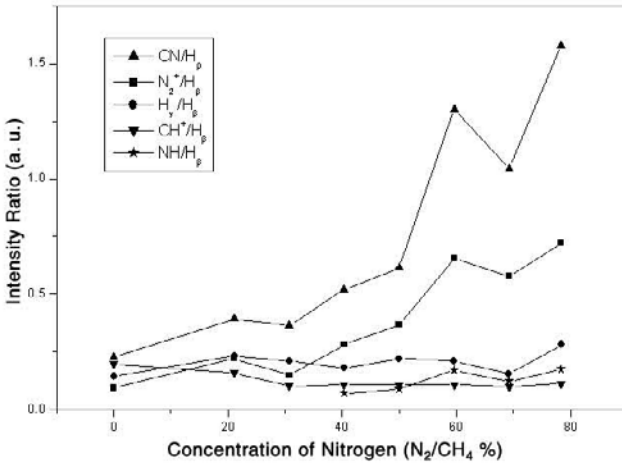


Fig. 4.19. Effect of nitrogen concentration on the relative emission intensities [182]

CN and N₂⁺ species and a slight rise in NH species. During these processes, the electron temperature remains unchanged.

Bohr et al. (1996) reported the influence of N₂ admixtures (5% – 40% N₂/CH₄) on hot-filament CVD growth [170]. Small N₂ additions (5% – 10% N₂/CH₄) improved the diamond phase purity, high concentration (20% – 40% N₂/CH₄) revealed a deterioration of the diamond phase purity and low growth rate. As shown in Fig. 4.19, CH⁺ falls to a relatively low concentration level when the input nitrogen gas concentration is increased to 30%, accompanied by the rapid rise in CN radicals at this point. The former species, CH⁺, have been attributed to being the active precursor for diamond growth by Cui and Fang (1997) [174]. Lower CH⁺ concentration is not favorable for diamond growth. Although CN can abstract adsorbed hydrogen from the diamond surface to create growth sites, and can increase diamond growth rate, with higher nitrogen gas input, too many CN radicals and growth sites are produced. Because CN radicals are not helpful for stabilizing diamond structure, the dangling bonds at growth sites may connect together to produce a graphite structure, and will deteriorate the diamond phase purity.

Figure 4.20 gives the spatial resolved optical emission spectroscopy between filament and substrate; the zero point is the filament position and the whole distance between the filament and the substrate is about 5 mm. For the detection position from filament to substrate, the H_γ (434.1 nm) line first increased to the peak intensity at a position 0.8 mm from the filament surface and then decreased near the substrate because of the consumption of atomic hydrogen in surface reactions. This is consistent with the LIF measurement results of Bertagnolli et al. (1998), as shown in Fig. 4.13. From this figure, we can clearly see that atomic H was created in the vicinity of the filament surface, and then diffused to the substrate. This process is very important to diamond growth. The heat transfer study gave a

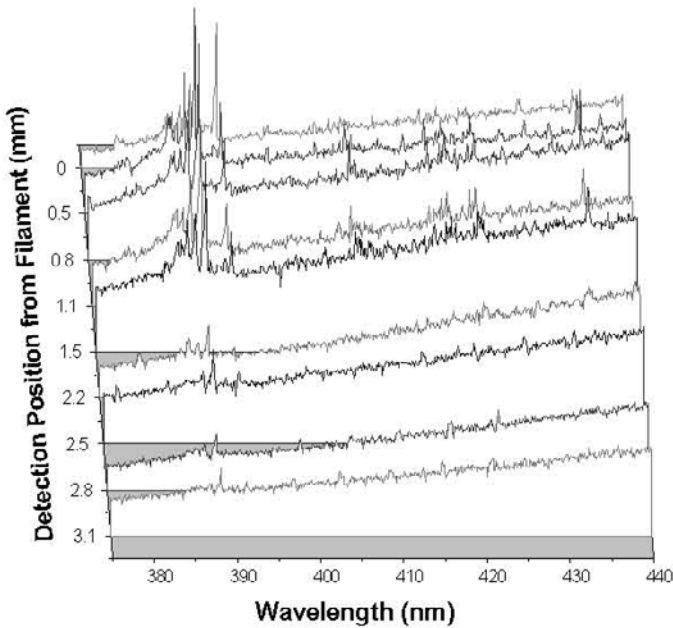


Fig. 4.20. Spatial resolved *in situ* emission spectroscopy [182]

complete energy balance for the filament and revealed that hydrogen dissociation accounts for 70% of the total power released from the filament, followed by radiation and conduction/convection at 15% each [187].

At the filament surface, the intensity of the N_2^+ line was higher than that of CN, but when the detection position was moved to 0.5 mm from the filament, this ratio was reversed. It shows that the $N\equiv N$ bond was broken near the filament surface and N was transferred from nitrogen to N-containing radicals, such as CN. Thus, CN lines still remained obvious near the substrate surface, whereas H_γ disappeared.

In order to get a better understanding of CN formation, the evolution of CN and other species were examined. For this purpose, after obtaining the steady-state flow of the gas mixture within the reactor, we abruptly stopped the CH_4 injection at time $t = 0$. As shown in Fig. 4.21, the intensities of H_2 and N_2^+ lines were kept unchanged, and we can see that the electron temperature remained constant. After closing off the methane, the intensity of the CN line vibrated at a high level, and 40 minutes later, it began to decrease. This result clearly shows that CN is already produced within the pure gaseous phase and its formation is influenced by the amount of methane. However, the concentration of CN was kept high and its OES intensity did not decay rapidly. This means that the solid carbon, graphite, or black carbon that grew on the holders of the filament and substrate in previous experiments act as a carbon source which is sufficiently large to maintain this new

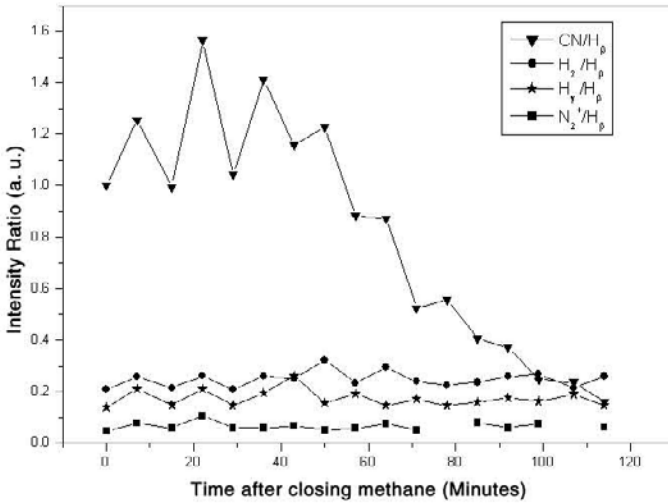


Fig. 4.21. Time evolution of the relative emission intensities after closing methane [182]

state of CN production for a very long time, because of the $C + N_2 \rightarrow CN + N$ reaction [184]. So the formation of CN can be produced in the gas phase as well as at the surface of the solid phase carbon. It is dissimilar to the formation of gas phase species in the conventional hydrocarbon/hydrogen mixture for diamond growth as shown in Fig. 4.10, in which most gas phase compositions are produced by gas phase reactions.

From these experiments and discussions, we can draw the conclusion that at low nitrogen concentrations, the CN radical behaves much like a growth accelerator, which is responsible for the magical increase in diamond growth rate. But nitrogen is not indispensable for diamond growth. The theoretical situation of a gas phase completely free of nitrogen would produce the lowest film growth rate, but of the best quality. Besides CN radicals, atomic H concentration has already been proposed as a key factor in diamond quality. Atomic H helps to etch surface graphite and stabilize diamond structure. So we can attribute the CN and atomic H lines to different aspects of diamond growth: CN is for diamond growth rate and atomic H is for diamond quality. By detailed controlling of these two emission lines, we can make the best choice between higher growth rate and good quality.

4.6 Summary

Diamond films have been successfully prepared using hot-filament CVD, microwave plasma-assisted CVD, DC arc plasma jet CVD, and other methods in recent decades. However, our understanding of the growth mechanism of metastable diamond is still vague. In order to find the answer to why diamond films can be

deposited from different gas sources by different synthesis techniques, scientists have studied the nucleation and growth process of diamond film from the two aspects of surface reaction and gas-phase reaction.

It is found that diamond nucleation density on the heterosubstrates can be greatly increased by the mechanical damage, the predeposited buffer layer, and the bias-enhanced nucleation methods. Of these methods the bias-enhanced method brings the best hope of realizing the heteroepitaxial growth of diamond films. The results of cross-section HRTEM imply that the diamond nucleation site is important to the heteroepitaxial growth of diamond. Under the CVD conditions, two growth modes, i.e., layer growth and spiral growth, were found in the growth process of diamond. In addition, substrate material selections with some novel considerations were attempted to deposit high-quality and epitaxial diamond films.

Many *in situ* diagnostic techniques have been employed for the growth environment evaluation, such as molecular beam mass spectroscopy, laser-induced fluorescence, and optical emission spectroscopy. These techniques can provide direct, quantitative, or semiquantitative information for a large number of stable and radical gas species about their energy and spatial distribution. With *in situ* diagnostics, we can efficiently correlate gas phase conditions with film properties such as growth rate, texture, morphology, and uniformity. It is found that many species, such as H, CH, CH⁺, CN, CH₃, C₂, and C₂H₂, have great influences on diamond growth, and it was generally believed that CH₃ and C₂H₂ are responsible for diamond growth.

Acknowledgment

The authors wish to acknowledge the support of the National Natural Science Foundation of China and the National Advanced Materials Committee of China.

References

1. Bundy FP, Strong HM (1962) Solid State Physics, Seitz F, Turnbull D (eds), Vol 13, 81, New York, Academic
2. Zhao XZ, Roy R, Cherian KA, Badzian A (1997) Hydrothermal growth of diamond in metal-C-H₂O systems, *Nature* 385:513
3. Spitsyn BV, Derjaguin BV (1980) USSR Patent 339134
4. Matsumoto S, Sato Y, Tsumi M, Setaka N (1982) *J Mater Sci* 17:3106
5. Kamo M, Sato Y, Matsumoto S, Setaka N (1983) *J Crystal Growth* 62:642
6. Stone BR, Tessmer GJ, Dreifus DL (1993) Bias assisted etching of diamond in a conventional chemical vapor deposition reactor, *Appl Phys Lett* 62:1803
7. Jing X, Klages C-P (1993) Epitaxial diamond thin films on (001) silicon substrates, *Appl Phys Lett* 62:3438
8. Wörner E, Wild C, Müller-Sebert W, Locher R, Koidl P (1996) Thermal conductivity of CVD diamond films: high-precision, temperature-resolved measurements, *Diamond Relat Mater* 5:688

9. Post P (1993) The business and technical outlook for CVD diamond and diamond-like carbon, Proc 2nd Gorham Advanced Materials Conf, Monterey, CA
10. Fünér M, Wild C, Koidl P (1998) Novel microwave plasma reactor for diamond synthesis, *Appl Phys Lett* 72:1149
11. Kurihara K, Sasaki K, Kawarada M, Koshino N (1988) High rate synthesis of diamond by DC plasma jet chemical vapor deposition, *Appl Phys Lett* 52:437
12. Hiraki A, Kawarada H, Wei J, Suzuki JI (1990) Preparation and characterization of wide area, high quality diamond film using magnetoactive plasma chemical vapor deposition, *Surface and Coating Technology* 43/44:10
13. Yara T, Yuasa M, Shimizu M, Makia H, Hatta A, Suzuki J, Ito T, Hiraki A (1994) Fabrication of diamond films at low pressure and low-temperature by magneto-active microwave plasma chemical vapor deposition, *Jpn J Appl Phys* 33(pt 1):4404
14. Mantei TD, Ring Z, Schweizer M, Tlali S, Jackson HE (1996) Low temperature synthesis of diamond films with electron cyclotron resonance plasma chemical vapor deposition, *Jpn J Appl Phys* 35:2516
15. Matsui Y, Yuuki A, Sahara M, Hirose Y (1989) Flame structure and diamond growth mechanism of acetylene torch, *Jpn J Appl Phys* 28:1718
16. Snail KA, Vardiman RG, Estrera JP, Glesener JW (1993) Diamond growth in turbulent oxygen-acetylene flames, *J Appl Phys* 74:7561
17. LeHuu T, Schmitt M, Paulmier D (1999) Combustion flame synthesis: a promising technique to obtain diamond single crystal, *Thin Solid Films* 356:122
18. Davanloo F, Lee TJ, Park H, You JH, Collons CB (1993) Protective films of nano-phase diamond deposited directly on zinc sulfide infrared optics, *J Mater Res* 8:3090
19. Joseph A, Wei J, Tanger C, Tzeng Y, Bozack M, Vohra Y (1993) High density diamond nucleation on unseeded substrates by a combined microwave and radio-frequency plasma, *Proc 3rd Internal Symp on Diamond Mater* 315
20. Fujimori N, Ikegaya A, Imai T, Fukushima K, Ota N (1989) in: J Dismukes et al. (eds) *Diamond and Diamond-like Films*, *Electrochem Soc Proc*, Vol PV 89-12, Pennington, NJ, p 465
21. Pan C, Withers JC, Stoessel CH, Loutfy RO (1995) Chemical vapor deposition of diamond using fullerenes for diamond nucleation and growth precursors, *Proc 4th Internal Symp on Diamond Mater* 130
22. Field JE (1979) *The Properties of Diamonds*, New York, Academic
23. Davis RF (1992) *Diamond Films and Coatings*, Noyes Publications, New Jersey
24. Graebner JE, Reiss ME, Seibles L, Hartnett TM, Miller RP, Robbison CJ (1994) Phonon scattering in chemical-vapor-deposited diamond, *Phys Rev B* 50:3702
25. Koidl P, Wild C, Fünér M, Müller-Sebert W (1998) *Proc Symp I Super Carbon of the IUMRS-ICA-97 in Japan*, September 1997, Fujiwara S (ed), MYU, Tokyo
26. Glover GH (1973) *Solid State Electronics* 16:973
27. Mort J, Kuhman D, Machonkin M, Moragan M, Jansen F, Okumura K, Legrice YM, Nemanich RJ (1989) Boron doping of diamond thin films, *Appl Phys Lett* 55:1121
28. Shiomi H, Nakahata H, Imai T, Nishibayashi Y, Fujimori N (1989) Electrical characteristics of metal contacts to boron-doped diamond epitaxial films, *Jpn J Appl Phys* 28:758
29. Miyata K, Kumagai K, Nishimura K, Kobashi K (1993) Morphology of heavily B-doped diamond films, *J Mater Res* 8:2845
30. Grot SA, Hatfield CW, Gildenblat GS, Badzian AR, Badzian T (1991) Electrical properties of selectively grown homoepitaxial diamond films, *Appl Phys Lett* 58:1542

31. Okano K, Naruki H, Akiba Y, Kkurosu T, Iida M, Hirose Y (1988) Synthesis of diamond thin films having semiconductive properties, *Jpn J Appl Phys, Part 2*, 27:L173
32. Locher R, Wagner J, Fuchs F, Wild C, Hiesinger P, Gonon P, Koidl P (1995) Boron doped diamond films: electrical and optical characterization and the effect of compensating nitrogen, *Mater Sci Eng B* 29:211
33. Pan C, Withers JC, Stoessel CH, Loutfy RO (1995) Proc 4th Internal Symp on Diamond Mater 130
34. Kalish R, Bernstein T, Shapiro B, Talmi A (1980) *Rad Effects* 52:153
35. Sandhu GS, Swanson ML, Chu WK (1989) Doping of diamond by coimplantation of carbon and boron, *Appl Phys Lett* 55:1397
36. Krutko OB, Kosel PB, Wu RLC, Fries-Carr SJ, Heidger S, Weimer J (2000) P-type polycrystalline diamond layers by rapid thermal diffusion of boron, *Appl Phys Lett* 76:849
37. Kajihara S, Antonelli A, Bernholc J (1989) Proc Fall 1989 MRS Meeting, Boston, MA, 162:315
38. Spitsyn BV, Aleksenko AE (1986) Physicochemical basis for doping diamond obtained from the gas phase, *Arch Naukio Materialach* 7:201
39. Okano K, Kiyota H, Iwasaki T, Kurosu T, Iida M, Nakamura T (1990) Proc Second Int Conf on the New Diamond Science and Technology, Washington DC, 23
40. Koizumi S, Murakami T, Inuzuka T, Suzuki K (1997) Growth and characterization of phosphorous doped (111) homoepitaxial diamond thin films, *Appl Phys Lett* 71:1065
41. Geis MW, Efremow NN, Woodhouse JD, McAleese MD, Marchywka M, Socker DG, Hochedez JF (1991) Diamond cold cathode, *IEEE Electron Device Lett* 12:456
42. Givargizov EI (1995) Silicon tips with diamond particles on them: new field emitters, *J Vac Sci Technol B* 13:414
43. Wang C, Garcia A, Ingram DC, Lake M, Kordesch ME (1991) Cold field emission from CVD diamond films observed in emission electron microscopy, *Electronics Lett* 27:1459
44. Xu NS, Tzeng Y, Latham RV (1993) Similarities in the 'cold' electron emission characteristics of diamond coated molybdenum electrodes and polished bulk graphite surfaces, *J Phys D* 26:1776
45. Okano K, Koizumi S, Silva SRP, Amaratunga GAJ (1996) Low-threshold cold cathodes made of nitrogen-doped chemical-vapor-deposited diamond, *Nature* 381:140
46. Geis MW, Twichell JC, Macaulay J, Okano K (1995) Electron field emission from diamond and other carbon materials after H₂, O₂, and Cs treatment, *Appl Phys Lett* 67:1328
47. Sowers AT, Ward BL, English SL, Nemanich RJ (1999) Field emission properties of nitrogen-doped diamond films, *J Appl Phys* 86:3973
48. Zhu W, Kochanski GP, Jin S, Seibles L (1995) Defect-enhanced electron field emission from chemical vapor deposited diamond, *J Appl Phys* 78:2707
49. Zhu W, Kochanski GP, Jin S, Seibles L (1995) Electron field emission from ion-implanted diamond, *Appl Phys Lett* 67:1157
50. Huang ZH, Cutler PH, Miskorvsky NM, Sullivan TE (1994) Theoretical study of field emission from diamond, *Appl Phys Lett* 65:2562
51. Pate BB (1986) The diamond surface atomic and electronic structure, *Surf Sci* 165:83
52. Zhu W, Kochanski GP, Jin S (1998) Low-field electron emission from undoped nanostructured diamond, *Science* 282:1471

53. May PW, Höhn S, Ashfold MNR, Wang WN, Fox NA, Davis TJ, Steeds JW (1998) Field emission from chemical vapor deposited diamond and diamond-like carbon films: Investigations of surface damage and conduction mechanisms, *J Appl Phys* 84:1618
54. de Heer WA, Chatelain A, Ugarte D (1995) A carbon nanotube field-emission electron source, *Science* 270:1179
55. Merkulov VI, Lowndes DH, Baylor LR (1999) Field-emission studies of smooth and nanostructured carbon films, *Appl Phys Lett* 75:1228
56. Shiomi H, Tanabe K, Nishibayashi Y, Fujimori N (1990) Epitaxial growth of high quality diamond film by the microwave plasma-assisted chemical-vapor-deposition method, *Jpn J Appl Phys* 29:34
57. Snail KA, Hanssen LM (1991) High temperature, high rate homoepitaxial growth of diamond in an atmospheric pressure flame, *J Crystal Growth* 112:651
58. Hayashi K, Yamanaka S, Watanabe H, Sekiguchi T, Okushi H, Kajimura K (1998) Diamond films epitaxially grown by step-flow mode, *J Crystal Growth* 183:338
59. Kamo M, Yurimoto H, Sato Y (1988) Epitaxial growth of diamond on diamond substrate by plasma assisted CVD, *Appl Surf Sci* 33/34:553
60. Chu CJ, D'Evelyn MP, Hauge R, Margrave JL (1990) *Carbon* 28:803
61. Geis MW (1990) Diamond, Boron Nitride, Silicon Carbide and Related High Bandgap Semiconductors, *Mater Res Soc Symp Proc* 162:15
62. Sutcu LF, Chu CJ, Thompson MS, Hauge RH, Margrave JL, D'Evelyn MP (1992) Atomic force microscopy of (100), (110), and (111) homoepitaxial diamond films, *J Appl Phys* 71:5930
63. DeNatale JF, Harker AB, Flintoff JF (1991) Microstructure and orientation effects in diamond thin films, *J Appl Phys* 69:6456
64. Williams BE, Glass JT, Davis RF, Kobashi K (1990) The analysis of defect structures and substrate/film interfaces of diamond thin films, *J Crystal Growth* 99:1168
65. Narayan J (1990) Dislocations, twins, and grain boundaries in CVD diamond thin films: Atomic structure and properties, *J Mater Res* 5:2414
66. Okubo T, Nakata S, Nagamoto H, Ihara HB, Komiyama H (1993) Synthesis of nanostructured diamond via controlled surface pretreatment in hexane medium, *Jpn J Appl Phys* 32:L1767
67. Barshilia HC, Mehta BR, Vankar VD (1996) Growth of diamond thin films by microwave plasma chemical vapor deposition process, *J Mater Res* 11:1091
68. Barnes PN, Wu RLC (1993) Nucleation enhancement of diamond with amorphous films, *Appl Phys Lett* 62:37
69. Tamaki K, Nakamura Y, Watanabe Y, Hirayama S (1995) Effect of hydrogenated amorphous carbon films on nucleation of diamond particles by hot-filament chemical vapor deposition, *J Mater Res* 10:431
70. Liao Y, Fang RC, Ye F, Shao QY, Wang GZ (1999) Nucleation and growth of diamond film on porous silicon substrate, *Modern Phys Lett B* 13:159
71. Li CH, Wang GZ, Liao Y, Ye F, Fang RC (2000) Diamond synthesis with hot filament chemical vapor deposition (HFCVD) in the presence of iron, *Modern Phys Lett B* 14:7
72. Cui JB, Fang RC (1996) Evidence of the role of positive bias in diamond growth by hot filament chemical vapor deposition, *Appl Phys Lett* 69:3507
73. John P, Milne DK, Roberts PG, Jubber MG, Liehr M, Wilson JJB (1994) Localized epitaxy of diamond on (100) silicon, *J Mater Res* 9:3083
74. Iijima S, Aikawa Y, Baba K (1990) *Appl Phys Lett* 57:2646

75. Yugo S, Kanai T, Kimura T, Muto T (1991) Generation of diamond nuclei by electric field in plasma chemical vapor deposition, *Appl Phys Lett* 58:1036
76. Stubhan F, Ferguson M, Fusser H-J (1995) Heteroepitaxial nucleation of diamond on Si(001) in hot filament chemical vapor deposition, *Appl Phys Lett* 66:1900
77. Tomellini M, Polini R, Sessa V (1991) A model kinetics for nucleation at a solid surface with application to diamond deposition from the gas phase, *J Appl Phys* 70:7573
78. Wang WL, Sanchez G, Polo MC, Zhang RQ, Esteve J (1997) Nucleation and initial growth of diamond by biased hot filament chemical vapor deposition, *Appl Phys A* 65:241
79. Sattel S, Gebber J, Ehrhardt H (1996) Ion induced nucleation of diamond, *Phys Stat Sol (a)* 154:141
80. Jing X, Zhang WJ, Klages C-P (1998) Effects of ion bombardment on the nucleation and growth of diamond films, *Phys Rev B* 58:7064
81. Fu GS, Wang XH, Han L, Dong LF, Li XW (1997) Textured diamond films growth on (100) silicon via electron-assisted hot filament chemical vapor deposition, *Appl Phys Lett* 70:1965
82. Wolter SD, Borst TH, Vescan A, Ohn EK (1996) The nucleation of highly oriented diamond on silicon via an alternating current substrate bias, *Appl Phys Lett* 68:3558
83. Chen QJ, Yang J, Lin ZD (1995) Synthesis of oriented textured diamond films on silicon via hot filament chemical vapor deposition, *Appl Phys Lett* 67:1853
84. Shigesato Y, Boekenhauer RE, Sheldon BW (1993) Emission spectroscopy during direct-current-biased, microwave-plasma chemical vapor deposition of diamond, *Appl Phys Lett* 63:314
85. Sheldon BW, Csencsits R, Rankin J, Boekenhauer PE, Shigesato Y (1994) Bias-enhanced nucleation of diamond during microwave-assisted chemical vapor deposition, *J Appl Phys* 75:5001
86. Stoner BR, Glass JT (1992) Textured diamond growth on (100) beta-SiC via microwave plasma chemical vapor deposition, *Appl Phys Lett* 60:698
87. Muller D, Tzou Y, Raj R, Sicox J (1993) Mapping sp^2 and sp^3 states of carbon at subnanometre spatial resolution, *Nature* 366:725
88. Stochel R, Stammler M, Janischowsky K, Ley L, Albrecht M, Strunk HP (1998) Diamond nucleation under bias conditions, *J Appl Phys* 83:531
89. Kim YK, Han YS, Lee JY (1998) The effects of a negative bias on the nucleation of oriented diamond on Si, *Diamond Relat Mater* 7:96
90. Cui JB, Shang NG, Liao Y, Li JQ, Fang RC (1998) Growth and characterization of diamond films deposited by dc discharge assisted hot filament chemical vapor deposition, *Thin Solid Films* 334:156
91. Shang NG, Fang RC, Han SJ, Liao Y, Cui JB (1998) Transverse bias-enhanced nucleation of diamond in hot filament chemical vapor deposition, *Mater Res Innov* 2:79
92. Cui JB, Shang NG, Fang RC (1998) Discharge induced enhancement of diamond nucleation on Si via hot filament chemical vapor deposition, *J Appl Phys* 83:6072
93. Reinke P, Oelhafen P (1997) Photoelectron spectroscopic investigation of the bias-enhanced nucleation of polycrystalline diamond films, *Phys Rev B* 56:2183
94. Chiang MJ, Hon MH (2000) X-ray photoelectron spectroscopy investigation of substrate surface pretreatments for diamond nucleation by microwave plasma chemical vapor deposition, *J Crystal Growth* 211:211

95. Geyber J, Weiler M, Sohr O, Jung K, Ehrhardt H (1994) Investigations of diamond nucleation on a-C films generated by dc bias and microwave plasma, *Diamond Relat Mater* 3:506
96. Zarrabian M, Fourches-Coulon N, Turban G, Marhic C, Lancin M (1997) Observation of nanocrystalline diamond in diamondlike carbon films deposited at room temperature in electron cyclotron resonance plasma, *Appl Phys Lett* 70:2535
97. Feng KA, Yang J, Lin ZD (1995) Interface study of heteroepitaxial diamond films on silicon (001) substrates, *Phys Rev B* 51:2264
98. Lee ST, Peng HY, Zhou XT, Wang N, Lee CS, Bello I, Lifshitz Y (2000) A nucleation site and mechanism leading to epitaxial growth of diamond films, *Science* 287:104
99. Kreuzt TJ, Clausing RE, Heathery Jr L, Warmack RJ, Thundat T, Feigerle CS, Wandelt K (1995) Growth mechanisms and defects in boronated CVD diamond as identified by scanning tunneling microscopy, *Phys Rev B* 51:14554
100. Sumant AV, Dharmadhikari CV, Godbole VP (1996) Some investigations on HF-CVD diamond using scanning tunneling microscopy, *Mater Sci Eng B* 41:267
101. Godbole VP, Sumant AV, Kshirsagar RB, Dharmadhikari CV (1997) Evidence for layered growth of (100) textured diamond films, *Appl Phys Lett* 71:2626
102. Zhu W, Ahn J, Tan HS, Tan BH (1992) Crystal growth of diamond films synthesized by oxygen acetylene combustion flames, *J Crystal Growth* 125:649
103. Tsuno T, Tomikawa T, Shikata S, Imai T, Fujimori N (1994) Diamond (001) single-domain 2 x 1 surface grown by chemical vapor deposition, *Appl Phys Lett* 64:572
104. Lee N, Badezian A (1995) Effect of misorientation angles on the surface morphologies of (001) homoepitaxial diamond thin films, *Appl Phys Lett* 66:2203
105. van Enkevort WJP, Janssen G, Vollenberg W, Giling LJ (1995) Anisotropy in monocrystalline CVD diamond growth. III: Surface morphology of hot filament grown films deposited on planar substrates, *J Crystal Growth* 148:365
106. Hayashi K, Yamanka S, Watanabe H, Sekiguchi T, Okushi H, Kajimura K (1998) Diamond films epitaxially grown by step-flow mode, *J Crystal Growth* 183:338
107. Han SJ, Fang RC, Liao Y, Le DF, Li FQ (1999) Observation of two types of growth modes on (111) face in CVD diamond films, *Modern Phys Lett B* 13:947
108. Pickett WE (1988) Thin superlattices and band-gap discontinuities: the (110) diamond-boron nitride interface, *Phys Rev B* 38:1316
109. Argoitia A, Angus JC, Ma JS, Wang L, Pirouz P, Lambrecht W (1994) Heteroepitaxy of diamond on c-BN: Growth mechanisms and defect characterization, *J Mater Res* 9:1849
110. Yang PC, Zhu W, Glass JT (1993) Nucleation of oriented diamond films on nickel substrates, *J Mater Res* 8:1773
111. Zhu W, Yang PC, Glass JT (1993) Oriented diamond films grown on nickel substrates, *Appl Phys Lett* 63:1640
112. Hartsell ML, Plano LS (1994) Growth of diamond films on copper, *J Mater Res* 9:921
113. Wang W, Liao K, Gao J (1991) High rate epitaxial growth of diamond on Si(100) by DC plasma CVD, *Phys Status Solidi A* 128:K83
114. Stoner BR, Glass JT (1992) Textured diamond growth on (100) beta-SiC via microwave plasma chemical vapor deposition, *Appl Phys Lett* 60:698
115. Argoitia A, Angus JC, Wang L, Nin XI, Pirouz P (1993) Diamond grown on single-crystal beryllium oxide, *J Appl Phys* 73:4305
116. Lambrecht WRI, Segall B (1989) Electronic structure of (diamond C)/(sphalerite BN) (110) interfaces and superlattices, *Phys Rev B* 40:9909

117. Lambrecht WRI, Segall B, Erratum: Electronic structure of (diamond C)/(sphalerite BN) (110) interfaces and superlattices [Phys Rev B 40:9909 (1989)], Phys Rev B 41:5409 (1990)
118. Lambrecht WRI, Segall B (1992) Electronic structure and total energy of diamond/BeO interfaces, J Mater Res 7:696
119. Shang NG, Fang RC, Hang Y, Li JQ, Han SJ, Shao QY, Cui JB, Xu CY (1998) Investigation of diamond films deposited on LaAlO₃ single crystal substrates by hot filament chemical vapor deposition, Chin Phys Lett 15:146
120. Liao Y, Fang RC, Chang C, Li CH, Wang GZ (2000) Influences of substrate orientations on heteroepitaxial growth of diamond films, International Conference on Engineering and Technological Sciences 2000 (ICETS 2000) Beijing, October
121. Dupuie JL, Gulari E (1991) Hot filament enhanced chemical vapor deposition of AlN thin films, Appl Phys Lett 59:549
122. Godbole VP, Jagannadham K, Naragan J (1995) Nucleation and growth of diamond films on aluminum nitride coated nickel, Appl Phys Lett 67:1322
123. Chen H, Zhang JF, Cui JB, Fang RC (1996) Deposition of diamond film on aluminum nitride ceramics and the study of their thermal conductance, Chin Phys Lett 13:625
124. Shang NG, Fang RC, Cui JB, Li JQ, Han SJ, Shao QY, Li M, Le DF (1998) Textured CVD diamond films grown on aluminum nitride (AlN) ceramics, Thin Solid Films 334:178
125. Shang NG, Fang RC, Liao Y, Cui JB (1999) Deposition of (100) and (110) textured diamond films on aluminum nitride ceramics via hot filament chemical vapor deposition, Jpn J Appl Phys 38:1500
126. Cui JB, Ma YR, Zhang JF, Chen H, Fang RC (1996) Growth and characterization of diamond film on aluminum nitride, Mater Res Bull 31:781
127. Liao Y, Fang RC, Ye ZY, Shang NG, Han SJ, Shao QY, Ji SZ (1999) Investigation of the thermal conductivity of diamond film on aluminum nitride ceramic, Appl Phys A 69:101
128. Lei T, Moustakas TD, Graham RJ, He Y, Berkowitz SJ (1992) Epitaxial growth and characterization of zinc-blende gallium nitride on (001) silicon, J Appl Phys 71:4933
129. Nakamura S (1991) GaN growth using GaN buffer layer, Jpn. J Appl Phys Lett 30:L1705
130. Liao Y, Chang C, Li CH, Ye ZY, Wang GZ, Fang RC (2000) Two-step growth of high quality diamond films, Thin Solid Films 368:303
131. Bachmann PK, Leers D, Lydtyan H (1991) Towards a general concept of diamond chemical vapor deposition, Diamond Relat Mater 1:1
132. Balestrino G, Marinelli M, Milani E, Paoletti A, Paroli P, Pinter I, Tebano A (1993) Diamond Relat Mater 2:389
133. Marinelli M, Milani E, Monuori M, Paoletti A, Tebano A, Balestrino G, Paroli P (1994) Compositional and spectroscopic study of the growth of diamond films from several gaseous mixtures, J Appl Phys 76:5702
134. Hwang NM, Hahn JH, Bahang GW (1993) Thermodynamic approach to the C-H-O deposition diagram in the diamond chemical vapor deposition process, Diamond Relat Mater 3:163
135. Varnin VP, Derjaguin VV, Fedoseev DV, Teremetskaya IG, Khodan AN, Sov Phys Crystallogr 22:513 (1977)

136. Reynolds WC (1986) The Element Potential Method for Chemical Equilibrium Analysis: Implementation in the Interactive Program STANJAN, Version 3, Stanford University
137. Chang C, Fang R-C, Liao Y, Wang G-Z, (to be published)
138. Goodwin DG, Gavillet GG (1990) Numerical modeling of the filament-assisted diamond growth environment, *J Appl Phys* 68:6393
139. Luque J, Juchmann W, Jeffries JB (1997) Spatial density distributions of C_2 , C_3 , and CH radicals by laser-induced fluorescence in a diamond depositing dc-arcjet, *J Appl Phys* 82:2072
140. Butler JE, Woodin RL (1993) Thin film diamond growth mechanisms, *Philos Trans R Soc London, Ser A* 342:209
141. Angus JC, Hayman CC (1988) Low-pressure, metastable growth of diamond and diamond like phases, *Science* 214:913
142. Chu CJ, Hauge RH, Margrave JL, D'Evelyn MP (1992) Growth kinetics of (100), (110), and (111) homoepitaxial diamond films, *Appl Phys Lett* 61:1393
143. Hsu WL, Tung DM (1992) Application of molecular beam mass spectrometry to chemical vapor deposition studies, *Rev Sci Instrum* 63:4138
144. Hsu WL, McMaster MC, Coltrin ME, Dandy DS (1994) Molecular beam mass spectrometry studies of chemical vapor deposition of diamond, *Jpn J Appl Phys* 33:2231
145. Hsu WL (1992) Gas-phase kinetics during microwave plasma-assisted diamond deposition: Is the hydrocarbon product distribution dictated by neutral-neutral interactions? *J Appl Phys* 72:3102
146. Hsu WL, McMaster MC, Coltrin ME, Dandy DS (1994) Molecular beam mass spectrometry studies of chemical vapor deposition of diamond, *Jpn J Appl Phys* 33:2231
147. McMaster MC, Hsu WL, Coltrin ME, Dandy DS, Fox C (1995) Dependence of the gas composition in a microwave plasma-assisted diamond chemical vapor deposition reactor on the inlet carbon source: CH_4 versus C_2H_2 , *Diamond Relat Mater* 4:1000
148. Rego CA, Tsang RS, May PW, Ashfold MNR, Rosser KN (1996) Gas-phase composition measurements during chlorine assisted chemical vapor deposition of diamond: A molecular beam mass spectrometric study, *J Appl Phys* 79:7264
149. Tsang RS, Rego CA, May PW, Thumim J, Ashfold MNR, Rosser KN, Younes CM, Holt MJ (1996) Gas-phase concentration measurements and diamond film composition from chlorine assisted CVD, *Diamond Relat Mater* 5:359
150. Tsang RS, Rego CA, May PW, Ashfold MNR, Rosser KN (1997) Examination of the effects of nitrogen on the CVD diamond growth mechanism using *in situ* molecular beam mass spectrometry, *Diamond Relat Mater* 6:247
151. Harris SJ, Weiner AM, Perry TA (1988) Measurement of stable species present during filament-assisted diamond growth, *Appl Phys Lett* 53:1605
152. McMaster MC, Hsu WL (1994) Experimental measurements and numerical simulations of the gas composition in a hot-filament-assisted diamond chemical-vapor-deposition reactor, *J Appl Phys* 76:7567
153. Sommer M, Smith FW (1990) Activity of tungsten and rhenium filaments in CH_4/H_2 and C_2H_2/H_2 mixtures: Importance for diamond CVD, *J Mater Res* 5:2433
154. Dandy DS, Coltrin ME (1994) Effects of temperature and filament poisoning on diamond growth in hot-filament reactors, *J Appl Phys* 76:3102
155. Jin S, Moustakas TD (1994) Effect of nitrogen on the growth of diamond films, *Appl Phys Lett* 65:403

156. Atakan B, Beuger M, Kohse-Hoinghaus K (1999) Nitrogen compounds and their influence on diamond deposition in flames, *Phys Chem Chem Phys* 1:705
157. Spear KE (1989), Diamond — ceramic coating of the future, *J Am Ceram Soc* 72:171
158. Celii FG, Butler JE (1991) Diamond chemical vapor deposition, *Annu Rev Phys Chem* 42:643
159. Yarbrough WA, Messier R (1990) Current issues and problems in the chemical vapor deposition of diamond, *Science* 247:688
160. Lucht RP, Salmon JT, King GB, Sweeney DW, Laurendeau NM (1983) *Opt Lett* 8:365
161. Alden M, Schawlow AL, Svanberg S, Wendt W, Zhang PL (1984) *Opt Lett* 9:211
162. Goldsmith JEM (1985) Two-step saturated fluorescence detection of atomic hydrogen in flames, *Opt Lett* 10:116
163. Bertagnolli KE, Lucht RP, Bui-Pham MN (1998) Atomic hydrogen concentration profile measurements in stagnation-flow diamond-forming flames using three-photon excitation laser-induced fluorescence, *J Appl Phys* 83:2315
164. Goodwin DG (1991) Simulations of high-rate diamond synthesis: methyl as growth species, *Appl Phys Lett* 59:277
165. Goodwin DG (1993) Scaling laws for diamond chemical-vapor deposition II: Atomic hydrogen transport, *J Appl Phys* 74:6895
166. Brenner DW, Robertson DH, Carty RJ, Srivastava D, Garrison BJ (1992) *Computational Methods in Materials Science*, Materials Research Society, Pittsburgh, PA
167. Klein-Douwel RJH, Schermer JJ, ter Meulen JJ (1998) CN distribution in flame deposition of diamond and its relation to the growth rate, morphology, and nitrogen incorporation of the diamond layer, *Diamond Relat Mater* 7:1118
168. Chatei H, Bougdira J, Remy M, Alnot P, Bruch C, Kruger JK (1997) Effect of nitrogen concentration on plasma reactivity and diamond growth in a H_2 - CH_4 - N_2 microwave discharge, *Diamond Relat Mater* 6:107
169. Badzian A, Badzian T, Lee S-T (1993) Synthesis of diamond from methane and nitrogen mixture, *Appl Phys Lett* 62:3432
170. Bohr S, Haubner R, Lux B (1996) Influence of nitrogen additions on hot-filament chemical vapor deposition of diamond, *Appl Phys Lett* 68:1075
171. Klein-Douwel RJH, Spaanjaars JLL, ter Meulen JJ (1995) Two-dimensional distributions of C_2 , CH, and OH in a diamond depositing oxyacetylene flame measured by laser induced fluorescence, *J Appl Phys* 78:2086
172. Lang T, Stiegler J, Kaenel YV, Blank E (1996) Optical emission diagnostics and film growth during microwave-plasma-assisted diamond CVD, *Diamond Relat Mater* 5:1171
173. Gruen DM, Zuiker CD, Krauss AR, Pan X (1995) Carbon dimer, C_2 as a growth species for diamond films from methane/hydrogen/argon microwave plasmas, *J Vac Sci Technol A* 13:1628
174. Cui J-B, Fang R-C (1997) Characterization of the diamond growth process using optical emission spectroscopy, *J Appl Phys* 81:2856
175. Shang N-G, Fang R-C, Han S-J, Liao Y, Cui J-B (1998) Transverse bias-enhanced nucleation of diamond in hot filament chemical vapor deposition, *Mat Res Innovat* 2:79
176. Luque J, Juchmann W, Brinkman EA, Jeffries JB (1998) Excited state density distributions of H, C, C_2 , and CH by spatially resolved optical emission in a diamond depositing dc-arcjet reactor, *J Vac Sci Technol A* 16:397
177. Raiche GA, Jeffries JB (1993) Laser-induced fluorescence temperature measurements in a DC arcjet used for diamond deposition, *Appl Opt* 32:4629

178. Reeve SW, Weimer WA (1995) Plasma diagnostics of a direct-current arcjet diamond reactor II: Optical emission spectroscopy, *J Vac Sci Technol A* 13:359
179. Cui Jingbiao, Ma Yurong, Fang Rongchuan (1996) Study of electron-enhanced hot-filament CVD diamond growth via *in situ* optical emission spectroscopy (Chinese), *Science in China (A)* 26:1038
180. May PW, Burrige PR, Rego CA, Tsang RS, Ashfold MNR, Rosser KN, Tanner RE, Cherns D, Vincent R (1996) Investigation of the addition of nitrogen-containing gases to a hot filament diamond chemical vapor deposition reactor, *Diamond Relat Mater* 5:354
181. Chang C, Ye Z-Y, Liao Y, Wang G-Z, Fang R-C (1999) Programming control of hot-filament chemical vapor deposition diamond film growth process via *in situ* optical emission spectroscopy, *Proceeding of Asian Conference on Chemical Vapor Deposition (Asian CVD'99)*, Shanghai, P R China
182. Chang C, Fang R-C, Liao Y, Wang G-Z (to be published)
183. Pearse RWB, Gaydon AG (1976) *The Identification of Molecular Spectra*, 4th Edition, 83, John Wiley & Sons, Inc, New York
184. Smith GP, Golden DM, Frenklach M, Moriarty NW, Eiteneer B, Goldenberg M, Bowman CT, Hanson RK, Song S, Gardiner Jr WC, Lissianski VV, Qin Z, GRI-Mech 3.0, http://www.me.berkeley.edu/gri_mech/
185. Ricard A, Malvos H, Bordeleau S, Hubert J (1994) Production of active species in a common flowing post-discharge of an Ar-N₂ plasma and an Ar-H₂-CH₄ plasma, *J Phys D: Appl Phys* 27:504
186. Locher R, Wild C, Herres N, Behr D, Koidl P (1994) Nitrogen stabilized <100> texture in chemical vapor deposited diamond films, *Appl Phys Lett* 65:34
187. Li J (1997) Design of multi-filament arrays and substrate holders in hot-filament CVD reactors for large area diamond film deposition, PhD dissertation, University of Arkansas
188. Skokov S, Weimer B, Frenklach M (1994) Elementary reaction mechanism of diamond growth from acetylene, *J Phys Chem* 98:8

5 Laser-Assisted Growth and Characterization of Multicomponent Lead-Zirconate-Titanate Films

Jyrki Lappalainen, Johannes Frantti, and Vilho Lantto

Microelectronics and Materials Physics Laboratories, P.O. Box 4500, University of Oulu, FIN-90014, Finland

5.1 Introduction

Soon after the invention of the ruby laser in 1960, the first theoretical and experimental studies concerning the interaction between laser light and solid material and the evaporation of the material into the form of thin film were published [1,2]. Although the laser facilities were at the prototype level with a low output power of unstable radiation at that time, the fundamental processes of laser-assisted material evaporation and laser-ablation deposition could be performed. Also, the very complex nature of the physical and chemical reactions on the surface of the material being exposed to the intense, highly-oriented coherent and monochromatic beam of photons was revealed. However, due to the modest laser technology and to the fast development and extensive research work in the fields of other thin-film deposition methods, including sputtering technologies as well as molecular beam epitaxy (MBE), little research work on laser-ablation technique as a method for thin-film deposition was made until the technique was utilized successfully in the deposition of high- T_c superconductors by Venkatesan in the late 1980s [3]. During the last ten years, there has been rapid development both in the theory of ablation process and experimental methods as well as in the field of lasers and deposition-equipment technology. Also, a large variety of materials, including single-component materials along with multicomponent semiconductors and dielectrics, have been deposited successfully using the laser-ablation deposition technique.

5.1.1 Laser-assisted growth of thin films

In pulsed-laser deposition, short and intense laser pulses are used to evaporate and ablate the surface of the desired target material. Typically, deposition is done using UV-wavelength lasers due to their high absorption coefficient for a large variety of materials. The most common laser type is the excimer gas laser with a wavelength from 151 to 351 nm depending on the selected gas mixture, or frequency-tripled or -quadrupled Q-switched Nd:YAG lasers with wavelengths of

355 and 266 nm, respectively. In the discussion here, all the laser-ablation deposition was carried out using a XeCl excimer gas laser with a wavelength of 308 nm and pulse duration of around 20 ns. These laser pulses have a peak power on the order of 10^8 W and, with appropriate optical manipulation and focusing, are capable of evaporating practically any kind of material. At low-pressure conditions, the evaporation leads to the formation of an adiabatically expanding plasma that is mainly composed of neutral atoms and various ionized and neutral species of the target material that can be collected onto a substrate to form a thin film. The main advantages of the pulsed-laser-deposition technique include experimental simplicity, the capability of evaporating materials with a high melting point and the ease of stoichiometric deposition of multicomponent compounds such as modified lead zirconate titanates (PZTs). However, the formation of large particulates (i.e., splashing) and the non-uniform film-thickness distribution are the main problems involved in this laser-assisted growth of thin films.

5.1.2 Ferroelectric PZT thin films

Ferroelectric lead-zirconate-titanate ceramics in the form of thin films have been studied intensively for various applications over the past few years. Their electrical and electromechanical properties, such as a remanent polarization, a high dielectric constant, piezoelectricity, strong electro-optic and acousto-optic effects, and pyroelectricity offer a wide variety of applications in microelectronics and micromechanics.

Lead-zirconate-titanate ceramics, $\text{Pb}(\text{Zr}_x\text{Ti}_{1-x})\text{O}_3$, are a solid solution of PbTiO_3 and PbZrO_3 with a perovskite ABO_3 crystal structure with Pb^{2+} ions in *A* sites, Zr^{4+} and Ti^{4+} ions in *B* sites, and oxygen octahedra formed by O^{2-} ions around the *B* cations. Between the composition-dependent Curie temperature (about 230°C for PbZrO_3 and 490°C for PbTiO_3) and room temperature, PZT ceramics actually have five different phases that include antiferroelectric orthorhombic and tetragonal crystal structures in Zr-rich compositions, ferroelectric rhombohedral (trigonal) high- and low-temperature phases in lower Zr compositions, and a tetragonal phase in compositions with a higher Ti content. Above the Curie temperature, PZT ceramics are always in the paraelectric cubic structure [4]. The phase boundary between the ferroelectric rhombohedral (trigonal) and tetragonal phases, with the value of $x \approx 0.53$ at room temperature, is known as the morphotropic phase boundary (MPB), which is very important for the electrical and mechanical properties utilized in the component applications. At the MPB, both phases are in thermal equilibrium in the ceramics and the phases form a coexistence region in the composition range of $0.49 \leq x \leq 0.64$ where PZT ceramics possess an increased capability of polarization and thus a high electromechanical coupling coefficient [5]. From the application point of view, the modification of PZT ceramics with rare-earth elements like Nd^{3+} (PNZT) and La^{3+} (PLZT), substituting Pb^{2+} ions in *A* sites, further improves the properties of the ceramics.

The ferroelectric nonlinear polarization effect with nonzeroremanent polarization and hysteresis is utilized in nonvolatile ferroelectric random-access (FERAM)

memory applications. In the capacitor structure, the direction of the remanent polarization is set by the last polarizing electric field, e.g., 5 V for a film 300 nm thick. In the dielectric material between the electrodes, the polarization state can be deduced from the amount of the charging current directed to the subsequent electric field, e.g., 3 V for the 300 nm film, thus determining the state “1” or “0” for the individual memory cell [6,7]. On the other hand, inverse piezoelectric phenomena causing elongation or shrinkage under an external electric field that depends on the mutual orientation of the field and the remanent polarization of the PZT material can be exploited in various multilayer-stack or mono- and bimorph-type actuator applications to generate accurately-controlled movement from a few nanometers up to several hundreds of micrometers. This is useful, for example, in atomic-force microscopy (AFM), photolithography systems for semiconductor manufacturing, and light-beam deflectors [8–10]. Due to their pyroelectric effect, PZT thin films, especially those with Zr-rich compositions, are sensitive when used in infrared temperature and motion sensors and are, for example, used as detector elements in alarm systems [11,12]. In addition to the group of applications utilizing the piezoelectric effect in PZT ceramics, different kinds of devices based on the surface-acoustic waves (SAW) in film surfaces can be used for RF signal filtering in telecommunication applications, the optical manipulation of light beams, and for gas detection and analyses, just to mention a few applications [13]. Also, the many excellent optical properties of La-modified PZT (PLZT) thin films, such as their high transmittance and low reflectance, together with their strong electro-optic Kerr effect, i.e., the change of the refractive index Δn which is proportional to the square of the applied electric field E^2 , are used in fast optical shutters, modulators, and waveguides [14–16].

5.2 Film Deposition Process

In the pulsed-laser deposition with UV lasers, one uses the short and intense laser pulse to both evaporate and ablate the surface of a desired target material. Pulsed-laser ablation (sputtering) without any evaporation can also remove material from the target surface. At low-pressures, laser-ablation forms an adiabatically expanding plasma that mainly consists of neutral atoms and various ionized and neutral species of the target material [17]. This plasma expands in the direction perpendicular to the target surface and can be collected onto a substrate to form a thin film a short distance away from the target.

5.2.1 Principles of pulsed-laser-deposition technique

The underlying mechanism in the process of laser-beam interaction with the target material is based on the photoexcitation of electrons. Different possibilities in this excitation process include electronic transitions from valence-band states as well as from the occupied surface and defect states to conduction-band states, leading

to the formation of electron-hole pairs and excitons. Assuming an initially perfect crystal structure, the relaxation of these excitations can occur simply through radiative or nonradiative recombination, thus restoring the system basically to the nondisturbed ground state. On the other hand, the relaxation process can result in a metastable state in the surface layer of the material leaving the original surface structure distorted with a number of defects. Under these metastable conditions, when the optical absorption properties of the material are changed and the surface layer of the target consists of a large number of loosely bound atoms, even a weak photoexcitation can easily create a vacancy and a free atom. When the excitation process is strong enough to cause direct formation of vacancy clusters and consequently multiple-emitted atoms in the form of larger uniform clusters (molecules) and dissociated atoms, the ablation process itself turns on [18]. Different steps of the pulsed-laser-deposition (PLD) process are described in Fig. 5.1.

In addition to the characteristic properties of the ablation process mentioned above, one important feature is the existence of the material-dependent threshold laser-beam fluence I_{th} . This laser-beam fluence can be determined as a minimum onset fluence to start the ablation process; it is strongly dependent on the target material properties and on the properties of the laser pulse. In the case where laser-beam interaction with the target surface is a thermal ablation process mainly due to the thermal conductivity and the radiation losses of the target, the surface temperature obtains the vaporization temperature T_v at the time t_{th} after the beginning of the laser-beam exposure. Because the laser-pulse length t_p is fixed (≈ 10 ns), a threshold value of the laser-beam fluence I_{th} is necessary for a sufficient amount of energy to evaporate the target surface [19].

Typically, for the semiconductors and insulators, like the PNZT ceramics, the adiabatic heating-model condition $2(k_d t_p)^{1/2} < \alpha^{-1}$, where k_d is the thermal diffusivity, α is the absorption coefficient, and t_p is the length of the laser pulse, is a good assumption [20]. In the adiabatic heating model, the temperature increase inside the target material is due to direct heating by the laser light instead of thermal diffusion from the target surface. Thus, the energy of the laser pulse is mainly absorbed in the thin surface layer of the target.

Under the conditions where the laser-ablation process is possible during the time of laser-beam exposure, a thin plasma layer is formed on the surface of the target as a result of the interaction of the incident laser beam with the ablated and evaporated particles. Initially, the particles emitted from the surface of the target form a thin Knudsen layer where thermal equilibrium among the particles is established through collisions. Initially, the velocity ($v_x \geq 0$) of the particles is perpendicularly pointed out from the target surface and the velocity distribution obeys Maxwellian distribution for the particles emitted through thermal ablation and evaporation, but does not necessarily do so for the emission due to photoexcitation [21]. However, quickly after a few collisions, thermal equilibrium is reached at the outer boundary of the Knudsen layer. A negative velocity component $-v_x$ is developed and the high temperature T_k of the plasma is converted into the form of kinetic energy giving the plasma a flow velocity u_k that always obeys the Maxwell-Boltzmann velocity distribution. At this point, due to the negative

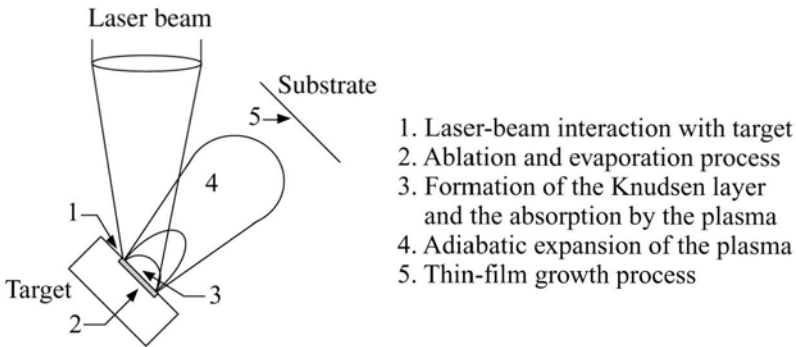


Fig. 5.1. Schematic description of different parts of the pulsed-laser-deposition process. In the case of an excimer laser, the pulse duration is around 10 ns and the flight time of the particles from the target to substrate is typically less than 5 μ s.

velocity component of the plasma, some of the particles are repelled back to the direction of the target and a part of the emitted material recondenses on the target surface.

The plasma layer is typically 100 μ m, which is thin compared to the dimensions of the plasma in the plane of the target surface that is determined by the spot size of the laser beam (e.g., 1 mm \times 2 mm in the case study in Section 5.3). The pressure gradient inside the plasma is greatest in the direction perpendicular to the target surface [22]. Thus, the adiabatic expansion of the plasma is fastest in this direction leading to a non-uniform thickness distribution of the film on the substrate. A typical thickness distribution of the laser-ablated thin film obeys a cosine-power law that can be used to evaluate the quality factor describing the flatness of the deposited thin film.

5.2.2 Growth and structure of thin films

The growth of the thin film begins as soon as the edge of the ablation plume reaches the substrate and the first species hit its surface. The actual mechanism of the film-growth process depends strongly on the conditions present in the ablation chamber, and also depends on the ablated material characteristics. In addition to the laser-beam fluence at the target surface, also the choice of the substrate material and temperature, as well as, the ambient gas atmosphere have a significant effect on the crystal structure and surface morphology of the growing thin film. Thus, the film deposition with the laser-ablation process is divided into the post-annealing heat-treatment process and *in situ* process according the specific growth parameters.

In the post-annealing process, as is done through the experiments in the case study in Section 5.3, the thin film itself is grown using a simplified process, where the substrate is kept at room temperature, and the chamber is evacuated to the pressure of around 10^{-5} mbar without any background gas. Under such conditions,

the thermal energy on the substrate surface is too low to initiate nucleation and thus the resulting films are generally amorphous, but can contain crystalline particulates originating from the target surface [23]. On the other hand, the most important parameter affecting the composition and the structure of the thin film during the ablation process is the laser-beam fluence. Post-annealing of films gives still another possibility to control the composition and crystal structure of the films. For example, in order to achieve PNZT films with the desired crystal structure, a subsequent annealing process was needed at temperatures between 600 and 900°C [8]. The annealed films are polycrystalline and the grain size is dependent on the annealing temperature and time and, in the case of PZT films discussed here, also on the atomic ratio of titanium and zirconium Ti/Zr [24]. In titanium-rich PZT films, the nucleation of the grains starts more easily, the number of grains is much higher, and the grains are smaller compared to those in zirconium-rich films.

The crystallization of the amorphous PZT film proceeds so that the film first forms a pyrochlore phase at temperatures between 400 and 500°C. Then, at higher temperatures, the upper face of the film starts to crystallize in some ferroelectric phase of perovskite PZTs, and the crystallization emerges deeper into the film during the annealing process [24]. An AFM micrograph of an amorphous PNZT film surface is shown in Fig. 5.2. In the case of the *in situ* deposition process, the substrate is heated up to temperatures from 550 to 750°C and the chamber is partially filled with oxygen gas in order to ensure sufficient nucleation energy for direct crystal growth during the film-deposition process starting from the substrate surface. An appropriate choice of the substrate with the lattice constants close to those of PZT promotes the growth of high-quality epitaxial thin films. Also, by varying the oxygen pressure, substrate temperature, and laser-beam fluence, the crystal structure of the film can be varied [23,25].

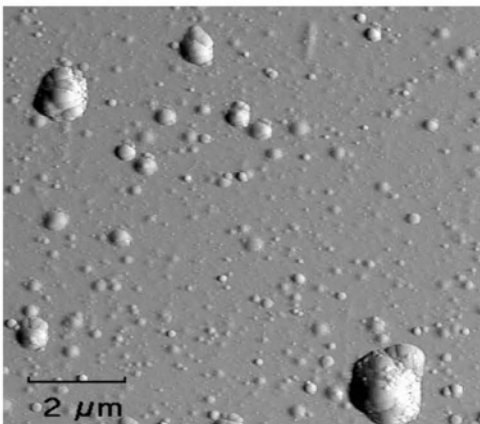


Fig. 5.2. AFM micrograph of an amorphous PNZT thin film with thickness of 390 nm after deposition at room temperature. The film was deposited at a laser-beam fluence of 1.0 J/cm² using 37,500 laser pulses.

5.3 Case Study: Nd-Modified PZT Films

The use of the pulsed-laser-deposition technique in the growth of post-annealed Nd-modified PZT thin films, hereafter PNZT, is considered here as a case study. Deposited PNZT films are in the form of single thin films on various substrates and also inside multilayer capacitor structures with platinum thin-film electrodes. Some features and results of the deposition process of films and the characterization of their structural and electrical properties are discussed.

Various $\text{Pb}_{0.97}\text{Nd}_{0.02}(\text{Zr}_{0.55}\text{Ti}_{0.45})\text{O}_3$ targets with different densities were prepared from a PNZT powder with this composition. Targets were first pressed into the form of pellets under a pressure of 500 kPa at room temperature. In order to adjust the density of the PNZT targets, the sintering was carried out at different temperatures between 900 and 1200°C for 20 minutes at the maximum temperature. The sintering process was carried out under an inverted zirconia crucible together with some extra PNZT powder in order to prevent an excess loss of lead. The quality of the PNZT targets was tested with the X-ray-diffraction method and with the energy-dispersive spectroscopy of X-rays (EDS). For the platinum-electrode deposition, a polished platinum disk was used as a target.

A pulsed XeCl-excimer laser with a wavelength of 308 nm and pulse duration of 20 ns was used for the film deposition processes. The laser-pulse repetition rate was 25 Hz and the laser-ablation process was carried out in a vacuum chamber at a pressure between 4×10^{-5} and 6×10^{-5} mbar at room temperature. The distance between the target surface and the substrate was varied between 20 and 35 mm and the angle between the target surface and incident laser beam was 45°. The laser-beam fluence on the PNZT target surface was varied between 0.2 and 3.0 J/cm² by adjusting the spot size of the laser beam on the target surface with a focusing quartz lens. Typically, for the capacitor application experiments, a laser-beam fluence of around 1.0 J/cm² was used. The deposition of the films was carried out with the scanning laser-beam condition at a constant scanning speed of 8 mm/s. However, the laser beam was scanned only in one horizontal direction parallel to the target surface so that the spot size of the laser beam and, thus, the laser-beam fluence was kept constant during the ablation process. In some experiments, the local laser-beam condition was also used in order to study the phenomena on the target surface during the ablation process. In the local laser-beam condition, both the target and the position of the laser spot were kept fixed so that the laser pulses hit the target always at the same surface area.

Single-crystal sapphire (Al_2O_3) substrates with (1 $\bar{1}$ 02) surfaces, MgO(100) and thermally oxidized Si(100) substrates were placed parallel to the target surface after a cleaning treatment. For silicon substrates, an oxide layer was grown by a dry-oxidation method in order to form a buffer layer between the silicon and the Pt/PNZT structure.

After deposition, a part of the PNZT thin-film samples were left amorphous and the rest were post annealed in air at various maximum temperatures between 600 and 900°C for a period of 10 to 20 minutes under an inverted zirconia crucible with some PNZT powder. The thickness of the PNZT thin films varied from 25 to

1200 nm, depending on the experiment. In the post-annealing heat treatment, a heating rate of 400°C/h was found to be appropriate for the single-layer PNZT films on sapphire and MgO substrates. In order to achieve an oriented polycrystalline PNZT thin film with a perovskite-type tetragonal or trigonal lattice structure, maximum annealing temperatures of at least 675 to 900°C had to be used. On silicon substrates, the PNZT films exceeding 300 nm in thickness were annealed at 650°C and the thinner films at 675°C. In order to avoid cracking due to the unequal thermal expansion between the silicon substrate and the PNZT layer, a low cooling and heating rate of 50°C/h had to be used.

For the deposition of the electrode layers in capacitor structures a polished platinum disk was used as a target. The fluence of 2.5 J/cm² was found to be appropriate to produce a smooth conductive platinum film. After deposition, platinum bottom electrodes, about 200 nm thick, were annealed in air atmosphere at 700°C. The top electrode was left amorphous. In the fabrication of a Pt/PNZT/Pt capacitor structure, a temperature difference of 25°C or more between the maximum annealing temperatures of the platinum bottom electrode and the PZT film was found necessary to prevent the mixing of the separate layers.

The growth rate of the deposited films as a function of the laser-beam fluence and time was determined with two different methods. The average growth rate was determined from the thickness of the deposited films measured with a Dektak 3030ST profilometer. The growth rate as a function of the number of laser pulses (or time) was measured in the *in situ* ablation process by replacing the substrates with a quartz-crystal sensor connected to the Sycon STM-100 Thickness/Rate monitor.

The structure of the PNZT films was studied with X-ray-diffraction experiments using CuK α -doublet (1.540562 and 1.544390 Å) radiation and a Phillips X-ray diffractometer. The measurements consisted usually of recording the X-ray diffraction intensities at 2 θ angles from 10 to 80° with a constant speed of 1°/min. Measurements with greater accuracy were carried out manually, e.g., by measuring an integration time corresponding to 20000 pulses. A commercial curve-fit program (Jandel Scientific PeakFit 4.0) was used to determine the accurate positions of the measured diffraction peaks.

Macroscopic mechanical stresses in PNZT thin films were determined from the diffraction patterns of the CuK α ₁-rays. The shifts in the diffraction-peak position from the tetragonal (413) planes at around 2 θ = 148° were measured as a function of the tilt angle for the stress analysis [26]. The XRD patterns were measured at the tilt angles of 0°, 30°, 45°, and 60° from both PNZT/Pt/MgO and PNZT/Pt/SiO₂/Si structures with various PNZT film thicknesses.

The structure and composition of the films were also studied with a scanning electron microscope (SEM) and EDS measurements using the JEOL JSM-6400/LINK AN10-85 facility with a thin-film analysis program. In some compositional analyses, an electron-probe microanalyzer (EPMA) JEOL JCSA-733 was also utilized. For high-resolution SEM micrographs of the ablation-target surfaces, a field-emission microscope (FESEM) JEOL JSM-6300F was used.

In order to study the surface morphology and, especially, the effect of the particulate formation on the quality of the thin-film surface, atomic force microscopy (Digital Instruments Nanoscope II) was used.

Visible laser light (514.532 nm) was used for Raman measurements. The spectrometer used was the Jobin Yvon T64000 model. The resolution of the Raman spectrometer was about 1 cm^{-1} . The spectra between -800 cm^{-1} and 1350 cm^{-1} were measured using a triple monochromator with a grating of 1800 grooves per mm. The data were collected using output power of 50 mW (laser beam power was a fraction of this in the case of micro-probing) and acquisition time $3 \times 600 \text{ s}$. All measurements were carried out under the microscope (laser spot diameter $1-2 \mu\text{m}$).

The determination of the dielectric properties of the PNZT thin films was done with an LCR meter (Hewlett Packard 4284A) using a signal amplitude of 1 V and frequencies of 1 and 10 kHz. The measurements of capacitance and loss angle were carried out between 22 and 500°C . The polarization behavior at room temperature was measured by a modified Sawyer-Tower circuit with a frequency of 165 Hz [27].

The leakage current as a function of the voltage applied across the Pt/PNZT/Pt capacitor structure was measured with a circuit composed of a voltage source (Keithley 263) and a digital current meter (Hewlett Packard 3458A) connected in series with the sample. The value of the current was measured 30 s after each voltage change so that the initial charging current of the capacitor had decayed and the leakage current stabilized. The conductivity measurements were also carried out at several elevated temperatures below the Curie temperature in order to identify the possible thermally activated charge-transport mechanisms.

Raman measurements were carried out at the Microelectronics and Materials Physics Laboratories, University of Oulu, Finland, and at the Materials and Structures Laboratory at the Tokyo Institute of Technology, Japan. The other measurements and preparation of samples were carried out at the Microelectronics and Materials Physics Laboratories, University of Oulu.

5.4 Results from XRD and EDS Measurements

The crystal structure of the post-annealed PNZT films was studied with conventional X-ray-diffraction measurements. The films deposited at higher laser-beam fluences above 1.5 J/cm^2 showed a polycrystalline, high-temperature trigonal structure independent of the annealing temperature [see Fig. 5.3(c)]. Deposition at lower laser-beam fluences [Fig. 5.3(a)] gave films with lower Zr contents and tetragonal crystal structure where the axis ratio c/a increased with increasing annealing temperature. However, from the films annealed at 600 and 650°C , only weak X-ray-diffraction intensities were measured, which showed that the films also contained the pyrochlore phase.

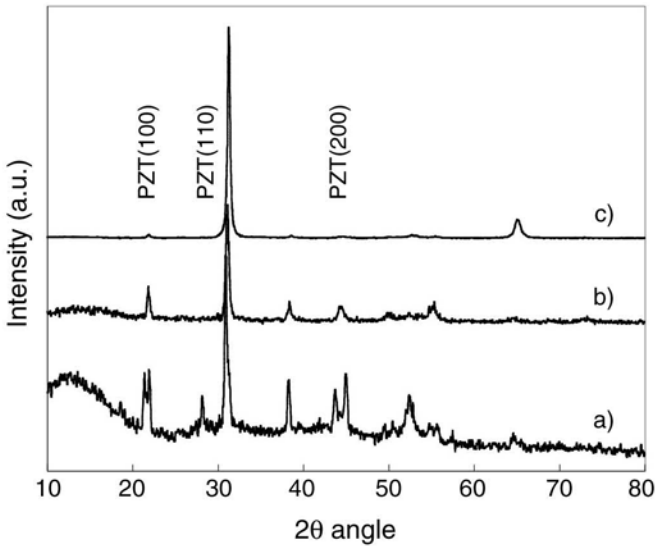


Fig. 5.3. XRD patterns from PNZT films deposited on the sapphire substrate at laser-beam fluences of (a) 0.4 (annealed at 850°C), (b) 1.3 (annealed at 850°C) and (c) 2.4 J/cm² (annealed at 800°C). The intensity values of the curve (c) were divided by a factor of 10 as compared with the intensity values of other curves (Reprinted from Ref. 30 with permission from Elsevier Science)

The atomic lead content Pb/(Zr+Ti) of amorphous as-deposited PNZT thin films as a function of laser-beam fluence was also studied. At fluences around 0.4 J/cm², the atomic lead content of the films was about 4.0 but decreased with increasing fluence to a value close to 1.0 at the laser-beam fluence of 0.75 J/cm². This behavior can be explained by a two-component model for the ejection of material from the target surface. At low laser-beam fluences (below 0.75 J/cm²) the material removal from the target is a thermal evaporation process and thus the composition of the ejected material flux is determined by the characteristic vapor pressures of the elements in the target. The relatively high vapor pressure of the PbO compound from the target leads to film compositions with lead contents exceeding its value in the initial PNZT target [28].

On the other hand, the segregation of lead into separate droplets and the formation of ZrO₂ and TiO₂ phases with high melting temperatures at the PNZT target surface during the ablation process [29] can also increase the amount of lead in the films at low laser-beam fluences. Higher surface temperatures at laser-beam fluences above 0.75 J/cm², on the other hand, ensure a more uniform evaporation of different elements from the target and the process resembles now more of an ablation process [28]. However, the surface temperature of the PNZT target also increases with the increasing laser-beam fluence and the material removal from the target is always a combination of thermal evaporation and ablation processes.

The final chemical composition of the PNZT films also changed during the post-annealing treatment, and the lead content of films annealed at high temperatures was less sensitive to laser-beam fluence. At low fluences, the as-deposited PNZT films contained excess lead and, thus, the ratio $Pb/(Zr+Ti)$ stabilizes close to the stoichiometric value during annealing. However, at high laser-beam fluences, the as-deposited PNZT films suffer from a lead content, which is too low, but at high annealing temperatures, the annealing atmosphere contains more lead evaporated from the extra PNZT powder under the inverted zirconia crucible. In this case, lead is incorporated from the vapor phase into the thin films; therefore, the lead content of the films increases with increasing annealing temperature. For films annealed at low temperatures, the high variation rate of lead content with fluence originates from the re-evaporation of lead (PbO) during the heat treatment; also, due to the low annealing temperature, the compensation from the vapor phase is smaller.

In addition, the enhanced formation of perovskite PZT phases at annealing temperatures above $650^{\circ}C$ leaves more lead in the crystal structure of the thin film and leads to compositions closer to that of the original PNZT target [28]. On the other hand, as shown in Fig. 5.4, the zirconium content $Zr/(Zr+Ti)$ of the post-

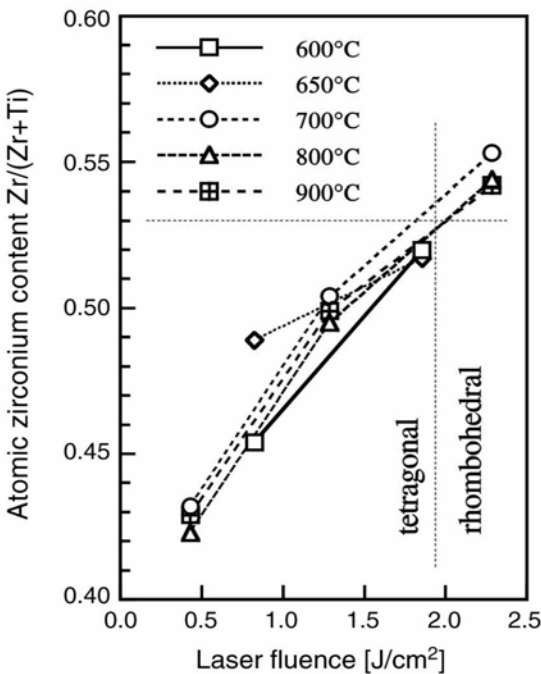


Fig. 5.4. Atomic zirconium content, $Zr/(Zr+Ti)$, of PNZT films as a function of laser-beam fluence used at the deposition. The films were post-annealed at various maximum temperatures between 600 and $900^{\circ}C$ (reprinted from Ref. 30 with permission from Elsevier Science)

annealed films increased monotonically from 0.43 up to 0.55 with increasing laser-beam fluences from 0.4 up to 2.4 J/cm², respectively. The zirconium content was also practically independent of the heat-treatment process [30].

This observation is consistent with the results of the composition measurements of the ablated target surface [29]. At higher laser-beam fluences above 1.0 J/cm², an increased evaporation of Zr and Ti further improves the compositional stability of the post-annealed PNZT thin films.

The dependence of zirconium content on the laser-beam fluence for films near the MPB with $x \approx 0.53$ also makes it possible to control the crystal structure of the film between the trigonal and tetragonal structures by choosing the correct deposition parameters. As shown in Fig. 5.3, the film deposited at the low fluence of 0.4 J/cm² has the tetragonal crystal structure, but the film deposited at the fluence of 2.4 J/cm² has the trigonal crystal structure [30].

5.5 Compositional and Structural Changes in the Target

Changes in the composition and structure of the PNZT target surface after the ablation process were studied by EDS analyses and XRD measurements. A PNZT target with a density of 7.4×10^3 kg/m³ was ablated with a fluence of 1.0 J/cm² for 25 minutes with up to 32700 pulses by using the scanning ablation process. Because of the higher evaporation rate of lead compared to that of zirconium and titanium, a strong lead deficiency was found in the surface layer of the target. Relative values between 0.17 and 0.26 were found for the atomic lead content Pb/(Zr+Ti) in the surface layer after ablation, which are low values when compared with the initial value of around 1.0. The corresponding values of the relative zirconium content Zr/(Zr+Ti) were close to the initial target composition (between 0.52 and 0.58). In this case, the compositional analyses were made on relatively large macroscopic areas at the target surface. The changes in the chemical composition of the PNZT target surface during ablation promote surface segregation and the development of new compounds and phases.

Figure 5.5 shows X-ray diffraction patterns measured with CuK α radiation from a PNZT target surface before and after ablation with various laser-beam fluences. In all patterns measured after the ablation, three additional twin peaks appear at 2θ angles of 35.7° and 36.3°, 51.3° and 52.3°, and 61.0° and 62.3°, respectively, indicating a slightly tetragonal new phase (indicated by the arrows in Fig. 5.5). Some changes in the shape and position of the PNZT peaks with increasing fluence are also seen in Fig. 5.5. The spreading of the PNZT peaks, e.g., the reflection from the (200) lattice planes at the 2θ angle of around 44° at the bottom of Fig. 5.5, also reveals the presence of both trigonal and tetragonal PZT phases in the clean target surface [31]. In the patterns measured from the target after the ablation with low fluences of 0.4 and 0.66 J/cm², an extra minor peak at the 2θ angle of 28.7° is also seen in Fig. 5.5, but it disappeared at higher fluences.

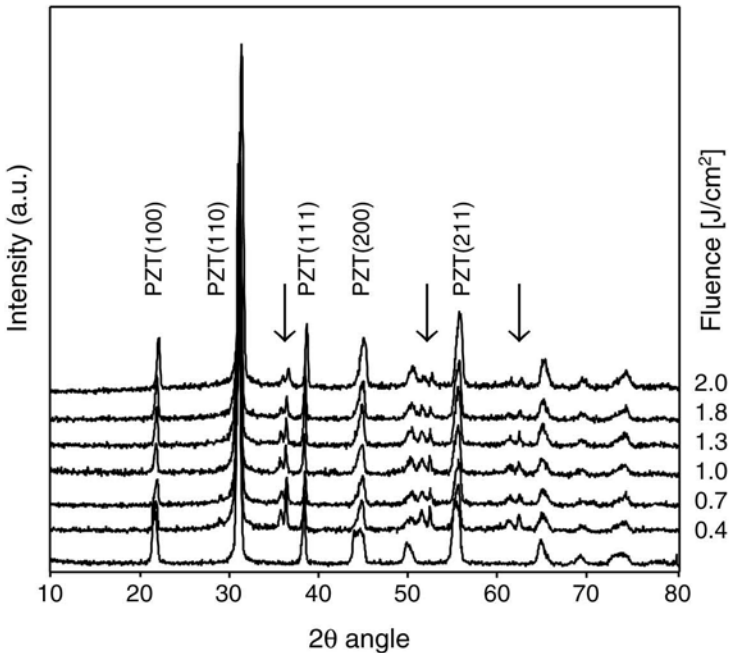


Fig. 5.5. X-ray diffraction patterns measured with $\text{CuK}\alpha$ radiation (1.54 \AA) from a PNZT-target surface before and after scanning laser ablation with various laser-beam fluences between 0.4 and 2.0 J/cm^2 . The arrows indicate three twin peaks from a new phase (tetragonal ZrO_2) formed in the laser-ablation process.

It is possible to conclude from the EDS results that the topmost target surface after ablation with the scanning process, and the top globules of the laser cones in the local ablation process, contain new Ti- and Zr-oxide compounds such as TiO_2 , ZrO_2 , and possibly ZrTiO_4 (Pb is found only in small droplets on the surface). However, at the high surface temperatures during the ablation process, the ZrTiO_4 phase should also decompose into the TiO_2 and ZrO_2 phases [32,33]. The intensities of the new XRD peaks in Fig. 5.5 are weak which may relate to an amorphous structure of the new surface layer. The three twin peaks in the XRD patterns agree with the (200), (220), and (311) reflections of a cubic structure with the face-centered-cubic (fcc) Bravais lattice after a slight distortion to a tetragonal structure with the body-centered-tetragonal Bravais lattice [29].

The lattice constants of the tetragonal structure are in this case $a \approx 4.941 \text{ \AA}$ and $c \approx 5.032 \text{ \AA}$, which are in close agreement with the values of the tetragonal ZrO_2 [34,35]. Therefore, the new peaks in the XRD patterns in Fig. 5.5 are related to tetragonal ZrO_2 because the cooling rate after laser-ablation process is fast. The intensity of the twin peaks also decreases with increasing fluence. An increase in the thickness of the new (amorphous) surface layer after ablation with increasing fluences may be the reason for the intensity decrease. Small amounts of crystalline

ZrO₂ and TiO₂ phases may be present at the bottom of the surface layer. An average grain size of 32 nm was calculated with the Scherrer equation [36] for this new phase in the surface layer of the ablated target. The EDS measurements from the top globules of the laser cones revealed a significant lead deficiency.

In fact, lead was missing in the top structure of the globules after both the local and scanning ablation processes. Instead, droplets of pure lead were found between the laser cones and on the walls of individual laser cones [see Figs. 5.6(a) and (b)]. On the other hand, the relative zirconium content $Zr/(Zr+Ti)$ was around 0.56 in all cases, which is close to the initial value in the target. These results also support the presence of both TiO₂ and ZrO₂ compounds in the top globules of the laser cones.

Raman spectra from a PNZT target surface before and after ablation were also measured [29]. The initial target surface had a typical Raman spectrum from PNZT ceramics with a trigonal structure as the main phase [37]. After ablation with single laser pulse having a fluence of 1.0 J/cm², a similar Raman spectrum was obtained. However, after ablation with 50 laser pulses, no specific Raman modes were found in the Raman spectrum. On the other hand, TiO₂ and ZrO₂ phases have several Raman-active modes in the same Raman-shift region [38]. The penetration depth of the applied argon-ion laser light with the wavelength of 514.532 nm was only a few hundred nanometers, which means that the top layer of the ablated target was either amorphous or possibly metallic. However, surface conductivity measurements from the ablated targets did not show any major conductivity changes with respect to the initial target surface. Thus, the combined information from the XRD and Raman measurements, and also from the EDS analyses, makes it possible to conclude that, because of the high cooling rate after the laser-beam exposure, the topmost surface layer of the ablated target is an amorphous mixture of different oxide compounds such as TiO₂ and ZrO₂ with small lead droplets on its surface. At the bottom of this amorphous surface layer, there is also a small amount of crystallized tetragonal ZrO₂ phase and possibly also a small amount of TiO₂ phase in the rutile structure in targets ablated with low laser-beam fluences.

In addition to the neutral and ionized atoms, molecular species and electrons, particulates up to micrometer-scale are generated in the laser-ablation process. The formation of these particulates impairs the surface morphology and quality of the growing thin film. The particulates are formed and ejected when the laser beam interacts with the molten surface layer of the target. The existence of the particulates (see Fig. 5.2) impairs the properties of the thin-film structure, especially for optical applications [39]. The explosions of the molten target surface due to the superheating of the subsurface layer and a rapid expansion of gas pores buried below the target surface inside a ceramic polycrystalline target are considered to be the dominant mechanisms responsible for the particulate formation [40,41]. On the other hand, the formation of a laser-cone structure on the target during a pulsed-laser deposition process generates large-scale particulates on the growing thin-film surface. In the case of metal targets, hydrodynamic sputtering has been considered to be a mechanism responsible for the particulate formation [42]. The dependence of the particulate density on the target density is assumed to relate

also to pores inside the sintered ceramic PNZT targets. The concentration of pores decreases with the increasing density of the PNZT ceramics and thus the number of particulates from the explosions of the pores under the target surface decreases.

Changes in the chemical composition of the PNZT target surface during ablation promote surface segregation and the development of new compounds and phases. XRD and EDS studies have revealed that new compounds are formed in a surface layer of the target as a result of changes in the chemical surface composition caused by differences in the evaporation rates of the elements. On the other hand, the surface segregation of certain elements and the fast cooling rate of the molten target surface after laser-beam exposure further promote a formation of amorphous structures and unstoichiometric compounds. These new compounds and phases in the surface layer which have higher melting points than that of the bulk target prevent the etching of the underlying layers of the target in the ablation process [43]. Thus, the etching of the target surface becomes non-uniform and laser-cone structure starts to develop in the target surface. Once the formation of the laser-cone structure is initiated, the laser-beam fluence dilution in the steep walls of the individual laser cones further strengthens the effect. The laser-cone structure in the case of a scanning laser beam is shown in Fig. 5.6. The larger magnifications reveal explosion holes with a diameter between 100 and 200 nm as a result of subsurface heating and a rapid expansion of the gas in the pores below the target surface.

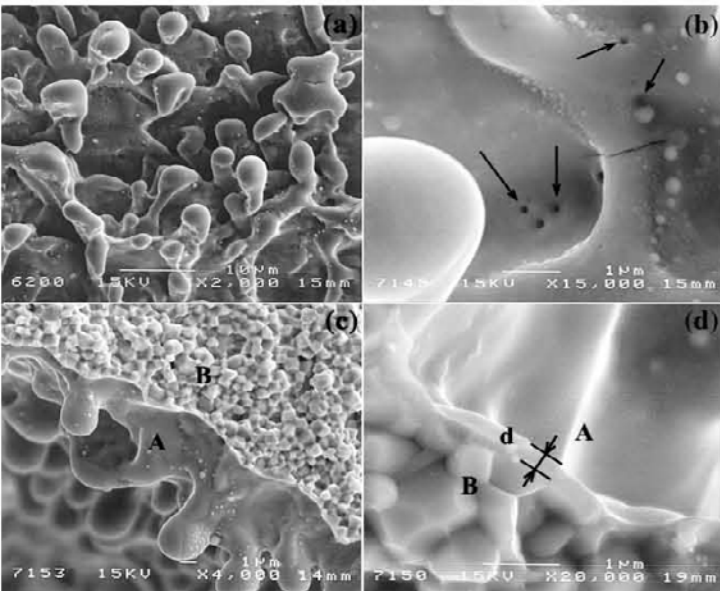


Fig. 5.6. SEM micrographs (a) and (b) show surface morphologies with different magnifications and (c) and (d) cross sections of a PNZT target after a scanning laser-ablation process

These explosions at the target surface generate the smaller particulates found on the PNZT thin-film surfaces. The surface of the targets had also numerous microcracks after ablation, which indicates a fast cooling and solidification rate of the molten layer at the target surface. Figures 5.6(c) and 5.6(d) show SEM micrographs of different cross sections of a PNZT target. The figures reveal the porous structure of the PNZT target with a density of $7.4 \times 10^3 \text{ kg/m}^3$ and sintered at 1100°C for 20 minutes. According to Fig. 5.6(d), the thickness d of the molten layer at the PNZT target surface had been less than 300 nm [29].

5.6 Raman Spectroscopy Studies of PZT Films

5.6.1 Basic concepts of the Raman effect

Despite the fact that most of the light traveling through a medium is either transmitted or absorbed by the medium, a small fraction is scattered, almost in all directions, by inhomogeneities inside the medium. These inhomogeneities may be static (like dislocations or point defects) or dynamic. Fluctuations in the density of the medium that are associated with atomic vibrations is an example of dynamic scattering. We consider the dynamic case and phonons. Inelastic scattering of light by acoustic phonons and optical phonons are called Brillouin and Raman scattering, respectively. The radiation produced in Raman scattering can further be divided to *Stokes* (light scattered with lower energy than the energy of the incoming light) and *anti-Stokes* scattering (light scattered with higher energy).

Raman scattering in crystals can be explained from the classical and from the quantum theoretical point of view. Classically, one determines the dipole moment p by the equation $p = \alpha E$, where α is the polarizability and the atoms of the sample are subjected to an electric field E . Polarizability α is modulated by the thermal excitations (phonons in crystals) present in the sample. The scattered radiation is produced by re-radiation of energy by the oscillating dipole moment p , the scattered intensity I being proportional to $|p|^2$ and inversely proportional to the fourth power of the wavelength of the scattered light [44]. The angular dependence of the intensity I of the oscillating dipole is given by the relation $I \propto \sin^2\theta d\omega$, where θ is the angle between the dipole moment axis and the given direction, and $d\omega$ is a solid angle increment (see, e.g., Ref. 45). Now, considering the modulation of a particular component α_{ij} as an example, we can see that this component is concerned with an exciting electric field along j and a resultant dipole along i . The dipole is modulated in the same way as the component, so that light at the Raman-shifted frequency is emitted as from a dipole of direction i . The Raman scattered light is polarized in the plane containing i and the propagation direction [45]. The intensity of the Raman scattered light can be calculated from the time-averaged power radiated by the induced polarizations into unit solid angle. Denoting the polarization of the incident and scattered light as e_i and e_s , respectively, the scattered intensity $I_s \propto |e_i \cdot (\partial\alpha/\partial Q)_0 Q(\omega) \cdot e_s|^2$, where Q is the vibration amplitude of a vibration of frequency ω . The Raman tensor R is defined by the equation $R =$

$(\partial\alpha/\partial Q)_0 \hat{Q}(\omega)$, where $\hat{Q}(\omega)$ is a unit vector parallel to phonon displacement. By measuring the dependence of the scattered intensity on the incident and scattered polarizations, one can deduce the symmetry of the Raman tensor and hence the symmetry of the corresponding Raman-active phonon. This, however, necessitates single crystals. The case of ceramics is described below.

It is tempting to consider Raman scattering as an interaction involving photons and phonons only. However, this interaction is very weak for visible light. Direct scattering of light by phonons necessitates that phonons and photons have comparable frequencies. Thus, this kind of process could arise at the far-infrared region. A theoretical model for this ionic Raman effect is reported in Ref. 46, but experimental verification seems to be lacking. From the quantum theory point of view, it is usually assumed that the radiation interacts with the lattice vibrations through the intermediary of the electrons in the crystal [44,47]. Loudon [44] has given three different elementary first order Raman scattering processes in terms of the elementary interactions between the radiation, the electrons, and the lattice. The most common of these three processes is the one where a photon with an angular frequency ω_i is present in the initial state and a photon with an angular frequency ω_s together with a phonon having an angular frequency of ω is present in the final state (so that this process is particularly for the Stokes component, but the corresponding process for the anti-Stokes component can be obtained by simple substitutions). The process involves three virtual electronic transitions accompanied by the following photon and phonon transitions: (1) a photon ω_i is absorbed, (2) an optical phonon ω is created, (3) a photon ω_s is emitted. Thus, in a quantum picture the scattering should be viewed as a third-order process. In the first step an electron-hole pair is created and this pair is scattered into another state by emitting a phonon in the second step. The electron-hole pair recombines radiatively in the third step with emission of the scattered photon. The third step involves a spontaneous emission of the scattered photon and thus this process is known as *spontaneous Raman scattering*.

In fact, when electromagnetic waves are propagating in a crystal they propagate only as *polaritons*. However, in the usual Raman scattering setup the wave-vector of the phonons involved is so large that the measured frequency is essentially that of the transverse optical (TO) phonon. Longitudinal optical (LO) phonons do not couple to transverse photons and thus do not participate in the polariton process. Strictly speaking, Raman scattering with phonons is the scattering of *exciton polaritons* under emission or absorption of a *phonon polariton* [48]. An exciton polariton is a coupled state of an exciton with a photon and a phonon polariton is a coupled state of a transverse phonon with a photon. In the weak coupling picture one can say that a photon creates a virtual exciton (electron-hole pair in the treatment given above) and is scattered by emission or absorption of an optical phonon. Polariton dispersion curves can be determined experimentally by forward Raman scattering. The understanding of these experiments necessitates strong-coupling or polariton picture. Since we are not involved in polariton experiments, the weak-coupling picture given above is valid.

5.6.2 Raman active modes

The exciting radiation in Raman experiments has a long wavelength; therefore, because of the wave-vector conservation law the wavelength of phonons in the first-order Raman scattering is practically infinite as compared with the dimensions of the unit cell of the crystal. Now, the group theory considerations are restricted to normal modes at the center of the Brillouin zone (in fact, to modes near the zone center, in a region where the polaritons are essentially phonon-like) that are those normal modes transforming as the irreducible representations of the point group of the space group. For general k directions, the phonons have mixed symmetries. Since optical modes have only nonzero frequencies at $k = 0$, these modes may only scatter light in a first-order scattering process. Thus, for k in any crystal direction, only a maximum of $3 \times (r-1)$ (r is the number of atoms in the crystal basis) optical modes may be observable. By changing the crystal orientation with respect to the polarization and propagation directions of the incident light, it is possible to observe another set of modes.

The criterion which determines whether or not a phonon mode is active in *first order* Raman scattering is the condition that it transforms in the same way as the tensor components α_{ij} under the point group of the lattice. This means that the irreducible representation, according to which the normal modes transform, must be contained in the irreducible representation for which the tensor components α_{ij} form a basis. The components of the polarizability tensor transform like products of coordinates (xx , xy , xz , and so on), whereas the components of the electric dipole moment transform like the coordinates (x , y , z). So, the phonons (normal modes) with even symmetry are Raman active, whereas phonons with odd symmetry are Raman inactive. Similarly, a phonon is IR active if it belongs to an irreducible representation which is contained in the representation for which the components of the electric dipole moment form a basis. In centrosymmetric crystals (like the cubic phase of lead titanate and PZT), IR and Raman activities are complementary, i.e., modes which are Raman active are IR inactive and vice versa. However, also in these crystals some modes may be both Raman and IR inactive and are called silent (like the T_{2u} -mode in the high temperature phase of lead titanate and PZT). Actually, the high temperature phase of PZT is an extreme example of this complementary property, since all atoms lie at the centers of symmetry (as long as the local distortions are neglected) and thus no first order Raman scattering can occur.

5.6.3 Raman spectra of ceramics

In the case of a polycrystalline material, Raman active modes for different directions and polarizations are, in principle, simultaneously observable. Further, Burns and Scott showed [49] how peaks in the Raman spectra of ceramics occur at just those frequencies corresponding to the actual modes propagating along the principal crystal axes. This makes the identification of Raman peaks measured from ceramics possible by directly comparing single crystal spectra and a spectrum measured from ceramics. However, it is not always possible to obtain single crystals, so

another method is needed. In the case of PZTs, this can be done by studying the spectra measured from lead titanate single crystals, and comparing them with the spectra measured from polycrystalline lead titanate. By replacing Ti ions by Zr ions in the structure of PbTiO_3 , peaks start to shift toward lower frequencies and become broader. However, as long as the symmetry is kept the same ($P4mm$ in this case), most of the peaks can be identified by this simple method. Particular care must be taken, since there are several other processes which might lead to the formation of peaks in the Raman spectra. For example, second or higher order modes might arise more easily in polycrystalline samples than in single crystals. Also peaks due to the other minor phases, which may not be easily seen by X-ray diffraction techniques, may have such large scattering cross sections that the possible Raman active modes appear in the measurements. Symmetry breaking (such as the breaking of translational symmetry by substitution of titanium by zirconium in lead titanate) may also lead to the cases, where some of the modes become Raman active. Optical transitions can also cause extra peaks. This necessitates a higher order process, and as a result, lower or even higher energy photons can be emitted. In order to study the origin of the peaks, several measurements can be used to find out whether a mode is a true Raman mode or not. Simple ways to verify this are to measure both anti-Stokes and Stokes spectra, to carry out the measurement with several wavelengths; to vary thermodynamic variables such as temperature, pressure, and electric field during the measurement; and plot the mode frequencies and intensities as a function of the selected variable.

5.6.4 Raman active phonons of PZT ceramics

Because the compositions of the thin films considered in this chapter are limited to $x \leq 0.55$, we will limit our discussion to the symmetries of these materials. These are cubic $Pm3m$ (high temperature paraelectric phase), tetragonal $P4mm$, and trigonal $R3m$ phases. Table 5.1 below summarizes first order Raman active modes in each phase.

In addition, long-range Coulomb forces lift the degeneracy of the T_{1u} modes in the cubic phase into a doubly degenerate $T_{1u}(\text{TO})$ mode (polarization transverse to k) and a single $T_{1u}(\text{LO})$ mode (polarization parallel to k). Similarly, the degeneracy of the transverse and longitudinal modes in tetragonal and trigonal phases is lifted by the long-range Coulomb forces. The frequencies of long wavelength longitudinal and transverse optical vibrations are related by the Lyddane-Sachs-Teller (LST) relationship provided that the wavenumber is above the polariton region of the dispersion curve. The following labelling scheme in the tetragonal phase was introduced [50] for the optical A_1 and E modes, originating from the three T_{1u} representations:

$A_1(3\text{TO})$	$A_1(3\text{LO})$	$E(3\text{TO})$	$E(3\text{LO})$
$A_1(2\text{TO})$	$A_1(2\text{LO})$	$E(2\text{TO})$	$E(2\text{LO})$
$A_1(1\text{TO})$	$A_1(1\text{LO})$	$E(1\text{TO})$	$E(1\text{LO})$

where the numbers in the parentheses increase with the increase of the particular mode frequency. LO and TO refer to longitudinal and transverse modes, respectively. Because the E and B_1 modes from the splitting of the T_{2u} modes are essentially degenerate, they are labelled $E\oplus B_1$ or “silent”.

Table 5.1. Classification of normal modes of vibrations for different phases of PZT at Γ ($k = 0$). Each listed phase has one formula unit in the primitive unit cell. The dimensions of the irreducible representations T_{1u} , T_{2u} , E , A_1 , A_2 , and B_1 are 3, 3, 2, 1, 1, and 1, respectively.

Phase	Normal modes of vibration	Remarks
Pm3m	$4T_{1u}\oplus T_{2u}$	Optical modes in three T_{1u} are IR active, but in T_{2u} they are neither Raman nor IR active (silent). Modes in the fourth T_{1u} correspond to three acoustic modes.
P4mm	$4E\oplus 4A_1\oplus E\oplus B_1$	Optical modes in E , A_1 , and B_1 are both Raman and IR active. Modes in a representation $A_1\oplus E$ correspond to three acoustic modes.
R3m	$4E\oplus 4A_1\oplus E\oplus A_2$	Optical modes in E and A_1 are both Raman and IR active. The mode A_2 is neither IR nor Raman active. Modes in a representation $A_1\oplus E$ correspond to three acoustic modes.

5.6.5 Characteristic features of the Raman scattering from the structural point of view

Traditionally, Raman scattering measurements have been used for the studies of first order Raman active modes as a function of various thermodynamic variables, such as temperature, electric field, and pressure. This has offered an experimental way to gain information related to the phase transitions. More recently, it has become possible to study the electronic energy band structure using resonance-Raman spectroscopy techniques. In the case of thin films, Raman imaging has proven to be an efficient way to study polycrystalline films and crystal orientation on a micrometer scale.

Since our studies are related to the structural features of these ceramics, we will discuss the symmetry breaking on a local scale. These local defects or distortions have a very crucial role in the formation of ferroelectric domains, or even in the determination of stable crystal symmetries.

As the name scattering suggests, the information obtainable from Raman scattering is very different in nature from that obtainable from diffraction experiments. Raman scattering can be described as a very local probe, yielding information of a unit cell scale phenomena (such as distortions due to the substitute atoms), whereas the information obtainable from conventional X-ray or neutron diffrac-

tion experiments tells about the average crystal structure. This is clearly demonstrated by observations that show peaks above the Curie temperature T_C in KTaO_3 [51] (where no first order Raman scattering should occur, by symmetry). Uwe et al. [51] related the origin of polar nanoregions even far above the bulk T_C to symmetry-breaking defects which induce randomly-oriented local domains. There were also found broad peaks in the Raman spectra of PZT ceramics above T_C at roughly the same energies as the first order Raman peaks occur in a ferroelectric phase below T_C [52]. Thus, these peaks might originate from higher order Raman scattering, or due to the symmetry-breaking defects. This latter explanation is more likely once one takes into consideration the fact that the peak positions were nearly the same below and above T_C .

A second example that shows clearly how Raman scattering yields information related to the local defects is the splitting of E -symmetry modes in tetragonal PZTs [53]. This splitting was observed to increase with increasing Zr concentration and decreasing temperature. Further, a clear frequency jump in the higher frequency peak of the doublet due to the splitting of the $E \oplus B_1$ mode (which is degenerate in pure lead titanate [50]) occurred when Zr concentration x changed from 0.40 to 0.50 [54]. This supposes an idea that the increasing amount of symmetry distortions in ab -basal planes will finally lead to the phase transition, and so one could consider this kind of symmetry breaking to be an example of precursor effects.

When one is studying the lattice dynamics of crystals, Raman scattering is again a powerful tool. The $A_1(1\text{TO})$ mode of tetragonal PZT ceramics has a particularly interesting role, since it is the soft mode, which is also related to polarization behavior of PZTs. The strong anharmonicity of this mode was clearly demonstrated by the Raman measurements, which were performed as a function of temperature and Zr concentration [54].

5.6.6 Raman spectra of PZT thin films

Figure 5.7 shows the Raman spectra measured from four samples deposited under the experimental conditions mentioned in Table 5.2. All the intensities are comparable to each other except the lowest spectrum, which has to be multiplied by a factor of five. These Nd-doped PZT thin films were deposited by pulsed laser ablation without substrate heating at a pressure of 6 to 8×10^{-6} mbar. Polished MgO plates (thickness $500 \mu\text{m}$) with (100) surfaces were used as substrates. The ablation target with the trigonal $R3m$ structure as the major phase had a composition $\text{Pb}_{0.97}\text{Nd}_{0.02}(\text{Zr}_{0.55}\text{Ti}_{0.45})\text{O}_3$, and an XeCl-excimer laser with the wavelength 308 nm was used in the ablation process. After ablation, the amorphous films were annealed at 700°C for 20 minutes with Nd-doped PZT powder in order to crystallize the films in a composition with equal amounts of A - and B -site cations.

We made a curve fit using Gaussians, except for sample A (see Table 5.2), where the peak at around 284 cm^{-1} was fit with a sum of a Gaussian and Lorentzian line shapes. This peak at around 280 cm^{-1} was fitted with two peaks, since the

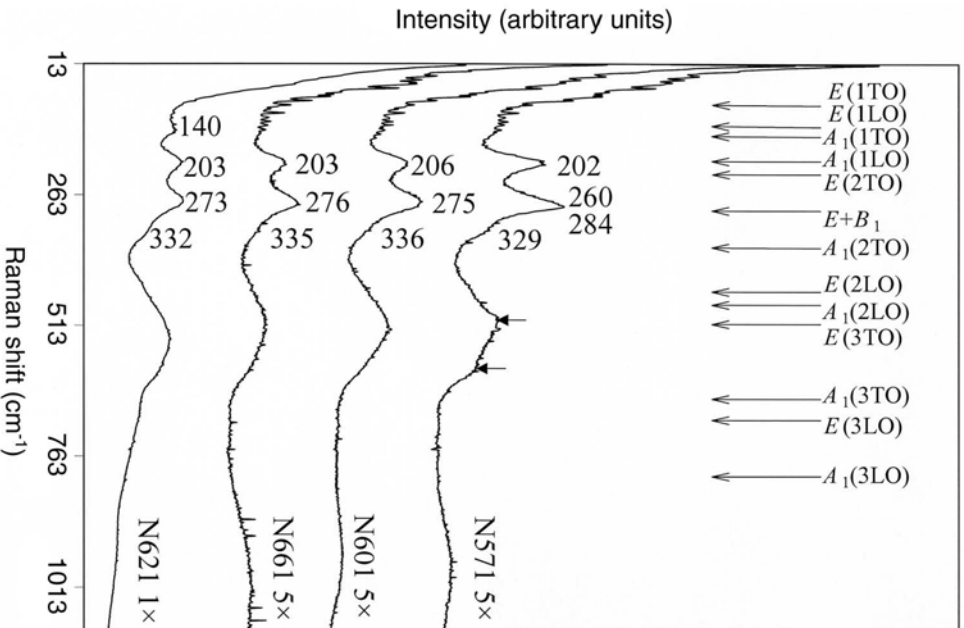


Fig. 5.7. Raman spectra measured from four PNZT thin films on the MgO substrate. The positions of different Raman peaks at room temperature in PbTiO_3 (Ref. 50) are also shown at the top.

fit with one peak was not able to yield a proper fit. Fontana et al. [55] conclude from their computed components of the effective charge of lead ions in PbTiO_3 that the bonds between lead and oxygen in tetragonal PbTiO_3 are mainly covalent and ionic, respectively, for directions parallel and normal to the polar c axis. It was possible to conclude from the high sensitivity of the $E(1\text{TO})$ -mode frequency on the Zr concentration in PZT that the addition of Zr considerably softens the “ionic” force constant of vibrations with displacement polarization in the direction of the a axis. For $A_1(1\text{TO})$ -mode vibrations with polarization in the direction of

Table 5.2. Film thickness and laser-beam fluence for four films ablated from a $\text{Pb}_{0.97}\text{Nd}_{0.02}(\text{Zr}_{0.55}\text{Ti}_{0.45})\text{O}_3$ target. Also, the sintering temperature of the target used at pulsed-laser deposition is given.

Sample	Films thickness/nm	Laser beam fluence/ Jcm^{-2}	Sintering temperature of the target/ $^{\circ}\text{C}$	Density of the target/ kgm^{-3}
A	388	1.0	1100	7400
B	451	0.66	1100	7400
C	328	1.0	1000	6340
D	294	0.4	1100	7400

the c axis, the force constant, originating primarily from covalent bonding between lead and oxygen, was found to be insensitive to Zr addition [56]. On the other hand, we found that the $A_1(\text{1TO})$ mode is sensitive to the addition of Nd to replace Pb in Nd-doped PbTiO_3 .

The low-frequency background is mainly due to the subpeaks of the $A_1(\text{1TO})$ mode. These subpeaks originate from the anharmonicity and double-well character of the potential energy of this mode, as discussed in more detail in Refs. [52,54,57]. Low-temperature Raman measurements made for the bulk ceramics showed that the anharmonicity model was able to describe qualitatively and even quantitatively the behavior of this low-frequency background [54]. This simple model was capable of describing the intensity behavior of the background as a function of temperature and Zr and Nd concentration.

It is seen that the $E\oplus B_1$ mode is asymmetrical, which is likely due to the splitting of this mode. This mode is degenerate in PbTiO_3 single crystals, but this degeneracy is obviously broken. This is the reason why we used two peaks in the fit of the $E\oplus B_1$ mode of the sample A. In the case of other samples this asymmetry was not so clear, and this peak was fit with one Gaussian peak. Similar observations have also been found from bulk ceramics [52–54], where the peaks were often more clearly split into two parts (particularly the peaks corresponding to the $E(\text{1TO})$ and the $E\oplus B_1$ mode at low temperatures). Further, the existence of $A_1(\text{1TO})$ mode indicates that the films contain both tetragonal and trigonal phases. This mode at around 135 cm^{-1} does not appear in pure trigonal samples. Also, the shoulder of the $E\oplus B_1$ mode at around 330 cm^{-1} disappears from the samples containing only trigonal phase. It is interesting to note, that the peaks at around 750 cm^{-1} have practically vanished, although their intensity in the bulk ceramics is roughly half of the intensity of the band centered around 550 cm^{-1} .

Thus, Raman spectroscopy gives information from the two phase coexistence, which is not always easily extractable by X-ray diffraction technique [56,58,59]. This is the case when the tetragonal axis ratio c/a is close to 1, and the detailed phase analysis by X-ray diffraction necessitates rather tedious calculations. On the contrary, the existence of both phases is seen by inspection from the Raman spectrum.

The main differences in the Raman spectra between trigonal and tetragonal phases are in the low- and high-frequency regions. The transverse modes $A_1(1TO)$ and $E(1TO)$ from the lowest T_{1u} representation correspond to the soft modes. However, the soft modes are missing in the Raman spectrum from the trigonal $R3m$ phase. Soft modes have been found in the low-temperature trigonal $R3c$ phase [60] and their frequency decreases with increasing temperature, approaching the zero frequency at the transition temperature to the $R3m$ phase. The splitting of the peak at about 550 cm^{-1} in the trigonal phase into the $E(3TO)$ and $A_1(3TO)$ peaks at about 500 and 600 cm^{-1} , respectively, in the tetragonal phase is the other clear difference in the Raman spectra between trigonal and tetragonal phases. This is seen from the Raman spectrum of sample A in Fig. 5.7 and is indicated by small arrows.

5.7 Electrical Properties of PNZT Films

5.7.1 Permittivity and spontaneous polarization

The dielectric properties of PZT thin films are typically found to be somewhat moderate as compared with the properties of bulk ceramics. Values of the dielectric constant and the remanent polarization of thin films are lower, and dielectric losses are higher. However, high values of the breakdown field have been obtained in thin-film capacitor structures. The dielectric constant and the loss angle of PNZT thin films as a function of the film thickness on both MgO and silicon substrates are shown in Fig. 5.8. In the case of the MgO substrate, the relative dielectric constant increases nearly linearly from 440 to 560 with increasing film thickness. A similar behavior was found also in PZT thin films fabricated with the sol-gel spin-coating and organo-metallic decomposition techniques [61]. Different mechanisms, including the formation of an interfacial layer with a high defect concentration between the electrode and the PZT film, Schottky-barrier formation, differences in the grain size and film density, and the presence of mechanical stresses, have been proposed to be responsible for this behavior [61,62]. As described later in Section 5.7.3, the dielectric constant decreased with increasing compressive stress in PNZT films on the MgO substrate. However, in the films deposited on the silicon substrate, much lower values of the relative dielectric constant between 100 and 200 were obtained, and no clear dependence of the values on the film thickness was found.

According to the results in Fig. 5.8, loss-angle values of about 0.09 and 0.03, with simultaneous impedance values of 2 and 25 $M\Omega$, were measured in the films on the MgO and silicon substrates, respectively. Typical hysteresis loops for the polarization of films in the Pt/PNZT/Pt capacitor structures on both substrate materials are shown in Fig. 5.9. A remanent polarization of $18\text{ }\mu\text{C}/\text{cm}^2$ and a coercive field of about $100\text{ kV}/\text{cm}$ were found in the films on the MgO substrate. In addition, it was found that the value of the coercive field depended also on the

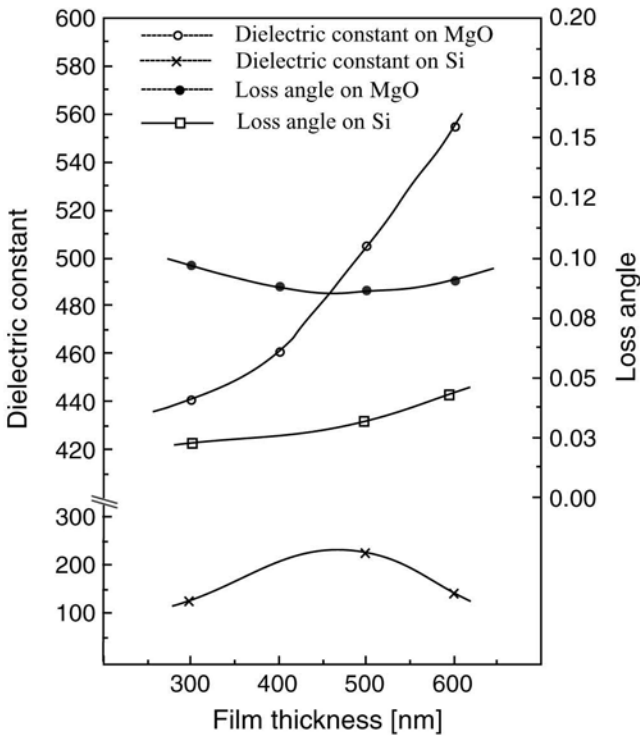


Fig. 5.8. Relative dielectric constant and loss angle measured from PNZT thin films on silicon and MgO substrates as a function of the film thickness (reprinted from Ref. 66 with permission from AIP)

compressive stress in the PNZT film. For films on the silicon substrate, a narrow hysteresis loop with a modest remanent polarization of $3 \mu\text{C}/\text{cm}^2$ and a coercive field of about $100 \text{ kV}/\text{cm}$ were measured. So far, all the results given to the dielectric properties of PNZT films on the silicon substrate were measured from films with a good morphology and uniform structure.

The dielectric constant of PNZT films was also measured as a function of temperature. A Pt/PNZT/Pt structure with a film thickness of 500 nm was fabricated on the silicon substrate, and measurements were carried out at the frequencies of 1 kHz and 10 kHz . The transition from the ferroelectric tetragonal phase to the paraelectric cubic phase was found to appear in a narrow temperature range, and the Curie temperature was found to be about 360°C .

Dielectric losses $\tan\delta$ as a function of frequency were also measured for the Pt/PNZT/Pt capacitor structures on both MgO and silicon substrates with various film thicknesses. At low frequencies, all samples had quite low $\tan\delta$ values below 0.06 . For films on the MgO substrate, the increase of the relative dielectric constant

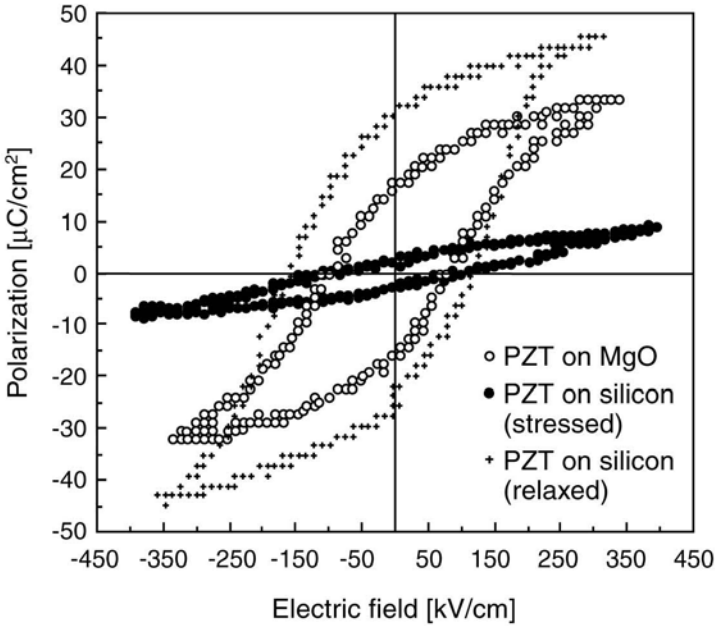


Fig. 5.9. Polarization vs. electric field hysteresis loops of the Pt/PNZT/Pt capacitor structures on MgO and silicon substrates. In the case of the silicon substrate, hysteresis loops measured from both stressed and relaxed PNZT films are shown (reprinted from Ref. 66 with permission from AIP)

ϵ_r with increasing film thickness (Fig. 5.8) is also shown in the behavior of $\tan\delta$ with increasing frequency: the value of $\tan\delta$ increased from about 0.06 to 0.3 with increasing film thickness at the frequency of 10^6 Hz. On the other hand, a typical behavior of $\tan\delta$ with frequency for stressed PNZT films with a high resistivity on the silicon substrate was similar to that of a 300 nm thick film on the MgO substrate, where the loss angle was almost constant with the frequency up to 10^6 Hz.

5.7.2 Electronic conduction

The pure ferroelectric $\text{Pb}(\text{Zr}_x\text{Ti}_{1-x})\text{O}_3$ bulk ceramics with compositions near to the MPB ($x \approx 0.53$) show p-type electronic conductivity due to nonstoichiometry. High values of conductivity impair the dielectric and piezoelectric properties of the ceramics. The poling process becomes difficult and PZT samples with high conductivity have rounded sluggish hysteresis loops due to the space-charge response out of phase relative to the alternating external electric field [62]. Also, high dielectric losses and overheating of samples even at low frequencies are typical problems in PZT ceramics with high extrinsic conductivity. However, the substitution of trivalent lanthanide ions like La^{3+} and Nd^{3+} for Pb^{2+} sites tends to de-

crease the p-type conductivity by incorporating excess electrons and thus compensating the effect of holes.

The current response of the Pt/PNZT/Pt structure to the external electric field possesses a typical behavior of a metal-insulator-metal (MIM) capacitor. The time dependence of the current in Pt/PZT/Pt structures can be divided into three different regions. After the introduction of an electric field, a fast-decaying charging current of the capacitor begins to flow. Next, a stabilized long-term leakage current is observed. Finally, after about 100 hours, an electrical degradation of the PZT thin film leads to a strong increase in the leakage current, causing a destructive breakdown [63]. An understanding of the conduction mechanism during the stabilized long-term leakage current gives useful information, not only about the PZT film itself, but also about the properties of the interfaces between the electrodes and the film.

At low electric fields, PZT films exhibit an ohmic (linear) conduction with resistivity values from 10^8 to 10^{13} Ωcm depending on the structure and defects of the film and also on the substrate and the electrode material and structure. The nonlinear behavior of the leakage current at electric fields exceeding about 50 kV/cm may relate to space-charge-limited current (SCLC), ionic conduction, Poole-Frenkel emission, Schottky-barrier emission or tunneling. In the case of the SCLC process, the carriers injected from the electrode form a quite freely moving space charge due to the reduced conductivity of the insulator. The trap states inside the dielectric decrease the conductivity; thus, the SCLC conduction is bulk controlled and also dependent on temperature. Ionic conduction takes place typically at elevated temperatures only due to a high activation energy ($\sim 1\text{--}3$ eV) needed for the ions or vacancies to move through the crystal structure. In the case of a high field across a thin insulating film, Schottky emission of electrons may occur from the metal-cathode contact into the conduction band of the insulator (or, in the case of hole injection, from the valence band of the insulator into the metal cathode).

Characteristic leakage currents as a function of voltage for the Pt/PNZT/Pt capacitor structures on both MgO and silicon substrates are shown in Fig. 5.10. From the linear parts of the curves in Fig. 5.10, low-field resistivity values ρ of 2.18×10^{11} and 2.97×10^{12} Ωcm were obtained for the films on the MgO and silicon substrates, respectively. For the film on the MgO substrate, the current-voltage curve in Fig. 5.10 is quite symmetric, but for the film on the silicon substrate, an asymmetric current response is seen. This asymmetry is assumed to relate to differences in the hole emission at the bottom and top interfaces between the Pt electrode and PNZT film [64]. At positive voltages seen in Fig. 5.10 the bottom electrode is the cathode. This electrode interface was annealed during the heat treatment of the PNZT film. On the other hand, the top Pt/PNZT interface had not been annealed after the room temperature processing. This electrode is the cathode at the negative voltage values in Fig. 5.10. As described in Ref. 64, oxygen vacancies V_o^{2+} become mobile at elevated annealing temperatures and drift to the bottom PNZT/Pt interface to compensate the contact potential and cause a band bending and possible hole accumulation (ohmic contact) at the heat-treated PNZT/Pt contact.

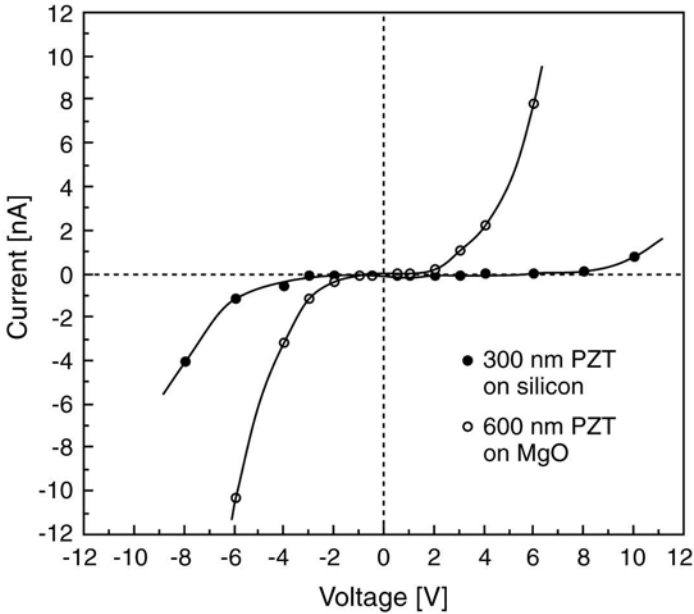


Fig. 5.10. Current-voltage characteristics measured at room temperature from a 300 nm thick PNZT film in the Pt/PNZT/Pt structure on the silicon substrate and from a similar structure with a 600 nm thick film on the MgO substrate (reprinted from Ref. 66 with permission from AIP)

Conversely, at the top Pt-electrode contact without any heat treatment there is no band bending because of the lack of positive donors and holes for the compensation of the contact potential. This asymmetric contact structure is assumed to be the reason for the asymmetry in the current response to applied voltage in Fig. 5.10. An ohmic linear current response is seen at low voltages.

It was also found from the leakage-current measurements in the uniformly stressed PNZT thin films on the MgO substrate that the current density at a constant external electric field increased with increasing film thickness. For example, an increase of the current density from 22 to 9820 nA/cm² was found with increasing film thickness from 350 to 600 nm at an electric field of 100 kV/cm [65]. This result is an indication of a bulk-limited conduction mechanism, e.g., the Poole-Frenkel conduction. On the other hand, the asymmetry found in the current-voltage characteristics of the Pt/PNZT/Pt capacitor structures, especially on the silicon substrate, should be interpreted as evidence of an electrode-interface-controlled conduction mechanism, such as the Schottky-emission conduction.

The leakage-current density as a function of applied electric field was measured at 295, 323, and 423 K for various PNZT films deposited on both silicon and MgO substrates. From the measurements at elevated temperatures, it was possible to deduce that the Poole-Frenkel conduction is most probably the mechanism responsi-

ble for the leakage currents in the PNZT films at electric fields below 150 kV/cm [65,66]. Assuming the Poole-Frenkel emission mechanism for the long-term leakage conduction, the activation energies of conductivity were calculated to be between 0.15 and 0.18 eV. These values are in agreement with the estimates in Ref. 67 for the binding energies of the Pb^{3+} hole traps in PZT ceramics. Two Raman peaks at around 1200 and 1500 cm^{-1} (quantum energies about 0.15 and 0.18 eV, respectively) appeared in the Raman spectra from different PNZT samples at exposure with 3.41 eV UV quanta and were related to the trap energies of the Pb^{3+} hole traps in Ref. 68. The present conduction results are also in good agreement with the results of Wouters et al. [64].

Both the results for the current-voltage characteristics in Fig. 5.10 and the results from the leakage-current measurements at elevated temperatures support the conclusion that under low-field conditions below 150 kV/cm, the leakage conduction in PNZT thin films occurs through the Poole-Frenkel mechanism due to the hopping of holes between Pb^{3+} hole traps with activation energies between 0.15 and 0.18 eV. Although the experimentally obtained results at electric fields above 150 kV/cm suggests Schottky-emission conduction, assuming an abrupt change in the conduction mechanism may be unrealistic. However, external electric fields below 150 kV/cm are the most important from the application point of view.

5.7.3 Role of macroscopic residual stresses

In the multilayer capacitor structure, electrical properties of the PNZT thin film are also affected by the substrate material and processing conditions during the fabrication steps. Especially, the thermal stresses originating from unequal thermal expansion coefficients of the substrate and film during a heat treatment above 500°C can lead to a formation of hillocks or cracks, respectively, when high compressive or tensile stresses appear. Stresses in thin films are usually considered to be biaxial, acting only in the plane of the film and being relaxed in the direction perpendicular to the substrate surface. For instance, in the case of the silicon substrate both in sputtered platinum electrodes and in PNZT films deposited by the sol-gel technique, stresses were found to be tensile with values on the order of 1 GPa and 100 MPa, respectively [69]. Typically, the remanent polarization decreases and the Curie temperature increases with increasing stress. Furthermore, some electrical properties like the low-field dielectric constant, loss angle and remanent polarization have been reported to vary with the film thickness [62].

The origin of stresses in a thin film is related, in addition to the thermal expansion, to structural changes in the film during the growth and annealing processes and to the interactions between the film and the substrate or some other underlying layer. The stress can be divided into three different groups according to the phenomena causing the stress. Extrinsic stress is generated during the film-growth process and is strongly dependent on the deposition parameters. Intrinsic stress arises from dimensional changes in the film caused by densification, crystallization, and phase transformations during the heat-treatment procedure. Finally, thermal stresses are produced during a heat-treatment procedure due to unequal

thermal expansions of the film and the substrate [70]. In the case study, the Nd-modified PZT films were deposited at room temperature and were amorphous after deposition. Moreover, the films were post annealed in order to achieve the desired crystal structure. Therefore, the total macroscopic stress in the films can be considered to be a sum of the intrinsic and thermal stresses.

As already discussed, the post-annealed PNZT thin films grown with the pulsed-laser-deposition technique are typically under a macroscopic residual stress due to different thermal processing steps. The (413) lattice planes of the tetragonal crystal structure with a diffraction peak at around $2\theta = 148^\circ$ in the case of $\text{CuK}\alpha_1$ radiation were used for the stress analysis of the PNZT films [66]. The XRD patterns were measured at the tilt angles of 0° , 30° , 45° , and 60° from both PNZT/Pt/MgO and PNZT/Pt/SiO₂/Si structures with various PNZT film thicknesses. An increase in the Bragg angle 2θ with increasing tilt angle, means a decrease in the distance d_{413} between the (413) planes, and is an indication of a compressive stress in PNZT films on the MgO substrate. An opposite behavior in films on the silicon substrate indicates a tensile stress. By applying Hooke's law, the macroscopic stress in the films was calculated. In the PNZT thin films deposited on the MgO substrate, the compressive stress was found to vary between 352 and 226 MPa with increasing film thickness as shown in Fig. 5.11. Although the dependence is not unambiguous, the stress clearly decreases with increasing film thickness. For PNZT films on the silicon substrate, tensile stresses of 415 and 405 MPa were measured with film thicknesses of 400 and 500 nm, respectively. Thus, the stress is assumed to decrease with increasing film thickness in the PNZT films on the silicon substrate as well [66].

On the other hand, it was found from the X-ray-diffraction results that in the PNZT films on the MgO substrate, the relaxation of the compressive stress favors the formation of ferroelectric tetragonal structure with the c -axis perpendicular to the film surface. In the case of the silicon substrate, the PNZT thin film is under a tensile stress, which favors the formation of tetragonal structure with the c -axis parallel to the film surface [66]. Then, the external electric field in the capacitor structure is mainly in the ab -plane of the tetragonal crystal structure and the polarization by the movement of both A - and B -site cations in the direction of the ferroelectric polarization (c -axis) is prohibited. This leads to moderate values for the permittivity and remanent polarization as shown in Fig. 5.9. Especially, in the PNZT films on the silicon substrate, a relaxation of stress due to cracking of the film or increasing the film thickness seems to release the crystal structure for a more effective polarization under an external electric field. For instance, the relative dielectric constant increased from around 100 to 530 and the remanent polarization, respectively, from 3 to 25 $\mu\text{C}/\text{cm}^2$ after a stress relaxation, as shown in Fig. 5.9.

In the case of compressive macroscopic stress, the directions of the c -axis and external electric field are the same, which makes the polarization through movement of A - and B -site cations easy in the Pt/PNZT/Pt capacitor structures on the MgO substrate. The effects of stress on the polarization and other dielectric properties are much lower in the films on the MgO substrate as compared to the effects

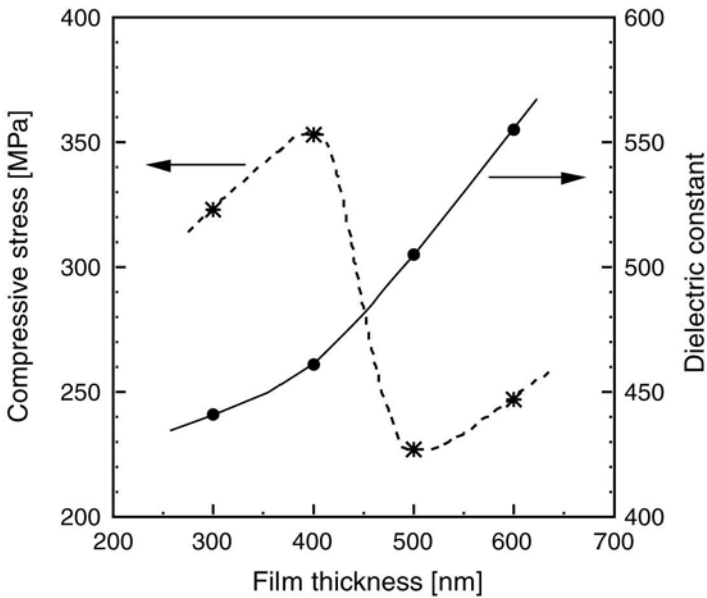


Fig. 5.11. Compressive stress and relative dielectric constant as a function of film thickness measured from PNZT films on the MgO substrate (reprinted from Ref. 66 with permission from AIP)

in films on the silicon substrate. However, the relative dielectric constant of films on the MgO substrate increased quite linearly from 440 to 560 with increasing film thickness and with decreasing compressive stress, respectively. It was also found that the value of the coercive field increased from 80 to 150 kV/cm with increasing compressive stress in the Pt/PNZT/Pt capacitor structures on the MgO substrate [66].

Also, the leakage current was found to change drastically with changes in the stress state in PNZT thin films. A strong decrease in the leakage current was found as a result of stress in PNZT films in the Pt/PNZT/Pt capacitors on the silicon substrate. In the case of a PNZT film with a thickness of 300 nm and tensile stress of about 400 MPa, very low values of the leakage current below 50 pA, up to electric fields of 120 kV/cm, were found. The relative dielectric constant ϵ_r in these capacitor films with a high tensile stress was typically between 100 and 200 together with a $\tan\delta$ value of about 0.03 for the dielectric losses and a modest remanent polarization $P_r < 5 \mu\text{C}/\text{cm}^2$. The current-voltage characteristics were also measured from a capacitor structure fabricated near a crack in the same PNZT film (the film was annealed with a higher temperature gradient of 100°C/h). In this case, the stress was relaxed in the film due to cracking. The leakage currents in this capacitor were about three orders of magnitude higher. The resistivity ρ calculated from the linear part of the current-voltage characteristics at low electric fields for this capacitor structure was found to be $3.6 \times 10^8 \Omega\text{cm}$ [65]. As mentioned before,

stressed PNZT films on the silicon substrate favor an orientation with the c -axis parallel to the film surface. As a result, the external electric field in the capacitor structure is mainly in the ab -plane of the tetragonal crystal structure; also, the polarization by the movement of both A - and B -site cations in the direction of the c -axis is prohibited causing the moderate values of the dielectric constant. However, the stress relaxation of the PNZT film had such drastic effects on the leakage current that the possibility of a different conduction mechanism was also studied. Other possible conduction mechanisms include the Schottky emission and the SCLC where the existence of space charge originates from the trapping of charge carriers at possible shallow traps in the PNZT film generated by the relaxation process [71]. Dielectric-loss measurements gave some support for the SCLC mechanism [66]. Stress-induced leakage current has been found also in ultra-thin SiO_2 layers in metal-oxide-semiconductor (MOS) capacitor structure on silicon single crystal [72].

5.8 Summary

Pulsed-laser deposition was found to be a versatile method for the fabrication of modified PZT thin films for different applications. It makes possible a congruent deposition of complex target materials like modified PZTs on different substrates with good stoichiometry.

Ferroelectric Nd-modified $\text{Pb}(\text{Zr}_x\text{Ti}_{1-x})\text{O}_3$ thin films have been used as a case study to consider laser-assisted growth and characterization of multicomponent lead-zirconate-titanate films. The film growth was based on pulsed-laser deposition on various single-crystal substrates including sapphire, MgO , and silicon; the films were grown into the form of single layer PNZT thin films and multilayer capacitor structures with platinum electrodes. The deposition was done from sintered ceramic targets with a nominal composition of $\text{Pb}_{0.97}\text{Nd}_{0.02}(\text{Zr}_{0.55}\text{Ti}_{0.45})\text{O}_3$ for the ferroelectric films and from a polished platinum disk for the electrode layers using a pulsed XeCl excimer laser with a wavelength of 308 nm and 20 ns pulse duration. Especially, the discussion concentrated on the properties of post-annealed thin films, which were deposited at room temperature.

EDS analyses revealed that the atomic lead content $\text{Pb}/(\text{Zr}+\text{Ti})$ in amorphous as-grown PNZT films was about 4.0 after ablation with low laser-beam fluences, but decreased rapidly with increasing laser-beam fluence and reached nearly stoichiometric composition of the target at the laser-beam fluence of 0.7 J/cm^2 . Atomic lead content of the post-annealed PNZT films varied also as a function of the annealing temperature, whereas the atomic zirconium content $\text{Zr}/(\text{Zr}+\text{Ti})$ was found to be quite insensitive to the annealing temperature, but it increased linearly as a function of laser-beam fluence. Using this dependence of the zirconium content, it was possible to control the crystal structure of the PNZT film between tetragonal and rhombohedral phases by adjusting the laser-beam fluence on the target surface properly.

XRD and EDS studies revealed that new oxide compounds (TiO_2 and ZrO_2) were formed on the surface layer of the target during the ablation process as a result of changes in the chemical surface composition caused by differences in the evaporation rates of the elements. New compounds and structures cause a shielding effect, which makes it possible to form regular laser-cone structure in the case of the local ablation process. Raman measurements together with XRD results from the ablated targets revealed that the topmost layer of the target surface was amorphous.

The different nature of X-ray diffraction and Raman scattering was discussed. It was found that X-ray diffraction results were inadequate for a proper interpretation of the two-phase (tetragonal and trigonal) coexistence in the films. Measured Raman spectra gave useful information about the two-phase coexistence in the films. For instance, it was found that the $A_1(\text{ITO})$ mode peak at about 140 cm^{-1} in PNZT films was the most sensitive indication of the presence of the tetragonal phase in the film. Also, some common examples of the various sources for light scattering in PNZT samples were given.

Electrical properties of the PNZT thin films were studied by fabricating multi-layer capacitor structures of ferroelectric films with platinum electrodes using pulsed-laser deposition and post-annealing techniques on MgO and oxidized silicon substrates. The relative dielectric constant of the PNZT films on the MgO substrate was found to increase linearly from 440 to 560 with increasing film thickness. The remanent polarization was around $18\text{ }\mu\text{C}/\text{cm}^2$ and the coercive field between 75 and 150 kV/cm. The smooth, uniform PNZT films on the silicon substrate had dielectric constants between 100 and 200 and remanent polarization around $3\text{ }\mu\text{C}/\text{cm}^2$. However, when the tensile stress of the film was relaxed by cracking, values of 530 and $25\text{ }\mu\text{C}/\text{cm}^2$ were measured for the relative dielectric constant and the remanent polarization, respectively. In order to determine the corresponding conduction mechanism for the leakage current, the current-voltage characteristics were measured at several temperatures. At higher temperatures, the Poole-Frenkel type conduction mechanism was observed with activation energies between 0.15 and 0.18 eV. The low-field resistivity of these films varied between 2.2×10^{11} and $2.9 \times 10^{12}\text{ }\Omega\text{cm}$.

The state of macroscopic stress in PNZT thin films due to the fabrication process was also discussed on the basis of X-ray-diffraction measurements. In PNZT films deposited on the MgO substrate, compressive stresses between 226 and 352 MPa were measured. In films on the silicon substrate, tensile stresses of about 400 MPa were found. The stress in the films decreased with increasing thickness and the leakage current also increased with increasing film thickness. The dielectric constant was found to depend inversely on the mechanical stress in the PNZT films. The coercive field also increased with increasing mechanical stress. Thus, the mechanical stress induced by different fabrication steps was found to have a strong effect on the dielectric properties of the PNZT thin films. Typically, in the uniform stressed films deposited on silicon substrates, the remanent polarization was quite modest. However, in the films on the silicon substrates where the tensile stress was relaxed due to cracking, much higher values for the remanent polariza-

tion and for the dielectric constant were measured. Furthermore, the leakage current in the Pt/PNZT/Pt-capacitor structure was found to be sensitive to the stress in the PNZT film and decreased with increasing stress. In addition, the leakage current in these capacitor structures increased by three orders of magnitude after cracking as compared to values in stressed-film capacitors without cracking, and the low-field resistivity was around $3.6 \times 10^8 \Omega\text{cm}$. According to the results of the loss-angle measurements, a possibility for the leakage current in these capacitors is the SCLC conduction mechanism.

References

1. Maiman TH (1960) Stimulated optical radiation in ruby, *Nature* 187(4736):493–494
2. Smith HM, Turner AF (1965) Vacuum deposited thin films using a ruby laser, *Applied Optics* 4(1):147–148
3. Cheung JT (1994) History and fundamentals of pulsed laser deposition. In: Chrisey DB, Huber GK (eds) *Pulsed Laser Deposition of Thin Films*, John Wiley & Sons, New York, pp 1–22
4. Jaffe B, Cook WR, Jaffe H (1971) *Piezoelectric Ceramics*, Academic Press, London, p 136
5. Ari-Gur P, Benguigui L (1974) X-ray study of the PZT solid solutions near the morphotropic phase transitions, *Solid State Commun* 15(6):1077–1079
6. Chen HM, Lee JY (1997) The temperature dependence of the transient current in ferroelectric $\text{Pb}(\text{Zr},\text{Ti}_{1-x})\text{O}_3$ thin films for memory devices applications, *J App Phys* 82(7):3478–3481
7. Sudhama C, Kim J, Khamankar R, Chikarmane V, Lee JC (1994) Thickness-scaling of sputtered PZT films in the 200 nm range for memory applications, *J Elec Mater* 23(12):1261–1268
8. Lappalainen J, Frantti J, Moilanen H, Leppävuori S (1995) Excimer laser ablation of PZT thin films on silicon cantilever, *Sens Actuators A* 46,47:104–109
9. Lee C, Itoh T, Suga T (1999) Self-excited piezoelectric PZT microcantilevers for dynamic SFM - with inherent sensing and actuating capabilities, *Sens Actuators A* 72:179–188
10. DeVoe DL, Pisano AP (1997) Modeling and optimal design of piezoelectric cantilever microactuators, *IEEE J Microelectromech Syst* 6(3):266–270
11. Chang CC, Tang CS (1998) An integrated pyroelectric infrared sensor with a PZT thin film, *Sens Actuators A* 65:171–174
12. Lin H, Wu NJ, Geiger F, Xie K, Ignatiev A (1996) A ferroelectric-superconducting photodetector, *J Appl Phys* 80(12):7130–7133
13. Shih WC, Wu MU (1998) Theoretical investigations of the SAW properties of ferroelectric film composite structures, *IEEE Trans Ultrason, Ferroelect, Freq Contr* 45(2):305–316
14. Meyer-Arendt JR (1989) *Introduction to Classical and Modern Optics*, Prentice-Hall, New Jersey, p 317
15. Potter Jr BG, Sinclair MB, Dimos D, Tuttle BA, Schwartz RW (1994) Electro-optical and optical evaluation of $\text{Pb}(\text{Zr},\text{Ti})\text{O}_3$ thin films using waveguide refractometry, *J Non Cryst Solids* 178:69–76

16. Peng CH, Chang JF, Desu SB (1992) Optical properties of PZT, PLZT, and PNZT thin films, *Mat Res Soc Symp Proc* 243:21–26
17. Leuchtner RE, Horwitz JS, Chrisey DB (1992) Dynamics of laser ablation and vaporization of $\text{PbZr}_{0.54}\text{Ti}_{0.46}\text{O}_3$: Laser fluence and ambient gas effects, *Mat Res Soc Symp Proc* 243:525–530
18. Haglund Jr RF, Itoh N (1994) Electronic processes in laser ablation of semiconductors and insulators. In: Miller JC (ed) *Laser Ablation*, Springer-Verlag, Berlin, pp 11–52
19. Tokarev VN, Lunney JG, Marine W, Sentis M (1995) Analytical thermal model of ultraviolet laser ablation with single-photon absorption in the plume, *J Appl Phys* 78(2):1241–1246
20. Ohring M (1992) *The Materials Science of Thin Films*, Academic Press, San Diego, p 599
21. Kelly R (1990) On the dual role of the Knudsen layer and unsteady, adiabatic expansion in pulse sputtering phenomena, *J Chem Phys* 92(8):5047–5056
22. Singh RK, Holland OW, Narayan J (1990) Theoretical model for deposition of superconducting thin films using pulsed laser evaporation technique, *J Appl Phys* 68(1):233–247
23. Leuchtner RE, Grabowski KS (1994) Ferroelectrics. In: Chrisey DB, Huber GK (eds) *Pulsed Laser Deposition of Thin Films*, John Wiley & Sons, New York, pp 473–508
24. Kwok CK, Desu SB (1992) Pyrochlore to perovskite phase transformation in sol-gel derived lead-zirconate-titanate thin films, *Appl Phys Lett* 60(12):1430–1432
25. Tseng TF, Yang RP, Liu KS (1997) Ferroelectric properties of $(\text{Pb}_{0.97}\text{La}_{0.03})(\text{Zr}_{0.66}\text{Ti}_{0.34})_{0.9875}\text{O}_3$ films deposited on Si_3N_4 -coated Si substrates by pulsed laser deposition process, *Appl Phys Lett* 70(1):46–48
26. Miller MH (1967) Stress measurement in metals. In: Kaelble EF (ed) *Handbook of X-rays*, McGraw-Hill, New York, p 19-1
27. Carrano J, Sudhama C, Chikarmane V, Lee J, Tasch A, Shepherd W, Abt N (1991) Electrical and reliability properties of PZT thin films for ULSI DRAM applications, *IEEE Trans Ultrason, Ferroelect, Freq Contr* 38(6):690–703
28. Saenger KL, Roy RA, Etzold KF, Cuomo JJ (1990) Lead zirconate titanate films produced by pulsed laser deposition, *Mat Res Soc Symp Proc* 200:115–120
29. Lappalainen J, Frantti J, Lantto V (1999) Surface structure and particulate generation in $\text{Pb}_{0.97}\text{Nd}_{0.02}(\text{Zr}_{0.55}\text{Ti}_{0.45})\text{O}_3$ ablation targets during pulsed laser deposition, *J Am Ceram Soc* 82:889–896
30. Lappalainen J, Lantto V (2000) Composition and phase structure in laser deposited and post-annealed $\text{Pb}_{1-3y/2}\text{Nd}_y(\text{Zr}_x\text{Ti}_{1-x})\text{O}_3$ thin films, *Appl Surf Sci* 154,155:118–122
31. Frantti J, Lantto V, Lappalainen J (1996) Symmetry consideration of Raman modes in Nd-doped lead zirconate titanate thin films for structure characterization, *J Appl Phys* 79(2):1065–1072
32. Levin EM, Robbins CR, McMurdie HF (1964) *Phase Diagrams for Ceramists*, The American Ceramic Society, Ohio, p 143
33. Bhattacharya EK, Mallick KK, Hartridge A, Woodhead JL (1996) Sol-gel preparation, structure and thermal stability of crystalline zirconium titanate microspheres, *J Mater Sci* 31:267–271
34. Powder Diffraction File no 17-923, *Inorganic Phases*, JCPDS International Centre for Diffraction Data (1995)
35. Wu JC, Chung CS, Ay CL, Wang I (1984) Nonoxidative dehydrogenation of ethylbenzene over $\text{TiO}_2\text{-ZrO}_2$ catalysts, *J Catal* 87:98–107

36. Warren BE (1969) X-ray Diffraction, Addison-Wesley, Reading, pp 251–254
37. Frantti J, Lantto V (1997) Structural studies of Nd-modified lead zirconate titanate ceramics between 11 and 680 K at the morphotropic phase boundary, *Phys Rev B* 56(1):221–236
38. Krebs A, Condrate Sr RA (1988) A Raman spectral characterization of various crystalline mixtures in the ZrO_2 - TiO_2 and HfO_2 - TiO_2 systems, *J Mater Sci Lett* 7:1327–1330
39. Venkatesan T (1994) Pulsed-laser deposition of high-temperature superconducting thin films. In: Miller JC (ed) *Laser Ablation*, Springer-Verlag, Berlin, pp 85–106
40. Cheung JT, Sankur H (1988) Growth of thin films by laser-induced evaporation, *CRC Crit Rev Solid State Mater Sci* 15(1):63–109
41. Singh K, Bhattacharya D, Narayan J (1990) Subsurface heating effects during pulsed laser evaporation of materials, *Appl Phys Lett* 57(19): 2022–2024
42. Kelly R, Miotello A (1994) Mechanisms of pulsed laser sputtering. In: Chrisey DB, Huber GK (eds) *Pulsed Laser Deposition of Thin Films*, John Wiley & Sons, New York, pp 55–87
43. Foltyn SR (1994) Surface modification of materials by cumulative laser irradiation. In: Chrisey DB, Huber GK (eds) *Pulsed Laser Deposition of Thin Films*, John Wiley & Sons, New York, pp 89–113
44. Loudon R (1964) The Raman effect in crystals, *Advan Phys* 13:423–482
45. Long DA (1977) *Raman Spectroscopy*, McGraw-Hill, London, pp 32–35
46. Humpreys LB (1972) Ionic Raman effect. III. First- and second-order ionic Raman effects, *Phys Rev B* 6:3886–3897
47. Yu PY, Cardona M (1996) *Fundamentals of Semiconductors*, Springer-Verlag, Berlin, pp 379–385
48. Klingshirn CF (1995) *Semiconductor Optics*, Springer-Verlag, Berlin, pp 181–185
49. Burns G, Scott BA (1970) Raman spectra of polycrystalline solids; application to the $PbTi_{1-x}Zr_xO_3$ system, *Phys Rev Lett* 25:1191–1194
50. Burns G, Scott BA (1973) Lattice modes in ferroelectric perovskites: $PbTiO_3$, *Phys Rev B* 7:3088–3101
51. Uwe H, Lyons KB, Carter HL, Fleury PA (1986) Ferroelectric microregions and Raman scattering in $KTaO_3$, *Phys Rev B* 33:6436–6440
52. Frantti J, Lantto V (1997) Structural studies of Nd-modified lead zirconate titanate ceramics between 11 and 680 K at the morphotropic phase boundary, *Phys Rev B* 56:221–236
53. Frantti J, Lantto V, Nishio S, Kakihana M (1999) Effect of A- and B-cation substitution on the phase stability of $PbTiO_3$ ceramics, *Phys Rev B* 59:12–15
54. Frantti J, Lappalainen J, Lantto V, Nishio S, Kakihana M (1999) Low-temperature Raman studies of $Pb(Zr_xTi_{1-x})O_3$ and $Pb_{1-3y/2}Nd_yTiO_3$ ceramics, *Jpn J Appl Phys* 38:5679–5682
55. Fontana MD, Idrissi H, Kugel GE, Wojcik K (1991) Raman spectrum in $PbTiO_3$ re-examined: Dynamics of the soft phonon and the central peak, *J Condens Matter* 3:8695–8705
56. Frantti J, Lappalainen J, Lantto V (1996) Symmetry consideration of Raman modes in Nd-doped lead zirconate titanate thin films for structure characterization, *J Appl Phys* 79:1065–1072
57. Frantti J, Lantto V (1996) Raman studies between 11 and 300 K of the effects of Nd additive in ferroelectric lead-titanate ceramics, *Phys Rev B* 54:12139–12150

58. Frantti J, Lantto V (1994) Characterization of $\text{Pb}_{0.97}\text{Nd}_{0.02}(\text{Zr}_{0.55}\text{Ti}_{0.45})\text{O}_3$ thin films prepared by pulsed laser ablation, *J Appl Phys* 76:2139–2143
59. Frantti J, Lantto V, Lappalainen J (1996) Group-theoretical consideration of Raman modes in Nd-doped PZT thin films for structure characterization, *Ferroelectrics* 184:69–78
60. Bäuerle D, Pinczuk A (1976) Low frequency vibrational modes and the phase transition of rhombohedral $\text{PbTi}_{1-x}\text{Zr}_x\text{O}_3$, *Solid State Commun* 19:1169–1171
61. Lee JJ, Thio CL, Desu SB (1995) Electrode contacts on ferroelectric $\text{Pb}(\text{Zr}_x\text{Ti}_{1-x})\text{O}_3$ and $\text{SrBi}_2\text{Ta}_2\text{O}_9$ thin films and their influence on fatigue properties, *J Appl Phys* 78(8):5073–5078
62. Udayakumar KR, Schuele PJ, Chen J, Krupanidhi SB, Cross LE (1995) Thickness-dependent electric characteristics of lead zirconate titanate thin films, *J Appl Phys* 77(8):3981–3986
63. Al-Shareef HN, Dimos D (1997) Leakage and reliability characteristics of lead zirconate titanate thin-film capacitors, *J Am Ceram Soc* 80(12):3127–3132
64. Wouters DJ, Willems GJ, Maes HE (1995) Electrical conductivity in ferroelectric thin films, *Microelectron Eng* 29:249–256
65. Lappalainen J, Lantto V (1999) Extrinsic conductivity in ferroelectric PZT film capacitors made by laser ablation deposition, *Phys Scr* T79:220–224
66. Lappalainen J, Frantti J, Lantto V (1997) Electrical and mechanical properties of ferroelectric thin films laser ablated from $\text{Pb}_{0.97}\text{Nd}_{0.02}(\text{Zr}_{0.55}\text{Ti}_{0.45})\text{O}_3$ target, *J Appl Phys* 82:3469–3477
67. Robertson J, Warren WL, Tuttle BA (1995) Band states and shallow hole traps in $\text{Pb}(\text{Zr}, \text{Ti})\text{O}_3$ ferroelectrics, *J Appl Phys* 77(8):3975–3980
68. Frantti J, Lantto V, Kakihana M (1998) Raman scattering studies of $\text{Pb}(\text{Zr}_x\text{Ti}_{1-x})\text{O}_3$ and $\text{Pb}_{1-3y/2}\text{Nd}_y(\text{Zr}_x\text{Ti}_{1-x})\text{O}_3$ ceramics with uv and visible laser lights, *Jpn J Appl Phys* 37(9B):5406–5409
69. Spierings GA, Dormans GJ, Moors WG, Ulenaers MJ, Larsen PK (1995) Stresses in $\text{Pt}/\text{Pb}(\text{Zr}, \text{Ti})\text{O}_3/\text{Pt}$ thin-film stacks for integrated ferroelectric capacitors, *J Appl Phys* 78(3):1926–1933
70. Desu SB (1993) Influence of stresses on the properties of ferroelectric BaTiO_3 thin films, *J Electrochem Soc* 140(10):2981–2987
71. Lamb DR (1967) *Electrical Conduction Mechanism in Thin Insulating Films*, Methuen and Co Ltd, London, p 74
72. Chou AI, Lai K, Kumar K, Chowdhury P, Lee JC (1997) Modeling of stress-induced leakage current in ultrathin oxides with the trap-assisted tunneling mechanism, *Appl Phys Lett* 70(25):3407–3409

6 Silicon Carbide Crystals — Part I: Growth and Characterization

G. Dhanaraj¹, X.R. Huang¹, M. Dudley¹, V. Prasad³, and R.-H. Ma²

Center for Crystal Growth Research, ¹Department of Materials Science and Engineering, ²Department of Mechanical Engineering, State University of New York at Stony Brook, Stony Brook, NY 11794-2200

³College of Engineering, Florida International University, Miami, FL 33174

6.1 Introduction

Silicon carbide (SiC), one of the oldest known semiconductor materials, has received special attention in recent years because of its suitability for electronic and optoelectronic devices operating under high temperature, high power, high frequency, and/or strong radiation conditions, where the conventional semiconductor materials like Si, GaAs, and InP are considered to have reached their limits. SiC exists as a family of crystal with more than 200 polytypes and a bandgap range of 2.4 to 3.3 eV. As a wide bandgap material, SiC possesses many superior properties, such as a larger operating temperature range, a high critical breakdown field (E_{cr}), high resistance to radiation and the ability to construct visible-range light-emitting devices [1]. It also distinguishes itself by a combination of high thermal conductivity (higher than that of copper), hardness second to diamond, high thermal stability, and chemical inertness. Some of the basic properties of SiC in comparison with many other semiconductor materials are presented in Table 6.1a, and the crystallographic unit cell parameters of the most common polytypes are listed in Table 6.1b. Owing to its outstanding properties, silicon carbide is expected to bring significant breakthroughs in the areas of high temperature applications, power devices, microwave devices, and LEDs. Some of the SiC-based devices and elements that have been developed thus far are listed in Table 6.2. Several review articles devoted to the growth, properties and device applications of SiC have been published in the last five years [2–6].

Table 6.1a. The basic parameters of some semiconductors [1,7]

Material	E_g eV	T_m °K	T_D °K	T_w °K	K W/[cm ·°K]	ϵ	μ_e cm ² / [V·s]	μ_h cm ² / [V·s]	$E_{cr} \times 10^5$ V/cm	$V_s \times 10^7$ cm/s
Ge	0.7	1210	374	280	0.6	16	3800	1800	1.0	0.6
Si	1.1	1690	645	410	1.35	12	1350	480	2.0	1.0
GaAs	1.43	1510	400	570	0.45	12	6000	320	2.6	1.0
BP	2.0	2300	1140	720	2.5	11	1500	300	4.0	2.0
GaP	2.2	1740	520	800	0.7	11	250	150	4.5	1.5
CdS	2.3	2020	290	840	0.2	11	350	15	10.0	1.0
3C-SiC	2.3	3100	1430	840	3–5	9.8	750	40	7	2.5
6H-SiC	3.0	3100	1200	1200	5–7	9.8	370	90	21	2.0
4H-SiC	3.2	3100	1200	—	5–7	9.8	800	115	20	2.0
GaN	3.45	1800	710	1250	1.0	9.5	400	—	14	2.2
ZnS	3.6	2200	340	1300	0.03	10	140	5	—	—
C	5.45	>3300	2230	2100	14	5.7	1800	1500	7.5	2.7
AlN	6.2	3100	1100	2100	2.0	9.1	—	—	—	1.5
BN	10.0	3300	1700	3300	3.0	7.1	—	—	—	1.5

Note: E_g — band gap; T_m — melting temperature; T_D — Debye temperature; T_w — working temperature; K — thermal conductivity; ϵ — permittivity of the semiconductor; μ_e and μ_h — electron and hole mobilities, respectively; E_{cr} : critical electric breakdown field; V_s : saturated carrier velocity

Table 6.1b. Unit cell parameters of the most commonly studied SiC polytypes [8,9]

Polytypes	a[Å]	b[Å]	c[Å]	α	β	γ
3C	4.439	4.439	4.439	90°	90°	90°
4H	3.073	3.073	10.053	90°	90°	120°
6H	3.073	3.073	15.08	90°	90°	120°
15R	12.69	12.69	12.69	13° 55'	13° 55'	13° 55'

Table 6.2. Selected SiC-based devices

Device or element type	Material	Reference
JFET	6H-SiC	(7,12)
UV photo detector	6H-SiC	(7,12)
MOSFET	6H-SiC	(7,12)
p-n-diodes	4H-SiC/6H-SiC	(7)
Vertical MOSFET	4H-SiC	(7)
Operational amplifiers IC	6H-SiC	(7)
Schottky diodes	6H-SiC	(7,10)
Blue/green LEDs	6H-SiC	(13)
MESFET	6H-SiC	(11,12)
BJT		(12)
Thyristor	4H-SiC	(11,12)
SIT		(11)
Schottky rectifier	4H/6H-SiC	(11,12)
MOSFET	15R-SiC	(14)
Sensors	3C	(15)

Note: JFET — Josephson field effect transistor; MOSFET — metal oxide field effect transistor; MESFET — metal field effect transistor; BJT — bipolar field effect transistor; SI — static induction transistor

6.1.1 Applications of SiC

High temperature applications

Current and future applications of electronic components have placed much more critical environmental requirements on semiconductors [7]. For example, high temperature electronic components and systems can play an important role in many areas, such as aircraft, spacecraft, automotive, defense equipment, power systems, and so forth. For reliable functioning of electronic devices under extreme conditions they need to withstand high temperatures. SiC appears to be a desirable candidate because of its high working temperature as well as Debye temperature. As reported by Chelnokov et al. [7], 6H-SiC is superior to Si, GaAs, GaN, and AlN for high temperature applications.

SiC can also find applications in sensors for high temperature, high pressure, and highly corrosive environments (e.g., combustion systems, gas turbines and the oil industry) [10]. For example, pressure sensors based on SiC thin layers deposited on an insulator structure have been successfully used to measure the combustion engine pressure up to 200 bar at temperatures up to 300°C [11].

High power devices. Power semiconductor devices are important for regulation and distribution of electricity. Since the efficient use of electricity depends on the performance of power rectifiers and switches, further improvements in efficiency, size, and weight of these devices are quite desirable. SiC has a high breakdown strength and therefore, it is possible to dope it at higher concentration, and still

have thinner layers for a given blocking voltage compared with the corresponding Si devices [11]. Indeed, the power losses can decrease dramatically with the use of SiC-based devices. Another desirable property of SiC for power application is its high thermal conductivity, which can facilitate the heat generated in the component to dissipate quickly. SiC power MOSFETs, diode rectifiers, and thyristors are expected to function over higher voltage and temperature ranges with superior switching characteristics. The size of these devices are expected to become significantly smaller compared to correspondingly rated Si-based devices [12]. This is due to the fact that SiC devices will not require heat dissipating components.

Although GaN and AlN are considered better than SiC in terms of several parameters [1] (see Table 6.1a), substrates of these materials are currently not available. Also, they are grown only heteroepitaxially using substrates of other materials, including SiC [1]. This leads to a very high dislocation density in the films, which limits the application of these materials for high power semiconductor devices. Moreover, high power is often coupled with high temperature where SiC is considered superior to GaN and AlN.

High frequency devices. Cellular phones, digital TV, telecommunication systems, and radars have made microwave technology an essential part of everyday life. Although some high power microwave semiconductor components have existed for a long time, such as Gunn, IMPATT, and TRAPATT diodes, these devices can only operate in parametric amplifiers, which are much more difficult to manufacture and tune. SiC-based microwave transistors are predicted to produce more efficient microwave systems and further expand their existing applications [11]. Silicon carbide SITs and MESFETs have already been developed for these applications. Indeed, silicon carbide SITs are challenging devices for high power applications up to 900 MHz. Interestingly, the first microwave MESFETs fabricated on a high resistivity 6H-SiC substrate showed a measured radio frequency gain of 8.5 dB at 10 GHz and f_{\max} of 25 GHz [12]. Further development of SiC-based microwave devices is underway.

Optoelectronic applications. The special physical and optical properties of SiC have been further exploited to fabricate bright blue and green light emitting diodes (LEDs) [13]. From manufacturing considerations there are several advantages in using SiC as a substrate material such as easier handling and cheaper processing. SiC is also being used as a substrate for the growth of GaN, an important material for LEDs. Compared to GaN growth on sapphire substrates, it is possible to obtain structurally more perfect epitaxial GaN layers on SiC due to smaller lattice mismatch and closer match of thermal expansion coefficients.

The primary requirement for SiC-based devices is the production of high quality thin films, which in turn require high quality substrates. Although serious efforts have been made on SiC growth and significant progress has been achieved, the application of SiC-based devices remains limited because of the non-availability of SiC wafers of high quality at a cheaper price.

6.1.2 Historical development of SiC crystal growth

Although SiC is considered a new entrant to the electronics industry, it is, in fact, not a newcomer to the materials world. It was first reported in 1824. SiC was recognized as a silicide of carbon in 1895 and could be synthesized successfully by the Acheson process [16] using sand and coke. The SiC-based LEDs were made as early as 1907 using small SiC crystals obtained from the cavities formed in the Acheson system. However, further research on the development of SiC as a semiconductor material was not pursued for several decades because of the difficulty of growing good quality single crystals. In 1955, Lely demonstrated the growth of SiC on a porous SiC cylinder by vapor condensation [17]. This method was further refined by Hamilton et al. [18] and Novikov et al. [19], and is commonly referred to as the Lely method. Based on this method SiC platelets were prepared in the laboratory for several different applications. Halden [20] grew single crystals of SiC using Si melt solutions but this method was not continued because of the difficulty in obtaining bigger crystals. Kendal [21] later proposed a method of cracking gaseous compounds containing C and Si at high temperatures to form SiC crystallites, which is probably the basis for today's SiC CVD technology.

A real breakthrough occurred in 1978 when Tairov and Tsvetkov [22] demonstrated the seeded growth of SiC using the sublimation method. This was the milestone for SiC technology. Since Tairov and Tsvetkov used Lely's concept of vapor condensation, their method is commonly known as the modified Lely method. Further research on bulk growth is only a refinement and improvement of this technology. Commercially, SiC wafers were first made available by Cree Research, Inc., in 1991 [23]. The availability of SiC wafers in recent years has

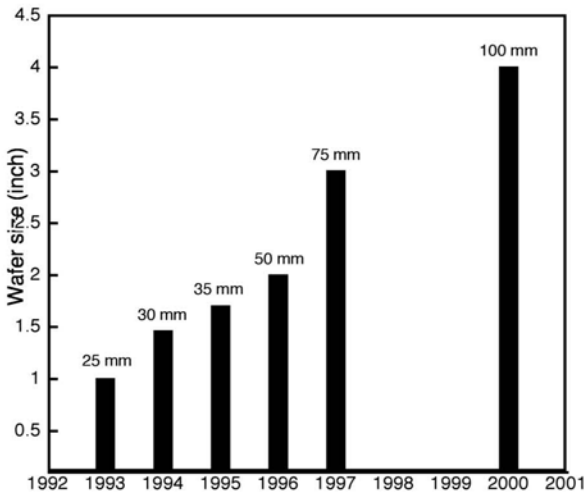


Fig. 6.1. Progress in the increase of diameter of SiC wafers [2]

spurred extensive research on epitaxial growth. Matsunami group's [24] research in establishing step-controlled epitaxy is a notable development in optimizing SiC epitaxial growth morphology.

Even though SiC has been used as an abrasive for a long period, specific interest in SiC semiconductors was shown only in the early 1950s by the space and military establishments in the former U.S.S.R. and a little later in the U.S.A. Civil nuclear industries invested substantially in the development of SiC electronics for their use in high radiation areas; Westinghouse in the U.S. and Siemens in Europe being the pioneering companies. Today there is an international consensus that the application of SiC will increase exponentially in a wide variety of applications. As a result, several companies in the U.S., Japan, Europe, and Russia have started producing SiC wafers commercially (Fig. 6.1).

6.2 Vapor Growth

Commercially, most of the semiconductor crystals are grown using one of the various melt methods, such as Czochralski, liquid-encapsulated Czochralski, Bridgman, and gradient freeze methods. However, these methods cannot be adopted for the growth of silicon carbide since it is not possible to melt SiC under easily achievable process conditions. The calculated values show that the stoichiometric SiC would melt only at above 100,000 atm and 3200°C [3]. Because of these reasons, single crystals of silicon carbide are grown using the techniques based on vapor growth, high temperature solution growth, and their variants. Since SiC readily sublimates, physical vapor growth can be easily adapted, and has become the primary method for growing large size SiC boules. On the other hand, SiC can also dissolve in certain melts, such as silicon, that makes melt solution growth a possible technique. This method is predominantly used for growing single crystal films. This section will describe the techniques based on vapor transport whereas the melt solution methods are discussed in Section 6.3.

6.2.1 Acheson method

The commercial production of SiC was established as early as 1892 [16] using a process known as the Acheson method. This process is primarily used for the synthesis of low purity polycrystalline material. The Acheson method also yields spontaneously nucleated SiC platelets of incomplete habit. In this process, a pre-determined mixture of silica, carbon, sawdust, and common salt [25] (e.g., 50% silica, 40% coke, 7% sawdust, and 3% salt) is heated by resistive heating of the core of graphite and coke placed at the center of the furnace. The mixture of reactants is filled around the core (Fig. 6.2). The furnace is heated to 2700°C, maintained at that temperature for a certain amount of time and then the temperature is gradually decreased. The sawdust creates porosity in the mixture through which

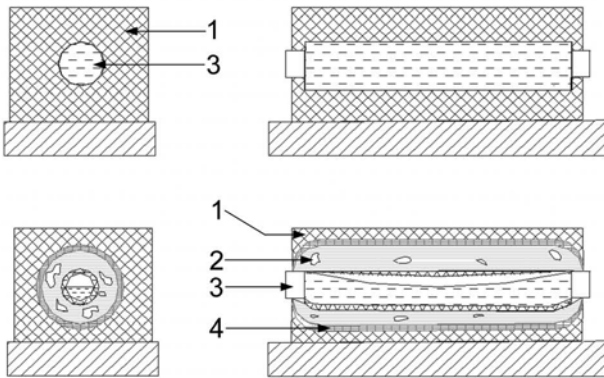


Fig. 6.2. Acheson method: (1) unreacted mixture, (2) SiC crystals nucleated in cavities, (3) carbon core with electrodes, and (4) amorphous SiC [25]

carbon monoxide and other gases can escape. The gaseous byproducts, resulting from the reaction in the charge, build up pressure locally, and also form voids and channels. During the thermal cycle, different regions of the reactants are subjected to different temperatures. Because of the lower temperatures in the outermost region, the charge there remains unreacted. In between the outermost and innermost regions the temperature reaches above 1800°C and the mixture transforms to amorphous SiC. In the core region, SiC is formed first but as the temperature increases it decomposes into graphite and silicon. The decomposed graphite remains at the core and the silicon vapor reacts with the carbon in the adjacent cooler regions to form SiC. Crystalline SiC is therefore formed outside the graphite layers. The common salt reacts with the metallic impurities and escapes in the form of chloride vapors improving the overall purity of the charge. The reaction yields predominantly 6H SiC polycrystalline materials. Platelet crystals up to 2–3 cm are formed in some hollow cavities, created by the escape of carbon monoxide. The size of the crystallites decreases with the increasing distance from the core of the furnace. The crystals are carefully extracted and after suitable processing some of these thin platelets are used as substrates. However, this method does not yield reproducible quality and dimensions of single crystals, and hence, is not suitable for commercial production, although one can obtain SiC platelets, suitable for the use as seeds in physical vapor growth.

6.2.2 Lely method

In 1955 Lely [17] developed a method that was considered to have a major advantage over the Acheson process. In the Lely method, SiC lumps are filled between two concentric graphite tubes [18] (Fig. 6.3a). After proper packing the inner tube is carefully withdrawn leaving a porous SiC layer inside the outer

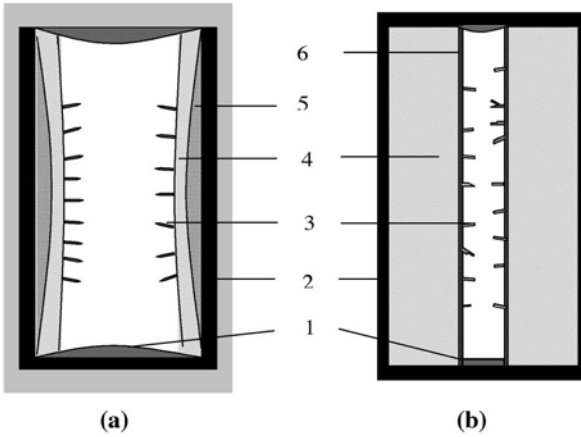


Fig. 6.3. (a) Original Lely method, (b) Improved Lely method; (1) SiC deposit, (2) graphite crucible, (3) SiC platelets, (4) SiC lump, (5) carbon from decomposed SiC, (6) graphite porous cylinder

graphite tube called the crucible. The crucible with the charge is closed with a graphite or SiC lid and is loaded vertically into a furnace. The furnace is then heated to approximately 2500°C in an Argon environment at atmospheric pressure. The SiC powder near the crucible wall sublimates and decomposes because of a higher temperature in this region. Since the temperature at the inner surface of the charge is slightly lower, SiC crystals start nucleating at the inner surface of the porous SiC cylinder. The nucleation phenomenon, in principle, is similar to that observed in the voids and channels of the Acheson system, except for the difference in the region of formation of SiC crystallites due to a different heating configuration. These thin platelets subsequently grow larger in areas if the heating is prolonged at this temperature. High purity crystals can be obtained using better grade SiC charge and Ar gas. Since crystals are nucleated on the lumps of SiC (at the inner surface) and it is difficult to impose higher supersaturation, there is no control over the nucleation process. The Lely method therefore produces platelets of incomplete hexagonal habit.

The original Lely method was later improved by Hamilton [18], and others [19]. In this improved version, SiC charge is packed in between the two annular graphite cylinders (Fig. 6.3b). The outer cylinder (crucible) is thick and the inner cylinder is thin and porous, and acts as a diaphragm. The sublimed SiC vapor passes through the small holes in the diaphragm and crystals are nucleated at the inner surface. Thick layers of SiC are also deposited on the lids at both ends. This modification offers slightly better control over the number of nucleation sites and yield, and crystals up to 20 × 20 mm² have been grown using this method. Good quality, larger crystals are obtained when the temperature variation in the cavity is small and the Ar pressure is maintained at about one atmosphere [19]. Similar to the Acheson process, crystals of 6H polytype are predominantly produced by this

method. The amount of crystals of other polytypes such as 15R and 4H, depend on the growth temperature and dopant. The main drawback of this method is still the lack of control over spontaneous nucleation. However, the crystals grow in isothermal conditions and practically at very low growth rates.

Even though Lely platelets show good structural perfection, they have non-uniform physical and electrical characteristics. Also, since the yield is low (~3%), this method is not suitable for industrial production. The Lely method is, however, ideal for producing platelets of high structural perfection suitable for use as seed crystals in bulk growth using other methods, as discussed later, and high quality substrates for epitaxial growth.

6.2.3 Modified Lely method

Even after Lely demonstrated better growth of SiC crystals, the research on bulk growth did not pick up due to the fact that size and yield could not be improved to a desired level. In fact, research on bulk growth of SiC slowed down in the 1970s until Tairov and Tsvetkov [22] developed the seeded sublimation growth technique, commonly known as the modified Lely method. They succeeded in suppressing the widespread spontaneous nucleation occurring on the (inner) graphite cylinder wall and achieved controlled growth on the seed (Fig. 6.4). This method also led to the control of polytypes to some extent. In the modified Lely method, growth occurs in an argon environment at 10^{-4} to 760 Torr in the temperature range of 1800–2600°C and the vapor transport is facilitated by a temperature differential, $\Delta T = T_2 \sim T_1$, between the seed and the source material. The seed temperature, T_1 , is maintained slightly lower than the source temperature. The kinetics of the transport of Si and C containing species are primarily controlled by the diffusion process.

There are two different designs of the seeded sublimation growth system based on the locations of the charge and seed. In earlier research [26–28] on seeded growth, after the pioneering work of Tairov and Tsvetkov [22], the source SiC was placed in the upper half of the graphite crucible in a circular hollow cylindrical configuration between the crucible and a thin walled porous cylinder (Fig. 6.4a). The seed platelet was held on a pedestal in the lower half of the crucible. Using this configuration, Ziegler et al. [26] grew 20 mm diameter and 24 mm long crystals at 20°C/cm temperature gradient and 2 mbar of Ar pressure, at a growth temperature of about 2200°C. Later, Barrett et al. [27] succeeded in growing 6H-SiC of 33 mm in diameter and 18 mm long at a temperature gradient of 20–30°C/cm and pressure of 20 Torr in the temperature range of 2100–2400°C.

In the second configuration [3,29,30–33] (Fig. 6.4b), that is commonly used today, the source material is held at the bottom of the crucible and the seed plate on the top. No graphite diaphragm is used in this configuration. This arrangement has a high yield (90%) [34], and has therefore become the industry standard for the production of SiC boules. Since this is the process that has attracted significant research efforts in recent years and has shown the most promise, it will be discussed in more detail in Section 6.4.

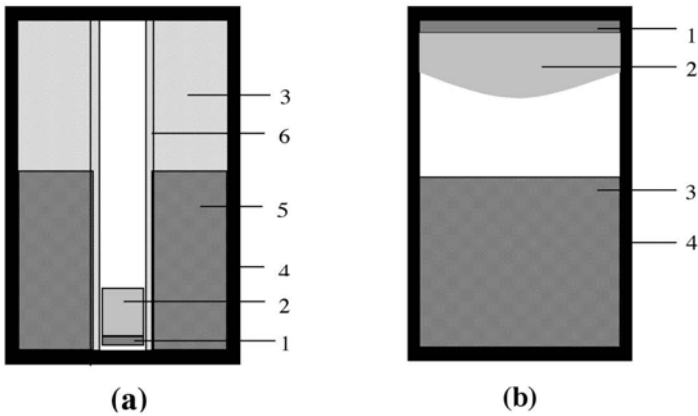


Fig. 6.4. Modified Lely method, (a) seed at the bottom, and (b) seed at the top; (1) seed, (2) crystal boule, (3) source material, (4) graphite crucible, (5) graphite powder, (6) porous graphite cylinder

6.2.4 Sublimation sandwich method

The sublimation sandwich method (SSM) is another variant of the physical vapor transport (PVT) growth. It was proposed in 1970 for the growth of thin epitaxial layers of SiC. In this design, the growth cell is partially open and the environment containing Si vapor may be used to control the gas-phase stoichiometry [35–39] (Fig. 6.5). The source material consists of SiC single crystal or polycrystalline plate with a small source to crystal distance (0.02–3 mm). There are several parameters, such as the source to substrate distance, small temperature gradient, and the presence of Ta for gettering of excess carbon that can control the growth process. Even though it has been shown that the process can be used for bulk growth of SiC crystals, growth of large size boules is yet to be realized. The high growth rate is achieved mainly due to the small source-to-seed distance and a large heat flux onto a small amount of source material with a low to slightly moderate temperature differential between the substrate and the source, 0.5–10°C. These facts make the growth of large boules quite difficult. The method is, however, quite promising for better quality epitaxial films with uniform polytype structures. The research on this sandwich sublimation technique includes theoretical models [35,39], and use of Ta as a crucible material for controlling graphitization [37].

Recently, Syvajarvi et al. [40] have reported growth rates as high as 2 mm/h using the so-called sublimation epitaxy method for 4H and 6H SiC. The growth cell construction is similar to the modified Lely technique but retains the feature of low source to seed distance (1 mm) of SSM. This technique is probably easy to implement but does not give much freedom to vary the vapor conditions. Interestingly, using the sublimation epitaxy method, Khlebnikov et al. [41] have

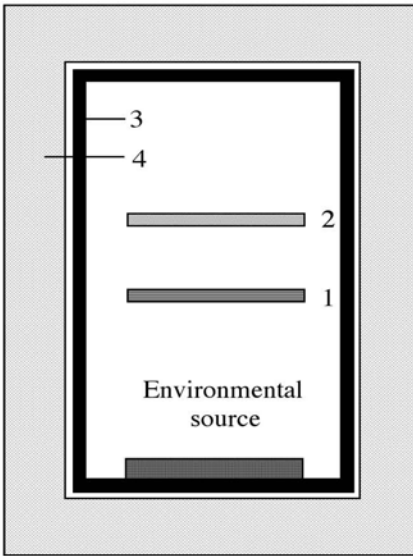


Fig. 6.5. Sublimation sandwich method: (1) source wafer, (2) substrate, (3) graphite container, and (4) insulation material

successfully demonstrated the filling of micropipe by depositing a thick film, however, its effect on device performance needs to be tested.

6.2.5 Chemical vapor deposition

Chemical vapor deposition (CVD) is a popular method for growing thin crystalline layers directly from the gas phase [24,42–44]. In this process a mixture of gases (source gases for Si and C, and a carrier gas) is injected into the growth chamber with substrate temperatures above 1300°C . Silane is the common Si source and a hydrocarbon is used for C. Propane is quite popular, but methane is of interest because of its availability with very high purity although it has a lower carbon cracking efficiency. The carrier gas is high purity H_2 , which also acts as a coreactant. Conventional Si and C source molecules, called multiple-source precursors have been used successfully and reproducible CVD epitaxial films have been produced. However, the single-source CVD SiC precursor shows several advantages over the multiple-source precursors, including a lower growth temperature (less than 1100°C).

Initially, the available SiC substrates were limited by the size and irregular shapes of the Lely and Acheson plates. SiC epitaxial films were then grown on other substrate materials. The first successful large area, heteroepitaxially grown 3C SiC was obtained by Nishinov et al. [45] on a high quality commercial Si wafer. Growth of 3C SiC was also tried on closely lattice-matched TiC, which

yielded slightly better results. With the availability of 6H SiC wafers grown by the modified Lely method, homoepitaxial growth of 6H SiC and heteroepitaxial growth of 3C SiC have been achieved with good success [24]. SiC epitaxial growth is mainly performed on 4H and 6H substrates. Growth on several crystallographic planes of 6H have also been investigated. However, the growth on the Si face of 6H SiC is preferred because of the superior quality and well understood doping behavior. In general, the quality of films obtained on the (0001) face is poor because of the complex surface morphology resulting from two-dimensional nucleation phenomena on the substrate, which leads to poor device performance. Inclusions of other polytypes like 3C SiC in the grown film has also been observed. This problem can be overcome by adopting a method developed by Matsunami's group [24] in which the wafer misoriented by 3–8° from the basal plane is used to control the morphology of the deposited epilayer. The complex surface morphology is transformed into a smooth stripe pattern and this method is referred to as step controlled epitaxy. True homoepitaxy can be obtained by this process leading to high quality epitaxial films. Doping of the film is obtained *in situ* during the growth of each epilayer by flowing either a p-type or n-type source gas. Nitrogen is commonly used as the n-type dopant. The amount of dopant incorporation and reproducibility can be improved by using a site-competition epitaxy [46]. Further details on doping are presented in Section 6.5.

The growth rates of CVD processes are low, a few tens of microns per hour, making it unsuitable for boule production. It can be increased by increasing the deposition temperature, but that makes the control of the process much more difficult, and also results in many other problems such as homogeneous nucleation in the gas phase. The high temperature CVD (HTCVD) [6,47] is an improved version that can yield thicker films and higher growth rates. In HTCVD the substrate is placed at the top of a vertically held graphite susceptor, similar to the crucible used in the modified Lely method, with holes at the bottom and top. The gaseous reactants are passed from the bottom of the susceptor upwards through the hole at the bottom. To maintain the growth for a long time and obtain the maximum deposition on the substrate, the temperature of the susceptor wall is kept high and the substrate temperature is kept slightly lower. This is basically an inverted stagnant flow reactor operating in the temperature range of 2200–2300°C. In principle, SiC growth by this method can be continued for longer periods and bulk crystals can be obtained. To date, 4H crystals of 35 mm diameter and a few millimeters thickness have been obtained at a growth rate of 0.3 to 0.6 mm/h [6].

The hot-wall CVD reported by Kordina et al. [48] is probably a good method to produce uniform epitaxial films on large diameter wafers. Here the CVD reactor is made of a single graphite block with a protective SiC layer. It has an elliptical outer cross section with a rectangular tapered hole, which runs through the entire length. The substrate wafers are placed appropriately on both sides of the rectangular slit. The mixture of gaseous precursors with a carrier gas is passed through the reactor from the end containing the larger hole. The tapered hole compensates for severe depletion of Si and C content in the reactant. The flow rate of the gas can be sufficiently large. This design provides good temperature homogeneity, and epitaxial films of excellent thickness uniformity can be obtained. The surface

morphology of the film can be controlled by choosing off-C-oriented substrate. Recent technological developments have allowed the growth of uniform epitaxial films on wafers as large as 50 mm in diameter [2,49].

6.3 High Temperature Solution Growth

6.3.1 Bulk growth

Melt growth is not suitable for SiC because of the fact that realizing its melting temperature and maintaining stoichiometry is beyond the reach of current industrial technologies. However, carbon is soluble in a Si melt that can allow growth of SiC from a high temperature solution. The solubility ranges from 0.01% to 19% in the temperature interval of 1412–2830°C [3]; although at high temperatures the evaporation of silicon makes the growth unstable. The solubility of carbon can be increased by adding certain transition metals to the Si melt [50]. In principle, this can enable the growth of SiC from the saturated solution by seeded solution growth. Unfortunately, there is no crucible material that can remain stable at the required temperatures and with these melts, and also the evaporation of the Si melt poses a serious problem at higher temperatures. It is also speculated that the incorporation of the added metals in the growing crystal is too high to be acceptable in semiconductor applications [3]. These difficulties restrict the application of this method to bulk growth of SiC. Halden [20], however, has grown SiC platelets from Si melt at 1665°C on a graphite tip in a Czochralski configuration. Epelbaum et al. [51] have obtained SiC boules of 20–25 mm diameter and 20 mm long at the pull rate of 5–15 mm/h in the temperature range of 1900–2400°C at Ar pressure of 100–120 bar. Even though solution grown crystals have been produced free of micropipes, they contain a number of flat silicon inclusions and show rather high rocking curve width. Because of the high temperature and high pressure involved in this process the method is not considered economic for large-scale production.

6.3.2 Liquid phase epitaxy

Even though the high temperature solution method for SiC poses enormous difficulties and is not popular for bulk growth, it has been successfully adopted for the growth of thin films by liquid phase epitaxy (LPE). Indeed, LPE has been used for the production of several SiC-based optoelectronic devices [26]. In LPE, semiconductor-grade silicon is used as a solvent in a graphite crucible. Carbon from the graphite crucible dissolves in Si melt and is transported to the surface of the SiC substrate, which is placed at the bottom of the crucible at a relatively lower temperature. Bright LEDs have been fabricated using this process. However this method suffers from several setbacks, like cracking of the film due to differential thermal contraction while solidifying, and the cumbersome process of extraction of the substrate containing the epitaxial film by etching off the solidified Si. These

problems can be overcome using a dipping technique [52]. In this improved process a SiC substrate attached to a graphite holder is dipped into the molten Si heated by an induction furnace, and is kept in the lower temperature region of the crucible. The substrate is withdrawn from the melt after obtaining the growth of the epitaxial film of a desired thickness. The growth is performed in Ar environment at 1650–1800°C, and the typical growth rate is 2–7 microns/hour. Doping is obtained by adding Al to the Si melt for p-type layer, and Si₃N₄ powder into Si for n-type. It is also possible to obtain n-type film by passing N₂ gas along with Ar. Epitaxial films obtained on (0001) of 6H SiC substrate have shown degradation in LED performance. This problem can be resolved by using substrates misoriented with respect to the *c* axis by a few degrees (3–10°), which leads to better polytype control and improved surface morphologies [24]. The method is known as step-controlled epitaxy, and has led to improved quality of the film and thereby reliable device performance. A better epitaxial surface morphology is obtained by this process, which has been explained based on the nucleation concept [24].

It is possible to lower the growth temperature range by selecting an alternate melt, which has a higher solubility than Si. Tairov et al. [53] have used Sn and Ga melts in the temperature range of 1100–1400°C and have produced LPE layers by using a sliding boat technique. Dmitriev et al. [54] have grown p-n junctions in the temperature range of 1100–1200°C. In addition they have also demonstrated a container-free epitaxial growth of 6H and 3C SiC films in which the melt is held by the electromagnetic field. It has the advantage of mixing induced by the electromagnetic forces [55]. Recently, Syvajarvi et al. [56] used a special sandwich configuration in LPE and succeeded in obtaining growth rates as high as 300 microns/h. One of the main attractions of LPE of SiC is the potential for filling of micropipes. The substrate after filling of micropipes do not reveal the presence of micropipes by either the optical microscopy or etching [6]. However, a detailed analysis is needed to understand the defect configuration around the filled core of the micropipes.

6.4 Bulk Growth by Seeded Sublimation: The Industrial Process

Out of all the methods investigated thus far for bulk growth, the only method that has been implemented by industry is the seeded sublimation growth, commonly known as the modified Lely method. The method has spurred intense worldwide research activity in recent years and has become a standard method for growing SiC crystals [3,22,26–33,57–59]. However, scaling-up of the production has been difficult because of the stringent growth conditions, slow growth rate, and presence of a large number of growth defects in the crystal.

The instrumentation and technology involved in the bulk growth of SiC are complex, and hence, the availability of large size crystals is still limited. This is primarily due to the fact that the operating temperatures are extreme and the monitoring and control are difficult [3]. Even today only a few companies are suc-

cessful in producing SiC boules of reasonable quality and size. The main constraint is the difficulty of finding out the optimum growth conditions for the modified Lely method such as a right combination of pressure, temperature, temperature gradient, charge size, geometric configuration, and so forth. It is not feasible to determine experimentally the exact thermal conditions in the growth zone due to high operating temperatures and the opacity of the graphite crucible. In spite of these limitations, great success has been achieved in the industrial production of SiC crystals in terms of crystal perfection and size [60–63]. Numerical modeling and simulation has been of great help in this endeavor [64]. Figure 6.1 shows the progress made in increasing the boule diameter over the last ten years.

6.4.1 Growth system

As described earlier, there are two main configurations for seeded sublimation growth (Fig. 6.4). The second configuration [3,29,58,62,63], where the source material is held at the bottom of the crucible and the seed plate is fixed onto the crucible lid, is the system commonly used today (Fig. 6.4b). This arrangement yields a higher growth rate compared to the other because of a smaller source to seed distance. Also, since the growing surface is facing downwards there is no danger of the incorporation of charge particles into the growing crystal as in the first case (Fig. 6.4a) where particulates can fall from the top. The main disadvantage of this configuration is that in a system for growing larger diameter boules, maintaining temperature uniformity in the source material becomes difficult. The first configuration is slightly less susceptible to temperature and pressure fluctuations. The operating temperature range of seeded sublimation growth is 1800–2600°C [22], with the actual temperature for growth depending on many different process conditions. Different groups grow SiC crystals at different temperatures by finding narrow windows of process parameters for successful growth.

In spite of some attempts to use a resistively heated furnace, this is not popular because at these high operating temperatures the graphite heating elements are not reliable. As a result, induction furnaces operating at lower frequencies (4 kHz to 300 kHz) [26,65] are commonly used for the modified Lely method. The optimum operating frequency of the induction furnace is 10 kHz, which has a reasonably high skin depth for a graphite crucible. Recently, efficient solid state induction furnaces have become easily available and these low-frequency generators preferentially couple with the susceptor and crucible, with minimum induction on the graphite insulator. Additionally, in an induction furnace it is possible to vary the temperature gradient at the initial stage as well as during the run. Another advantage of the induction furnace over the resistive furnace is the minimal thermal insulation required as the heat is generated directly on the susceptor and crucible. The dimensions and number of turns of the induction coil are selected based on the geometric considerations, temperature, and temperature gradients desired and heat losses. Often, low coil voltage is selected to reduce arcing due to electrical discharge inside the growth chamber at high vacuum used during the degassing and baking of the hot zone. An optimum capacity of the induction furnace and the

number of coil turns and their dimensions are arrived at through experience, along with the simulation results.

The main chamber of the SiC growth system (Fig. 6.6) is a vertically mounted, double walled, water cooled assembly that consists of two concentric quartz tubes sealed with vacuum tight end flanges using double O-ring seals on ground surfaces of the quartz tubes. Cooling water is circulated between the concentric quartz tubes from bottom to the top, although Yakimova et al. [57] have shown that it is also possible to use an air-cooled quartz enclosure. The hot zone consists of a high-density graphite crucible and susceptor surrounded by a rigid graphite insulation. Because of the higher resistivity of the rigid insulation compared to that of the graphite susceptor and crucible, heat is generated primarily on the susceptor by the eddy currents induced by the low frequency magnetic field. The graphite components of the growth chamber, particularly the crucible and susceptor, are treated at high temperatures in fluorine atmosphere to remove metallic impurities. The design of the hot zone is modified based on the requirements of the axial and radial gradient. This is accomplished with the help of computer modeling [64], and prediction of the temperature profile as a function of the growth front, since it is impossible to experimentally find the thermal conditions of the hot zone because of the measurement constraints.

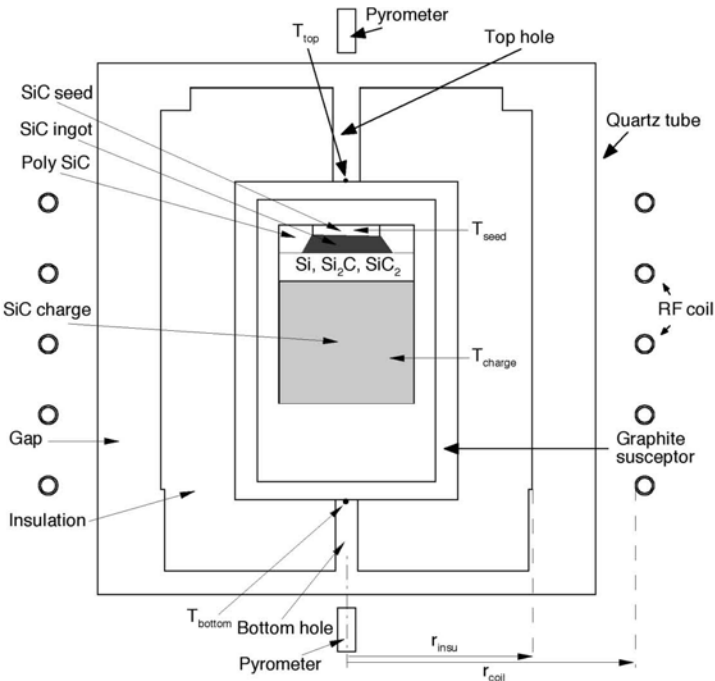


Fig. 6.6. Schematic of the SiC growth system

The normally practiced measurement procedure is to monitor temperatures of the top (T_1) and bottom (T_2) surfaces of the graphite crucible using two color pyrometers (Fig. 6.6). The temperatures are controlled by varying the output power of the induction furnace. Often, the induction coil is mounted on a motorized linear vertical translation stage and the position of the coil is changed during the growth to vary the temperature gradient and the seed temperature. This option is quite useful in achieving the optimized seeding.

The vertical growth chamber is connected to a high vacuum system for obtaining initial degassing (at 10^{-7} Torr) as well as maintaining the required vacuum (e.g., 10 to 100 Torr) conditions during growth. Maintaining vacuum at a predetermined value, as closely as possible, is essential to control the growth rate. This is achieved by using a vacuum throttle valve, a capacitance manometer, and a pressure controller.

6.4.2 Seeding and growth process

After repeated degassing and baking of the growth zone, the chamber is filled with Ar gas. The Ar partial pressure is maintained at about 600 Torr–1 atm while heating up to the maximum required growth temperature (2200–2400°C). The coil position is adjusted such that a desirable temperature gradient of 10 to 20°C/cm can be obtained. The seed temperature, T_1 , and the temperature differential, ΔT , can be varied by changing the coil position, however T_1 and T_2 cannot be controlled independently. The Ar pressure is brought down to a lower value between 1 to 40 Torr at a predetermined pumping speed to initiate the growth smoothly. The axial temperature gradient influences the growth rate, whereas the radial temperature gradient changes the diameter of the crystal (see Chen et al. [64], part II of this paper).

The main stages of growth are: (1) dissociative sublimation of SiC source, (2) mass transfer of gaseous species, and (3) crystallization onto the seed. At a high temperature, the SiC source material decomposes into several Si and C containing species such as Si, C, SiC₂, and Si₂C. Since the crucible is made of graphite, vapor species will react with the graphite wall and form Si₂C and SiC₂, with the graphite crucible acting like a catalyst. Details of the reaction kinetics are described in the companion paper by Chen et al. [64]. The differential temperature between the seed and source, ΔT , works as a driving force and facilitates transport of vapor species, mainly Si, Si₂C, SiC₂. The presence of a temperature gradient leads to supersaturation of the vapor and controlled growth occurs at the seed.

Initially, a high quality Lely plate is used as the seed crystal, and the diameter of the growing crystal is increased by properly adjusting the thermal conditions. For growing larger boules of approximately uniform diameter, wafers from previously grown boules are used as seed disks.

The seed crystal is attached to the graphite top using a sugar melt [66], which decomposes into carbon and gets bonded with the graphite lid. Optimizing this bonding process is quite important since the differential thermal expansion between the seed and the graphite lid can cause bending of the seed plate, leading to formation of domain-like structure, low angle boundaries, and polygonization

[67]. Micropipes can form at these low angle boundaries. Any non-uniformity in seed attachment, like a void between the seed and the lid, can cause variation in the temperature distribution, and the heat dissipation through the seed may get altered. It can result in uneven surfaces and depressions in the growth front corresponding to the void. Evaporation of the back surface of the seed crystal can create thermally decomposed voids, which can propagate further into the bulk [66]. These voids can then become a source for the generation of micropipes. Protecting the back surface of the seed by a suitable coating eliminates these voids. Seed platelet attachment to the graphite lid is one of the important technical aspects of industrial growth.

If the growth process is not optimized, it can lead to polycrystalline deposition due to uncontrolled nucleation. In addition to optimizing the Ar pressure and temperature gradient to achieve controlled nucleation, removal of a thin layer of the seed surface by thermal etching, obtained by imposing a reverse temperature gradient [68], has been found helpful. Etching is also possible by oscillatory motion of the induction coil. The *in situ* thermal etching helps in cleaning the surface of the seed crystal before starting the growth. In some cases, a small amount of excess silicon is added to the charge in order to maintain the Si vapor concentration and stabilize the growth of certain polytypes. The growth of boules is initiated at a very slow rate and is increased progressively by decreasing the pressure.

The dimensions of available Lely plates are very small (approximately 10 mm size hexagonal platelet with thickness less than 0.5 mm), and hence the boule diameter has to be increased. Depending on the design of the crucible and supersaturation ratio, simultaneous growth of polycrystalline SiC, predominantly 3C, occurs particularly on the graphite lid surrounding the seed crystal. If the growth conditions are not optimal, the polycrystalline SiC can get incorporated into the boule near the periphery, leading to cracking due to high stresses. If the growth rate of the boule is higher than the growth rate of polycrystalline SiC, it favors a smooth growth of the boule dominating over the polycrystalline mass. The design of the crucible for increasing the diameter of the boule is normally accomplished through modeling [64].

Bahng et al. [69] have proposed a method of rapid enlargement of the boule using a cone-shaped platform, where enlargement depends on the taper angle of the cone. It has been reported that in this technique, the broadening of the boule is not affected by the growth of the polycrystalline SiC. After obtaining the required diameter of the boule, the seed disks of larger diameter are prepared from these boules for further growth in a specifically designed hot-zone suitable for promoting predominantly the axial growth. As the growth of the boule progresses, the temperature of the growing surface changes, which can be compensated by moving the induction coil. It is evident that the process parameters must be optimized for a particular crucible design, system geometry, and boule dimension. A detailed discussion of these issues and effects of various process parameters are presented in Reference [64].

Among the numerous SiC polytypes, only 6H, 4H, 15R, and 3C have been studied for different applications. 6H, 4H have been studied extensively in the bulk crystal form as well as exipitaxy, whereas 3C has been investigated predomi-

nantly in the epitaxial form. Recently, work on bulk growth of 15R has been initiated for MOSFET applications [14]. Crystals of 4H polytype are grown in a narrow temperature range of 2350–2375°C at 5 mbar using (0001)C face of 4H seed plates [6]. A lower growth rate (0.1 mm/h) is used in the beginning and the growth rate is increased to 0.5 mm/h after growing a 1 mm long boule. Above 2375°C the 4H transforms into 6H; below 2350°C the crystal quality becomes a limiting factor. Among the SiC polytypes 6H is the most extensively studied and the reported growth temperature range varies widely. Perhaps this is due to the difference in the growth cell configuration and temperature measurement conventions. Snyder et al. [61] have reported the growth of 100 mm 6H boules at 2100–2200°C and 5–30 Torr of Ar pressure with 10°C to 30°C/cm temperature gradient. The clearly established result is that (0001)Si face should be used for the growth of 6H whereas (0001)C face is needed for the growth of 4H. It seems that for the bulk growth of 15R seed platelets of the same polytype are required. Schulze et al. [70] have demonstrated the growth of 15R crystals on (0001)Si seed face at 2150–2180°C, 5°C/cm gradient. However, Nishiguchi et al. [65] have shown that 15R polytypes can grow stably on both C and Si of (0001) face at the seed temperature not exceeding 2000°C with the growth rate controlled between 0.1 mm/h to 0.5 mm/h. In addition to temperature there are several other parameters that control the polytypes formation (see Section 6.6.2 for details).

Growth of SiC boule depends on many parameters, such as growth temperature, temperature gradient, Ar pressure, crystal temperature, source to crystal distance, and porosity of the source material [64]. Preparative conditions of the source material alter the vapor species concentrations and vary the growth conditions. The deviation of the stoichiometry can lead to a lower growth rate. The growth rate increases as the seed crystal temperature increases. It also increases with the temperature differential ($T_2 \sim T_1$) and the temperature gradient, but decreases with the source to seed distance. The growth rate varies almost inversely with the Ar pressure and the trend is consistent with $1/\text{Pa}$ dependence on the molecular diffusion coefficient [58]. There exists a saturation of growth rate at very low pressures and one would tend to select this growth regime but control of the vapor composition becomes more difficult.

The growth rates have been measured by inducing growth bands by instantly introducing N_2 gas along with the Ar flow at different intervals and subsequent postmortem studies. In general, (0001) plate is used as a seed and growth proceeds along the c direction. Even though the crystal grows smoothly on (0001) plate, it is also the favorable orientation for the nucleation of micropipes. There have been several attempts [71,72] to grow crystals on non-(0001) orientation. Even though micropipe density reduced in the bulk, the generation of other types of defects such as stacking faults on the basal plane, which hinder electron transport in device application, increased. Presently, the seeding is restricted to (0001) orientation for industrial production of SiC boules.

Monitoring and controlling the growth of SiC is very difficult because of the usage of opaque graphite materials in the hot zone. Recently, radiography has been employed to study the growth interface during the growth process [73]. This imaging technique also revealed the graphitization of SiC source material that

could reduce the growth rate as well as affect the structural perfection of the growing boule. Attempts have also been made to study the defect generation during the growth process by *in situ* X-ray topography [74].

6.5 Doping in Bulk and Epitaxial Growth

6.5.1 Doping in modified Lely method

Doping in SiC is obtained either by containing the dopant in the source material or by passing it in the gaseous form along with argon. The common dopants are N₂ and Al that give rise to n and p type conductivity. The characteristics of dopant incorporation are in general similar for 6H and 4H polytypes. However, there is a significant variation in N₂ and Al incorporation in sublimation growth for the different crystallographic faces [3]. For example, nitrogen incorporation is greater on (0001)Si face compared to (000 $\bar{1}$)C face, whereas the Al incorporates more on (000 $\bar{1}$)C face. Undoped crystals grown on (000 $\bar{1}$)C face show n-type conductivity while the crystals grown on (0001)Si are p-type. This is due to the preferential incorporation of residual dopants present in the graphite components of the hot zone or in the source material. Nitrogen doping concentration in the grown crystal is approximately a function of the square root of the N₂ partial pressure. Aluminum concentration in the bulk linearly varies with the amount present in the source material. The conductivity of the crystal decreases as the N concentration increases, however beyond 60% of nitrogen there is no considerable increase in the carrier density, and hence growth of low resistive SiC growth can be carried out at this nitrogen partial pressure along with the Ar under stable growth conditions [62]. The incorporation of Al is roughly linear with its concentration in the source up to 10²⁰ cm⁻³. Aluminum concentration increases with the increase in growth temperature. However, the nitrogen concentration has exactly the reverse behavior. Low resistive wafers that are required for vertical power devices, are prepared by maximizing the dopant concentration. In the case of microwave devices semi-insulating SiC crystals are required. These are obtained by using a combination of deep level dopants and intrinsic point defects. Wafers of high resistivity ~10⁵ Ω cm (measured at 350°C) are made by deep level doping using vanadium. However, recently Mitchel et al. [75] have demonstrated the growth of semi-insulating 4H-SiC without using V doping.

6.5.2 Doping in epitaxial films

In LPE growth, Al is added to Si to obtain p-type conductivity, and adding Si₃N₄ powder into Si or passing N₂ leads to n-type epitaxial films [43,44]. In CVD, doping is obtained by passing gas phase dopant sources. Trimethyl aluminum and diborane (B₂H₆) are the common p-type dopant sources. Nitrogen is used as n-type dopant, and phosphorous (PH₃) is less commonly used. Conventional methods of

varying the dopant concentration by varying the flow rate do not yield reproducible results, and in addition, it is difficult to increase the dopant concentration. It has been reported that using the site-competition epitaxial technique [46] it is possible to achieve both the reproducibility as well as extended doping range. In this technique Si to C ratio is varied within the reactor to control the dopant incorporation during the growth. This technique has been successfully used on SiC (0001) Si-face using either propane or methane, and also in the growth on SiC substrates of different crystallographic orientation. This technique is based on approximately adjusting the Si/C ratio (e.g., 0.1 to 0.5) within the reactor to effectively control the amount of dopant substitutionally incorporated in the SiC lattice. (For nitrogen, varying the Si/C ratio from 0.1 to 0.5 increases the dopant incorporation (N_D) from $1 \times 10^{15} \text{ cm}^{-3}$ to $1 \times 10^{17} \text{ cm}^{-3}$ [43]). The principle is that there is a competition between the N and C for the C site, and between Al and Si for the Si site during the growth of the epilayer.

6.6 Growth Defects

6.6.1 Growth spirals and micropipes

The observation of growth spirals on the natural faces of SiC crystals grown from the vapor was reported by Verma [76] and Amelinckx [77] in the early 1950s. These are due to screw dislocations emerging at the growing surface. They play an important role in crystal growth as predicted by Charles Frank through his well-known dislocation theory of crystal growth [78]. More details on this topic are presented in Section 6.7.1. The emergence of screw dislocations on a habit face produces a ledge of height equal to the Burgers vector. Crystal grows by the attachment of molecules to the edge of this ledge. The ledge is self-perpetuating and continues to be present on the surface as long as the dislocation line intersects the surface. The ledge winds itself into a circular or polygonal spiral with the dislocation line at the center, and as the growth proceeds the spiral apparently revolves. The step height of these spirals is equal to an integer times c . Depending on the sign of the Burgers vector the spiral can revolve in clockwise or anti-clockwise direction, and depending on the magnitude of the Burgers vector the dislocation present at the center of the spiral can have a closed core or hollow core [79]. These hollow core screw dislocations are known as micropipes or pinhole defects. These micropipes propagate into the bulk and the presence of such defects is detrimental to device fabrication. Frank has predicted that for crystals such as SiC, where the Burgers vectors are large, a stable hollow core would form along the dislocation line as a result of the reduction in the local strain energy of the dislocation. Detailed studies on growth spirals in SiC have been made by several investigators including Sunagawa and Bennema [80].

In the modified Lely method, the supersaturation is imposed by the temperature gradient and it is normally higher than that in the Lely method. Formation of a larger number of nucleation sites are expected at higher supersaturations. If the

screw dislocation mechanism is operative, it will lead to more spirals. This is in agreement with the experimental observations reported by Tairov and Tsvetkov [81]. The high resolution HRD study shows that there exists a domain-like structural behavior in the grown crystal. These slightly misoriented domains are surrounded by low angle boundaries containing high dislocation density, perhaps formed by the relaxation process [67]. Etch pits observed in SiC crystals correspond to elementary and large screw dislocations. The etch pits formed on the core of super screw dislocations continue to be present in the bulk, whereas the etch pits formed because of elementary dislocation do not show one to one correspondence after the removal of a certain amount of thickness of the bulk crystal. The origin of micropipes can be classified into three main categories: (a) thermodynamic, (b) kinetic, and (c) technological cause. *In situ* X-ray characterization methods are being attempted to understand the formation of these defects during growth [74]. It has been observed that micropipes are predominantly formed at the seed/boule interface and propagate along the growth direction. Takahashi et al. [71] have demonstrated that with the use of seed plates of orientations perpendicular to [0001], it is possible to suppress the micropipes, however the crystals contained large number of stacking fault defects. Tanaka et al. [82] showed how some micropipes can get terminated at the planar defects, however the details of planar defect formation was not discussed. Recently Khlebnikov et al. [41] demonstrated a new technique for filling up the micropipes by rapidly growing a thick epitaxial film. Even though some work has been carried out [83] on device fabrication using the micropipe filled epitaxy, this method has not gained popularity.

While micropipes are formed during the growth, it is possible that simultaneously occurring processes such as micropipe dissociation, migration, transformation, and coalescence, can progressively reduce the micropipe density. Indeed, by optimizing the growth parameters the micropipe density has been steadily brought down to $0.5/\text{cm}^2$ [60]. Further discussions on micropipes are presented in Section 6.7.

6.6.2 Polytypism

One of the most unique properties of SiC is its ability to exist in over 200 different polytypes. These polytypes possess the same chemical makeup, but the stacking sequence varies along the *c*-axis of the lattice, and hence, they demonstrate different physical properties. Even though the fact that easy formation of different SiC polytypes due to low stacking fault energy makes it possible to obtain a variety of SiC crystals for different applications, the same fact places severe demands on the thermodynamic, kinetic, and thermal conditions of the process and design of the growth cell [3]. If the growth conditions are not optimized, inclusions of different polytypes occur and thereby deteriorate the growing crystal. Among these polytypes, 6H is the most extensively studied, followed by 4H. Other polytypes that are grown are 3C and 15R. Temperature is one of the important parameters that influences the formation of polytypes [84]. It should be noted that more than one polytype can coexist within the same temperature range. Selection of the right

temperature range and proper seed and seed polarity are critical to obtaining the desired polytype. Other growth parameters that influence the stability of polytypes are supersaturation, vapor phase stoichiometry [81], growth pressure, pumping speed, and dopants [5,6,81].

Systematic studies to understand favorable growth conditions for obtaining a specific polytype have been carried out on 6H [58] and 15R [70] by placing two seeds adjacent to each other on the crucible lid. These two seeds are cut from the same wafer, one with a C face and the other with a Si face. Growth results obtained on two seeds of different polarities under identical growth parameters reveal the ideal seed orientation required for obtaining a single polytype. In general, 6H SiC crystals are grown on the (0001)Si face of 6H SiC seed, whereas 4H [58] crystals are grown on the (0001)C face of 6H crystal. When the growth parameters and seed polarity are not optimized, the grown crystals may contain inclusions of other polytypes and these can become the source for the generation of micropipes. Schulze et al. [85] have grown 6H SiC boules on Si face as well as on C face of 6H SiC seed at very low growth rate, which also led to micropipe-free growth in certain regions. The presence of the polytypes can be easily revealed using the differential oxidation, micro-Raman, and X-ray diffraction techniques. Maintaining growth of one polytype is essential to obtain high quality bulk crystals.

6.6.3 Graphitization

In PVT growth of SiC, the charge dissociates into different forms of Si- and C-containing molecules and condenses onto the seed. The vapor pressure of Si is higher compared to that of all other species, and therefore if there is any loss of vapors during the growth (due to the leakage), the vapor concentration can become carbon-rich. Similarly, during the thermal etching process, the seed surface becomes carbon-rich due to premature breakdown of the seed surface by the loss of Si from the seed surface [3]. The presence of excess carbon in vapors, seed surface, or source material is known as graphitization. Growth initiated on a carbon-rich seed surface can lead to polycrystalline growth. Carbon-rich vapors can produce inclusions of carbon clusters in the growing boule, which can act as the source for micropipe generation. On the other hand, the graphitization of source material can reduce the growth rate by reducing the sublimation rate of the charge. These problems can be controlled in many different ways. The loss of SiC vapor can be minimized by properly sealing the crucible with the lid, whereas the Si concentration can be maintained by adding excess Si into the charge. However, if the Si concentration is increased beyond a certain limit, the growth rate reduces, and also it favors the formation of 3C SiC polytypes as inclusions in 6H. A recent study [37] shows that the excess carbon concentration can be controlled by using a Ta crucible; the excess carbon atoms are adsorbed by the inner surface of the crucible by the gettering process. Crystals of better structural quality have been obtained using Ta crucibles. However, the growth rate reduces by about 10% due to the reduction in C concentration in the crucible. This method of controlling carbon concentration is successfully used in the sublimation sandwich method.

6.7 Defect Analysis

A vital component of the study of crystal growth is an assessment of crystalline imperfections and growth inhomogeneities. This is most evident in the SiC semiconductor industry, which requires wafers of high quality for the fabrication of a variety of devices. SiC crystals grown using different techniques can contain crystalline imperfections such as growth dislocations of screw character with closed cores and hollow cores (micropipes), deformation induced basal plane dislocations, parasitic polytype inclusions, planar defects (stacking faults, microscopic twins, and small angle boundaries), hexagonal voids, and so forth. These defects affect the device performance; in particular, growth dislocations with hollow cores are detrimental to power devices. It is essential to study these defects and understand their origins to develop better crystal growth strategies. The techniques that are commonly used for imaging defects are based on electron and optical microscopy and X-ray diffraction. Each has its own range of capabilities and shortcomings. When it comes to actually solving the problems associated with crystal growth, it is not always obvious which technique is the most appropriate for a particular problem. However, recent developments in defect characterization of SiC crystals have clearly established that X-ray topography, particularly synchrotron white beam X-ray topography (SWBXT) [79,86,87], is superior to other techniques such as chemical etching, AFM, SEM, TEM, and optical microscopy based methods, although these techniques can be used in a complementary manner.

6.7.1 Micropipes and closed core screw dislocations

Origin of the hollow core and Frank's theory

Among the various defects that exist in SiC crystals, screw dislocations lying along the [0001] axis are the most significant and are generally considered to be one of the major factors limiting the extent of the application of SiC. These screw dislocations have been shown to have Burgers vectors equal to nc (where c is the lattice parameter along the [0001] direction in the hexagonal coordinate space and n is an integer), with hollow cores becoming evident with $n \geq 2$ for 6H SiC and $n \geq 3$ for 4H SiC [79]. These latter screw dislocations are generally referred to as micropipes, and their hollow cores can be understood from Frank's theory [78]. This theory predicted that a screw dislocation whose Burgers vector exceeds a critical value in crystals with large shear modulus should have a hollow core with the equilibrium diameter D related to the magnitude of the Burgers vector b by

$$D = \frac{\mu b^2}{4\pi^2 \gamma}, \quad (6.1)$$

where μ is the shear modulus and γ is the specific surface energy. Experimentally, the diameter D can be directly measured by SEM or AFM, while the Burgers

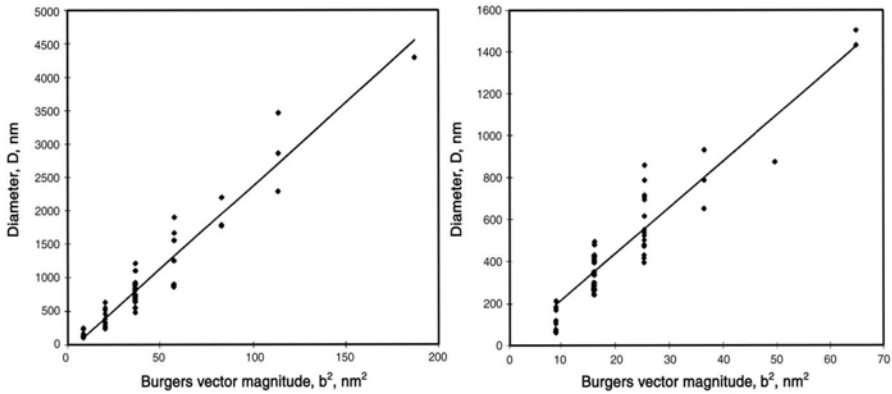


Fig. 6.7. Relationship between the magnitudes of screw dislocation Burgers vectors, b , and the diameters of the associated hollow cores, D . (a) 6H SiC, (b) 4H SiC [79]

vector magnitude b can be obtained by determining the step height of the growth spiral on the as-grown surface using optical interferometry or AFM, or directly using the X-ray topography. Detailed experimental results indicate a direct proportional relationship between D and b^2 for micropipes in both 6H- and 4H-SiC [79,86,87]. In these studies, the magnitudes of the Burgers vectors were obtained using a set of SWBXT methods including back-reflection topography, transmission topography, and section topography, as described in the following. The D versus b^2 correlation obtained experimentally for 6H SiC and 4H SiC is given in Fig. 6.7, this both explicitly verifies Frank's theory and simultaneously reveals that micropipes in SiC are screw dislocations with large Burgers vectors (super-screw dislocations).

Growth spirals and screw dislocations

Growth spirals have been observed on habit faces of as-grown crystals, but not much attention was paid until Frank [78] proposed the dislocation theory to explain the growth of crystals at very low supersaturations. Spirals observed on the habit faces of the as-grown crystal are a clear manifestation of screw dislocations emerging on the surface contributing to the growth by providing everlasting steps for the attachment of units. Hence they are called growth spirals.

Verma [76] and Amelincx et al. [77] have studied the growth spirals from SiC polytypes in detail. In fact, their study is the direct experimental evidence of Frank's theory suggesting the role of screw dislocations in crystal growth, particularly at very low supersaturations. These spirals have been studied using the phase contrast microscope [88], the scanning electron microscope (SEM) [88], and recently by the atomic force microscope (AFM) [89]. The spirals had different shapes ranging from circular shape (Fig. 6.8) to hexagonal. Often, these spirals show crystallographic symmetry. The center of the spiral coincides with the core

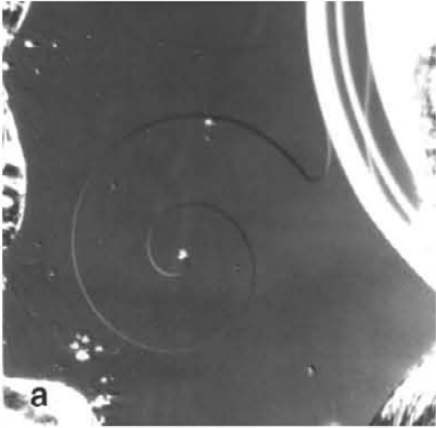


Fig. 6.8. Optical micrograph of a growth spiral on (0001) face of 6H SiC [93]

of the dislocation emerging out of the habit face. The spiral spins either clockwise or anticlockwise depending on the sign of the dislocation. The elementary spiral is of circular shape matching the theoretical shape, and the step height (Burgers vector) equals the lattice parameter along the c direction. Often it is possible to observe steps which are equal to several times the lattice parameter along c axis. When the Burgers vector is more than the unit cell parameter it will be energetically unfavorable unless it has an open core. These open cores have been observed as black dots with phase contrast microscopes [88,90–91]. As the step height increases the spacing of interlaces increases. The spirals interact with each other depending on the sign of the spiral and the pattern of interlace changes, and they have been studied in detail [88]. When two screw dislocations of the same sign are present very close to each other their spirals spin without intersecting each other, which are called cooperative spirals. If the distance between the two screw dislocations is more than the critical value, the shape of the resultant spirals changes because of the interaction. Two dislocations of opposite sign can form a closed loop.

In hexagonal SiC polytypes the step height (Burgers vector of the screw dislocation) is equal to nc , where n is an integer (where as in rhombohedral polytype the step height is $1/3$ of the unit cell parameter c). Tanaka et al. [92] have shown by optical microscopic study that the core radius of the spiral increased with the step height. Dudley et al. [93] have established that the micropipes are hollow core screw dislocations with Burgers vector 3–7 times that of the lattice parameter along c , to be discussed in more detail later. This was also confirmed by Giocondi et al. [89] by studying the step height of the spiral by AFM study. It is possible to observe giant spirals containing a micropipe at the center as well as minute spirals having no micropipes [94]. It is interesting to note that this study of the growth spiral can also be extended to find out the polytype by calculating the step height [90,91,95].

Back-reflection observation of screw dislocations: Intersections with (0001) substrate surface. Screw dislocations in (0001)SiC wafers, both closed core and hollow core (micropipes), can be characterized effectively using back-reflection geometry in synchrotron white beam X-ray topography (SWBXT) [96]. Figure 6.9, a typical back-reflection topograph taken from a (0001) SiC wafer (grown by Cree Research, Inc.) clearly reveals the screw dislocations, both hollow core or closed core, as white circular spots surrounded by black rings. The distribution of the micropipes and screw dislocations as well as their detailed structures can be obtained from such images.

It is noticeable that the circular white spots in Fig. 6.9 are not the images of the hollow cores of the micropipes, because the dimensions of these white spots range from several tens to hundreds of microns, while the actual dimensions of micropipes observed by SEM and AFM are on the order of several microns or less.

On the other hand, the smallest white spots in Fig. 6.9 are images of closed core screw dislocations. These two facts indicate that the circular images of micropipes and closed core screw dislocations are related to the diffraction effects associated with the long-range strain fields of the screw dislocations. In fact, the formation mechanism of the circular images can be described using a simple geometric X-ray diffraction model [97–100].

As indicated in Fig. 6.10(a), due to the lattice displacement of the screw dislocation, the normal \mathbf{n} to the (0001) lattice plane varies from point to point near the dislocation core. Consider a screw dislocation coinciding with the z axis (perpendicular to the (0001) surface). The displacement field u can be expressed in the xyz coordinate space as:

$$u_x = u_y = 0, \quad u_z = \frac{b}{2\pi} \tan^{-1} \frac{y}{x} \quad (6.2)$$

where b is the Burgers vector of the screw dislocation. Due to this displacement field, the distorted diffraction vector becomes [101],

$$\bar{\mathbf{g}} = \bar{\mathbf{g}}_0 - \nabla(\bar{\mathbf{g}}_0 \cdot \bar{\mathbf{u}}), \quad (6.3)$$

where $\bar{\mathbf{g}}_0$ is the undistorted diffraction vector of the perfect lattice. Eqs. (6.2) and (6.3) lead to the position-dependent $\bar{\mathbf{n}} = \bar{\mathbf{g}} / |\bar{\mathbf{g}}|$ as:

$$\begin{aligned} n_x &= \frac{by}{r(b^2 + 4\pi^2 r^2)^{1/2}} \\ n_y &= \frac{-bx}{r(b^2 + 4\pi^2 r^2)^{1/2}}, \\ n_z &= \frac{2\pi r}{(b^2 + 4\pi^2 r^2)^{1/2}}, \end{aligned} \quad (6.4)$$

where $r = (x^2 + y^2)^{1/2}$.

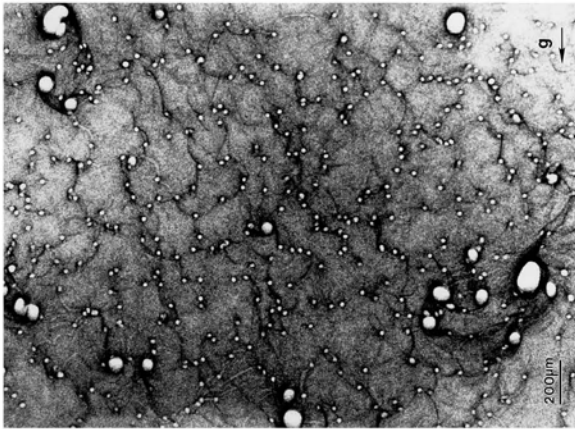


Fig. 6.9. SWBXT back-reflection images of close core (smaller white spots) and hollow core (large white spots) screw dislocations in a (0001) 6H SiC wafer. The faint lines connecting these screw dislocation images are basal plane dislocation images [93]

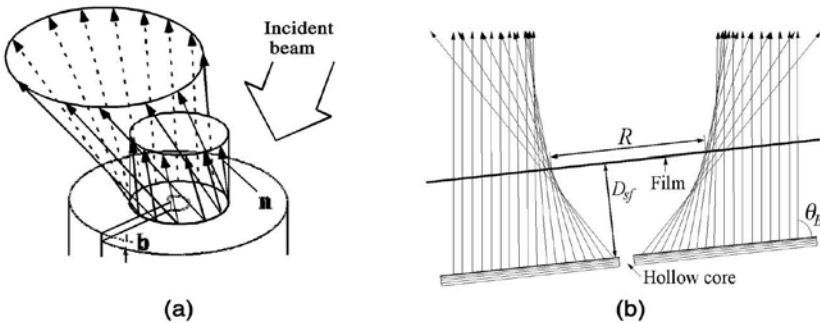


Fig. 6.10. The contrast formation mechanism of micropipes on SWBXT back-reflection topographs. (a) Diffraction geometry: b is the Burgers vector; \vec{n} is the position-dependent normal to the (0001) lattice plane; (b) Schematic representation of overlap of the twisted cones in space

In SWBXT, as the effective divergence of the synchrotron radiation beam is usually around 10^{-5} or less, it is accurate enough to assume that all the incident X-rays have the same direction s_0 . Therefore, the continuous variation of \vec{n} in the distorted lattice makes both the directions and the wavelengths of the diffracted X-rays vary continuously from point to point. However, the direction \vec{s}_g of the diffracted X-rays from an arbitrary point on the surface can be simply described by the geometrical diffraction principle:

$$\vec{s}_g(x, y) = \vec{s}_0 + 2\sin\theta_B(x, y) \vec{n}(x, y), \tag{6.5}$$

where $\theta_B(x, y) = \pi/2 - \cos^{-1}[-\bar{s}_0 \cdot \bar{n}(x, y)]$ is the Bragg angle. Thus, we can divide the crystal surface into a set of small squares of constant area and calculate the direction \bar{s}_g for each square. Since the intensity variation of the incident synchrotron spectrum is slow within the small wavelength range of diffraction, all the squares may be assumed to have the same diffraction power. In order to determine how the diffracted rays intersect the X-ray film, we can further divide this film into a set of squares. Then the computing process is to project the intensities from all the squares on the crystal surface onto the corresponding squares on the X-ray film according to the diffraction direction \bar{s}_g . The sum of the intensities of each square on the film received after the projection represents the local contrast level.

Detailed calculations based on this simulation principle indicate that when a nearly parallel white synchrotron beam is incident on the surface, the X-rays diffracted from successive circular regions surrounding the core form numerous twisted cones [one of these cones is schematically shown in Fig. 6.10(a)]. The overlap of these cones in space results in the formation of the circular images [see Fig. 6.10(b)]. Based on this principle, the images of micropipes and screw dislocations can be rigorously simulated. Fig. 6.11(a) shows a magnified image of an $8c$ micropipe in 6H SiC, while Fig. 6.11(b) is the simulated image of screw dislocation with the Burgers vector being $8c$ ($b \approx 12.1$ nm). It is apparent that the simulation is in excellent agreement with the recorded micropipe image. This proves that micropipes in SiC are indeed pure screw dislocations.

Back-reflection SWBXT images of micropipes or close-core screw dislocations contain abundant information concerning the dislocation structures. The most important information is that the diameter of a screw dislocation image quantitatively indicates the magnitude of the Burgers vector. From Fig. 6.10(b) one can see that two factors determine the image diameter: one is the Burgers vector magnitude of the dislocation and the other is the film-to-sample distance (D_{sf}). The relationship between these three quantities is shown in Fig. 6.12. From the curves in this figure it is easy to estimate the Burgers vector magnitude of any micropipe or screw dislocation revealed in the back-reflection topograph taken at a specific film-to-sample distance. For example, the smallest white spots, which have the highest density in Fig. 6.9, can be determined to be the images of $1c$ screw dislocations (elementary screw dislocations), while the larger spots are images of micropipes with Burgers vectors ranging from $2c$ to $8c$ (micropipes with Burgers vector as large as several tens of the c lattice parameter can also occasionally be found in low-quality SiC crystals).

The other kind of structural information that can be obtained by back-reflection SWBXT is that the twist direction of the diffraction cones unambiguously indicates the dislocation sense, that is, the direction of the Burgers vector. The clockwise twist of the diffracted X-rays (viewed toward the surface) in Fig. 6.10(a) actually results from a right-handed screw dislocation. For a left-handed dislocation, the twist direction is opposite. Figure 6.13(a) shows a back-reflection section topographic image of a micropipe obtained by a slit-limited synchrotron beam of about $20 \mu\text{m}$ in width, while Fig. 6.13(b) is the corresponding simulation. Compared with Fig. 6.11(a), only two “tails” of the overall dislocation image remain in

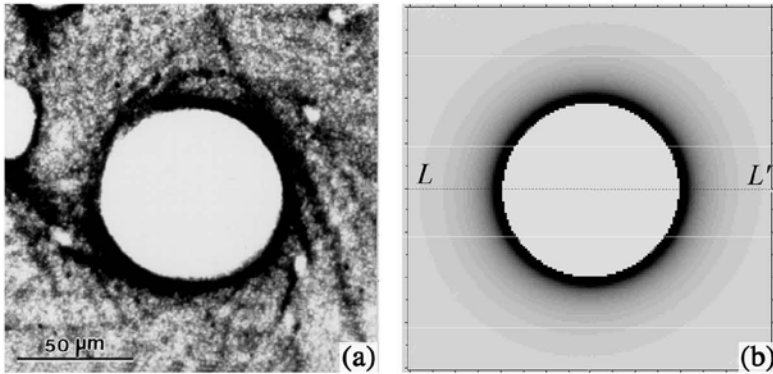


Fig. 6.11. (a) Back-reflection SWBXT image of an $8c$ micropipe taken from a (0001) surface of a 6H-SiC crystal. Sample-to-film distance 20 cm; (b) Simulation of a screw dislocation with Burgers vector $|b| = 8c$ [98]

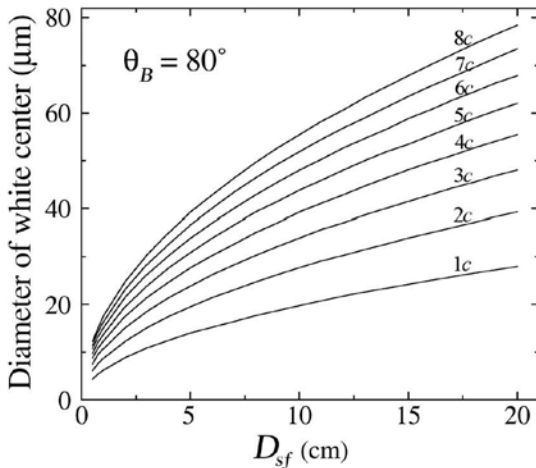


Fig. 6.12. Variation of the diameter of the circular micropipe white contrast as a function of the sample-to-film distance (D_{sf}) and the Burgers vector magnitude [99]

the section topograph. The presence of the tails stretching in directions out of their illuminated sides indicates that the diffracted rays are indeed twisted. Since the twist is along the clockwise direction, the actual micropipe is a right-handed screw dislocation. Figures 6.13(c) and 6.13(d) show the section topograph and the corresponding simulation of a micropipe that is a left-handed screw dislocation.

An isolated micropipe appears as a circular black ring surrounding a white center under the symmetric back reflection, but noncircular white spots are also frequently observed (see Fig. 6.9). Observations of etched crystal surfaces using

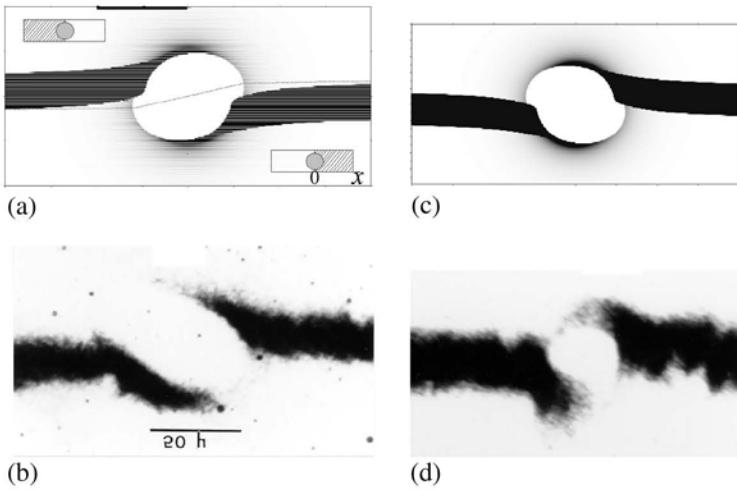


Fig. 6.13. Section topographs showing the senses of screw dislocations associated to micropipes. (a) and (b) are the simulated and recorded images of a right-handed screw dislocation, respectively; (c) and (d) are the simulated and recorded images of a left-handed screw dislocation [98]

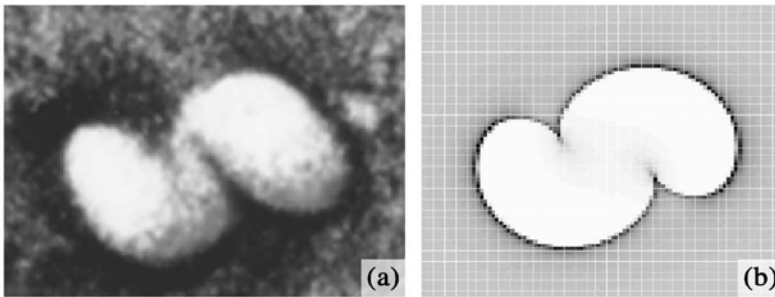


Fig. 6.14. Recorded (a) and simulated (b) images of a micropipe with the same dislocation Burgers vector magnitude and sense [99]

SEM show that the noncircular white regions generally contain several micropipe etch pits close to each other, indicating that these images correspond to groups of micropipes.

Figure 6.14(a) shows a SWBXT image of two identical micropipes ($b_1 = b_2 = 4c$, 6H-SiC) separated by a distance of 25 μm , and Fig. 6.14(b) is the image simulated on the basis of the superimposition of the two independent strain fields of the two micropipes. It is apparent that the two images exactly coincide with each other. The corresponding image and simulation of two opposite-sense screw

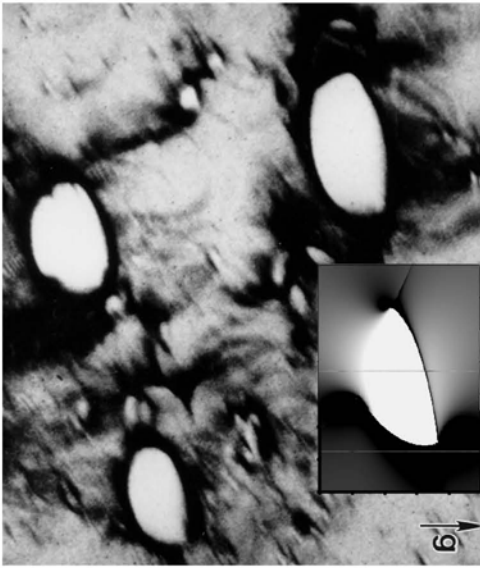


Fig. 6.15. 1126 grazing-reflection topograph of micropipes. Inset is the simulated contrast of a $4c$ screw dislocation with surface relaxation effect considered [97]

dislocations ($b_1 = -b_2$) will be presented below. From this principle, one can actually simulate images of arbitrarily distributed micropipe groups so as to extract the configurations of the individual dislocations.

Grazing incidence imaging of screw dislocations. In addition to the above SWBXT methods, another useful diffraction geometry is the grazing-reflection geometry. In this geometry the incident beam makes an extremely small angle (less than 1°) with respect to the (0001) surface, but there is no limitation for the exit angle of the diffracted beam. This is an especially useful geometry for characterizing micropipes and screw dislocations in SiC films since one can control the penetration depth of X-rays at will by adjusting the incidence angle. Figure 6.15 is a 1126 topograph taken with the recording X-ray film parallel to the (0001) surface, in which the three oval-shaped white spots are images of micropipes. The simulated image based on the geometrical diffraction principle is shown in the inset of Fig. 6.15. Evidently, the shape of the simulated white contrast is similar to that of the recorded images.

Defects revealed by etching. One of the complementary techniques that has been used for evaluating the dislocation density is chemical etching, which is based on the preferential dissolution around the dislocation core due to the stress field. This can also provide information about the kind [102], configuration [103], and inclination [104]. The important task is to find out suitable etchant and etching conditions, and ensure that the etch pits are due to dislocations [105]. Numerous etchants have been reported in the literature for etching of SiC. The most widely

used etchant is KOH in the temperature range of 600–800°C [95]. This has become a routine technique used for the analysis of micropipes in industries. The (0001)Si face reveals the etch pits very clearly compared to poor etching on the (0001)C face [95]. Normally, the etching in SiC is optimized with the help of proven back reflection synchrotron white beam X-ray topography (BR-SWBXT) and is used for quick in-house evaluation of wafers. Depending on the sizes of the etch pits, one can classify them as: (a) large size hexagonal pits that are due to micropipes, (b) medium size pits caused by small spirals that have closed core screw dislocations, or (c) small pits due to edge dislocations [94]. It is also possible to observe process-induced dislocations in the form of dislocation pile-ups and polygonization [91]. Tuominen et al. [72] have revealed domain boundaries and micropipes using etching and SEM study. The domains are of the order of a millimeter with slight misorientation, which can result from the interaction of micropipes.

Transmission Observation of Screw Dislocations of $\{11\bar{2}0\}$ Substrate Wafers.

The true nature of the screw dislocations in SiC is readily revealed by examining longitudinally cut $\{11\bar{2}0\}$ wafers in transmission geometry, that is, wafers cut parallel to the [0001] growth axis [86,87,93]. In one such topograph, long straight segments of dislocation are observed, with line directions close to the growth axis (Fig. 6.16a). These dislocations have clearly not been created by plastic deformation in the classic sense, that is, via the operation of dislocation sources (such as Frank-Read sources) under the action of stress. Rather they are the dislocations produced during growth via phenomena occurring on the growth surface. These phenomena can include replication of dislocations intersecting the growth face, or dislocation nucleation processes involving incorporation of inclusions onto the growth face, or other “growth accidents”. Such “grown-in” dislocations are often observed in crystals grown from solution, vapor, or flux, and typically propagate at a small angle (usually not greater than $\sim 15^\circ$) to the growth axis [106].

Examples of SWBXT images of growth dislocations, recorded using the symmetric 0006 reciprocal lattice vector, from a $(11\bar{2}0)$ 6H-SiC wafer (cut from a boule grown by Cree Research, Inc.) are shown in Fig. 6.16(a). Each screw dislocation image along the [0001] axis exhibits double contrast with a bimodal intensity profile. Micropipes with Burgers vectors $b \geq 2c$ (for 6H-SiC), tend to run exactly parallel to [0001]; while closed core screw dislocations ($b = 1c$, for 6H-SiC) are only approximately parallel to [0001] (deviating by up to $\sim 15^\circ$). This is due to the fact that deviation from [0001] for the micropipes would cost too much energetically due to the much higher line energy. Such transmission images make it possible to observe the nucleation (and potentially, annihilation) and propagation of the screw dislocations during the growth process.

Again, the transmission image can be rigorously simulated using the geometrical diffraction method, as plotted in Fig. 6.16(b). It should be noted that the vertical shift of the double contrast columns is related to the fact that the diffracting planes besides the dislocation center are tilted in opposite senses in the plane of incidence (the plane containing both the incident beam and the principal diffracted

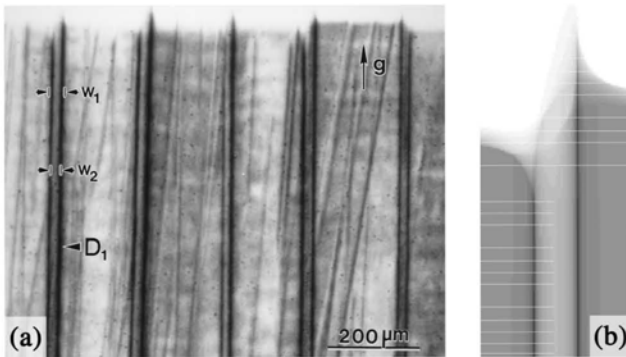


Fig. 6.16. Synchrotron transmission topograph showing the double contrast images of micropipes in a longitudinally cut SiC wafer; (b) simulated image of a micropipe in the transmission geometry [99]

beam), and the distance and direction of this shift are determined by the magnitude of the Burgers vector and the dislocation sense, respectively. This enables us to obtain both the dislocation distributions as well as the Burgers vector magnitudes of individual dislocations. Moreover, the vertical shift of the double contrast of each dislocation image unambiguously indicates the dislocation sense. For example, micropipes 1, 2, 3, and 4 in Fig. 6.16(a) are right-handed screw dislocations while micropipe 5 is a left-handed screw dislocation [87,99].

Micropipes and other defects like thermally decomposed voids running parallel to the surface have also been studied using transmission optical microscopy. Using optical microscopy, Sanchez et al. [66] have shown that thermal decomposition cavities in the bulk can be minimized by using a graphite coating on the seed. It is also possible to observe micropipes and other dislocations on (0001) surface under crossed polarizers [107]. The interference contrast in the image reveals the strain associated with the dislocations through the photoelastic effect. If the micropipe is filled with certain laser dyes, it can be easily observed by the fluorescence using laser scanning confocal microscopy.

Dislocations in epilayers and device structures

SWBXT can also be used to examine dislocation configurations in epilayers and in substrate/epilayer systems that have devices fabricated upon them. Such epilayer and device structures are typically fabricated upon (0001) oriented wafers. In reflection geometry, SWBXT samples defect structures down to the effective penetration depth of the X-ray beam, integrating all the information gathered into a single image. The effective penetration depth, which is controlled in large part by absorption, can be varied by changing the incident grazing angle. By recording images at successively greater penetration depths, one can look for the appearance of new contrast features, and in this way perform a depth profile of the

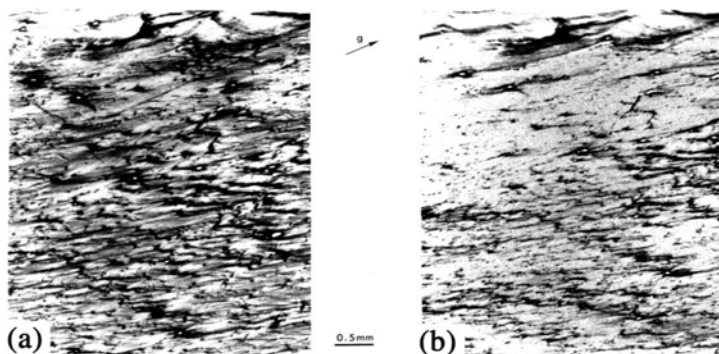


Fig. 6.17. Grazing incidence reflection topographs ($g = 1126$, $\lambda = 0.70 \text{ \AA}$) recorded from (a) a 6H-SiC substrate before epilayer growth; (b) the same region after growth of a $6 \mu\text{m}$ thick epilayer [109].

defect structure [108]. Limiting the penetration depth through control of the grazing angle also makes it feasible to record images exclusively from an epilayer. Figure 6.17 shows an example where images were recorded in grazing incidence geometry from a (0001)6H-SiC crystal before and after the growth of a $6 \mu\text{m}$ thick epilayer [109]. The penetration depth in each case is around $6 \mu\text{m}$, and so one can compare the microstructure in the epilayer to that in the substrate. Close examination of this figure reveals that all of the threading screw dislocations present in the substrate [see Fig. 6.17(a)], which appear as white elliptically shaped rings with white centers, are replicated, as expected, in the epilayer [Fig. 17(b)]. On the other hand, the basal plane dislocations, some of which are visible in Fig. 6.17(a) appear not to be present in Fig. 6.17(b). This is to be expected since most of these dislocations do not thread the surface (note that a finite number will, due to the offcut angle of the crystal). This also can be interpreted to provide some insight as to the mechanism of formation of the basal plane dislocations.

The CVD epilayer growth process is carried out at temperatures several hundred degrees lower than the PVT substrate growth. Since the basal plane dislocations are clearly generated by plastic deformation processes, as evidenced by the dislocation morphology comprising concentric loops piling up on the (0001) slip plane, this suggests two things: (1) that the temperature of CVD growth is not sufficiently high to provide the thermal stresses necessary to drive dislocation motion, and (2) the temperature is not high enough to sufficiently depress the yield stress to a level that is exceeded by the extant thermal stresses. Detailed stress modeling is required to determine the most significant factors controlling the appearance of basal plane dislocations.

Reflection geometry can also be used to examine substrate/epilayer systems that have devices fabricated upon them. The features that make up the device topology typically provide contrast on X-ray topographs. The contrast usually

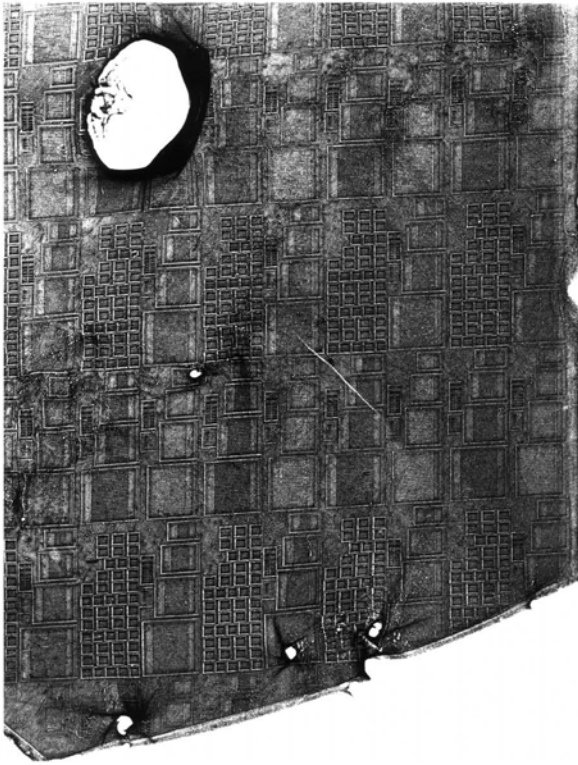


Fig. 6.18. SWBXT back reflection image recorded from a 6H-SiC single crystal that has thyristors fabricated upon it (devices fabricated at U.S. Army Research Laboratory). The small white spots distributed over the image are $1c$ and larger screw dislocations. The location of these dislocations with respect to the device topology can be clearly discerned, enabling the influence of the defects on device performance to be determined. The large white feature corresponds to damage inflicted by a probe.

originates from the strain experienced by the crystal at the edges of growth mesas, or metallization layers, although some absorption contrast may also superimpose on this. Topographs recorded from such structures provide an image of the defect microstructure superimposed on the backdrop of the device topology. This means that direct comparisons can be drawn between the performance of specific devices and the distribution of defects within their active regions. This has made it possible to determine the influence of threading screw dislocations (closed core and hollow core) on device performance [110,111]. The back reflection geometry is particularly useful here, since it gives a clear image of the distribution of screw dislocations on the background device topology that is imaged with sufficient clarity to unambiguously identify the device. An example of a back reflection image recorded from a crystal with devices fabricated on it is shown in Fig. 6.18.

Model for the origin of screw dislocations and micropipes

It has been frequently observed that screw dislocation (including micropipe) nucleation can occur at foreign material inclusions incorporated into the SiC crystal during growth. However, the general mechanisms by which these inclusions, which could be, for example, graphite particles, silicon droplets, or even voids, can lead to screw dislocation nucleation are not clear. Dudley et al. [112] recently proposed a model for the mechanism of screw dislocation nucleation at such inclusions. This model is based on the previously proposed theory for nucleation of screw dislocations at foreign material (solvent, impurity, or void) inclusions during the growth of crystals from solution [113].

A typical example of the nucleation of screw dislocations (including micropipes) at inclusions in SiC can be clearly seen in Fig. 6.19(a), which is a transmission optical micrograph recorded from a (1-100) thin longitudinal-cut section from a *c*-axis 6H-SiC boule grown by the PVT method at Advanced Technology Materials, Inc. (in 1995). Here it is apparent that a group of micropipes has nucleated at the site of a group of what appears to be overlapping inclusions or voids. This phenomenon was observed to occur throughout this crystal, and many other similar crystals, with nucleation being observed at inclusions of various sizes. While optical microscopy is only able to reveal large micropipes, SWBXT can be employed to image screw dislocations in all their forms (including those with closed cores). A SWBXT image recorded in transmission geometry from the same sample is shown in Fig. 6.19(b). Here the total (micropipe and closed-core) dislocation density is much higher than that observed in Fig. 6.19(a), indicating that a large number of $1c$ dislocations have also nucleated at these inclusions.

Due to the close proximity of the micropipes shown in Figs. 6.19(a) and 6.19(b), it is difficult to discern the details of the nucleation process. However, these details can be clearly revealed in the nucleation of micropipes at isolated inclusions. Figure 6.20(a) shows a pair of micropipes emanating from a small isolated inclusion, and this phenomenon can be frequently observed in PVT grown SiC crystals. In a reverse process, inclusions are also observed to terminate micropipe pairs. Evidence for the production of opposite sign, screw dislocation pairs can also be found from the frequent observation of mesa structures on the (0001) growth surface in the early stages of PVT-growth of SiC crystals. A typical mesa developed through the interaction between the growth spirals of two closely spaced screw dislocations on the as-grown surface is shown in Fig. 6.20(b). This type of mesa structure indicates the presence of two screw dislocations with the same Burgers vector magnitude but opposite signs [114].

The formation of micropipe pairs is also observable in Lely platelets of SiC. Figure 6.21(a) is an enlarged back-reflection SWBXT image of one of a number of screw dislocation pairs on the (0001) surface of a 6H-SiC Lely platelet. Here the equal Burgers vector magnitudes and the opposite senses of the two dislocations can be verified by the corresponding simulation shown in Fig. 6.21(b) (for comparison, see the images of two screw dislocations with the same sense in Fig. 6.14) [98,99]. It should be noted that in Lely platelets, both the micropipe density

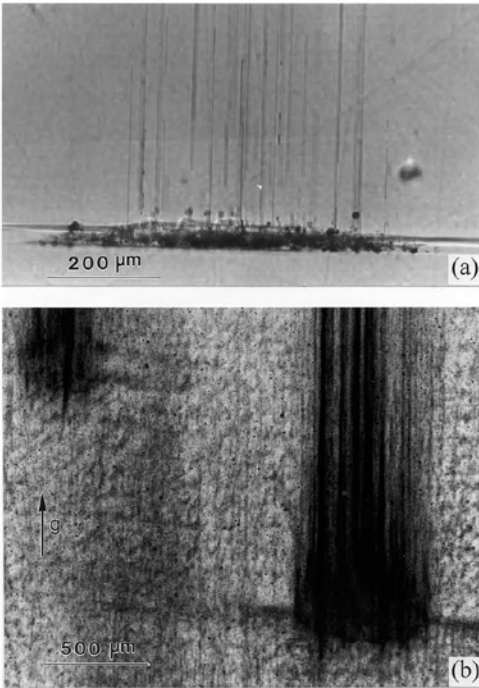


Fig. 6.19. (a) Optical micrograph of a part of a (1-100) 4H-SiC wafer showing the nucleation of micropipes at a group of inclusions during growth. (b) SWBXT image recorded in transmission geometry showing the same region as Fig. 6.1(a). (The upper-left region is another group of inclusions at which micropipes nucleate) [112].

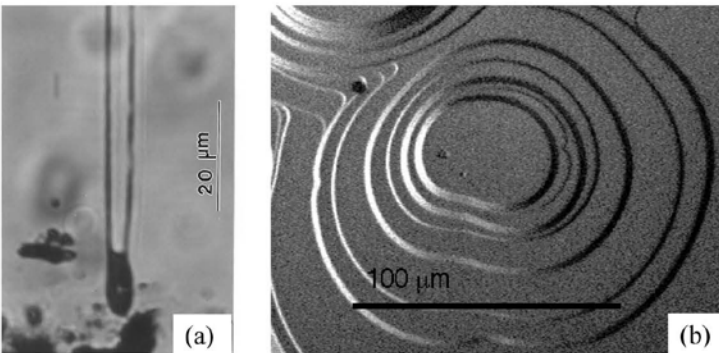


Fig. 6.20. (a) Nucleation of a pair of micropipes at an inclusion in 4H-SiC; (b) AFM image showing a typical mesa structure on the growth face of a 4H SiC crystal [112]

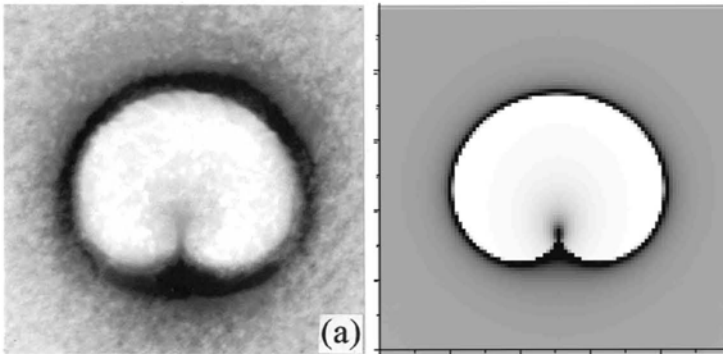


Fig. 6.21. (a) SWBXT image recorded in back-reflection geometry from a (0001) Lely platelet showing a pair of opposite-sign screw dislocations; (b) simulation of the image of two opposite-sign screw dislocations ($b_1 = -b_2 = 12c = 18.2$ nm) with $30\ \mu\text{m}$ spacing. Image dimensions $200 \times 200\ \mu\text{m}^2$ [112]

and $1c$ dislocation density are very low, and the occurrence of isolated dislocation pairs indicates that the two closely spaced dislocations are most likely produced simultaneously, for example, at the same inclusion, and their close proximity cannot be attributed to the merging of two dislocations generated from different sites.

Systematic observations of screw dislocation (micropipe) formation processes using a variety of techniques thus suggest, in agreement with earlier reports [85,89,115–117], that a possible mechanism for nucleation of micropipes in SiC involves the incorporation of inclusions into the crystal lattice. In the case of small isolated inclusions, it is found that the screw dislocations (micropipes) nucleate in pairs.

The nucleation of screw dislocations at inclusions has been observed in several systems [118–120]. The formation of screw dislocation pairs from inclusions has been briefly proposed by Chernov [113] for the crystals grown from solution. Here we extend this approach in detail to explain the observed nucleation of screw dislocations in SiC. As shown in Fig. 6.22(a), this model assumes that two macrosteps of different height, approaching each other on the growth surface, trap a layer of foreign material (solvent, void, or impurity) on the growth surface. As a result of the higher rate of feeding of the protruding edge than the re-entrant edge, an overhanging ledge can subsequently be produced as the crystal attempts to overgrow the inclusion and incorporate it into its lattice. This overhanging ledge is vulnerable to deformation and vibrations and when the macrostep EG meets the approaching macrostep E'F', horizontal atomic planes which were at the same original height may no longer meet along the line where the two steps meet. If the layer of foreign material constituted a void (or transport gases), downward depression of the overhanging ledge may be expected, whereas if it constituted impurity, deformation of the opposite sense dislocations might be expected. In order to accommodate this misalignment, screw dislocations of opposite sign are created

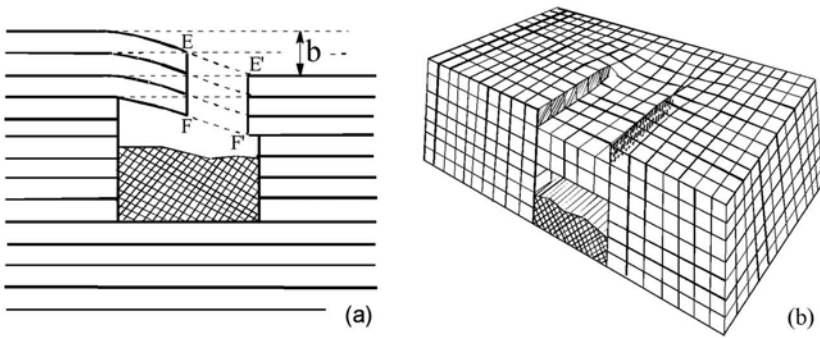


Fig. 6.22. Schematic diagram illustrating the creation of a pair of opposite-sign screw dislocations during the process of inclusion overgrowth. (a) Sectional view through the inclusion parallel to the dislocation line. (b) Perspective view from above [112]

which have Burgers vector magnitudes equal to the magnitude of the misalignment. The configurations of the two created dislocations can be seen more clearly in Fig. 6.22(b). Since the degree of misalignment depends on the relative size of the two approaching steps and the lateral and vertical extent of the inclusion, the production of dislocations with a range of Burgers vectors becomes possible. In fact, micropipe-related screw dislocations in SiC can have Burgers vectors as large as several tens times the basic lattice constant along the c axis [121]. It seems more likely that these very large Burgers vector screw dislocations are created by this kind of mechanism rather than one involving the merging of groups of same-sign dislocations.

In addition, in cases of large inclusions or groups of inclusions, the deformation of the protruding ledge may be spread over the length of the line along which they meet, resulting in the creation of distributed groups of opposite-sign screw dislocations. These groups may not necessarily be distributed symmetrically, but in all cases, the sum of all the Burgers vectors of the dislocations created must equal zero.

In SiC, the sources of the growth steps involved in the above model can be the vicinal nature of the growth surface (which tends to be slightly dome-shaped), 2D nucleation, as well as spiral steps associated with the intersections of screw dislocations with the surface. Differences in step height are certainly conceivable when a vicinal step meets a spiral step and can even occur when two spiral steps associated with screw dislocations of different Burgers vector magnitude meet or if step bunching occurs for a group of dislocations. Moreover, the merging of 2D-grown islands also play an important role in the formation of growth steps as well as voids. These various sources in conjunction with the formation of inclusions thus provide opportunities for micropipes as well as closed-core screw dislocations to be created during growth.

6.7.2 Basal plane dislocations

The primary slip plane for hexagonal 4H and 6H SiC is the basal plane. It is therefore not surprising that deformation-induced dislocations on the basal plane are observed in both structures [122,123]. An example is shown in Fig. 6.23, a transmission topograph recorded from a 6H-SiC basal plane wafer (grown by Cree Research, Inc.). Also shown in this figure is a reflection topograph recorded from the same region of the 6H-SiC crystal.

Detailed Burgers vector analysis of these dislocations can be easily performed. Observation of the morphologies of the basal plane dislocation loops clearly indicates that they are deformation-induced and appear to have been nucleated both at the crystal edges and at the sites of micropipes. This is an interesting phenomenon and is the subject of ongoing study.

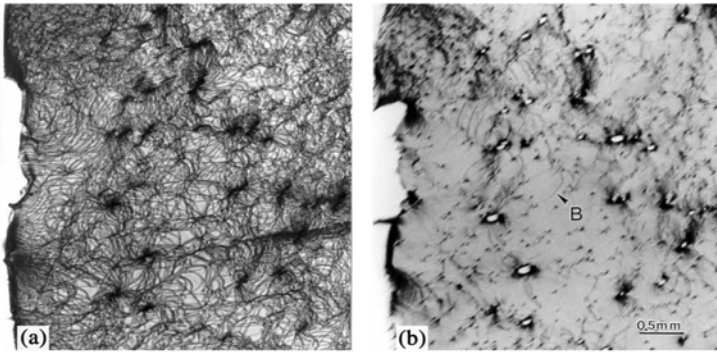


Fig. 6.23. (a) Transmission topograph recorded from a basal plane wafer, showing basal plane dislocation loops; (b) the corresponding reflection image, revealing the screw dislocations as well as a few basal plane dislocations [93,122]

6.7.3 Small angle boundaries

Another defect, which is receiving increasing attention in 4H-SiC, is the small angle boundary. Preliminary characterization using X-ray topography indicates that the tilt angles associated with these boundaries are only a few seconds of arc, although detailed analysis of the nature of these defects has not yet been completed [124]. Examples of this kind of defect are shown in Fig. 6.24.

Detailed studies carried out by Ha et al. [125], suggest that the small angle boundaries are composed of edge dislocations running approximately along the growth axis. These edge dislocations are believed to have been originally produced by plastic deformation processes occurring on nonbasal planes. These edge dislocations are postulated to subsequently undergo polygonization to form the small

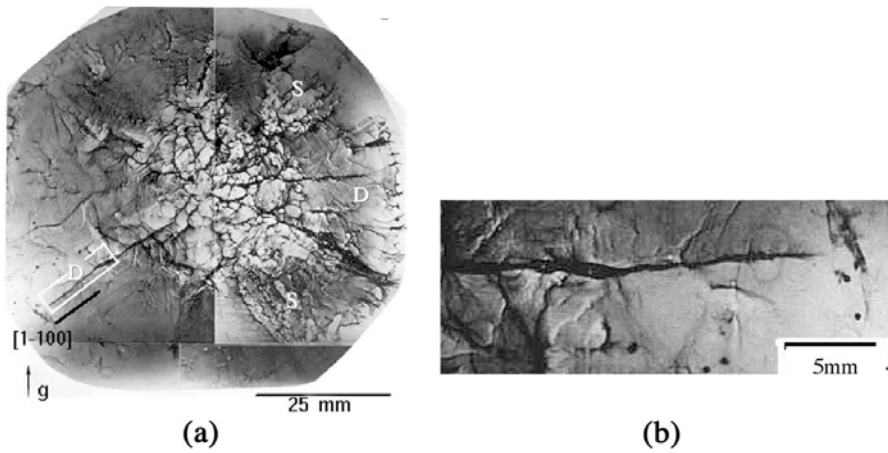


Fig. 6.24. (a) Back-reflection topograph of experimental 3-inch 4H-SiC wafer [(00016), $\lambda = 1.26 \text{ \AA}$] showing several small angle boundaries; (b) enlargement from framed section on Fig. 6.17(a), clearly showing the orientation contrast (image overlap) from one of the boundaries [122]

angle boundary structures. The spacing between dislocations within the boundaries is shown by etching to be on the order of 1 micron. This is just below the resolution limit for SWBXT, but while the individual dislocations within the boundaries cannot be resolved, the tilt associated with the boundaries is clearly revealed.

6.7.4 Hexagonal voids

Another defect that is sometimes observed in PVT-grown SiC boules is the hexagonal void; a flat, hexagonal, platelet-shaped cavity oriented parallel to the basal plane (with lateral sizes between 50 and 750 μm and thickness along the c -axis between 5 and 25 μm). As shown by Kuhr et al. [126], these voids are nucleated at imperfections in the attachment layer between the seed and crucible cap. Growth steps are observed on the void facets closest to the seed, and evaporation steps are found on void facets closest to the growth surface, providing evidence for void movement during the growth. AFM images have revealed that the growth steps, nucleated at the sidewall of the void, flow across the bottom of the void and terminate in a trench-like depression. KOH etching of wafers between the void and seed further reveal the dislocations lining up along the trace of the void path, often with higher densities corresponding to the location of the trench. In addition, the SWBXT images recorded from wafers above and below the void show a random distribution of screw dislocations in the crystal volume above the void, and an absence of screw dislocations in the volume directly below the void, except for hollow core superscrew dislocations, which are found at the corners of the void trace

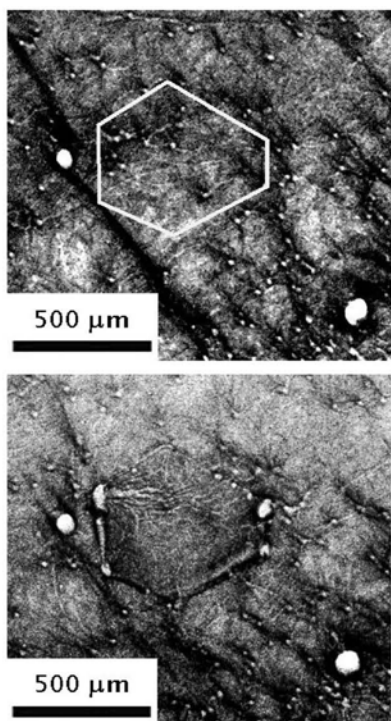


Fig. 25. Back-reflection X-ray topographs ($g = 00024$, $\lambda = 1.24 \text{ \AA}$) of the area above (a) and below (b) a hexagonal void (a). The projected passage of the void has been traced in white. The screw dislocations visible above the void in (a) are not visible beneath the void in (b) [126]

(see Fig. 6.25). In this way, groups of closed core dislocations, intersected by the hexagonal voids as they sweep through the crystal, are forced to coalesce to produce fewer, larger Burgers vector screw dislocations (whilst conserving the Burgers vector).

6.8 Summary

An extraordinary combination of physical and electronic properties makes silicon carbide a unique material for devices in high power, high frequency, high temperature, and intense-radiation applications. Recent developments in SiC bulk growth and epitaxial film technology have greatly advanced the SiC-based device technology. Although the device potential of SiC was realized long ago from the SiC platelets grown by Acheson and Lely methods, the breakthrough occurred only when the seeded sublimation growth was demonstrated by Tairov and Tsvet-

kov in 1978. Since then research in the area of SiC crystal growth and device fabrication has increased substantially all over the world. The modified Lely method has now become a standard process for industrial production of SiC boules. Wafers of 50 mm diameter are commercially available, and 75 mm and 100 mm diameter wafers have also been grown on an experimental basis. It is expected that 75 mm SiC wafers will be commercially available soon in the market. This has been made possible by optimizing the crystal growth technology in conjunction with modeling and computer simulation. Details on process physics, modeling development, and simulation schemes, together with the description of the effects of various process parameters, are presented in Chapter 7.

The defects, particularly micropipes, have been significantly reduced by improving the growth technique, optimizing the process parameters, and developing better understanding of the defect generation and propagation. The undesirable polytype inclusions have been understood reasonably well, and now it is possible to grow a single polytype using the modified Lely method. Today, wafers of micropipe density as low as $0.5/\text{cm}^2$ are available commercially. This development is considered quite important for most of the nonpower devices. Indeed, a remarkable advancement has been made in crystal growth technology for both 6H- and 4H-SiC crystals. Now efforts are being devoted to grow 15R SiC, which has a great potential for MOSFET applications. The other common polytype, 3C, is predominantly grown using heteroepitaxy.

With the availability of 6H-SiC wafers, research on epitaxial growth has increased tremendously. High quality films are being produced for different device applications using CVD techniques; in particular, HTCVD and hot-wall CVD have yielded films of good uniformity. Even though LPE of SiC is not as successful as CVD, recent developments such as container-free LPE growth show promise for better quality films. In addition, the quality of the epitaxial film and thereby the functioning of the device have been improved greatly by step-controlled epitaxy. High dopant incorporation can be achieved using the site-competition technique.

Defects present in the SiC crystals have been characterized using X-ray topography, and microscopy-based techniques such as chemical etching, AFM, SEM, TEM, reflection and transmission optical microscopy. Even though many of these techniques are used in a complementary manner to obtain detailed information on defects present in the crystal, X-ray topography, particularly SWBXT, is quite superior to other methods in revealing defects present in the SiC crystals. Indeed, SWBXT has provided complete quantitative characterization of both closed core and hollow core (micropipes) screw dislocations as well as basal plane dislocations. It has also given insights into the formation mechanisms of these defects. Since SWBXT is capable of imaging defects in a full size wafer with devices fabricated on it, the technique can be successfully used to study the influence of various defects on device performance.

The challenge in SiC growth still remains the quality, size, and cost. For widespread use of SiC as a semiconductor, it is important that further progress is made in all of these areas. Since the presence of micropipes is detrimental for device performance, micropipe density must be brought down to a much lower value.

Also, other defects such as basal plane dislocations, inclusions, and voids need to be reduced substantially. Another area that is important is the control of polytype and infringement of polycrystalline growth directly under the seed. Since different polytypes of SiC have different properties and also polytype inclusions can become a potential source for defect generation, it is critical that a single polytype is maintained throughout the growth of the boule.

Control of the growth process requires sensing, measurement, and control strategies. However, the process does not allow much measurement, in fact, nothing inside the growth zone. Measurement of temperatures at only two locations, far away from the growth surface and the bulk of the SiC charge, gives very little information on the actual growth temperature and temperature gradient, two critical growth parameters. Also, it is difficult to experimentally find out the rate of sublimation, chemical composition of vapor, and growth interface shape, etc., which make the control of the process very difficult.

Further, it is well known that the size of the semiconductor wafer has great influence on the cost of the device fabrication. Any improvement in the size of the wafer increases its use by a large factor. For widespread use of SiC, it is believed that 100 mm wafers should be made available immediately followed by 150 mm within five years. Indeed, an increase in SiC boule size and reduction in its price are essential if the SiC semiconductor market is to reach its forecast of \$4 billion by 2004 and \$8 billion by 2008.

Acknowledgments

Support is acknowledged from the U.S. Army Research Office under contract number DAAG559810392 (Contract monitor Dr. John Prater), partially funded by the DARPA Electronics Technology Office (Order#E111/3 monitored by Dr. Dan Radack) and NASA Glenn Research Center, from NSF grant DMR99003702 (subcontract 54406855242), and from ONR grants N0001140010348 and N000140110302 (contract monitor Dr. Colin Wood). Topography carried out at the Stony Brook Topography Facility (beamline X-19C) at the National Synchrotron Light Source, which is supported by the U.S. Department of Energy, Division of Materials Sciences and Division of Chemical Sciences.

References

1. Lebedev AA, Chelnokov VE (1999) Wide-gap Semiconductors for High-power Electronics. *Semiconductor* 33(9):999–1001
2. Carter Jr CH, Tsvetkov VF, Glass RC, Henshall D, Brady M, Muller StG, Kordina O, Irvine K, Edmond JA, Kong HS, Singh R, Allen ST, Palmour JA (1999) Progress in SiC: from Material Growth to Commercial Device Development. *Mater Sci Eng B* 61–62:1–8

3. Glass RC, Henshall D, Tsvetkov VF, Carter Jr CH (1997) SiC-Seeded Crystal. *MRS Bulletin* 22(3):30–35
4. Koga K, Yamaguchi T (1991) Single Crystals of SiC and Their Application to Blue LEDs. *Prog Crystal Growth and Charact* 23:127–151
5. Dmitriev VA, Spencer MG (1998) SiC Fabrication: Growth and Doping. *Semiconductors and Semimetals* 52:21–75
6. Yakimova R, Janzen E (2000) Current Status and Advances in the Growth of SiC. *Diamond and Related Materials* 9:432–438
7. Chelnokov VE, Syrkin AL (1997) High Temperature Electroics Using SiC: Actual Situation and Unsolved Problems. *Mater Sci Eng B46*:248–253
8. Baumhauer H (1915) Über die verschiedenen Modifikationen des Carborundums und die Erscheinung der Polytypie. *Z Krist* 55:249–259
9. Otto H (1926) Das Gitter des Karborunds (SiC) III (Modifikation und das “amorphe Karbid”). *Z Krist* 63:1–18
10. Spetz AL, Tobias P, Baranzahi A, Martensson P, Lundström I (1999) Current Status of Silicon Carbide Based High-Temperature Gas Sensors. *IEE Transactions on Electron Devices* 46:561–565
11. Harris CI, Konstantinov AO (1999) Recent Developments in SiC Device Research. *Physica Scripta* T79:27–31
12. Neudeck PG (1995) Progress in Silicon Carbide Semiconductor Electronics Technology. *J Electronic Materials* 24:283–288
13. Harle V, Hiller N, Kugler S, Hahn B, Stath N (1999) Industrial Aspects of GaN/SiC Blue Light Emitting Diodes in Europe. *Mater Sci Eng B61–62*:310–313
14. Schorner R, Friedrichs P, Peters D, Stephani (1999) Significantly Improved Performance of MOSFETs on Silicon Carbide using the 15R-SiC. *IEEE Electronic Device Letters* 20:241–244
15. Krotz G, Wagner C, Legner W, Sonnatag H, Moller H, Muller G (1996) Micro-machining Applications of Heteroepitaxially Grown b-SiC Layers on Silicon. *Inst Phys Conf Ser No 142*:829–83
16. Acheson AG (1892) British Patent 17:911
17. Lely JA (1955) Darstellung von Einkristallen von Siliziumcarbid und Beherrschung von Art und Menge der eingebauten Verunreinigungen. *Berichte Deutsche Keramik Gesellschaft* 32:229–231
18. Hamilton DR (1960) The Growth of Silicon Carbide by Sublimation. In: Connor JR, Smilestens J (eds) *Silicon Carbide, A High Temperature Semiconductor*. Pergamon, Oxford, pp 45–51
19. Novikov VP, Ionov VI (1968) Production of Monocrystals of alpha-Silicon Carbide. *Growth of Crystals* 6b:9–21
20. Halden FA (1960) The Growth of Silicon Carbide from Solution. In: Connor JR, Smilestens J (eds) *Silicon Carbide, A High Temperature Semiconductor*. Pergamon, Oxford, pp 115–123
21. Kendal JT (1960) The Growth of Silicon Carbide from Gaseous Cracking. In: Connor JR, Smilestens J (eds) *Silicon Carbide, A High Temperature Semiconductor*. Pergamon, Oxford, pp 67–72
22. Tairov YM, Tsvetkov VF (1978) Investigation of Growth Processes of Ingots of Silicon Carbide Single Crystals. *J Crystal Growth* 43:209–212
23. Cree Research, Inc, 2810 Meridian Parkway, Suite 176, Durham, NC 27713

24. Matsunami H, Kimoto T (1997) Step Controlled Epitaxial Growth of SiC: High Quality Homoepitaxy. *Mater Sci Eng R20*:125–166
25. Knippenberg WF (1966) Growth Phenomena in Silicon Carbide: Preparative Procedures. *Philips Res Rept* 18:170–179
26. Ziegler G, Lanig P, Theis D, Weyrich C (1983) Single Crystal Growth of SiC Substrate Material for Blue Light Emitting Diodes. *IEEE Trans Electron Device ED-30*:277–281
27. Barrett DL, Seidensticker RG, Gaida W, Hopkins RH (1991) SiC Boule Growth by Sublimation Vapor Transport. *J Crystal Growth* 109:17–23
28. Stein RA, Lanig P, Leibenzeder S (1992) Influence of Surface Energy on the Growth of 6H and 4H-SiC Polytypes Sublimation. *Mater Sci Eng B11*:69–71
29. Glass RC, Henshall D, Tsvetkov VF, Carter Jr CH (1997) SiC Seeded Crystal Growth. *Phys Stat Sol (b)* 202:149–162
30. Barrett DL, Mchugh JP, Hobgood HM, Hopkins RH, McMullin PG, Clarke RC (1993) Growth of Large SiC Single Crystals. *J Crystal Growth* 128:358–362
31. Powell AR, Wang S, Fechko G, Brandes GR (1998) Sublimation Growth of 50mm Diameter SiC Wafers. *Materials Science Forum* 264–268:13–16
32. Garcon I, Rouault A, Anikin M, Jaussaud C, Madar R (1995) Study of SiC Single-Crystal Sublimation Growth Conditions. *Mater Sci Eng B29*:90–93
33. Tairov YuM, Tsvetkov VF (1981) General Principles of Growing Large-size Single Crystals of Various Silicon Carbide Polytypes. *J Crystal Growth* 52:146–150
34. Tairov YuM (1995) Growth of Bulk SiC. *Mater Sci Eng B29*:83–89
35. Karpov SYu, Makarov YuN, Mokhov EN, Ramm MG, Ramm MS, Roenkov AD, Talalaev RA, Vodakov YuA (1997) Analysis of Silicon Carbide Growth by Sublimation Sandwich Method. *J Crystal Growth* 173:408–416
36. Karpov SYu, Makarov YuN, Ramm MS (1997) Simulation of Sublimation Growth of SiC Single Crystals. *Phys Stat Sol (b)* 202(1):201–220
37. Vodakov YuA, Roenkov AD, Ramm MG, Mokhov EN, Makarov YuN (1997) Use of Ta-container for Sublimation Growth and Doping of SiC Bulk Crystals and Epitaxial Layers. *Phys Stat Sol (b)* 202(1):177–200
38. Mokhov EN, Ramm MG, Roenkov AD, Vodakov YuA (1997) Growth of Silicon Carbide Bulk Crystals by the Sublimation Sandwich Method. *Mater Sci Eng B46*:317–323
39. Karpov SYu, Makarov YuN, Ramm MS, Talalaev RA (1997) Control of SiC Growth and Graphitization in Sublimation Sandwich System. *Mater Sci Eng B46*:340–344
40. Syvajarvi M, Yakimova R, Tuominen M, Kakanakova-Georgieva, MacMillan MF, Henry A, Wahab Q, Janzen E (1999) Growth of 6H and 4H-SiC by Sublimation Epitaxy. *J Crystal Growth* 197:155–162
41. Khlebnikov I, Madangarli VP, Khan MA, Sudharshan TS (1998) Thick Flim Epitaxy for ‘Filling Up’ Micropipes. *Materials Science Forum* 264–268:167–170
42. Henry A, Ivanov IG, Egilsson T, Hallin C, Ellison A, Kordina O, Lindefelt U, Janzen E (1997) High Quality 4H-SiC Grown on Various Substrate Orientations. *Diamond and Related Materials* 6:1289–1292
43. Larkin DJ (1997) An Overview of SiC Epitaxial Growth. *MRS Bulletin* 22(3):36–41
44. Matsunami H (1993) Progress in Epitaxial Growth of SiC. *Physica B* 185:65–74
45. Nishinov S, Powell JA, Will HA (1983) Production of Large-area Single-crystal Wafers of Cubic SiC for Semiconductors. *Appl Phys Lett* 42:460–462
46. Larkin DJ, Neudeck PG, Powell JA, Matus LG (1993) Site Competition Epitaxy for Doping of CVD Silicon Carbide. *Inst Phys Conf Ser* 137:51–54

47. Kordina O, Hallin C, Ellison A, Bakin AS, Ivanov IG, Henry A, Yakimova R, Touminen M, Vehanen A, Janzen E (1996) High Temperature Chemical Vapor Deposition of SiC. *Appl Phys Lett* 69:1456–1458
48. Kordina O, Hallin C, Henry A, Bergman JP, Ivanov I, Ellison A, Son NT, Janzen E (1997) Growth of SiC by “Hot-Wall” CVD and HTCVD. *Phys Stat Sol (b)* 202:321–334
49. Janzen E, Kordina O (1997) SiC Material for High-power Applications. *Mater Sci Eng B* 46:203–209
50. Syvajarvi M, Yakimova R, Ivanov IG, Janzen E (1997) Growth of 4H SiC from Liquid Phase. *Mater Sci Eng B* 46:329–332
51. Epelbaum BM, Hofmann D, Muller M, Winnacker A (2000) Top-seeded Solution Growth of Bulk SiC: Search for the Fast Growth Regimes. *Materials Science Forum* 338–342:107–110
52. Suzuki A, Ikeda M, Nagoa NT, Matsunami H, Tanaka TJ (1976) Liquid Phase Epitaxial Growth of 6H-SiC by the Dipping Technique for Preparation of Blue-light-emitting Diodes. *J Appl Phys* 47:4546–4550
53. Tairov YuM, Raihel FI, Tsvetkov VF (1982) Silicon Solubility in Tin and Gallium. *Neorganicheskie Materiali* 1390–1391
54. Dmitriev VA, Elfimov LB, Il'inskaya ND, Rendakova SV (1996) Liquid Phase Epitaxy of Silicon Carbide at Temperatures of 1100–1200C. *Springer Proceedings in Physics* 56:307–311
55. Dmitriev VA, Cherenov A (1993) Growth of SiC and SiC-AlN Solid Solution by Container Free Liquid Phase Epitaxy. *J Crystal Growth* 128:343–348
56. Syvajarvi M, Yakimova R, Radamsom HH, Son NT, Wahab Q, Ivanov IG, Janzen E (1999) Liquid phase epitaxial growth of SiC. *J Crystal Growth* 197:147–154
57. Yakimova R, Syvjarvi M, Tuominen M, Iakimov T, Råback R, Vehanen A, Janzen, E (1999) Seeded Sublimation Growth of 6H and 4H-SiC Crystals. *Mater Sci Eng B* 61–62:54–57
58. Augustine G, Hobgood HM, Balakrishna V, Dunne G, Hopkins RH (1997) Physical Vapor Transport Growth and Properties of SiC Monocrystals of 4H Polytype. *Phys Stat Sol (b)* 202:137–148
59. Nishizawa SI, Kitou Y, Bahng W, Oyanagi N, Khan MN, Arai K (2000) Shape of SiC Bulk Single Crystal Grown by Sublimation. *Material Science Forum* 338–342:99–102
60. Hobgood D, Brady M, Brixius W, Fechko G, Glass R, Henshall D, Jenny J, Leonard R, Malta D, Muller StG, Tsvetkov V, Carter Jr C (2000) Status of Large Diameter SiC Crystal Growth for Electronic and Optical Applications. *Materials Science Forum* 338–342:3–8
61. Snyder DW, Heydemann VD, Everson WJ, Barret DL (2000) Large Diameter PVT Growth of Bulk 6H SiC Crystals. *Materials Science Forum* 338–342:9–12
62. Siergiej RR, Clarke RC, Sriram S, Aggarwal AK, Bojko RJ, Morse AW, Balakrishana V, MacMillan MF, Burk Jr AA, Brandt CD (1999) Advances in SiC Materials and Devices: An Industrial Point of View. *Mater Sci Eng B* 61–62:9–17
63. Muller StG, Glass RC, Hoobgood HM, Tsvetkov VF, Brady M, Henshall D, Jenny JR, Malta D, Carter Jr CH, The Status of SiC Bulk Growth from an Industrial Point of View. *J Crystal Growth* 211:325–332
64. Chen Q-S, Prasad V, Zhang H, Dudley M (2002) Silicon Carbide Crystals — Part II: Process Physics and Modeling. In: Byrappa K, Ohachi T (eds) *Crystal Growth for Modern Technology*. William Andrew Publishing, Norwich, NY

65. Nishiguchi T, Okada S, Sasaki M, Harima H, Nishino S (2000) Crystal Growth of 15R-SiC Boules by Sublimation Method. *Material Science Forum* 338–342:115–118
66. Sanchez EK, Kuhr T, Heydemann D, Snyder W, Rohrer S, Skowronski M (2000) Formation of Thermal Decomposition Cavities in Physical Vapor Transport of Silicon Carbide. *J Electronic Materials* 29(3):347–351
67. Tuominen M, Yakimova R, Glass RC, Tuomi T, Janzen E (1994) Crystalline Imperfections in 4H SiC Grown with a Seeded Lely Method. *J Crystal Growth* 144:267–276
68. Anikin M, Madar R (1997) Temperature Gradient Controlled SiC Crystal Growth. *Materials Science and Engineering B*46:278–286
69. Bahng W, Kitou Y, Nishizawa S, Yamaguchi H, Nasir Khan M, Oyanagi N, Nishino S, Arai K (2000) Rapid Enlargement of SiC Single Crystal Using a Cone-shaped Platform. *J Crystal Growth* 209:767–772
70. Schulze N, Barrett D, Weidner M, Pensl G (2000) Controlled Growth of Bulk 15R SiC Single Crystals by the Modified Lely Method. *Materials Science Forum* 338–342:111–114
71. Takahashi J, Kanaya M, Fujiwara Y (1994) Sublimation Growth of SiC Single Crystalline Ingots on Faces Perpendicular to the (0001) Basal Plane. *J Crystal Growth* 135:61–70
72. Touminen M, Yakimova R, Prieur E, Ellison A, Toumi T, Vehanen A, Janzen E (1997) Growth-related Structural Defects in Seeded Sublimation-grown SiC. *Diamond and Related Materials* 6:1272–1275
73. Oyanagi N, Nishizawa SI, Kato T, Yamaguchi H, Arai K (2000) SiC Single Crystal Growth Rate by *in situ* Observation Using the Transmission X-ray Technique. *Materials Science Forum* 338–342:75–78
74. Kato T, Oyangi N, Yamaguchi H, Takano Y, Nishizawa S, Arai K (2000) *In situ* Observation of SiC Bulk Single Crystal Growth by X-Ray Topography. *Materials Science Forum* 338–342:457–460
75. Mitchel WC, Saxler A, Perrin R, Goldstein J, Smith SR, Ewvaraye AO, Solomon JS, Brady M, Tsvetko V, Carter Jr CH (2000) Vanadium-free Semi-insulating 4H-SiC Substrate. *Materials Research Forum* 338–342:21–24
76. Verma AR (1951) Spiral Growth on Carborundum Crystal Faces. *Nature* 167:939
77. Amelinck S (1951) Spiral Growth on Carborundum Crystal Faces. *Nature* 167:939–940
78. Frank FC (1951) Capillary Equilibria of Dislocated Crystals. *Acta Crystallography* 4:497–501
79. Si W, Dudley M, Glass R, Tsvetko V, Carter Jr H (1998) Experimental Studies of Hollow Core Screw Dislocations in 6H-SiC and 4H-SiC Single Crystals. *Materials Science Forum* 264–268:429–432
80. Sunagawa I, Bennema P (1981) Observation of the Influence of Stress Fields on the Shape of Growth and Dissolution Spirals. *J Crystal Growth* 53:490–504
81. Tairov YuM, Tsvetkov VF (1983) *Progr Crystal Growth Characterization* 7:111
82. Takanaka N, Nishino S, Saraie J (1996) Sublimation Growth of 6H-SiC Bulk. In: Nakshima H, Matsunami S, Yoshida Harima, (eds) *Proceedings of 6th Int Conf SiC Related Materials*. *Inst of Phys Conf Ser* 142:49–52
83. Schattner TE, Casady JB, Smith MCD, Mazzola MS, Dmitieva VA, Rentakova SV, Sadow SE (2000) 4H-SiC Device Scaling Development on Repaired Micropipe Substrates. *Materials Science Forum* 338–342:1203–1206

84. Knippenberg WF (1966) Growth Phenomena in Silicon Carbide: Discussion of Results and Conclusions. *Philips Res Rept* 18:268–274
85. Schulze N, Barret DL, Pensl G (1998) Near-equilibrium Growth of Micropipe Free 6H-SiC Single Crystals by Physical Vapor Transport. *Appl Phys Lett* 72:1632–1634
86. Si W, Dudley M, Glass R, Tsvetkov V, Carter Jr CH (1997) Hollow-Core Screw Dislocations in 6H-SiC Single Crystals, A Test of Frank's Theory. *J Electronic Materials* 26:128–133
87. Dudley M, Si W, Wang S, Carter Jr CH, Glass R, Tsvetkov VF (1997) Quantitative Analysis of Screw Dislocations in 6H-SiC Single Crystals. *Il Nuovo Cimento* 19D:153–164
88. Verma AR (1953) *Crystal Growth and Dislocations*. Butterworths Scientific Publications, London
89. Giocondi J, Rohrer GS, Rhorer, Skowronski M, Balakrisna V, Augustine G, Hobgood HM, Hopkins RH (1997) An AFM Study of Super-dislocation/ Micropipe Complexes on the 6H-SiC(0001) Growth Surfaces. *J Crystal Growth* 181:351–362
90. Verma AR (1960) Polytypism and Surface Structure of Silicon Carbide Crystals-Interferometric and X-ray Studies. In: Connor JR, Smilestens J (eds) *Silicon Carbide, A High Temperature Semiconductor*. Pergamon, Oxford, pp 202–206
91. Amelinckx S, Strumane G (1960) Surface Features on Silicon Carbide Crystal Faces. In: Connor JR, Smilestens J (eds) *Silicon Carbide, A High Temperature Semiconductor*. Pergamon, Oxford, pp 202–206
92. Tanaka H, Uemura Y, Inomata Y (1981) Observation of Holes Around Dislocation Core in SiC. *J Crystal Growth* 53:630–632
93. Dudley M, Wang S, Huang W, Carter Jr CH, Tsvetko VF, Fazi C (1995) White Beam Synchrotron Topographic Studies of Defects in 6H-SiC Single Crystals. *J Phys D: Appl Phys* 28:A63–A68
94. Sugiyama N, Okamoto A, Okumura K, Tani T, Kamiya N (1998) Step Structures of SiC Single Crystals Grown by Modified Lely Method. *J Crystal Growth* 191:84–91
95. Faust JW, Tung Y, Liaw HM (1973) A Study of Etch Pits on Pure Polytypes of SiC. In: *Silicon Carbide-1973*. University of South California
96. Dudley M, Huang W, Wang S, Powell JA, Neudeck P, Fazi C (1995) White Beam Synchrotron Topographic Analysis of Multipolytype SiC Device Configurations. *J Phys D: Appl Phys* 28:A56–A62
97. Huang XR, Dudley M, Vetter WM, Huang W, Carter Jr CH (1998) Contrast Mechanism in Superscrew Dislocation Images on Synchrotron Back-Reflection Topographs. *Mat Res Soc Symp Proc* 524:71–76
98. Huang XR, Dudley M, Vetter WM, Huang W, Wang S, Carter Jr CH (1999) Direct Evidence of Micropipe-Related Pure Superscrew Dislocations in SiC. *Appl Phys Lett* 74:353–356
99. Huang XR, Dudley M, Vetter WM, Huang W, Si W, Carter Jr CH (1999) Superscrew Dislocation Contrast on Synchrotron White-Beam Topographs: An Accurate description of the Direct Dislocation Image. *J Appl Cryst* 32:516–524
100. Dudley M, Huang XR, Huang W (1999) Assessment of Orientation and Extinction Contrast Contributions to the Direct Dislocation Image. *J Phys D: Appl Phys* 32:A139–A144
101. Authier A (1996) Dynamical Theory of X-Ray Diffraction—II. Deformed Crystal. In: Authier A, Lagomarsino S, Tanner BK (eds) *X-Ray and Neutron Dynamical Diffraction Theory and Application*. Plenum, New York, pp 43–62

102. Gilman JJ, Jhonson WG, Sears SW (1958) Dislocation Etch Pit Formation in Lithium Fluoride. *J Appl Phys* 29:747
103. Sagar JW, Faust Jr JW (1967) Dislocation Studies in Bi_2Te_3 by Etch Pit Technique. *J Appl Phys* 38:482
104. Amelinckx S, Struman G, Webb WW (1960) Behavior of Individual Dislocations in Strain-Hardened LiF Crystals. *J Appl Phys* 31:687
105. Dhanaraj G, Shripathy T, Bhat HL (1992) Defect Characterization of KTP Single Crystals. *Bull Materials Science* 15:219–227
106. Klapper H (1980) Defects in Non-Metal Crystals. In: Tanner BK, Bowen DK (eds) *Characterization of Crystal Growth Defects by X-ray Methods*. NATO ASI Series B, Physics, v 63, Plenum, New York and London, pp 133–160
107. Takahashi J, Kanaya M, Hoshino T (1993) Sublimation Growth and Characterization of SiC Single Crystalline Ingots on Faces Perpendicular to the (0001) Basal Plane. *Inst Phys Conf Ser* 137:13–16
108. Yao G-D, Dudley M, Wu J (1990) Synchrotron White Beam Topographic Imaging in Grazing Bragg-Laue Geometries. *J X-ray Science & Technology* 2:195–213
109. Wang S, Dudley M, Carter Jr CH, Kong HS (1994) X-ray Topographic Studies of Defects in PVT 6H-SiC Substrates and Epitaxial 6H-SiC Thin Films. *Mat Res Soc Symp Proc* 339:735–740
110. Neudeck PG (2000) Electrical Impact of SiC Structural Defects on High Electric Field Devices. *Materials Science Forum*, 338–342:1161–1166
111. Neudeck PG, Huang W, Dudley M (1998) Breakdown Degradation Associated with Elementary Screw Dislocations in 4H-SiC P+N Junction Rectifiers. *Mat Res Soc Symp Proc* 483:285–294
112. Dudley M, Huang XR, Huang W, Powell A, Wang S, Neudeck P, Skowronski M (1999) The Mechanism of Micropipe Nucleation at Inclusions in Silicon Carbide. *Appl Phys Lett* 75:784–786
113. Chernov AA (1989) Formation of Crystals in Solutions. *Contemp Phys* 30:251–276
114. Burton WK, Cabrera N, Frank FC (1951) The Growth of Crystals and the Equilibrium Structure of Their Surfaces. *Philos Trans R Soc London, Ser A* 243:299–358
115. Tsvetkov V, Glass R, Henshall D, Asbury D, Carter Jr CH (1998) SiC Seeded Boule Growth. *Materials Science Forum* 264–268:3–8
116. Heydemann VD, Sanchez EK, Rohrer GS, Skowronski M (1998) The Structural Evolution of Lely Seeds During the Initial Stages of SiC Sublimation Growth. *Mat Res Soc Symp Proc* 483:295–298
117. Balakrishna V, Hopkins RH, Augustine G, Donne GT, Thomas RN (1998) Characterization of 4H-SiC Monocrystals Grown by Physical Vapor Transport. *Inst Phys Conf Ser* 160:321–331
118. Gits-Leon S, Lefauchaux F, Robert MC (1978) Effect of Stirring on Crystalline Quality of Solution Grown Crystals—Case of Potash Alum. *J Crystal Growth* 44:345–355
119. Klapper H, Kuppers H (1973) Directions of Dislocation Lines in Crystals of Ammonium Hydrogen Oxalate Hemihydrate Grown From Solution. *Acta Cryst A* 29:495–503
120. Neuroth G (1996) Der Einfluß von Einschlußbildung und mechanischer Verletzung auf das Wachstum und die Perfektion von Kristallen. PhD thesis, University of Bonn, Germany
121. Krishna P, Jiang S-S, Lang AR (1985) An Optical and X-Ray Topographic Study of Giant Screw Dislocations in Silicon-Carbide. *J Crystal Growth* 71:41–56

122. Wang S (1995) Characterization of Growth Defects in Silicon Carbide Single Crystals by Synchrotron X-ray Topography. PhD thesis, State University of New York at Stony Brook, USA
123. Vetter WM (1999) Characterization of Dislocation Structures in Silicon Carbide Crystals. PhD thesis, State University of New York at Stony Brook
124. Kuhr TA, Vetter WM, Dudley M, Skowronski M (2000) X-ray Characterization of 3 Inch Diameter 4H and 6H-SiC Experimental Wafers. *Materials Science Forum* 338–342:473–476
125. Ha S, Nuhfer NT, De Graef M, Rohrer GS, Skowronski M (2000) Origin of Threading Dislocation Arrays in SiC Boules Grown by PVT. *Materials Science Forum* 469–472:477–480
126. Kuhr TA, Sanchez EK, Skowronski M, Vetter WM, Dudley M (2000) Hexagonal Voids and the Formation of Micropipes During SiC Sublimation Growth. Submitted to *J Appl Phys*

7 Silicon Carbide Crystals — Part II: Process Physics and Modeling

Q.-S. Chen¹, V. Prasad³, H. Zhang¹, and M. Dudley²

Center for Crystal Growth Research, ¹Department of Mechanical Engineering,
²Department of Materials Science and Engineering, State University of New York
at Stony Brook, Stony Brook, NY 11794-2200
³College of Engineering, Florida International University, Miami, FL 33174

Nomenclature

a	activity
A	area (m^2)
\mathbf{A}	magnetic vector potential (Wb/m)
A_{SiC}	growth area (m^2)
\mathbf{B}	magnetic flux density (T)
c_p	isobaric specific heat, (J/kg/K)
d_p	mean diameter of the charge particles (m)
D	diffusion coefficient (m^2/s)
D_c	diameter of crucible (m)
f	frequency (Hz)
F	radiation view factor
g	gravitational acceleration (m/s^2)
Gr	Grashof number, $\rho^2 g \beta R^3 \Delta T / \mu^2$
G_{SiC}	growth rate (m/s), dissolving rate of particles (m/s)
ΔG_T^0	isobaric-isothermal Gibbs-function
h	heat transfer coefficient ($\text{W/m}^2/\text{K}$)
$\Delta h_{f, 298}^0$	heat of formation
H	latent heat (J/kg)
I	current (A)
\mathbf{J}	current density (A/m^2)
k	thermal conductivity (W/m/K)
K	equilibrium constant of a chemical reaction
L	gap between the charge and seed (m)
M	molecular weight (kg/mol)
p	pressure (Pa)
P	partial pressure (Pa)
Pe	mass Péclet number (UL/D)

Pr	Prandtl number ($\mu c_p / k$)
q	heat flux (W/m^2)
q''_{eddy}	heat generated by eddy currents (W/m^3)
q''_{radi}	radiative heat flux (W/m^2)
Q	heat flux (W)
r	radial coordinate (m)
R	universal gas constant, 8.314 ($\text{J}/\text{mol}/\text{K}$); heat resistance (K/W)
R_s	radius of susceptor (m)
Ra	Rayleigh number ($Gr \cdot Pr$)
t	time (s)
T	temperature (K)
ΔT	temperature difference between the charge and seed (K)
u	displacement component
U	advective velocity (m/s), activation energy (J/mol)
v	displacement component
z	axial coordinate (m)

Greek Symbol

α	absorptivity, thermal expansion coefficient, sticking coefficient
β	volumetric expansion coefficient ($1/\text{K}$)
ε	emissivity, strain
ε_m	permittivity (F/m)
ε_p	porosity of SiC charge
μ	viscosity ($\text{kg}/\text{m}/\text{s}$)
μ_m	magnetic permeability (H/m)
ρ	density (kg/m^3)
ρ_c	density of crystal (kg/m^3)
σ_c	electrical conductivity ($1/\Omega/\text{m}$)
σ	Stefan-Boltzmann constant 5.670×10^{-8} ($\text{W}/\text{m}^2/\text{K}^4$), stress
ω	angular frequency (rad/s)

Subscripts

∞	ambient
<i>boun</i>	boundary
<i>coil</i>	induction coil
<i>cond</i>	conductive
<i>conv</i>	convective
<i>eddy</i>	eddy current
<i>eff</i>	effective
<i>gas</i>	gas
<i>insu</i>	insulation material

<i>radi</i>	radiative
<i>real</i>	real part of a complex quantity
<i>s</i>	solid
<i>Ste</i>	Stefan
θ	angular direction

7.1 Introduction

Silicon carbide crystals of 50–100 mm diameter are now commercially grown using the method of physical vapor transport, commonly known as the modified Lely method. A detailed review of the historical development of SiC growth, micropipes and other defects in as-grown crystals, issues and challenges of the current process technology, and characteristics of the present industrial growth systems is presented in a companion article (Chapter 6) by Dhanaraj et al. [1]. Any advancement in crystal growth technology in terms of the boule size (diameter and length) and defect density strongly depends on the understanding of the process physics, better design of the growth system and effective control of the growth process. Since direct measurement of temperature, flow, species concentration, and growth rate is extremely difficult, if not impossible, physics-based modeling is the only way that one can develop an understanding of the transport mechanisms in a SiC growth system. The models can also help in process optimization and system design.

Modeling and simulation of SiC crystal growth has attracted significant research interests in last five years or so, and growth models have been developed by several investigators, namely, Hofmann et al. [2,3], Pons et al. [4,5], Egorov et al. [6], Müller et al. [7,8], Karpov et al. [9], Chen and co-workers [10–15], Selder et al. [16], and Råback et al. [17–19]. Various degrees of system complexity have been considered by these authors, such as electromagnetic field produced by RF heating, generated heat power in the graphite susceptor, conduction and radiation heat transfer, temperature distribution, and growth kinetics.

Hofmann et al. [2,3] modeled the temperature distributions for a growth temperature of 2573 K and system pressure of up to 3500 Pa. Pons et al. [4,5] calculated the electromagnetic field and temperature distribution, and found that the predicted temperatures for the seed and powder surface (2920 K and 3020 K) are much larger than the external temperatures measured at the top and bottom of the crucible (2390 K and 2500 K), while the maximum temperature of the insulation foam on its periphery is about 1000 K. The total pressure is around 30 Torr (4000 Pa) and the growth rate is 1.55 mm/h. Egorov et al. [6] modeled the global heat transfer inside the system for SiC growth in a tantalum container. Müller et al. [7,8] calculated the temperature distributions in inductively heated SiC growth reactors at temperatures of 2373–2673 K, and found that the temperatures in the powder are highly nonuniform, and predicted radial variations of 30–50 K along the powder surface. Karpov et al. [9] predicted growth rate in the growth of SiC in a tantalum container.

Ma et al. [10] performed an order-of-magnitude analysis of parameters in the SiC PVT growth, and used a one-dimensional network model and two-dimensional finite-volume model to predict the temperature distribution in a 75 mm growth system. Chen and co-workers [11–15] proposed a kinetics model for SiC vapor growth, predicted growth rate as a function of temperature, temperature gradient, and inert gas pressure, and obtained a growth rate profile across the seed surface from the temperature distribution in a 75 mm growth system. The powder charge is modeled as a solid matrix with a porosity and an effective conductivity that accounts for both the conduction and radiation in the powder.

Selder et al. [16] introduced a modeling approach for the simulation of heat and mass transfer during SiC bulk crystal growth and compared calculated results with the experimental data. Råback et al. [17–19] presented a model for the growth rate of the SiC sublimation process and estimated the parametric dependencies of the growth rate.

7.2 Modeling of Heat and Mass Transfer and Growth Rate

7.2.1 Growth process

A typical SiC growth system consists of an RF copper coil, quartz tube, graphite susceptor, graphite insulation, crucible, and some other components (Fig. 7.1). The graphite crucible is filled with a SiC powder charge, and a SiC seed is placed on the bottom of the lid of the crucible as shown in Fig. 7.1. The seed is cooled by heat loss through the top hole. The SiC powder charge is heated by RF induction heating that is generated by passing through the coil a radio-frequency current. The current required depends on the number of turns of coil and distance between the coil and the susceptor. The time-harmonic electromagnetic field induces eddy currents in the graphite susceptor that has a high electrical conductivity, and heat is generated in a thin (skin) layer of the susceptor. Sometimes a double-walled water-cooled quartz tube is used to seal the system [5,20,21] that enables us to reduce the thickness of the insulation, and enhance the coupling between the coil and the susceptor. The system is maintained at a very low pressure using a vacuum pump, and an argon container is linked to the end plate to control the pressure inside the quartz tube and create an inert gas environment. Two holes are bored in the graphite insulation above and below the crucible to monitor the temperatures of the seed and the charge using pyrometers. The temperature inside the top hole is controlled, which is lower than the seed temperature.

The growth process consists of several steps [22,23]: (a) *vacuum degassing stage*—a low gas pressure (10^{-3} Pa) and an evacuation temperature of $1073\text{ K} < T < 1273\text{ K}$ are applied to reduce the background nitrogen contamination; (b) *pre-heating stage*—temperature is gradually increased in high-purity argon environment (about 10^5 Pa) to the growth temperature and stabilized to achieve an optimum ΔT between the source and the seed; (c) *growth stage*—a programmed

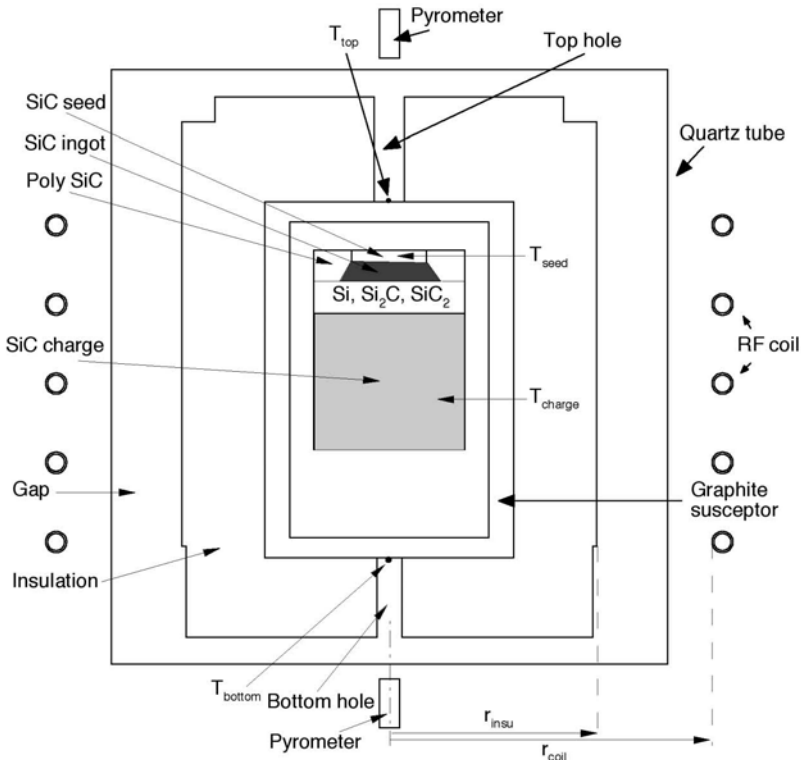


Fig. 7.1. Schematic of an RF-heated furnace for the growth of single SiC crystals by PVT

pressure reduction is used to achieve low-defect nucleation and uniform epitaxy on the oriented seed crystal, and argon pressure is decreased to $10 < p < 2.66 \times 10^4$ Pa, and boule growth begins; and (d) *cooling stage*—the temperature is reduced. The temperature difference between the charge and the seed during the growth stage depends on the system configuration. According to Lilov [24], SiC dissociates completely into liquid silicon and solid carbon at $T > 3150$ K and therefore the growth temperature must lie below 3150 K. Various growth systems used by industry employ different growth temperatures depending on the temperature gradient in the growth chamber; a higher growth temperature is usually associated with a lower temperature gradient and a higher pressure. Although a model can account for various stages of the growth as outlined above, those reported in the literature have thus far primarily focused on step (c), the growth stage.

7.2.2 Flow and heat transfer parameters

The flow in a silicon carbide growth system is induced by: (a) the buoyancy force that is produced by the variations in temperature on crucible walls, and (b) the ad-

vection due to sublimation of SiC charge. The flow is essential to bring the SiC vapor and other species from the charge at the bottom to the growth surface at the top. The effect of buoyancy can be determined by the Grashof number,

$$Gr = \frac{\rho^2 g \beta D_c^3 \Delta T}{\mu^2} = \frac{\rho^2 g D_c^3}{\mu^2} \frac{\Delta T}{T}, \quad (7.1)$$

where the isobaric expansion coefficient, $\beta = \frac{1}{\rho} \frac{\partial \rho}{\partial T} = \frac{1}{T}$, if the argon-vapor mixture is considered as an ideal gas, and the Prandtl number,

$$Pr = \frac{\mu c_p}{k} \quad (7.2)$$

For a typical process condition of 3×10^4 Pa as the system pressure, 2900 K as the growth temperature, 30 K as the temperature difference (ΔT), the Prandtl number is obtained as 0.66 while the Grashof number is estimated to be 3 and 24 for crucible (inner) diameters of 50 mm and 100 mm, respectively. These values of the Grashof number are far below the threshold at which natural convection can be considered appreciable [4,10]. Even though in the case of a cylinder heated on the outer wall natural convection can occur at any Rayleigh number, Ra must be above 1707 for the onset of convection in an enclosure heated from below and cooled at the top (Bénard convection). The present configuration does not conform to any of these two classical cases. It is still reasonable to consider that buoyancy flow plays a far less important role than radiative and conductive heat transfer in a SiC growth system. However, in the next generation systems for large diameter SiC crystal growth, the Grashof number may not remain this small. For example, if the crucible (inner) height becomes 500 mm, Gr based on height will increase to about 3000 leading to appreciable buoyancy effects. Even though $Gr = 3000$ is not very large, the complex temperature boundary conditions can lead to complex flows, a combination of Bénard convection and vertical boundary layer flows. For such convective flow analysis, a model based on fluid-superposed porous layer theory as outlined by Prasad [25] and Chen et al. [26,27] can be used.

The Stefan flow on the other hand is caused by volumetric expansion of silicon carbide species due to dissolving and sublimation of the charge. The species mainly include gaseous Si, Si₂C, SiC₂, and SiC. The partial pressure of each species in the charge reaches an equilibrium value, which is a strong function of temperature. The transport of species from the charge to seed is determined by the Stefan flow and growth kinetics. The Stefan flow is therefore very important for mass transfer and growth rate.

If leakage and diffusion are neglected, the advective velocity of SiC vapor flow can be estimated from,

$$U = \rho_{SiC} G_{SiC} A_{SiC} / \alpha \rho_{gas} A_{gas}, \quad (7.3)$$

where the vapor density is $\rho_{gas} = pM/RT$, A_{SiC} is the growth area, and α is the sticking coefficient. This leads to the mass Péclet number,

$$Pe = UL/D, \quad (7.4)$$

where the diffusion coefficient can be obtained from $D = D_0(T/T_0)^n (p_0/p)$ [28], with $D_0 = 5 \times 10^{-6} \sim 2 \times 10^{-4} \text{ m}^2/\text{s}$, $n = 1.8$, $T_0 = 273 \text{ K}$, and $p_0 = 1 \text{ atm}$. Using $D_0 = 5 \times 10^{-6} \sim 1 \times 10^{-5} \text{ m}^2/\text{s}$ and $L = 50 \text{ mm}$, Chen et al. [13] have calculated the advective velocity, diffusion coefficient, density, and Péclet number for two operating conditions, one with a low growth temperature and low gas pressure and another with a high growth temperature and high gas pressure (Table 7.1).

If the buoyancy effects are neglected, the heat transfer in the SiC growth system will depend on the latent heat released during the deposition (or absorbed during the sublimation), heat transfer by Stefan flow (advective mass transport), and radiative heat transfer inside the growth system. These three heat transfer quantities can be estimated from,

$$Q_{\text{latent}} = \rho_{\text{SiC}} G_{\text{SiC}} A_{\text{SiC}} \Delta H_{\text{vs}}, \quad (7.5a)$$

$$Q_{\text{Stefan}} = \rho_{\text{SiC}} G_{\text{SiC}} A_{\text{SiC}} c_p \Delta T, \quad (7.5b)$$

$$Q_{\text{radi}} = \varepsilon A_{\text{SiC}} \sigma (T_{\text{charge}}^4 - T_{\text{seed}}^4) \quad (7.5c)$$

For a growth rate of $G_{\text{SiC}} = 1 \text{ mm/h}$, a diameter of 50 mm, $\Delta T = 30 \text{ K}$, $\varepsilon = 0.8$, and $T_{\text{seed}} = 2900 \text{ K}$, Q_{latent} , Q_{Stefan} , and Q_{radi} are estimated to be 0.01 W, 0.1 W, and 1000 W, respectively. It is therefore reasonable to neglect the latent heat released and heat transfer by Stefan flow while calculating the temperature distribution. It should, however, be noted that the temperature distribution inside the crucible will depend on the temperature conditions on the inner surfaces of the crucible and conduction and radiation in the SiC charge. As shown later, these heat transfer mechanisms can be easily included in a physics-based mathematical model for the system. Another important issue to keep in mind is the effect of latent heat release on the growth phenomena since a small change in temperature gradient (due to condensation) in the vicinity of the growth interface can significantly affect the growth behaviors. It has also been commonly assumed that the chemical reaction, both exothermic and endothermic, does not contribute much to the heat transfer and temperature distribution [4].

Table 7.1. Advective flow parameters for two different operating conditions [13]

	U [m/s]	D [m ² /s]	ρ [kg/m ³]	α	Pe
2600 K, 20 Torr (2666 Pa)	0.178	2.16×10^{-2}	4.92×10^{-3}	1	0.41
2900 K, 200 Torr (26,666 Pa)	0.0199	3.98×10^{-4}	4.41×10^{-2}	1	2.5

7.2.3 One-dimensional network model

As a first approximation, a heat resistance network analysis can be very useful in developing a basic understanding of the thermal behavior of a SiC growth system [10]. In the absence of convective heat transfer, the thermal field in a SiC growth system is dominated by the interplay of conduction and radiation within and between the different components.

A typical SiC system, as shown schematically in Fig. 7.2(a), can be easily represented by a heat resistance network (Fig. 7.2b). For this simple analysis, the inner surfaces of the upper and lower graphite susceptors can be treated at fixed temperatures, T_a and T_b . The heat resistances for conduction, convection, and radiation are given by

$$R_{cond} = \frac{L}{kA}, \quad R_{conv} = \frac{1}{hA}, \quad (7.6a, b)$$

$$R_{radi} = \frac{1}{\epsilon\sigma(T_1 + T_2)(T_1^2 + T_2^2)A} \approx \frac{1}{4\epsilon\sigma T_{av}^3 A}, \quad (7.6c)$$

where L is the thickness, k is the thermal conductivity, A is the area, h is the heat transfer coefficient, ϵ is emissivity, σ is the Stefan-Boltzmann constant, and T_{av} is the average temperature of two surfaces under consideration, $T_{av} = \frac{T_1 + T_2}{2}$, where T_1 and T_2 are the temperatures of the two surfaces.

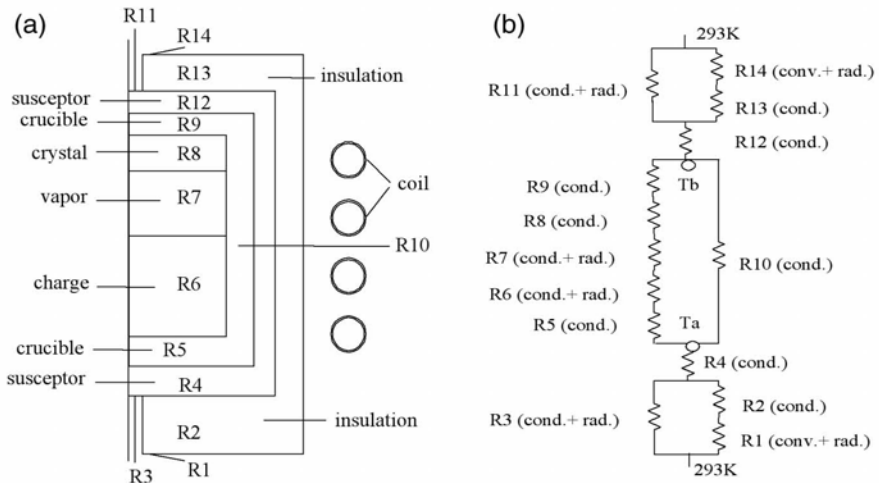


Fig. 7.2. (a) Schematic and (b) thermal network of a SiC growth system (cond. — conduction, conv. — convection, rad. — radiation) [10]

It is necessary to consider both conduction and radiation from particle to particle to account for the heat transfer within the SiC charge. Several correlations for

the effective heat transfer coefficient due to radiation in a porous matrix have been reported in the literature [29]. One of these correlations valid for spherical particles is given by Kansa et al. [30],

$$h_{radi, porous} = \frac{8}{3} \varepsilon \varepsilon_p \sigma 4 T_{av}^3 d_p \quad (7.7)$$

where ε_p is the porosity for a randomly packed spherical bed, T_{av} is the average temperature of the charge, and d_p is the average particle diameter.

Figure 7.2(b) shows the thermal network diagram for a typical SiC growth system using the electrical circuit analogy. The resistances in various components of a typical growth system have been calculated by Ma et al. [10], which give a good indication of the magnitude of heat transfer through various components.

7.2.4 Thermal transport model

In developing a thermal transport model for SiC growth, it is important to consider the electromagnetic field generated by RF heating, heat generation, conduction and radiation in various parts of the growth system, and appropriate boundary conditions. The effects of convective heat transfer as discussed in Section 7.2.2 have been neglected by almost all investigators thus far. However, they may need to be considered as the PVT growth system is upscaled. A short discription of the major components of the model is given below.

Calculation of electromagnetic field

The electromagnetic field produced by an RF induction coil can be calculated by using Maxwell equations, and the generated heat power in the graphite susceptor can be predicted by low frequency eddy current theory ($f < 1$ MHz). For the present problem, the Maxwell equations can be simplified using the quasi-steady approximation. It is commonly assumed that the current in the coil is time-harmonic, and heat in the graphite susceptor is generated only by eddy currents [31]. Under such conditions, the magnetic flux density can be expressed as the curl of a magnetic potential vector, $\mathbf{B} = \nabla \times \mathbf{A}$, and the Maxwell equations can be written in terms of the vector potential, \mathbf{A} , as,

$$\nabla \times \left(\frac{1}{\mu_m} \nabla \times \mathbf{A} \right) + \varepsilon_m \frac{\partial^2 \mathbf{A}}{\partial t^2} + \sigma_c \frac{\partial \mathbf{A}}{\partial t} = \mathbf{J}_{coil} \quad (7.8)$$

Assuming that the coil and the electromagnetic field are axi-symmetric, such that both \mathbf{A} and the current density, \mathbf{J}_{coil} , have only one angular component each with an exponential form,

$$\mathbf{A} = \begin{Bmatrix} 0 \\ A_0 e^{i\alpha z} + cc \\ 0 \end{Bmatrix}, \quad \text{and} \quad \mathbf{J}_{coil} = \begin{Bmatrix} 0 \\ J_0 e^{i\alpha z} + cc \\ 0 \end{Bmatrix}, \quad (7.9)$$

where i is the complex unit, and cc denotes the complex conjugate. The final equation for \mathbf{A} is obtained by substituting Eqs. (7.9) in Eq. (7.8),

$$\left(\frac{\partial^2}{\partial r^2} + \frac{1}{r} \frac{\partial}{\partial r} - \frac{1}{r^2} + \frac{\partial^2}{\partial z^2}\right)\left(\frac{A_0}{\mu_m}\right) + \varepsilon_m \omega^2 A_0 - i\omega\sigma_c A_0 = -J_0 \tag{7.10}$$

In an axisymmetric system, the following boundary conditions can be used to solve equation (7.10),

$$A_0 = 0, \quad \text{at } r = 0, \text{ and } (r^2 + z^2) \rightarrow \infty \tag{7.11}$$

After solving equations (7.10) for A_0 , the generated heat power by eddy currents in the graphite susceptor can be obtained from [31,32],

$$q''_{eddy} = \frac{1}{2} \sigma_c \omega^2 A_0 A_0^* \tag{7.12}$$

where $*$ denotes the complex conjugate. Further details of the electromagnetic field formulation can be found in Bíró and Preis [31], Pons et al. [4] and Chen et al. [13].

Energy transport

In the absence of convective flows, temperature distribution in the growth system can be calculated using an energy transport equation,

$$(\rho c_p)_{eff} \frac{\partial T}{\partial t} = \nabla \cdot (k_{eff} \nabla T) + q'''_{eddy} - (q''_{radi} + q''_{insu}) \delta A / \delta V, \tag{7.13}$$

where q''_{radi} is the radiative heat flux normal to the inner surface of the radiation enclosure, and δA and δV are the area over a finite-volume face and finite volume near the gas/solid interface (see Fig. 7.3a), respectively. In Eq. (7.13), q''_{insu} is the radiative heat flux on the outer surface of the insulation,

$$q''_{insu} = \varepsilon_{eff} \sigma (T^4 - T_\infty^4), \tag{7.14}$$

where ε_{eff} is effective emissivity. For surfaces exposed to the ambient air, the effective emissivity can be chosen as that of the material, $\varepsilon_{eff} = \varepsilon_{insu}$. On the other hand, for surfaces exposed to the copper coil, the effective emissivity can be calculated from [33],

$$\varepsilon_{eff} = \frac{1}{1/\varepsilon_{insu} + r_{insu}/r_{coil}(1/\varepsilon_{coil} - 1)}, \tag{7.15}$$

so that the reflection of energy by the inner surface of the copper coil can be included in the formulation [13]. Here ε_{insu} and ε_{coil} are the emissivities of graphite insulation and copper coil, respectively, and r_{insu} and r_{coil} are the radii of the outer surface of insulation and inner surface of coil (as shown in Fig. 7.1).

Suitable boundary conditions must be used to solve Eq. (7.13). The computational domain for the energy equation is set as inside the quartz tube (Fig. 7.1), and the temperature on the quartz tube is set as 293 K. If it can be assumed that the three-dimensional effects are negligible, the symmetric condition

$$\frac{\partial T}{\partial r} = 0, \quad \text{at } r = 0 \quad (7.16)$$

can be used at the central axis. This condition is certainly applicable for good quality, slow growth as is evident from the symmetric growth striations reported in the literature (Selder et al., [16]). However, three-dimensional effects can become important if the growth system becomes larger, the material uniformity cannot be maintained, and/or there are fluctuations in power supply.

The thermal properties of various components (i.e., graphite susceptor, graphite insulation, crucible, and SiC charge) in the growth system should be considered as a function of temperature. Although most of the modeling studies consider SiC charge as a solid, Chen et al. [11,13] have considered the porosity of the charge and radiation from particle-to-particle. The effective heat capacity of the SiC powder charge can be estimated using the mixture theory,

$$(\rho c_p)_{eff} = (1 - \epsilon_p) (\rho c_p)_{SiC} + \epsilon_p (\rho c_p)_{gas}, \quad (7.17)$$

whereas the thermal conductivity can be obtained by considering the conduction-radiation heat transfer among the particles [30],

$$k_{eff} = (1 - \epsilon_p) k_{SiC} + \epsilon_p (k_{gas} + \frac{8}{3} \epsilon \sigma 4 T^3 d_p) \quad (7.18)$$

Many other correlations for k_{eff} can be found in Kaviany [29].

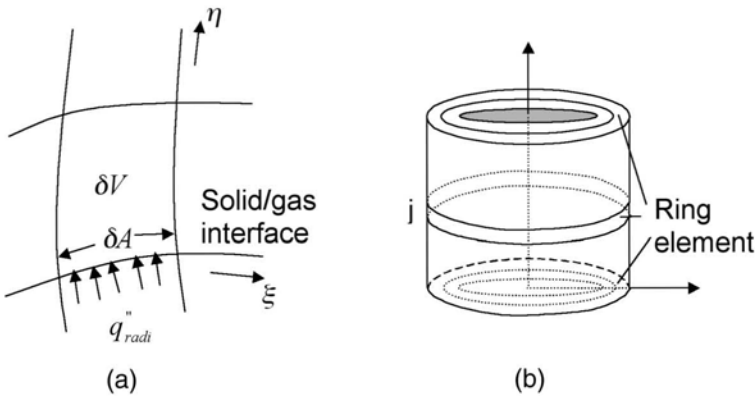


Fig. 7.3. (a) Heat flux on the radiation surface and curvilinear grid system, and (b) schematic of ring elements on radiative surfaces. The ring elements coincide with the finite volume grids for conduction calculation [13].

Radiative heat transfer

Radiation is the dominant mode of heat transfer inside the crucible and requires special attention while developing a model for the SiC growth.

Pons et al. [4] have not considered the wall-to-wall radiation in the gas region, but assumed an apparent conductivity, greatly simplifying the energy equation [13] in their model. On the other hand, Hoffman et al. [2], Egorov et al. [6], and Chen and co-workers [13] have considered grid-to-grid gray-diffuse radiation together with appropriate view factors. This approach requires that all radiation surfaces be divided into grids and radiation view factors between each pair of these grids be calculated. In two-dimensional calculations, this, however, reduces to circular rings as shown in Fig. 7.3(b). It is also important that radiation heat transfer is calculated not only in the growth chamber but also in the bottom and top holes, as emphasized by Chen et al. [13].

Here, we describe the radiation model as adopted by Chen and co-workers [13], which is based on the method of discrete exchange factors (DEF) [34–36]. It is assumed that the radiation surfaces are gray, diffusely emitting and reflecting, and opaque. The radiation surface is broken into a number of rings each with uniform properties, and view factors between each pair of rings are calculated using appropriate relations [37]. The absorptivity α_j is assumed to be equal to the emissivity ϵ_j in each ring. The integral equation for radiative heat transfer is then obtained as [33],

$$\frac{q_{radi j}}{\epsilon_j} - \sum_{k=1}^N F_{j,k} \frac{1-\epsilon_k}{\epsilon_k} q_{radi k} = \sigma T_j^4 - \sum_{k=1}^N F_{j,k} \sigma T_k^4 \tag{7.19}$$

where $F_{j,k}$ is the view factor from ring j to ring k [37]. The above equations can be solved numerically by writing,

$$(A_{jk}) \cdot (q''_{radi k}) = (B_{jk}) \cdot (\sigma T_k^4), \tag{7.20}$$

where $A_{jk} = \frac{\delta_{jk}}{\epsilon_k} - F_{j,k} \frac{1-\epsilon_k}{\epsilon_k}$, $B_{jk} = \delta_{jk} - F_{j,k}$, and $\delta_{j,k}$ is Kronecker's delta. The radiative heat flux can be written in the tensor form as,

$$q''_{radi j} = (\mathbf{A}^{-1} \cdot \mathbf{B})_{jk} \cdot (\sigma T_k^4) \tag{7.21}$$

The radiative heat flux is used as a source term in each computational element when solving the energy equation (7.13).

It should be noted that the spectral (wavelength dependence) behavior of radiation heat transfer is not accounted for in the above model although the radiative properties of SiC surfaces may be spectral. Secondly, the decomposition of SiC and accumulation/deposition of carbon particles can change the radiative properties inside the crucible significantly as the growth proceeds. Finally, the chemical species in the gas/vapor region may also participate in heat transfer by volumetric radiation. Since nothing is known of the participating behavior of any species other than carbon, this is a difficult task at present.

7.2.5 Mass transport model

Once the temperature field inside the crucible is obtained, a mass transport model can be used to calculate the distribution of species in the system. Hofmann et al.

[2], Pons et al. [4], and Chen et al. [11–14] have all considered the transport of species with various degrees of complexity. Since sublimation of SiC particles is associated with decomposition in various species and chemical reactions, a thermodynamic analysis is necessary for the calculations of partial pressures and species transport.

Equilibrium processes

Mass spectrometric investigations conducted by Drowart and De Maria [38] have shown that the basic components of the evaporation of SiC are Si, Si₂C, SiC₂, and SiC. The content of the other components of evaporation (Si₂, C, C₂, C₃) in the vapor is insignificant and can be neglected. The following reactions are considered [38,24]:



The equilibrium constant of a chemical reaction can be calculated from,

$$K_i = \exp(-\Delta G_T^0 / RT). \quad (7.27)$$

The change in isobaric-isothermal Gibbs-function ΔG_T^0 for the reaction is given by,

$$\Delta G_T^0 = \sum_{\text{prod}} \nu_i (\Delta h_{f,298}^0 + h_T - h_{298} - Ts_T^0) - \sum_{\text{reac}} \nu_i (\Delta h_{f,298}^0 + h_T - h_{298} - Ts_T^0), \quad (7.28)$$

where $\Delta h_{f,298}^0$ is the heat of formation, ν_i is the stoichiometric coefficient, and h_T is the enthalpy of the reacting species.

Lilov [24] has conducted a thermodynamic study on the partial pressure of each species. Up to 2546 K the pressure of silicon vapor above the silicon carbide is determined only by reaction (7.23) because the pressure of silicon ensured by (7.25) is less than the pressure of Si due to reaction (7.23). Therefore, in the temperature interval of 1500–2546 K, both reactions (7.23) and (7.25) take place simultaneously and the partial pressures of Si and SiC₂ are determined by, $P_{\text{Si}} = K_2$, $P_{\text{SiC}_2} = K_4 / P_{\text{Si}}$, respectively. In Table 7.2, the underlined values represent the real pressures at equilibrium; from 1500–2546 K, the silicon partial pressures due to reaction (7.23) are the real ones. The pressures of silicon vapor under these conditions are less than the pressure at saturated conditions, and therefore, in this temperature interval the dissociation takes place in the gas phase. As a result of reactions (7.23) and (7.25), carbon gradually accumulates in the silicon carbide charge.

At temperatures above 2546 K, the partial pressure of silicon due to reaction (7.25) becomes greater than that by reaction (7.23). Therefore, reaction (7.23) cannot take place ($\Delta G_T^0 > 0$) and the pressure of silicon above SiC is regulated only by reaction (7.25). In Table 7.2, the values due to reaction (7.25) are underlined from 2546–2900 K, which represent the real ones. According to Lilov [24], above 2546 K, silicon is separated in the form of the solution saturated with carbon. In this case, the activity of Si in the solution is equal to the equilibrium constant of reaction (7.22), $K_1 = a_{Si}$. The partial pressure of silicon can be obtained according to Henry's law $P_{Si} = P_{Si}^{Sat} a_{Si}$ and the partial pressure of SiC₂ can be determined from the equation, $P_{SiC_2} = \frac{K_4}{K_1 P_{Si}^{sat}}$.

Table 7.2. Partial pressures of Si and SiC₂ (Pa) (Lilov [24])

T [K]	$P_{Si}^{Sat} a_{Si}$	P_{Si} reaction (7.23)	P_{Si} reaction (7.25)	P_{SiC_2} reaction (7.25)
1500	3.5×10^{-5}	<u>3.0×10^{-6}</u>	3.9×10^{-7}	5.1×10^{-8}
1600	4.4×10^{-4}	<u>4.2×10^{-5}</u>	7.6×10^{-6}	1.4×10^{-6}
1700	4.0×10^{-3}	<u>4.3×10^{-4}</u>	1.0×10^{-4}	2.5×10^{-5}
1800	2.5×10^{-2}	<u>3.4×10^{-3}</u>	1.0×10^{-3}	3.2×10^{-4}
1900	0.11	<u>2.2×10^{-2}</u>	8.3×10^{-3}	3.2×10^{-3}
2000	0.47	<u>0.11</u>	5.3×10^{-2}	2.5×10^{-2}
2100	1.8	<u>0.52</u>	0.28	0.16
2200	5.8	<u>2.0</u>	1.3	0.84
2300	17	<u>7.0</u>	5.2	3.8
2400	47	<u>22</u>	18	15
2500	116	<u>61</u>	58	56
2546	173	<u>97</u>	96	96
2600	270	161	<u>170</u>	170
2700	588	391	<u>456</u>	456
2800	1210	890	<u>1138</u>	1138
2900	<u>2366</u>	1914	2659	2659
3000	<u>4419</u>	3904	5855	5855
3100	<u>7922</u>	7604	12250	12250
3150	<u>10477</u>	10477	17418	17418

At temperatures above 2900 K, the partial pressure of Si determined by the equilibrium constant of reaction (7.25) becomes more than the pressure of silicon saturated vapor and therefore the dissociation of SiC takes place in the condensed phase accompanied by the separation of liquid silicon. In Table 7.2, these values are underlined in the column $P_{Si} = P_{Si}^{Sat} a_{Si}$, that are obtained using Henry's law.

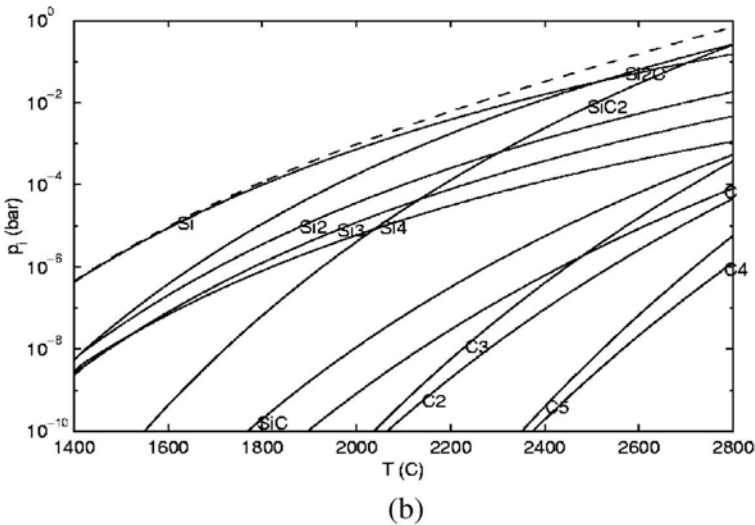
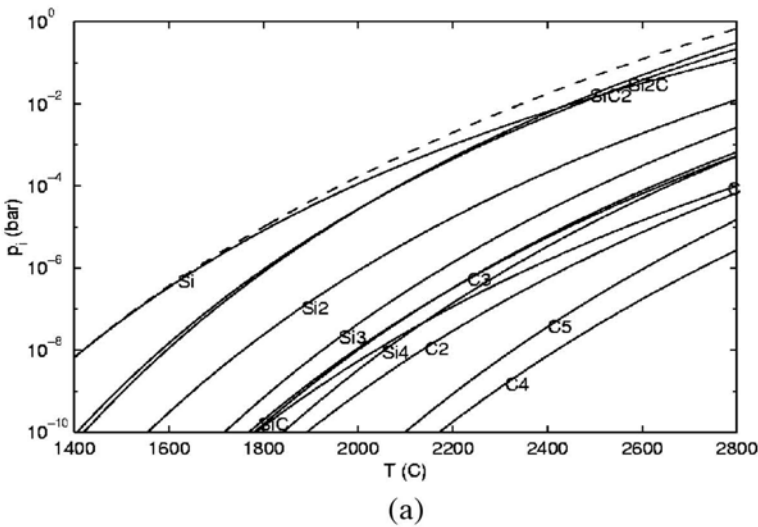


Fig. 7.4. Equilibrium partial pressures for various species in a Si-C system assuming (a) condensed SiC and carbon, (b) condensed SiC and silicon. The dashed line is the total pressure [19].

At 3150 K, $K_1 = a_{Si} = 1$ and $P_{SiC_2} = K_4/P_{Si}^{Sat}$, the solution of C in Si becomes mutually saturated. At $T > 3150$ K, ΔG_T^0 of reaction (7.22) is less than zero, and therefore, SiC under these conditions dissociates completely. Hence, 3150 K is the limiting temperature for the existence of SiC in the condensed phase.

Figure 7.4(a) shows the equilibrium pressures of a Si-C system at constant pressure. The gaseous species include C, C₂, C₃, C₄, Si, Si₂, Si₃, SiC, SiC₂, and Si₂C, and the condensed species are SiC and carbon. Among individual species gaseous silicon dominates at temperatures below 2673 K, while SiC₂ and Si₂C have larger partial pressures at higher temperatures. Figure 7.4(b) shows the system with condensed SiC and silicon. Since liquid silicon is energetically less favorable, it only occurs when there is excess of silicon and no carbon source. The partial pressures are higher as shown in Fig. 7.4(b).

Growth kinetics

As explained above, reaction (7.25) is considered most important for the deposition process (Lilov [24]). The vapor pressure of silicon is larger than that of SiC₂ at temperatures below 2546 K, and less than that of SiC₂ at temperatures above 2900 K. The rate-determining species, A, is therefore chosen as SiC₂ at $T < 2546$ K, and as Si at $T > 2900$ K. A can be either of the two at $2546 \text{ K} < T < 2900 \text{ K}$, since they have the same vapor pressure (Table 7.2). Introducing z' coordinate, which is set as 0 at the charge and L at the seed, vapor pressures of various species can be considered as a function of z' .

To develop a growth kinetics model, Chen et al. [11,13] have assumed that the species transport rate near the seed is proportional to supersaturation of A, such that [39],

$$J_A = \chi_A (p_A(L) - p_A^*(L)), \quad (7.29)$$

where p_A^* is the equilibrium vapor pressure of A, $\chi_A = \frac{1}{\sqrt{2\pi M_A RT}}$. If SiC₂ and Si vapors can be assumed to have an identical transport rate, i.e., $J_{SiC_2} = J_{Si}$, the growth rate of SiC crystal will become,

$$G_{SiC} = \frac{2M_{SiC}}{\rho_{SiC}} \chi_A [p_A(L) - p_A^*(L)] \quad (7.30)$$

A multiple 2 is introduced on the right side of Eq. (7.30) since one SiC₂ molecule and one Si molecule form 2 SiC molecules.

Assuming that advective velocities of the species SiC₂ and Si are the same, the distribution of vapor pressure can be obtained from a one-dimensional mass transfer equation for Stefan flow as,

$$p_{SiC_2}(z') + p_{Si}(z') = p - [p - p_{SiC_2}(0) - p_{Si}(0)] \exp(Pe \cdot z'/L) \quad (7.31)$$

The advective velocity, U , in Pe can be expressed as a function of transport rate of SiC₂ and Si,

$$U = J_{SiC} RT/p = 2\chi_A (p_A(L) - p_A^*(L))RT/p \quad (7.32)$$

From the above equation, one can obtain,

$$p_A(L) = p_A^*(L) + Up/(2\chi_A RT) \quad (7.33)$$

If Si_2C and Si can be assumed to have an identical vapor pressure in the growth chamber, equation (7.31) will reduce to,

$$U = D/L \ln((p - 2p_A(L))/(p - 2p_A(0))) \quad (7.34)$$

Even if there exists a difference between the equilibrium vapor pressures of the two species at the charge, the above equation is still valid.

Furthermore, if the vapor pressure at the source is assumed to be the same as the equilibrium vapor pressure, such that $p_A(0) = p_A^*(0)$, U and $p_A(L)$ can be obtained from Eqs. (7.33) and (7.34) by solving them in an iterative fashion. First, by setting U as 0, $p_A(L)$ can be calculated using (7.33), the advective velocity U can then be obtained by substituting (7.33) in (7.34), and finally the growth rate can be calculated using (7.30). Here the equilibrium vapor pressures of species Si, SiC, Si_2C , and SiC_2 can be taken from (7.24) as partly shown in Table 7.2.

7.2.6 Numerical method

The transport equations for electromagnetic field, heat transfer, and species transport can be solved by using a numerical scheme based on either finite element (Pons et al. [4]; Egorov et al. [6]) or finite volume method (Hofmann et al. [2]; Chen et al. [13]). Pons et al. [4] have used an FEM package “Flux-Expert”, which alternately solves the electromagnetic and thermal equations without an external iterative scheme. Once the temperature field is obtained, the mass transfer equations are solved in an uncoupled manner. The computer model developed by Hofmann et al. [2] uses the basic finite volume code FASTEST (developed at the University of Erlangen) that also employs multigrid techniques.

Chen and co-workers [13], on the other hand, have developed their computer model for SiC growth using MASTRAPP (Multizone Adaptive Scheme for Transport and Phase Change Processes). MASTRAPP employs high-resolution schemes for grid refinement and clustering for phase-change and moving boundary problems and has been extensively used for crystal growth modeling by Zhang et al. [40,41] and many others. MASTRAPP-based crystal growth simulations have been well tested against the experimental data, and the model is being used for a variety of industrial problems.

The integrated radiative heat transfer equations using the DEF method require special treatment. The coupling between the solvers of energy Eq. (7.13) and radiation Eq. (7.21) is obtained through nodal temperatures and heat fluxes in an iterative fashion. Refer to Chen et al. [13] and Naraghi et al. [34,35] for details on the solution scheme.

A suitable grid distribution with finer mesh in the regions of large temperature and species gradients needs to be used for accurate predictions. For example, Chen

et al. [13] have used a grid of 198×147 for most of their calculations (Fig. 7.5). Other investigators have also used very fine grids to perform the growth simulation [2,4,6]. Furthermore, since the electrical and thermal conductivities of the graphite susceptor strongly depend on the temperature (Table 7.3), the heat power generated in the graphite susceptor changes significantly with time. It is therefore necessary to use a small time step, e.g., 2 s for the transient calculations.

A typical solution procedure is adopted as follows: The electromagnetic field (Eq. 7.10) is solved to obtain the heat generated by induction heating (Eq. 7.12), which is added as a heat source term in the energy equation (Eq. 7.13) to obtain the temperature distribution solved together with Eq. (7.21). After obtaining the temperature field, mass transfer, and vapor species concentration, growth rate can be obtained using a one-dimensional mass transfer model coupled with a growth kinetics model (Section 7.2.5). The radial variation of growth rate is considered by taking into account the temperature variation in the radial direction. The model can therefore predict two-dimensional growth interface profile except that mass transfer and thermal coupling are not allowed in the lateral direction.

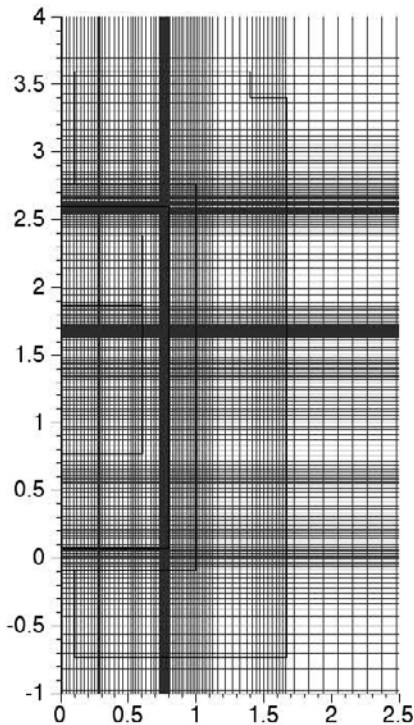


Fig. 7.5. Computational grids for finite volume method [13]. Grids are highly clustered in the regions of large temperature gradients.

Table 7.3. Material properties of various components [13]

Components	Electrical resistivity [Ωm] [500–3000°C]	Thermal conductivity [W/m/K] [500–3000°C]
Graphite	$0.8 \times 10^{-5} - 1 \times 10^{-5}$	50–20
Insulation	0.001	0.1–3
SiC crystal	1–0.001	100–50
SiC charge	1–0.001	20–5
Argon	—	0.03–0.05

7.3 Growth Simulation

7.3.1 Electromagnetic field and heat generation

In calculating the electromagnetic field, it is necessary to consider reasonable axial and radial distances in the computational domain such that most of the contours of magnetic potential vector, A , remain within the field of simulation. This is important for application of the boundary condition [11] and accurate calculation of the heat generated in the graphite susceptor. For example, Chen et al. [13] have taken the computational domain as $-20R_s < z < 20R_s$ and $r < 20R_s$ with the radius of the outer surface of the susceptor $R_s = 70$ mm for a 75 mm diameter crystal growth. In this case, the magnetic potential is diminished at a distance of $20R_s$ from the coil. Many times, it is necessary to perform calculations with different sizes of the computational domains to make an appropriate choice. Typical contours of magnetic vector potential for 5 turns of coil and current of 1200 A as obtained by Chen et al. [11] are shown in Fig. 7.6. The contour lines are concentrated along the outer portion of the graphite susceptor, and the contour of $(A_0)_{real} = 5 \times 10^{-5}$ Wb/m bends in the bottom and top portion of the susceptor and passes through the outer portion of the cylindrical susceptor. The graphite susceptor with a high conductivity serves as a shield, such that a large amount of energy is generated by eddy currents in the susceptor within a small skin depth, leaving less energy to be generated in the parts inside the susceptor (like the crucible, crystal, and charge).

The generated heat per unit volume for the case considered by Chen et al. [13] is shown in Fig. 7.7. Clearly, q''_{eddy} in the susceptor is several orders of magnitude larger than that in the SiC charge. The total amount of energy generated in the skin depth is much larger because of the volume for the same radial width becomes larger (second power) away from the central axis.

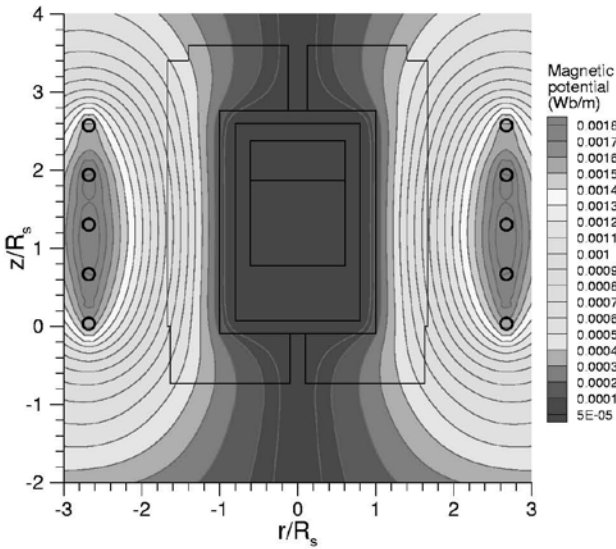


Fig. 7.6. magnetic potential contours, $(A_0)_{real}$, in a system with a coil of five turns, current of 1200 A and frequency of 10 kHz [13]. Only a portion of the computational domain, $r \leq 3R_s$, and $z \leq 4R_s$, is shown in this figure.

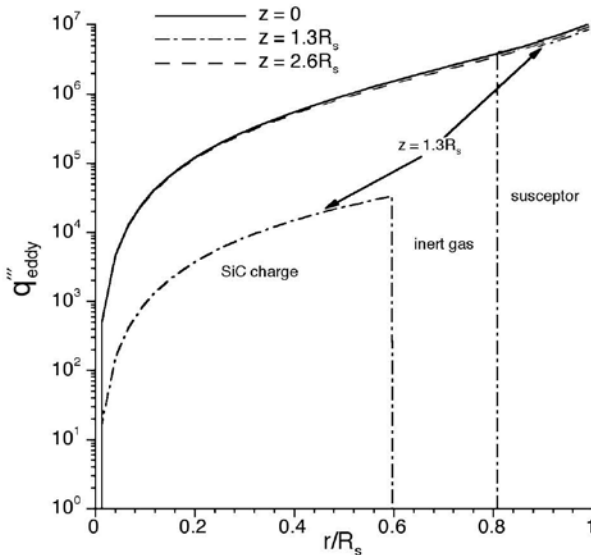


Fig. 7.7. Generated heat power, q'''_{eddy} , along the radial direction at different heights $z = 0, 1.3R_s$, and $2.6R_s$. The profile at $z = 1.3R_s$ has an inert gas gap between the powder charge and the susceptor [13].

7.3.2 Temperature field

Axial and radial temperature gradients are crucial for the successful growth and enlargement of SiC crystals. The SiC charge sublimates in the bottom of the container where the temperatures are higher than that in the seed, and saturation of the SiC vapor is thus produced in the SiC charge region. Since temperature on the seed surface is lower than that in the powder charge, the SiC vapor becomes supersaturated near the seed. The supersaturation of vapor species acts as a driving force for the deposition of SiC. The growth rate is therefore not only related to the temperature at the seed but also to the axial temperature gradient. Balkas et al. [42] have found that for a given seed temperature, the growth rate is a linear function of the temperature gradient in the growth chamber.

A positive radial temperature gradient at the seed surface can initiate an outward growth especially when a Lely seed is used to grow large size crystals, and depress the polytype growth on the graphite lid near the seed. The lower temperature at the center of the seed can ensure a higher growth rate on the seed than that on the graphite lid, because the supersaturation of the vapor species is higher on the seed.

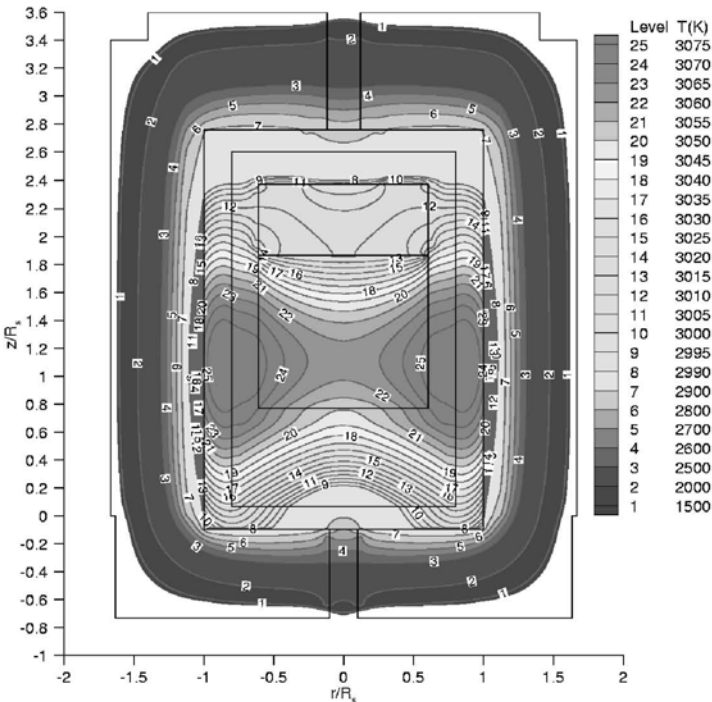


Fig. 7.8. Temperature contours for a system with a coil of five turns, current of 1200A, frequency of 10 kHz, and inert gas pressure of 26,666 Pa [11]

As shown by Chen and other investigators (Fig. 7.8), the maximum temperature exists in the graphite susceptor and always at the level of the geometric center of the induction coil. The positive temperature difference between the SiC charge and the seed allows the sublimation of SiC in the charge and deposition of SiC on the seed. A positive radial temperature gradient is also formed at the seed surface, which ensures an outward growth of the crystal [43]. As can be seen in Fig. 7.8, the temperature difference is less than 10 K at the seed surface. A proper radial temperature gradient at the seed has to be obtained to ensure a convex shape of the crystal interface and keep thermal stresses low in the crystal as well as low dislocation and micropipe densities.

Temperature distribution for different currents

The temperature distribution strongly depends on the power supply to the RF coil (see Fig. 7.9 for $I = 1000$ A and 1100 A and Fig. 7.8 for $I = 1200$ A). The magnitude of the temperature increases with the current. The growth temperature for the modified Lely method ranges from 1800 K to 2900 K as reported by Tairov and Tsvetkov [44,45]. The temperature distribution for the case of $I = 1200$ A corresponds to an upper limit growth condition for the modified Lely method in the system considered by Chen et al. [11]. The growth temperature depends on the temperature gradient that is related to the system design. For systems with a large temperature gradient, the growth temperatures are low (2100–2800 K) (Tairov and Tsvetkov [44,45]; Barrett et al. [22,23]; Hofmann et al. [2,3]; Müller et al. [7]),

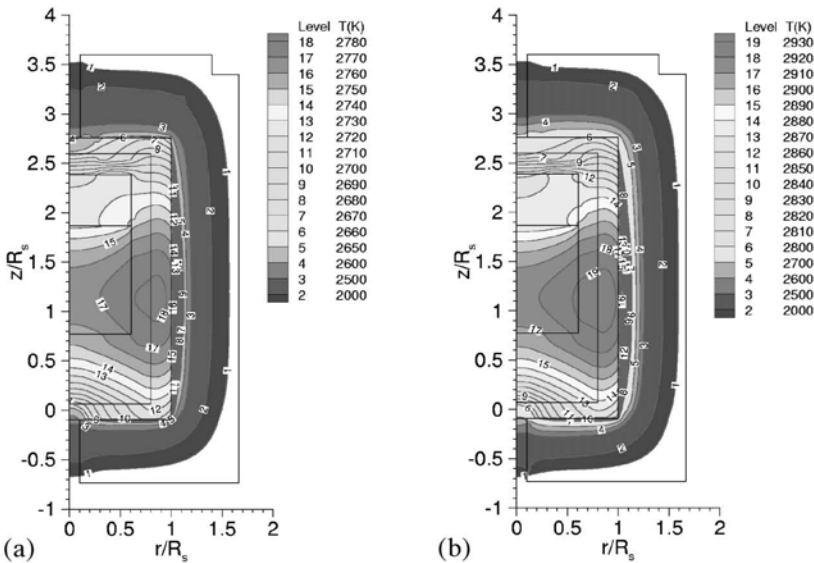


Fig. 7.9. Temperature distributions for different currents, (a) $I = 1000$ A, and (b) $I = 1100$ A [13]

while the growth temperatures range from 2700 K to 2900 K for systems that have smaller temperature gradients (Pons et al. [4,5]). For a low growth temperature, the inert gas pressure required is lower than that required for the high temperature growth.

As can be seen in Figs. 7.8 and 7.9, the temperature has a lower value at the center of the seed because of the cooling effect of the upper hole. The temperature increases along the radial direction on the seed surface, reaches a high value before the inner wall of the growth chamber. The lower temperature at the center of the seed can ensure an outward growth in radial direction, because of higher supersaturation of the vapor species at the center of the seed than that near the edge of the seed. Management of heat loss is crucial to control the growth of SiC crystals. However, it is not an easy task since thermal characteristics of the upper portion of the crucible change significantly as the growth proceeds and thermal resistance due to as-grown crystal increases. This task is made further difficult because currently the heat loss system used for PVT growth is passive.

Temperature for different coil positions

As is well known, by moving the induction coil upward/downward, the temperature difference between the charge and the seed can be easily changed. Figure 7.10 presents the temperature distributions for two different positions ($z_{coil} = 0, 10$ mm), while the temperature on the top of the crucible is kept at 2400 K. A PID (propor-

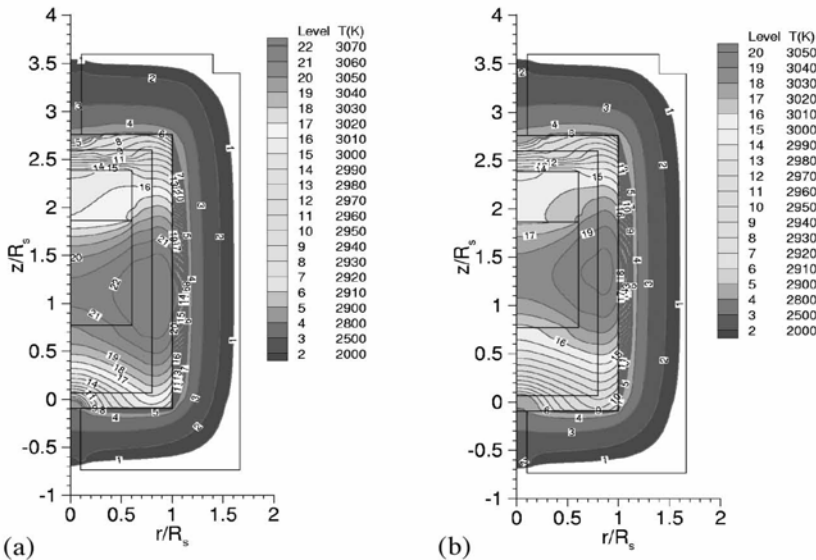


Fig. 7.10. Temperature distributions for different coil positions. The coil positions are (a) $z_{coil} = 0$ and (b) 0.01 m, respectively. The temperature on top of the crucible is kept at 2400 K for all the cases [13].

tional, integral, and derivative) control strategy has been used numerically to keep the temperature on top of the crucible constant by changing the current. With the coil moved up, the location of the maximum temperature in the charge moves up and the temperature difference between the charge and the seed decreases. In Figs. 7.10(a–b), the temperature difference between the charge and the seed, $T_{charge} - T_{seed}$, is a linear function of the coil position, z_{coil} . It should be noted that the temperature difference may not remain a linear function of the coil position if the coil is moved further up. Since the growth rate depends on the temperature difference between the charge and the seed (Eq. 7.35), the change in coil position will certainly affect the growth rate.

Temperature distribution for different ingot length

The temperature distribution also changes with the growth of crystal (Fig. 7.11). A large radial temperature gradient during the initial growth is important for enlargement of the crystal. After the ingot length of the crystal reaches 5 mm for the system considered here, the radial temperature gradient decreases (Figs. 7.11a–b). A small radial temperature gradient ensures a constant diameter of the crystal and relatively flat growth interface. More importantly, the thermal stress in as-grown crystal caused by temperature gradient decreases after the ingot length exceeds 5 mm. The axial temperature gradient in the ingot crystal is about 15 K/cm after the ingot of 25 mm has been grown (Figs. 7.11a–b).

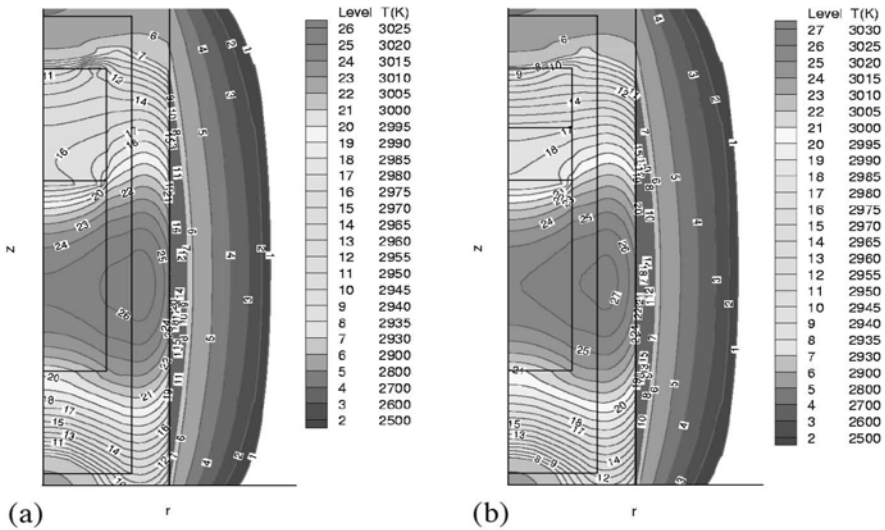


Fig. 7.11. Temperature distributions in a 35mm system when $I = 1350$ A, and ingot length (a) $L_{in} = 0$ and (b) $L_{in} = 25$ mm

Simulations reported by various investigators demonstrate that the temperature and temperature gradient inside the crucible are strong functions of system design, coil position, power supply, charge size, and ingot length. In addition, the temperature field continuously changes with an increase in the crystal length. The simulations reported in literature thus far give a good qualitative understanding of the effect of these parameters. However, simulations need to be performed every time a change in the design of the system is contemplated.

7.3.3 Growth rate calculations

The experimental data of Balkas et al. [42] indicate that the growth rate is a linear function of the temperature difference between the seed and source, ΔT , and an exponential function of the inverse of growth temperature with the following expression,

$$G_{SiC} = A(p, S, t) \Delta T \exp(-U/RT), \quad (7.35)$$

where U is the activation energy, $A(p, S, t)$ is a coefficient that depends on the inert gas pressure p , the effective source surface area S , and the duration of the growth, t . Balkas et al. [42] found that $U = 5.99 \times 10^5$ J/mol based on their experiment data.

Dependence of growth rate on growth temperature

Chen et al. [11] have investigated the dependence of growth rate on growth temperature for a range of axial temperature gradients. They have considered two cases, one with a small axial temperature gradient of 2 K/cm, and the other with a large axial temperature gradient of 20 K/cm. The distance between the seed and the charge surface is taken as 5 cm (2 inch).

The growth rate predicted by Chen et al. [11] shows an Arrhenius-type dependence on the growth temperature for inert gas pressures ranging from 666 Pa (5 Torr) to 40,000 Pa (300 Torr) (Fig. 7.12). The growth rate curves, however, deviate from the Arrhenius behavior when the temperature becomes too high. The Arrhenius-type growth curve for a given pressure shifts towards the low temperature region when the axial temperature gradient increases (compare Fig. 7.12b with 7.12a). The low temperature growth, that is usually associated with small-scale systems, therefore, requires a larger axial temperature gradient (Fig. 7.12b). The experimental data for 700 Pa argon pressure in Fig. 7.12b taken from Nakata et al. [46] support the prediction of Chen et al. [11] at low pressures.

In the growth rate–growth temperature map, the curves merge at high temperatures where the total vapor pressure of species is larger than the inert gas pressure (Fig. 7.12). In this case, if the crucible is not properly sealed, the pressure inside the crucible will fluctuate since the pressure inside the crucible will be higher than the system pressure. The fluctuation of pressure inside the crucible can cause unsteady species transport in the growth chamber by Stefan flow and growth fluctuations.

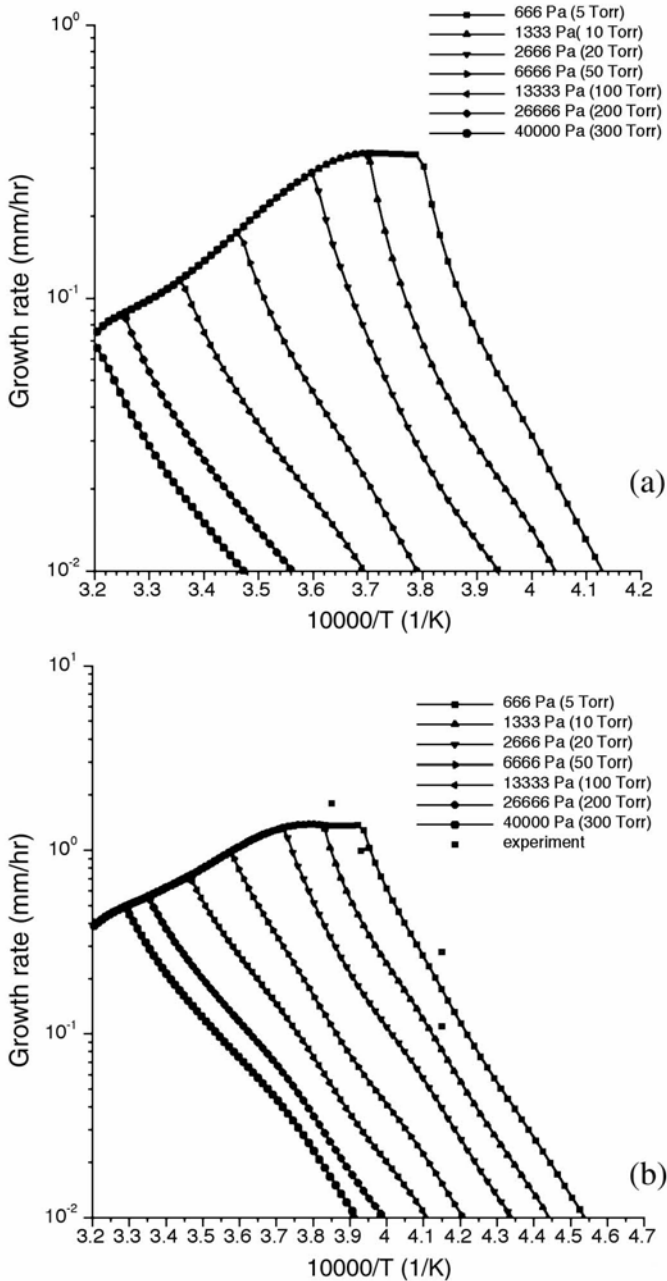


Fig. 7.12. Predicted growth rate versus inverse of growth temperature for different gas pressures for axial temperature gradients of (a) 2 K/cm and (b) 20 K/cm [11]. Experimental data for inert gas pressure of 700 Pa in (b) are taken from Nakata et al. [46]

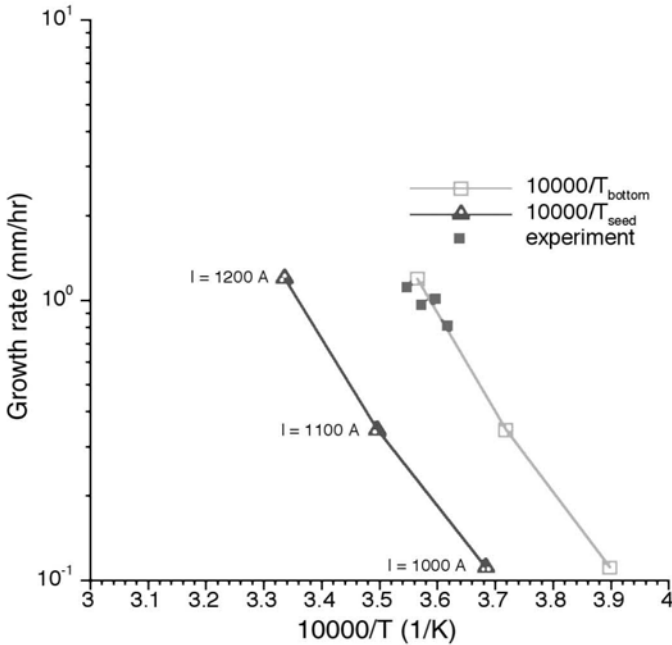


Fig. 7.13. Dependence of the growth rate on the seed temperature, T_{seed} , and the temperature on the bottom of the crucible, T_{bottom} in a 75 mm system [15]. The symbols from top to bottom correspond to currents of 1200 A, 1100 A, and 1000 A, respectively. Experimental data are taken from Balkas et al. [42]

The growth rate versus growth temperature curve in Fig. 7.13 is an Arrhenius-type curve and yields an activation energy of 5.5×10^5 J/mol, close to 5.44×10^5 J/mol as reported by Syväjärvi et al. [47]. The growth rate versus the inverse of the temperature at the bottom is also plotted in Fig. 7.13 and yields the same activation energy as the previous curve. The predicted growth rate at high pressures strongly depends on the diffusion coefficient D_0 , which is in the range of $5 \times 10^{-6} \sim 2 \times 10^{-4}$, taken as 1×10^{-5} m²/s by Chen et al. [13] to better correlate the prediction with experimental data of Balkas et al. [42].

Influence of inert gas pressure on growth rate

Chen et al. [11] have also examined the dependence of growth rate on inert gas pressure for the previous two cases. The growth rate curves become flat when the inert gas pressure is low. Although the growth rate of about 1 mm/h cannot be achieved for an axial temperature gradient of 2 K/cm (Fig. 7.12a), it is possible to obtain such a growth if the axial temperature gradient of 20 K/cm can be maintained at $T_{seed} > 2400$ K (Fig. 7.12b). From Fig. 7.14, it is evident that it is theoretically

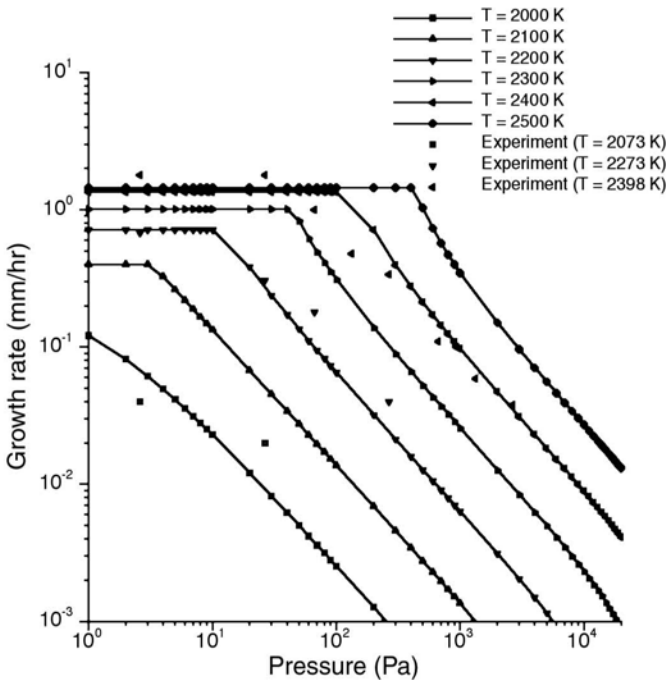


Fig. 7.14. Growth rate versus gas pressure for different growth temperatures at axial temperature gradient of 20 K/cm [11]

possible to grow SiC crystals at elevated inert gas pressures, such as 26,666 Pa (200 Torr), if the growth temperature is high. On the other hand, the growth at pressures less than 133 Pa (1 Torr) and temperatures below 2500 K is also possible, as shown in Fig. 7.14.

Figure 7.14 also shows that when the inert gas pressure is low, the growth rate does not increase as the pressure is decreased. This is because the total vapor pressure of SiC species is larger than the inert gas pressure. The growth is therefore unstable in this case, and a leak in the crucible will cause fluctuations in the pressure inside the crucible and unsteady growth conditions.

Dependence of growth rate on temperature gradient

As is well known, the temperature gradient in the substrate region is an important parameter for CVD growth, but in the PVT growth of SiC crystals, the effect of this parameter has not been examined carefully. Chen et al. [11] have made the first attempt to study the importance of temperature gradient as presented in Fig. 7.15 where the growth rate versus inert gas pressure is presented for several different temperature gradients, for the growth temperature of 2400 K. With an increase

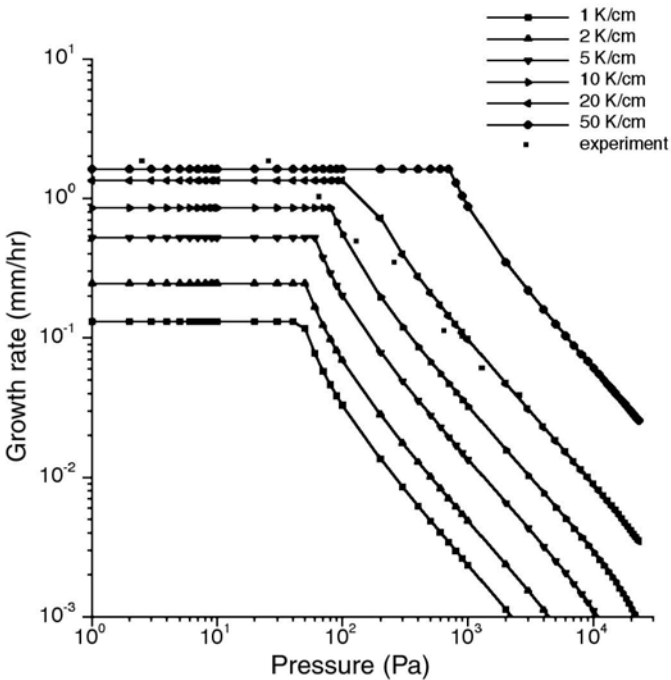


Fig. 7.15. Growth rate versus gas pressure for different axial temperature gradients at growth temperatures of 2400 K [11]. Experimental data are taken from [17]

in temperature gradient, the growth rate curve moves upward towards the high growth rate region. Again, in the growth rate–inert gas pressure map, the region where the growth rate curves become flat will have unstable growth, since the total vapor pressure of SiC species will be higher than the inert gas pressure.

Effect of coil position on temperature distribution and growth rate profile

Since $T_{charge} - T_{seed}$ is related to the coil position, the growth rate can be changed by moving the coil upward or downward. There are different control strategies, such as keeping the temperature on the top of the crucible, T_{top} , constant (Chen et al. [13]), or by keeping the power supply constant (Selder et al. [16]). The growth rate versus temperature difference between the charge and the seed is shown in Fig. 7.16 for different coil positions when T_{top} is kept constant, at 2400 K or 2300 K. In a certain range of coil position, the growth rate is a linear function of coil position, z_{coil} . For example, for $T_{top} = 2400$ K, the growth rate is almost a linear function of z_{coil} when $0 < z_{coil} < 0.03$ m; and for $T_{top} = 2300$ K, the growth rate is a linear function for -0.03 m $< z_{coil} < 0$. The growth rate can be less than zero representing etching of the seed (not shown here), if the coil is moved further up.

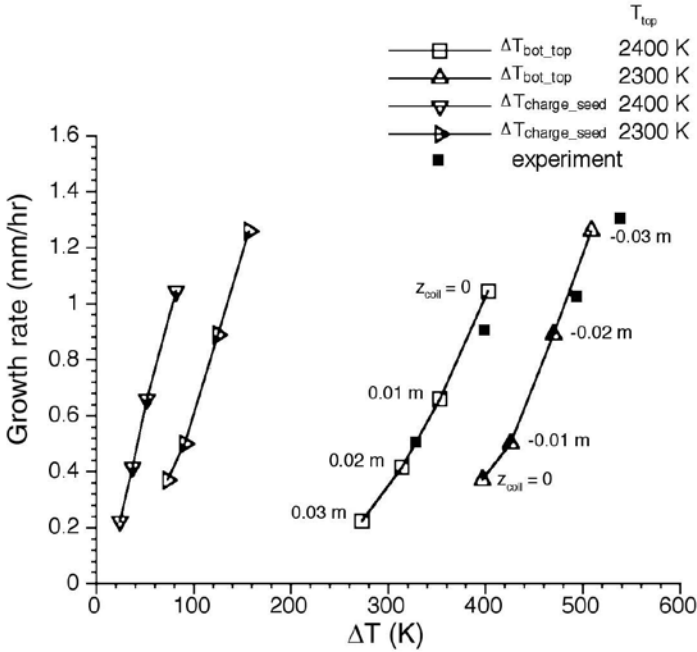


Fig. 7.16. Dependence of growth rate, G_{SiC} , on temperature difference between the charge and seed, $T_{charge} - T_{seed}$, and on temperature difference between the bottom and top of the crucible, $T_{bottom} - T_{top}$. The coil positions, z_{coil} , are denoted besides the symbols on the curve of $G_{SiC} \sim T_{bottom} - T_{top}$. The temperature on the top of the crucible, T_{top} , is maintained at either 2400 K or 2300 K [13]. Experimental data are taken from Balkas et al. [42]

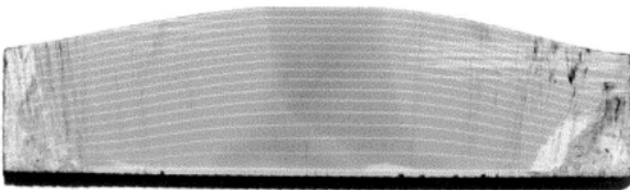


Fig. 7.17. Slice of a SiC crystal marked during growth by interface demarcation technique. The seed is positioned at the bottom. Dark horizontal regions are nitrogen-rich SiC material, undoped regions exhibit a bright contrast (Selder et al. [16])

The effect of coil position has also been studied by Selder et al. [16] who used an interface demarcation technique to achieve the experimental surface shape. During the growth experiment, nitrogen was added to the inert gas in the growth cell at fixed time steps. After the growth experiment, a slice was cut from the grown crystal along its growth direction as shown in Fig. 7.17.

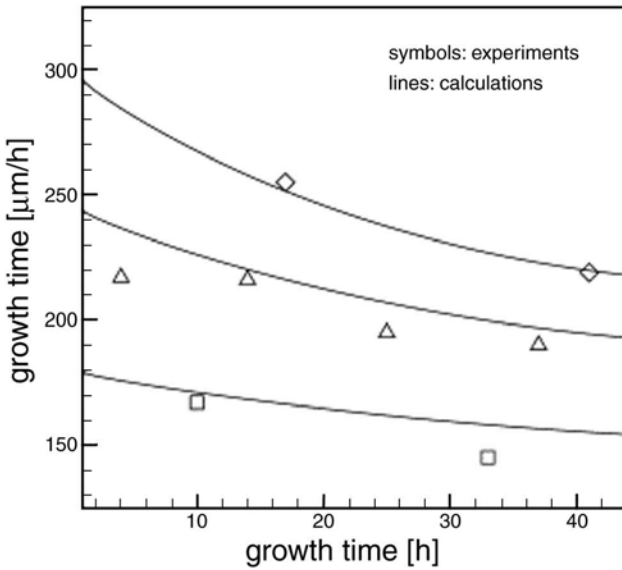


Fig. 7.18. Measured and predicted growth rates for different coil positions. Starting from a symmetrical coil position (upper curve), the coil is successively shifted downwards (Selder et al. [16])

Growth rate evolution in the center of the crystal was measured and computed for different coil positions while keeping the induction power constant. Figure 7.18 shows that the growth rate decreases with increasing crystal length. As can be seen, the growth rate also decreases by shifting the coil downward while the power supply is held constant. This is because the growth temperature, T_{seed} , decreases although $T_{charge} - T_{seed}$ may increase.

7.3.4 Thermally induced stress

Thermal stresses in SiC crystal with nonuniform temperature gradient can cause plastic deformation and generation of dislocations during the growth. Müller et al. [8] have used a thermoelastic model to calculate the thermal stress based on the temperature field from their 2D model. The stress-strain relation for a thermoelastic anisotropic solid body is taken as [48,49]:

$$\begin{pmatrix} \sigma_{rr} \\ \sigma_{\varphi\varphi} \\ \sigma_{zz} \\ \sigma_{rz} \end{pmatrix} = \begin{pmatrix} c_{11} & c_{12} & c_{13} & 0 \\ c_{12} & c_{22} & c_{23} & 0 \\ c_{13} & c_{23} & c_{33} & 0 \\ 0 & 0 & 0 & c_{44} \end{pmatrix} \begin{pmatrix} \varepsilon_{rr} - \alpha(T - T_{ref}) \\ \varepsilon_{\varphi\varphi} - \alpha(T - T_{ref}) \\ \varepsilon_{zz} - \alpha(T - T_{ref}) \\ \varepsilon_{rz} \end{pmatrix} \quad (7.36)$$

In the above equation, α is the thermal expansion coefficient, $T_{ref} = 0.5(T_{min} + T_{max})$ is a reference temperature, and

$$\epsilon_{zz} = \frac{\partial u}{\partial z}, \quad \epsilon_{rr} = \frac{\partial v}{\partial r}, \quad \epsilon_{\phi\phi} = \frac{v}{r}, \quad \epsilon_{rz} = \frac{\partial v}{\partial z} + \frac{\partial u}{\partial r}, \quad (7.37)$$

c_{ij} are the elastic material constants in the Voigt notation and u, v are the displacement components in axial and radial direction, respectively. Figure 7.19 shows the calculated 2D temperature distribution and the corresponding 2D distribution of the normal component ϵ_{rr} , and shear stress ϵ_{rz} in the crystal area, with positive values corresponding to tension and negative values to compression [8]. The calculated level of thermoelastic stress up to ~ 100 MPa in the SiC crystal during growth is well above the critical resolved shear stress σ_{CRS} , ~ 8 MPa (4H-SiC) and ~ 13 MPa (6H-SiC) at 1300°C (Samant and Pirouz [50]). The resolved shear stress at $2200\text{--}2500^\circ\text{C}$ is < 1 MPa by extrapolating the experimental values according to Müller et al. [8]. The generated dislocations are estimated to be $N \propto (|\sigma_{RS}| - \sigma_{CRS})$.

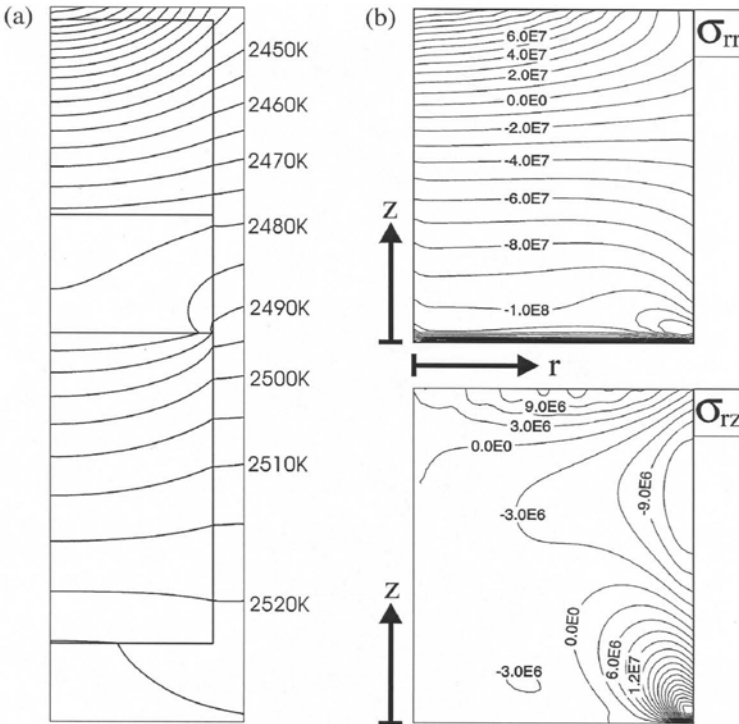


Fig. 7.19. (a) Numerical simulation of the axisymmetric temperature distribution inside a growth cell, and (b) resulting thermoelastic stress inside a 6H-SiC crystal: normal stress, σ_{rr} , and shear stress, σ_{rz} (Müller et al. [8])

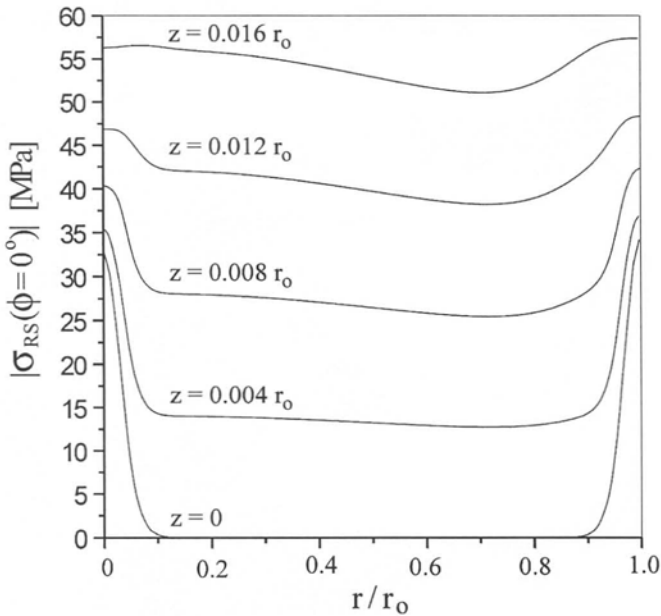


Fig. 7.20. Radial dependence of the resolved shear stress in the $\langle 1120 \rangle$ direction at different distances from the growth interface ($z = 0$) (Müller et al. [8])

For the three primary (0001) $\langle 1120 \rangle$ slip systems σ_{RS} is given by $\sigma_{RS} = (\sigma_{rr} + \sigma_{zz}) \cos\phi - \sigma_{\phi\phi} \sin\phi$. Figure 7.20 shows the radial dependence of $|\sigma_{RS}|$ for $\phi = 0^\circ$, corresponding to the $\langle 1120 \rangle$ direction, for different z -positions within a thin boundary layer ($\sim 500 \mu\text{m}$) at the growth interface.

Modeling of stresses during the growth of SiC crystals is quite challenging and not much has been reported on this problem except the work of Müller et al. [8]. It is expected that this topic will receive significant attention in the near future because of the direct relationship between the stresses and defects.

7.4 Summary

The vapor transport growth of silicon carbide crystals involves induction heating, electromagnetic field, radiative and conductive heat transfer, sublimation and condensation, chemical reaction, stoichiometry, mass transport, thermal stresses, as well as defect and micropipe generation and propagation. The irregular geometry, complicated boundary conditions, and lack of information on thermophysical properties at high temperatures make this process very difficult to understand, model, and control. Since defects and micropipes in SiC crystals are directly related to transport phenomena, it is critical to develop better understanding of these

phenomena to grow crystals of higher quality and larger size and to examine the effects of various parameters individually and collectively.

Models of sufficient complexity have been developed to simulate the sublimation SiC growth [2–19]. These models account for the RF heating, heat generation in graphite susceptor by eddy currents, heat transfer by conduction and radiation, species transport, growth kinetics, and stress analysis. The predictions made by these models are generally in good agreement with experimental data. The growth kinetics and mass transport from the charge to seed determine the growth rate and the shape of the crystal. The growth rate is a strong function of the interface temperature, temperature gradient, inert gas pressure, and the gap between the charge and seed, as well as the charge properties (particle size, height).

Modeling and simulation has been widely used in industry to optimize the system geometry and growth processes. The components of the growth system can be redesigned in order to grow crystals with low thermal stresses. Industry has used the model to design the furnace for growing 50–100 mm diameter SiC crystals. It is observed that a convex shape of interface can ensure an outward growth to expand a small size seed into a large diameter crystal. However, it can generate large thermal stresses and cause higher defect density. The mechanism of defects and screw dislocations is still not well understood and requires a strong coupling among modeling, growth, and characterization. Only then can a direct correlation among the process conditions, transport phenomena, chemistry, growth behavior, stresses, and defects be developed.

Acknowledgments

Acknowledgements are due to Sterling Semiconductor, Inc. and Advanced Technology Materials, Inc. for supporting this work through grants from BMDO/IST (managed by ONR, N00014-98-C-0176) and from Defense Advanced Research Projects Agency (F33615-98-C-5412), respectively, to NSF (CTS9876198), to AFOSR and DARPA for a MURI grant (F496209510407), and to ONR (grants N0001140010348 and N000140110302, contract monitor Dr. Colin Wood). Special thanks are also due to C. Balkas and N.K. Yushin of Sterling Semiconductor for helpful discussions and to M. Jacobs of AFOSR for encouragement and support of research on modeling in crystal growth.

References

1. Dhanaraj G, Huang XR, Dudley M, Prasad V, Ma R-H (2002) Silicon Carbide Crystals — Part I: Growth and Characterization. In: Byrappa K, Ohachi T (eds) *Crystal Growth for Modern Technology*. William Andrew Publishing, Norwich, NY
2. Hofmann D, Heinze M, Winnacker A, Durst F, Kadinski L, Kaufmann P, Makarov Y, Schäfer M (1995) On the Sublimation Growth of SiC Bulk Crystals: Development of a Numerical Process Model. *J Crystal Growth* 146:214–219

3. Hofmann D, Eckstein R, Kölbl M, Makarov Y, Müller StG, Schmitt E, Winnacker A, Rupp R, Stein R, Völkl J (1997) SiC-Bulk Growth by Physical-Vapor Transport and its Global Modeling. *J Crystal Growth* 174:669–674
4. Pons M, Blanquet E, Dedulle JM, Garcon I, Madar R, Bernard C (1996) Thermodynamic Heat Transfer and Mass Transport Modeling of the Sublimation Growth of Silicon Carbide Crystals. *J Electrochem Soc* 143(11):3727–3735
5. Pons M, Blanquet E, Dedulle JM, Madar R, Bernard C (1997) Different Macroscopic Approaches to the Modeling of the Sublimation Growth of SiC Single Crystals. *Mater Sci and Eng B* 46:308–312
6. Egorov YuE, Galyukov AO, Gurevich SG, Makarov YuN, Mokhov EN, Ramm MG, Ramm MS, Roenkov AD, Segal AS, Vodakov YuA, Vorob'ev AN, Zhmakin AI (1998) Modeling Analysis of Temperature Field and Species Transport Inside the System for Sublimation Growth of SiC in Tantalum Container. *Materials Science Forum* 264–268:61–64
7. Müller StG, Eckstein R, Hofmann D, Kadinski L, Kaufmann P, Kölbl M, Schmitt E (1998) Modeling of the PVT-SiC Bulk Growth Process Taking into Account Global Heat Transfer, Mass Transport and Heat of Crystallization and Results on its Experimental Verification. *Materials Science Forum* 264–268:57–60
8. Müller StG, Glass RC, Hobgood HM, Tsvetkov VF, Brady M, Henshall D, Jenny JR, Malta D, Carter Jr CH (2000) The Status of SiC Bulk Growth From an Industrial Point of View. *J Crystal Growth* 211:325–332
9. Karpov SYu, Kulik AV, Zhmakin IA, Makarov YuN, Mokhov EN, Ramm MG, Ramm MS, Roenkov AD, Vodakov YuA (2000) Analysis of Sublimation Growth of Bulk SiC Crystals in Tantalum Container. *J Crystal Growth* 211:347–351
10. Ma R-H, Chen Q-S, Zhang H, Prasad V, Balkas CM, Yushin NK (2000) Modeling of Silicon Carbide Crystal Growth by Physical Vapor Transport Method. *J Crystal Growth* 211:352–359
11. Chen Q-S, Zhang H, Prasad V, Balkas CM, Yushin NK, Wang S (2001) Kinetics and Modeling of Sublimation Growth of Silicon Carbide Bulk Crystals. *J Crystal Growth* 224:10–110
12. Chen Q-S, Zhang H, Ma R-H, Prasad V, Balkas CM, Yushin NK (2001) Modeling of Transport Processes and Kinetics of Silicon Carbide Bulk Growth. *J Crystal Growth* 225:299–306
13. Chen Q-S, Zhang H, Prasad V, Balkas CM, Yushin NK (2001) Modeling of Heat Transfer and Kinetics of Physical Vapor Transport Growth of Silicon Carbide Crystals. *J Heat Transfer* 123:1098–1109
14. Chen Q-S, Zhang H, Prasad V (2001) Heat Transfer and Kinetics of Bulk Growth of Silicon Carbide. *J Crystal Growth* 230:239–246
15. Prasad V, Chen Q-S, Zhang H (2001) A Process Model for Silicon Carbide Growth by Physical Vapor Transport. *J Crystal Growth* 229:510–515
16. Selder M, Kadinski L, Makarov Yu, Durst F, Wellmann P, Straubinger T, Hofmann D, Darpov S, Ramm M (2000) Global Numerical Simulation of Heat and Mass Transfer for SiC Bulk Crystal Growth by PVT. *J Crystal Growth* 211:333–338
17. Råback P, Nieminen R, Yakimova R, Tuominen M, Janzén E (1998) A Coupled Finite Element Model for the Sublimation Growth of SiC. *Materials Science Forum* 264–268:65–68

18. Råback P, Yakimova R, Syväjärvi M, Nieminen R, Janzén E (1999) A Practical Model for Estimating the Growth Rate in Sublimation Growth of SiC. *Mater Sci and Eng B* 61–62:89–92
19. Råback P (1999) Modeling of the Sublimation Growth of Silicon Carbide Crystals. Doctoral dissertation, Helsinki University of Technology, Espoo, Finland
20. Augustine G, Hobgood HMcD, Balakrishna V, Dunne G, Hopkins RH (1997) Physical Vapor Transport Growth and Properties of SiC Monocrystals of 4H Polytype. *Phys Stat Sol (b)* 202:137–148
21. Siergiej RR, Clarke RC, Sriram S, Agarwal AK, Bojko RJ, Morse AW, Balakrishna V, MacMillan MF, Burk Jr AA, Brandt CD (1999) Advances in SiC Materials and Devices: An Industrial Point of View. *Mater Sci and Eng B* 61–62:9–17
22. Barrett DL, Seidensticker RG, Gaida W, Hopkins RH, Choyke WJ (1991) SiC Boule Growth by Sublimation Vapor Transport. *J Crystal Growth* 109:17–23
23. Barrett DL, McHugh JP, Hobgood HM, Hopkins RH, McMullin PG, Clarke RC (1993) Growth of Large SiC Single Crystals. *J Crystal Growth* 128:358–362
24. Lilov SK (1993) Study of the Equilibrium Processes in the Gas Phase During Silicon Carbide Sublimation. *Mater Sci and Eng B* 21:65–69
25. Prasad V (1991) Convective Flow Interaction and Heat Transfer Between Fluid and Porous Layers. In: S Kakaç et al (eds) *Convective Heat and Mass Transfer in Porous Media*. Kluwer, Netherlands 563–615
26. Chen Q-S, Prasad V, Chatterjee A (1999) Modeling of Fluid Flow and Heat Transfer in a Hydrothermal Crystal Growth System: Use of Fluid-Superposed Porous Layer Theory. *J Heat Transfer* 121:1049–1058
27. Chen Q-S, Prasad V, Chatterjee A, Larkin J (1999) A Porous Media-Based Transport Model for Hydrothermal Growth. *J Crystal Growth* 198/199:710–715
28. Kaldis E, Piechotka M (1994) Bulk Crystal Growth by Physical Vapor Transport, Hurlé DTJ (ed) *Handbook of Crystal Growth* 2:615–658
29. Kaviany M (1995) *Principles of Heat Transfer in Porous Media*. Springer-Verlag, New York
30. Kansa EJ, Perlee HE, Chaiken RF (1977) Mathematical Model of Wood Pyrolysis Including Internal Forced Convection. *Combust Flame* 29:311–324
31. Bíró O, Preis K (1989) On the Use of the Magnetic Vector Potential in the Finite Element Analysis of Three-Dimensional Eddy Currents. *IEEE Transactions on Magnetics* 25:3145–3159
32. Kraus JD, Carver KR (1973) *Electromagnetics*. McGraw-Hill
33. Siegel R, Howell JR (1992) *Thermal Radiation Heat Transfer*. Hemisphere Publishing
34. Naraghi MHN, Chung BTF (1984) A Stochastic Approach for Analysis of Radiative Heat Transfer in Enclosures with Non-participating Media. *J Heat Transfer* 106:690–698
35. Naraghi MHN, Chung BTF, Litkouhi B (1988) A Continuous Exchange Factor Method for Radiative Exchange in Enclosures with Participating Media. *J Heat Transfer* 110:457–462
36. Nunes EM, Naraghi MHN (1998) Numerical Model for Radiative Heat Transfer Analysis in Arbitrarily Shaped Axisymmetric Enclosures with Gaseous Media. *Num Heat Transfer A* 33:495–513
37. Modest MF (1988) Radiative Shape Factors between Differential Ring Elements on Concentric Axisymmetric Bodies. *AIAA J of Thermophysics and Heat Transfer* 2:86–88

38. Drowart J, De Maria G (1960) *Silicon Carbide*. Pergamon, Oxford University Press
39. Kaneko T (1993) Growth Kinetics of Vapor-grown SiC. *J Crystal Growth* 128:354–357
40. Zhang H, Prasad V, Moallemi MK (1996) Numerical Algorithm Using Multizone Adaptive Grid Generation for Multiphase Transport Processes with Moving and Free Boundaries. *Num Heat Transfer, Part B* 29:399–421
41. Zhang H, Prasad V (2000) Modeling of High Pressure Liquid-encapsulated Czochralski Crystal Growth Processes. In: Szmyd JS, Suzuki K (eds) *Modeling of Transport Phenomena in Crystal Growth*. WIT Press 323–362
42. Balkas CM, Maltsev AA, Roth MD, Yushin NK (2000) Role of Temperature Gradient in Bulk Crystal Growth. *Materials Science Forum* 338–342:79–82
43. Anikin M, Madar R (1997) Temperature Gradient Controlled SiC Crystal Growth. *Mater Sci and Eng B* 46:278–286
44. Tairov YuM, Tsvetkov VF (1978) Investigation of Growth Processes of Ingots of Silicon Carbide Single Crystals. *J Crystal Growth* 43:209–212
45. Tairov YuM, Tsvetkov VF (1981) General Principles of Growing Large-size Single Crystals of Various Silicon Carbide Polytypes. *J Crystal Growth* 52:146–150
46. Nakata T, Koga K, Matsushita Y, Ueda Y, Niina T (1989) Single Crystal Growth of 6H-SiC by a Vacuum Sublimation Method, and Blue LEDs. In: Rahman MM, Yang CY-W, Harris GL (eds) *Amorphous and Crystalline Silicon Carbide II*. Springer Proc Phys 43:26
47. Syväjärvi M, Yakimova R, Kakanakova-Georgieva A, MacMillan MF, Janzén E (1999) Kinetics and Morphological Stability in Sublimation Growth of 6H and 4H SiC Epitaxial Layers. *Mater Sci and Eng B* 61–62:161–164
48. Lambropoulos JD (1987) The Isotropic Assumption During the Czochralski Growth of Single Semiconductors Crystals. *J Crystal Growth* 84:349–358
49. Fainberg J, Leister H-J (1996) Finite Volume Multigrid Solver for Thermo-elastic Stress Analysis in Anisotropic Materials. *Comput Methods Appl Mech Engrg* 137:167–174
50. Samant AV, Pirouz P (1998) Activation Parameters for Dislocation Glide in α -SiC. *Int J Ref Metals and Hard Materials* 16:277–289

8 Thermodynamics of Multicomponent Perovskite Synthesis in Hydrothermal Solution

Malgorzata M. Lencka¹ and Richard E. Riman²

¹OLI Systems, Inc., 108 American Road, Morris Plains, NJ 07950, USA

²Department of Ceramic and Materials Engineering, 607 Taylor Road, Rutgers University, Piscataway, NJ 08854-8065, USA

8.1 Introduction

In this chapter, we will focus on the hydrothermal synthesis of smart ceramic materials with a perovskite-type structure. Perovskite compounds have the general formula ABO_3 , where the A cation is relatively large and of low valence (such as Ba^{2+} , Sr^{2+} , Ca^{2+} , Pb^{2+} , La^{3+} , Sm^{3+} , Nd^{3+} , Bi^{3+} , K^+ , and the B cation is relatively small (such as Ti^{4+} , Zr^{4+} , Sn^{4+} , W^{6+} , Nb^{5+} , Ta^{5+} , Fe^{3+} , Mn^{3+} , Mg^{2+} , Zn^{2+} , Ni^{2+}).

Hydrothermal synthesis involves numerous simultaneous reactions between dissolved and solid species in an aqueous system to form anhydrous multicomponent oxides. Hydrothermal media may provide an effective reaction environment for the synthesis of numerous smart ceramic materials from a variety of precursor reagents (e.g., water-soluble salts, hydroxides, oxides) in the form of polycrystalline solids [1–15], thin films [16–22], and single crystals [23–25].

In particular, phase-pure ceramic materials with controlled stoichiometry and morphology can be hydrothermally synthesized in a single experimental step from simple and inexpensive precursors at moderate temperatures and pressures [26] far below those required for conventional techniques. To take advantage of the opportunities offered by hydrothermal synthesis, it is important to select a precursor system that is both reactive and cost-effective. However, the reactivity of a precursor system can only be judged by optimizing the processing variables such as reagent (precursor) concentrations and ratios, pH, temperature, and pressure, which can be extremely time consuming due to the large number of variables involved. To improve the efficiency of evaluating a precursor system, a comprehensive thermodynamic model that simulates hydrothermal reactions has been developed [27–29]. This model is a part of the OLI software [30]. Our simulation approach has been validated for numerous perovskite-type multi-component oxide systems, which include alkaline-earth titanates and zirconates [11,13,15], lead titanate [12], various solid solutions of lead zirconate titanate [14], lead magnesium niobate [31], and lead zinc niobate [31]. In this chapter, modeling and experimental validation of selected hydrothermal systems will be presented.

8.2 Thermodynamic Model

Prior to utilizing the thermodynamic model, we select candidate-starting materials (i.e., an appropriate precursor system) for hydrothermal synthesis. The thermodynamic model is used subsequently to predict the concentrations and activities of both ionic and neutral species in multicomponent systems that may contain an aqueous phase, any number of solid phases, and, if necessary, a vapor and a nonaqueous liquid phase. The starting point for the equilibrium calculations in the hydrothermal system is the computation of speciation in the investigated system. For this purpose, a realistic model of electrolyte systems is used. This model combines information about standard-state properties of all species of interest with a formulation for the excess Gibbs energy, which accounts for the solution nonideality. The model has been described in detail by Zemaitis et al. [28] and Rafal et al. [27].

In a multicomponent system, the partial molal Gibbs energy of the i -th species is related to the molality (m_i) by

$$\bar{G}_i = \bar{G}_i^0 + RT \ln m_i \gamma_i \quad (8.1)$$

where \bar{G}_i^0 is the standard-state partial Gibbs energy and γ_i is the activity coefficient. Thus, the thermodynamic properties of the system can be calculated if the standard-state Gibbs energies are available for all species as functions of temperature and pressure [i.e., $\bar{G}_i^0(T, P)$] and the activity coefficients are known as functions of the composition vector m and temperature [i.e., $\gamma_i(m, T)$]. From basic thermodynamics, the standard-state Gibbs energy of formation $\bar{G}_i^0(T, P)$ can be calculated as a function of temperature and pressure if the following data are available:

1. Gibbs energy of formation at a reference temperature T_r and pressure P_r (usually 298.15 K and 1 bar, respectively)
2. Enthalpy of formation at T_r and P_r
3. Entropy at T_r and P_r
4. Heat capacity as a function of temperature and pressure
5. Volume as a function of temperature and pressure

The key to representing the standard-state properties over substantial temperature and pressure ranges is the accurate knowledge of the heat capacity and volume. For this purpose, the Helgeson-Kirkham-Flowers-Tanger (HKFT) equation of state [32–33] is used. This equation accurately represents the standard-state thermodynamic functions for aqueous, ionic, and neutral species as functions of both temperature and pressure. In its revised form [33], the HKFT equation is capable of reproducing the standard-state properties up to 1000°C and 5 kbar.

The HKFT equation is based on the solvation theory and expresses the standard-state thermodynamic functions as sums of structural and solvation contributions, the latter being dependent on the properties of the solvent (i.e., water). The standard partial molal volume (\bar{V}^0) and heat capacity (\bar{C}_p^0) are given by

$$\bar{V}_0 = a_1 + \frac{a_2}{\Psi + P} + \left(a_3 + \frac{a_4}{\Psi + P} \right) \left(\frac{1}{T - \Theta} \right) - \omega Q + \left(\frac{1}{\varepsilon} - 1 \right) \left(\frac{\partial \omega}{\partial P} \right)_T \quad (8.2)$$

$$c_p^0 = c_1 + \frac{c_2}{(T - \Theta)^2} - \left(\frac{2T}{(T - \Theta)^3} \right) \left(a_3(P - P_r) + a_4 \ln \frac{\Psi + P}{\Psi + P_r} \right) + \omega T X + 2TY \left(\frac{\partial \omega}{\partial T} \right)_P - T \left(\frac{1}{\varepsilon} - 1 \right) \left(\frac{\partial^2 \omega}{\partial T^2} \right)_P \quad (8.3)$$

where a_1 , a_2 , a_3 , a_4 , c_1 , and c_2 represent species-dependent nonsolvation parameters, T_r is the reference temperature of 298.15 K, P_r is the reference pressure of 1 bar, Ψ and Θ refer to solvent parameters equal to 2600 bars and 228 K, respectively. Q , X , and Y denote the Born functions given by

$$Q = \frac{1}{\varepsilon} \left(\frac{\partial \ln \varepsilon}{\partial P} \right)_T \quad (8.4)$$

$$X = \frac{1}{\varepsilon} \left[\left(\frac{\partial^2 \ln \varepsilon}{\partial T^2} \right)_P - \left(\frac{\partial \ln \varepsilon}{\partial T} \right)_P^2 \right] \quad (8.5)$$

$$Y = \frac{1}{\varepsilon} \left(\frac{\partial \ln \varepsilon}{\partial T} \right)_P \quad (8.6)$$

where ε is the dielectric constant of water and ω stands for the Born coefficient, which is defined for the j -th aqueous species by

$$\omega_j \equiv \omega_j^{abs} - Z_j \omega_{H^+}^{abs} \quad (8.7)$$

In Eq. (8.7), Z_j is the charge on the j -th aqueous species, $\omega_{H^+}^{abs}$ refers to the absolute Born coefficient of the hydrogen ion and ω_j^{abs} designates the absolute Born coefficient of the j -th species given by

$$\omega_j^{abs} = \frac{N^0 e^2 Z_j^2}{2r_{e,j}} \quad (8.8)$$

where N^0 is the Avogadro number, e is the electron charge and $r_{e,j}$ denotes the effective electrostatic radius of the j -th species, which is related to the crystallographic radius $r_{x,j}$ by

$$r_{e,j} = r_{x,j} + |z_j| (k_z + g) \quad (8.9)$$

where k_z represents a charge-dependent constant equal to 0.0 for anions and 0.94 for cations, and g denotes a generalized function of temperature and density. Thus, the HKFT equation expresses the heat capacity and volume as functions of pure water properties and seven empirical parameters, which have been tabulated for large numbers of ions, complexes, and both inorganic and organic neutral molecules. The remaining thermodynamic properties are obtained by thermodynamic integration using the values of the Gibbs energy, enthalpy and entropy at reference temperature and pressure as integration constants.

The activity coefficient model used for representing the solution nonideality is an extended form of an expression developed by Bromley [34]. The Bromley

equation is a combination of the Debye-Hückel term for long-range electrostatic interactions and a semi-empirical expression for short-range interactions between cations and anions. In a multicomponent system, the activity coefficient of an ion i is given by

$$\log \gamma_i = \frac{-Az_i^2 I^{1/2}}{1+I^{1/2}} + \sum_j \left[\frac{|z_i|+|z_j|}{2} \right]^2 \left[\frac{(0.06+0.6B_{ij})|z_i z_j|}{\left(1+\frac{1.5}{|z_i z_j|} I\right)^2} + B_{ij} + C_{ij} I + D_{ij} I^2 \right] m_j \quad (8.10)$$

where A is the Debye-Hückel coefficient that depends on temperature and solvent properties, z_i is the number of charges on ion i , I is the ionic strength (i.e., $I = 0.5 \sum z_i^2 m_i$), N is the number of ions with charges opposite to that of ion i , and B_{ij} , C_{ij} and D_{ij} are empirical, temperature-dependent cation-anion interaction parameters. Bromley's [34] original formulation contains only one interaction parameter, B_{ij} , which is sufficient for systems with moderate ionic strength. For concentrated systems, the two additional coefficients C_{ij} and D_{ij} usually become necessary. The three-parameter form of the Bromley model is capable of reproducing activity coefficients in solutions with ionic strength up to 30 mol/kgH₂O. The temperature dependence of the B_{ij} , C_{ij} and D_{ij} parameters is usually expressed using a simple quadratic function.

The Bromley model is restricted to interactions between cations and anions. For ion-molecule and molecule-molecule interactions, the well-known model of Pitzer [35] is used. To calculate the fugacities of components in the gas phase, the Redlich-Kwong-Soave [36] equation of state is used.

In the absence of sufficient experimental data, reasonable predictions can be made using a method due to Meissner [37], which makes it possible to extrapolate the activity coefficients to higher ionic strengths based on only a single, experimental or predicted, data point.

8.2.1 Computational method

The thermodynamic model is formulated for k independent reactions, each of which can be written as

$$\sum_{i=1}^{n_j} \nu_i^{(j)} A_i^{(j)} = 0 \quad (j = 1, \dots, k) \quad (8.11)$$

where $A_i^{(j)}$ is the i -th chemical species participating in the j -th reaction, $\nu_i^{(j)}$ is the stoichiometric number of species $A_i^{(j)}$, and n_j is the total number of species undergoing the j -th reaction.

The equilibrium state of the j -th reaction is defined by the standard Gibbs energy change of the reaction

$$\Delta G_j^\circ = \sum_{i=1}^{n_j} \nu_i^{(j)} \Delta G_f^\circ(A_i^{(j)}) = -R T \ln K_j(T, P) \quad (j = 1, \dots, k) \quad (8.12)$$

where $\Delta G_f^\circ(A_i^{(j)})$ is the standard Gibbs energy of formation of species $A_i^{(j)}$ and K_j is the equilibrium constant of the j -th reaction. Since molality m is used in this work as the concentration unit, the equilibrium constant is expressed as

$$K_j = \prod_{i=1}^{n_j} (m_{A_i^{(j)}} \gamma_{A_i^{(j)}})^{\nu_i^{(j)}} \quad (j = 1, \dots, k) \quad (8.13)$$

where $\gamma_{A_i^{(j)}}$ is the activity coefficient of species $A_i^{(j)}$.

Table 8.1. Reaction equilibria in the Pb-Ti hydrothermal system with TiO_2 and PbAc_2 and/or $\text{Pb}(\text{NO}_3)_2$ as starting materials

$\text{H}_2\text{O} = \text{H}^+ + \text{OH}^-$	$\text{PbAc}_{2(\text{aq})} = \text{PbAc}^+ + \text{Ac}^-$
$\text{H}_2\text{O}_{(\text{g})} = \text{H}_2\text{O}$	$\text{PbAc}_3^{2-} = \text{Pb}^{2+} + 3\text{Ac}^-$
$\text{TiO}_{2(\text{s})} + \text{OH}^- = \text{HTiO}_3^-$	$\text{PbAc}_{2(\text{s})} = \text{Pb}^{2+} + 2\text{Ac}^-$
$\text{Ti}^{4+} + \text{H}_2\text{O} = \text{TiOH}^{3+} + \text{H}^+$	$\text{PbNO}_3^+ = \text{Pb}^{2+} + \text{NO}_3^-$
$\text{TiOH}^{3+} + \text{H}_2\text{O} = \text{Ti}(\text{OH})_2^{2+} + \text{H}^+$	$\text{Pb}(\text{NO}_3)_{2(\text{aq})} = \text{PbNO}_3^+ + \text{NO}_3^-$
$\text{Ti}(\text{OH})_2^{2+} + \text{H}_2\text{O} = \text{Ti}(\text{OH})_3^+ + \text{H}^+$	$\text{Pb}(\text{NO}_3)_{2(\text{s})} = \text{Pb}^{2+} + 2\text{NO}_3^-$
$\text{Ti}(\text{OH})_3^+ + \text{H}_2\text{O} = \text{Ti}(\text{OH})_{4(\text{aq})} + \text{H}^+$	$\text{HAc}_{(\text{g})} = \text{HAc}_{(\text{aq})}$
$\text{Ti}(\text{OH})_{4(\text{aq})} + \text{OH}^- = \text{HTiO}_3^- + 2\text{H}_2\text{O}$	$\text{HAc}_{(\text{aq})} = \text{H}^+ + \text{Ac}^-$
TiO_2 (rutile) + $2\text{H}_2\text{O} = \text{Ti}(\text{OH})_{4(\text{aq})}$	$\text{Ac}_{2(\text{aq})} = 2\text{HAc}_{(\text{aq})}$
TiO_2 (anatase) + $2\text{H}_2\text{O} = \text{Ti}(\text{OH})_{4(\text{aq})}$	$\text{Ac}_{2(\text{vap})} = \text{Ac}_{2(\text{aq})}$
PbO (litharge) + $\text{H}_2\text{O} = \text{Pb}^{2+} + 2\text{OH}^-$	$\text{HNO}_{3(\text{g})} = \text{HNO}_{3(\text{aq})}$
PbO (massicot) + $\text{H}_2\text{O} = \text{Pb}^{2+} + 2\text{OH}^-$	$\text{HNO}_{3(\text{aq})} = \text{H}^+ + \text{NO}_3^-$
$\text{PbO}_{(\text{aq})} + \text{H}_2\text{O} = \text{PbOH}^+ + \text{OH}^-$	$\text{KOH}_{(\text{s})} = \text{K}^+ + \text{OH}^-$
$\text{Pb}(\text{OH})_{2(\text{s})} = \text{Pb}^{2+} + 2\text{OH}^-$	$\text{KOH} \cdot \text{H}_2\text{O} = \text{K}^+ + \text{OH}^- + \text{H}_2\text{O}$
$\text{PbOH}^+ = \text{Pb}^{2+} + \text{OH}^-$	$\text{KOH} \cdot 2\text{H}_2\text{O} = \text{K}^+ + \text{OH}^- + 2\text{H}_2\text{O}$
$\text{Pb}^{2+} + 2\text{OH}^- = \text{HPbO}_2^- + \text{H}^+$	$\text{KAc}_{2(\text{aq})} = \text{K}^+ + \text{Ac}^-$
$\text{Pb}_2\text{OH}^{3+} + \text{H}^+ = 2\text{Pb}^{2+} + \text{H}_2\text{O}$	$\text{KNO}_{3(\text{s})} = \text{K}^+ + \text{NO}_3^-$
$\text{PbTiO}_{3(\text{s})} + 3\text{H}_2\text{O} = \text{Pb}^{2+} + 2\text{OH}^- + \text{Ti}(\text{OH})_{4(\text{aq})}$	$\text{K}_2\text{TiO}_{3(\text{s})} + 3\text{H}_2\text{O} = 2\text{K}^+ + \text{Ti}(\text{OH})_{4(\text{aq})} + 2\text{OH}^-$
$\text{PbAc}^+ = \text{Pb}^{2+} + \text{Ac}^-$	

The chemical equilibrium Eqs. (8.12) and (8.13) are solved simultaneously with mass and electroneutrality balance equations. To solve this system of equations, the standard Gibbs energies of formation and activity coefficients are calculated as described above.

For example, let us consider a system obtained by mixing soluble salts of lead (e.g., lead acetate or lead nitrate) with titanium dioxide. Table 8.1 contains equilibrium equations between 42 aqueous and solid species that may exist in the Pb-Ti-H₂O system. The presence of nitric acid and potassium hydroxide (cf. Table 8.1) results from the fact that the formation of ceramic materials (e.g., lead titanate) may require pH-adjusting agents such as acids, alkaline hydroxides, or ammonia. For completeness, the data for gaseous species are also included even though the gas phase plays a secondary role in perovskite synthesis under the *T-P* conditions of interest. As we can see in Table 8.1, even a relatively simple hydrothermal system such as Pb-Ti-H₂O contains a large number of species and a correspondingly large number of equations to be solved.

8.2.2 Standard-state properties

The standard Gibbs energy of formation at the temperature and pressure of interest is calculated from the standard Gibbs energy ΔG_f° and enthalpy ΔH_f° of formation, and entropy S° at a reference temperature (usually 298.15 K) as well as the partial molar volume V° and heat capacity C_p° as functions of temperature. The OLI data bank contains information for many aqueous, gaseous, and solid compounds. Whenever possible, data should be taken from critically evaluated and consistent sources. These compilations were discussed previously along with criteria for selecting the most reliable data [29]. Extensive works on the application of the HKFT equation [38–39] serve as a main source of data for aqueous species. Data for solid compounds are usually taken from the compilations of NBS [40–41], JANAF [42], Medvedev et al. [43], and Robie and Hemingway [44]. For ceramic materials, especially double oxides (e.g., lead and alkaline-earth titanates), most of the data are available in the book of Barin [45].

In the case of solid compounds, solubility data in pure water as well as in alkaline or acidic solutions at different temperatures are the best source of data for standard-state properties. These data are available in books of Seidell and Linke [46–47] and in the current literature. Whenever possible, regression of solubility data are performed using the OLI software [30] to obtain accurate and consistent thermochemical data for solid compounds.

In many cases, no experimental data are available for aqueous and solid species of interest; therefore predictive methods are necessary. If the HKFT equation parameters are not available from the regression of experimental data, they can be estimated. For this purpose, Shock and Helgeson [38–39] presented correlations for most solution species except for complexes. Sverjensky [48] developed an estimation method for several classes of complexes. In addition to the HKFT equation parameters, these methods make it possible to predict the reference-state en-

thalpy and entropy if the reference-state Gibbs energy is known. These and other estimation techniques have been reviewed in detail by Rafal et al. [27].

At the same time, empirical procedures for calculating the standard-state properties of perovskite-type multicomponent (double) oxides of the general formula ABO_3 ($A = Ca, Sr, Ba, Pb, \text{etc.}$; $B = Ti, Zr, \text{etc.}$) have been developed [49]. They are based on a family analysis [50–51] or group contribution methods [52]. In our work, unavailable thermochemical properties for lead zirconate and lead, magnesium, zinc niobates, and lead zirconate were estimated using these methods.

For solid solutions (e.g., PZT, PMN, PZN), no thermodynamic properties are available and no experimental solubilities were measured. Therefore, estimation methods are necessary. They include calculations of thermochemical data based on the ideal-solid solution approximation. A less sophisticated alternative is the use of group contribution methods. A more rigorous approach is based on the analysis of the thermodynamic properties of solid solutions in terms of the thermodynamic functions of mixing. This approach was applied to calculate standard-state properties of the PZT solid solutions [14].

It should be noted that the number of potentially stable solid phases in some multicomponent systems can be very large. For example, in the Pb-Mg-Nb-K hydrothermal system we are dealing with a large number of solid phases (i.e., oxides, hydroxides, niobates, etc.). Therefore, in the case of such a complicated system for which a great deal of estimation is necessary, it is useful to utilize the model interactively with experimentation to establish the solid phases that are likely to form. Experiments may greatly suppress or increase the number of phases included in the model, whose properties can be estimated as mentioned earlier. Furthermore, experimentation can provide feedback for adjusting the magnitude of certain thermochemical data, which may have questionable origin.

8.2.3 Stability and yield diagrams

The purpose of our work was to calculate the optimum synthesis conditions for the formation of phase-pure materials. This information can be obtained from the knowledge of stability and yield diagrams calculated for hydrothermal systems involving ceramic materials. In the past, stability diagrams were considered for a limited number of hydrothermal systems by assuming that the aqueous solutions were ideal [8,53].

Repetitive application of the model for different input concentrations of the A-site and B-site precursors as well as pH-adjusting agents (mineralizers) makes it possible to construct stability and yield diagrams. Stability diagrams show the ranges of equilibrium conditions for which various aqueous and solid species are stable in the hydrothermal system. Equilibrium conditions include the total molality of a selected aqueous metal precursor, solution pH, and temperature. The total molality of the aqueous metal precursor is the sum of the equilibrium concentrations of all dissolved metal species and does not include the species that precipitate from the solution as solids. While the stability diagrams provide information about the conditions for incipient precipitation of various solid phases, they do not

specify the reaction conditions required for an assumed yield of a reaction product. To accomplish this goal, the idea of yield diagrams was conceived [12]. In contrast to stability diagrams, yield diagrams are shown with the total input concentration of the metal precursor as the independent variable instead of the equilibrium (total) concentration of all dissolved metal species. The metal precursor can be converted to the desired product (e.g., ABO_3) with a certain yield, while the remainder of the metal precursor can remain in the solution. For the purpose of yield analysis, it is necessary to use the input concentration because we are concerned not only with the equilibrium concentration of species in saturated solution but also with the conversion of the precursor system into a phase-pure product. Thus, the input concentration of the metal precursor takes into account all metal-containing solution and solid species. In our previous papers [11–14], yield diagrams were constructed point by point, whereas later, a computer program has been developed for the automatic generation of these diagrams [15].

As the y -axis variable of yield diagrams, the program uses the input concentrations of one or more starting materials, which is equal to the initial concentration of the metal precursor. To simplify the graphical output in multicomponent metal oxide systems, the ratios of the input precursor concentrations are held constant at a predetermined value. As the y -axis variable of stability diagrams, the program uses the total concentrations of one or more metal precursors. As the x -axis variable, the program can use either pH or the input concentration of a mineralizer. All concentrations are expressed in molalities because such units are easily measurable. Also, temperature can be used as the y -axis variable and all precursor concentrations can be used as the x -axis or y -axis variables. If pH is chosen as the x -axis variable, the program changes the equilibrium pH by adding varying amounts of a selected acid (e.g., HNO_3) and a base (e.g., KOH). It should be noted that the pH values are calculated at the temperature of an experiment at equilibrium. For example, pH values in alkaline solutions at 433–473 K are smaller by about 2–3 pH units than those for the same solutions at room temperature.

If the input concentration of a pH-adjusting agent is chosen as the x -axis variable, it is varied by the program on a linear or logarithmic scale. It should be noted that the diagrams developed in previous papers [29,11–14] were constructed always with the total or input concentration of the metal precursor, equilibrium pH or temperature as the y -axis variable and with equilibrium pH or temperature as the x -axis variable. The automatic generation of diagrams allows us to be more flexible in the choice of independent variables. This is particularly useful when it is necessary to determine the amount of a pH-adjusting agent that is needed to obtain a certain yield of the product.

The stability diagrams include two types of lines: the solid lines denote the states of incipient precipitation of solids, whereas the dotted lines show the loci where two aqueous species have equal concentrations. In practice, an equilibrium point is assumed to lie on the solid-aqueous species boundary (solubility curve) when less than 0.25% of the precursor is found to be in the form of a solid phase. The yield diagrams show the areas where the desired product precipitates with a yield greater than or equal to an assumed value (e.g., 99%). At the solubility curve (shown in both stability and yield diagrams), the yield is very small because the

solubility curve corresponds to incipient precipitation of the desired product. The yield increases as we move beyond the solubility curve into the solid-liquid region. This yield is calculated by dividing the number of moles of the product by the total number of moles of the input metal precursor. The yield areas are shown in the diagrams as shaded fields. Usually, the boundaries between aqueous species are not shown in the yield diagrams. It should be noted that yield diagrams provide direct guidance for the experimental synthesis, because the shaded area of the yield diagram shows the range of input precursor concentrations that can produce a phase-pure product.

A certain ratio of metals in the starting materials (i.e., A/B) is assumed by choosing the precursor system for hydrothermal synthesis. It may correspond to the stoichiometric ratio in the formula of the perovskite (i.e., ABO_3) or can be greater or lower than one. If the ratio is lower than one, the formation of the perovskite phase does not go to completion. If it is greater than one, the formation of the perovskite and possibly additional phases containing A-site metals takes place. If the ratio is equal to one, we may expect the formation of phase-pure ABO_3 if thermodynamics drives the following reaction to completion, i.e., if reaction (8.14) has a large equilibrium constant:



Thus, for making phase-pure ABO_3 , reaction conditions where the ratio A/B equals or exceeds one are the most useful to optimize. In the section that follows, we will present examples where we have achieved this.

8.2.4 Stability and yield diagrams for the stoichiometric ratio of precursors (A/B = 1)

Figure 8.1 shows the stability diagram calculated for the hydrothermal system obtained by mixing lead nitrate or lead acetate and titanium dioxide at $T = 433$ K. The stoichiometric molar ratio Pb/Ti = 1 is employed. The total molality of all lead species that may occur in the solution and the solution pH are used as independent variables. The solid curved line on the stability diagram corresponds to the states of incipient precipitation of $PbTiO_3$. On the other hand, the vertical straight lines correspond to the loci where two aqueous species have equal concentrations. As shown in Fig. 8.1, the chemical identity of these species varies with pH. While Pb^{2+} dominates at pH below 4.3, it becomes hydrolyzed to $PbOH^+$ at $4.3 < \text{pH} < 7.8$. Further, the neutral species $PbO_{(aq)}$ becomes predominant at $7.8 < \text{pH} < 9.2$ and is, in turn, replaced by $HPbO_2^-$ at pH above 9.2. The formation of the desired product, $PbTiO_3$, is strongly dependent on pH. Crystalline $PbTiO_3$ can be obtained at pH higher than ca. 4.0. The stability of $PbTiO_3$ increases with rising pH and reaches a maximum at pH equal to 8.5. In this range of pH, $PbTiO_3$ precipitates when the concentration of lead in solution is as low as 10^{-7} m. The stability of $PbTiO_3$ somewhat decreases at pH above 10 because of the amphoteric character of lead. Thus, the solubility curve of $PbTiO_3$ has a parabolic shape.

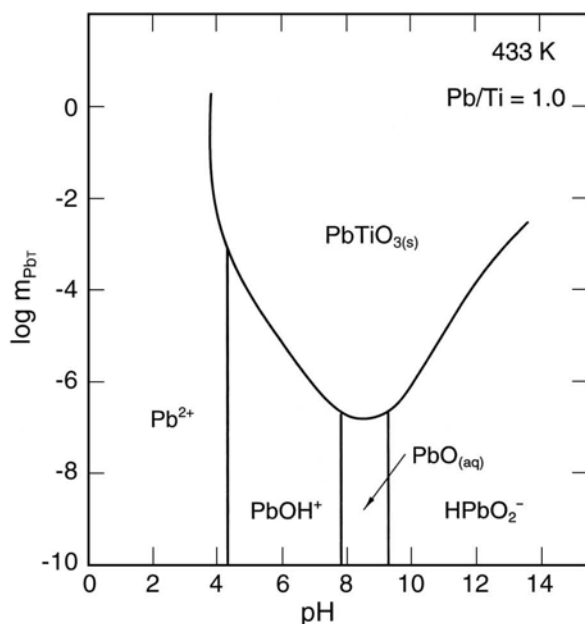


Fig. 8.1. Calculated stability diagram for the Pb-Ti system at 433 K. PbAc_2 and TiO_2 are used as starting materials and the ratio of total molalities is equal to 1.0

The incipient precipitation line of PbTiO_3 is practically insensitive to the chemical identity of lead precursors. A very small shift in pH (about 0.2 units) is caused by the existence of various lead nitrate and lead acetate complexes in this system (cf. Table 8.1).

Figure 8.2 shows the comparison of the conditions for the synthesis of the alkaline-earth titanates, CaTiO_3 , SrTiO_3 , and BaTiO_3 . It combines the calculated phase stability diagrams for three hydrothermal systems Ca-Ti, Sr-Ti, and Ba-Ti at 433 K. The diagrams are qualitatively similar because of the chemical similarity of the Ca, Sr, and Ba cations. The total molality of the alkaline-earth metal precursor and the pH of the solution adjusted by KOH are chosen as independent variables. Three incipient precipitation lines are shown in this figure. The beginning of precipitation lines of CaTiO_3 and SrTiO_3 are very close to each other. The BaTiO_3 line is located at somewhat higher pH. Its distance from the SrTiO_3 line is about 1.2 pH units. The relative location of the incipient precipitation lines is a result of an interplay of several independent factors. Among them, most important are the relative magnitude of standard-state thermodynamic functions, alkalinity of the Ba, Sr, and Ca species as well as specific interactions between ions that determine the activity coefficients. It is apparent that the incipient precipitation line for the titanate of the most alkaline metal (i.e., Ba) lies at higher pH values. The differences between the CaTiO_3 and SrTiO_3 lines become visible only at relatively high

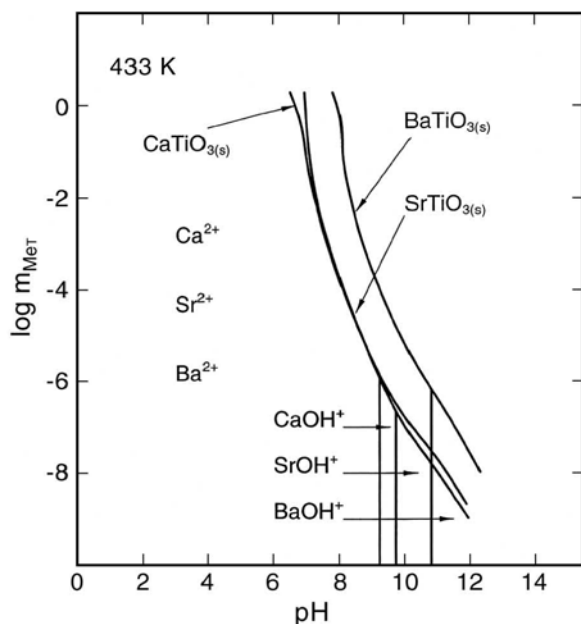


Fig. 8.2. Comparison of calculated phase stability diagrams for the hydrothermal systems Ca-Ti, Sr-Ti, and Ba-Ti at 433 K for the stoichiometric molar ratios of precursors

or low (but not intermediate) concentrations. The $CaTiO_3$ and $SrTiO_3$ lines cross each other. If the input concentration of titanium dioxide is 0.1 m, barium titanate precipitates at pH above 8, strontium titanate begins to form at pH above 7.5 and calcium titanate occurs at pH above 7.3 at 433 K. The predominant areas of alkaline-earth cations and their hydroxycomplexes are also shown in this figure.

Figure 8.3 shows a yield diagram for the Pb-Zr-Ti hydrothermal system calculated at 433 K [14]. Lead acetate and zirconium and titanium dioxide with a molar ratio equal to 0.52/0.48 were used as precursors. KOH was used to adjust pH and the Pb/(Zr+Ti) ratio was equal to one. The area of stability of a solid solution $PbZr_{0.52}Ti_{0.48}O_3$ (PZT) is encompassed by a parabolic-shaped solid line. The exact pH value at which precipitation begins depends on the total concentration of Pb in the aqueous phase. For example, if the concentration of lead precursor is equal to 0.1 m, the precipitation of the solid solution starts at pH values above 4.9. If lead nitrate is used, the left boundaries are shifted toward lower pH values by about 0.3–0.4 pH units while the right boundaries remain the same. The area of PZT solid solution stability increases with higher concentration. For relatively concentrated solutions, dissolution of solid PZT phases occurs at pH values above 14.0. The effect of temperature on the diagram is minimal in the range from ca. 433 K to 573 K. At 573 K, the incipient precipitation lines shift toward lower pH values by about 0.2–0.4 units. The area of PZT yield greater than 99.0% is much smaller

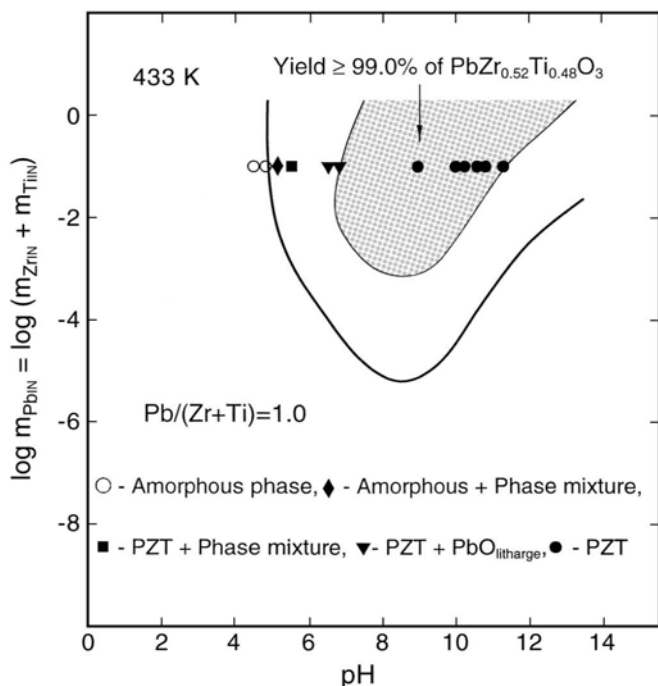


Fig. 8.3. Calculated yield diagram of $\text{PbZr}_{0.52}\text{Ti}_{0.48}\text{O}_3$ at 433 K. PbAc_2 , TiO_2 , and ZrO_2 are used as starting materials for the calculations. Symbols denote various solid phases that were experimentally obtained using PbAc_2 and coprecipitated the Zr-Ti hydrous oxide $\text{Zr}_x\text{Ti}_{1-x}\text{O}_2 \cdot n\text{H}_2\text{O}$

than the stability region. It is illustrated in Fig. 8.3 as a shaded region encompassed by a solid line. For the input concentration of lead and, subsequently, the sum of the input concentrations of Ti and Zr equal to 0.1 m, phase-pure PZT forms at pH values above 6.8 and below 11.4. Since the yield diagrams are somewhat sensitive to the chemical identity of precursors [12], calculations were performed with lead nitrate as a precursor. In this case, the area of PZT yield greater than 99% is shifted toward lower pH values by about 0.8–0.9 pH units.

One of the possible ways of presenting yield diagrams is by performing calculations of stability and yield of ceramic materials at different temperatures as a function of the solution pH. Figure 8.4 summarizes theoretical findings pertaining to the synthesis of PbTiO_3 from lead acetate or lead nitrate and titanium dioxide for the Pb/Ti ratio equal to 1. Figure 8.4 is valid for the input reagent concentrations ranging from 0.05 to 0.2 m, which are convenient for carrying out the reactions in practice. The dashed line corresponds to the beginning of precipitation of lead titanate. The solid lines encompass the region of greater than 99.99% yield of PbTiO_3 , which is appropriate for performing practical syntheses. The areas

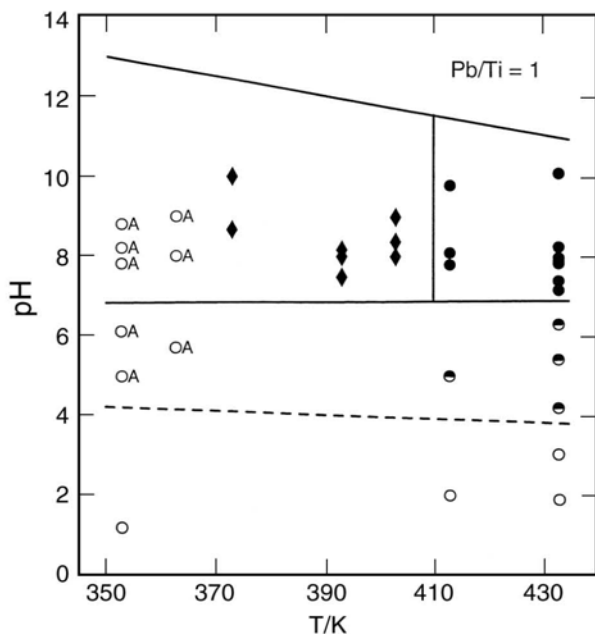


Fig. 8.4. Solid products of hydrothermal reactions of PbAc_2 and/or $\text{Pb}(\text{NO}_3)_2$ and TiO_2 for the input molality of lead equal to 0.05–0.2 m at different temperatures and pH values: solid circles — crystalline PbTiO_3 , A — amorphous PbTiO_3 , hollow circles — TiO_2 , semi-solid circles — $\text{PbTiO}_3 + \text{TiO}_2$, solid diamonds — $\text{PbTiO}_3 + \text{TiO}_2 + \text{PbO}$ (massicot) + $\text{Pb}_2\text{Ti}_2\text{O}_6$. The dashed line denotes the beginning of precipitation of PbTiO_3 and the solid lines encompass the region where the yield of PbTiO_3 exceeds 99.99%

between the dashed and lower solid lines and upper solid line and $\text{pH} = 14$ correspond to the precipitation of PbTiO_3 along with unreacted solid titanium dioxide. The region between the $\text{pH} = 0$ axis and the dashed line shows the conditions for which the synthesis reaction does not occur. In this region, unreacted solid titanium precursor and aqueous species coexist. For clarity, aqueous lines are not shown in the yield diagrams.

The stability and yield diagrams with pH as an independent variable (i.e., Figs. 8.1–8.4) do not indicate the concentration of a pH -adjusting agent necessary to synthesize the desired product. Figure 8.5 shows calculated phase stability and yield of strontium zirconate obtained by mixing strontium hydroxide and zirconium oxide at 473 K. In this figure, the Sr and Zr precursors, with a fixed molar ratio (i.e., $\text{Sr}/\text{Zr} = 1$), are used as y -axis variables and pH is replaced with the molality of a base (i.e., KOH) as an x -axis variable. The solid line in Fig. 8.5 denotes the beginning of precipitation of strontium zirconate. In the area above the solid line, strontium zirconate and zirconium oxide coexist. As we move closer to the shaded area, the yield of strontium zirconate increases while the amount of

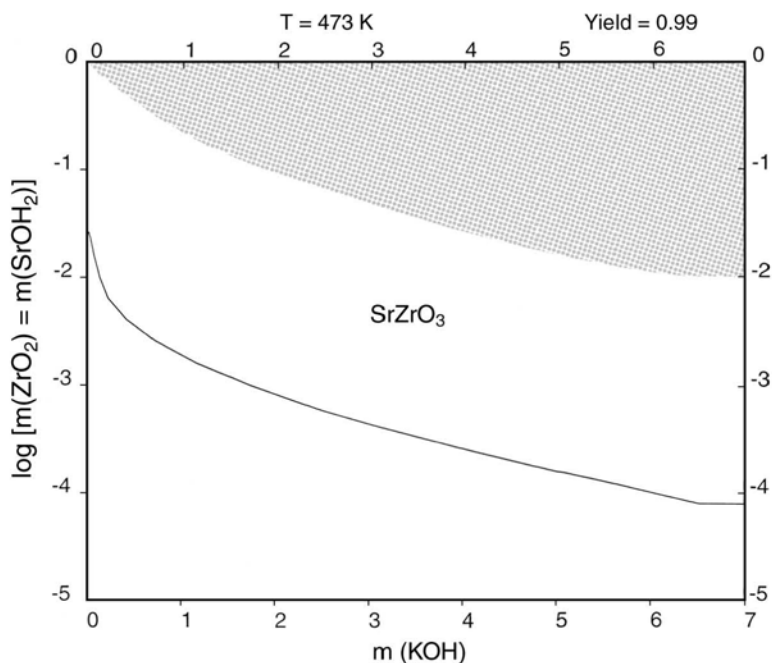


Fig. 8.5. Calculated phase stability and yield diagram as a function of the input amount of KOH at 473 K for Sr/Zr = 1 using Sr(OH)₂ as a source of strontium

zirconium dioxide decreases. The shaded region shows the optimum synthesis conditions (i.e., input molality of strontium hydroxide and potassium hydroxide) for the formation of phase-pure strontium zirconate (yield greater than 99%) at 473 K. The amount of KOH necessary to form phase-pure SrZrO₃ from Sr(OH)₂ is much smaller than that from strontium nitrate [15] but cannot be completely eliminated (cf. Fig. 8.5). The minimum amount of KOH is as low as 0.2 m when the input concentration of Sr(OH)₂ is 1 m but rises to 1.6 m for an input concentration of 0.1 m.

All the above diagrams showed that it is possible to synthesize phase-pure titanates and zirconates if the synthesis conditions are carefully chosen. Compositions in the perovskite family with the general formula Pb(B₁B₂)O₃ are known as ferroelectric relaxors and are of considerable interest. It has been reported in the literature [54] that these materials are difficult to fabricate reproducibly without the appearance of a pyrochlore phase that can be detrimental to the dielectric properties. Lead magnesium niobate [Pb(Mg_{1/3}Nb_{2/3})O₃ or PMN] attracted our attention because it has never been obtained hydrothermally at moderate temperatures. An analysis of the stability of perovskite materials in vacuum based on quasi-thermodynamics and crystal chemical arguments performed by Shrout and Halliyal [55] showed that the problem of pyrochlore formation in the preparation

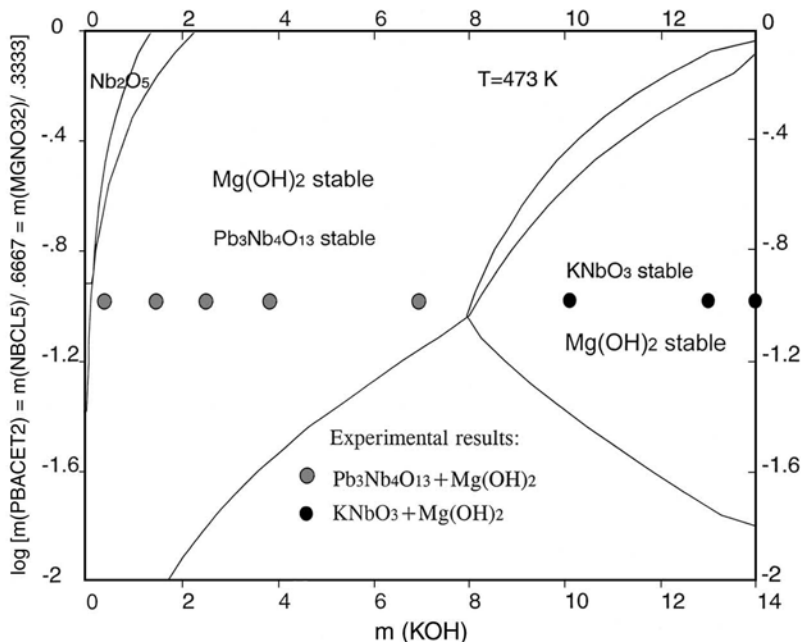


Fig. 8.6. Stability of various solid phases in the Pb-Mg-Nb-K-H₂O system at 473 K

of PZN and PMN is primarily thermodynamic in nature. Therefore, it was of interest to study whether high stability of pyrochlores (such as $\text{Pb}_{1.83}\text{Mg}_{0.29}\text{Nb}_{1.71}\text{O}_{6.39}$ or $\text{Pb}_3\text{Nb}_4\text{O}_{13}$) in the Pb-Mg-Nb-H₂O system is also responsible for the failure of obtaining phase-pure tetragonal PMN hydrothermally. One of the main steps in calculating the stability of the phase of interest (i.e., PMN) is to find or estimate thermochemical data for solid phases that are likely to form at hydrothermal conditions. It should be noted that the number of potentially stable solid phases in this system is very large and consists of oxides and hydroxides of lead, magnesium, and niobium; various niobates of magnesium, lead, and potassium; and solid solutions, which include a tetragonal and a cubic PMN pyrochlore phase and possibly a solid solution between potassium niobate and lead magnesium niobate.

Our original databank did not contain thermochemical properties of most of the above solids except for magnesium and lead oxides and hydroxides. Therefore, thermochemical data for Nb_2O_5 , $\text{Pb}(\text{NbO}_3)_2$, and KNbO_3 were calculated from the reported solubilities of these species in aqueous solutions [46–47,31]. Thermochemical properties of multicomponent oxides (niobates) were calculated using a group contribution method [30,51]. Then, based on the new values for the end-members, thermochemical properties of the solid solutions were calculated using an ideal solid solution approximation. Figure 8.6 shows the calculated stability of various solid phases in the Pb-Mg-Nb-K-H₂O system at 473 K. Input molality of lead, magnesium, and niobium precursors with a ratio corresponding to the

stoichiometry of tetragonal PMN is shown on the y -axis and the KOH concentration is shown on the x -axis. The solid lines encompass the regions where various solid materials are stable. For example, Nb_2O_5 is stable in an acidic environment at low amounts of KOH and at relatively high concentration of niobium in the solution. Lead niobate, $\text{Pb}_3\text{Nb}_4\text{O}_{13}$, is extremely stable and starts to precipitate at very low concentrations of KOH. At high concentrations of KOH, lead niobate dissolves to release Nb ions into the solution to form potassium niobate (KNbO_3). The stability regions of $\text{Mg}(\text{OH})_2$ and the $\text{Pb}_3\text{Nb}_4\text{O}_{13}$ pyrochlore phase overlap at low pH values, but magnesium hydroxide is very stable at highly alkaline solutions and overlaps in this region with KNbO_3 . These calculations are summarized in Fig. 8.6, which shows that tetragonal PMN is not thermodynamically stable. This is because magnesium hydroxide and lead niobate are more stable than tetragonal PMN in basic aqueous solutions. Furthermore, the use of KOH mineralizer causes the formation of KNbO_3 . Organic mineralizers such as tetramethylammonium hydroxide (Me_4NOH) do not form niobates but they still cause the formation of $\text{Pb}_3\text{Nb}_4\text{O}_{13}$ and $\text{Mg}(\text{OH})_2$ instead of tetragonal PMN [31]. It should be noted that standard-state properties for many solid compounds in this system were estimated. Therefore, this is a preliminary phase and stability diagram of the Pb-Mg-Nb-K hydrothermal system, which may be fine-tuned in the future.

8.2.5 Stability and yield diagrams for the nonstoichiometric ratio of precursors ($A/B > 1$)

When the A/B ratio is above one, we expect the area of phase-pure product in the yield diagrams to increase. This is because an excess of A-site metal in solution shifts the equilibrium so that pure perovskite phase precipitates at lower pH values, which also reduces the amount of required mineralizer. However, an excess amount of metal A can also cause the precipitation of secondary phases. In the lead-containing hydrothermal systems, an excess of lead will form lead hydroxide or lead oxide (litharge) [12]. Hydrated and nonhydrated forms of hydroxides can precipitate together with desired ceramic material in the systems containing alkaline-earth metal [29,13,15]. While some of these impurities can be eliminated with washing, the leaching of A-site ions from the perovskite lattice is also an important concern [56]. Thus, an excess of A metal is useful provided that syntheses are performed in the pH region where additional solid phases do not precipitate.

Figure 8.7 shows a yield diagram in the Pb-Ti- H_2O system constructed using lead acetate and titanium oxide with the Pb/Ti ratio equal to 1.5. This figure shows the pH-T regions where different solid phases can be obtained for the input concentration of lead precursor equal to 0.1 m. The dashed line represents the beginning of precipitation of PbTiO_3 . The region between the axis $\text{pH} = 0$ and the dashed line shows conditions where the reaction does not occur. In the area between the dashed and solid lines, PbTiO_3 will precipitate along with unreacted TiO_2 . In Fig. 8.7, the dot-dashed line shows the beginning of precipitation of PbO (litharge). Phase-pure perovskite precipitates between the solid and dot-dashed

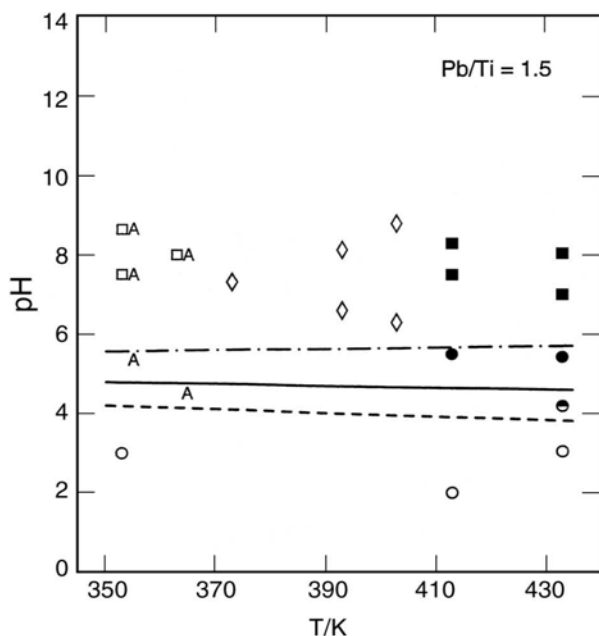


Fig. 8.7. Solid products of hydrothermal reactions of PbAc_2 and TiO_2 for the input concentration of lead equal to 0.1 m at different temperatures and pH values: solid circles — crystalline PbTiO_3 , A — amorphous PbTiO_3 , hollow circles — TiO_2 , semi-solid circles — $\text{PbTiO}_3 + \text{TiO}_2$, open diamonds — PbO (litharge and massicot) + $\text{Pb}_2\text{Ti}_2\text{O}_6 + \text{TiO}_2$, hollow squares — PbO (litharge and massicot), solid squares — $\text{PbTiO}_3 + \text{PbO}$ (litharge and massicot). The dashed line denotes the beginning of precipitation of PbTiO_3 , the solid and dot-dashed lines encompass the region where the yield of PbTiO_3 exceeds 99.99%, and the dot-dashed line denotes the beginning of precipitation of PbO .

lines. Thus, the area above the dot-dashed line corresponds to the region where phase-pure PbTiO_3 cannot be obtained because of the presence of an additional solid phase, PbO . A comparison of Figs. 8.4 and 8.7 shows that an excess of Pb decreases the pH for the formation of phase-pure PbTiO_3 by about 2 pH units. Consequently, less mineralizer is necessary to obtain pure phase. However, the region of phase-purity is relatively small and limited to one pH unit. At higher alkalinities, lead oxide precipitates along with lead titanate. The extent of the phase-purity region depends strongly on the Pb/Ti ratio [12,57–58].

Figure 8.8 shows calculated phase stability and yield diagram as a function of the input molality of KOH at 473 K for the Sr/Zr ratio equal to 2.0 in the Sr - Zr hydrothermal system. Strontium hydroxide and zirconium dioxide were used as precursors. In comparison with the Sr/Ti ratio equal to 1.0 (cf. Fig. 8.5), the beginning of precipitation of SrZrO_3 shifts very slightly towards lower concentrations of the input metal precursors thus suggesting that a slightly lower pH is necessary

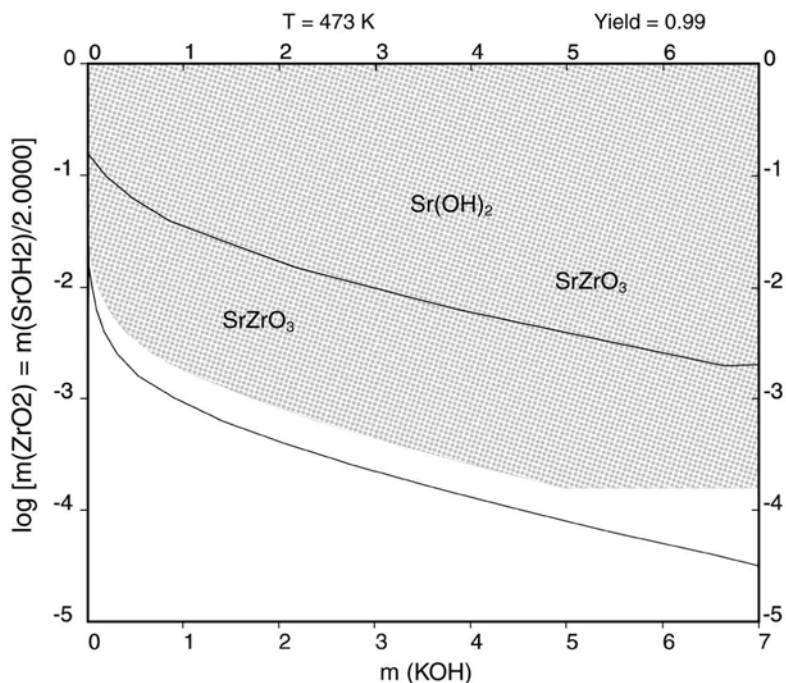


Fig. 8.8. Calculated phase stability and yield diagram as a function of the input amount of KOH at 473 K for Sr/Zr = 2.0 using Sr(OH)₂ as a source of strontium. The solid circle denotes experimental conditions for which phase-pure SrZrO₃ was obtained.

for the formation of pure strontium zirconate. The region of nearly complete yield of SrZrO₃ (> 99%) is much greater than for Sr/Zr = 1.0 and starts at lower amounts of KOH (cf. Fig. 8.5) and correspondingly lower pH values [15]. No mineralizer is necessary when the input concentration of Zr exceeds 0.02 m. The upper solid line in Fig. 8.8 represents the incipient precipitation line of strontium hydroxide. In the area above this line, SrZrO₃ is always contaminated with SrOH₂.

Our work has also examined the possibility of utilizing organic mineralizers [58]. The next diagram shows the calculated yield of lead zirconate titanate (PbZr_{0.6}Ti_{0.4}O₃) at 433 K with the ratio of lead acetate to a sum of titanium and zirconium dioxide equal to 1.1. In Fig. 8.9, the input molalities of Ti precursor are plotted against the molality of tetramethylammonium hydroxide (Me₄NOH). The upper left and lower solid lines encompass the region of stability of rhombohedral PZT. They belong to the incipient precipitation line. Phase-pure PbZr_{0.6}Ti_{0.4}O₃ can form in a relatively wide region of input precursor and mineralizer molalities (cf. shaded area in Fig. 8.9). PbZr_{0.6}Ti_{0.4}O₃ precipitates along with PbO in the small region shown on the top of the phase-purity region. The stability area of PbO is

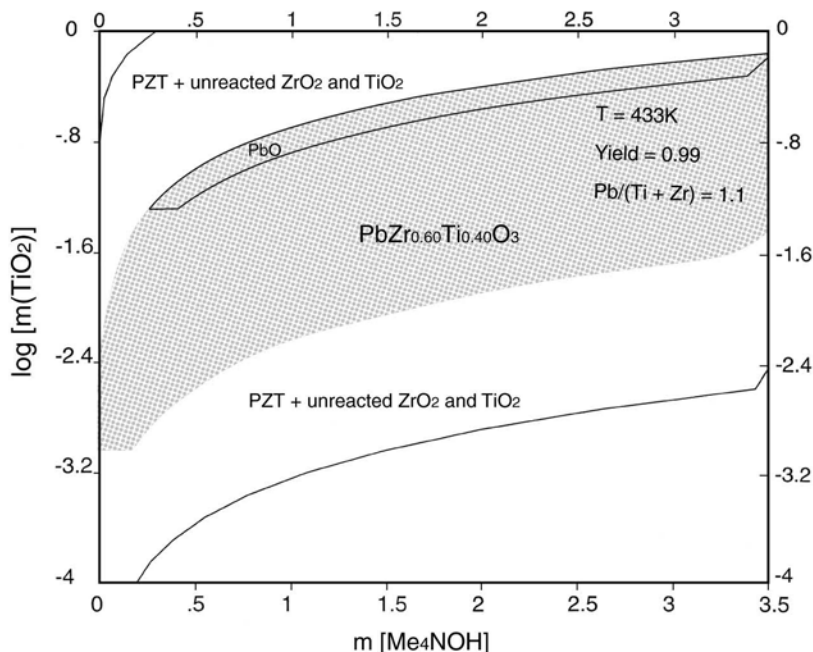


Fig. 8.9. Calculated yield diagram of $\text{PbZr}_{0.6}\text{Ti}_{0.4}\text{O}_3$ at 433 K. PbAc_2 , TiO_2 , and ZrO_2 are used as starting materials for the calculations

relatively small and limited to a high concentration of precursors. In highly alkaline solutions, lead oxide dissolves. When the ratio of metals in precursor materials is greater than one, the area of the perovskite phase-purity region widens. However, at some reaction conditions it causes contamination of ceramic materials with additional phases.

8.2.6 Carbon dioxide contamination

There are three general ways to introduce CO_2 into a hydrothermal product. They are as follows:

1. Contaminated starting materials (e.g., alkaline and alkaline-earth hydroxides, hydrous oxides)
2. Synthesis unit operation into a high pH precursor solution (the absorption of CO_2)
3. Post-synthesis unit operations (i.e., during washing, filtration, etc.)

To eliminate the risk of carbonate contamination with starting materials, all reagents should be free from carbonates. However, carbonate-free alkaline-metal hydroxides (i.e., precursors) and alkaline hydroxides (i.e., mineralizers) are not

available commercially. For example, according to the manufacturer (Aldrich), the 99.99% (adjusted to cation) electronic grade KOH contains 0.4 wt% of K_2CO_3 . On the other hand, commercially available alkaline-earth hydroxides usually contain 0.5–3 wt% of CO_2 . The weight percent of alkaline-earth carbonate in the final product can be calculated assuming that all K_2CO_3 contained in KOH converts to ACO_3 ($A = Ba, Sr, Ca$). In principle, carbonates can be removed from the final product by washing with a weak acid but the risk of dissolving ceramic materials with acids is very high as suggested in the stability and yield diagrams (cf. Figs. 8.1–8.10). Therefore, it is advisable to purify commercial hydroxides and hydrates. It can be done by filtering metal carbonate contaminants from a hot stock solution of the corresponding hydroxide and hydrate.

The problem of contamination of the solution with carbonates during preparation of starting materials has been discussed in our previous papers [11,13]. Unless the system is isolated from the atmosphere, contact with CO_2 may occur during precursor solution preparation. The effect of atmospheric CO_2 on the purity of alkaline-earth titanates and zirconates is different for the Ca-, Sr-, and Ba-containing hydrothermal systems. It is directly correlated with the alkalinities of Ca, Sr, and Ba because the absorption of CO_2 is facilitated by the alkalinity of the solution. Accordingly, the metal concentration thresholds above which carbonates precipitate are different for the three systems. For example, the contact of alkaline strontium precursors with an open CO_2 -containing air atmosphere will lead to a contamination with $SrCO_3$ when the input concentration of Sr is above about 10^{-4} m [11,15]. Thus, it is beneficial to avoid contact with atmosphere during the preparation of reagents. This is also the case when alkaline-earth metal salts (e.g., nitrates or acetates) are used as precursors in conjunction with NaOH or KOH as mineralizers because the presence of the mineralizers makes the solutions alkaline. However, our practical observations show that the absorption of atmospheric CO_2 may require a substantial amount of time, which could be much longer than the time required for experimental manipulations.

Washing and vacuum filtering of the synthesis products in air may cause additional contamination, especially when an excess amount of the A-site cation is present in alkaline environments. However, our study [15] shows that the existing carbonate content of the starting materials appears to be the major determinant of the purity of the product.

For our thermodynamic simulations, we assume that the carbonate contamination results primarily from the CO_2 content of the starting materials. We have constructed stability diagrams for the Sr-Zr- CO_2 - H_2O system in which the amount of CO_2 is varied proportionally to the amount of the Sr and Zr precursors [15]. This simulates a real-world situation in which CO_2 is a fixed fraction of a reactant. Figure 8.10 shows the effect of CO_2 on the stability and yield diagram plotted against the pH when the input amount of CO_2 is equal to 0.085 times the amount of ZrO_2 . This amount corresponds to the average concentration of carbon dioxide typically found in hydrous ZrO_2 and KOH in our reactions [15]. In Fig. 8.10, the stability region of strontium carbonate has a parabolic shape. Despite the small CO_2 content of the system, $SrCO_3$ is very stable and its stability range almost overlaps with

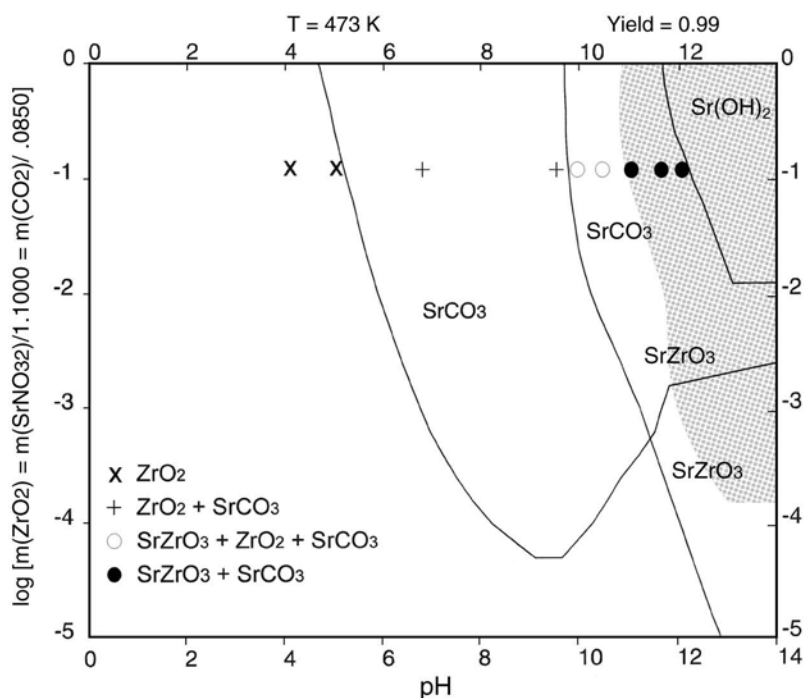


Fig. 8.10. Calculated phase stability and yield diagram at 473 K for Sr/Zr = 1.1 using $\text{Sr}(\text{NO}_3)_2$ as a source of strontium when the amount of CO_2 in the starting materials is equal to 0.085 times the amount of ZrO_2 . The symbols denote experimental conditions for which the following products were obtained: (x) ZrO_2 , (+) $\text{SrCO}_3 + \text{ZrO}_2$, (Y) $\text{SrZrO}_3 + \text{ZrO}_2 + \text{SrCO}_3$, (●) $\text{SrZrO}_3 + \text{SrCO}_3$

the nearly complete yield range of strontium zirconate denoted by the shaded area. At very high pH values, strontium hydroxide is stable and its stability region overlaps with those of strontium zirconate and strontium carbonate. Thus, SrZrO_3 is predicted to be carbonate-free only in dilute solutions at high pH values.

The hydrothermal equilibrium systems discussed in this chapter provide representative examples of what can be achieved using our methodology. These examples show that for a given precursor system, thermodynamic calculations can be used to specify the optimum synthesis conditions for the formation of phase-pure smart perovskite materials. However, electrolyte thermodynamics computations alone are not sufficient. Sluggish reaction kinetics at low temperatures as well as the limited availability of thermochemical data for some species in the hydrothermal system can render questionable conclusions derived from computations. Therefore, experimental evaluation of the thermodynamic predictions is necessary.

8.3 Validation and Applications of Thermodynamic Modeling

In order to validate the theoretical predictions, experiments are performed using the calculated stability and yield diagrams as a guide. In particular, hydrothermal syntheses are carried out at various metal precursor concentrations and ratios (A/B) for a wide pH range (mineralizer concentration) at each temperature. Thus, hydrothermal reactions are performed to investigate whether the location of the various stability and yield regions agrees with the experimental findings. Soluble salts of lead and alkaline-earth metals are used as sources of the A-site cation in the hydrothermal synthesis. Such starting materials are inexpensive and easy to handle. Also, alkaline-earth metal hydroxides can be used for this purpose [11,13,15]. However, they usually contain carbonates [15] and, therefore, should be purified prior to use. Also, their low solubility is of concern [15]. As a convenient source of the B-site cation, commercial anhydrous or freshly precipitated hydrous oxides are used, the latter considered more reactive [12,14–15]. From a practical point of view, the starting material concentration above 0.02 m is recommended. Reaction products are identified using X-ray diffraction technique. To further verify phase purity, other techniques such as wet chemical methods, thermogravimetric analysis, electron diffraction, energy dispersive spectroscopy, and other methods are employed. These tools are important if X-ray diffraction patterns are inconclusive. Experimental points are plotted in the corresponding regions of the yield diagrams (cf. Figs. 8.4, 8.7, 8.10).

Our simulation approach has been validated for numerous perovskite systems, which include BaTiO_3 [59], CaTiO_3 [13], SrTiO_3 [11], SrZrO_3 [15], PbTiO_3 [12,57–58], various solid solutions of PZT [14,60], PMN [31], and PZN [31]. The results indicate a very good agreement between theoretical predictions and experimental results for all investigated systems.

It is noteworthy that in some cases this agreement takes place only above a certain temperature that is characteristic for a precursor system (cf. Figs. 8.4, 8.7) or in certain regions of the stability and yield diagrams (e.g., in the phase-pure region or at high pH values, cf. Fig. 8.3). For example, there is an excellent agreement between predictions and experiments at temperatures above 410 K in the Pb-Ti- H_2O system [12] (cf. Fig. 8.4). However, the same agreement can be reached even at lower temperatures (above 363 K) in the same system with complexing agents [57]. The discrepancies at lower temperatures may be caused by sluggish reaction kinetics that can lead to the formation of metastable crystalline or amorphous products (cf. Figs. 8.4 and 8.7) that cannot be inferred from thermodynamic computations. Also, the lack of thermodynamic data (e.g., for $\text{Pb}_2\text{Ti}_2\text{O}_6$ or amorphous precursors) and inaccurate data may contribute to the disagreement.

Possible sources of disagreement may also result from a fact that the complexity of the thermodynamic system depends on the scale of mixing of all reagents. It is worth noting that thermodynamic calculations assume that all reagents are mixed on a microscopic scale. This is especially important in the case of solid solutions. In practice, the mixture may not be homogenous. Thus, instead of a phase-

pure product, phase separation results [14] such as precipitation of the end-members of the solid solution system (e.g., PT and PZ instead of PZT) or formation of multiple phases (e.g., CaTiO_3 and $\text{Ca}(\text{OH})_2$), which are likely far from equilibrium [12,14].

To validate the thermodynamic predictions with greater accuracy, a special option called “an expert system” has been developed as a part of the OLI program. It makes it possible to design experiments that test the position of the yield boundary (cf. the shaded areas in Figs. 8.3–8.10). For this purpose, the expected yield and amount of ceramic material as well as the number of tests inside and outside the yield boundary is specified by the user in conjunction with the allowed variation in temperature and precursor concentration. As a result, the recommended metal precursor and mineralizer concentrations at each temperature are calculated.

Our computations for numerous systems have uncovered a series of thermodynamic trends. The systems investigated so far belong to two categories: alkaline-earth metal and lead-containing perovskites. Stability diagrams for alkaline-earth titanates (i.e., CaTiO_3 , SrTiO_3 , and BaTiO_3) are qualitatively similar because of the chemical similarity of the Ca, Sr, and Ba cations. Their stability and yield regions are limited by lower boundaries with respect to pH [11,13] (cf. Figs. 8.2, 8.10). In other words, alkaline-earth titanates and zirconates are stable in alkaline solutions and dissolve in either acids or CO_2 -containing water, or both. The formation of phase-pure alkaline-earth titanates from metal hydroxides instead of metal nitrates or acetates at high input metal concentrations (above 0.1 m) does not require the addition of a mineralizer because the necessary concentration of OH^- groups is readily provided by the hydroxide precursor [13]. The presence of excess A-site ions in precursor reagents (i.e., $A/B > 1$) expands the width of the yield region closer to the incipient precipitation line. Thus, phase-pure products can form at less alkaline solution, which is very important from economic and environmental points of view. However, if the pH becomes too high, alkaline-earth hydroxides precipitate as an impurity phase (cf. Fig. 8.10). Alkaline-earth metal-Ti-Zr- H_2O systems also proved to be very vulnerable to contamination with carbonates [11,13,15] (cf. Fig. 8.10).

In contrast to the alkaline-earth metals, lead is amphoteric. Its hydroxy complexes are relatively stable in highly alkaline environments. Therefore, the stability areas of PT, PZ, and PZT are parabolic in shape (cf. Figs. 8.1, 8.3, 8.10). In other words, the stabilities of lead-containing perovskites are bounded by lower and upper pH limits. Although the presence of excess lead widens the yield region, it can also cause the precipitation of an unwanted PbO phase in the middle of the yield region [12]. However, this problem has been solved with the aid of complexing agents and our simulation-based approach [57]. In contrast to alkaline-earth perovskites, carbonate contamination is not an issue in the Pb-Ti-Zr- H_2O systems because lead-containing carbonates (i.e., $2\text{PbO}\cdot\text{PbCO}_3$, $\text{PbO}\cdot\text{PbCO}_3$, PbCO_3 , $2\text{PbCO}_3\cdot\text{Pb}(\text{OH})_2$, and PbCO_3) are less stable than their corresponding perovskites.

8.4 Summary

A thermodynamic model of heterogeneous aqueous electrolyte systems, coupled with a facility for the automatic generation of stability and yield diagrams, provides a powerful tool for predicting the effect of various process conditions on the synthesis of smart ceramic materials. In particular, it makes it possible to determine the optimum conditions (T, pH, input precursor concentrations, and ratios) for the synthesis of various perovskite-type materials from simple precursors. The model is particularly valuable for analyzing the effects of changing the chemical identity and relative amounts of starting materials as well as for predicting the possibility of contamination with carbonates. The theoretical predictions allow us to formulate synthesis guidelines. In order to validate the results of theoretical predictions, experimental syntheses were performed in the whole temperature and pH range and for various input amounts of starting materials. Experience has demonstrated that this first-principles based approach provides a very successful means to find optimum synthesis conditions for the formation of perovskite-type multicomponent oxides.

References

1. Peterson JH (1940) Process for Producing Insoluble Titanates, US Pat No 2216655, Oct 22
2. Christensen AN, Rasmussen SE (1963) Hydrothermal Preparation of Compounds of the Type ABO_3 and AB_2O_4 . *Acta Chem Scand* 17(3):845
3. Christensen AN (1970) Hydrothermal Preparation of Barium Titanate by Transport Reactions. *Acta Chem Scand* 24:2447–2452
4. Kutty TRN, Vivekanandan R, Murugaraj P (1988) Precipitation of Rutile and Anatase (TiO_2) Fine Powders and Their Conversion to $MTiO_3$ (M = Ba, Sr, Ca) by the Hydrothermal Method. *Mater Chem Phys* 19:533–546
5. Kutty TRN, Balachandran R (1984) Direct Precipitation of Lead Zirconate Titanate by the Hydrothermal Method. *Mat Res Bull* 19:1479–1488
6. Dawson WJ Swartz SL (1992) Process for Producing Submicron Ceramic Powders of Perovskite Compounds with Controlled Stoichiometry and Particle Size. US Pat No 5 112 433, May 12
7. Beal KC (1987) Precipitation of Lead Zirconate Titanate Solid Solutions Under Hydrothermal Conditions. In: Messing GL, Mazdiyasi KS, McCauley JW, Haber RA (eds) *Advances in Ceramics, Vol 21, Ceramic Powder Science*. American Ceramic Society, Westerville, OH, p 33
8. Watson DJ, Randall CA, Newnham RE, Adair JH (1988) Hydrothermal Formation Diagram in the Lead Titanate System. In: Messing GL, Mazdiyasi KS, McCauley JW, Haber RA (eds) *Ceramic Transactions, Vol 1, Ceramic Powder Science IIA*. American Ceramic Society, Westerville, OH, p 154
9. Kaneko S, Imoto F (1978) Reactions between PbO and TiO_2 under Hydrothermal Conditions. *Bull Chem Soc Jpn* 51(6):1739–1742

10. Komarneni S, Li Q, Stefansson KM, Roy R (1993) Microwave-Hydrothermal Processing for Synthesis of Electroceramic Powders. *J Mater Res* 8(12):3176–3183
11. Lencka MM, Riman RE (1994) Hydrothermal Synthesis of Perovskite Materials: Thermodynamic Modeling and Experimental Verification. *Ferroelectrics* 151:159–164
12. Lencka MM, Riman RE (1993) Synthesis of Lead Titanate: Thermodynamic Modeling and Experimental Verification. *J Am Ceram Soc* 76(10):2649–2659
13. Lencka MM, Riman RE (1995) Thermodynamics of the Hydrothermal Synthesis of Calcium Titanate with Reference to Other Alkaline-Earth Titanates. *Chem Mater* 7(1):18–25
14. Lencka MM, Anderko A, Riman RE (1995) Hydrothermal Precipitation of Lead Zirconate Titanate Solid Solutions: Thermodynamic Modeling and Experimental Verification. *J Am Ceram Soc* 78(10):2609–2618
15. Lencka MM, Nielsen E, Anderko A, Riman RE (1997) Hydrothermal Synthesis of Carbonate-Free Strontium Zirconate: Thermodynamic Modeling and Experimental Verification. *Chem Mater* 9(5):1116–1125
16. Graham B, Patterson GD (1958) Film-Forming Hydrosols of Barium Titanate, their Preparation and a Substrate Coated Therewith. US Patent No 2841503, July 1
17. Kajioshi K, Ishizawa N, Yoshimura M (1991) Heteroepitaxial Growth of BaTiO₃ Thin Films on SrTiO₃ Substrates under Hydrothermal Conditions. *Jpn J Appl Phys* 30(1B):L120–L123
18. Kajioshi K, Ishizawa N, Yoshimura M (1991) Preparation of Tetragonal Barium Titanate Thin Film on Titanium Metal Substrate by Hydrothermal Method. *J Am Ceram Soc* 74(2):369–374
19. Bendale P, Venigalla S, Ambrose JR, Verink Jr ED, Adair JH (1993) Preparation of Barium Titanate Films at 55°C by an Electrochemical Method. *J Am Ceram Soc* 76(10):2619–2627
20. Kajioshi K, Yoshimura M, Hamaji Y, Tomono K, Kasanami T (1996) Growth of (Ba,Sr)TiO₃ Thin Films by the Hydrothermal-Electrochemical Method and Effect of Oxygen Evolution on Their Microstructure. *J Mater Res* 11(1):169–183
21. Bacsá R, Ravindranathan P, Dougherty JP (1992) Electrochemical, Hydrothermal, and Electrochemical-Hydrothermal Synthesis of Barium Titanate Thin Films on Titanium Substrates. *J Mater Res* 7(2):423–428
22. Chien AT, Speck JS, Lange FF (1997) Hydrothermal Synthesis of Heteroepitaxial PbZr_xTi_{1-x}O₃ Thin Films at 90–150°C. *Mater Res Bull* 12(5):1176–1178
23. Laudise RA (1987) Hydrothermal Synthesis of Crystals. *Chem Eng News* 28:30–43
24. Marshall DJ, Laudise RA (1966) The Hydrothermal Phase Diagrams K₂O-Nb₂O₅ and K₂O-Ta₂O₅ and the Growth of Single Crystals of K(Ta,Nb)O₃. *Proceedings of an International Conference on Crystal Growth*, p 557, Boston, June 20–24
25. Yanagisawa K, Kanai H (1997) Crystal Growth of Lead Zirconate Titanate with Additives under Hydrothermal Conditions. *Jpn J Appl Phys* 36(1-9B):6031–6034
26. Dawson WJ (1988) Hydrothermal Synthesis of Advanced Ceramic Powders. *Ceram Bull* 67(10):1673–1678
27. Rafal M, Berthold JW, Scrivner NC, Grise SL (1995) Models for Electrolyte Solutions. In: Sandler SI (ed) *Models for Thermodynamic and Phase Equilibria Calculations*. Marcel Dekker, New York, pp 601–670
28. Zemaitis Jr JF, Clark DM, Rafal M, Scrivner NC (1986) *Handbook of Aqueous Electrolyte Thermodynamics: Theory & Application*. AIChE, New York

29. Lencka MM, Riman RE (1993) Thermodynamic Modeling of Hydrothermal Synthesis of Ceramic Powders. *Chem Mater* 5(1):61–70
30. Environmental and Corrosion Simulation Programs (ESP/CSP), OLI Systems, Inc, Morris Plains, NJ, 1996
31. Lencka MM, Cho SB, Riman RE, Equilibria in the Pb-Mg-Nb and Pb-Zn-Nb Hydrothermal Systems, to be published
32. Helgeson HC, Kirkham DH, Flowers GC (1981) Theoretical Prediction of the Thermodynamic Behavior of Aqueous Electrolytes at High Pressures and Temperatures: IV. Calculation of Activity Coefficients, Osmotic Coefficients, and Apparent Molal and Standard and Relative Partial Molal Properties to 600°C and 5 kb. *Am J Sci* 281:1249–1428
33. Tanger JC, Helgeson HC (1988) Calculation of the Thermodynamic and Transport Properties of Aqueous Species at High Pressures and Temperatures: Revised Equations of State for the Standard Partial Molal Properties of Ions and Electrolytes. *Am J Sci* 288:19–98
34. Bromley LA (1973) Thermodynamic Properties of Strong Electrolytes in Aqueous Solutions. *AIChE J* 19(2):313–320
35. Pitzer KS (1973) Thermodynamics of Electrolytes. I. Theoretical Basis and General Equations. *J Phys Chem* 77(2):268–277
36. Soave G (1972) Equilibrium Constants from a Modified Redlich-Kwong Equation of State. *Chem Eng Sci* 27:1197–1203
37. Meissner HP (1980) in Newman SA (ed) Thermodynamics of Aqueous Systems with Industrial Application. *Am Chem Soc Symp Ser* 133:495–511
38. Shock EL, Helgeson HC (1988) Calculation of the Thermodynamic and Transport Properties of Aqueous Species at High Pressures and Temperatures: Correlation Algorithms for Ionic Species and Equation of State Predictions to 5 kb and 1000°C. *Geochim Cosmochim Acta* 52:2009–2036
39. Shock EL, Helgeson HC, Sverjensky DA (1989) Calculation of the Thermodynamic and Transport Properties of Aqueous Species at High Pressures and Temperatures: Standard Partial Molal Properties of Inorganic Neutral Species. *Geochim Cosmochim Acta* 53:2157–2183
40. Wagman DD, Evans WH, Parker WB, Halow I, Bailey SM, Schumm RH (1968–1982) Selected Values of Chemical Thermodynamic Properties, NBS Technical Note 270/3-8
41. Wagman DD, Evans WH, Parker WB, Schumm RH, Halow I, Bailey SM, Churney KL, Nuttall RL (1982) The NBS Tables of Chemical Thermodynamic Properties. *J Phys Chem Ref Data* 11:Suppl No 2
42. Chase Jr MW, Davies CA, Downey Jr JR, Frurip DJ, McDonald RA, Syverud AN (1985) JANAF Thermochemical Tables, 3rd ed. *J Phys Chem Ref Data* 14:Suppl No 1
43. Medvedev VA, Bergman VA, Gurvich LV, Yungman VS, Vorobiev AF, Kolesov VP (1962–82) *Termicheskie Konstanty Veshchestv* (Thermal Constants of Substances), Vols 1-10. Glushko VP (ed), Russian Academy of Sciences, Viniti, Moscow, USSR
44. Robie RA, Hemingway BS, Fisher JR (1995) Thermodynamic Properties of Minerals and Related Substances at 298.15 K and 1 Bar (10^5 Pascals) Pressure and at Higher Temperatures. US Geological Survey Bulletin 1452, US Government Printing Office, Washington, DC
45. Barin I, in collaboration with Sauert F, Schultze-Rhonhof E, Shu Sheng W (1993) Thermochemical Data of Pure Substances. VCH Publishers, New York

46. Seidell A (1940) *Solubilities of Inorganic and Metal Organic Compounds*, 3rd ed, Vol 1, D. Van Nostrand Company, Inc, New York
47. Linke WF, Seidell A (1965) *Solubilities of Inorganic and Metal-Organic Compounds*, 4th ed, Vol 2. American Chemical Society, Washington, DC
48. Sverjensky DA (1987) Calculations of the Thermodynamic Properties of Aqueous Species and the Solubilities of Minerals in Supercritical Electrolyte Solutions. In: Carmichael ISE, Eugster HP (eds), *Reviews in Mineralogy, Thermodynamic Modeling of Geologic Materials: Minerals, Fluids and Melts*, Vol 17. Mineralogical Society of America, Chelsea, MI, pp 177-209
49. Lencka MM, Riman RE (1995) Estimation of Thermochemical Properties for Ceramic Oxides: A Focus on PbZrO_3 . *Thermochim Acta* 256:193–203
50. Sverjensky DA (1984) Prediction of Gibbs Free Energies of Calcite-type Carbonates and the Equilibrium Distribution of Trace Elements between Carbonates and Aqueous Solutions. *Geochim Cosmochim Acta* 48:1127–1134
51. Sverjensky DA, Molling PA (1992) A Linear Free Energy Relationship for Crystalline Solids and Aqueous Ions. *Nature* 356:231–234
52. Latimer W (1952) *The Oxidation State of Elements and Their Potentials in Aqueous Solutions*, 2nd ed. Prentice-Hall, New York
53. Osseo-Asare K, Arriagada FJ, Adair JH (1988) in Messing GL, Fuller Jr ER, Hausner H (eds) *Ceramic Transactions, Vol I, Ceramic Powder Science IIA*. American Ceramic Society, Westerville, OH, p 47
54. Halliyal A, Kumar U, Newnham RE, Cross LE (1987), Stabilization of the Perovskite Phase and Dielectric Properties of Ceramics in the $\text{Pb}(\text{Zn}_{1/3}\text{Nb}_{2/3})\text{O}_3$ - BaTiO_3 System. *Am Ceram Soc Bull* 66(4):671–676
55. Shrout TR, Halliyal A (1987) Preparation of Lead-Based Ferroelectric Relaxors for Capacitors. *Am Ceram Soc Bull* 66(4):704–711
56. Hung CC (1990) Hydrothermal BaTiO_3 Synthesis: The Effect of Aqueous Rinsing on Surface Chemistry. MSc Thesis, Rutgers University, New Brunswick, New Jersey, October
57. Gersten B, Lencka MM, Riman RE (2002) Engineered Low Temperature Hydrothermal Synthesis of Phase-Pure Lead-Based Perovskites using Ethylenediaminetetraacetic Acid Complexation. *Chem Mater*, in press
58. Cho SB, Lencka MM, McCandlish LE, Riman RE, Low Temperature Hydrothermal Synthesis and Formation Mechanisms of Lead Titanate Particles using Tetramethylammonium Hydroxide: Thermodynamic Modeling and Experimental Verification, in preparation
59. Eckert Jr JO, Hung-Houston CC, Gersten BL, Lencka MM, Riman RE (1996) Kinetics and Mechanism of Hydrothermal Synthesis of Barium Titanate. *J Am Ceram Soc* 79(11):2929–2939
60. Oledzka M, Lencka MM, Pinceloup P, Mikulka-Bolen K, McCandlish LE, Riman RE, (2002) The Influence of Precursor on Microstructure and Phase Composition of Epitaxial, Hydrothermal $\text{PbZr}_{0.7}\text{Ti}_{0.3}\text{O}_3$. *Chem Mater*, in press

9 Growth of Multicomponent Perovskite Oxide Crystals: Synthesis Conditions for the Hydrothermal Growth of Ferroelectric Powders

Bonnie L. Gersten

ARL, ATTN: AMSRL-WM-MD, Building 4600, APG, MD 21005-5069

9.1 Introduction

In this chapter a general description of the hydrothermal process and ferroelectric materials will be presented. An overview of the approaches used for the synthesis will be outlined in table form. In addition, the specifics of the synthesis for controlled chemical and phase purity, kinetics and rate controlling mechanisms, controlled morphology, and controlled particle size will be discussed. Finally, conclusions about the synthesis of the hydrothermal growth of ferroelectric powders will be made.

9.2 General Overview

9.2.1 Description

Hydrothermal synthesis is accomplished by the use of suspensions or homogeneous solutions subjected to temperature and pressure to induce rapid phase transformation kinetics. This synthesis method falls under the category of wet chemical methods that includes sol-gel and coprecipitation. The wet chemical routes achieve purer and finer powders than the conventional solid-state calcination route. Unlike other wet chemical methods, the hydrothermal method can be used to prepare anhydrous phase-pure oxides in a single step synthesis route from inexpensive precursors. During the process, no hazardous volatiles are produced. Furthermore, the water-based solvent can be recycled. All of these advantages make hydrothermal processing an environmentally friendly manufacturing process. The method has been used to prepare powders as reviewed in Dawson [1] and Riman [2]. Crystals have been discussed by Yanagisawa et al. [3–5], and films by Bendale et al. [6], Chien et al. [7–8], Kajiyoshi et al. [9], Pilleux et al. [10], Roeder et al. [11], and Yoshimura et al. [12].

Hydrothermal processes can further be categorized into oxidation, precipitation, decomposition, and crystallization processes as described by Somiya [13]. The oxidation requires a metal powder to transform to an oxide while in water (e.g., an oxidation equation: $\text{PbO} + \text{Zr} + 2\text{H}_2\text{O} \rightarrow \text{PbZrO}_3 + 2\text{H}_2$ (Somiya [13])). In the precipitation process, two metal salts dissolve in water and coprecipitate under hydrothermal conditions (e.g., a precipitation equation: $\text{Pb}(\text{NO}_3)_2 + 0.5\text{ZrOCl}_2 + 0.5\text{TiCl}_4 + \text{KOH} + \text{H}_2\text{O} \rightarrow \text{Pb}(\text{Zr}_{0.5}\text{Ti}_{0.5})\text{O}_3 + \text{H}_2\text{O} + \text{ions}$ (Lee et al. [14])). In the decomposing process a precursor (e.g., an oxalate or carboxalate) decomposes under hydrothermal conditions (e.g., a decomposition equation: $\text{SrTiO}_{(2-x/2)}(\text{OH})_{1+x}\text{OOC-}n\text{-C}_7\text{H}_{15}$ ($0 < x < 2$) $+\text{H}_2\text{O} \rightarrow \text{SrTiO}_3 + \text{H}_2\text{O} + \text{other species}$ (Riman et al. [15])). In the crystallization process a hydrous precursor crystallizes to form a crystallite while in water (e.g., a crystallization equation: $\text{PbO} + \text{ZrO}_2 \cdot n\text{H}_2\text{O} + \text{H}_2\text{O} \rightarrow \text{PbZrO}_3 + n\text{H}_2\text{O}$ (Somiya [13])).

9.2.2 Perovskite ferroelectrics

The perovskites are of interest to the electronics industry because of their structure that gives them unique electronic properties. The ABO_3 perovskite unit cell is illustrated in Fig. 9.1. Each 'A' site ion is surrounded by twelve nearest neighbor oxygen ions, while, each 'B' site ion has six oxygen ions in an octahedral coordination. The 'A' site ions and oxygen ions together form a face centered cubic lattice, with 'B' site ions fitting into octahedral interstices. Since the 'B' site ion is much smaller than the 'A' site ion, the 'B' site ion can rattle within the octahedral interstices which suggests minimum energy positions for the 'B' site that are off-center and consequently give rise to an electric dipole. When a stress is applied, the dipoles align in one direction to provide a polarization that is called the piezoelectric effect. The ferroelectric state is when the crystals contain a spontaneous reversible electric dipole moment. The paraelectric state is when the dipoles in neighboring cells are randomly oriented relative to each other. The change from paraelectric to ferroelectric state occurs at the Curie temperature and corresponds to the change in dielectric constant. Therefore, many perovskite materials are used for applications in electronics (e.g., nonvolatile memories, transducers, actuators, and capacitors) based on their special electronic properties. Jaffe et al. [16] provides a more detailed description of ferroelectrics in his book on piezoelectrics.

The hydrothermal method allows for the tailoring of electronic properties of the ferroelectric materials by varying the composition of the 'A' and 'B' site cations and allows for a controlled dopant distribution. Furthermore, the production of more reactive-controlled, nano-sized particles allows for lower temperature sintering so that co-firing can be accomplished with less expensive electrodes (e.g., 30%Pd with 70%Ag). The control of particle size also prevents exaggerated grain growth and allows for thinner layers of materials for a better control of electronic materials and better mechanical stability.

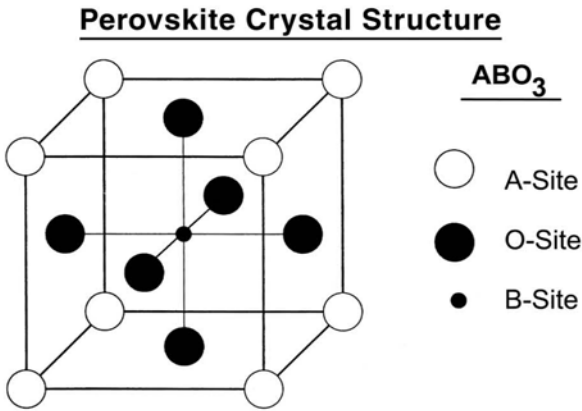


Fig. 9.1. ABO₃ perovskite unit cell [20]

9.2.3 History

Flaschen [17] in 1955 was the first to publish an article written about the hydrothermal synthesis of the ferroelectric materials. Flaschen [17] prepared BaTiO₃ from titanium ester and soluble barium salt at a pH of 11–14 at a temperature greater than 80°C for 1–2 h. Since then many other perovskite ferroelectric materials have been prepared by the hydrothermal method by many others (cf. Table 9.1).

The conditions of the preparation however have varied. Tables 9.2–9.4 outline some of the conditions used in the hydrothermal synthesis of PbTiO₃, Pb(Zr,Ti)O₃, and BaTiO₃, respectively. These variables include time, temperature, pH, mineralizer type, mineralizer concentration, type of ‘A’ site precursor, type of ‘B’ site precursor, ‘A’/‘B’ molar ratio in the precursor, concentration of ‘A’ site precursor, and the use of additives or stirring.

Table 9.1. Ferroelectric Powders Prepared by the Hydrothermal Method

SrTiO ₃ [18–24]	BaTiO ₃ [6–8,17–19,20,23,25–65]	PbTiO ₃ [18,20,23,28,45,66–84]
CdTiO ₃ [18]	CaTiO ₃ [18,24,45,85–86]	BaSnO ₃ [87]
SrZrO ₃ [23,88]	BaZrO ₃ [18,23,89]	CaZrO ₃ [18]
PbZrO ₃ [20]	(Ba,Sr)TiO ₃ [11,20,23,90,11]	Ba(Ti,Zr)O ₃ [33,60]
Ba(Ti,Sn)O ₃ [91]	(Ba,Sr)(Ti,Zr)O ₃ [34]	Pb(Zr,Ti)O ₃ [20,23,92–102]
Pb(Zr,Ti)O ₃ –Nb ₂ O ₃ [3]	Pb(Sc,Nb)O ₃ [5]	(Pb,La)(Zr,Ti)O ₃ [4,100]
Pb(Zr,Ti)O ₃ –MnO [3]		

Table 9.2. Synthesis Conditions for PbTiO₃

Author	Time [h]	T [°C]	pH	Min. [type]	[Min] [M]	'Pb'	'Ti'	Pb/Ti	[Pb] [M]	Stir
Kaneko & Imoto [76]	5	100–500				oxide	SO ₃	1–1.8		No
Takai et al. [77]	1–3	100–160				oxide	NO ₃			Yes
Suzuki et al. [75]	6–8	100–220	11–14	KOH		acetate	Cl	1	0.15	Yes
Walton et al. [74]	1	200–300	9.5–9.6	NH ₃		acetate	isopropoxide	1	0.5–1	Yes
Rossetti et al. [80]	0–367	225–250	9.5–9.6	NH ₃		acetate	isopropanol	1	0.1–1	Yes
Li & Yao [79]	1–4	180–200	13.6–13.8	KOH	0.4–1	acetate	butoxide	1.2–2	0.1–0.5	No
Lencka & Riman [66]	24–72	90–160	9–11	KOH NH ₃		acetate NO ₃	oxide, isopropoxide	1–1.5	0.05–0.2	No
Sato et al. [70]	2–8	150–300		K, Na, Li-OH NH ₃		NO ₃	Cl	1		Yes
Ohara et al. [69]	24	150				OH	K-Ti	1		No
Cheng et al. [68]	2	220		KOH	4	oxide	oxide	0.5–1.05	5	Yes
Choi et al. [28]	16	220		KOH		acetate	Cl	1	0.15	Yes
Moon et al. [72–73]	0–18	150	> 14	KOH	1	acetate	acetylacetone	1.5	0.025–0.125	Yes
Gersten et al. [67]	72	70–200	7–14	KOH	0–10	acetate	oxide, isopropoxide	1–2	0.05–0.1	No
Gelabert et al. [78]	96–144	200		KOH KF		NO ₃	CH ₃ CH ₂ C H ₂ O	2		No

Table 9.3. Synthesis Conditions for $\text{Pb}(\text{Zr,Ti})\text{O}_3$

Author	Time [h]	T [°C]	pH	Min. [type]	[Min] [M]	'Pb'	'B'	Pb/'B'	[Pb] [M]	Stir
Kutty et al. [92]	6–8	150–350				oxide	Cl	1		Yes
Lee et al. [14]	0.5–96	70–200		KOH, NaOH	2–10	NO_3	Cl	1	1	No
Beal [75]	0.5	300	> 12	Many	0.1–0.66	oxide	Cl	1.1	0.5	Yes
Lencka et al. [93]	24–48	90–200	8.5–12	KOH		acetate NO_3	pro- poxide	1	0.1	Yes
Ichihara et al. [98]	0.5–48	70–200		KOH	4–10	NO_3	Cl	1–1.2		Yes
Cheng et al. [97]	2	150		KOH	1–5	acetate	Cl, butyl	1–1.9	0.5	No
Ohba et al. [99]	4	150, 180		KOH	0.001–10	NO_3	hydrous	1.1	0.0275–0.55	Yes
Su et al. [102]	6	350		KOH, NaOH	1	acetate	acetyla- cetone			Yes
Lee & Yen [100]	2–48	160–260		KOH	0.5	NO_3	Cl	1	0.05	No
Chen et al. [96]	35–70	160–240				acac	hydrous	1	0.13	No
Traianidis [101]	2	265		KOH	1–10	NO_3	hydrous	1–2	0.13	No

Table 9.4. Synthesis Conditions for BaTiO₃

Author	T [h]	T [°C]	pH	Min. [type]	[Min] [M]	'Ba'	'Ti'	Ba/Ti	[Ba] [M]	Stir
Flaschen [17]	1–2	80		KOH		Salt	ester	1		No
Christensen et al. [18]	70–125	350–490		NaOH, KF	1–4	OH	O ₂ *H ₂ O	1–2	0.05–0.24	No
Yamamura et al. [62]		120				OH	Cl	1		No
Kaneko & Imoto [39]	0.5–12	200–600				OH	oxide	1–2		No
Matsuoka et al. [48]	0–1.5	78–370				OH	oxide	1–1.2		Yes
Ovramenko et al. [52]	0–40	200–500			0.4–1	OH	oxide			Yes
Hertl [35]	12–72	70–103				OH	oxide	>1	0.2–6.94	No
Kutty et al. [44]	3–10	180–280				OH	hydrous, oxide	1	0.23	Yes
Klee et al. [41]	Many	80–150		TMAH, NH ₃		OH	hydrous	1–2		No
Bagwell et al. [26]	1–24	90	13.6–13.9			OH	oxide	1/1.23	0.64–0.16	No
Gersten et al. [20]	8	150–300	7–14	KOH		acetate	oxide, alk	1–2	0.05–1	Yes
Hu et al. [37]	24	90–100	10–12	KOH		OH	Cl	1	0.2	No
Um et al. [56]	0–12	150–300				OH	alkoxide			Yes
Wada et al. [59]	4	150	>13	KOH		OH	Ti-Chelate oxide	5		Yes
Shi et al. [55]	4–72	75–200		NH ₃		OH	oxide	1		No
Asiaie et al. [25]	1–8	240		NaOH	0.3–4	Cl	isopropoxide	>1	.005	No
Kumazawa et al. [42–43]	8	150–300				OH	oxide, alk	1–4		Yes
Vivekanandan et al. [60]	2–10	90–180				OH	hydrous	1	0.2, 1	Yes
Fukai et al. [33]	5	200				OH	Cl	1.5	0.9	No
Pfaff [53]	6–36	60–250				OH	oxide, Cl	1–1.2	0.25	Yes
Hennings et al. [36]	10–15	150	>13	TMAH	25 wt%	acetate	acetate, alkoxide	1	0.03	No
Dutta & Gregg [31]	12–168	240		NaOH	0.01	OH, Cl	oxide	1	0.25	No
Hung et al. [38]	4–56	90				OH	oxide	1		No
Lencka et al. [45]	72	100–200	7–17	KOH, NaOH		NO ₃	hydrous, oxide	1	0.05–0.1	Yes
Komarneni et al. [23]	0.5–2	109–194	>13	KOH	10	NO ₃	Cl	1–2	0.35	micro-wave

Some authors have written papers [1–2,13,89,103] that reviewed the synthesis method. This chapter will review the hydrothermal synthesis of complex perovskite powders with an emphasis on the variables that control chemical phase, morphology, and size. Discussion of the rate controlling mechanism will also be addressed.

9.3 Synthesis Conditions for Controlled Chemical and Phase Purity

Chemical purity and phase purity of the perovskite ferroelectric is of the utmost importance to control since it will directly influence the electronic properties (e.g., dielectric constant, Curie temperature, etc.). The synthesis conditions (e.g., pH, temperature, and concentration) as well as the purity of the precursor materials significantly affect the chemical and phase purity of the resultant powders. The variables and strategies to control phase and chemical purity of hydrothermally synthesized ferroelectric powders will be discussed in this section.

9.3.1 Thermodynamic conditions

The optimal approach to control the chemical phases of the ferroelectric perovskite under equilibrium conditions is to calculate the stability and yield conditions of the perovskite by a thermodynamic model. Lencka et al. [19,93] described a thermodynamic model for aqueous solutions. Calculations were performed using software from OLI systems, Inc. [104] for many perovskite systems: PbTiO_3 [45,66,67], BaTiO_3 [45], SrTiO_3 [45], $(\text{Ba,Sr})\text{TiO}_3$ [20], CaTiO_3 [45], $\text{Pb}(\text{Zr,Ti})\text{O}_3$ [20,93], and SrZrO_3 [88]. The model requires the following information for all species in the solution: the standard Gibbs energies ΔG_f° and enthalpies ΔH_f° of formation, entropies S_o at a reference temperature (298.15 K), and the partial molar volumes V_o and heat capacities C_p° as functions of temperature. Equilibrium equations for all the species in the solution are set up. For example, Table 9.5 lists all the reaction equilibria for the system with feedstocks of titania, Ba-acetate, Sr-acetate, and ethylene diamine tetra acetic acid (EDTA), hereafter referred to as the EDTA-Ba-Sr-Ti hydrothermal system [20]. The model considers all the activity coefficients of aqueous species [104]. When the thermodynamic values are not known, estimation methods can be used to obtain the values [20,93].

Table 9.5. Reaction Equilibria in the EDTA-Ba-Sr-Ti Hydrothermal System with TiO_2 , BaAc_2 , and SrAc_2 as Feedstocks

(1) $(\text{C}_{10}\text{H}_{14}\text{N}_2\text{O}_8)^{-2} = \text{H}^+ + (\text{C}_{10}\text{H}_{13}\text{N}_2\text{O}_8)^{-3}$	(2) $(\text{C}_{10}\text{H}_{15}\text{N}_2\text{O}_8)^{-1} = \text{H}^+ + (\text{C}_{10}\text{H}_{14}\text{N}_2\text{O}_8)^{-2}$
(3) $(\text{C}_{10}\text{H}_{17}\text{N}_2\text{O}_8)^{+1} = \text{H}^+ + \text{C}_{10}\text{H}_{16}\text{N}_2\text{O}_{8(\text{aq})}$	(4) $\text{C}_{10}\text{H}_{16}\text{N}_2\text{O}_{8(\text{s})} = \text{C}_{10}\text{H}_{16}\text{N}_2\text{O}_{8(\text{aq})}$
(5) $\text{C}_{10}\text{H}_{16}\text{N}_2\text{O}_{8(\text{vap})} = \text{C}_{10}\text{H}_{16}\text{N}_2\text{O}_{8(\text{aq})}$	(6) $(\text{C}_{10}\text{H}_{18}\text{N}_2\text{O}_8)^{+2} = \text{H}^+ + (\text{C}_{10}\text{H}_{17}\text{N}_2\text{O}_8)^{+1}$
(7) $(\text{C}_{10}\text{H}_{13}\text{N}_2\text{O}_8)^{-3} = \text{H}^+ + (\text{C}_{10}\text{H}_{12}\text{N}_2\text{O}_8)^{-4}$	(8) $\text{K}(\text{C}_{10}\text{H}_{12}\text{N}_2\text{O}_8)^{-2} = \text{K}^+ + (\text{C}_{10}\text{H}_{13}\text{N}_2\text{O}_8)^{-3}$
(9) $\text{Ba}(\text{C}_{10}\text{H}_{12}\text{N}_2\text{O}_8)^{-2} = \text{Ba}^{+2} + (\text{C}_{10}\text{H}_{13}\text{N}_2\text{O}_8)^{-3}$	(10) $\text{Ba}(\text{HC}_{10}\text{H}_{12}\text{N}_2\text{O}_8)^{-1} = \text{H}^+ + \text{Ba}(\text{C}_{10}\text{H}_{12}\text{N}_2\text{O}_8)^{-2}$
(11) $\text{Sr}(\text{C}_{10}\text{H}_{12}\text{N}_2\text{O}_8)^{-2} = \text{Sr}^{+2} + (\text{C}_{10}\text{H}_{13}\text{N}_2\text{O}_8)^{-3}$	(12) $\text{Sr}(\text{HC}_{10}\text{H}_{12}\text{N}_2\text{O}_8)^{-1} = \text{H}^+ + \text{Sr}(\text{C}_{10}\text{H}_{12}\text{N}_2\text{O}_8)^{-2}$
(13) $\text{H}_2\text{O} = \text{H}^+ + \text{OH}^-$	(14) $\text{H}_2\text{O}_{(\text{g})} = \text{H}_2\text{O}$
(15) $\text{TiO}_{2(\text{s})} + \text{OH}^- = \text{HTiO}_3^-$	(16) $\text{Ti}^{4+} + \text{H}_2\text{O} = \text{TiOH}^{3+} + \text{H}^+$
(17) $\text{TiOH}^{3+} + \text{H}_2\text{O} = \text{Ti}(\text{OH})_2^{2+} + \text{H}^+$	(18) $\text{Ti}(\text{OH})_2^{2+} + \text{H}_2\text{O} = \text{Ti}(\text{OH})_3 + \text{H}^+$
(19) $\text{Ti}(\text{OH})_3^+ + \text{H}_2\text{O} = \text{Ti}(\text{OH})_{4(\text{aq})} + \text{H}^+$	(20) $\text{Ti}(\text{OH})_{4(\text{aq})} = \text{TiO}_{2(\text{s})} + 2\text{H}_2\text{O}$
(21) $\text{BaO}_{(\text{s})} + 2\text{H}^+ = \text{Ba}^{2+} + \text{H}_2\text{O}$	(22) $\text{BaOH}^+ = \text{Ba}^{2+} + \text{OH}^-$
(23) $\text{Ba}(\text{OH})_{2(\text{s})} = \text{Ba}^{2+} + 2\text{OH}^-$	(24) $\text{Ba}(\text{OH})_2 \cdot 8\text{H}_2\text{O}_{(\text{s})} = \text{Ba}^{2+} + 8\text{H}_2\text{O} + 2\text{OH}^-$
(25) $\text{Ba}(\text{OH})_2 \cdot 3\text{H}_2\text{O}_{(\text{s})} = \text{Ba}^{2+} + 3\text{H}_2\text{O} + 2\text{OH}^-$	(26) $\text{Ba}(\text{OH})_2 \cdot \text{H}_2\text{O}_{(\text{s})} = \text{Ba}^{2+} + \text{H}_2\text{O} + 2\text{OH}^-$
(27) $\text{BaTiO}_{3(\text{s})} + \text{H}_2\text{O} = \text{Ba}^{2+} + 2\text{OH}^- + \text{TiO}_{2(\text{s})}$	(28) $\text{Ba}_2\text{TiO}_{4(\text{s})} + 2\text{H}_2\text{O} = 2\text{Ba}^{2+} + 4\text{OH}^- + \text{TiO}_{2(\text{s})}$
(29) $\text{Ba}(\text{NO}_3)_{2(\text{s})} = \text{Ba}^{2+} + 2\text{NO}_3^-$	(30) $\text{CO}_{2(\text{g})} = \text{CO}_{2(\text{aq})}$
(31) $\text{CO}_{2(\text{aq})} + \text{H}_2\text{O} = \text{H}^+ + \text{HCO}_3^-$	(32) $\text{HCO}_3^- = \text{H}^+ + \text{CO}_3^{2-}$
(33) $\text{BaCO}_{3(\text{s})} = \text{Ba}^{2+} + \text{CO}_3^{2-}$	(34) $\text{BaCO}_{3(\text{aq})} = \text{Ba}^{2+} + \text{CO}_3^{2-}$
(35) $\text{BaHCO}_3^+ = \text{Ba}^{2+} + \text{HCO}_3^-$	(36) $\text{BaAc}_2 \cdot 2\text{H}_2\text{O} = \text{Ba}^{2+} + 2\text{H}_2\text{O} + 2\text{Ac}^-$
(37) $\text{BaAc}_2 \cdot 3\text{H}_2\text{O} = \text{Ba}^{2+} + 3\text{H}_2\text{O} + 2\text{Ac}^-$	(38) $\text{BaAc}^+ = \text{Ba}^{2+} + \text{Ac}^-$
(39) $\text{BaAc}_{2(\text{s})} = \text{Ba}^{2+} + 2\text{Ac}^-$	(40) $\text{BaAc}_{2(\text{aq})} = \text{Ba}^{2+} + 2\text{Ac}^-$
(41) $\text{SrO}_{(\text{s})} + 2\text{H}_2\text{O} = \text{Sr}^{2+} + 2\text{OH}^-$	(42) $\text{SrOH}^+ = \text{Sr}^{2+} + \text{OH}^-$
(43) $\text{Sr}(\text{OH})_{2(\text{s})} = \text{Sr}^{2+} + 2\text{OH}^-$	(44) $\text{Sr}(\text{OH})_2 \cdot 8\text{H}_2\text{O}_{(\text{s})} = \text{Sr}^{2+} + 8\text{H}_2\text{O} + 2\text{OH}^-$
(45) $\text{Sr}(\text{OH})_2 \cdot \text{H}_2\text{O}_{(\text{s})} = \text{Sr}^{2+} + \text{H}_2\text{O} + 2\text{OH}^-$	(46) $\text{SrTiO}_{3(\text{s})} + \text{H}_2\text{O} = \text{Sr}^{2+} + 2\text{OH}^- + \text{TiO}_{2(\text{s})}$
(47) $\text{Sr}_2\text{TiO}_{4(\text{s})} + 2\text{H}_2\text{O} = 2\text{Sr}^{2+} + 4\text{OH}^- + \text{TiO}_{2(\text{s})}$	(48) $\text{Sr}(\text{NO}_3)_{2(\text{s})} = \text{Sr}^{2+} + 2\text{NO}_3^-$
(49) $\text{Sr}(\text{NO}_3)_{2(\text{aq})} = \text{SrNO}_3^+ + \text{NO}_3^-$	(50) $\text{SrNO}_3^+ = \text{Sr}^{2+} + \text{NO}_3^-$
(50) $\text{Sr}(\text{NO}_3)_2 \cdot 4\text{H}_2\text{O} = \text{Sr}^{2+} + 4\text{H}_2\text{O} + 2\text{NO}_3^-$	(51) $\text{SrAc}_2 \cdot 4\text{H}_2\text{O} = \text{Sr}^{2+} + 4\text{H}_2\text{O} + 2\text{Ac}^-$
(52) $\text{SrAc}_2 \cdot 0.5\text{H}_2\text{O} = \text{Sr}^{2+} + 0.5\text{H}_2\text{O} + 2\text{Ac}^-$	(53) $\text{SrAc}^+ = \text{Sr}^{2+} + \text{Ac}^-$
(54) $\text{SrCO}_{3(\text{s})} = \text{Sr}^{2+} + \text{CO}_3^{2-}$	(55) $\text{SrCO}_{3(\text{aq})} = \text{Sr}^{2+} + \text{CO}_3^{2-}$
(56) $\text{SrHCO}_3^+ = \text{Sr}^{2+} + \text{HCO}_3^-$	(57) $\text{HAc}_{(\text{g})} = \text{HAc}_{(\text{aq})}$
(58) $\text{HAc}_{(\text{aq})} = \text{H}^+ + \text{Ac}^-$	(59) $\text{HNO}_{3(\text{g})} = \text{HNO}_{3(\text{aq})}$
(60) $\text{HNO}_{3(\text{aq})} = \text{H}^+ + \text{NO}_3^-$	(61) $\text{KOH}_{(\text{s})} = \text{K}^+ + \text{OH}^-$
(62) $\text{KOH} \cdot \text{H}_2\text{O}_{(\text{s})} = \text{K}^+ + \text{OH}^- + \text{H}_2\text{O}$	(63) $\text{KOH} \cdot 2\text{H}_2\text{O}_{(\text{s})} = \text{K}^+ + \text{OH}^- + 2\text{H}_2\text{O}$
(64) $\text{KNO}_{3(\text{s})} = \text{K}^+ + \text{NO}_3^-$	(65) $\text{KAc}_{(\text{aq})} = \text{K}^+ + \text{Ac}^-$
(66) $\text{KAc}_2^- = \text{K}^+ + 2\text{Ac}^-$	(67) $2\text{Ba}_{0.5}\text{Sr}_{0.5}\text{TiO}_3 + 2\text{H}_2\text{O} = \text{Ba}^{2+} + \text{Sr}^{2+} + 2\text{HTiO}_3^- + 2\text{OH}^-$

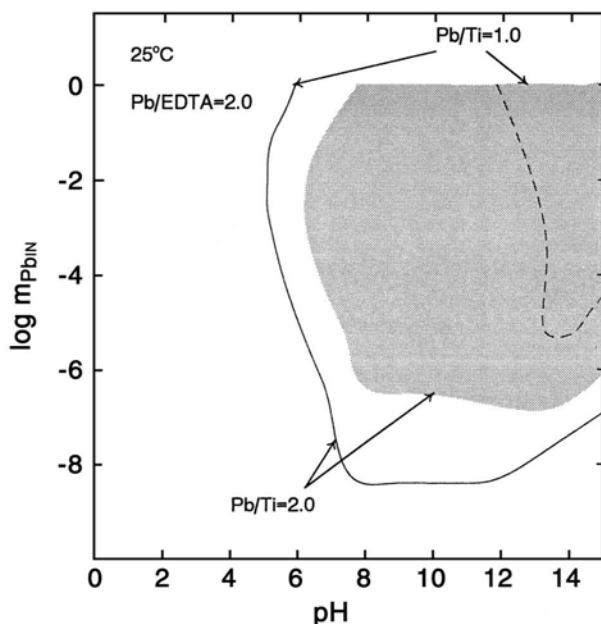


Fig. 9.2. Yield diagram for PbTiO_3 . The yield diagram depicts the input concentration of Pb on the y-axis and pH on the x-axis at the particular temperature of 25°C . The shaded region denotes greater than 99% phase-pure PbTiO_3 yield for Pb/Ti molar ratio equal to 2 and Pb/Ti molar ratio equal to 1. The lines represent the beginning of precipitation of PbTiO_3 [20].

The results of the calculation of the model are the equilibrium concentrations of all species as a function of pH, temperature, and initial reagent concentrations. The conditions for phase-pure perovskites can be represented in a yield diagram as shown in Fig. 9.2 for PbTiO_3 . This yield diagram depicts the input concentration of lead on the y-axis and pH on the x-axis at the particular temperature of 25°C . The shaded region denotes greater than 99% phase-pure PbTiO_3 yield for Pb/Ti molar ratio equal to 2 and Pb/Ti molar ratio equal to 1. The lines represent the beginning of precipitation of PbTiO_3 . In this case, the input reagent included EDTA in a Pb/EDTA molar ratio equal to 2.0. Apparent from the diagram is that there is a larger area in the yield diagram for the phase pure region of PbTiO_3 with the Pb/Ti molar ratio equal to 2 rather than 1. This highlights the influence of the molar ratios of the input reagent concentrations on the reaction conditions for obtaining chemically pure material. A second variable is the actual reagents used in producing the yield diagram. In this case, EDTA, lead acetate, titania, and potassium hydroxide were used as the initial reagents. However, reactions without the additive of EDTA would have produced a yield diagram with PbO precipitate [20]. Another yield diagram is shown in Fig. 9.3 with the y-axis as temperature and the x-axis as KOH concentration [20]. The input variables are Sr concentration

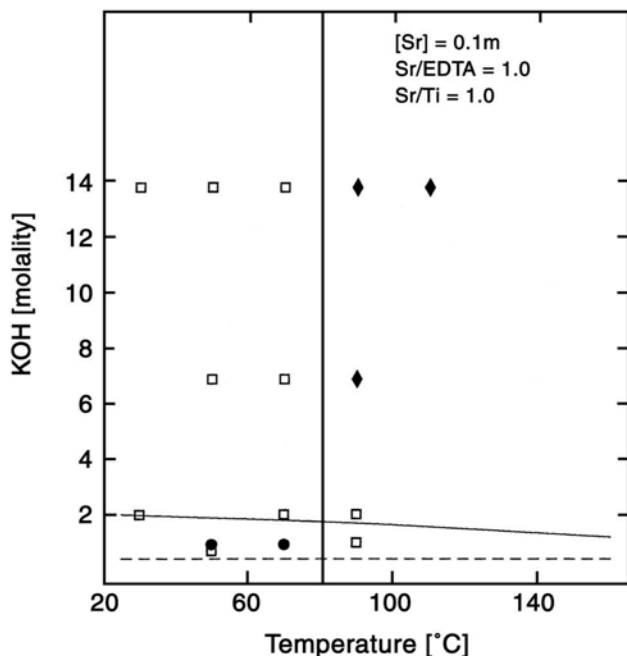


Fig. 9.3. Yield diagram for SrTiO_3 . The input variables are Sr concentration of 0.1 *m*, the Sr/Ti molar ratio is 1 and the Sr/EDTA molar ratio is 1. The dashed line represents the beginning of precipitation of SrTiO_3 . The horizontal solid line represents the beginning of greater than 99% yield of SrTiO_3 . The vertical line represents the minimum reaction temperature for SrTiO_3 synthesis. The experimental points are denoted by points as follows: λTiO_2 , $\circ\text{SrTiO}_3+\text{TiO}_2$, and τSrTiO_3 (After [20])

of 0.1 *m*, the Sr/Ti molar ratio is 1, and the Sr/EDTA molar ratio is 1. The dashed line represents the beginning of precipitation of SrTiO_3 . The horizontal solid line represents the beginning of greater than 99% yield of SrTiO_3 . The vertical line represents the minimum reaction temperature for SrTiO_3 synthesis. The experimental points are denoted with points as follows: λTiO_2 , $\circ\text{SrTiO}_3+\text{TiO}_2$, and τSrTiO_3 .

The yield diagram is only useful in obtaining pure materials if pure precursors are used. If carbon dioxide from the air or are in the mineralizers during or after the hydrothermal reaction, the product can contain a layer of carbonate contamination. Urek et al. [57] found that carbonate contamination is reduced by increasing the pH. Similarly, Gersten [20] found that the use of chelating agents such as EDTA could reduce the carbonate contamination. For example, from thermodynamic calculations of the hydrothermal preparation of BaTiO_3 from TiO_2 , Baacetate, and KOH without EDTA, BaCO_3 will form with only 0.001 mol% K_2CO_3 present. However, with EDTA present 4.5 mol% K_2CO_3 must be present before BaCO_3 will appear [20].

Often when a carbonate-rich perovskite or a nonstoichiometric phase with excess 'A' site is produced the situation is "fixed" by washing the perovskite with acid (Li and Yao [79] in preparing PbTiO_3 ; Kutty and Balachandran [92] in preparing $\text{Pb}(\text{Zr},\text{Ti})\text{O}_3$; and Ovramenko et al. [52] in preparing BaTiO_3). However, this approach without guidance from equilibrium conditions may also leach away the desired perovskite phase causing exaggerated grain growth on sintering as described in Hung et al. [38] and Pinceloup et al. [54].

9.3.2 Mineralizers and additives

The type of mineralizer (pH adjusting agent) can affect the final purity of the perovskite powders. For example, in the case of $\text{Pb}(\text{Zr},\text{Ti})\text{O}_3$, Beal [95] used several different mineralizers (i.e., NaF , NaCl , NaOH , KF , KCl , KBr , KOH , LiF , LiCl , and LiOH). He found that the ionic radius of the alkali mineralizers of Na, K, and Li correlated directly to the impurity concentrations. The smaller Li ion was retained in the structure of the powders at higher levels (i.e., 0.4–0.5 mol%) compared with the K ion (0.03 mol%) that is twice as large [95]. It was also found that fluoride-based mineralizers contaminated greater than the other halides. He suggested that there was a stronger bonding of the F ion to the structure. The presence of Zr increased the contamination potential of the F ion. However, fluoride-based mineralizers do promote the formation of pure perovskite [95]. Yanagisawa and Kanai [3] also found the incorporation of K ion (i.e., 0.37 wt%) from the KF mineralizer used (i.e., 25–45 wt%) to prepare $(\text{Pb}, \text{La})(\text{Zr},\text{Ti})\text{O}_3$ and $(\text{Pb}, \text{Mn})(\text{Zr},\text{Ti})\text{O}_3$. The contamination by the K ion was significantly higher in the preparation of $\text{Pb}(\text{Nb},\text{Zr},\text{Ti})\text{O}_3$ (i.e., 1.1–1.5 wt%) since the K ion incorporates in the 'A' site of the perovskite, while the Nb is in the 'B' site [3]. The larger incorporation of K ion in the $\text{Nb-Pb}(\text{Zr},\text{Ti})\text{O}_3$ may be a result of the charge neutrality.

To avoid the impurity from the alkali mineralizer, either no mineralizer [96], an organic mineralizer (e.g., tetramethylammonium hydroxide (TMAH) [36,46,41,57]) or another base (e.g., NH_3) have been used. The use of no mineralizer has been used extensively in the preparation of BaTiO_3 ; for example, Flaschen [17] and Eckert et al. [32] used $\text{Ba}(\text{OH})_2$ to raise the pH for the hydrothermal synthesis of BaTiO_3 . However, when the source of pH and concentration are coupled, it is not possible to independently evaluate the effects of these variables. Furthermore, the unreacted hydroxide requires washing that can leach the BaTiO_3 , as discussed by Hennings et al. [36]. Instead, Hennings et al. [36] used TMAH to increase the pH and a stoichiometric BaTi -acetate gel was used as the precursor for pure phase BaTiO_3 at 150°C within 10–15 h. However, Urek et al. [57] found that TMAH requires a burnout step at 800°C before the sintering of a ceramic material. Another limitation is that it will decompose above 150°C . Therefore, when the minimum reaction temperature of some of the hydrothermal synthesis conditions for preparing perovskites approach these temperatures alternative methods need to be found. One alternative is to find other precursors. For example, Chen [96] used precursors of 0.03 m Pb -acetylacetonate and Zr-Ti hydrous gel to form $\text{Pb}(\text{Zr},\text{Ti})\text{O}_3$.

at 160°C within 70 h and at 200°C within 30 h. However, when Pb-acetate was used instead of the Pb-acetylacetonate, the perovskite would not form [96].

If additives are used during the hydrothermal reaction, the reaction could be hindered. For example, Kiss et al. [40] found that Cynamer P-250 and Elvanol 50-42 prevented the complete reaction of BaTiO₃.

9.3.3 Homogeneity

Another variable in the final product is the homogeneity of the starting precursor. The starting precursor for the synthesis of Pb(Zr,Ti)O₃ [93,96] or (Pb,La)(Zr,Ti)O₃ [100] requires molecular scale mixing in order for the pure-phase product to occur. For example, Lencka et al. [93] found that a hydrous ZrO₂-TiO₂ prepared from a coprecipitate of titanium isopropoxide and zirconium propoxide in 2-propanol mixed with Pb-acetate and heated for 3 days at 150°C resulted in pure phase Pb(Zr,Ti)O₃. However, when precursors of hydrous TiO₂ and ZrO₂ were prepared separately and then mixed with Pb-acetate under the same conditions, PbTiO₃ and PbZrO₃ precipitated out separately. The same results were corroborated with the hydrothermal procedure used by Chen et al. [96]. Similarly, in the preparation of (Pb,La)(Zr,Ti)O₃, Lee and Yen [100] found that the precursor prepared from a coprecipitated stoichiometric gel resulted in pure phase (Pb,La)(Zr,Ti)O₃, while the mixture of individually precipitated Pb, La, Zr, and Ti gels resulted in a phase mixture of PbTiO₃ and PbZrO₃ (cf. Fig. 9.4). The reason

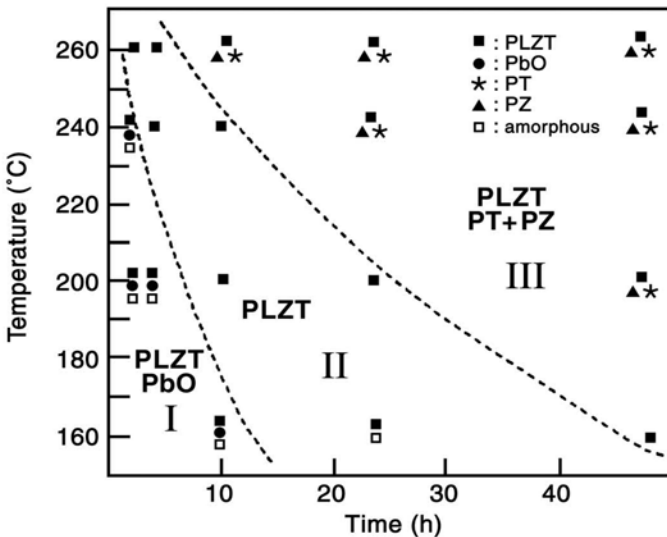


Fig. 9.4. TTT (fraction transformation, temperature, time) diagram of (Pb,La)(Zr,Ti)O₃ (PLZT) phase formation under hydrothermal conditions [100]

for this required homogeneity may be explained on the basis of kinetics: PbTiO_3 and PbZrO_3 are more stable than $(\text{Pb,L a})(\text{Zr,Ti})\text{O}_3$ [100]. Further evidence for the metastable nature of $(\text{Pb,L a})(\text{Zr,Ti})\text{O}_3$ is that powders prepared from coprecipitated gel at high temperatures (e.g., 200 to 240°C) or long times (e.g., 10 to 40 h) will phase separate [100].

9.3.4 Reaction time and temperature

Reaction time is another variable that affects the chemical purity of the perovskite. Although the thermodynamic model predicted the possibility of the phase-pure perovskites at all temperatures greater than 25°C, in reality, temperatures greater than 25°C were required for phase pure synthesis. In the case of PbTiO_3 , Gersten [20] found that the minimum reaction temperatures varied between 140 and 70°C. In the case of SrTiO_3 and BaTiO_3 however, the minimum reaction temperature was found to be 90°C (cf. Fig. 9.3). Below the minimum reaction temperature, incomplete reactions resulted probably due to sluggish reaction kinetics (e.g., short reaction time).

9.3.5 Hydroxyl groups

An unavoidable contaminant of the hydrothermal process is the hydroxyl groups that attach to the lattice of the crystal structure and adsorb on the surface. There has been some disagreement in the literature [25,27,58–60,91] as to the affect of the lattice hydroxyls on the phase structure of hydrothermally prepared BaTiO_3 . Vivekanandan and Kutty [91] found the cubic-tetragonal transformation of hydrothermally prepared BaTiO_3 was a function of hydroxyl concentration. In agreement with this study, Wada et al. [59,105] studied these water groups for a particular size of hydrothermally prepared BaTiO_3 (89.72 nm) and found that they contribute to the crystal structure (being cubic rather than tetragonal) and defects. The hydroxyls can be removed by heat treatments up to 600°C. Shi et al. [55] also supposed that a cubic phase rather than a tetragonal phase is stabilized by defects from OH ions and Ba ion vacancies. He based his supposition on his findings that at a Ba/Ti molar ratio equal to 1 a cubic phase was formed, while Ba/Ti equal to 3 gave tetragonal phase and higher synthesis temperatures stabilized the tetragonal phase. Kaneko and Imoto's [39] studies agreed with the findings of Shi et al. [55].

However, Begg et al. [27] argues that the structure transformation is a function of particle size. Below 0.19 μm the particles are cubic and above 0.27 μm the particles are completely tetragonal [27]. In support of this argument, Dutta and Gregg [31] synthesized tetragonal BaTiO_3 of particle size 1 μm stabilized with chloride ions, but synthesized metastable cubic phase BaTiO_3 of particle size 0.2 μm without the chloride. Asiaie et al. [25] is in agreement that the hydroxyl defects do not induce the tetragonal–cubic transformation and it is not an effect of strain, or the presence of amorphous impurities. After analysis of tetragonal particles of various

sizes (i.e., 0.3 and 0.5 μm) they support the transition being particle size dependent [25].

9.3.6 Summary

In summary, the variables that can affect the purity and phase of the hydrothermally grown ferroelectric can be divided into categories of thermodynamics and kinetics. The thermodynamic variables include the following: temperature, pH, precursor type, mineralizer type, precursor concentration, purity of precursors, and ratios of the precursor concentrations (including additives). The kinetic variables include all the above, as well as time and homogeneity of the initial precursors. The unavoidable impurities that result in the product are the hydroxyls in the crystal lattice, impurities in the precursors, and impurities that result from the mineralizer to adjust the pH.

9.4 Kinetics and Rate Controlling Mechanisms

As already mentioned, the reaction time actually contributes to the phase-purity of the hydrothermal reaction. Without the appropriate length of time, the reaction will not be complete even with the correct synthesis conditions (i.e., pH, temperature, initial reagent concentration). Furthermore, the reaction time will also contribute to the resulting powder morphology and size of the product. Therefore, before further discussing some of the variables that control morphology and size, a discussion on the kinetics and possible rate controlling mechanisms will be presented.

Some of the rate-controlling mechanisms have been hinted at in the introduction in the classification of hydrothermal reactions. These include oxidation, decomposition, coprecipitation, and crystallization. However, most of the synthesis conditions (cf. Tables 9.2–9.4) used for the synthesis of the ferroelectric powders have been through the coprecipitation or crystallization routes. Therefore, the discussion of the mechanisms will focus on these.

9.4.1 Rate determining step in the mechanisms

Two main mechanisms or a combination of these mechanisms have been suggested in the literature as rate determining for the hydrothermal reaction of ferroelectric powders: dissolution-precipitation and *in situ* transformation [2,32] (cf. Fig. 9.5). A dissolution-precipitation mechanism occurs when soluble reactants are heated over time. As a result, the concentration in the hydrothermal solution increases. When there is sufficient dissolution of the ions, supersaturation is achieved and the product is formed. On the other hand, an *in situ* transformation mechanism assumes a surface (topochemical) reaction of cations (i.e., Ba) with a

less soluble species (i.e., TiO_2) in water. The reaction proceeds by the diffusion of cations through the structure of insoluble species until the completion of the reaction.

The rate limiting process for dissolution and precipitation is either the dissolution of the oxide phase and/or the precipitation from solution, or both. However, these processes are only broad descriptions that can be divided into other mechanisms. For example, within the dissolution mechanism, mass transport (i.e., diffusion or convection) or surface mechanisms may control the rate. Furthermore, within the surface chemical mechanism the following mechanisms can be rate controlling: nucleophilic or electrophilic attack, surface reconstruction, or transfer of charge reactions [106]. Once the conditions of supersaturation of a critical nuclei is obtained, precipitation may occur. The supersaturation is the metastable state of a solution in which soluble species remain in solution even though their thermodynamic equilibrium limit is exceeded. Nuclei may form homogeneously or heterogeneously. Growth of the nuclei may be limited by the following mechanisms: mass transport of the ions from solution to the nuclei, adsorption of ions on the crystal surface, diffusion of the ions through the adsorption layer of the crystal, dissolution of the nuclei, nucleation on the crystal surface, and by surface spiral growth of the crystals [107]. Also growth can be limited by continuous precipitation of new nuclei [108–110]. There also may be more than one mechanism that can control the rate [107].

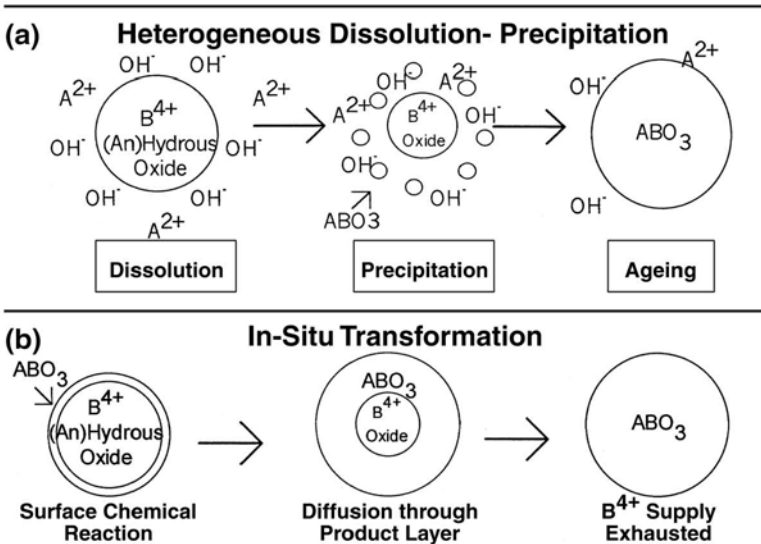


Fig. 9.5. Two mechanisms: (a) dissolution-precipitation and (b) *in situ* transformation (After [2])

9.4.2 Precipitation

A typical kinetic process for precipitation is shown in Fig. 9.6. The process (cf. Fig. 9.6 in ref. [111]) includes an initial induction time due to the creation of supersaturation, primary and secondary nucleation, and growth stages. In the primary stage, critically sized nuclei form by homogenous or heterogeneous nucleation. In the secondary stage, Ostwald ripening occurs, where dissolution is followed by re-deposition. Additionally, in the secondary stage an aggregation process dominates, where agglomeration and coagulation of particles occur. The final effect of this growth stage is the redistribution of solid phase of the precipitate to form a low energy morphology.

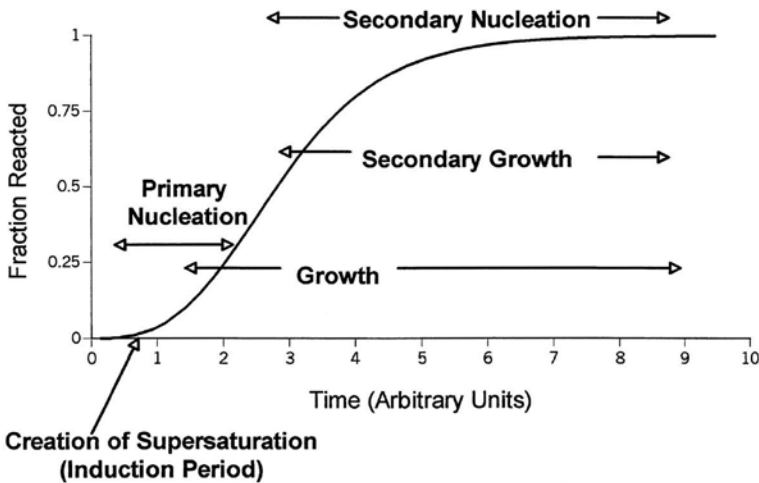


Fig. 9.6. A typical kinetic process for precipitation (fraction reacted vs. time) (After [111])

9.4.3 Reaction rate

The reaction rate for the hydrothermal synthesis can be described as a function of the concentration of species in the aqueous environment and the reaction temperature. The part of the rate equation that is dependent on concentration is expressed as fraction reacted with time. There are many different rate equations depending on the physical model. One model is the Johnson-Mehl-Avrami (JMA) [108–110] where growth and nucleation are simultaneous given by

$$df/dt = kt^m(1-f), \quad (9.1)$$

where t is time, f is the fraction reacted, and k and m are fit parameters. The JMA equation can be solved for time as

$$t = t_{ind} + [-1/k (\ln(1 - f))]^{1/m} \tag{9.2}$$

where, t is the time for f fraction perovskite to react, and t_{ind} , k , and m are the three fit parameters. t_{ind} represents the induction time, m represents a geometric constant, and k represents a constant that depends on nucleation frequency and rate of grain growth. Hancock and Sharp [112] generalized the approach and used the value of m to differentiate between various possible mechanisms (cf. Table 9.6).

Table 9.6. Reaction Rate Slope m for the Johnson-Mehl-Avrami Equation $-\ln \ln(1 - f) = \ln(k) + m \ln(t)$ (After Hancock and Sharp [112])

Implied Mechanism	m
Diffusion controlled	0.54–0.62
Phase boundary	1.07–1.11
Nucleation and growth	2.00, 3.00
Zero order	1.24
First order	1.00

Table 9.7. Rate Determining Mechanisms

Material	Mechanism	Evidence	Condition [cf. Tables 9.2-9.4]	Reference
BaTiO ₃	Surface Reaction	H&S, size	Ba(OH) ₂ > 0.1M	Hertl [35]
	Diffusion	H&S, size	Ba(OH) ₂ < 0.1M	Hertl [35]
	Combination	H&S, size & morphology	Ba(OH) ₂ > 0.1M	Eckert [32]
	Diffusion	Size & morphology	Ba(OH) ₂ = 0.1M	Hu [37]
	Dissolution	H&S, comparison of E _a		Ovramenko [52]
	Dissolution	Size with time	Ba(OH) ₂ > 0.1M	Kumazawa [42]
	Dissolution	H&S, size & morphology	Ba(OH) ₂ > 0.1M	Bagwell [26]
PbTiO ₃	Dissolution	H&S, size & morphology	[PbAc ₂] = 0.1, 1.0M	Rossetti [80]
	Dissolution	H&S, size & morphology	[PbAc ₂] = 0.025, 0.125; KOH = 1.0 m	Moon [73]
	Ion exchange	Morphology & size		Ohara [69]
	Dissolution	H&S, Nielsen, size & morphology	[PbAc ₂] = 0.1 m , KOH = 2.5, 7.8 m	Gersten [20]
	Precipitation	Size & morphology	[PbAc ₂] = 0.1 m	Gelabert [78]
Pb(Zr,Ti)O ₃	Combination	H&S, morphology		Lee & Yen [100]
	Dissolution	Same morphology as precursor		Kutty [92]
	Dissolution		KOH > 5M, Pb = 0.5M	Cheng [97]

Many have used the method of Hancock and Sharp (H&S) [112] (cf. Table 9.6) along with particle characterization (size or morphology or both) to suppose a rate determining mechanism for synthesis of perovskites (cf. Table 9.7).

Most authors that suggested a dissolution rate determining mechanism also pointed out the very low solubility of TiO_2 (and ZrO_2) precursor. Therefore, instead the precursor may not fully dissolve, but A (where $A = \text{Ba}, \text{Pb}$) ions may cause structural rearrangement within the precursor followed by dehydration [24,92,100].

Hertl [35] used a Hancock and Sharp (H&S) [112] type method and suggested that the rate-determining step for the hydrothermal synthesis of BaTiO_3 above a $\text{Ba}(\text{OH})_2$ concentration of 0.1 m may be the reaction of $\text{Ba}(\text{OH})_2$ with TiO_2 at the solid-liquid interface. However, below 0.1 m $[\text{Ba}(\text{OH})_2]$ the rate-determining step is diffusion through the product layer. Eckert et al. [32] points out that the change in kinetic mechanism may be a result of the OH ions that changes the solubility of the TiO_2 rather than the influence of the Ba ions. They suggested a combination mechanism of diffusion and dissolution control based on H&S results and microstructure. Bagwell et al. [26] suggested a dissolution reprecipitation mechanism for the synthesis of BaTiO_3 after using the H&S method and evaluating the microstructure. However, the reaction slowed due to polymers adsorbed on the TiO_2 precursor. These polymers inhibit the dissolution of the TiO_2 . Kumazawa et al. [42] also suggested a dissolution rate limiting mechanism based on evidence from differences in the particle size of the resulting BaTiO_3 powders from amorphous and crystalline precursors. Rossetti et al. [80] supposed a mechanism of dissolution-precipitation from homogeneous solution for the hydrothermal synthesis of PbTiO_3 . Support for this mechanism was the data from the H&S method along with microstructure data that showed that the particle size decreased with a decrease in feedstock concentration. Particle size should decrease with an increase in feedstock concentration in order to support a nucleation and growth mechanism. From the crystallization fraction as a function of time and a microscope study, a dissolution rate determining mechanism was suggested. Similarly Moon et al. [72] used this approach and confirmed a dissolution-precipitation mechanism. However, they suggested a chemical reaction at the interface of the growing particles is the rate-limiting step. They recommend increasing the lead concentration and alkalinity to increase the solubility that results in an increase in supersaturation, thereby promoting PbTiO_3 precipitation.

Support for the “shrinking core” diffusion reaction mechanism was also presented. For example, Hu et al. [37] aged 0.1 M $\text{Ba}(\text{OH})_2$ solution and 0.1 M monodispersed TiO_2 0.1–1 μm for 24 h at 100°C to form BaTiO_3 monodispersed microspheres of the same size and shape indicating a diffusion-reaction mechanism. Su et al. also suggest an *in situ* transformation mechanism for the synthesis of $\text{Pb}(\text{Zr},\text{Ti})\text{O}_3$ from an amorphous zirconia-titania gel by the diffusion of PbO into the amorphous network, which by expulsion of water will crystallize [102]. Somewhat like the diffusion rate limited reaction, Ohara [51,69], suggested an ion exchange mechanism to predominate for the transformation of fibrous potassium titanate into fibrous BaTiO_3 and PbTiO_3 under hydrothermal conditions.

Table 9.8. Rate Controlling Mechanisms for the Nielsen Equation $df/dt = kf^q(1-f)^p$ [107,113–115] for Different Values of q and p

Implied mechanism	q	p	E_a [kJ/mol]
Growth by diffusion through the solution	0.33	1.0	~6–20
Surface adsorption growth	0.67	1.0	~45
Integration growth			~30–75
Mononuclear growth	1.33	≥ 0.0	
Spiral growth	0.67	2.0	
Polynuclear growth	0.67	≥ 1.0	
Surface diffusion controlled growth			

Recently, Gersten [20] showed that a Nielsen [107] growth model could equally be applied to rate data to distinguish between physical mechanisms. The growth model presented by Nielsen [107] is represented by the differential equation

$$df/dt = kf^q(1-f)^p \quad (9.3)$$

where f is the fraction reacted, t is the time, and k , p , and q are fit parameters. For diffusional growth q is equal to $1/3$ and p is equal to 1. For mononuclear surface growth, q is equal to $4/3$ and p is an integer. For polynuclear surface growth, q is equal to $2/3$ and p is an integer [107]. The various mechanisms based on this model are presented in Table 9.8. The model assumes all the growth occurs after a nucleation step.

Gersten [20] used the H&S method along with a Nielsen [107] approach (cf. Tables 9.6 and 9.8) to determine the rate determining mechanism for the hydrothermal synthesis of PbTiO_3 in the Pb-Ti-K-EDTA- H_2O system and (Ba,Sr) TiO_3 in the Ba-Sr-Ti-K-EDTA- H_2O system. Both systems were found to be of the dissolution-precipitation type. They exhibited an induction time indicative of the creation of a supersaturation. Furthermore, the reaction time, as a function of the fraction reacted, best fit a Nielsen's equation for adsorption and integration by polynuclear controlled growth (i.e., $p = 0.75$, $q = 0.67$). This can include adsorption (via electrostatic, chemical, and "ligand-like" effects), and integration by dehydration. The values for E_a also agreed with this mechanism (i.e., $E_a \sim 50$ – 100 kJ/mol). The presence of 1 nm particles on the surface of the precursor after 1 min also confirmed this mechanism.

The part of the function that is dependent on temperature can be written as the Arrhenius equation. The Arrhenius equation is given by

$$k(T) = A \exp(E_a/RT), \quad (9.4)$$

where R equals 8.314 J/mol K, T is temperature, A is a constant, and E_a is the apparent activation energy.

Gersten [20] found that the activation energy was dependent on the KOH concentration. It was found to decrease from 101 to 47 kJ/mol with an increase in KOH from 2.5 to 7.8 *m*. Rossetti et al. [80] found an even lower magnitude of apparent activation energy, 30.1 kJ/mol, under varied conditions (cf. Table 9.3). Other apparent activation energies for hydrothermally-formed BaTiO₃ were 105.5 kJ/mol [35], 107 kJ/mol [20], 56 kJ/mol [52], and 20.9 kJ/mol [48]; for SrTiO₃ it was 72 kJ/mol [22] and 91 kJ/mol [20]. Gersten [20] attributed the variations in the apparent activation energies for each system to the different synthesis conditions (cf. Tables 9.3, 9.5).

9.4.4 Variables affecting the reaction rate

The reaction time can be affected by the types of precursors, concentrations of the precursors, proportions of the concentrations of precursors, concentrations of mineralizers, type of mineralizer, types of additives, and temperature. Gersten [20] found that the rank of importance of the variables studied for the hydrothermal preparation of PbTiO₃ from Pb-acetate, titania, EDTA, and KOH were (1) the change in titanium species precursor, (2) an increase in temperature, (3) the concentration of KOH, (4) the Pb/Ti molar ratio, and (5) the concentration of Ti and Pb species.

As expected, the larger the precursor, the longer the reaction will take. This is due to the longer time required for dissolution or diffusion in larger sized precursors. Also, if the precursor is more reactive (e.g., higher surface area, more defects in the precursor, metastable phase of the precursor) the reaction will be shorter. Pfaff [53] found that the larger sized rutile titania would not form as much BaTiO₃ compared with the more reactive anatase titania under hydrothermal conditions. Also as expected, if there is a hindering material (e.g., polymer, ion) adsorbed on the surface of the precursor, the reaction will take longer. For example, Li and Yao [79] found that the type of mineralizer (LiOH vs. KOH) influences the reaction time of PbTiO₃ powders. Li⁺ easily absorbs on the surface of the particles, and because of its small radius it resists crystal growth so that the reaction time is longer. Beal et al. [95] found that the reaction time was hindered by chloride-containing mineralizers compared with sodium and lithium fluoride mineralizers.

A way to increase the reaction time is to increase the heat up rate of the reaction. This can be accomplished by the novel microwave approach as developed by Komarneni et al. [23] and Abthu et al. [94] for the preparation of a wide variety of perovskite materials (cf. Table 9.1). Another modification of the hydrothermal process is the electrochemical-hydrothermal method that combines the hydrothermal process with an electric field [12]. Yoo et al. [63] used an electric field (50 mA/cm²) for the anodic oxidation of a Ti metal plate in the formation of BaTiO₃ powders at 250°C with 0.5 N Ba(NO₃)₂.

9.5 Synthesis Conditions for Controlled Morphology

The control of the morphology of hydrothermally grown powders is closely related to the growth mechanism of the reaction, which in turn is a function of the supersaturation [106,113–116]. Walton [116] provided a summary of the effects of initial supersaturation and interfacial energy on the growth mechanism and morphology crystal growth of a general material. He summarizes as follows: with an initial supersaturation (S) 1–2 and a low interfacial energy (IE) the morphology will be discrete, well formed crystals with no agglomerates. The nucleation is heterogeneous, and the growth is slow and predominantly occurs by screw dislocation. However, with S between 2–5 and a high IE , the growth changes to surface nucleation. With a low IE or a high IE , but with S between 10–50 the growth changes to dendritic and the morphology changes to poorly formed dendritic crystals. With S between 10–50 and a low IE or with a $S > 1000$ and a high IE , the nucleation becomes homogeneous and the morphology would be both stability-dependent and agglomerated [116].

Although the supersaturation is the driving force for the growth of the powders, there are many related factors that contribute as well to the morphology of the final hydrothermal product. These include initial reagent, initial reagent concentration, pH, temperature, stir rate, and time. The supersaturation increases with a decrease in temperature and an increase in concentration of soluble species. In the presence of low-soluble species (e.g., TiO_2), the supersaturation may be increased by the pH that will increase the dissolution of the mostly insoluble species. Additives also prevent or enhance the dissolution of the essentially nondissolving species by either surface adsorbing or chelating the species, respectively. Additives or mineralizers occupy reaction sites necessary for the product formation. Stirring and time also increase the rate of dissolution thereby increasing the supersaturation. The initial morphology of the precursor may also greatly contribute to the final morphology because dissolution may be limited, thereby a diffusion mechanism may result. The resultant mechanism could be the diffusion of the soluble species, the structural rearrangement within the precursor, followed by dehydration. The contributions of these variables to the particle morphology will be discussed in detail in the following sections.

9.5.1 Precursor

The initial shape and size of the essentially nondissolving initial precursor reactants (such as ZrO_2 or TiO_2 in the case of zirconates and titanate perovskites) can play an important role in the final morphology and size of the perovskite. These precursors can act as templates for the final product. For example, Choi et al. [28] found that spherical perovskite powders of $PbTiO_3$, $BaTiO_3$, $SrTiO_3$, $Pb(Zr,Ti)O_3$, $PbZrO_3$, and $Ba(Zr,Ti)O_3$ were hydrothermally prepared from precursors of spherical gel powders of hydrous titania and zirconia hydrolyzed from titanium tetrachloride and zirconium oxychloride, lead acetate trihydrate, barium hydrox-

ide, and strontium hydroxide. Hu et al. [37] found that monodispersed microspheres of TiO_2 under hydrothermal conditions reacted with barium to form BaTiO_3 with the same size and shape as the initial powders. Similarly, Gersten et al. [20,90] prepared spherical PbTiO_3 (cf. Fig. 9.7) and $(\text{Ba,Sr})\text{TiO}_3$ powders (cf. Fig. 9.8) from spherical precursors of hydrous titania. Furthermore, Ohara et al. [51] synthesized BaTiO_3 from a precursor of fibrous potassium titanate hydrate and barium hydroxide with Ba/Ti molar ratio equal to 1 at 150°C for 24 h. The fibrous potassium titanate was 1 to 10 mm long and 1–100 μm in diameter, whereas the BaTiO_3 product was 100 μm to 1 mm long and 1–10 μm in diameter composed of fine crystals of average 270-nm size. A similar method was used to prepare fibrous PbTiO_3 [69].

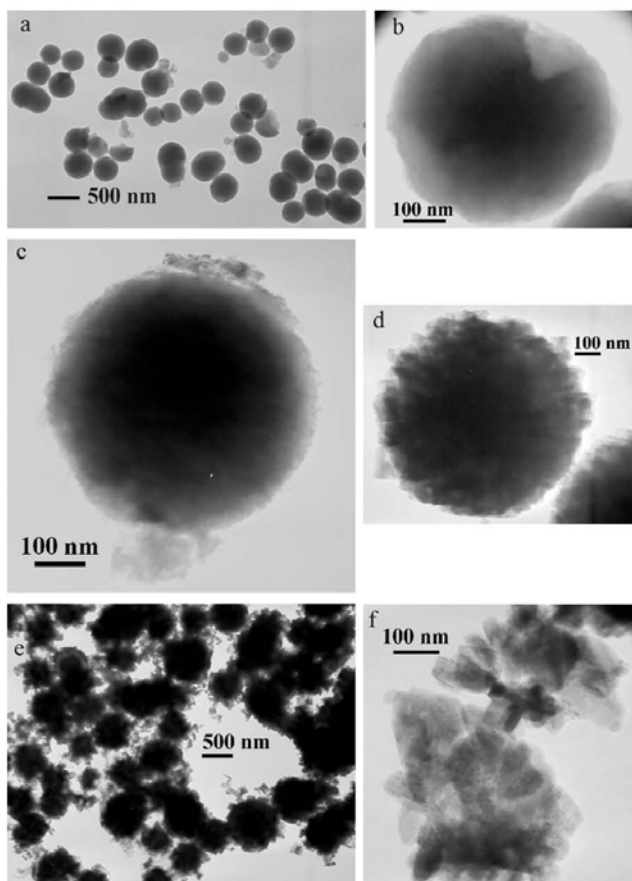


Fig. 9.7. TEM micrographs of (a) and (b) spherical hydrous titania precursor, (c) and (f) partially reacted spherical PbTiO_3 powder, (d) and (e) fully reacted spherical PbTiO_3 powder [20]

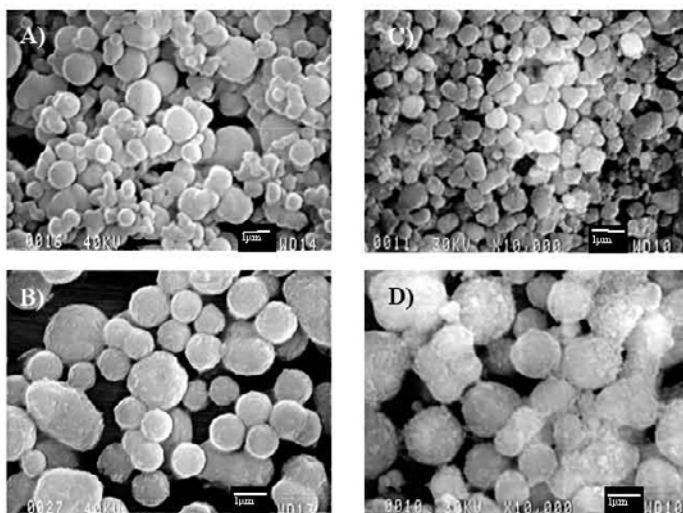


Fig. 9.8. SEM micrographs of precursors of spherical titania with particle size of (a) 1 μm , (b) 1.5 μm , and respective product of $(\text{Ba,Sr})\text{TiO}_3$ with corresponding particle sizes (c) 1 μm , (d) 1.5 μm

9.5.2 Temperature

The influence of temperature on the morphology of the perovskite has been demonstrated in preparation of BaTiO_3 by MacLaren et al. [46] from Ba-acetate, TMAH, and hydrous TiO_2 ; after 2 h at 120 or 160°C, the particles were round, whereas at 200°C the powder formed a facet on low index planes towards cubic morphology (cube faces parallel to $\{100\}$ planes). In another study, Xia et al. [61] found a similar progression occurred from spherical clusters at 75°C to cubes or spheres at 400°C after a 4 h reaction with equimolar amounts of $\text{Ba}(\text{OH})_2$ and TiO_2 . Kutty and Balachandran [92] studied the effects of temperature and $\text{Pb}/(\text{Ti}+\text{Zr})$ molar ratio on the morphology in the precipitation of $\text{Pb}(\text{Zr,Ti})\text{O}_3$ from PbO , and on hydrous- $\text{TiO}_2\text{-ZrO}_2$ derived from chlorides after 8 h. The crystallites formed a tabular shape (0.3 μm) at 300°C with $\text{Pb}/(\text{Ti}+\text{Zr})$ equal to 1 but were cubic (0.4 μm) at 400°C with a molar ratio of 1.2. Gelabert et al. [78] found that dendritic growth occurred in the preparation of PbTiO_3 from homogeneous mixture of precursors. They attributed the growth to inefficient heat dissipation or a high supersaturation. Dendritic growth could be minimized by more accurate temperature control, prevention of thermal gradients by agitation, or incorporation of stronger ligands [78].

9.5.3 Reagent concentration

The reagent concentration can significantly change the morphology. For example, Moon et al. [73] found that tabular PbTiO_3 was produced at 0.05 M feedstock concentrations, whereas cubic particles were prepared at 0.1 M and aggregate tabular particles were synthesized at 0.125 M. The feedstock was Pb-acetate, Ti-isopropoxide acetylacetonate, and KOH or NaOH with 1.5 molar ratio of Pb/Ti, and was heated to 150°C for 12 h. Bagwell et al. [26] also found that the concentration of the precursor in the synthesis of BaTiO_3 influenced the final morphology. As an example, a change in concentration from 1.62 to 0.64 M changed the particle morphology from round to octahedral for particles synthesized at 90°C for 24 hrs from solution containing TiO_2 , Ba(OH)_2 , NH_3 , and polymers adsorbed on the TiO_2 (i.e., polyacrylic acid and polyethylene oxide-block-polymethacrylic acid). This also may be the result of the adsorbed polymers that reduce the surface energy of various growth planes [26].

9.5.4 Additives

Polymeric additives such as polyacrylic acid and polyethylene oxide-block-polymethacrylic acid make BaTiO_3 particles more round [26]. Li and Yao [79] used water-soluble polymers (e.g., PVP, PEG, etc.) as protecting agents during hydrolysis in the preparation of PbTiO_3 between 180–240°C for 1–4 hours. With the addition of PVP, the powders synthesized were tabular perovskite powders. Under similar synthesis conditions, PEG formed acicular powders of an unknown lead titanate phase. Kutty et al. [44,85,87] and Vivekanandan et al. [60,91] used poly-vinyl-alcohol (PVA) in the synthesis of BaTiO_3 , BaZrO_3 , BaSnO_3 , Ba(Sn,Ti,Zr)O_3 , and CaTiO_3 ; they found that the polymer changed the morphology of the growth of the perovskite. For example, irregular, acicular-shaped crystals of CaTiO_3 formed without PVA, but in its presence rectangular platelets formed [87]. This was attributed to the steric hindrance due to the polymers on the surface of the precursor that prevented aggregation, so that the small particles could be more reactive. Also the polymers could act as growth modifiers on certain habits of the crystals to limit crystal size (and growth directions). In general, the polymer molecular structure may also act as a morphology template for the crystal.

9.5.5 Mineralizer type and concentration

The type and concentration of mineralizer was also found to affect the morphology of the powders. In a study conducted by Beal [95] on the synthesis of Pb(Zr,Ti)O_3 from KBr, KOH, and KF, it was determined that KBr and KOH produced random morphologies (1 μm –10 μm elongated) and KF produced cubic. However, for KF the mineralizer concentration influenced the morphology. With low concentrations, rounded (μm) particles grew, while with greater concentrations

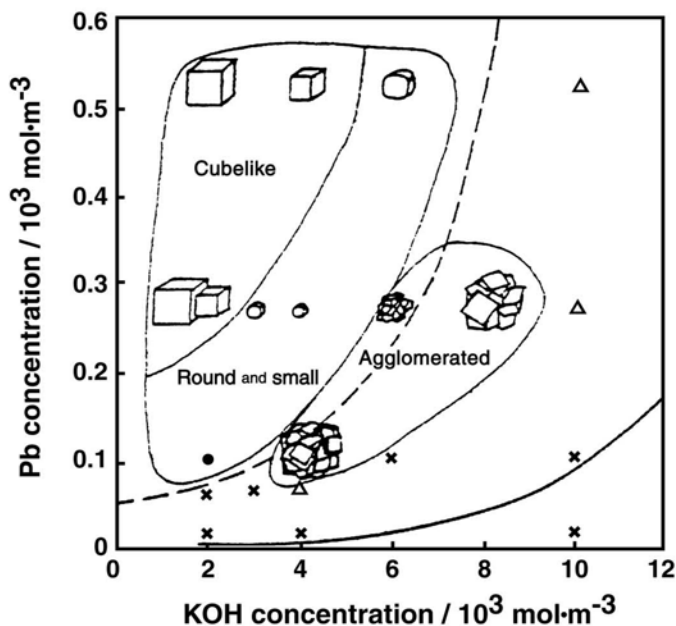


Fig. 9.9. Schematic representation of the morphology of $\text{Pb}(\text{Zr},\text{Ti})\text{O}_3$ powders synthesized at 150°C for 4 hours. Solid line and dashed line are for the Pb concentration saturated with PbO and $\text{Pb}(\text{Zr},\text{Ti})\text{O}_3$ powder, respectively. Phases of $\text{Pb}(\text{Zr},\text{Ti})\text{O}_3$ (λ), and $\text{Pb}(\text{Zr},\text{Ti})\text{O}_3$ with other crystalline solids (triangles), and amorphous (\times) [99]

cube-like (mm) particles grew [95]. Gelabert et al. [78] also found that the mineralizer concentration influenced the morphology. They found that PbTiO_3 changed from spherical agglomerates with dendrites at 0.8 M KOH to square platelets with dendrites at 1.2 M KOH. In another study of $\text{Pb}(\text{Zr},\text{Ti})\text{O}_3$, Ichihara et al. [98] formed $\text{Pb}(\text{Zr},\text{Ti})\text{O}_3$ powders with complicated folded cubes at high concentrations of KOH (4 M) which became dice shaped forms with small folded cubes at low concentrations of KOH (< 4 M). In another study of $\text{Pb}(\text{Zr},\text{Ti})\text{O}_3$, Cheng et al. [97] found that an increase in 1–2 M KOH to 5 M KOH transformed cubic-like particles to a smaller random morphology that formed larger aggregates. In yet another study, Traianidis et al. [101] found that in the synthesis of $\text{Pb}(\text{Zr},\text{Ti})\text{O}_3$ powder from $\text{Pb}(\text{NO}_3)_2$ and hydrous $\text{TiO}_2\text{-ZrO}_2$ at 265°C with Pb/Ti molar ratio equal to 2, after 2 h cubic shaped particles were made with 1 M KOH and turned platelet with KOH concentrations greater than 2 M. Ohba et al. [99] found the morphology conditions of $\text{Pb}(\text{Zr},\text{Ti})\text{O}_3$ were outlined as a function of Pb concentration and KOH concentration (cf. Fig. 9.9). For values between 0.3 and 0.6 m Pb concentration and 2 and 4 m KOH a cubic-like morphology was dominant. For values between 0.1 and 0.2 m Pb and 2 and 6 m KOH a rounded morphology was dominant. For values of 0.1 Pb m and between 4 and 8 m KOH an agglomerated

morphology was dominant. This was found correlated with the solubility of PbO [99]. Zhao [65] suggested that BaTiO₃ formed {111} octahedrons under the high alkaline processing conditions from Ba-hydroxide, and titania (anatase) powder at 90°C under hydrothermal conditions, and suggested this is the only stable surface under these processing conditions.

9.5.6 Summary

In summary, the morphology of perovskite powders produced by the hydrothermal method has been shown to be controllable by the initial reagent types, initial reagent concentration, pH, temperature, stir rate, and time that are parameters of the supersaturation. Polymer additives may control the morphology by acting as growth modifiers, steric stabilizer, and/or template. The insoluble precursor may also act as a template assisting to preserve the morphology for the product.

9.6 Synthesis Conditions for Controlled Particle Size

The particle size and morphology is also dependent on the supersaturation and the growth mechanism. This can be affected by initial precursor, ratio of precursors, temperature, time, additives, mineralizer type, and mineralizer concentration. Under the mechanism of nucleation and growth, the particle size is expected to decrease with an increase in supersaturation. Therefore, the particle size is expected to decrease with a decrease in temperature and an increase in concentration of soluble species. However, in the presence of slightly soluble species, particle size is expected to increase with an increase in pH (mineralizer concentration) and an increase in reaction time. However, if the reaction proceeds by a diffusion-limited mechanism, the starting size of the precursor should be the main contribution to the final particle size.

Just as expected from nucleation and growth kinetics, the parameters that effect the particle size in the hydrothermal synthesis of BaTiO₃ and SrTiO₃ were noted by Um, Kumazawa, and others [42,43,56]. These parameters included an increase in size with temperature and time and a decrease with Ba/Ti or Sr/Ti molar ratio and Ba(OH)₂ concentration.

9.6.1 Precursor

As discussed previously, the size, shape, and phase of the initial precursor of the mostly nondissolving precursor can greatly influence the resultant product size and shape with almost any perovskite. Hu et al. [37] found that monodispersed microspheres of TiO₂ under hydrothermal conditions reacted with barium to form BaTiO₃ with the same size and shape as the initial powders. Likewise, Gersten et

al. [90] prepared $(\text{Ba,Sr})\text{TiO}_3$ powders (cf. Fig. 9.8) from spherical precursors of hydrous titania with the same size and shape.

In the hydrothermal preparation of BaTiO_3 powders from $\text{Ba}(\text{OH})_2$ and amorphous titania (particle size $0.65 \mu\text{m}$), Kumazawa et al. [42] found that the particle ranged in size from 0.03 to $0.11 \mu\text{m}$ depending on the hydrothermal conditions. However, when a rutile TiO_2 precursor (particle size $0.49 \mu\text{m}$) was used in the synthesis, the resultant particles were 0.2 – $0.7 \mu\text{m}$. Similarly, Klee et al. [41] found that powders of BaTiO_3 prepared from hydrous titania had a higher surface area ($56 \text{ m}^2/\text{g}$) than the particles prepared from titania ($10.6 \text{ m}^2/\text{g}$).

9.6.2 Concentration and molar ratio

Concentration can affect the particle size. For example, Moon et al. [72] found that the particle size decreased from 3 nm to 1.5 nm for PbTiO_3 with an increase in concentration from 0.05 M and 0.1 M feedstocks of Pb-acetate and Ti-acetyl acetone. The molar ratio of the precursors can affect the particle size. In the case of hydrothermally prepared BaTiO_3 , Wada et al. [59] found that the particle size decreased with increasing Ba/Ti molar ratio of the precursors of Ba-hydroxide and titania; however, above a Ba/Ti molar ratio of 20, the size remained a constant 20 nm . Wada et al. [58] also found that with a different set of precursors using Ba-hydroxide and Ti chelated with nitrilotriacetic acid (NTA) and with a Ba/Ti molar ratio equal to 5, the average particle size of the BaTiO_3 that formed remained at 19 nm .

9.6.3 Mineralizer type and concentration

The mineralizer type or additives of organic materials may stabilize smaller particles by the steric effect. For example, Urek et al. [57] found a smaller particle size for the hydrothermal synthesis of BaTiO_3 from Ba-acetate, Ti-ethoxide, and TMAH compared with synthesis from Ba-hydroxide, Ti-ethoxide, and ammonia. Similarly, Kutty, Vivekanandan and others [44,85,87,60,91], found that small amounts of poly-vinyl-alcohol (PVA) (0.01 – $0.05 \text{ wt}\%$) decreased the particle size for the preparation of BaTiO_3 , BaZrO_3 , BaSnO_3 , $\text{Ba}(\text{Sn,Ti,Zr})\text{O}_3$, and CaTiO_3 . Kiss et al. [40] also noticed that the addition of isopropyl alcohol for the hydrolysis of Ti-ester in highly alkaline solutions of $\text{Ba}(\text{OH})_2$ decreased the particle size due to the decrease in polarity of the suspension that hindered the condensation of neighboring particles.

The concentration of mineralizer affects the particle size. In the preparation of BaTiO_3 from NaOH , BaCl_2 , and Ti-isopropoxide, Asiaie et al. [25] found that an increase in NaOH concentration from 0.003 to 0.005 m increased the particle size from 0.09 to $0.3 \mu\text{m}$. In the synthesis of $\text{Pb}(\text{Zr,Ti})\text{O}_3$, Ohba et al. [99] found an increase in the concentration of mineralizer resulted in larger particles as expected from a mechanism of nucleation and growth. Similarly, Beal et al. [95] found that when the concentration of mineralizer was increased and the pH was raised, the particles grew larger.

Dutta and Gregg [31] noticed a decrease in particle size from 1 μm to 0.2 μm of hydrothermally prepared BaTiO_3 and attributed it to the presence of Cl ion from the synthesis of BaCl_2 , TiO_2 , and NaOH compared with the preparation from $\text{Ba}(\text{OH})_2$. However, for both syntheses the concentration of Ba and NaOH was kept a constant, 0.25 m and 1 m, respectively, without considering an increase in pH due to an increase in the hydroxide concentration from the $\text{Ba}(\text{OH})_2$.

9.6.4 Reaction time

The particle size of the hydrothermally prepared perovskite was found to increase as a function of time. For example, Asiaie et al. [25] found that BaTiO_3 particles increased from 0.3 to 0.5 μm by increasing the reaction time from 1 week to 2 weeks.

9.6.5 Temperature

The crystallite size is affected by temperature. For example, MacLaren et al. [46] studied hydrothermal BaTiO_3 , and found the powders formed with TMAH, Ba-acetate, and hydrous TiO_2 after 2 h at 120 and 160°C were 15–50 nm, but were larger at 200°C (the size increase was not noted). Ichihara et al. [98] also found that the grain size of $\text{Pb}(\text{Zr,Ti})\text{O}_3$ prepared by reacting $\text{Pb}(\text{NO}_3)_2$ with ZrOCl_2 and TiCl_4 with 4 M KOH for 4 h decreased from 2–3 μm to 1–2 μm with an increase in reaction temperature from 180 to 200°C. However, Ohba [99] found that an increase in temperature can increase or decrease the size of the $\text{Pb}(\text{Zr,Ti})\text{O}_3$ particles depending on the synthesis conditions. For example, the particle size increased for an increase in temperature from 150 to 180°C when KOH was 4 m and Pb was 0.1 and 0.275 m. However, the particles became smaller for an increase in temperature from 150 to 180°C when the Pb concentration was 0.5 m and the KOH concentration was 2–4 m [99]. The suggested reason for the change in particle size with respect to conditions is due to the degree of saturation of PbO. At higher temperatures, there is a decrease in the degree of PbO saturation that results in a decrease in size and a higher degree of agglomeration [99].

9.6.6 Summary

Particle size has been shown mostly to follow trends expected for supersaturation under the conditions for precipitation. Therefore, as expected with increases in temperature, time, and mineralizer concentration, the particle size increases, but the particle size decreases with an increase in concentration. Any additive that enhances the supersaturation decreases the particle size and vice versa.

9.7 Summary

The processing parameters for the synthesis of ferroelectric perovskite powders by the hydrothermal method have been reviewed. In conclusion, the first step in processing of chemically phase pure materials is the thermodynamic verification of the correct processing conditions for the reaction of the desired product. The chemical purity of the precursors should be high, and the pH adjusters or other additives should be decomposable at calcination temperatures. For multicomponent oxides (e.g., $\text{Pb}(\text{Zr},\text{Ti})\text{O}_3$), the starting precursors must be intimately mixed. The reaction time must be long enough for complete reaction. The time can be predicted if the mechanism is known, but can be shortened by an increase in concentration or temperature. Knowledge of the supersaturation can be helpful in the control of the morphology and particle size. The supersaturation is influenced by the initial reagent concentration, pH, temperature, stir rate, and time. An increase in supersaturation will result in a decrease in particle size. Therefore, to obtain fine particles, the temperature should be kept at a minimum and the concentration at a maximum. Other variables to keep in mind when trying to produce nano-sized particles are the mineralizer concentration, reaction time, and additives.

References

1. Dawson WJ (1988) Hydrothermal Synthesis of Advanced Ceramic Powders. *Ceram Bull* 67:1673–1677
2. Riman RE (1990) Hydrothermal Synthesis of Ceramic Powders, Proc 11th Riso Int Symp Metall and Mat Sci, Structural Ceramics-Processing, Microstructure and Properties, Bentzen JJ, Blide-Sorensen JB, Christiansen N, Horsewell A, Ralph B (eds) 111–72126
3. Yanagisawa K, Kanai H (1997) Crystal Growth of Lead Zirconate Titanate with Additives under Hydrothermal Conditions. *Jpn J Appl Phys* 36 Part 1(9B):6031–6034
4. Yanagisawa K, Kanai H, Yamashita Y (1995) Hydrothermal Crystal Growth of Lanthanum Modified Lead Zirconate Titanate. *Jpn J Appl Phys* 34 Part 1(9B):5346–5348
5. Yanagisawa K, Rendon-Angeles JC, Kanai H, Yamashita Y (1998) Stability and Single Crystal Growth of Lead Scandium Niobate and Its Solid Solution with Lead Titanate under Hydrothermal Conditions. *J Mater Res* 13(4):875–879
6. Bendale P, Venigalla S, Ambrose JR, Vernick Jr ED, Adair JH (1993) Preparation of Barium Titanate Films at 55°C by an Electrochemical Method. *J Am Ceram Soc* 76:2619–2627
7. Chien AT, Speck JS, Lange FF (1997) Hydrothermal Synthesis of Heteroepitaxial $\text{Pb}(\text{Zr}_x\text{Ti}_{1-x})\text{O}_3$ Thin Films at 90–150°C. *J Mat Res* 12(5):1176–1178
8. Chien AT, Speck JS, Lange FF, Daykin AC, Levi CG (1995) Low Temperature/Pressure Hydrothermal Synthesis of Barium Titanate: Powder and Heteroepitaxial Thin Films. *J Mat Res* 10:1784–1789
9. Kajiyoshi K, Tomono K, Hamaji Y, Kasanami T, Yoshimura M (1995) Short-Circuit Diffusion of Ba, Sr, and O During ATiO_3 (A = Ba, Sr) Thin Film Growth by the Hydrothermal-Electrochemical Method. *J Am Ceram Soc* 78(6):1521–1531

10. Pilleux ME, Grahmann CR, Fuenzalida VM, Avila RE (1993) Hydrothermal ABO_3 Ceramic Thin Films. *Appl Surf Sci* 65/66:283–288
11. Roeder RK, Slamovich EB (1997) Low Temperature Hydrothermal Processing (100°C) of Stoichiometric $(Ba_xSr_{1-x})TiO_3$ Thin Films and Powders. Proceedings of the Aqueous Chemistry and Geochemistry of Oxides, Oxyhydroxides, and Related Materials, Materials Research Society Symposium Proceedings 432:195–200
12. Yoshimura M, Suchanek W, Watanabe T, Sakurai B, Abe M (2000) Functionally Graded $SrTiO_3$ - $BaTiO_3$ Thin Films Prepared by the Hydrothermal-Electrochemical Method under Flowing Solution. *J Mater Sci* 35(4):3011–3015
13. Somiya A, Hishinuma K, Akiba T (1995) A New Materials Processing-Hydrothermal Processing. *Bull Mater Sci* 18(6):811–818
14. Lee KH, Asaga K, Ichihara T, Daimon M (1987) Synthesis of PZT Crystalline Powders by Reaction of Aqueous Solutions below 200°C . *Yogyo-Kyokai Shi* 95:74–78
15. Riman RE, Landham RR, Bowen HK (1989) Synthesis of Uniform Titanium and 1:1 Strontium-Titanium Carboxyhydrosols by Controlled Hydrolysis of Alkoxy metal Carboxylate Precursors. *J Am Ceram Soc* 72(5):821–826
16. Jaffe B, Cook Jr WR, Jaffe H (1971) *Piezoelectric Ceramic*. Academic Press, New York
17. Flaschen SS (1955) An Aqueous Synthesis of Barium Titanate. *J Am Chem Soc* 77:6194
18. Christensen AN, Rasmussen SE (1963) Hydrothermal Preparation of Compounds of the Type ABO_3 and AB_2O_4 . *Acta Chem Scand* 17(3):845
19. Lencka MM, Riman RE (1995) Thermodynamics of the Hydrothermal Synthesis of Calcium Titanate with Reference to Other Alkaline-Earth Titanates. *Chem Mater* 7:18–25
20. Gersten BL (1999) Influences of the A and B Site Cation Species in the Kinetics of Hydrothermal Synthesis of ABO_3 Perovskite-Type Materials. PhD thesis, Rutgers University, Piscataway
21. Avudaithai M, Kutty TRN (1987) Ultrafine Powders of $SrTiO_3$ from the Hydrothermal Preparation and Their Catalytic Activity in the Photolysis of Water. *Mat Res Bull* 22:641–650
22. Lee KH, Lee BH, Kim, JS (1985) A Study of $SrTiO_3$ Synthesis by Direct Wet Process (II). *J Korean Ceram Soc* 22:19–24
23. Komarneni S, Li Q, Stefanesson KM, Roy R (1993) Microwave-Hydrothermal Processing for Synthesis of Electroceramic Powders. *J Mater Res* 8(12):3176–3183
24. Kutty TRN, Vivekanandan R (1988) Precipitation of Rutile and Anatase (TiO_2) Fine Powders and their Conversion to $MTiO_3$ ($M = Ba, Sr, Ca$) by the Hydrothermal Method. *Mat Chem Phys* 19:533–546
25. Asiaie R, Zhu W, Akbar SA, Dutta PK (1996) Characterization of Submicron Particles of Tetragonal $BaTiO_3$. *Chem Mater* 8:226–234
26. Bagwell RB, Sindel J, Sigmund W (1999) Morphological Evolution of Barium Titanate Synthesized in Water in the Presence of Polymeric Species. *J Mat Res* 14(5):1844–1851
27. Begg BD, Vance ER, Nowotny J (1994) Effect of Particle Size on the Room Temperature Crystal Structure of Barium Titanate. *J Am Ceram Soc* 77(12):3186–3192
28. Choi JY, Kim CH, Kim DK (1998) Hydrothermal Synthesis of Spherical Perovskite Oxide Powders using Spherical Gel Powders. *J Am Ceram Soc* 81:1353–1356

29. Chun C-M (1997) Hydrothermal Crystallization of Barium Titanate: Mechanisms of Nucleation and Growth. PhD thesis, Princeton University
30. Christensen AN (1970) Hydrothermal Preparation of Barium Titanate by Transport Reactions. *Acta Chem Scand* 24(7):2447–2452
31. Dutta PK, Gregg JR (1992) Hydrothermal Synthesis of Tetragonal Barium Titanate. *Chem Mater* 4:843–846
32. Eckert Jr JO, Hung-Houston CC, Gersten BL, Lencka MM, Riman RE (1996) Kinetics and Mechanisms of Hydrothermal Synthesis of Barium Titanate. *J Am Ceram Soc* 79:2929–2939
33. Fukai K, Hidaka K, Aoki M, Abe K (1990) Preparation and Properties of Uniform Fine Perovskite Powders by Hydrothermal Synthesis. *Cer Int* 16:285–290
34. Chaput F, Boilot JP (1987) Chemical Processing of (Ba,Sr)(Ti,Zr)O₃ Perovskite Ceramics. *J Mater Sci Lett* 6(1):1110–1112
35. Hertl W (1988) Kinetics of Barium Titanate Synthesis. *J Am Cer Soc* 71(10):879–883
36. Hennings D, Rosenstein G, Schreinemacher H (1991) Hydrothermal Preparation of Barium Titanate from Barium-Titanium Acetate Gel Precursors. *J Europ Ceramic Soc* 8:107–115
37. Hu MZC, Kurian V, Payzant EA, Rawn CJ, Hunt RD (2000) Wet-Chemical Synthesis of Monodispersed Barium Titanate Particles — Hydrothermal Conversion of TiO₂ Microspheres to Nanocrystalline BaTiO₃. *J Chem Phys* 8:212–224
38. Hung CC, Riman RE, Caracciolo R (1993) An XPS Investigation of Hydrothermal and Commercial Barium Titanate Powders. *Ceramic Powder Science III* 17–24
39. Kaneko S, Imoto F (1975) Synthesis of Fine Grained Barium Titanate by Hydrothermal Reaction. *Nippon Kagaku Kaishi* 6:985–1000
40. Kiss K, Magder J, Vukasovich MS, Lockhart RJ (1966) Ferroelectrics of Ultrafine Particle Size: I, Synthesis of Titanate Powders of Ultrafine Particle Size. *J Am Ceram Soc* 49(6):291–295
41. Klee M (1989) Low Temperature Processing of BaTiO₃, Ba(Ti_{1-x}Zr_x)O₃ and (Ba_{1-x}Sr_x)TiO₃ Powder. *J Mater Sci Lett* 8:985–988
42. Kumazawa H, Annen S, Sada E (1995) Hydrothermal Synthesis of Barium Titanate Fine Particles from Amorphous and Crystalline Titania. *J Mater Sci* 30:4740–4744
43. Kumazawa H, Kagimoto T, Kawabata A (1996) Preparation of Barium Titanate Ultrafine Particles from Amorphous Titania by a Hydrothermal Method and Specific Dielectric Constants of Sintered Discs of the Prepared Particles. *J Mater Sci* 31:2559–2602
44. Kutty TRN, Murugaraj P (1988) Hydrothermal Precipitation and Characterization of Polytitanates in the System BaO-TiO₂. *J Mat Sci Lett* 7:601–603
45. Lencka MM, Riman RE (1993) Thermodynamic Modeling of Hydrothermal Synthesis of Ceramic Powders. *Chem Mater* 5:61–70
46. MacLaren I, Ponton CB, Elgy CN, Knott PR (1996) The Effects of Synthesis Temperature upon Hydrothermally Produced BaTiO₃ Powders, *Electroceramics V, International Conference on Electronic Ceramics and Applications*. Portugal, Book 2:375–378
47. Maurice AK, Buchanan RC (1987) Preparation and Stoichiometry Effects on Microstructure and Properties of High Purity BaTiO₃. *Ferroelectrics* 74:61–75
48. Matsuoka K, Sakuragi S, Yamazaki J (1978) Hydrothermal Synthesis of BaTiO₃. *Reports of the Research Laboratory of Hydrothermal Chemistry of Japan* 2(15):45–47

49. Moon J, Kerchner JA, Krarup H, Adair JH (1999) Hydrothermal Synthesis of Ferroelectric Perovskites from Chemically Modified Titanium Isopropoxide and Acetate Salts. *J Mat Res* 14(3):425–435
50. Nanni P, Leoni M, Buscaglia V, Aliprandi G (1994) Low Temperature Aqueous Preparation of Barium Metatitanate Powders. *J Eur Cer Soc* 14:85–90
51. Ohara Y, Miyayama M, Shimizu T, Yanagida H (1996) Barium Titanate Fabricated from Fur-Fibres. *Mat Sci* 7:27–33
52. Ovramenko NA, Shvets LI, Ovcharenko FD, Kornilovich BYu (1979) Kinetics of Hydrothermal Synthesis of Barium Metatitanate. *Inorg Mat* 15:1560–1562
53. Pfaff G (1991) BaTiO₃ Preparation by Reaction of TiO₂ with Ba(OH)₂. *J Eur Cer, Soc* 8:35–39
54. Pinceloup P, Courtois C, Leriche A, Thierry B (1996) Hydrothermal Synthesis of Barium Titanate Powders: Influence of Final Washing Step on Sintering Behavior and Dielectric Properties, *Electroceramics V, International Conference on Electronic Ceramics and Applications*. Portugal, Book 2:363–366
55. Shi EW, Xia CT, Zhong WZ, Wang BG, Feng CD (1997) Crystallographic Properties of Hydrothermal Barium Titanate. *J Am Ceram Soc* 80(6):1567–1572
56. Um MH, Kumazawa H (2000) Hydrothermal Synthesis of Ferroelectric Barium and Strontium Titanate Extremely Fine Particles. *J Mater Sci* 35(5):1295–1300
57. Urek S, Drofenik M (1998) The Hydrothermal Synthesis of BaTiO₃ Fine Particles from Hydroxide Alkoxide Precursors. *J Europ Ceram Soc* 18:279–286
58. Wada S, Chikamori H, Noma T, Suzuki T (2000) Hydrothermal Synthesis of Barium Titanate Crystallites using New Stable Titanium Chelated Complex in Aqueous Solution. *J Mat Sci Lett* 19:245–247
59. Wada S, Suzuki T, Noma T (1995) The Effect of the Particle Sizes and the Correlational Sizes of Dipoles Introduced by the Lattice Defects on the Crystal Structure of Barium Titanate Fine Particles. *Jpn J Appl Phys* 34 Part 1(9B):5368–5379
60. Vivekanandan R, Philip S, Kutty TRN (1986) Hydrothermal Preparation of Ba(Ti,Zr)O₃ Fine Powders. *Mat Res Bull* 122:99–108
61. Xia CT, Shi EW, Zhong WZ, Guo JK (1995) Preparation of BaTiO₃ by the Hydrothermal Method. *J Eur Cer Soc* 30(1):1171–1176
62. Yamamura H, Shiraski SI, Takahashi K, Takagi M (1974) Aqueous Synthesis of Barium Titanate And Its Dielectric Properties. *Nippon Kagaku Kaishi* (7):1155–1159
63. Yoo SE, Yoshimura M, Somiya S (1989) Direct Preparation of BaTiO₃ Powders from Titanium Metal by Anodic Oxidation under Hydrothermal Conditions. *J Mat Sci Lett* 8:530–532
64. Yoshimura M, Suchanek W (1997) *In Situ* Fabrication of Morphology Controlled Advanced Ceramic Materials by Soft Solution Processing. *Solid State Ionics* 98(3–4):197–208
65. Zhao L, Chien AT, Lange FF, Speck JS (1996) Microstructural Development of BaTiO₃ Powders Synthesized by Aqueous Methods. *J Mat Res* 11(6):1325–1328
66. Lencka MM, Riman RE (1993) Synthesis of Lead Titanate: Thermodynamic Modeling and Experimental Verification. *J Am Ceram Soc* 76(10):2649–2659
67. Gersten B, Lencka MM, Riman RE (1996) ISAF '96: Proceedings of the Tenth IEEE International Symposium on Applications of Ferroelectrics, Vol 2, Bulwicki BM, Amin A, Safari A (eds) IEEE, New York
68. Cheng H, Ma J, Zhao Z, Qi L (1996) Hydrothermal Synthesis of PbTiO₃ from PbO and TiO₂. *J Mater Sci Lett* 15(14):1245–1246

69. Ohara Y, Koumoto K, Shimizu T, Yanagida H (1995) Hydrothermal Synthesis of Fibrous Lead Titanate Powders. *J Mat Sci* 30:263–266
70. Sato S, Murakata T, Yanagi H, Miyasaka F, Iwaya S (1994) Hydrothermal Synthesis of Fine Perovskite PbTiO_3 Powders with a Simple Mode of Size Distribution. *J Mat Sci* 29:5657–5663
71. Peterson CR (1998) Hydrothermal Processing of Lead Titanate Powders and Thin Films. PhD thesis, Purdue University, West Lafayette, IN, Aug
72. Moon J, Carasso ML, Krarup HG, Kerchner JA, Adair JH (1999) Particle-Shape Control and Formation Mechanisms of Hydrothermally Derived Lead Titanate. *J Mater Res* 14(3):866–875
73. Moon J, Li T, Randall CA, Adair JH (1997) Low Temperature Synthesis of Lead Titanate by the Hydrothermal Method. *J Mat Res* 12:189–197
74. Walton DJ, Randall CA, Newnham RE, Adair JH (1988) Hydrothermal Formation Diagram in the Lead Titanate System, *Ceramic Transactions, Vol 1, Ceramic Powder Science IIA*, Messing GL, Fuller Jr ER, Hausner H (eds) Westerville, OH: Amer Ceram Soc 154–161
75. Suzuki M, Uedaira S, Masuya H, Tamura H (1987) Hydrothermal Synthesis of Lead Titanate Fine Powders, *Ceramic Transactions, Ceramic Powder Science II*. Westerville, OH: Amer Ceram Soc 163–170
76. Kaneko S, Imoto F (1978) Reactions between PbO and TiO_2 under Hydrothermal Conditions. *Bull Chem Soc Jpn* 51:1739–1742
77. Takai K, Shoji S, Naito H, Sawaoka A (1982) Fine Powder PbTiO_3 Obtained by Hydrothermal Technique and Its Sinterability, *Proc 1st Intern Symp Hydrothermal Reactions*. Tokoyo Inst Technology, Somiya, 877–885
78. Gelabert MC, Gersten BL, Riman, RE (2000) Hydrothermal Synthesis of Lead Titanate from Complexed Precursor Solutions. *J Crystal Growth* 211:497–500
79. Li YX, Yao X (1993) Lead Titanate Powders Derived from Hydrothermal Treatment. *Sensors and Actuators A* 35:255–258
80. Rossetti Jr GA, Watson DJ, Newnham RE, Adair JH (1992) Kinetics of the Hydrothermal Crystallization of the Perovskite Lead Titanate. *J Crystal Growth* 116:251–259
81. Fox GR, Adair JH, Newnham RE (1990) Effects of pH and H_2O_2 upon Coprecipitated PbTiO_3 Powders: Part I: Properties of As-Precipitated Powders. *J Mater Sci* 25:3634–3640
82. Fox GR, Breal E, Newnham RE (1991) Crystallization of Nanome-Size Coprecipitated PbTiO_3 Powders. *J Mater Sci* 26:2566–2572
83. Kim MJ, Matijevic E (1989) Preparation and Characterization of Uniform Submicrometer Lead Titanate Particles. *Chem Mater* 1:363–369
84. Shvets LI, Ovramenko NA, Ovcharenko FD (1979) Reactions between PbO and TiO_2 under Hydrothermal Conditions. *Doklady Akademii Nauk SSSR* 248(4):889–891
85. Kutty TRN, Vivekanandan R (1987) Preparation of CaTiO_3 Fine Powders by the Hydrothermal Method. *Mat Lett* 5(3):79–83
86. Kim MJ, Matijevic E (1994) Preparation of Uniform Submicrometer Particles of Calcium Titanate and Lead Niobate by Replacement Reactions. *J Am Ceram Soc* 77(7):1950–1953
87. Kutty TRN, Vivekanandan R (1987) BaSnO_3 Fine Powders from Hydrothermal Preparation. *Mat Res Bull* 22(3):1457–1465

88. Lencka MM, Nielson E, Anderko A, Riman RE (1997) Hydrothermal Synthesis of Carbonate-Free Strontium Zirconate: Thermodynamic Modeling and Experimental Verification. *Chem Mat* 9:1116–1125
89. Phule PP, Grundy DC (1994) Pathways for the Low Temperature Synthesis of Nano-Sized Crystalline Barium Zirconate. *Mat Sci Eng B: Sol State Mat Adv Tech* B23(1):29–35
90. Gersten B, Synowczynski J (2000) Hydrothermal Synthesis of Pure Barium Strontium Titanate, ISAF 2000: Proceedings of the 12th IEEE International Symposium on Applications of Ferroelectrics. IEEE, New York
91. Vivekanandan R, Kutty TRN (1988) Hydrothermal Ba(Ti,Sn)O₃ Fine Powders and Dielectric Properties of the Corresponding Ceramics. *Ceram Intern* 14:207–216
92. Kutty TRN, Balachandran R (1984) Direct Precipitation of Lead Zirconate Titanate by the Hydrothermal Method. *Mat Res Bull* 19:1479–1488
93. Lencka MM, Anderko A, Riman RE (1995) Hydrothermal Precipitation of Lead Zirconate Titanate Solid Solutions: Thermodynamic Modeling and Experimental Synthesis. *J Am Ceram Soc* 78: 2609–2618
94. Abthu IR, Liu SF, Komarneni S, Li QH (1999) Processing of Pb(Zr_{0.52}Ti_{0.48})O₃ (PZT) Ceramics from Microwave and Conventional Hydrothermal Powders. *Mat Res Bull* 34(9):1411–1419
95. Beal KC (1987) Precipitation of Lead Zirconate Titanate Solid Solution under Hydrothermal Conditions, *Advances in Ceramics, Ceramic Powder Science*. The American Ceramic Society 21:33–41
96. Chen DR, Jiao XL, Xu RR (1998) Hydrothermal Synthesis of PbZr_xTi_{1-x}O₃ (x = 0.45–0.65) Powders Without Using Alkaline Mineralizer. *J Mat Sci Lett* 17:53–56
97. Cheng H, Ma J, Zhu B, Cui Y (1993) Reaction Mechanism in the Formation of Lead Zirconate Titanate Solid Solution under Hydrothermal Conditions. *J Am Ceram Soc* 76:625–29
98. Ichihara T, Tsurumi T, Asaga K, Lee KH, Daimon M (1990) Hydrothermal Synthesis of PZT Crystalline Powder and Piezoelectric Property of Ceramics. *J Ceram Soc Jpn Inter Ed* 98:155–160
99. Ohba Y, Rikitoku T, Tsurumi T, Daimon M (1996) Precipitation of Lead Zirconate Titanate Powders under Hydrothermal Conditions. *J Ceramic Soc Jpn* 104(1):6–10
100. Lee Y-J, Yen F-S (1997) Phase Formation Mechanism for Hydrothermally Synthesizing Lanthanum Modified Lead Zirconate Titanate Powders. *J Crystal Growth* 178:335–344
101. Traianidis M, Courtois C, Leriche A, Thierry B (1999) Hydrothermal Synthesis of Lead Zirconium Titanate (PZT) Powders and Their Characteristics. *J Eur Cer Soc* 19(6–7):1023–1026
102. Su B, Button TW, Ponton CB (1998) Hydrothermal Formation of Perovskite Lead Titanate (PZT) Powders, *Proc International Conference AIRAPT-16 and HPCJ-38 on High Pressure Science and Technology, Kyoto, Japan, 25-29, August 1997. Review of High Pressure Science and Technology* 7:1348–1355
103. Shrout TR, Swartz SL (1992) Processing of Ferroelectric and Related Materials: A Review. *IEEE* 80–88
104. Environmental and Corrosion Simulation Program (ESP/CSP) version 6.0, OLI Systems, Inc, Morris Plains, NJ (1998)
105. Wada S, Suzuki T, Noma T (1996) Role of Lattice Defects in the Size Effect of Barium Titanate Fine Particles. *J Ceram Soc Jpn* 104(5):383–392

106. Blesa MA, Morando PJ, Ragazzoni AE (1994) *Chemical Dissolution of Metal Oxides*. Boca Raton, FL: CRC Press
107. Nielsen AE (1964) *Kinetics of Precipitation*. Oxford, England: Pergamon Press L
108. Avrami MJ (1939) Kinetics of Phase Change I, General Theory. *J Chem Phys* 7:1103–1112
109. Avrami MJ (1940) Kinetic of Phase Change II. *J Chem Phys* 8:212–224
110. Erofe'ev BV (1946) Generalized Equations of Chemical Kinetics and Its Application in Reactions Involving Solids. *Compt Rend Acad Sci USSR* 52:511–514
111. Sohnel O, Mullin JW (1988) Interpretation of Crystallization Induction Periods. *J Coll Interf Sci* 123:43–50
112. Hancock JD, Sharp JH (1972) Method of Comparing Solid-State Kinetic Data and Its Application to the Decomposition of Kaolinite, Brucite, and BaCO₃. *J Am Ceram Soc* 55(6):74–77
113. Nielsen AE (1983) Precipitates: Formation, Coprecipitation, and Aging. In: Kolthoff IM, Elving PJ (eds) *Treatise on Analytical Chemistry*, 2nd ed, pt 1, Vol 3. New York: John Wiley and Sons, pp 269–347
114. Nielsen AE (1984) Electrolyte Crystal Growth Mechanisms. *J Crystal Growth* 67:289–310
115. Nielsen AE, Christoffersen J (1982) The Mechanisms of Crystal Growth and Dissolution, Biological Mineralization and Demineralization, Nancollas GH, Konferenzen D (eds) New York: Springer-Verlag, pp 37–77
116. Walton AG (1967) *The Formation of Precipitates*. New York: Wiley

10 Crystal Growth, Size, and Morphology Control of Nd:RVO₄ Under Hydrothermal Conditions

K. Byrappa¹, B. Nirmala¹, K.M. Lokanatha Rai², and M. Yoshimura³

¹Department of Geology, University of Mysore, Manasagangotri, Mysore-570 006, India

²Department of Chemistry, University of Mysore, Manasagangotri, Mysore-570 006, India

³Materials Structures Laboratory, Center for Materials Design, Tokyo Institute of Technology, 4259, Nagatsuta, Midori, Yokohama 226, Japan

10.1 Introduction

Growth of solid-state laser host crystals is an attractive field in solid-state science owing to its technological significance. Laser diode pumped solid-state lasers have a wide variety of applications in military, industrial, medical treatment, and scientific fields due to their advantages of high stability, compactness, high efficiency, and long life time and have become one of the frontier areas of research [1]. There exists a large number of solid-state laser host crystals. In this context, the rare earth vanadates are of great interest due to their useful luminescent and magnetic properties [2]. These materials have been employed as highly efficient laser diode pumped microlasers [3], an efficient phosphor [4], and as very attractive polarizer materials [5]. The rare earth vanadates are known as the high temperature materials and their synthesis by any technique insists on high temperature conditions. That is the reason why most of the earlier workers have obtained these laser crystals by flux or melt methods at elevated temperatures [6–9]. In spite of its excellent physical properties, the high-tech applications have not been realized due to crystal growth difficulties. One of the major problems encountered in RVO₄ crystals is the presence of oxygen imperfections (color centers and inclusions) introduced during the crystal growth processes. Although YVO₄ melts congruently [10], certain vanadium oxides vaporize incongruently, causing changes in Y/V ratio and oxygen stoichiometry in the melt. These undesired effects could generate additional phases and oxygen defects in YVO₄ crystals especially those grown from the melt [11]. Efforts to eliminate these defects did not yield significant success in the flux and melt techniques. Rubin and Van Uitert (1966) were the first to obtain large bulk crystals of Nd:YVO₄ using the Czochralski (Cz) technique [12]. But problems related to the oxygen deficiency and inclusions could not be eliminated. This is emphasized by the numerous reports of Cz growth [12–14] and

other melt growth methods like Verneuil [15], modified floating zone [16,17], laser heated pedestal growth [18,19], and Bridgman [13]. The flux growth experiments did not yield adequate results due to inclusion and size problems. The hydrothermal method was not attempted to grow these crystals and it might be due to the fact that their growth insists on high temperature and high-pressure conditions and also, a strong belief that their growth under mild hydrothermal conditions will introduce water into the structure or interstices. There is a growing tendency in recent years to obtain crystals under mild hydrothermal conditions. The method involves the use of aqueous solvent or mineralizers under lower temperature and pressure to dissolve and recrystallize materials that are relatively insoluble under ordinary conditions.

The hydrothermal method has an advantage over the earlier methods because of its suitability and perfection in obtaining a desired polymorphic modification. It is well known that in vanadate crystals grown at much higher temperature, there is a rapid fall in the fluorescent lifetime because of various physical defects.

This motivated the present authors to obtain rare earth vanadates under lower pressure and temperature conditions by the hydrothermal method. Detailed studies of the growth mechanism, role of pH, morphology control, X-ray diffraction, and luminescent properties are discussed here.

10.2 Technologically Important Vanadates

The synthesis of vanadates began in the 19th century [20]. In recent years several new rare earth vanadates have been reported from time to time. Among these, Nd:YVO₄ and Nd:GdVO₄ are the prominent ones. YVO₄ was first synthesized by Goldschmidt and Harlidsen in 1928 [20]. However, the growth of Nd:YVO₄ crystals of high optical quality encounters a lot of difficulties, which hinder their application. Nd:GdVO₄ crystal was first introduced by Zagumennyi et al. (1992) as a new laser material [21]. This material offers large effective absorption and emission cross-sections coupled with a relatively broad absorption line. The laser performance is expected to be much more tolerant to diode wavelength variation than Nd:YAG, and is therefore an interesting material for future applications [22–25].

10.3 Phase Equilibria

The study of the phase equilibria of a given system helps to understand the phases crystallizing and their crystallization boundaries. This is one of the first and foremost requirements for the successful growth of any compound in the form of single crystals. Failures in the growth of single crystals are largely due to the lack of phase equilibria data for the corresponding systems and also the growth technology. Although the study of vanadate systems started as far back as the 1950s, the systems bearing V₂O₅ studied up to now are the following: Y₂O₃-V₂O₅ [10], Y₂O₃-

V₂O₅-V₂O₃ [26], and Y₂O₃-V₂O_{5-y} [27]. It is known that among the vanadium oxides V₂O₅ has the highest equilibrium O₂ partial pressure, while V₂O₃ has the lowest. V₂O₃ is the most stable form in the V₂O₅-V₂O₃ system, and is the only congruently vaporizing phase. Other vanadium oxide phases vaporize incongruently, transforming in a stepwise manner into V₂O₃. Since high-temperature systems containing V₂O₅ always have intermediate vanadium oxide phases, it is more appropriate to consider Y₂O₃-V₂O₅ as a ternary system Y₂O₃-V₂O₅-V₂O₃ [18]. Although an equilibrium phase diagram cannot be constructed due to the incongruent vaporization of the metastable vanadium oxides, a ternary depiction of the quasi-equilibrium system representing the various yttrium-vanadium compounds involved is useful for better understanding of the processes. Figures 10.1 and 10.2 show the binary and ternary systems of YVO₄ [10,26]. The phase relations can be interpreted through the ternary system (Fig. 10.2) where the direction of melt composition modification is indicated by a small arrow. Although a number of black YVO_{4-x} phases have not yet been identified precisely, the existence of a minimum of two kinds of black crystal phases along the YVO₄-YVO₃ line has been confirmed.

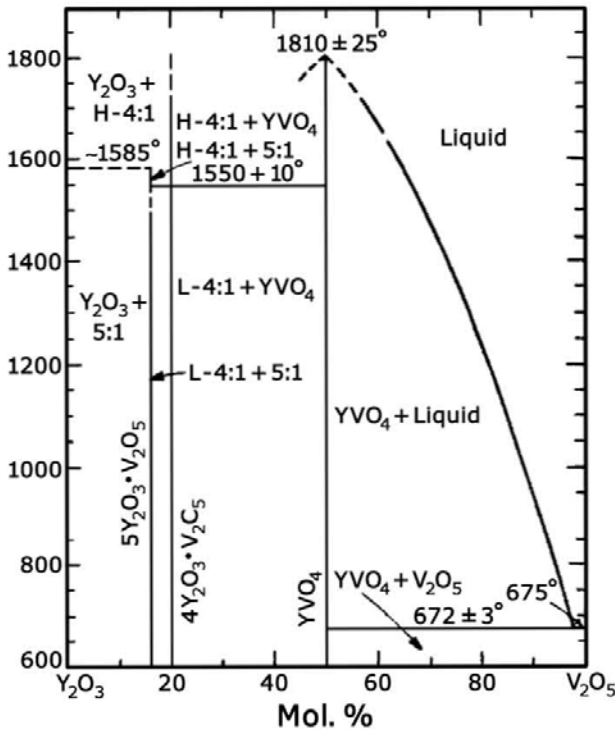


Fig. 10.1. Y₂O₃ - V₂O₅ binary system [10]

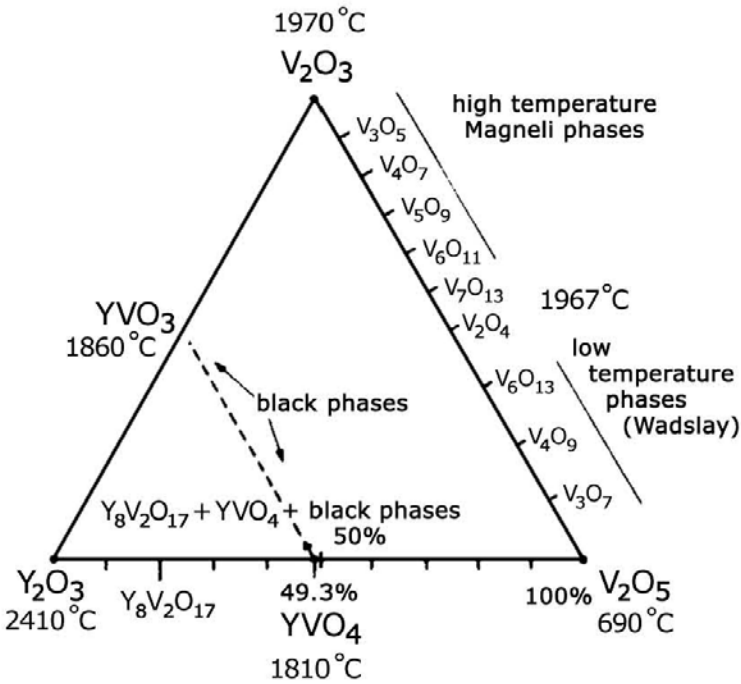


Fig. 10.2. $Y_2O_3 - V_2O_5 - V_2O_3$ ternary system [26]

10.4 Structure of $Nd:RVO_4$

RVO_4 belongs to a large family of tetragonal compounds with the $I4_1/amd$ space group [28]. The rare earth ions occupy the positions with D_{2d} symmetry and the vanadium ions have tetrahedral symmetry. Theoretically, rare earth ions in these compounds are trivalent and the valency of vanadium ions is equal to five. Therefore, the external electronic configuration of rare earth ions can be ascribed to $4f^n 5s^2 5p^6$ and the vanadium ions to $3d^6$. The rare earth bonds are realized by the 6s and 5d orbitals because of the fact that 4f and 5d levels are energetically close to each other and 4f-5d electronic transfers may take place. Energetic separations between 4f and 5p levels are in the range of 20 eV. Then the 4f electrons participate in the chemical bonds. The values of the lattice parameters of RVO_4 crystals are close to 7.2 Å (*a* parameter) and 6.35 Å (*c* parameter). Both parameters decrease with the atomic number of the rare earth ion. The tetragonal unit cells containing four YVO_4 molecules are shown in Fig. 10.3. The principal structural unit of YVO_4 is a chain of alternating edge sharing VO_4 tetrahedra and YO_8 polyhedra,

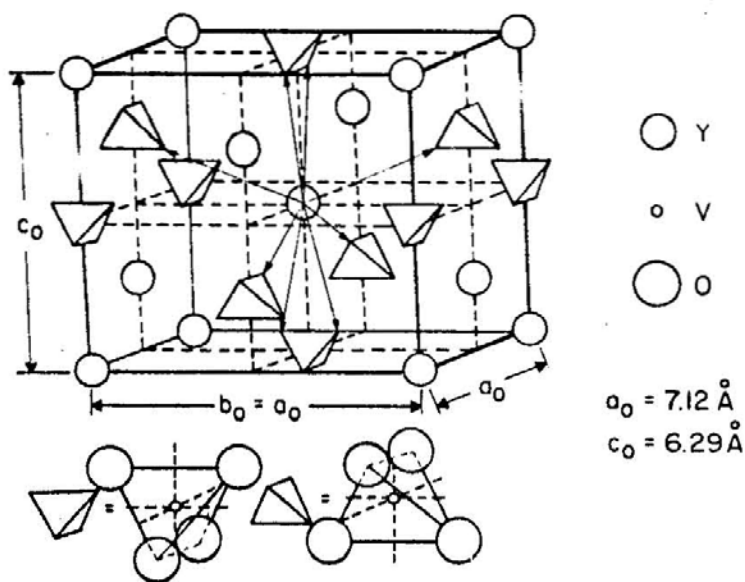


Fig. 10.3. Tetragonal unit cell of YVO₄. VO₄ arrangements are represented by schematic tetrahedra: eight arrows indicate oxygen positions around the central Y of the YO₈ polyhedron [28]

which can be best described as a triangular dodecahedron [29]. Two edges are shared with VO₄ groups and four with dodecahedra. Nevertheless, 12 (8+4) edges are unshared. The chains are joined laterally by the edge sharing YO₈ dodecahedra, causing specific cleavage characteristics in YVO₄ crystals [29].

10.5 Synthesis and Growth of Rare Earth Vanadates

The methods used in the synthesis and growth of rare earth vanadates are discussed below.

10.5.1 Zone melting

Good quality rare earth orthovanadate crystals have been prepared by the relatively inexpensive method of zone melting with dynamic immersion by means of an iridium plate heater [16,17]. The growth of rare earth vanadates by this technique is a complex combination of physicochemical incongruent evaporation and crystallization from a multicomponent Y₂O₃-V₂O₃-V₂O₅ system. The process requires a careful maintenance and control of oxygen partial pressure.

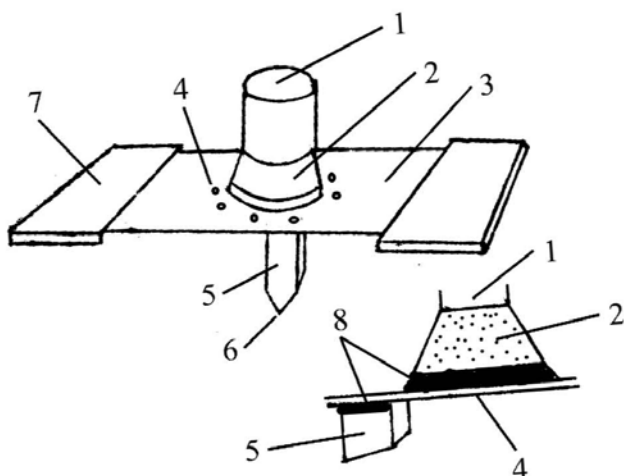


Fig. 10.4. Experimental set up for zone melting [17]: (1) polycrystalline feed rod, (2) rod section impregnated by the melt, (3) opening for melt passage, (4) iridium plate, (5) crystal, (6) seed crystal, (7) platinum leads, (8) melt

The single crystal synthesis was carried out in a universal vacuum/compression chamber (type T-935) constructed by the Kharkov Physicotechnical Institute of the Academy of Sciences of the Ukrainian SSR. A $8.0 \times 1.4 \times 0.05$ cm iridium plate was fastened to water-cooled copper leads (Fig 10.4). The chamber was first evacuated under oxygen partial pressure control followed by admission of argon to yield a total pressure equal to atmospheric pressure. Pentavalent vanadium is known to be unstable at high temperature [30,31]. So the initial composition obviously becomes enriched with V_2O_5 due to the selective volatility of vanadium oxides. The crystal develops colors immediately during and after growth varying from a light honey yellow to a dark brown. Therefore, preparation of colorless crystals evidently requires tighter control as to oxygen partial pressure, excess V_2O_5 , and geometric parameters of the molten zone, along with its rate of movement.

10.5.2 Czochralski technique

Rare earth vanadates were obtained by the Czochralski technique of pulling from the melt [32,33]. For high melting oxides, iridium crucibles are generally used to hold and directly or indirectly heat the melt. The heating arrangements are such that the central region of the surface of the melt is its coolest part. For vanadates, the melt is not stable under atmospheric conditions. Temperature in excess of 2000°C is required to keep the material molten. At these temperatures, there is a continuous evolution of oxygen from the depths of the melt. The crystals are annealed for 12 hours to remove any discoloration.

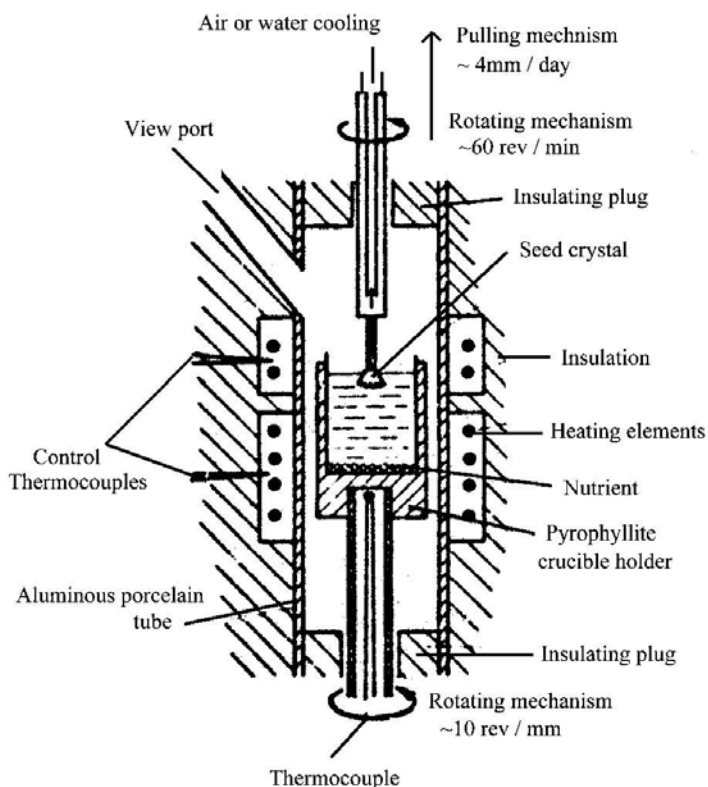


Fig. 10.5. Pulling furnace [32]

Though this method produced the layered and relatively highest quality crystals, oxygen loss and inclusion problems could not be eliminated [30,34]. The crystals grown by the conventional Cz method exhibited severe spiral growth, which retarded the continuing growth; no more than 20% of the melt was consumed at the onset of spiral growth. However, nearly 50% of the melt was consumed for the growth without a spiral mode [3]. The schematic diagram of the pulling furnace is shown in Fig. 10.5.

10.5.3 Flux growth

The flux method is popular to grow rare earth vanadates [35]. It can be defined as high temperature solution growth, which allows the growth of materials in the form of single crystals of sufficiently large size. The experiments were carried out in a specially designed crystallization chamber. The crucible-containing nutrient

Table 10.1. Starting Composition and Experimental Conditions for the Growth of Nd:RVO₄ under Flux Growth

Nutrient	Flux	Initial temp [°C]	Duration [h]	Final temp [°C]	Compound	Ref.
Y ₂ O ₃ + Nd ₂ O ₃	PbO + V ₂ O ₅ + PbF ₂	1350	20	1000	Nd:YVO ₄	[36]
Dy ₂ O ₃ + Nd ₂ O ₃	PbO + PbF ₂ + V ₂ O ₅	1350	20	950	Nd:DyVO ₄	[37]
Gd ₂ O ₃ + Nd ₂ O ₃	Bi ₂ O ₃ + V ₂ O ₅	1320	14	950	Nd:GdVO ₄	[38]
Pr ₂ O ₃ + Nd ₂ O ₃	PbO + V ₂ O ₅	1360	12	980	Nd:PrVO ₄	[39]

Cooling rate = 1°C/h

material was placed inside the crystallization chamber. The mixture was heated up to 1200°C at the rate of 300°C/h and held for 20 to 24 hours until the complete dissolution of the oxide took place. Later on, the temperature was slowly decreased at the rate of 1°C/h up to 800°C followed by a fast cooling. The crystals obtained were cleaned using hot dilute 1:5 HNO₃.

In most of the experiments, lead vanadate (Pb₂V₂O₇) was used as the flux agent rather than bismuth vanadate. Although, this method gives fairly good quality crystals, the method lacks popularity because of:

- Difficulties in maintaining the oxygen stoichiometry and controlling the loss of vanadium oxide,
- The presence of mixed phases,
- The presence of ions of the flux impurities in the crystals,
- Problems in removing flux agents.

YVO₄ melt continuously transforms into a multiphase system during the growth process, since undesired Y₈V₂O₁₇ and black YVO_{4-x} (0 < x ≤ 1) phases are formed by incongruent vanadium oxide vaporization [26].

10.5.4 Top seeded solution growth (TSSG)

Rare earth vanadate single crystals were grown using lithium meta vanadate (LiVO₃) flux, dissolved and purified in hot water. Since LiVO₃ has excellent water solubility, its dissolution in water and subsequent filtering and drying minimized impurities in TSSG. The TSSG pulling rate was approximately 0.02 mm/h.

The UV absorption edge of RVO₄ crystals grown by Cz and TSSG was compared by Erdei et al. (1997) [40]. TSSG-RVO₄ crystal grown from LiVO₃ flux has a broader optical transmittance in UV than the Cz crystal, implying that the TSSG-YVO₄ has better Y-V-O stoichiometry than the Cz crystal. Since, the crystal grown by this method is at 1800°C, appearance of the metastable phase relations, precipitates, and oxygen deficiency could not be eliminated.

Thus the rare earth vanadates obtained by flux, Cz, TSSG, zone melting belong to high temperature growth techniques and are relatively poor in crystal quality. This prompted the present authors to an alternative technique, wherein most of these problems have easily been overcome.

In spite of a very long history behind the development of the hydrothermal technique and its adoptability to modern technological requirements, still it remains as a recent technique, especially for the growth of vanadates.

10.6 Solubility Study

This is one of the most important aspects of the hydrothermal growth of crystals. Due to the lack of proper data on the type of solvents, the solubility and solvent solute interaction, the hydrothermal growth of a specific compound initially failed. Despite the large amount of literature data available, still it is a highly attractive field in hydrothermal research not only for crystal growers, but also for the corrosion scientists, hydro metallurgists, geoscientists, and so on. Unfortunately, most of the studies have been performed only at the saturated vapor pressure of the system and very few combined high-temperature high-pressure experiments have been designed to yield thermodynamical data.

The real hydrothermal solutions are different from the ideal solutions and their understanding relies upon the knowledge of the influence of the solvent in the process of dissolution and crystallization of various compounds. Obviously, as shown in most of the experiments, the type of solvent and its concentration determine the specific hydrothermal process and its important characteristics, such as the solubility of the starting materials, quantity of the phases, their composition, output of the phases, kinetics, and growth mechanism of single crystals.

The synthesis of a specific compound is carried out using different solvents on the basis of physicochemical considerations. The following conditions are adopted in selecting the most suitable mineralizers:

1. Congruence of the dissolution of the test compounds
2. A fairly sharp change in the solubility of the compounds with changing temperature or pressure
3. A specific quantitative value of the absolute solubility of the compound being crystallized
4. The formation of readily soluble mobile complexes in the solution
5. A specific redox potential of the medium ensuring the existence of ions of the required value.

Besides, the solvent should have a desired viscosity, insignificant toxicity, and very weak corrosion activity with respect to the apparatus. These factors may fulfill the requirement of the hydrothermal mineralizers in addition to determining the values of solubility of the compound under investigation.

A successful growth of any crystal relies on the availability of solubility data. In fact, the earlier workers did not attempt the hydrothermal growth of rare earth

vanadate crystals due to the lack of solubility data on these compounds. The authors [41] carried out a systematic study of the solubility of Nd:RVO₄. Several mineralizer solutions like HCl, HNO₃, HCOOH, H₂SO₄, NaOH, NaF, and NH₄Cl were tried. Since the Nd:RVO₄ compounds did not have any solubility data under hydrothermal conditions, the authors have selected the solvents on the empirical basis and found that Nd:RVO₄ shows good solubility essentially in the acidic solvents. However, HCl or HNO₃ or H₂SO₄ or HCOOH alone did not show considerable solubility. The resultant products obtained were essentially fine crystalline mass without any morphology. It is interesting to note that the use of alkaline solvent did not result in the crystallization of rare earth vanadates, but instead rare earth hydroxides, R(OH)₃, or hydrous rare earth vanadates, RVO₄·nH₂O (where R = rare earths) were formed. These results provided a stimulus for the authors to carry out the growth of M:RVO₄ (where M = Nd, Eu; R = Y, Gd) using mainly the acidic solvents. The use of a single acid solvent with a varying molarity did not substantially enhance the solubility. Therefore, attempts were made to use the mixed acid mineralizers. The acids like HCl+HNO₃, HCl+HCOOH, HNO₃+HCOOH were mixed in different molarity and ratios in order to find the most suitable mineralizer for Nd:RVO₄. The solubility measurements were carried out by the weight loss method. Here a crystal is kept in equilibrium with an appropriate solution at the desired pressure and temperature conditions for a period of time greater than that necessary to establish equilibrium. All the solubility measurements were carried out in Morey type autoclaves. The experimental temperature to study the solubility was up to 350°C. Nd:RVO₄ shows negative solubility. The enthalpy of dissolution calculated from an Arrhenius plot, log S vs. 10³/T, for Nd:YVO₄ was found to be 16.345 kJ/mole. The solubility of Nd:RVO₄ has been studied with reference to temperature, pressure, concentration of the solution, and so forth. The corresponding solubility curves are represented in Figs. 10.6–10.8. The study of the complexation process with reference to the solvent–solute interaction is of great importance in understanding the crystallization of rare earth

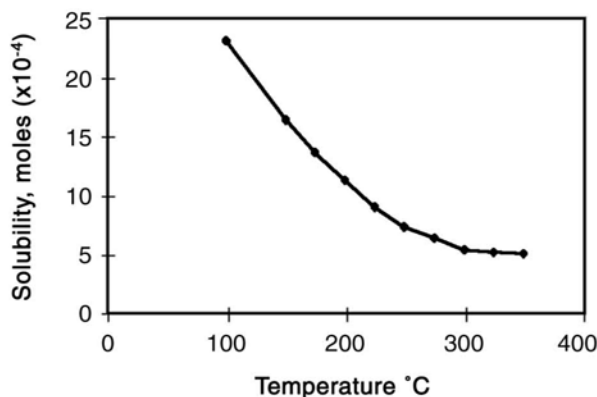


Fig. 10.6. Solubility curve of Nd:RVO₄ in 1.5 M HCl + 3.0 M HNO₃

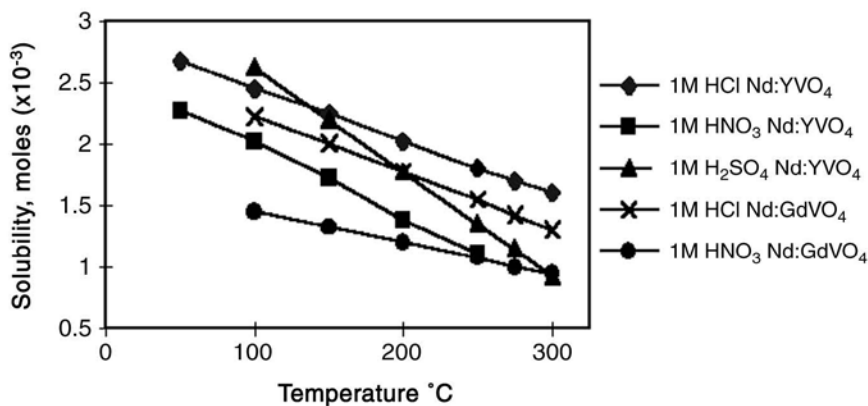


Fig. 10.7. Solubility of Nd:RVO₄ in different solvents

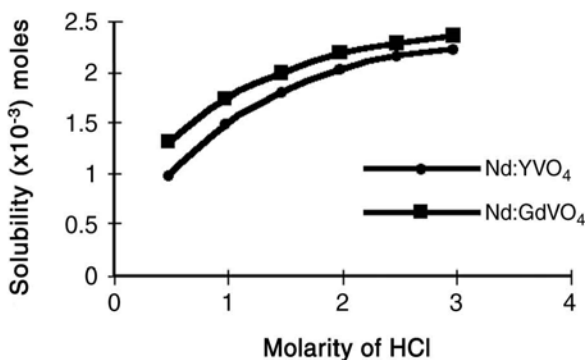


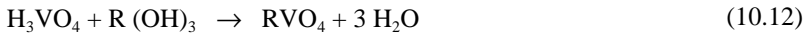
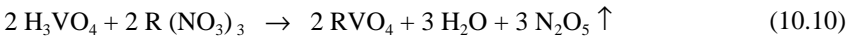
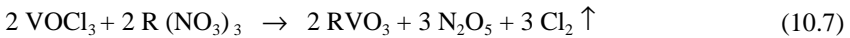
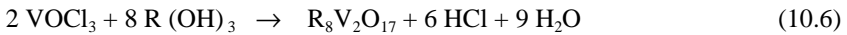
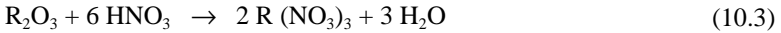
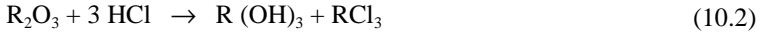
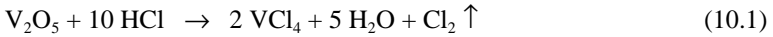
Fig. 10.8. Solubility curves for Nd:RVO₄ in HCl

vanadates. Reports on such studies are seldom found in the literature for rare earth vanadates. The authors [42] have made an attempt to study the solvent solute interaction, complexation, and related physicochemical aspects of crystallization.

In the experiments to grow Nd:RVO₄ (where R = Y, Gd) crystals, concentrated HCl and HNO₃ were used as the solvent. Con. HCl and Con. HNO₃ (1.5 M : 3.0 M) in the ratio 2:1 is the best solvent to grow Nd:YVO₄. Con. HCl and Con. HNO₃ (1.0 M : 1.0 M) in the ratio 1:2 is the best solvent for Nd:GdVO₄.

The choice of the solvent was determined by the solubility of the components of the most complex equilibrium systems. The solvent and solute are essentially linked by the coordination type and hence varied complexes of independent existence occur. In the complex systems considered here, consisting of more than four components, it is extremely difficult to precisely understand the formation of such coordination compounds and the interpretation given here is based on the compositions of the starting materials. The hard bases H₂O, OH⁻, NO₃⁻, SO₄²⁻ act in de-

termining the solubility of the final resultant stable complex [43]. The following reaction series can be proposed for the formation of Nd:RVO₄ (R = Y, Gd):



Note: Underlined formulas represent the solid precipitation

It is further presumed that the formation of a stable complex, Nd:RVO₄ at 240°C and 100 bars pressure must have undergone several intermediate stages of solvation, forming stable and unstable solvated complexes, at different temperatures (room temperature to 240°C) and pressures between 1 bar and 100 bars. It is not possible to write precisely all the intermediate stages of solvation taking place in such a complex system. Figure 10.9 is the composition diagram showing the crystallization boundaries. In general the crystallization fields for various phases are rather narrow, and a slight change in the nutrient will give rise to other phases shown in the diagram.

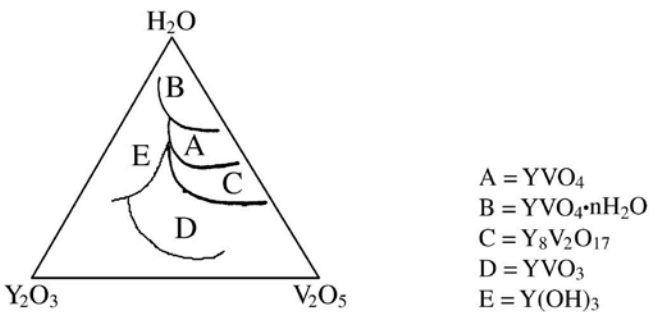


Fig. 10.9. Composition diagram for Y₂O₃ – V₂O₅ – H₂O system at T = 240°C and 60% fill

10.7 Crystal Growth

The authors [43] have obtained Nd:RVO₄ crystals under hydrothermal conditions using Morey type autoclaves provided with teflon liners of capacity 25 ml. The use of teflon liners has helped in overcoming the entry of inclusions from the autoclave material. Figure 10.10 shows the schematic diagram of the hydrothermal autoclave used in the present work. The starting materials such as R₂O₃ (where R = Y, Gd), V₂O₅, and Nd₂O₃ were taken in appropriate proportions in teflon liners. A suitable mineralizer solution of known concentration was added into the teflon liners and the entire mixture was stirred well until a homogeneous and less viscous solution was obtained. The temperature was kept constant at 240°C and the pressure generated depended on the fill (usually 50–60%). The pH of the growth medium was measured before and after each experiment and crystallization was carried out through spontaneous nucleation. Hence, an effort was made to reduce the number of nucleation centers by increasing the temperature of the crystallization reactor slowly at the rate of 10°C/h up to 100°C and beyond at the rate of 3°C/h. The nutrient materials were held at 240°C for a period of 3 days without any fluctuations in the temperature. From the fourth day onwards the temperature fluctuation to the tune of ±10°C to ±20°C was introduced periodically in order to reduce the number of nucleation centers. By this means, small crystallites, which had developed earlier, dissolve leaving only bigger crystallites to grow. The authors [8] had previously employed an oscillating temperature technique to obtain bigger crystals (3 × 0.5 × 7 mm) of yttrium orthovanadates from high temperature solution. In these experiments, it was observed that as the size of the crystal increases, the crystal quality reduces (4.2 × 4.2 × 4 mm).

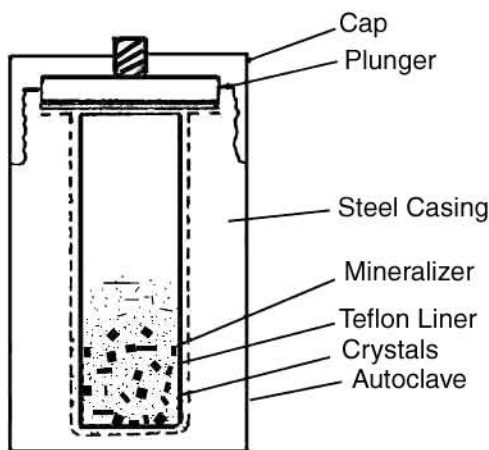


Fig. 10.10. Schematic diagram of the hydrothermal autoclave

Table 10.2. Experimental Conditions for the Growth of Nd: YVO₄ Crystals

Sl. No	Nutrient Composition	Mineralizer	P/bar	% fill	pH [i]	pH [f]	Size [mm]	Remarks
1.	Y ₂ O ₃ , V ₂ O ₅ Nd ₂ O ₃ – 5 wt% 1:2	0.75 M HCl: 1.5 M HNO ₃ 2:1	100	60	0.33	0.39	—	amorphous powder
2.	Y ₂ O ₃ , V ₂ O ₅ Nd ₂ O ₃ – 5 wt% 1:2	0.75 M HCl: 0.75 M HNO ₃ 2:1	100	60	0.30	4.70	0.1–0.25	tiny plate-like thin crystals
3.	Y ₂ O ₃ , V ₂ O ₅ Nd ₂ O ₃ – 10 wt% 1:2	1.0 M HCl: 2.0 M HNO ₃ 2:1	100	60	0.25	5.20	0.5–1.0	bulk crystals, plate-like, hexagonal
4.	Y ₂ O ₃ , V ₂ O ₅ Nd ₂ O ₃ – 10 wt% 1:2	1.5 M HCl: 3.0 M HNO ₃ 2:1	100	60	0.18	4.12	1.0–1.5	bulk crystals, plate-like, rhombohedral, thicker crystals
5.	Y ₂ O ₃ , V ₂ O ₅ Nd ₂ O ₃ – 5 wt% 1:2	1.5 M HCl: 3.0 M HNO ₃ 2:1	130	80	0.13	4.09	1.5–2.5	well developed, plate-like, rhombohedral, thicker crystals
6.	Y ₂ O ₃ , V ₂ O ₅ Nd ₂ O ₃ – 10 wt% 1:2	2 M HCl: 4 M HNO ₃ 2:1	100	60	0.08	3.02	2.5–3.0	irregular shaped thicker crystals
7.	Y ₂ O ₃ , V ₂ O ₅ Nd ₂ O ₃ – 5 wt% 1:2	1.5 M HCl: 3.0 M HNO ₃ 2:1	123	75	0.05	2.56	1.0-2.0	light brown, thick, not well developed, crystals
8.	Y ₂ O ₃ , V ₂ O ₅ Nd ₂ O ₃ – 5 wt% 1:2	1.0 M HCl: 1.0 M HNO ₃ 2:1	115	70	0.03	1.56	0.5–1.0	tiny irregular, light brown crystals
9.	Y ₂ O ₃ , V ₂ O ₅ Nd ₂ O ₃ – 5 wt% 1:2	0.5 M HCl: 1.0 M HNO ₃ 2:1	115	70	0.01	0.46	—	crystalline powder

T = 240°C, t(duration) = 8 days, pH (i) = initial, pH (f) = final

The rare earth concentrations are in the range 3–10 wt%. After the experimental run, the autoclaves were quenched initially using an air jet and then water, and the products were washed thoroughly in distilled water and ultrasonic cleaner to separate single crystals from the solution. The products obtained were well-faceted single crystals of 0.1 to 4 mm size. Tables 10.2 and 10.3 give experimental conditions for the growth of Nd:RVO₄ crystals.

Table 10.3. Experimental Conditions for the Growth of Nd: GdVO₄ Crystals

Sl. No	Nutrient Composition	Mineralizer	t [days]	pH [i]	pH [f]	Size [mm]	Remarks
1.	Gd ₂ O ₃ , V ₂ O ₅ Nd ₂ O ₃ – 5 wt% 1:2	1.0 M HCl: 1.0 M HNO ₃ 1:1	8	0.01	0.50	—	amorphous powder
2.	Gd ₂ O ₃ , V ₂ O ₅ Nd ₂ O ₃ – 5 wt% 1:2	1.5 M HCl: 1.5 M HNO ₃ 2:1	8	0.03	1.42	—	very fine crystalline powder
3	Gd ₂ O ₃ , V ₂ O ₅ Nd ₂ O ₃ – 5 wt% 1:2	1.0 M HCl: 2.0 M HNO ₃ 1:2	6	0.05	3.02	0.5–1.0	bulk plate-like, hexagonal crystals
4.	Gd ₂ O ₃ , V ₂ O ₅ Nd ₂ O ₃ – 5 wt% 1:2	1.5 M HCl: 1.5 M HNO ₃ 1:2	8	0.14	3.15	1.0–1.5	bulk crystals, small plate-like, rhombohedral
5.	Gd ₂ O ₃ , V ₂ O ₅ Nd ₂ O ₃ – 5 wt% 1:2	0.75 M HCl: 1.5 M HNO ₃ 1:2	6	0.23	3.35	1.5–2.5	bulk crystals, plate-like, hexagonal
6.	Gd ₂ O ₃ , V ₂ O ₅ Nd ₂ O ₃ – 5 wt% 1:2	1.0 M HCl: 1.0 M HNO ₃ 1:2	8	0.30	3.73	2.5–3.0	plate-like, rhombohedral, thick crystals
7.	Gd ₂ O ₃ , V ₂ O ₅ Nd ₂ O ₃ – 5 wt% 1:2	0.75 M HCl: 0.75 M HNO ₃ 1:2	8	0.38	3.90	1.0-2.0	bulk plate-like, rhombohedral
8.	Gd ₂ O ₃ , V ₂ O ₅ Nd ₂ O ₃ – 5 wt% 1:2	1.5 M HCl: 0.75 M HNO ₃ 1:2	8	0.46	2.90	0.5–1.0	bulk plate-like, rhombohedral
9.	Gd ₂ O ₃ , V ₂ O ₅ Nd ₂ O ₃ – 5 wt% 1:2	0.75 M HCl: 0.75 M HNO ₃ 1:2	8	0.50	1.90	—	fine crystalline powder

T = 240°C, P = 100 bars, pH (i) = initial, pH (f) = final

Here, the nutrient materials were taken directly in the teflon liners. The size of the crystals obtained was not more than 3 mm. R₂O₃+V₂O₅+Nd₂O₃ interact first with each other in the presence of a mineralizer to form Nd:YVO₄. Here structural units/growth units are formed first, followed by the further interaction of these growth units with the mineralizer to form bulk growth units or single crystals.

Table 10.4 gives experimental conditions for the growth of Nd:YVO₄ crystals using sintered nutrient. The starting materials such as Y₂O₃, V₂O₅, Nd₂O₃ were taken in an appropriate ratio (with a slight surplus of V₂O₅) and sintered at 900°C for 24 hours in a nitrogen atmosphere. In such a nutrient the Nd:YVO₄ structural

Table 10.4. Experimental Conditions for the Growth of Nd: YVO₄ Crystals Using Sintered Nutrient

Sl. No	Nutrient Composition	Mineralizer	P/bar	% fill	pH [i]	pH [f]	Size [mm]	Remarks
1.	Y ₂ O ₃ , V ₂ O ₅ Nd ₂ O ₃ – 5 wt% 1:2.5 H ₂ O ₂ 1 ml	0.5 M HCl: 1.0 M HNO ₃ 2:1	90	55	1.1	1.4	—	amorphous powder
2.	Y ₂ O ₃ , V ₂ O ₅ Nd ₂ O ₃ – 5 wt% 1:2.5 H ₂ O ₂ 1 ml	1.0 M HCl: 1.0 M HNO ₃ 2:1	100	60	0.9	2.01	0.25–0.5	small, light brown, cubic crystals
3.	Y ₂ O ₃ , V ₂ O ₅ Nd ₂ O ₃ – 10 wt% 1:2.5 H ₂ O ₂ 1 ml	1.5 M HCl: 3.0 M HNO ₃ 2:1	115	70	0.58	2.78	1.0–1.5	bulk crystals, small hexagonal, thick crystals
4.	Y ₂ O ₃ , V ₂ O ₅ Nd ₂ O ₃ – 5 wt% 1:2.5 H ₂ O ₂ 1 ml	1.5 M HCl: 3.0 M HNO ₃ 2:1	115	70	0.42	3.21	1.5–2.0	light brown, well developed, hexagonal, thick crystals
5.	Y ₂ O ₃ , V ₂ O ₅ Nd ₂ O ₃ – 5 wt% 1:2.5 H ₂ O ₂ 1 ml	1.5 M HCl: 3.0 M HNO ₃ 2:1	115	70	0.31	3.83	2.0–2.5	small plate-like, rhombohedral, thicker crystals
6.	Y ₂ O ₃ , V ₂ O ₅ Nd ₂ O ₃ – 5 wt% 1:2.5 H ₂ O ₂ 1 ml	1.5 M HCl: 3.0 M HNO ₃ 2:1	115	70	0.15	4.10	2.5–3.5	well developed, plate-like, rhombohedral, light brown, thick crystals
7.	Y ₂ O ₃ , V ₂ O ₅ Nd ₂ O ₃ – 5 wt% 1:2.5 H ₂ O ₂ 1 ml	1.5 M HCl: 1.5 M HNO ₃ 2:1	115	70	0.04	4.73	3.0–4.2	light brown, thicker crystals, plate-like, rhombohedral

T = 240°C, t (duration) = 8 days, pH (i) = initial, pH (f) = final

units pre-exist. During the crystal growth process under hydrothermal conditions, these structural units directly interact with the mineralizer solution at a higher growth rate. This facilitated the present authors to obtain fairly large size single crystals (4.2 × 4.2 × 4 mm) through a spontaneous nucleation process. If these large crystals are used as seed crystals, we can grow large crystals (size up to 1 cm) of rare earth vanadates under mild hydrothermal conditions. Such work would facilitate the growth of large high quality single crystals under milder hydrothermal conditions without going into the high temperature solution or melt techniques.

10.8 Morphology

The study of morphology is an important aspect in crystal growth, particularly in crystals carrying device potential. It also helps to understand the defects in crystals and their growth mechanism. The defects are directly revealed by the micro- and macro-morphology of crystals. The slowest growing faces having the lowest surface energy determine the habit of a crystal. A number of factors such as degree of supersaturation, type of solvent, pH of the mineralizer, and so forth affect the habit of a crystal.

The morphological analysis of these Nd:RVO₄ crystals show platelike, pseudocubic, or hexagonal habits. The size of the crystals varies from 0.1 to 4.2 mm from a typical experimental run of 8 days duration. The crystal faces are very well developed with highly polished surfaces in most of the cases and vitreous luster. The morphological forms of Nd:RVO₄ mainly depend upon the % fill, molarity of the mineralizer, and pH of the media (Figs. 10.11 to 10.15).

Figures 10.11 and 10.12 clearly show how the growth rate changes with pH of the growth media. As pH increases, the crystal morphology also varies. As evident from Table 10.5, plate-like rhombohedral Nd:YVO₄ crystals were obtained in the pH range 0.15 to 0.30 and Nd:GdVO₄ in the range 0.25 to 0.40. As pH increases, the morphology and also the growth rate of the crystals decline.

Figures 10.13 and 10.14 show the variation of morphology with pressure. As the pressure increases, morphology of rare earth vanadates changes from hexagonal plate-like to rhombohedral shape and also the growth rate increases. As the pressure increases beyond 125 bars, irregular shaped crystals are obtained.

Figure 10.15 shows morphology variation with pH for Nd:YVO₄ crystals obtained using sintered nutrient. The growth rate gradually decreases as the pH of the medium increases. The growth rate increases as the reaction involves direct interaction of Nd:YVO₄ with mineralizer. Figure 10.16a shows the characteristic photograph of Nd:YVO₄. When the initial pH is 0.25 in 1 M HCl + 2 M HNO₃ (2:1) solution, Nd:YVO₄ crystallizes as hexagonal platelets. Crystals are honey yellow colored with a vitreous surface. Figure 10.16b shows the characteristic

Table 10.5. Morphology of Rare Earth Orthovanadates

Composition	Initial pH	Common faces	Growth rate
Nd:YVO ₄	0.15 to 0.30	(001) (010) (110)	$\gamma(110) > \gamma(010)$
Nd:YVO ₄	0.13 to 0.08	(001) (100) (010)	$\gamma(100) > \gamma(010)$
Nd:GdVO ₄	0.05 to 0.20	(100) (010) (011)	$\gamma(011) > \gamma(010)$
Nd:GdVO ₄	0.25 to 0.40	(100) (001) (010)	$\gamma(001) > \gamma(010)$

T = 240°C, P = 100 bars

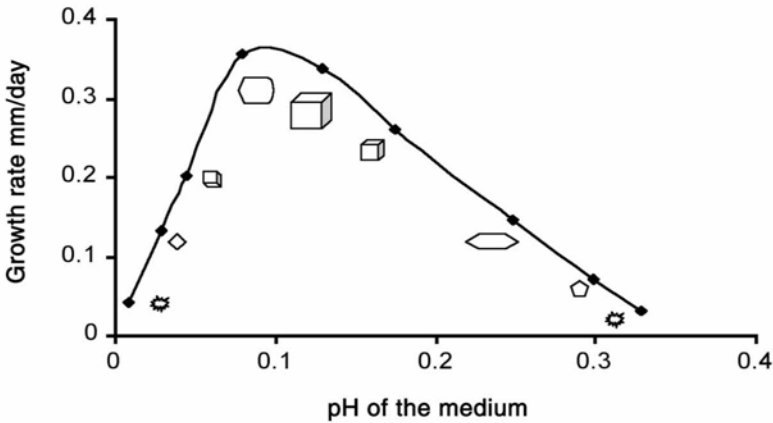


Fig. 10.11. Dependence of growth rate and pH of the media for Nd:YVO₄ 1.5 M HCl + 3.0 M HNO₃

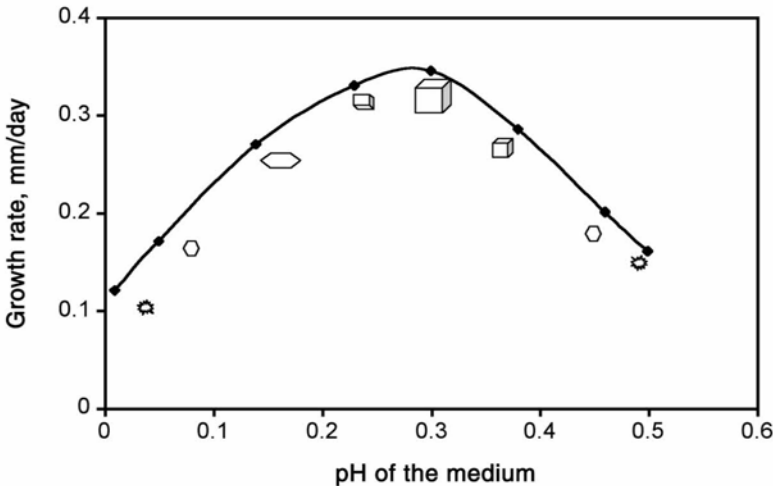


Fig. 10.12. Dependence of growth rate and pH of the growth media for Nd:GdVO₄ 1.0 M HCl + 1.0 M HNO₃

photograph of Nd:GdVO₄. When the initial pH is 0.05 in 1 M HCl + 2 M HNO₃ (1:2) solution, Nd:GdVO₄ crystallizes as hexagonal platelets. Crystals are honey yellow colored with a vitreous surface. When the initial pH is 0.13 in 1.5 M HCl + 3 M HNO₃ (2:1) solution, Nd:YVO₄ crystallizes as thick rhombohedral crystals. Crystals are honey yellow colored with a vitreous surface. The well-developed faces are: (100), (010), (001) (Fig.10.16c). The schematic diagrams of the crystals are shown in Fig. 10.17.

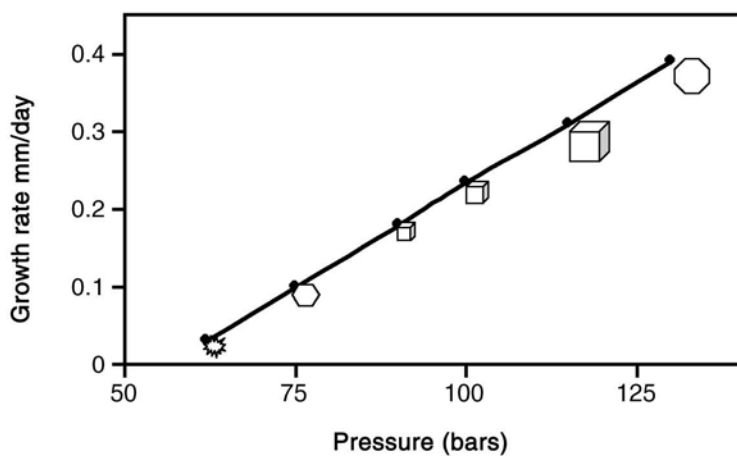


Fig. 10.13. Morphology variation with pressure for Nd:YVO₄ crystals

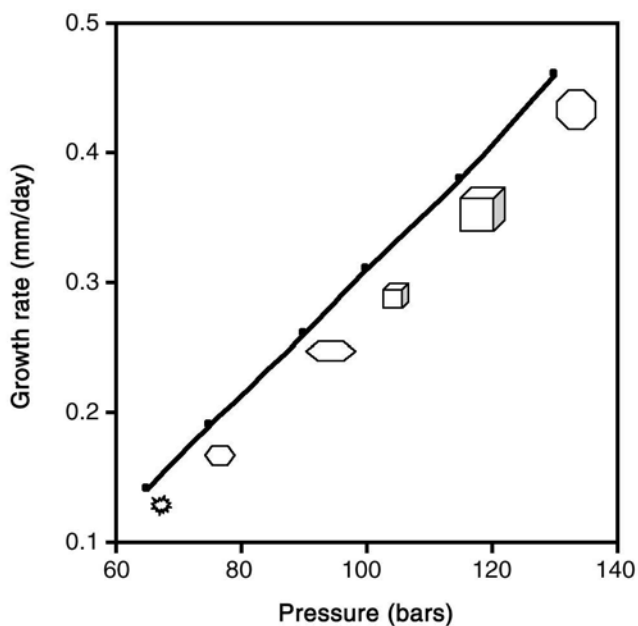


Fig. 10.14. Morphology variation with pressure for Nd:GdVO₄ crystals

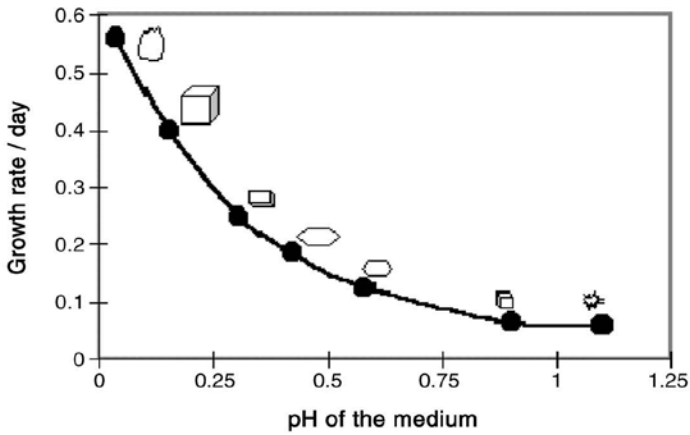


Fig. 10.15. Morphology variation with pH for Nd:YVO₄ crystals obtained from sintered nutrient

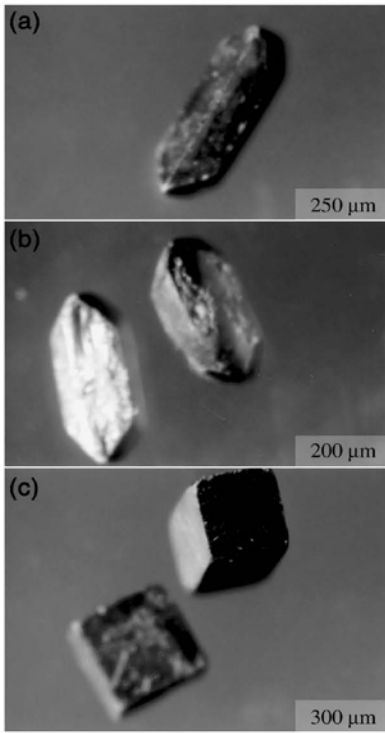


Fig. 10.16(a-c). Characteristic photographs of rare earth vanadate crystals obtained under mild hydrothermal conditions

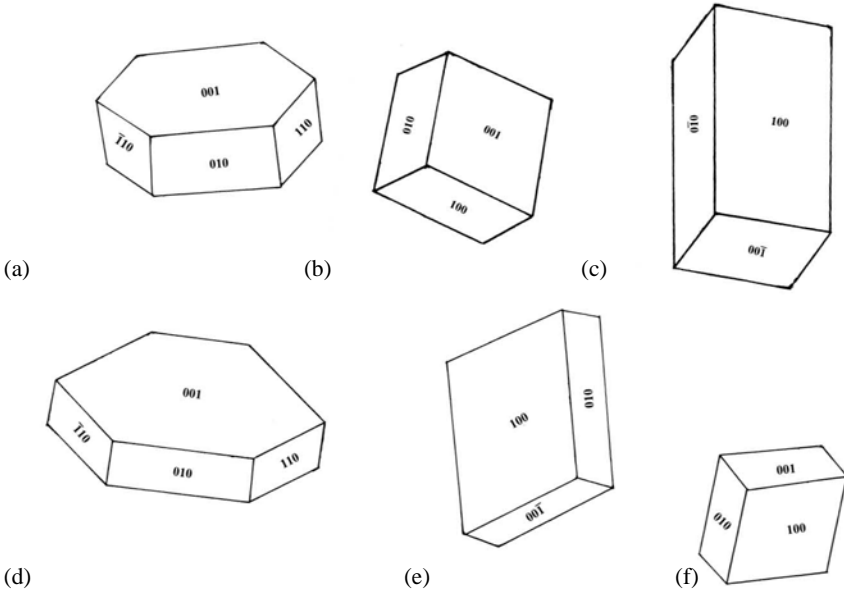


Fig. 10.17. Schematic diagrams of Nd:RVO₄ crystals

10.8.1 Surface morphology

Although, there are several reports on the growth and characterization of Nd:RVO₄ crystals, there are hardly any reports on the defect studies like surface morphology and micro-morphology of as-grown surfaces. The as-grown surfaces of Nd:RVO₄ crystals exhibit thick kinked layers; arrays of parallel layers on certain faces, isolated etch pits and etch pitch clusters. Crystals obtained from both slowly cooled and suddenly quenched autoclaves showed these characteristic features. However, as expected, the crystals obtained from quenched autoclaves showed less dissolution morphology in comparison with those from slowly cooled autoclaves. Figure 10.18(a-d) shows the surface morphology of slowly cooled rare earth vanadates. It is well known that rare earth vanadates show negative temperature coefficient of solubility. During cooling the crystals undergo dissolution and hence dissolution features are observed in most of the rare earth vanadates. Dissolution is seen more in the center on the surface of the (001) face than at the edge. The middle void surface corresponds to the dissolution pit (Fig. 10.18a). Consequently, the rare earth vanadates do not require further etching to study the surface morphology. The study of the surface morphology clearly indicated the requirement of rapid cooling of autoclaves after the experimental run, moderate supersaturation and a slow rate of growth to obtain high quality single crystals of rare earth vanadates.

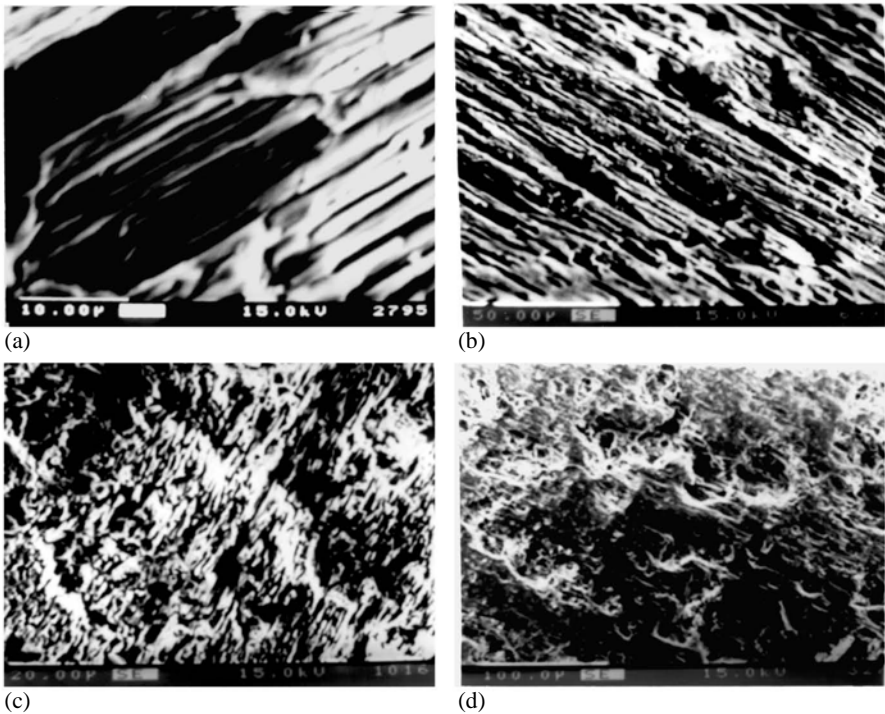


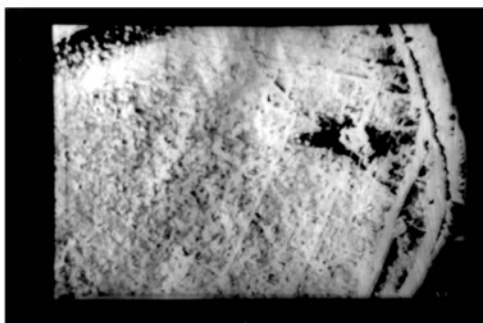
Fig. 10.18(a-d). Surface dissolution features in rare earth orthovanadate crystals

Crystals obtained from quenched autoclaves showed less dissolution morphology in comparison with those from slowly cooled autoclaves. Figure 10.19(a-c) shows the morphology of the crystals obtained from rapid quenching of autoclaves.

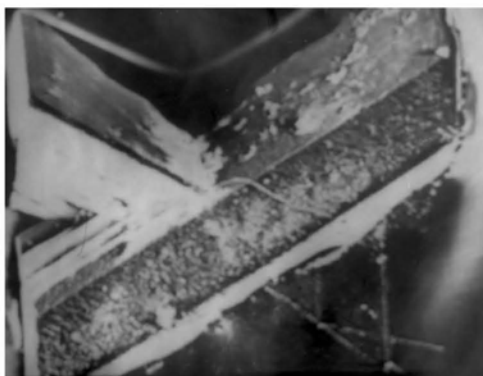
The surface morphology of the as-grown surfaces of rare earth vanadates consists of striations, micro steps, growth layers, block structures, and so forth. The surface morphology varies with pH, pressure, and molarity of the mineralizer. Figure 10.19a shows the striations at the edge. This surface morphology was obtained when the pH of the media was 0.05 and pressure 100 bars in 8 days of experimental duration. Figure 10.19b shows micro steps on the (001) surface. This morphology was obtained when the concentration of the mineralizer was 1.5 M HCl + 3 M HNO₃, pressure 130 bars, pH = 0.13 in an experimental duration of 10 days. Figure 10.19c shows twinning morphology. This was observed when the concentration of the mineralizer was low (0.75 M HCl + 0.75 M HNO₃ in the ratio 1:2), pressure 100 bars, pH = 0.05 in an experimental duration of 10 days. The temperature in all the experiments was maintained at 240°C.



(a)



(b)



(c)

Fig. 10.19(a-c). Surface morphology of rare earth vanadates after a rapid quenching of autoclaves

10.9 Characterization

10.9.1 XRD and IR studies

The authors [44] have carried out X-ray and infrared studies. The cell parameters were calculated for the representative samples and depicted in Table 10.6. These values are in correspondence with the reported values [45,46].

The infrared spectrum of rare earth vanadates shows more fineness and multiple splitting in the region of lower wave numbers. The most interesting feature of this spectrum is the absence of $(\text{OH})^-$ bands in the region $3000\text{--}3500\text{ cm}^{-1}$. This shows that water is not incorporated in the interstices of vanadates grown by hydrothermal technique in spite of the mild hydrothermal experimental conditions. In the range $950\text{--}1050\text{ cm}^{-1}$ and $400\text{--}600\text{ cm}^{-1}$, the compound shows 4 sharp absorption bands, which were formed by $[\text{VO}_4]^{3-}$ [47].

Compound	Coordination	$\gamma(\text{A}_1)$	$\gamma(\text{E})$	$\gamma(\text{F}_2)$	$\gamma(\text{F}_2)$
vanadate	$[\text{VO}_4]^{3-}$	870	345	825	480

Table 10.6. Cell Parameters for Rare Earth Vanadates Obtained Under Hydrothermal Conditions

Compound	a, Å	c, Å	V, Å ³
YVO ₄	7.118(3)	6.289(8)	318.64
Nd:YVO ₄ (3% Nd)	7.127(4)	6.297(5)	319.85
GdVO ₄	7.214(2)	6.348(4)	330.36
Nd:GdVO ₄ (3% Nd)	7.223(7)	6.359(7)	331.76

10.9.2 Laser spectroscopy

Laser spectroscopic experiments at $1.06\text{ }\mu\text{m}$ were performed on a 2 mm thick crystal sample. The crystal was oriented with the *c*-axis parallel to the polarization direction of the diode laser. Pump source was a SDL-2482 diode with an emitting area of $500\text{ }\mu\text{m} \times 1\text{ }\mu\text{m}$ and a CW power of 2.3 W at 808.4 nm. The pump beam was first collimated in one direction using a collimating optic with 5 mm focal length. The higher slope efficiency and the lower pump threshold of Nd:GdVO₄ result in an output power surplus of 100 mW at an absorbed pump power of 1500 mW [23]. Figure 10.20 shows an input-output curve of Nd:GdVO₄ and for comparison, a measurement with an identical Nd:YAG setup is shown (slope efficiency 53%).

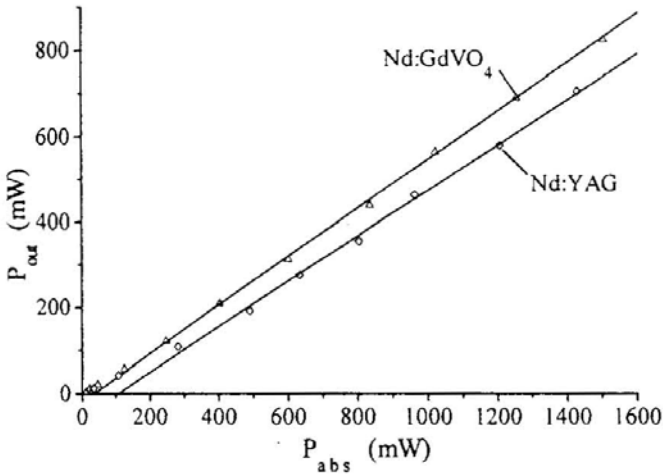


Fig. 10.20. Diode-laser pumped lasing of Nd:GdVO₄ and Nd:YAG at 1.06 μm under identical conditions [23]

The substitution of Gd for Y in these various crystals leaves the crystal field felt by the Nd ion largely unchanged and does not alter greatly the spectra that arise from doping of these crystals with Nd. However, as Gd³⁺ is closer in size to Nd³⁺ than Y³⁺, a larger concentration of Nd can be incorporated into the crystals, thereby enhancing the absorption coefficient [23]. Since this leads to an increased pumping efficiency, Gd-based crystals are good candidates for future use in miniaturized Nd lasers.

For Nd:YVO₄ and Nd:GdVO₄, accurate stark levels for ⁴I_J ($J = 9/2, 11/2, 13/2, 15/2$) and ⁴F_{3/2} multiplets have been determined from the spectra [48]. Representative spectra are shown in Fig. 10.21. The lines shown in these spectra arise from the ⁴I_{9/2} \rightarrow ⁴I_{13/2} transitions. The spectra are nearly identical between the Y and Gd counterparts with respect to peak position, relative strengths, and polarization dependence.

Table 10.7 shows the norms of the parameters for the Gd-based crystals, and are slightly less than those for the Y-based crystals. This suggests that the Nd ions experience a weaker average crystal field in the Gd-based crystals, and is consistent with the larger radius of Gd³⁺ ion compared to the Y³⁺ ion [49], which is expected to result in an increase in the lattice constants for the Gd-based crystals. For the vanadates, the lattice constants of GdVO₄ are larger than those of YVO₄ [50]. Thus, due to the increased distance between the Nd impurity and the neighboring host atoms, the strength of the crystal field is reduced, giving rise to (slightly) smaller crystal field parameters.

The parameters β and γ give energies of the t_2 and t_1 triplets respectively, resulting from the tetrahedral field B (t_2) and C (t_1); and Y (t_2 - t_1 mixing) results from the tetragonal distortion.

The absorption coefficient of 1% Nd:GdVO₄ was 59.3 cm⁻¹, twice that of 1% Nd:YVO₄, and approximately the same as that of 3% Nd:YVO₄ [3]. Slope efficiency, threshold pump power and output power of Nd:GdVO₄ exceeded those of Nd:YVO₄.

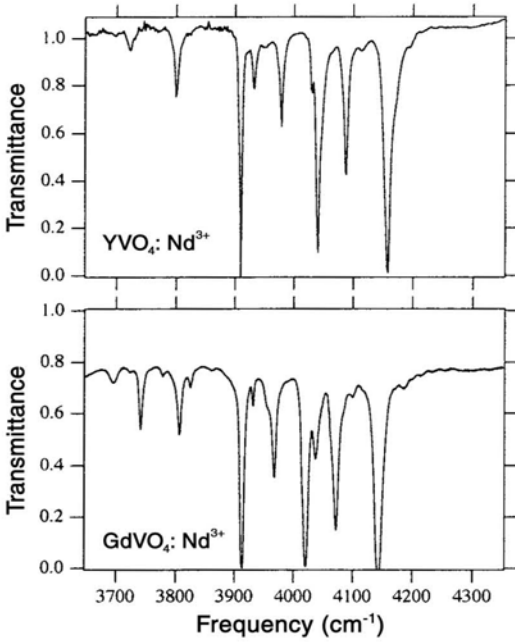


Fig. 10.21. Transmittance spectra for Nd- doped YVO₄ and GdVO₄ showing ⁴I_{9/2} → ⁴I_{13/2} transitions [48]

Table 10.7. Crystal Field Parameters for the Nd Impurity (values are in Cm⁻¹)

Parameter	YVO ₄	GdVO ₄
beta	190.6	157.3
gamma	-59.6	-37.6
B	-386.2	-384.5
C	30.4	76.2
Y	-99	-97.5
E(11/2)	1866	1866
E(13/2)	3836	3836
E(15/2)	5872	5872

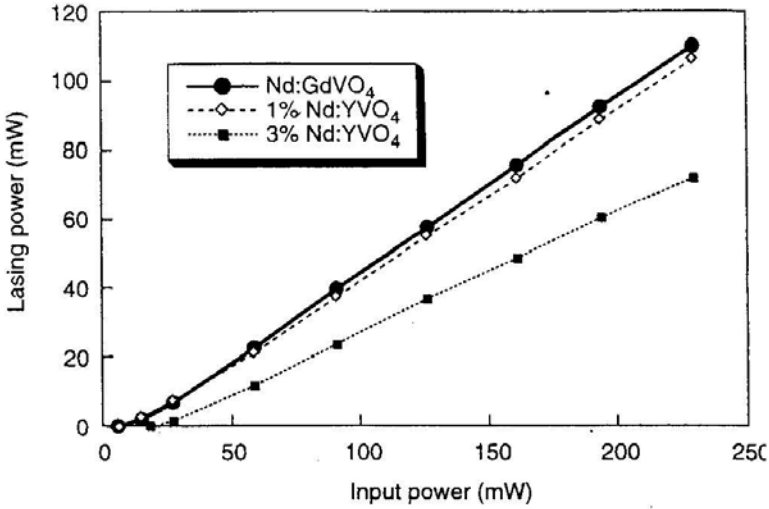


Fig. 10.22. Input–output CW characteristics of Nd:GdVO₄ compared with Nd:YVO₄ [3]

10.9.3 Absorption measurements

The uniaxial crystal Nd:GdVO₄ shows strong polarization dependent absorption transitions due to the anisotropic crystal field [23]. At 808.4 nm, the peak absorption cross section was $5.2 \times 10^{-19} \text{ cm}^2$. For σ -polarization the absorption coefficient is only 17 cm^{-1} . The absorption spectrum as a function of wavelength for both polarizations is shown in Fig. 10.23. The half width of the absorption at 808.4 nm is 1.6 nm. For comparison with Nd:YAG and Nd:YVO₄ some data are listed in Table 10.8 for active ion densities of $1.5 \times 10^{20} \text{ cm}^{-3}$.

At the same neodymium concentration, the absorption coefficient of Nd:GdVO₄ is seven times higher and the transition line is 80% broader in comparison with Nd:YAG.

Table 10.8. Comparison of Absorption in YAG, YVO₄, and GdVO₄ for Diode-laser Pumping near 808 nm

Crystal	Crystal ion density [10 ²⁰ cm ⁻³]	Polarization direction	Absorption Coefficient [cm ⁻¹]	Eff. Absorption cross section [10 ⁻¹⁹ Cm ²]	Half width [nm]
1.1% Nd:YAG	1.5	Unpolarized	11	0.7	0.9
1% Nd:YVO ₄ [51]	1.5	E c	40	2.7	2
1.2% Nd:GdVO ₄	1.5	E c	78	5.2	1.6

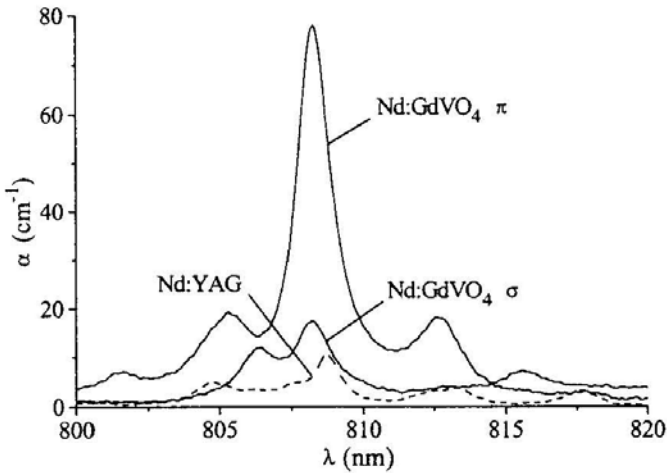


Fig. 10.23. Absorption spectra from the ground state ${}^4I_{3/2}$ into the ${}^4F_{5/2}$ multiplet for Nd:GdVO₄ in π - and σ -polarization [23]

10.10 Summary

The hydrothermal growth of rare earth vanadates has several advantages. Although, the rare earth vanadates have very high melting points ($> 1800^\circ\text{C}$) and very low solubility, these crystals could be obtained under mild hydrothermal conditions ($T = 240^\circ\text{C}$, $P \sim 100$ bars). One of the major problems encountered in the growth of rare earth vanadates is the presence of oxygen imperfections (color centers and inclusions) introduced during the crystal growth processes. Also a certain amount of vanadium oxide vaporizes incongruently, causing changes in Y/V ratio and oxygen stoichiometry in the melt. Further, vanadium is highly corrosive at high temperature. Adoption of the hydrothermal technique could eliminate all these problems. We have studied the ternary system $\text{Y}_2\text{O}_3 - \text{V}_2\text{O}_5 - \text{H}_2\text{O}$ under hydrothermal conditions at $T = 240^\circ\text{C}$, with 60% fill, and identified the crystallization field for the RVO₄ crystals. The problems encountered by melt and flux techniques have been completely eliminated by the authors by using hydrothermal technique. A systematic study of the growth rate and morphology has been carried out with respect to the type of mineralizer, % fill, pH of the growth media, and the nutrient type. Rare earth vanadates usually exhibit pseudo-cubic, rhombohedral, and prismatic habits, and the authors have succeeded in introducing the hexagonal and rectangular plate-like habit through careful controlling of the growth parameters. Such an *in situ* fabrication of the morphology is highly useful for device applications, which do not need further cutting, polishing, and so forth. Although spontaneous nucleation was used for the growth of these rare earth vanadates, a higher growth rate was accomplished to obtain large size single crystals

of $4.3 \times 4.3 \times 2$ mm in an experimental run of 8 days. The use of these spontaneously grown large crystals as seeds would facilitate the growth of bulk single crystals of rare earth vanadates up to 1 cm size in about 8 to 10 days. The infrared spectroscopic studies did not show the presence of any hydroxyl molecules in these crystals in spite of the mild hydrothermal growth conditions adopted. The laser spectroscopic properties of these crystals are found to be highly encouraging.

Acknowledgments

The authors wish to acknowledge the financial support of the Dept. of Atomic Energy, Government of India, under the National Laser Programme. Also, we wish to acknowledge Dr. B. Basavalingu, Mr. B.V. Suresh Kumar and Mr. R. Dinesh for their help in the preparation of this manuscript.

References

1. Zhang HJ, Meng XL, Zhu L, Zhang HZ, Wang P, Dawes J, Wang CQ, Chow YT (1998) *Cryst Res Technol* 33:801–806
2. Chakoumakos BC, Aabraham MM, Boatner LA (1994) *J Solid State Chem* 109
3. Shimamura K, Uda S, Kochurikhin VV, Taniuchi T, Fukuda T (1996) *Jpn J Appl Phys* 35:1832–1835
4. Prasad M, Pandit AK, Ansari TH, Singh RA, Wanklyn BM (1989) *Phys Lett A1* 38:61
5. Maunders EA, Deshaser LG (1971) *J Opt Soc* 61:684
6. Rubin JJ, Utiert LG (1966) *J Appl Phys* 37(7):2920
7. Bagdasarov KhS, Karylov VS, Popov VI (1972) *Nauka, Leningrad* 123
8. Hintzman W, Muller-Vogt G (1969) *J Crystal Growth* 5:274–278
9. Terado Y, Shimamura K, Kochurikhin VV, Barashov LV, Ivanov MA, Fukuda T (1996) *J Crystal Growth* 167:369–372
10. Levin FM (1967) *J Am Ceram Soc* 50:381
11. Van Uitert LG, Linares RC, Soden RR, Ballman AA (1962) *J Chem Phys* 36:702
12. Dess HM, Bolin SR (1967) *Trans Mat Soc AMIE* 239:359
13. Mcknight HG, Rothrock LR (1973) Technical Report No ECOM 0022f. US Army contract No DAAB 07-72-C-0022, April
14. Drafall LE, Belt RF (1978) Technical Report DELNV-TR-76-0908-F. US Army Electronics Command, Fort Monmouth, NJ, Sept
15. Popov VI, Bagdasarov KhS, Mokhosoev IV, Mokhosoev MV (1969) *Sov Phys Cryst* 13:974
16. Muto K, Awazu K (1969) *Jpn J Appl Phys* 8:1360
17. Udalov YuP, Aappen ZS (1982) *Izv Akad Nauk SSSR, Neorg Mater* 118:1349
18. Erdei S, Ainger FW (1993) *J Crystal Growth* 128:1025–1030
19. Nestor OH (1991) Final Technical Report, PP NASI NASA. Jet Propulsion Laboratory, Pasadena, NAS 7–1127, Oct
20. Broch Z (1932) *Z Physik Chem B* 20:345

21. Ostroumov VG, Shcherbakov IA, Zagumennyi AI (1993) OSA Proceedings on Advanced Solid State Lasers, Pinto A, Tso Yee Fan (eds) Vol 15
22. Zagumennyi AI, Ostroumov VG, Shcherbakov IA, Jensen T, Meyn JP, Huber G (1992) *Sov J Quantum Electronics* 22:1071
23. Jensen T, Ostroumov VG, Meyn JP, Huber G, Zagumennyi AI, Shcherbakov IA (1994) *Appl Phys B* 58:373
24. Studenikin PA, Zagumennyi AI, Zavartsev YuD, Popov PA, Shcherbakov IA (1995) *Quantum Electron* 25:1162
25. Chai BHT, Loutts G, Lefaucheur J, Zagumennyi AI (1994) in Fan TY, Chai BHT (eds) OSA Proceedings on Advanced Solid State Lasers. Optical Society of America, Washington, DC, 20:41
26. Erdei S (1993) *J Crystal Growth* 134:1–13
27. Erdei S, Jin BM, Ainger FW, Keszei B, Vandlik J, Veges AS (1997) *J Crystal Growth* 172:466–472
28. Jasiolek SG, Dabkouska HA (1986) *J Crystal Growth* 79:534–541
29. Hoad JL, Silverton JV (1963) *Inorg Chem* 2:235
30. Chow K, Macknight HC (1973) *Mater Res Bull* 8(12):1343
31. Milan EF (1929) *J Phys Chem* 33(4):498
32. Nassau K, Van Uitert LG (1960) *J Appl Phys* 31:1508
33. Rubin JJ, Thomas RA (1965) *J Am Ceram Soc* 48:100
34. Morrison AD (1973) *J Mat Sci* 8:1666
35. Byrappa K, Kulkarni AB, Gopalakrishna GS (1986) *J Crystal Growth* 5:347
36. Wanklyn BM (1981) *J Crystal Growth* 54:610–614
37. Wanklyn BM (1977) *J Crystal Growth* 37:334–342
38. Garton G, Smith SH, Wanklyn BM (1972) *J Crystal Growth* 13/14:588–592
39. Dabkowski A, Dabkowska H, Jasiolek G (1985) *J Less Common Metals* 110:255–257
40. Erdei S, Jin BM, Ainger FW (1997) *J Crystal Growth* 174:328–330
41. Byrappa K, Nirmala B (1999) *Ind J Phys* 73A(5):621–632
42. K. Byrappa (1992) *Ind J Phys* 66A(3):233
43. Byrappa K, Nirmala B, Yoshimura M (1999) *Materials Science Forum (Switzerland)* 506:315
44. Byrappa K, Nirmala B, Lokanatha Rai KM, Rao RV, *J Mater Res*, in press
45. Aldred AT (1984) *Acta Cryst B* 40:569–574
46. Brixner LH, Abramson E (1965) *J Electrochem Soc* 112(1):70
47. Siebert H (1954) *Z Anorg u Allgem Chem* 275:225
48. Anderson FG, Weidner H, Summers PL, Peale RE, Zhang XX, Chai BHT (1994) *J Luminescence* 60/61:150–153
49. Lide DR (ed) *CRC Handbook of Chemistry and Physics*. CRC Press, Boca Raton, FL, 1991, 72nd ed, 4–121
50. Wyckoff RWG (1965) *Crystal Structures Vol 3*. Wiley, New York, 2nd ed, 17
51. Randles MH, Creamer JE, Belt RF, Quarles GJ, Esterowitz L (1992) OSA Technical Ser, Vol 10. Optical Society of America, Washington, DC, 289

11 Hydrothermal Growth of Quartz Under Specific Conditions and the Raman Spectra of Ion Species in a Hydrothermal Growth Solution

M. Hosaka

Yamanashi Institute of Gemology and Jewelry Arts, Toukoji-machi 1955-1, Kofu, 400-0808, Japan

11.1 Introduction

Hydrothermal growth is suitable for synthesizing a material which cannot exist in stable form or which is highly soluble at a high temperature. The most typical example of electronic components synthesized by this method is synthetic quartz. Synthetic quartz is most often used as a quartz oscillator for frequency generators and as a filter for frequency controllers. They are used in both industrial electronic components and consumer electronic components.

The first to discover the method of using seed crystal for growing quartz crystal was an Italian crystal grower, G. Spezia from the University of Torino. H. Iwasaki and F. Iwasaki confirmed that the following three publications of Spezia have greatly contributed to the development of electronic components today.

1. G. Spezia: Contribuzioni di Geologia Chimica, La pressione e chimicamente inattiva nella solubilita e ricostituzione del quarzo, *Atti. Accad. Sci. Torino*, 40:254–262 (1905).
2. G. Spezia: Contribuzioni sperimentali alla cristallogenesi del quarzo, *Atti. Accad. Sci. Torino*, 41:158–165 (1906).
3. G. Spezia: Sull' accresimento del quarzo, *Atti. Accad. Sci. Torino*, 44:95–107 (1909).

The achievements of Spezia were described in detail by F. Iwasaki and H. Iwasaki [4]. According to the report, while the dissolved lasca is transported from the nutrient side to the seed crystal side by convection in the current growth method of synthetic quartz, the lasca is transported mainly by diffusion in Spezia's method. The growth rate in the z -direction is supposed to have been 0.02 mm/day on one side because the growth was realized by diffusion. British researchers, Wooster et al. [5], conducted their experiments applying Spezia's method. In Germany also, Nacken [6] carried out his studies on the growth of crystal on the basis of Spezia's method, by placing the nutrient and the seed crystal in isothermal conditions. After

World War II, on the basis of these achievements, studies were carried out in the United States to develop the hydrothermal temperature gradient method currently used, which consists of using the difference in solubility. This method, which consisted of placing the seed crystal on the upper part of an autoclave and the nutrient, i.e., silica, in the lower part with a temperature gradient between such parts, was highly suited to mass produce quartz of good quality. The earliest studies in this field in Japan started at Yamanashi University in 1953. Currently, Japan is the largest producer of synthetic quartz in the world.

Na_2CO_3 and NaOH are used as solvents to grow quartz on an industrial scale. Typical solvents other than alkaline solutions that have been used to grow quartz include NaCl developed by Corwin and Swinnerton [7] and Hosaka and Taki [8], RbOH developed by Kopp and Clark [9], NH_4F developed by Balitsky [10] and Hashimoto et al. [11], including experiments under isothermal conditions and those using a temperature gradient method. The grown crystal shows morphology specific to the solvent used.

A factor other than the solvent that influences the sound growth of α -quartz is the filling of the solution. Usually, at room temperature, the solution fills more than 75% of the free volume of the vessel. As the percentage of the solution at room temperature decreases the quality of grown quartz declines, and when the filling rate drops below 50%, the seed crystal suspended in the upper part of the autoclave dissolves. Even at such low filling below about 50%, however, quartz has been successfully grown by applying the so called hydrothermal reverse temperature gradient method, which consists of placing the nutrient on the lower temperature side and the seed crystal on the higher temperature side [12]. The pressure inside the autoclave at a high temperature varies with the rate at which the solution fills the vessel at room temperature. Kennedy's isobaric and isovolumic solubility curves [13] for a SiO_2 - H_2O system shows that, when the pressure is over 75 MPa, the temperature coefficient of solubility is positive at a constant pressure. The temperature coefficient of solubility is negative, however, below about 70 MPa. One realizes that in the ordinary temperature gradient method quartz is grown at a pressure of 75 MPa or more, where the temperature gradient of solubility is positive. On the other hand, at a lower pressure, one can grow quartz by placing the seed on the higher temperature side and the source material on the lower temperature side, since the temperature gradient of solubility is negative. The authors [12] have succeeded in growing quartz in a NaCl - H_2O system with a filling rate of less than 50% by using the hydrothermal reverse temperature method. The growth of quartz with a low rate of filling can be explained by the temperature gradient of solubility. However, the problem of existing species should be studied further since it is expected that ion species present in the solution are different between a high rate of filling (i.e., a high pressure) and a low rate of filling (i.e., a low pressure), at a high temperature. If it was possible to mass produce high-quality quartz with a low filling rate, it would make an excellent industrial method with lower heating costs, but crystals thus produced were often imperfect with crevice flawing in the z -direction. However, in natural quartz crystal, two phase fluid inclusions have less than 50% of liquid phase in some cases. Crystal with such a proportion of liquid phase in fluid inclusions is formed

in dike- and pike-like veins and may have been grown by the transport of silicic ions from the low temperature side to the high temperature side. Natural quartz crystal rarely has crevice flawing and achieves transparency, since it grows mainly in directions perpendicular to the r - and z -faces.

When a small amount of impurity is added into the solvent, the impurity enters into the structure of the quartz crystal as substitutional or interstitial type. The crystal gives various colors according to the quantity and type of such impurity. Lehmann and Bambauer [14] reported, for instance, that the purple color of amethyst is attributable to the presence of paramagnetic holes formed by exposure to radiation when Fe^{3+} is incorporated into the structure of quartz crystal as a substitute for Si^{4+} or an interstitial type filling the interstices in the structure. As is amethyst, smoky quartz which incorporated Al^{3+} substitutionally also has a hole color center formed by radiation. The color of citrine is attributable to substitutional Fe^{3+} . As for the color cause of rose quartz, Hosaka et al. [15] stated that it was attributable to charge transfer between interstitial Fe^{2+} and substitutional Ti^{4+} , and Balitsky et al. [16] reported that it was a complex color center attributable mainly to the phosphorous element, both based on their experiments. However, colored quartz obtained by the addition of impurities is used only as jewelry stone and is produced only in small quantity. Industrially, there are more demands today for synthetic quartz without impurities such as Fe^{3+} and Al^{3+} , which is used for the development of electronic components.

Today, the improvements in growing method allows the production of high quality quartz with less impurities and microscopic solid phase inclusions such as acmite ($\text{NaFeSi}_2\text{O}_6$) and emeleusite ($\text{Na}_4\text{Li}_2\text{Fe}_2\text{Si}_{12}\text{O}_{30}$) [17].

As there are a lot of technical reports written since Spezia about the growth of synthetic quartz used as electronic components and for the characterization of grown quartz crystals, the discussion is limited to the following studies carried out by the author.

11.1.1 Growth of quartz with small content of Al^{3+}

It is supposed that when Al^{3+} incorporated in synthetic quartz is of substitutional type, alkaline metal ions are incorporated for charge compensation and that, when such crystal is exposed to radiation, defects are caused in the form of holes or H^+ traps in the oxygen orbit neighboring the substitutional Al^{3+} and this affects the frequency change of oscillators. Concerning the effects of Al^{3+} on the growth of synthetic quartz, Brown and Thomas [18] reported that Al^{3+} enters into the crystalline structure as substitutional type when its concentration is low, while it fills the crystal lattice as interstitial type, and the unevenness on the Z -face increases as the concentration increases. Martin and Armington [19] also reported that the amount of the incorporated Al^{3+} increases and Q -value decreases as the growth rate increases. Further, Taki and Hosaka [20] reported that, when the concentration of Al^{3+} is 100 ppm or less, the S -region develops on the boundary between the $+X$ -region and the Z -region. The relation of Al^{3+} contents in these regions may be

written as $Z < X < S$. Iwasaki et al. [21] have stated that Al contents in Y-bar synthetic quartz may be expressed by the following formula:

$$\text{Al} = a \cdot \exp(b \cdot \text{Al}_{\text{lasca}}) \quad (11.1)$$

The values of a and b are dependent upon the growth conditions. The formula shows clearly that Al^{3+} impurities in synthetic quartz are largely dependent on the lasca used as nutrient.

The authors [22] have synthesized high purity α -quartz using powdered synthetic, high purity α -cristobalite containing 3.1 ppm of Al^{3+} .

11.1.2 Synthesis of micro α -quartz crystals by hydrothermal hot-pressing method

This experiment was conducted by the author [23] to see if quartz crystal can be synthesized by the hydrothermal hot-pressing method, which requires neither large vessels nor high temperatures/high pressures, but cannot produce a large single quartz crystal. Its advantage consists rather in its ability to synthesize in short time micro crystals, which can be used as filler.

11.1.3 Growth of quartz crystals above transition temperature and morphology of synthetic crystals

The transition from low quartz (α -quartz) to high quartz (β -quartz) takes place at a temperature of 573°C . The α -quartz belongs to the trigonal crystal system and exhibits a hexagonal prismatic habit with major and minor rhombohedral faces and prism faces. The β -quartz belongs to the hexagonal crystal system and exhibits a hexagonal dipyramidal habit which usually does not have prism faces, but may have extremely small faces in some rare cases. The sharp transition temperature between the α - and β -quartz is easily expected because they are of a framework structure consisting of SiO_4 tetrahedra, and the only difference between them is the angle between neighboring SiO_4 tetrahedra.

The structural similarity contradicts the long-held belief and observation that prism faces usually do not appear on β -quartz. The authors [24] have synthesized quartz crystals at a temperature higher than the transition temperature by applying the hydrothermal method and checked whether the morphologies of the as-grown crystals varied with temperature, as well as the validity of the long-held belief that prism faces do not appear on β -quartz and observed a hexagonal dipyramidal habit, and in a few cases, a hexagonal dipyramidal habit without prism faces. Swanson and Fenn [25] have synthesized β -quartz in silicate melts and observed only a hexagonal dipyramidal habit, but hydrothermal synthesis of quartz at a temperature higher than the transitional temperature has never been performed before.

11.1.4 Raman spectral studies of $\text{SiO}_2\text{-NaOH-H}_2\text{O}$ and $\text{SiO}_2\text{-Na}_2\text{CO}_3\text{-H}_2\text{O}$ system solutions under hydrothermal conditions

The morphology and the surface microtopography of a grown crystal reflect the environment in which the crystal grew. For example, on synthetic quartz grown in an alkaline solution, the rhombohedrons are usually composed of three rhombohedral faces. Pyramidal growth hillocks are observed on the prism faces.

These pyramids may have been developed by spiral growth or two-dimensional spread. On the other hand, natural quartz usually has six rhombohedral faces while the prism faces show striations running perpendicularly to the c -axis. The striations are relatively a few in number and flat or steep in shape. The distance between respective striations varies from crystal to crystal. In surface microtopography on their rhombohedrons, natural quartz and synthesized quartz grown in an alkaline solution differ from each other. The surface microtopography of natural quartz shows small growth hillocks and mosaic-like growth patterns which vary between places of origin, while, on the rhombohedrons of quartz grown in an alkaline solution, relatively large growth hillocks are observed. Figure 11.1 illustrates an experiment to show the surface microtopography varying with an alkaline concentration. The horizontal axis of the graph represents the concentration of Na_2CO_3 added into NaCl solution. The prism faces of quartz synthesized in NaCl solution simulating the growth conditions of natural quartz present fine parallel striations [26]. One realizes from the figure that, as the alkali content increases, the striations widen their respective distances to gradually form a pyramid as shown in the figure. When an alkaline solution such as NaOH or Na_2CO_3 was added into 10 wt% NaCl solution, no remarkable difference has been observed in

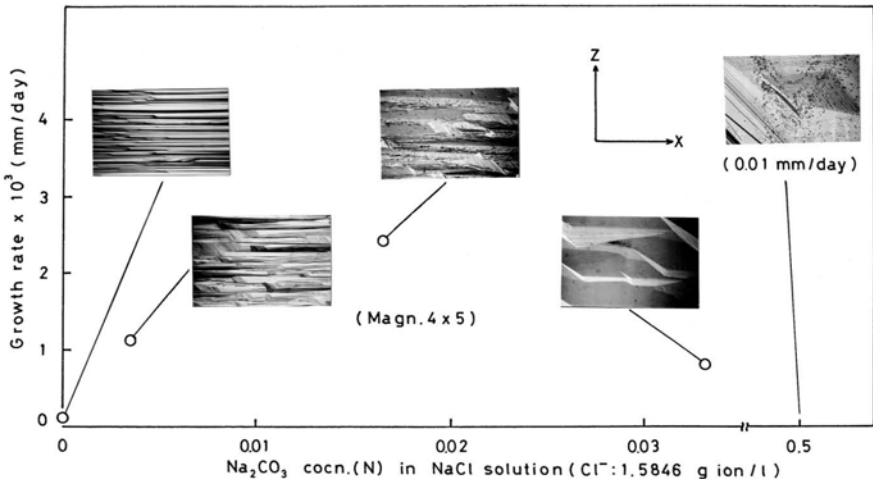


Fig. 11.1. Relation between the surface topography on the prism face and Na_2CO_3 concn. (N) in NaCl solution. Growth temp.: 400°C , Dissolving temp.: 425°C , Degree of fill: 70%

the distance between respective striations, but, when each of such alkaline solutions was added into H_2O , the distance between striations on the prism faces of the crystals grown in Na_2CO_3 became somewhat wider compared to that shown by the crystals grown in a solution to which the same content of $NaOH$ had been added. The surface microtopography is largely dependent upon the nature of the growth solution or solvent, that is to say, upon dissolved silicic ion species. As silicic ion species, there are SiO_4 , Si_2O_7 , Si_3O_{10} , $(SiO_3)_4$, and $(SiO_{4/2})_x$. The ratio of these ions varies between the types of solution. For example, based on the measurements of solubility Laudise [27] and Taki [28] performed, they supposed that Si_3O_7 occupies a large part in the $NaOH$ solution, because 3 mol of SiO_2 is dissolved into 2 mol of $NaOH$ there; and that SiO_3 is predominant in the Na_2CO_3 solution because there 1 mol of SiO_2 was dissolved in 1 mol of Na_2CO_3 . Under hydrothermal conditions, silicic ions other than these ions or amorphous sodium silicate ($Na_xSi_yO_z$) are supposed to be present. Lentz [29] analyzed trimethylsilyl derivatives of silicic ions in sodium silicate solutions by gas chromatography to examine the degree of polymerization of silicic ions. He reported that, when $Na_2O/SiO_2 \geq 2.0$, the proportion of monomers increases as the alkali content increases; when $Na_2O/SiO_2 \leq 1.0$, the proportion of chain or ring polysilicic ions increases as the alkali content decreases.

Hosaka and Taki [30] have designed an autoclave with optical windows resistant to high temperature and pressure as a means for *in situ* observation of solutions at high temperature and pressure. Using a Raman spectrometer, they tried to measure directly and optically the conditions of solutions at high temperature and pressure to check the correspondence between the previously confirmed chemical species [27,28,29] and Raman spectra.

11.2 Growth of Quartz with Poor Al^{3+} Content

11.2.1 Experimental method

The α -cristobalite used as the nutrient was amorphous silica particles sintered at 1,000–1,300°C with less than 1 ppm of Al^{3+} impurities [31]. Two compacted forms of α -cristobalite of 30–40 μm particle size were used in these experiments. One was sintered at more than 1,300°C into grains of 0.5–1.0 mm in diameter. The other one was also sintered at more than 1,300°C and compacted into lumps of about 1 cm in diameter. Figure 11.2 [22] shows the α -cristobalite used as nutrient. It would be possible to use high-purity glass as nutrient once it is transformed into α -quartz at high temperature and pressure [7], but, in such a case, transparent crystals could not be obtained until the glass is completely transformed into α -quartz, because glass is highly soluble. The advantage of α -cristobalite over glass is that it can be used as nutrient in an autoclave from the beginning of the experiment, because it has much lower solubility [32] and transforms into α -quartz at a temperature of about 300°C (measured on the outer wall of the autoclave). As seed

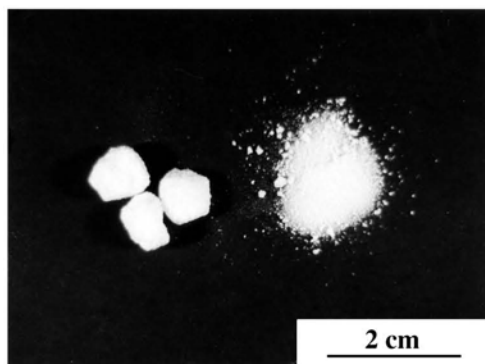


Fig. 11.2. α -cristobalite used as the source material. Right: compacted into lumpus (about 1 cm). Left: compacted into grains (0.5–1.0 mm)

crystal, Y-bar crystal was used. As solvent, 1 N NaOH solution was used. The experiment was performed at a growth temperature of 315°C, a dissolving temperature of 340°C, and a degree of filling of 83%.

11.2.2 Experimental results

Synthesized crystals were transparent and did not present any inclusions of microscopic size ($\times 100$) in their growth regions. The rate of growth was 0.20–0.60 mm/day in the Z-direction, but did not show any significant difference compared to the previous experiments conducted using lasca as nutrient.

The Al^{3+} content analyzed with inductively coupled plasma atomic emission spectrometry (ICAP-88, Nippon Jarrell-Ash Co., Ltd.) in each of both sides of the Z region, the +X, and -X regions, the Al^{3+} content was 2.9, 2.1, and 2.1 ppm, respectively. The Al^{3+} content included both substitutional and interstitial types. The low Al^{3+} content of the substitutional type in the Z and X regions was suggested, however, by the facts that the irradiation of CO^{60} γ -rays of 10 Mrad did not cause any coloration and that the absorption coefficients for 3304 cm^{-1} and 3364 cm^{-1} which were stated by Halliburton et al. [33] to be absorbed by $\text{Al-H}^+\cdots\cdots\text{OH}^-$ (Al in this case was a substitutional type) was extremely small except for in the -X direction. The release of Al^{3+} from the nutrient into the solution upon the dissolution of the nutrient does not mean that all of the released Al^{3+} is incorporated into the grown seed crystal: They are “purified,” so to speak [21]. The fact that the Al^{3+} content of the grown crystal was about 2 ppm in each region when α -cristobalite of less than 1 ppm of Al^{3+} content was used as nutrient suggests a contamination from the NaOH solution or the inner wall of the vessel.

The generation of the S-region was not observed between the Z- and X-regions of the synthetic quartz. Previous studies [20] have made it clear that with less than 10 ppm of Al^{3+} content, the S-region was not generated.

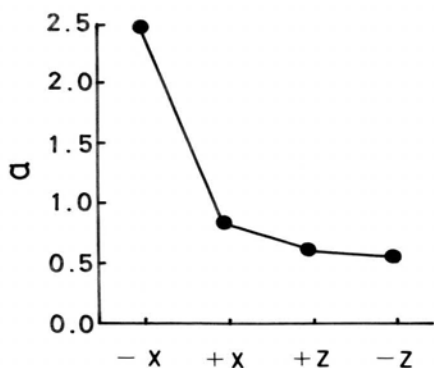


Fig. 11.3. Absorption coefficient at 3407 cm^{-1}

Figure 11.3 shows for each region the absorption coefficient (α) of 3407 cm^{-1} attributable to the presence of H_2O or its ion species. The measurement of infrared absorption spectra was performed in the region not affected by the change of Al^{3+} content, that is to say, at a distance of 0.3 mm apart from the seed crystal remaining in the grown crystal. The fact that the absorption coefficient for the $-X$ -region is larger than those in other regions seems to reflect the fact that H_2O particles, which are easily absorbed on the $-X$ face, are included in the crystal.

After the experiment, it was confirmed by means of X-ray diffraction that the α -cristobalite used as nutrient had recrystallized into α -quartz at a temperature of 300°C . The α -cristobalite remained as it was, however, at a temperature of 260°C . This suggests that when the temperature in the nutrient side was 270°C or less, the α -cristobalite does not recrystallize into α -quartz, but directly dissolves into silicic ions and that such dissolved silicic ions are transported to the seed crystal side. The fact that at a temperature of 300°C or more, the transformation from α -cristobalite to α -quartz takes place within 24 hours seems to suggest that, in this case, silicic ions dissolved from the transformed α -quartz are transported to the seed side. There was no evidence that the difference between the two forms of α -cristobalite used as nutrient had any particular effect on the grown crystal.

11.3 Synthesis of Micro α -Quartz Crystals by Hydrothermal Hot-Press Method

11.3.1 Experimental method

Figure 11.4 shows the hydrothermal hot-press used in the experiment [34]. The mixture of the nutrient and the solvent filled the space A of the figure. As nutrient [31], nonsintered α -cristobalite $200\text{ }\mu\text{m}$ in diameter and $0.5\text{--}1.0\text{ mm}$ in length was

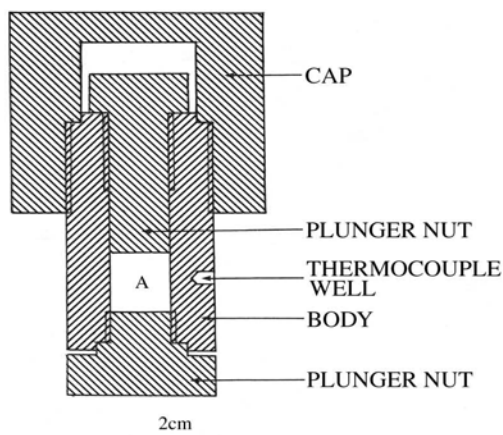


Fig. 11.4. Schematic diagram of hydrothermal hot-press

used. As solvent, 1 N NaOH, 1 N Na₂CO₃, and sodium formate were used. The NaOH and Na₂CO₃ were used in the state of aqueous solutions. The sodium formate was mixed with the nutrient in a ratio of 1:1 without water before being used. After the space A was filled with solvent and nutrient, the plunger nuts B and C were put in place and tightened with a constant torque of 500–1,000 kg·f·cm with a torque wrench. The device was set in an electric furnace and left for the reaction for 24–30 hours. After the experiment, the device was quenched and the reactant was examined by means of SEM and X-ray diffraction.

11.3.2 Experimental results

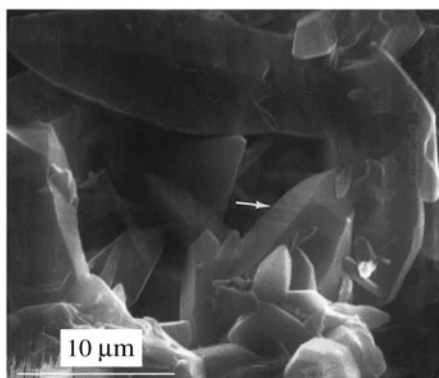
In the experiment using 1 N NaOH, 1 N Na₂CO₃, and sodium formate, a 100% crystallization was observed at a temperature of 300°C. The crystal thus grown was hexahedral and had a rhombohedron at one end or at both ends. The micro quartz was 20 μm in length and 5–8 μm in thickness. On the prism faces of the crystals synthesized in sodium formate, striations were observed running parallel to the boundary between the rhombohedron and the prism faces. Figure 11.5 shows the micro quartz synthesized from sodium formate. Table 11.1 shows the results of the experiment [34].

At a high temperature, sodium formate is supposed to decompose into sodium oxalate. Considering that the sodium oxalate may decompose secondarily, it seems quite probable that the solution contains complex ion species at temperatures above the melting point (253°C).

Sodium formate is a kind of fused salt. Probably, the experiment was the first to have used sodium formate as a solvent to grow quartz. When observed through SEM, the morphology of the micro quartz synthesized in each of 1 N NaOH and 1

Table 11.1. Results of Synthetic Micro Quartz Crystals

Solvent	Reaction temp. [°C]	Reaction time [h]	Results [X-ray diffraction]
1 N NaOH	250	24	α -cristobalite
Sodium formate	255	24	α -cristobalite
1 N NaOH	300	24	100% α -quartz
Sodium formate	300	30	100% α -quartz
1 N Na ₂ CO ₃	300	30	100% α -quartz

**Fig. 11.5.** SEM photograph of micro α -quartz crystals synthesized from sodium formate at a temperature of 300°C

1 N Na₂CO₃ solutions had no significant difference from that of crystals synthesized by convection. This suggests that the ion species present in each of 1 N NaOH and 1N Na₂CO₃ solutions used in this experiment were similar to the those previously examined [27,28].

11.4 Growth and Morphology of Quartz Crystals Synthesized Above Transition Temperature

11.4.1 Experimental method

The nutrient and the solvent were initially made to react for 58 hours at a soaking temperature exceeding the transition temperature, then were cooled down slowly to the quenching temperature at a constant speed (0.07°C/mm), and finally

Table 11.2. Experimental Data

Nutrient	α -cristobalite: 0.5 g (grains of 0.5–1.0 mm)
Solvent	10 wt% NaCl, 1 N NaOH 0.89 cm ³
Filling	30%
Soaking temperature	600–750°C, at every 50°C
Soaking duration	58 h
Quenching temperature	600–750°C, at every 50°C
Cooling rate	0.07°C/mm
Cooling duration	12 h
Quenching speed from a quenching temp. to 50–60°C	About 5.5°C/s, by running water

quenched at a speed of 5.5°C/s. The β -quartz is considered to grow principally during the slow cooling period. Table 11.2 summarizes part of the experimental conditions [24].

As nutrient, high-purity α -cristobalite was used to prevent the influence of impurities. The solvent filled 30% of the free volume of the reaction vessel. At this filling rate and high temperature, it takes the form of a fluid of very low density, i.e., vapor phase. In the growth of natural quartz, the same phenomenon is observed. This is evident from the observation of two phase fluid inclusions found in natural quartz. In some cases, the proportion of the liquid phase to the vapor phase in such two phase fluid inclusions reaches to 20–30% [35,36]. It is understood that quartz with inclusions of such a high proportion of vapor phase, or such a low proportion of liquid phase, grows under vapor phase at a high temperature. Therefore, one may consider that the growth of β -quartz in this experiment also took place under vapor phase. Considering this method similar to or an extension of the hydrothermal growth method, the author named it “hydrothermal vapor growth.”

The effects of the filling density in liquid phase, i.e., fluid density at a high temperature, upon the growth of quartz at a high temperature of 600°C or more is not yet clear.

As the temperature rises, the solvent reacts with α -cristobalite used as nutrient. Dissolved silicic ions dissolve into the vapor phase and grow during the slow cooling period. That is to say, the β -quartz grew during the period through which these ions were slowly cooled down from the soaking temperature. Since the transition from α -quartz to β -quartz occurs at a temperature of 573°C, one might suppose that quenching at a temperature sufficiently higher than 573°C allows one to see that the morphology of β -quartz is unchanged, in the same way as β -quartz in volcanic rocks is observed. The authors observed that the crystals thus quenched and characterized through SEM and X-ray diffraction are α -quartz transformed from α -cristobalite.

11.4.2 Experimental results

Table 11.3 summarizes the results of the experiment [24]. Crystals are roughly classified into the following two groups:

- Type 1: Most of these crystals show a long prismatic habit and rounded terminations. The hexagonal pyramidal faces of this type show $\{10\bar{1}\bar{1}\}$.
- Type 2: These crystals show a hexagonal or stout prismatic habit. They are larger than those of type 1. The photograph in Fig. 11.6 shows both types 1 and 2. The type 1 crystals have a thickness of 3 μm and a length of less than 25 μm . The type 2 crystals may be further classified into the following three subgroups:
 - Type 2N: As in Fig. 11.7, these crystals show a hexagonal dipyramidal habit without prismatic faces.
 - Type 2F: As in Fig. 11.8, these crystals show a stout prismatic habit with flat prismatic faces.
 - Type 2C: As in Fig. 11.9, these crystals show a spindle-like habit with tapering faces. Their prismatic faces tend to curve as their size grows.

Most of the hexagonal pyramidal faces of these Type 2N, Type 2F, and Type 2C crystals were $\{\text{hohl}\}$ faces, with $\{10\bar{1}\bar{1}\}$ faces appearing only as small faces at the terminations.

As is shown clearly in Table 11.3, there are more Type 1 crystals than Type 2 crystals. The table also shows that as the temperature rises (above 700°C), the Type F crystals increase and the Type N crystals decrease in number. At a soaking temperature of less than 700°C, Type C and F crystals were observed, but there were no Type N crystals. At a soaking temperature of 600°C and a quenching temperature of 550°C, the crystals showed a habit like α -quartz. No significant difference of morphology was observed that was attributable to the difference of solvent, but in the experiment with NaCl solution, striations were observed on the prismatic faces. While in the experiment with NaOH solution, pyramidal growth hillocks were observed on the prismatic faces. This indicates that, even at such a

Table 11.3. Summary of the Experiment Results

Soaking temperature [°C]	Quenching temperature [°C]	Solvent 10 wt% NaCl	Solvent 1 N NaOH
750	700	Type 1 > Type 2 (F > C >> N)	Type 1 > Type 2 (F > C >> N)
700	650	Type 1 > Type 2 (C > F)	Type 1 > Type 2 (C ~ F)
650	600	Type 1 > Type 2 (C ~ F)	Type 1 > Type 2 (C ~ F)
600	550	As α -quartz	As α -quartz

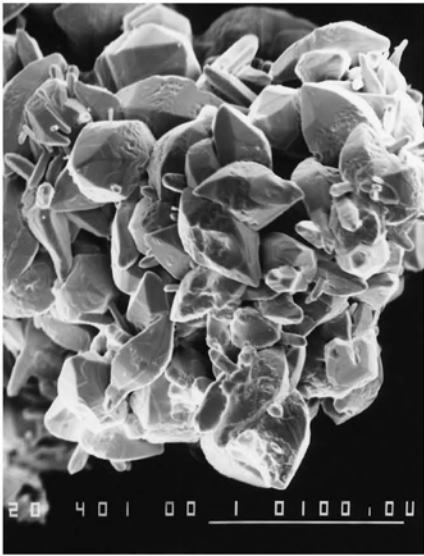


Fig. 11.6. SEM photograph of a crystal group showing Type 1 habit (larger crystals) and Type 2 habit (smaller crystals). 10 wt% NaCl solution, soaked at 700°C and quenched at 650°C

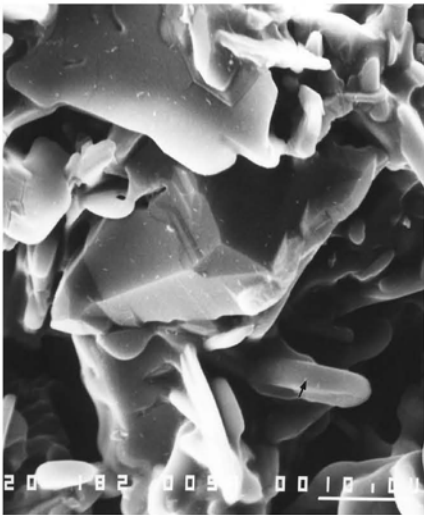


Fig. 11.7. SEM photograph of β -quartz crystal (Type 2N) without prism faces. 10 wt% NaCl solution, soaked at 750°C and quenched at 700°C. A black arrow indicates co-existing Type 1 crystal

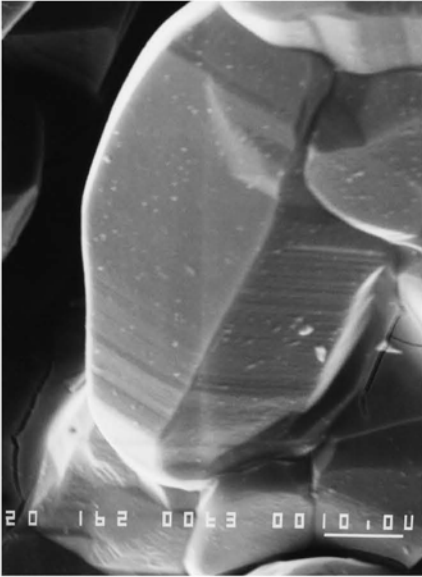


Fig. 11.8. SEM photograph of β -quartz crystal (Type 2F). 1 N NaOH solution, soaked at 750°C, and quenched at 700°C

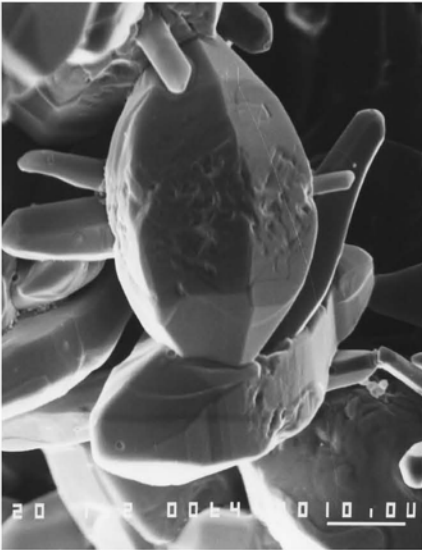


Fig. 11.9. SEM photograph of β -quartz crystal (Type 2C). 10 wt% NaCl solution, soaked at 700°C, and quenched at 650°C

high temperature as allows the growth of β -quartz, dissolved ion species are different from solution to solution.

In this experiment, β -quartz grown under “hydrothermal vapor phase” above the transitional temperature showed, in most cases, a hexagonal dipyramidal habit and, in few cases, a hexagonal dipyramidal habit without prism faces. Another remarkable morphological characteristic is that hexagonal dipyramidal faces were not $\{10\bar{1}1\}$ faces, but fundamentally $\{h0\bar{h}1\}$ faces. With the appearance of such highly indexed hexagonal pyramidal faces, crystals showed a tendency to show round forms as their size increased.

These observations and the discussions that followed suggest the following about the growing process of β -quartz: The habits shown by the Type 1 and Type 2 crystals represent the morphology of β -quartz. β -quartz starts with Type 1 habit and transforms into a stout Type 2 crystal. In other words, as the crystal grows, the growth rate perpendicular to the prism faces increases much faster than the growth rate perpendicular to the dipyramidal faces. As a result, hexagonal pyramidal faces and tapered prism faces of high indexes appear.

11.5 Raman Spectral Studies of the Solution Chemistry of $\text{SiO}_2\text{-NaOH-H}_2\text{O}$ and $\text{SiO}_2\text{-Na}_2\text{CO}_3\text{-H}_2\text{O}$ Systems Under Hydrothermal Conditions

11.5.1 Experimental method

In order to observe directly the state of an aqueous solution under hydrothermal conditions, it is necessary to construct an autoclave with optical windows. Figure 11.10 illustrates an autoclave with optical windows constructed of Cr-Mo steel. A small type autoclave (A) is placed in an electric furnace. The autoclave has a reaction chamber with an internal diameter of 3 mm and a total capacity of 0.5 cm³. At the upper and lower sides and a lateral side, the autoclave has mirror-finished, sapphire-plate optical windows (B) 9 mm in diameter and 7 mm in thickness. The material for such windows must not only resist high temperature and pressure, but also must satisfy many other conditions: They must have a high transmittance in an adequate range of light transmittance; the reflective index and its dispersion must be small; its own fluorescent characteristics must be low when Raman spectra is measured, and so forth. Diamond would be best suited as such a material considering all these requirements, but the authors [24] used sapphire plates in the experiment because it had been proven in preliminary experiments that they are quite satisfactory for the purpose. The electric furnace was made in a size, which can be placed in the sample room for the spectrophotometer. The heating in the electric furnace was realized by means of three 300 W and two 100 W parallel nichrome wires wound around the core tube. Around the outer surface of the electric furnace of the autoclave, a copper tube was wound to circulate cooling water

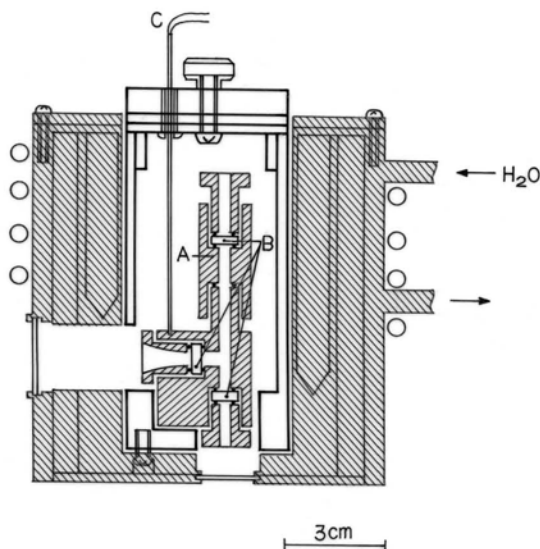


Fig. 11.10. Autoclave having optical windows for the measurement of Raman spectra at high temperature and high pressure and electrical furnace. (A) autoclave; (B) sapphire windows; (C) thermocouple

during the spectrophotometric measurement. Temperature was measured by inserting the tip of a thermocouple (C) into a well made on the top of the autoclave to a depth of about 2 mm.

Argon ion laser (Toshiba Co., Ltd.) with a wavelength of 514.5 nm, enabling the control of spontaneous emission in the range of $0\text{--}1,000\text{ cm}^{-1}$, was used in these experiments. The laser beam was led into the reaction chamber through the lower window of the small autoclave shown in Fig. 11.10. Scattered Raman light generated in the reaction chamber of the autoclave was picked up by a spectrophotometer (Nihon Denshi Co., Ltd.) through the left side window of the autoclave.

When put in direct reaction in the autoclave shown in Fig. 11.10, the quartz and the solution might form heavy cake, which would stick to the inner surface of the sapphire plates of the small autoclave, and reduce the intensity of the laser beam. The scattered laser beam from heavy cake might be picked up, too. For this reason, in the experiment, the author grew quartz for 3 days preliminarily by an ordinary temperature gradient method in an autoclave having an internal volume of 350 cm^3 and a platinum vessel having an internal volume of 100 cm^3 , with a filling rate of 60% and at a dissolving temperature of 350°C and a growing temperature of 330°C . The autoclave was then quenched. The solution was filtered and the filtered solution used as the sample solution, which was supposed to retain silicic ions present at the time the quartz crystals grew up. As solvent, aqueous solutions of 1 N NaOH and 0.5 N Na_2CO_3 were used. After having the solution and quartz made to react, the concentration of $\text{Na}_2\text{O}/\text{SiO}_2$ was calculated from each solution

filtered, respectively. The concentration was about 0.56 for the 1 N NaOH solution and about 2.50 for the 0.5 N Na_2CO_3 solution.

Spectrophotometric measurement was performed in the range of 50–4,000 cm^{-1} , maintaining the specimen at a measurement temperature for sometime and gradually increasing the temperature of the autoclave. The filtered solution filled 60% of the inner capacity of the small autoclave shown in Fig. 11.10. The spectra at each temperature were integrated 20 to 30 times with a Raman data analyzer and then averaged.

11.5.2 Experimental results

$\text{SiO}_2\text{-NaOH-H}_2\text{O}$ system [37, 38]

Figure 11.11 shows the Raman spectra at room temperature. Raman spectra were observed at 175, 430, 600, 780, 1035, 1645, 3200, and 3400 cm^{-1} . The Raman spectra shown in Fig. 11.12 were measured at temperatures of 150, 200, 250, 300, and 320°C. At each of the temperatures of 150, 200 and 250°C, spectra were observed at 430, 780, 1035, 3200, and 3400 cm^{-1} . Each of these spectra became feebler as the temperature was increased. At a temperature of 300°C, it was confirmed at 780 and 1035 cm^{-1} . At a temperature of 320°C, the spectral broadening centering around 1200 cm^{-1} was observed. The spectral pattern observed during temperature decrease was the same as that observed during temperature increase. Shifting of the spectral bands with temperature increase and temperature decrease was not observed.

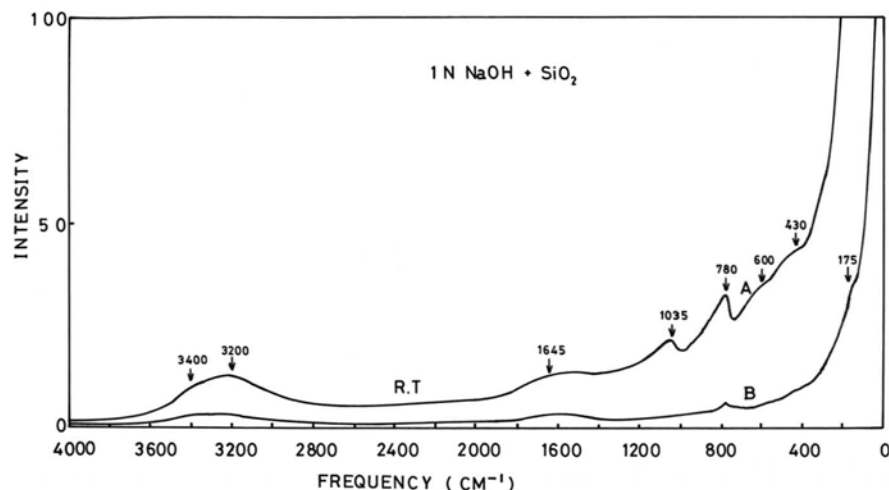


Fig. 11.11. Raman spectra of $\text{SiO}_2\text{-NaOH-H}_2\text{O}$ system at room temperature. Sensitivity: (A) 1,000 pulses/s; (B) 10,000 pulses/s

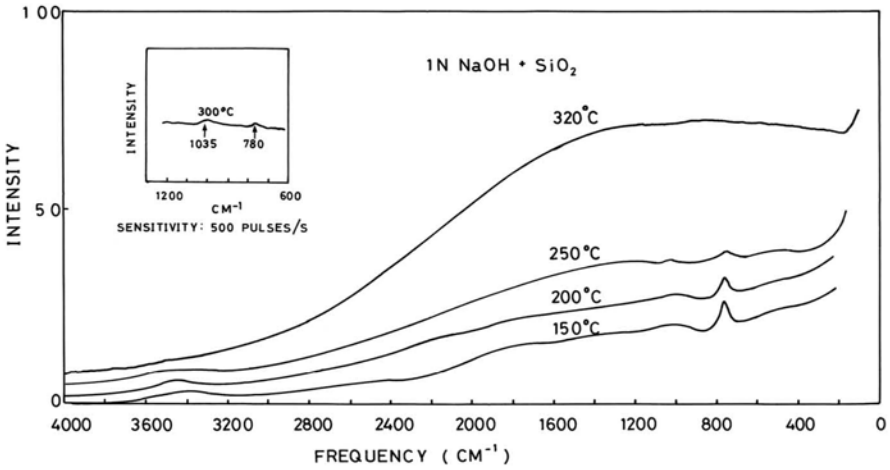


Fig. 11.12. Raman spectra of SiO₂-NaOH-H₂O system at a series of temperatures. Sensitivity: 1,000 pulses/s

SiO₂-Na₂CO₃-H₂O system [37]

Figure 11.13 shows Raman spectra recorded at room temperature, 250, and 300°C. At room temperature, Raman spectral bands were observed at 175, 450, 525, 780, 1020, 1070, 1645, 3250, and 3400 cm⁻¹. The spectrum at 780 cm⁻¹ was broad, different from the one shown with NaOH. Under hydrothermal conditions at 300°C,

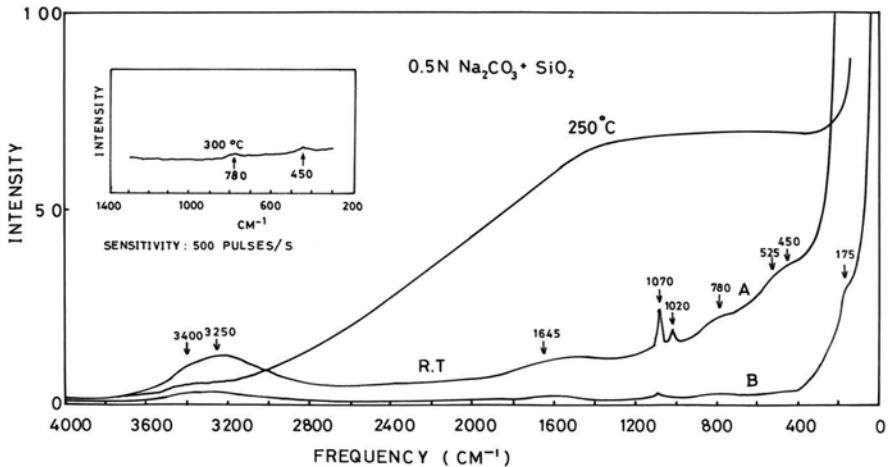


Fig. 11.13. Raman spectra of SiO₂-Na₂CO₃-H₂O system at room temperature and a series of temperatures. Sensitivity: (A) 1,000 pulses/s; (B) 10,000 pulses/s

broad spectra were observed at 450 and 780 cm^{-1} . Spectral patterns observed during temperature decrease was the same as that observed during temperature increase. Shifting of the spectra with temperature increase and temperature decrease was not observed.

11.5.3 Discussion

There are several reports on the Raman spectra of sodium silicate solution, like Fortnum and Edwards [39], and Earley et al. [40]. Fortnum and Edwards [39] observed Raman spectra at 448, 607, 777, and 935 cm^{-1} with 2.5 M sodium silicate solution. With 0.5–2.5 M sodium silicate solutions, Earley [40] observed Raman spectra at 616, 782, and 929 cm^{-1} at an $\text{Na}_2\text{O}/\text{SiO}_2$ ratio of 2.0 and at 456, 614, 779, 937, and 1030 cm^{-1} at an $\text{Na}_2\text{O}/\text{SiO}_2$ ratio of 1.0. The difference in the $\text{Na}_2\text{O}/\text{SiO}_2$ ratio caused the slight difference in wavelengths. In the experiment performed by the author with the $\text{SiO}_2\text{-Na}_2\text{CO}_3\text{-H}_2\text{O}$ system at an $\text{Na}_2\text{O}/\text{SiO}_2$ ratio of 0.56, the Raman spectra observed at 430, 600, 780, and 1035 cm^{-1} correspond to those reported by Fortnum and Edwards, and Earley et al. Other spectra correspond to those of water. The Raman spectrum observed at 780 cm^{-1} also corresponds to that of water. However, such a sharp and intensified spectrum of 780 cm^{-1} as is shown in the figure should not be attributed to water but to silicic ions, since water has a very broad pattern of spectra due to the hydrogen bond between the water molecules. Lentz reported that the proportion of monomers increases as the alkaline concentration increases when the molar ratio is $\text{Na}_2\text{O}/\text{SiO}_2 \geq 2.0$, and the proportion of chain or ring type polysilicic ions increases as the alkaline concentration decreases when the molar ratio is $\text{Na}_2\text{O}/\text{SiO}_2 \leq 1.0$ [29]. Therefore, the concentration of silicic ions in a solution of $\text{Na}_2\text{O}/\text{SiO}_2$ with a molar ratio of 0.56 ($\text{Na}:\text{Si} \approx 1:1$) is supposed to be in the following relation [29]:



The compliance between the Raman spectra of sodium silicate measured at room temperature with those measured under hydrothermal conditions, and the absence of shifting observed when Fig. 11.11 was compared to Fig. 10.10, shows that the Raman spectra with solutions of $\text{Na}_2\text{O}/\text{SiO}_2$ with a molar ratio of 0.56 measured under hydrothermal conditions below 300°C (Fig. 11.10, Fig. 11.11) represent Raman spectra of solutions which contain, in the order of appearance in the above relation, monomers, dimers, trimers, and polysilicic ions.

Raman spectra of reaction solution between a 0.5 N Na_2CO_3 solution and a $\text{Na}_2\text{O}/\text{SiO}_2$ molar ratio of 2.50, and quartz did not show any remarkable characteristics, as were shown with NaOH, and in most cases corresponded to those of water. According to Earley et al. [40], the Raman spectra at room temperature of sodium silicate with a $\text{Na}_2\text{O}/\text{SiO}_2$ molar ratio of 2.0 or more appear at 454, 614, 784, and 932 cm^{-1} . The spectra at 454 and 784 cm^{-1} thus correspond to the results of this experiment. The results of the experiments reported by Lentz [29] suggest the predominance of monomer ions for compositions of $\text{Na}_2\text{O}/\text{SiO}_2 \geq 2.0$.

Based on the measurement of the solubility [27,28], it is supposed that ring type $\text{Si}_3\text{O}_7^{2-}$, in the case of NaOH, and monosilicic ions of SiO_3^{2-} , in the case of Na_2CO_3 , exist in each solvent. This corresponds roughly to the results of the experiments performed by Lentz [29]. Raman spectra decreased their intensity as the temperature was increased and were observed at 780 and 1035 cm^{-1} at a temperature of 300°C in a SiO_2 -NaOH- H_2O system and at 450 and 780 cm^{-1} at the same temperature in a SiO_2 - Na_2CO_3 - H_2O system. At a temperature of 320°C, a broad pattern of spectra were observed in both solutions. This may be attributable to the following:

1. As a result of temperature change, the change of equilibrium constant altered the ratio of existing silicic ions.
2. As a result of temperature change, the vibration level of the Si-O bond altered.
3. Background light increased.

11.5.4 Summary

In the experiment, an autoclave, with optical windows resistant to high temperature and pressure of 350°C and 400 psi, respectively (at a filling rate of 60%), was constructed and used to measure Raman spectra under high temperature and pressures. The types of silicic ions present in aqueous solutions of sodium silicate vary with the $\text{Na}_2\text{O}/\text{SiO}_2$ molar ratio of such solutions. As the $\text{Na}_2\text{O}/\text{SiO}_2$ molar ratio increases, the chain of Si-O-Si is cut to generate monosilicic ions. As the $\text{Na}_2\text{O}/\text{SiO}_2$ molar ratio decreases, chain or ring type polysilicic ions are generated. A change in the type of these silicic ions causes some shifting or change in intensity of the Raman spectra specific to silicic ions. For example, the spectra of silicic ions with chain-like structure appear at the slightly lower frequency side, but such difference in wave number is small. Therefore, it may be supposed that spectra of silicic ions usually appear around 450, 600, 700, and 1035 cm^{-1} .

In this experiment, Raman spectra were measured for a SiO_2 -NaCl- H_2O system with a filtered solution obtained after the interaction between a quartz crystal and a NaCl solution at a temperature of 350°C, but no characteristic Raman spectra were observed. This might be because the solubility of quartz in NaCl solution at this temperature is too small to generate a large amount of silicic ions.

References

1. Spezia G (1905) *Atti accad sci Torino* 40:254
2. Spezia G (1906) *Atti accad sci Torino* 41:158
3. Spezia G (1909) *Atti accad sci Torino* 44:95
4. Iwasaki F, Iwasaki H (1998) *J Jap Assoc Crystal Growth* 25:66 (in Japanese)
5. Wooster N, Wooster WA (1946) *Nature* 157:297
6. Nacken R (1950) *Chemiker-Ztg* 74(50):745
7. Corwin JF, Swinnerton AC (1951) *J Am Chem Soc* 73:3598

8. Hosaka M, Taki S (1981) *J Crystal Growth* 52:837
9. Kopp OC, Clark GW (1968) *J Crystal Growth* 2:308
10. Balitsky VS (1977) *J Crystal Growth* 41:100
11. Hashimoto S, Yazaki E, Kodaira K (1993) *J Ceramic Soc Japan* 101(10):1120
12. Hosaka M, Taki S (1986) *J Crystal Growth* 78:413
13. Kennedy GC (1950) *Econ Geol* 45:629
14. Lehmann G, Bambauer HU (1973) *Angew Chem Internat Edit* 12:283
15. Hosaka M, Miyata T, Shimizu Y, Okuyama O (1986) *J Crystal Growth* 78:561
16. Balitsky VS, Makhina IB, Prygov VI, Mar'in AA, Emel'chenko AG, Fritsch E, McClure SF, Taijing L, DeGhionno D, Koivula JI, Shigley JE (1998) *Gem & Gemology* 34(1):34
17. Voigt DE, Brantley SL (1991) *J Crystal Growth* 113:527
18. Brown CS, Thomas LA (1960) *J Phys Chem Solids* 13:337
19. Martin JJ, Armington AF (1983) *J Crystal Growth* 62:203
20. Taki S, Hosaka M (1986) *Hydrothermal Reactions* 1:15 (in Japanese)
21. Iwasaki F, Iwasaki H, Suzuki CK (1989) *Jpn J Appl Phys* 28(1):68
22. Hosaka M, Miyata T (1993) *Mat Res Bull* 28:1201
23. Hosaka M (1991) *J Crystal Growth* 112:291
24. Hosaka M, Miyata T, Sunagawa I (1995) *J Crystal Growth* 152:300
25. Swanson SE, Fenn PM (1986) *Am Mineralogist* 71:331
26. Hosaka M, Miyata T, Taki S (1986) *J Crystal Growth* 75:473
27. Laudise RA, Ballman AA (1961) *J Phys Chem* 65:1396
28. Taki S, Yamada K (1961) *Rept Fac Educ Yamanashi Univ* 12:146 (in Japanese)
29. Lentz CW (1964) *Inorg Chem* 3:575
30. Hosaka M, Taki S (1990) *J Crystal Growth* 100:343
31. United States Patent-No 4853198. August 1, 1989
32. Avakov V, Vinogradov BN (1972) *Izv Vyssh Ucheb Zaved, Khim Teknol* 17(6):879 (in Russian)
33. Halliburton LE, Markes ME, Marten JJ (1980) *Proc 34th Ann Symp Freq Control* 1
34. Hosaka M (1991) *J Crystal Growth* 112:291
35. Yermakov NP (1961) *Intern Geol Rev* 3:575
36. Roedder E (1963) *Econ Geol* 58
37. Hosaka M (1982) Doctorial thesis, Hottkaido Univ, 212
38. Hosaka M (1990) *J Crystal Growth* 100:343
39. Fortnum D, Edwards JD (1956) *J Inorg Nucl Chem* 2:264
40. Early JE, Fortnum D, Wojciki A, Edwards JD (1965) *J Am Chem Soc* 81:1295

12 Growth and Characterization of Technologically Important Oxide Single Crystals

Krishan Lal, R.V. Anantha Murthy, Ashutosh Choubey, and Niranjana Goswami

Crystal Growth and Characterization Section, National Physical Laboratory, Dr. K. S. Krishnan Road, New Delhi-110012, India

12.1 Introduction

There is a wide variety of technologically important oxide single crystals, which find applications in diverse fields. These are employed as laser hosts, in nonlinear optical devices, optical wave guides and other components in optical communications, in memories, and numerous other applications. Many of the oxide crystals had been extensively used as substrates to prepare high T_c superconductors, blue light emitting lasers, magnetic bubble memories, and so forth. Lithium niobate [1–2], cadmium tungstate, sapphire, ruby, garnets [3], lithium tantalate, lead molybdate [4], bismuth germanate, potassium niobate, barium titanate [5], bismuth silicate [6], and others are being extensively used for making important devices. We shall discuss recent advances in growth and structural characterization of lithium niobate and bismuth germanate (BGO) crystals.

Lithium niobate (LiNbO_3) is an opto-electronic material. LiNbO_3 crystals with high degree of perfection, optical homogeneity, correct stoichiometry, and single ferroelectric domain are required for fabrication of surface acoustic wave devices (SAW), optical wave guides, photonic switches in telecommunication, as piezoelectric materials in tomography, and as second harmonic generators (SHG) [1]. LiNbO_3 single crystals have large electro-optic coefficients and do not need application of a high voltage. These crystals have received much attention as phase conjugate wave generators and real-time read-write holograms using the photorefractive effect [7]. Generally, to improve properties, LiNbO_3 crystals have been doped with transition metals. Iron doping has been utilized for making devices like second harmonic generators. Crystals grown from congruent melts are inherently metastable at room temperatures. Therefore, a strict control on composition of the charge for crystal growth experiments and physical parameters like temperature are very crucial for growing good quality single crystals.

Bismuth germanate is widely used as a scintillator due to its attractive properties like nonhygroscopic nature, high atomic number (Z), short decay time, and extremely short afterglow [8–15]. BGO scintillators are being widely used for positron emission tomography [16,17], mammography [18], X-ray computed to-

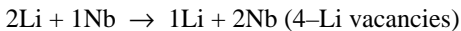
mography [19,20], calorimetry [21,22], and oil well logging [23]. Only colorless crystals grown from high purity oxides are useful as scintillators [9]. Crystals grown from low purity Bi_2O_3 and GeO_2 are yellowish in appearance. Study of influence of doping elements on sensitivity has shown that Gd and Ti improved sensitivity by 4% above that of pure BGO [24–26]. The fluorescence from BGO is similar to that reported for other materials where bismuth is present as a dilute activator ion. The BGO luminescence is assigned to $^3\text{P}_1 \rightarrow ^1\text{S}_0$ transitions of Bi^{3+} [8]. Fluorescence spectra of BGO gives a peak at a wavelength of 483.3 nm.

High resolution X-ray diffraction topography and diffractometry have been found to be useful for the direct observation of lattice defects in single crystals and provide valuable feedback for improving structural perfection of crystals [27].

In this chapter, we review recent advances made in growth and characterization of nearly perfect lithium niobate and bismuth germanate crystals.

12.2 Crystallographic Structure

At room temperature LiNbO_3 has rhombohedral structure. It belongs to the $3m$ point group and $R3c$ space group. In the $R3c$ space lattice Nb atoms occupy (0,0,0) positions, Li atoms occupy (0,0,1/4) positions and O atoms occupy (4,1/3,1/2) positions. The unit cell dimensions are: $a = 5.1494 \text{ \AA}$ and $c = 13.8620 \text{ \AA}$. At 1160°C , LiNbO_3 undergoes a first order phase transition. The polar ferroelectric $3m$ symmetry transforms into nonpolar paraelectric 3m symmetry above the Curie temperature. There is a substantial change in the volume of the unit cell at the phase transition due to which strain is produced in the crystals as these cross the Curie temperature. This strain has to be handled very carefully during growth experiments as it can lead to cracking or a high level of residual stress in the crystals. Lithium niobate is known to grow with lithium deficiency. The model for Li deficiency is as follows:



This results in a total of 5.9% Li missing from its regular sites and this is called antisite defects.

Menzer (1931) showed that $\text{Bi}_4\text{Ge}_3\text{O}_{12}$ (BGO) is isomorphous with $\text{Bi}_4\text{Si}_3\text{O}_{12}$ (eulytine) [28]. Eulytine belongs to the $\bar{1}43d$ space group [29,30]. Durif and Averbuch-Pouchot (1982) refined the atomic positions of BGO [30]. The cubic unit cell has a lattice constant, $a_0 = 10.497 \text{ \AA}$ and contains four formula units. Ge^{4+} with site symmetry $\bar{4}$ has an almost regular tetrahedral coordination of O^{2-} ions at distance 1.740 \AA . Bi^{3+} , site symmetry 3, is coordinated by three O^{2-} ions at 2.160 \AA and three O^{2-} ions at 2.605 \AA , in a highly deformed octahedron. One tetrahedron shares points with eight octahedra. One octahedron shares edges with three other octahedra and shares points with six tetrahedra. An interesting aspect of BGO is the presence of “holes” in its structure. These are empty sites with point symmetry

4 and are enclosed tetrahedrally by O^{2-} ions at 2.47 \AA [31]. No cleavage planes have been observed for BGO [32]. The atomic absorption coefficient for X-rays of wavelength 0.7 \AA is very high and calculated as 710 cm^{-1} .

12.3 Growth of Lithium Niobate Crystals: Earlier Work

Reisman and Holtzberg (1958) gave the first phase diagram of the system $\text{Li}_2\text{O-Nb}_2\text{O}_5$ [33]. However, Svaasand et al. (1973) worked out the phase diagram of LiNbO_3 , which was widely accepted [34]. Lerner et al. (1968) made a substantial improvement, showing that LiNbO_3 has a fairly large solid solution ranging from 44 to 55 mol % of Li_2O . The maximum melting temperature does not occur at the stoichiometric composition but rather at 48 to 49 mol % of Li_2O and tends to grow with variable stoichiometry [35]. Starting with Ballman in 1965, several investigators have carried out the growth of single crystals of LiNbO_3 [36]. The LiNbO_3 crystals were generally grown by the Czochralski (Cz) method, although other methods such as Verneuil, Bridgman/Stockbarger, and Stepanov techniques are possible and have been tried [37,38]. The materials aspect of LiNbO_3 were dealt with in the well-known series of five papers from the Bell Laboratories by Nassau et al. (1966) [39] and Abrahams et al. (1966) [40]. They could grow successfully single domain crystals by *in situ* poling during the growth. Baumann et al. (1993) had grown crystals with melt composition varying from 48.46–48.49% Li_2O [41]. They determined the congruent melt composition as $48.470 \pm 0.005 \text{ mol \% Li}_2\text{O}$ for the [00.1] growth direction. They have analyzed the compositional homogeneity along the crystal by analyzing the orthoscopic fringe patterns and found that the composition of the congruent melting point shifts from the stoichiometrical composition towards the niobium rich side. The precise congruent composition reported in the literature varies between 48.3 to 48.6 mol % Li_2O . Different methods were used to determine the exact value of the congruent composition by investigation of compositional variation on physical properties like Curie temperature [42,43], surface acoustic wave velocity [44], refractive index [45–48], birefringence [49], and phase matching temperature of the second harmonic generation [48,49].

Single crystals of high structural perfection without compositional inhomogeneities are required for device fabrication. The most serious problem concerning the quality of LiNbO_3 is the spatial variation of birefringence, which is considered to be related to thermal stress and compositional variation during crystal growth. Studies on spatial variations of the birefringence using optical techniques have been made by several workers [48,49]. Reich et al. (1991) studied the effect of electrical field on the growth of LiNbO_3 crystals [50]. Stoichiometry control plays a key role in property tailoring. To optimize the stoichiometry and grow nearly perfect crystals, we have grown LiNbO_3 crystals with variable composition from 45 to 55 mol % Li. X-ray diffractograms were recorded for each composition. It was seen that for a small change in Li/Nb ratio there was an appreciable change in the peak intensity particularly for 11.1 type reflections. Though

the bulk powder was LiNbO_3 , only Nb concentration varied in the different composition powders. The excess Nb concentration in the crystals gave different colors to the crystals.

12.4 Growth of Bismuth Germanate Crystals: Earlier Work

Nitsche (1965) had grown for the first time bismuth germanate ($\text{Bi}_4\text{Ge}_3\text{O}_{12}$) single crystals as a replacement for the bismuth silicon oxide (eulytite) [32]. Nitsche used a crucible-free technique as it was found to react with platinum. BGO crystal rods with a diameter of 4–5 mm and lengths of 10–12 mm were grown successfully. These were yellow in color and X-ray Laue patterns established that these were single crystals. It was found that the crystal was stable in air but dissolved easily in concentrated HCl. Research on the growth of good quality and large size BGO crystals was started after this initial work [51–53]. Dickinson et al. (1972) grew BGO crystals by the Cz method in air, thereby, suppressing the corrosion of the platinum crucible [54]. They could grow BGO crystals of 15 mm diameter and 25–38 mm length. These crystals were transparent and nearly colorless with a slightly yellowish tinge. Seed rotation rate was optimized at 30 rpm and the pulling rate was kept in the range of 3–4 mm/h. They used X-ray diffraction analysis to confirm the crystallinity. Mass spectrographic analysis showed that the total impurity concentration in the crystals ranged from 35 to 85 ppm. They found silicon was the major cation contaminant, and chlorine was the major anion impurity. In addition, aluminum, potassium, and calcium were detected in the 1–20 ppm range. Platinum contamination was below 1 ppm level.

Weber and Monchamp (1973) showed BGO as a laser host crystal for rare earth and iron group activator ions and also as a scintillator material [8]. This was the first paper to propose that BGO can be used as a scintillation material. The group compared $\text{Bi}_4\text{Ge}_3\text{O}_{12}$ with $\text{Bi}_{12}\text{GeO}_{20}$ and showed its superiority. Takagi et al. (1981) studied the influence of crystalline defects on scintillation conversion efficiency [24]. It was found that the efficiency decreases by shrinkage voids and impurities. This work suggested that shrinkage voids may be eliminated by making the growth interface flat and purifying the crystals. It was shown that the sensitivity can be brought up to 12% of that of NaI (Tl) by eliminating voids and purifying the crystals. Later, Barnes (1984) studied the influence of impurities on the quality of bismuth germanate, particularly on the scintillation property [55]. Al, Ca, Fe, Mg, Si, and Pt were among the major impurities investigated in Cz grown crystals. The impurity tolerance in the raw material was set at 1 ppm level.

Schmid et al. (1984) grew BGO crystals by the heat exchanger method (HEM) [56]. They compared their crystals with those grown by the Cz method. The crystals were transparent and free of dislocations. Control of stoichiometry was found to be a problem in the Cz grown crystals as there are a few more stable Bi_2O_3 - GeO_2 phases according to the phase diagram [54,57]. Schmid and co-workers suggested that variations in stoichiometry of the melt is less in the HEM method than that found in the case of the Cz method. In the Cz method, the melt surface had a

local temperature gradient and, therefore, secondary phases could be trapped in the grown crystal. These were not present in the crystals grown by the HEM method.

Van Hoof et al. (1985) characterized Bridgman grown crystals by X-ray diffractometry and topography techniques [58]. They found that the half width of the diffraction curves in the central region was only 10 arc sec, and for the entire crystal it was ~ 20 arc sec. They found that the Bridgman grown BGO crystals were dislocation free except at the outer edges. The dislocation density was estimated as less than 10 cm^{-2} at the center and about $10^2\text{--}10^3 \text{ cm}^{-2}$ at the outer edges. However, for Cz grown BGO crystals half widths of the diffraction curves were about 16 arc sec for the central region. Low angle boundaries were observed in the crystals. For the entire crystal the half width was 500 arc sec and the dislocation density was found to be in the range: $1\text{--}1.5 \times 10^4 \text{ cm}^{-2}$, which was almost 100 times of that observed with the Bridgman grown BGO crystals. X-ray diffraction topographs recorded with crystals grown by the Bridgman as well as Cz methods supported the results obtained by diffractometry [58]. Allegretti et al. (1989) also showed that the Bridgman grown BGO crystals exhibit less dislocation density than the Cz grown BGO single crystals [59]. Smet et al. (1988) found that the yellowish color of crystals was due to change in stoichiometry and also caused by impurities [60]. The formation of voids and inclusions was also observed in Bridgman grown BGO crystals. They characterized the crystals by the etching method. BGO crystals grown from the melt were always bounded by $\{112\}$ and $\{\bar{1}\bar{1}\bar{2}\}$ crystallographic facets. The formation of inclusions was concentrated at the edges of the growth facets and impurity segregation was maximum near the center of the facets. Van Enckevort et al. (1990) had also characterized Bridgman grown BGO single crystals by the etching method [61]. $1\text{N}\text{--}4\text{N}$ HCl etchant was used in this case. They also used the birefringence microscopy technique. Edge dislocations were observed in the Bridgman grown BGO single crystals.

Takagi et al. (1986) studied the effect of growth conditions on the shape of BGO single crystals [62]. They used the Cz method to grow BGO crystals. The rotation rate was varied from 27 rpm to 50 rpm. They observed an optimized rotation rate of 40 rpm to achieve a stable shape of the crystal. Otherwise the crystals were twisted and imperfect. By varying the position of the rf coil it was observed that the crystal shape could be improved by making the upper part of the crucible hotter than the lower part. They also suggested that the use of an after-heater on a crucible is an effective way of suppressing the heat loss from the melt and the crystal surfaces, and also prevented twisting of the crystal. Horowitz et al. (1986) studied the effect of precipitates and yellow color on crystal performance [63].

Ivleva et al. (1987) grew some of the multi-oxide single crystals like LiNbO_3 , $\text{Ca}_3(\text{VO}_4)_2$, $\text{Bi}_{12}\text{SiO}_{20}$, $\text{Bi}_4\text{Ge}_3\text{O}_{12}$, and $\text{Bi}_{12}\text{GeO}_{20}$ by Stepanov's technique [38]. In this method the melt is transported via a feed capillary to the meniscus on the top plane of a shaper. By this technique crystals of desired shapes can be grown. However, the quality of these crystals was not found to be high enough for device applications. Gopalkrishnan et al. (1994) made an attempt to grow BGO crystals by the Float zone method [64]. Later, this group made XPS studies on BGO and BSO crystals grown by the Cz and Float zone methods and found that the surfaces

of these crystals were contaminated [65]. The eulytite crystals are chemically more robust to degradation than the sellinite crystals. A research group at IIC, Novosibirsk (1996), (2001) has grown very large size BGO single crystals, weighing more than 30–50 kg, by the Low Thermal Gradient Cz (LTG Cz) technique [66]. They suggested that the LTG Cz method may be a suitable method for growing bismuth germanate single crystals of device quality. We have used this technique to grow nearly perfect BGO crystals [67–71]. These crystals have been extensively characterized by high-resolution X-ray diffraction techniques.

12.5 A Crystal Growth System for Cz Growth of Nearly Perfect Crystals

A versatile crystal puller designed, developed, and fabricated in our laboratory is shown in the Fig. 12.1. It has been extensively used for growth of single crystals using a resistance heating furnace as well as an rf induction heating system [72,73]. It is possible to continuously vary the seed pulling rates by a factor of ten around a given nominal growth rate. Different absolute values of growth rates can be obtained by selecting an appropriate set of gears. A high level of uniformity and smoothness of pulling motion is ensured by employing two stainless steel rods with surface flatness within $\pm 5 \mu\text{m}$ as guides to the motion.

The salient features of the crystal growth system are shown schematically in Fig. 12.2. The platinum crucible (C), ceramic holder (CH), and Pt / Pt-10% Rh thermocouple (TC) are enclosed in a quartz tube (QT). A window (W) had been provided in the quartz tube for viewing the crystal while it is being grown. The crucible assembly is surrounded by an rf coil (RF) for melting the charge. A platinum seed holder (SH) was fixed at one end of a ceramic rod (PR). The other end of the ceramic rod is fixed to a seed pulling and rotating assembly. A resistive furnace (F) was placed above the crucible set-up to ensure controlled post-growth cooling of the crystals.

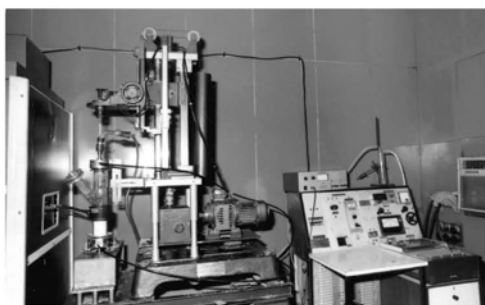


Fig. 12.1. A photograph of a crystal growth system designed and developed at NPL (National Physical Laboratory, New Delhi, India)

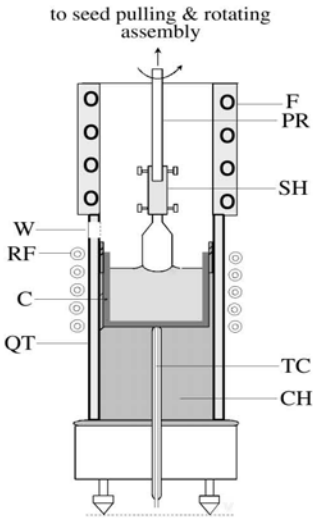


Fig. 12.2. A schematic line diagram of the crucible set-up of the crystal growth system developed at NPL

12.5.1 A crystal growth system for low thermal gradient Czochralski (LTG Cz) technique

The LTG Cz method employed for successful growth of high quality BGO crystal is a modification of the conventional Cz method [74]. It is well-known that in the usual Cz growth of crystals the temperature gradient across the seed–melt interface is important in deciding the rate of growth and the perfection of the grown crystals. The temperature gradient is particularly important for the growth of oxide single crystals [75]. For the growth of crystals like BGO, a low thermal gradient has enhanced the perfection of the crystals to the state-of-the-art level [68]. To achieve a low thermal gradient in Cz growth, special features have to be incorporated in the growth system. Figure 12.3 shows such a crystal growth system designed and developed at the Institute of Inorganic Chemistry, Novosibirsk, Russia. A block diagram of the crystal growth system is shown in Fig. 12.4. The main subassemblies of this system are: (1) the growth chamber SS; (2) the furnace F; (3) the crucible C; (4) the crystal pulling and rotation mechanism SH; and (5) the power supply and electronic controls [67].

The crystal growth chamber (SS) is essentially a double-walled stainless steel vertical cylinder 600 mm in diameter and 900 mm high. The crucible and the resistance furnace are housed in this chamber. Doors are provided to this chamber on two opposite vertical sides for taking out and putting in crucibles. For viewing the interior of the chamber, two windows, one on each door, are fixed. The chamber is mounted on a base plate. A weighing mechanism (WM) consisting of an electronic balance to weigh the crucible and charge is located below the base plate.



Fig. 12.3. A photograph of the crystal growth system employed for growth of crystals by the low thermal gradient Cz method

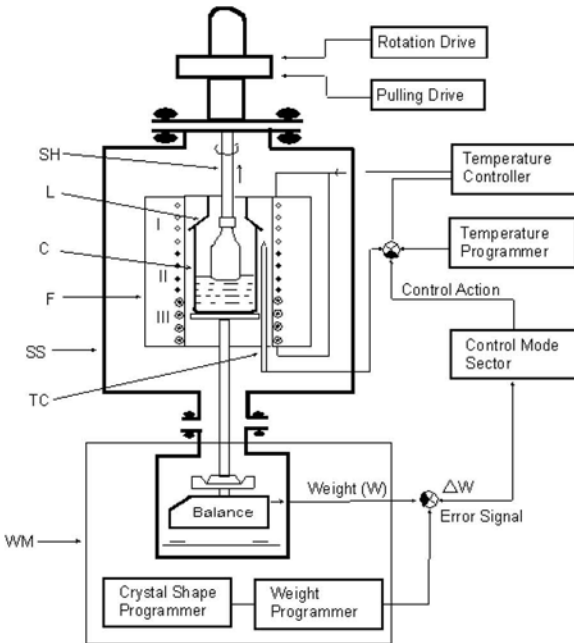


Fig. 12.4. A block diagram of the crystal growth system used for growth of crystals by the low thermal gradient Cz method

A three-zone muffle furnace (F) has been used. The electrical power fed to all the zones is controlled independently. The temperature of each zone is monitored by positioning the thermocouples (TC) radially to the furnace.

Cylindrical-shaped platinum crucibles (C) are employed. In some of the experiments for the growth of BGO crystals, crucibles with diameters of ~70 mm and lengths of ~150 mm were used [68]. The crucible is placed on one arm of the microbalance of the weighing mechanism. A tightly fitting platinum lid (L) was employed to cover the top of the crucible. This arrangement helps in maintaining the low temperature gradient above the melt.

A pull rod made of ruby, with a diameter of ~10 mm and length of ~35 cm, is fixed to the pulling assembly. A cylindrical platinum seed holder is attached to the other end of the pull rod. By varying the frequency of the input power of the motor, the pulling rates can be varied. Six different pull rates in the range of 0.1 mm/h to 6 mm/h and three different seed rotation speeds in the range of 7.5 rpm to 100 rpm are possible.

The central electronic control unit consists of: (1) a Seed Rotation Control Unit (SRCU); (2) a Seed Pulling Control Unit (SPCU); (3) an Electronic Weight Balancing Unit (EWBU); (4) a Crystal Weight Programmer Unit (CWPU); (5) an Error Signal Feedback Unit (ESFU); (6) Recording Instruments (RI), and (7) Temperature Controller-cum-Programmer Units (TCPU). These units are employed to control all the essential functions.

12.6 High Resolution X-ray Diffractometers

High resolution X-ray diffraction techniques are being extensively employed to evaluate crystalline perfection of single crystals and to characterize crystal defects [76]. In these experiments, the exploring X-ray beam is required to be highly collimated and monochromated. The divergence of the beam has to be reduced, keeping in view the theoretical half widths of the diffraction curves to be recorded. Ideally, it should be much lower than the theoretically expected half widths. Such systems are now available [77]. However, even if the divergence is comparable to the half width, the system can be used effectively. To achieve nearly parallel X-ray beams, combinations of X-ray sources with small sizes (microfocus or fine focus), long collimators, slits with small openings, and monochromator-collimator crystals are used.

Essential features of a double crystal X-ray diffractometer and a five crystal X-ray diffractometer, which were employed to characterize BGO and LiNbO₃ crystals, respectively, in the authors' laboratory are described in the following.

12.6.1 Double crystal X-ray diffractometer

Figures 12.5 and 12.6 show a photograph and a schematic line diagram of the double crystal X-ray diffractometer, respectively. The diffractometer has been de-

signed and developed at NPL [78]. It consists of: (1) an X-ray source; (2) the monochromator stage; (3) the specimen stage; (4) the traversing mechanism, and (5) the detector and the counting systems. A fine focus X-ray source was employed as the source of X-rays. The source size was $0.4 \times 0.4 \text{ mm}^2$ after foreshortening. A 50 cm long collimator fitted with a slit (S1) is used to reduce the divergence of the beam to ~ 300 arc sec in the horizontal plane, which is the plane of diffraction. One of the slits is vertical and is used to reduce the divergence in the horizontal plane. The other slit is horizontal and controls the vertical divergence. The jaws of both the slits are made of $\sim 1.6 \text{ mm}$ thick tantalum sheet. The edges of the jaws are prepared carefully by grinding and lapping.

The X-ray beam emerging from the first collimator slit (S1) falls on a plane (111) silicon monochromator-collimator. The crystal was mounted on a tilt stage, which in turn is fixed on the top of a turntable, which is essentially an optical spectrometer. The diffracting (111) planes of silicon were oriented to lie in a vertical plane. The angular orientation of the monochromator with respect to the collimated beam was adjusted for Bragg diffraction from (111) planes, which were nearly parallel to its surface. The diffracted beam from the monochromator contained well resolved $K_{\alpha 1}$ and $K_{\alpha 2}$ components of the characteristic K_{α} doublet. A

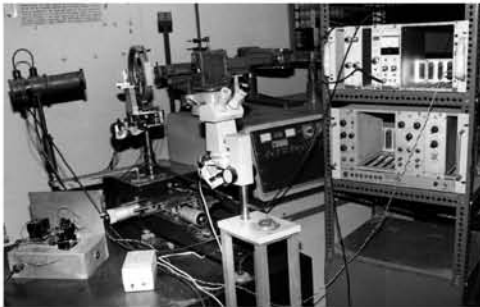


Fig. 12.5. A photograph of the double crystal X-ray diffractometer designed and developed at NPL

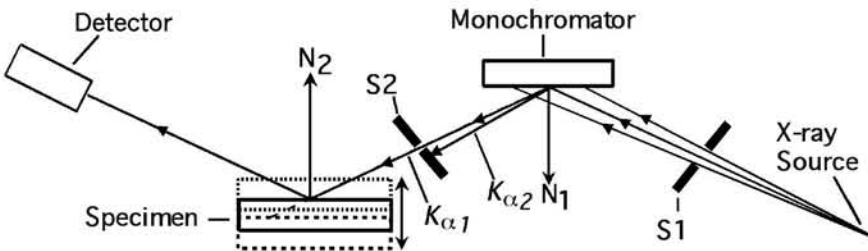


Fig. 12.6. A schematic diagram of the double crystal X-ray diffractometer developed at NPL

second collimator slit (S2), is placed in the path of the diffracted beam. The vertical slit was positioned to allow only the K_{α_1} beam to pass through. The K_{α_2} beam and the residual direct beam were blocked. The K_{α_1} beam so isolated was used as the exploring beam. The height of the exploring beam can be fixed as per the requirements of an experiment.

The specimen occupied the second crystal stage of the diffractometer. In all the experiments reported in the present work, the specimens were oriented for diffraction in (+, -) symmetrical Bragg geometry. However, this stage can be used to perform the experiments in Laue geometry also. The specimen was mounted on a tilt stage or a vertical circle goniometer, which is fixed on top of a traversing mechanism. This entire assembly is mounted on a central turntable, which has been designed and developed at NPL. This turntable is able to give small angular rotations of about 0.06 arc sec to the crystal around a vertical axis. The angular rotation of the crystal in the plane of diffraction (θ -motion) is measured accurately from the deflection of a graticule fixed at the end of a 1 m long radial arm of the turntable. The diffractometer was placed on a heavy granite surface plate. The top surface of the granite plate is flat within $\pm 8 \mu\text{m}$.

A scintillation counter designed, developed, and fabricated at NPL was used as the X-ray detector. In this counter a NaI (Tl) crystal was used as the scintillator. The diffractometer can be used for recording high resolution X-ray diffraction (rocking) curves and topographs, making absolute integrated intensity measurements and for measuring the radius of curvature of specimen crystals [67,68,71,79,80].

12.6.2 Five crystal X-ray diffractometer

A five crystal X-ray diffractometer, designed, developed, and fabricated at NPL (National Physical Laboratory, New Delhi, India) has been used for the high resolution X-ray diffractometric and topographic evaluation of crystalline perfection [77]. Figure 12.7 shows a photograph of this diffractometer. The results reported in this article were obtained by employing the diffractometer in a three crystal configuration. A schematic line diagram of the diffractometer in the three crystal configuration is shown in Fig. 12.8. The diffractometer was set in (+, -, +) geometry. A well collimated X-ray beam was achieved by employing a combination of a fine focus X-ray source, a long collimator, and two plane silicon monochromator-collimator crystals, which were set in (+, -) geometry of Bonse-Hart type [81]. The X-ray source and collimator details are the same as in the case of the double crystal X-ray diffractometer described above. With this arrangement, the K_{α} characteristic radiation is resolved into K_{α_1} and K_{α_2} components. Highly monochromated and well collimated K_{α_1} beam was isolated with the help of a fine slit and was used as the exploring X-ray beam. In the present set of investigations Mo K_{α_1} radiation was used. The specimen crystals formed the third crystal of the diffractometer. For X-ray diffractometric and topographic studies of crystals in



Fig. 12.7. A photograph of the five crystal X-ray diffractometer, designed, developed, and fabricated at NPL

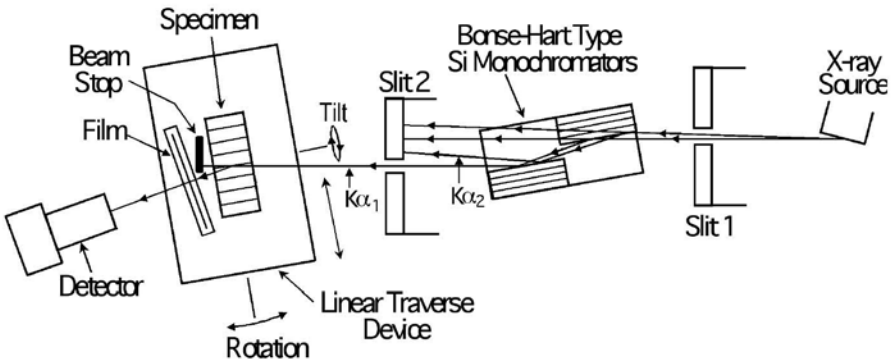
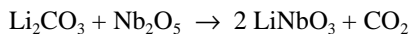


Fig. 12.8. A schematic diagram of the five crystal X-ray diffractometer in the three crystal configuration

transmission geometry, these were thinned down to 0.4 mm. Great care has been taken in mounting these thin wafers so that no appreciable strain is introduced during the mounting process [82]. Diffraction from (11.0) lattice planes was studied in symmetrical Laue geometry. These planes are normal to the growth direction [00.1]. The exploring X-ray beam had a width of 0.2 mm in the plane of diffraction and the height was adjusted according to the size of the sample.

12.7 Synthesis of Lithium Niobate and Bismuth Germanate Powders

The LiNbO_3 charge was prepared by the solid state reaction of Li_2CO_3 and Nb_2O_5 at 1000°C for 24 h according to the reaction:



To optimize the correct stoichiometry, Li_2CO_3 and Nb_2O_5 varying from 45 mol % to 55 mol % were mixed to prepare the charge. X-ray diffractograms were recorded for each charge composition. The phase change during the heating as well as the cooling cycle until the melting point were confirmed by DTA and TGA curves. A typical DTA curve is shown in Fig. 12.9.

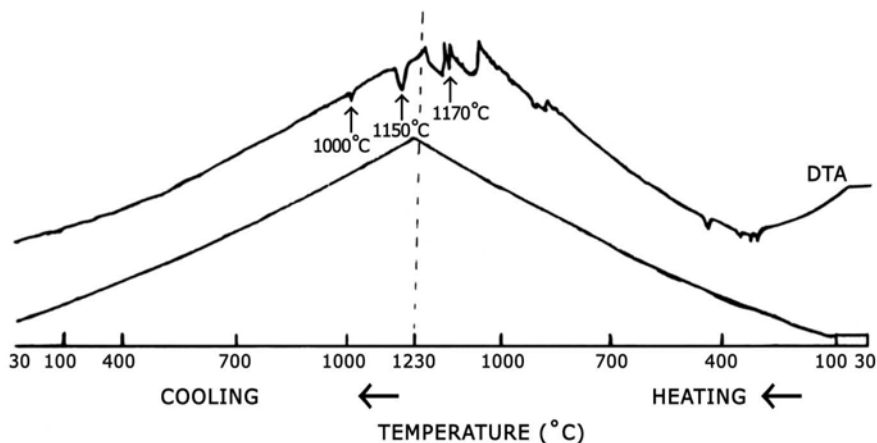
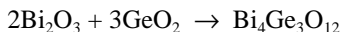


Fig. 12.9. A typical DTA curve recorded for lithium niobate powder

Bismuth germanate powder was prepared by high temperature solid-state reaction of Bi_2O_3 and GeO_2 powders. The binary system of Bi_2O_3 and GeO_2 can produce several stable compounds on reaction [31,53,57]. The molar ratios of the two constituents in these compounds are 1:1, 2:3, 6:1, 7:1, and 1:3. For the present series of experiments, the two powders were carefully weighed with molar ratio of 2:3 to achieve the desired phase with the composition $\text{Bi}_4\text{Ge}_3\text{O}_{12}$. The chemical reaction is given by:



The two powders in the molar ratio 2:3 were thoroughly mixed for 24 h. The purity of both the chemicals were 99.99%. The mixture was sintered at 850°C for 8 h. After the reaction, charge was cooled and once again powdered, remixed, and again sintered at 850°C for 8 h. The crystallographic phase was confirmed by powder X-ray diffraction. For the crystal growth experiments this powder was used as the charge material.

12.8 Growth of Nearly Perfect Crystals of LiNbO_3 and BGO

12.8.1 LiNbO_3 single crystals

LiNbO_3 single crystals were prepared by varying the molar fractions of Li_2CO_3 and Nb_2O_5 . The mol % of Li was varied from 45% to 55%. X-ray diffraction patterns were recorded to confirm all the compositions. Single crystals were grown with different Li to Nb ratios. The crystals were grown along the $[00.1]$ direction in air using platinum crucibles 50 mm in diameter and length of about 55 mm [73]. Experimental parameters were optimized for growth of nearly perfect crystals. The seed pulling rate was kept at ~ 10 mm/h and the rate of seed rotation was maintained at 30 rpm. Since these crystals have a first-order phase transition below melting point, these can easily crack during cooling to room temperature after the growth. The post-growth cooling rates were optimized in the following manner. After the growth, the crystals were first cooled down to about 900°C at the rate of 20°C/h over a period of 10–15 h in rf heating. Thereafter, the crystals were pulled up into the resistive furnace (F), which was positioned above the crucible set-up, and was preheated to 900°C . The crystal boules were cooled down to room temperature in about 30–40 h. The grown crystals were about 20 mm in diameter and 40 mm in length. The colors of the as-grown crystals for different compositions were slightly different. The colors of the as-grown crystals in the lower Li percentage side were light green, whereas when Li percentage was high the crystals were dark brown in color. Colorless and transparent crystals of LiNbO_3 were obtained for the charge composition of 48.6 mol % lithium oxide. In the as-grown stage these were pale yellow in color. The crystals grown under air are known to be deficient in oxygen. To remove oxygen deficiency, the crystals were heated under flowing oxygen at 1000°C for about 48 h. The crystals became colorless and transparent after annealing. Fig. 12.10 shows some of the typical crystals grown in these experiments.

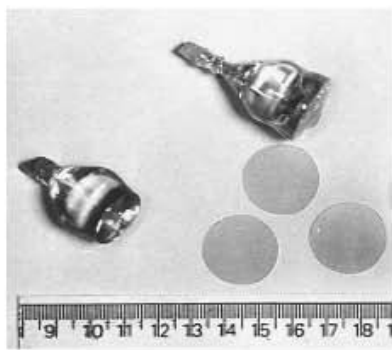


Fig. 12.10. LiNbO_3 crystals grown along the $[00.1]$ direction. A few polished wafers cut perpendicular to the growth direction are also shown.

Thin wafers with surfaces perpendicular to the [00.1] growth direction were cut using a diamond ID cutter. These wafers were lapped and polished to a thickness of ~ 0.4 mm for characterization by X-ray diffraction and optical examination. The mechanically damaged surface layers were etched off in a hot mixture of two parts of HF and one part of HNO_3 for about 2–5 min. at 100°C . This was found to be adequate to get damage-free crystals. High resolution X-ray diffractometry helps in giving the feedback in these experiments.

Iron doped LiNbO_3 crystals are particularly useful for nonlinear optical applications, such as in second harmonic generators. They were grown by using the technique described above. 5 N pure Fe_2O_3 powder was used as a dopant. Single crystals with doping level of 0.05 mol % iron have been grown. The doped crystals were pinkish in color. A doping level of more than 0.05 mol % Fe_2O_3 resulted in complete blackening of the crystal boules.

Special steps are needed to grow LiNbO_3 crystals, which have a single ferroelectric domain in their entire volume. Generally, as-grown crystals contain several small ferroelectric domains. As described later, high resolution X-ray diffraction topography has been employed to reveal ferroelectric domains. To obtain mono-domain crystals, poling was carried out *in situ*, by applying a high DC electric field across the crystal–melt system along the growth direction [00.1]. The crucible was connected to the positive polarity, whereas the seed holder was maintained at negative voltage. Experiments were performed with electric current densities in the growing crystal varying from 1.5 mA/cm^2 to 2.5 mA/cm^2 . X-ray topographs provided the feedback on the mono-domain nature of grown crystals. The results of investigations reported above have shown that colorless transparent pure crystals and iron doped crystals can be grown along the [00.1] direction in air for the charge composition of 48.6 mol % lithium. The crystalline perfection of LiNbO_3 crystals was found to be quite good, as indicated by the small half width of their diffraction curves. The traverse topographs of these crystals show the presence of ferroelectric domains if these are present. Adequate poling, however, enables growth of nearly perfect mono-domain crystals.

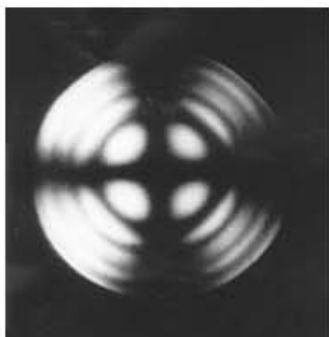


Fig. 12.11. A conoscopic interferogram for white light of LiNbO_3 sample cut perpendicular to the growth axis

To assess the optical quality of the crystals, conoscopic interferograms or optic-axis pictures were recorded using a high-resolution microscope. These were recorded with monochromatic as well as white light. The specimens were cut perpendicular to the growth axis [00.1]. Figure 12.11 shows a typical interferogram recorded with white light. The conoscopic interferogram recorded showed perfect symmetry and were quite sharp. This implies that the crystals exhibit pronounced birefringence and the optic axis is perpendicular to the wafer surface. This property is required for phase matching conditions in devices.

12.8.2 Bismuth germanate single crystals

For growing BGO crystals, the temperatures of the three zones of the LTG furnace were set near the melting point of the BGO (1040°C) in TCPU of control panel. The temperature of the middle zone was kept a little bit higher than that of the other two zones. The temperature profile of the furnace above the melt was measured to ensure a low thermal gradient. A typical temperature profile is shown in Fig. 12.12. The melt surface was taken as a reference point. The temperature is nearly constant over a length of ~ 4 cm above the melt surface and after that a temperature gradient of nearly $1.2^{\circ}\text{C}/\text{cm}$ is observed. It can be seen that the thermal gradient is quite low. This enables one to grow crystals in low thermal gradient conditions, a salient feature of these experiments.

The crystal growth experiments were started by weighing of the crucible carrying the charge. This weight was balanced by appropriate electronic weights in the other arm (EWBU). The powder was heated at a rate of $250^{\circ}\text{C}/\text{h}$ till the entire powder was melted at 1040°C . The melt temperature was stabilized for a few hours. Initially, only the platinum seed holder without the seed crystal was dipped into the melt to optimize the temperature of the melt for crystallization. The

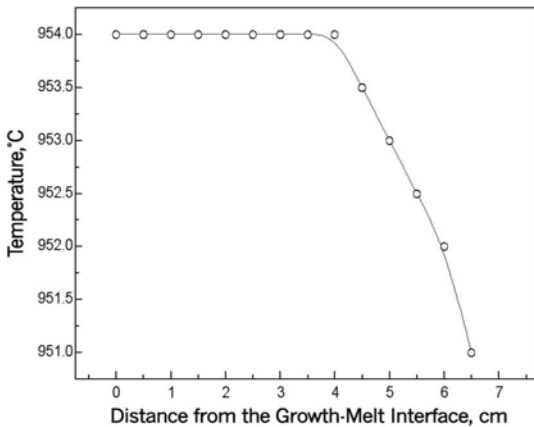


Fig. 12.12. A typical temperature profile of the low thermal gradient furnace

temperature was adjusted until crystallization was possible at its tip. The seed holder was pulled up slightly above the melt after dipping to cool the drop of melt at its tip. It was dipped again and the temperature of the melt was optimized by observing the growth of the drop. If the temperature of the melt is higher than the desired one, the drop will melt. If on the other hand, the temperature of the melt is lower than the optimum value many nucleation points will be created. So, the temperature of the melt was adjusted carefully to ensure that the droplet starts growing in a controlled manner. At this stage, the platinum seed holder was pulled out and a T-shaped Z-cut bismuth germanate seed crystal was fixed in the platinum seed holder with its axis along [001]. The growth experiment was initiated after dipping the seed and attaining the thermal equilibrium.

During the crystal growth experiment, the diameter of the crystal was controlled by the automatic diameter control mechanism of the crystal growth system. The rate of increase in crystal weight ($\Delta g/\Delta t$) had been programmed for a pre-set desired diameter of the crystal to be grown.

If S_k is the area of crystal cross-section (in cm^2), ρ is the density of the melt (in g/cm^3), V_p is the seed pulling rate (in cm/h), $\Delta H/\Delta t$ is the rate of decrease of melt height in the crucible (in cm/h). The value of $\Delta H/\Delta t$ is given by:

$$\frac{\Delta H}{\Delta t} = \frac{\Delta g / \Delta t}{\rho S_c} \quad (12.1)$$

Here S_c = cross-sectional area of the crucible. It can be easily shown that S_k is given by:

$$S_k = \frac{\Delta g / \Delta t}{\rho(V_p + \Delta H / \Delta t)} \quad (12.2)$$

Before the start of the crystal growth experiment, the growth rate ($\Delta g/\Delta t$) was calculated and the system was programmed accordingly. The rate of increase in crystal weight ($\Delta g/\Delta t$) for growing crystals of diameter 40 mm, has been worked out as 30 g/h. This growth rate was set in the CWPU module of the crystal growth system. During the growth, if there is any deviation in the cross-section of the crystal from the desired size, the error feedback control system ESFU modifies the power to the furnace and hence the crystal cross-section. For example, if there is an increase in cross-section of the crystal from the desired value, the temperature of the melt is increased suitably. Similarly, if the actual cross-section of growing crystal is smaller than that of the desired size, the temperature of the melt is decreased. The cross-section of the crystal can also be controlled by changing the seed pulling rate. However, in these experiments, the seed pulling rate was kept constant and the cross-section of the crystal was controlled by controlling the temperature of the melt. It may be mentioned that the weighing mechanism is quite sensitive and its limit of detection is 10 mg in 1 kg or 10 ppm level.

In a typical experiment, target diameter of crystal was kept as ~40 mm and the length aimed at ~80 mm. The growth experiments were programmed to run for nearly 33 h. The first five hours were utilized for growing the cone portion after the seed growth condition was attained. This stage is over once the desired di-

iameter of ~40 mm is reached. Thereafter, the growth experiment was continued for 28 h and the diameter was maintained at this value. The seed pull rate was fixed at the optimum value of 2.5 mm/h. The seed rotation rate was 38 rpm, which had been optimized separately. After the growth was over, the crystal was cooled to room temperature at a rate of 150°C/h.

Figure 12.13 shows a photograph of a typical boule grown under these conditions. This crystal was ~40 mm in diameter and ~80 mm in length. The crystal was colorless in appearance. Further, it can be seen that the shape is nearly circular at the top and almost rectangular at the bottom without any twist. The upper portion of the crystal towards the seed appears to be slightly bigger than the rest of the crystal. As mentioned above, initially the crystal diameter is increased gradually to attain the desired size of ~40 mm diameter. Thereafter, the automatic weight control feedback loop was utilized to maintain the diameter. This system essentially ensures a constant rate of weight addition. The cross-sectional area of the crystal remained reasonably constant. However, the cross-section is not absolutely circular due to faceting and appears to be of different dimensions when viewed from different directions. This is the primary reason why the diameter appears to be smaller in the middle region of Fig. 12.13. Depending upon this faceting, different crystals have slightly different appearance when viewed from different directions in spite of good weight control.



Fig. 12.13. A typical BGO crystal grown by low thermal gradient Czochralski method along the [001] direction

12.9 Evaluation of Perfection of Lithium Niobate and Bismuth Germanate Single Crystals by High Resolution X-ray Diffractometry and Topography

High resolution X-ray diffractometry and topography experiments were performed to evaluate the crystalline perfection of lithium niobate and bismuth germanate

single crystals and to directly observe and characterize defects in the same by employing multi-crystal X-ray diffractometers.

12.9.1 Characterization of lithium niobate crystals

For evaluation of the perfection of LiNbO_3 crystals a five crystal X-ray diffractometer was employed in a three crystal mode as described above (Figs. 12.7 and 12.8). The high resolution diffraction curves were quite sharp with half widths in the range of 10–30 arc sec [73]. Figure 12.14 shows a typical diffraction curve recorded with (11.0) diffracting lattice planes in symmetric Laue geometry in (+, -, +) configuration of the diffractometer. The specimen was at the third crystal stage. It is a single sharp peak with a half width of 12 arc sec. The theoretical half width of the diffraction curve calculated on the basis of plane wave dynamical diffraction theory for an ideally perfect lithium niobate crystal is 3.3 arc sec [83–86]. Under identical experimental conditions, half widths of diffraction curves of nearly perfect silicon single crystals are in the range of 5–10 arc sec [87,88]. A part of the broadening of such curves was due to the difference in lattice spacing of the diffracting planes of the specimen and those of the monochromator crystals. Also, the finite angular divergence and wavelength spread of the exploring $K_{\alpha 1}$ beam led to some broadening. Considering these factors, the diffraction curves of the specimens are quite sharp. Therefore, it can be concluded that these crystals possess a high degree of crystalline perfection. Results of high resolution X-ray topography experiments gave similar results.

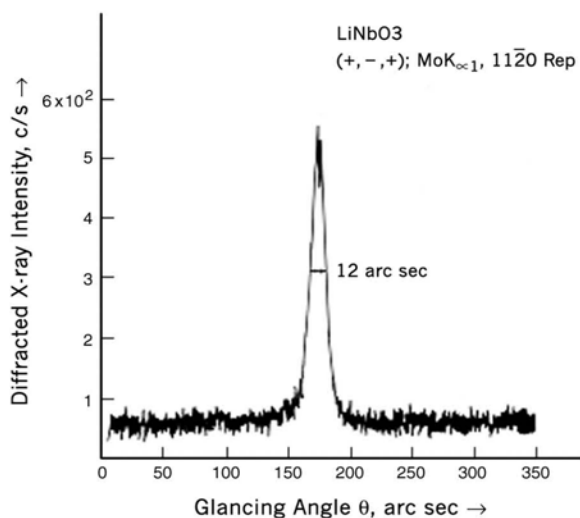


Fig. 12.14. A typical high resolution X-ray diffraction curve of a (00.1) LiNbO_3 crystal recorded with (11.0) diffracting planes in symmetrical Laue geometry. $\text{MoK}_{\alpha 1}$ radiation used

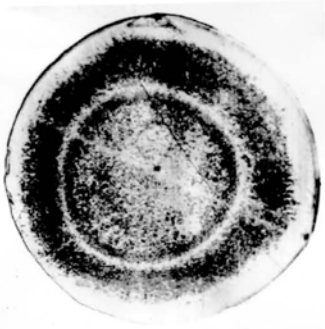


Fig. 12.15. A typical high resolution X-ray diffraction traverse topograph of an unpoled (00.1) LiNbO_3 crystal recorded in symmetrical Laue geometry with (11.0) diffracting planes and $\text{MoK}_{\alpha 1}$ radiation

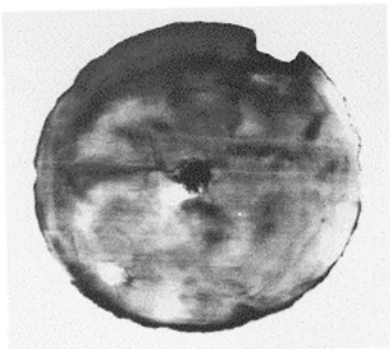


Fig. 12.16. A typical high resolution X-ray diffraction traverse topograph of a poled (00.1) LiNbO_3 crystal. Experimental conditions were the same as in Fig. 12.15.

High resolution X-ray topographs were recorded for both poled and unpoled crystals. Figure 12.15 shows a typical topograph recorded for an unpoled crystal sample and Fig. 12.16 for a poled crystal sample, using $\text{Mo K}_{\alpha 1}$ radiation with (11.0) diffracting planes. In the unpoled sample ferroelectric domains are randomly oriented. There is a concentric distribution of defects in an otherwise uniform intensity background. These may be due to segregation of impurity defects. The dark rings are due to ferroelectric domain boundaries with the opposite polarity to that of the matrix. Sugii et al. (1973) have also observed similar ferroelectric domain boundaries [89]. We have found experimentally that the strong contrast is independent of diffraction vectors. In the topograph of a poled sample the dark rings have disappeared and have nearly uniform intensity throughout, which clearly depicts absence of multiple domains. The domain vectors are now perfectly aligned along the electric field.

12.9.2 Characterization of bismuth germanate single crystals

A double crystal X-ray diffractometer described above was employed to characterize the BGO single crystals. Some of the specimens were rectangular in shape and a few nearly circular specimens were also used. Disk-shaped specimens with diameters of ~ 25 mm had been examined in detail. The exploring beam size was kept small: ~ 5 mm \times ~ 0.4 mm. The height of the beam was ~ 5 mm in the vertical direction, the plane of diffraction being horizontal. In a few experiments, the exploring beam height was increased to 30 mm so that it irradiated the entire specimen along the vertical direction. Different regions of the specimen surface were examined by selective irradiation.

Figure 12.17 shows a typical high resolution X-ray diffraction curve of a (001) BGO crystal. In this experiment, (004) planes, which were nearly parallel to the specimen surface, were selected for diffraction. The beam height was ~ 5 mm and it irradiated the central region of the specimen. The diffraction curve is quite sharp with a half width of ~ 9 arc sec. The theoretical value of the half width for the diffraction curve for (004) diffracting planes of an ideally perfect BGO crystal, calculated by using the plane wave dynamical theory is 3.8 arc sec [83–86]. Since the monochromator in the diffractometer was a (111) silicon crystal, some broadening is expected due to dispersion caused by the lattice mismatch ($d_{\text{Si}} = 3.1355$ Å, $d_{\text{BGO}} = 2.6307$ Å). Keeping this fact in view, the observed value of the half width is quite close to the theoretical value for a perfect BGO crystal. This indicates that the quality of the explored region of the specimen crystal is quite good.

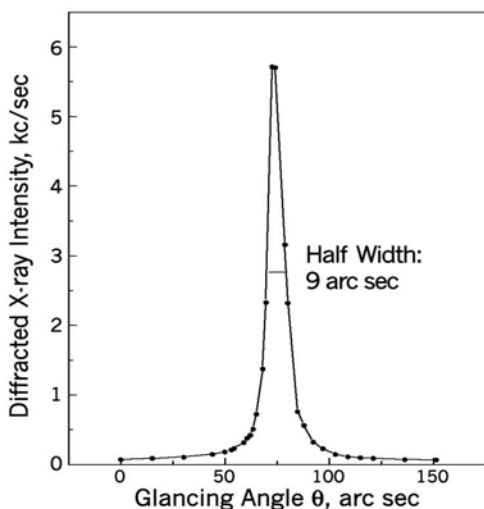


Fig. 12.17. A typical high resolution X-ray diffraction curve of a (001) BGO single crystal recorded with (004) planes from the central part of the specimen in symmetrical Bragg geometry

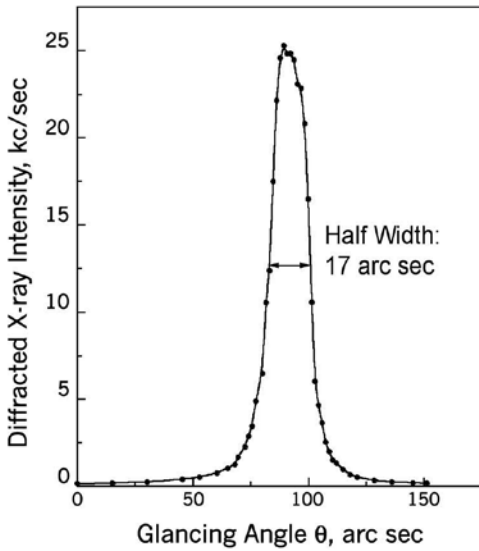


Fig. 12.18. A typical high resolution X-ray diffraction curve of a (001) bismuth germanate single crystal recorded with (004) diffracting planes in Bragg geometry when the exploring X-ray beam irradiated the entire specimen along the vertical direction on right hand side of the center.

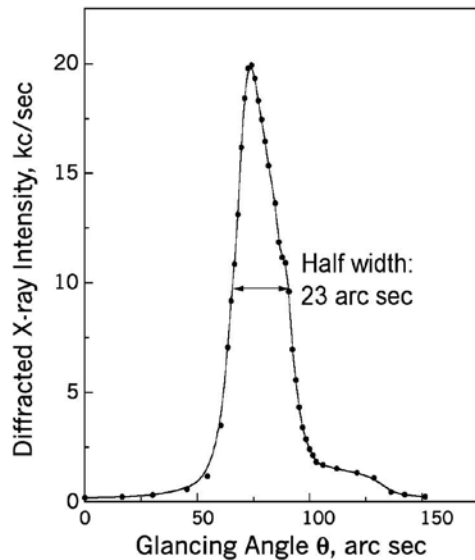


Fig. 12.19. A typical high resolution X-ray diffraction curve of a (001) bismuth germanate single crystal recorded with (004) diffracting planes in Bragg geometry from a region on the left hand side of the center.

The exploring beam height was increased from 5 mm to ~30 mm to observe overall perfection along the vertical direction. Figure 12.18 shows a typical diffraction curve recorded when the exploring beam was irradiating the right side of the central area of the specimen. It can be seen that the curve is considerably broader than the curve of Fig. 12.17. The half width of the diffraction curve has increased to 17 arc sec. A single peak was observed in the diffraction curve. Therefore, one can conclude that no boundary is present in the irradiated region. Figure 12.19 shows a typical diffraction curve recorded under conditions similar to those in Fig. 12.18. This curve was recorded from the left side of the central region of the specimen. The half width of this diffraction curve is 23 arc sec. This curve is broader than that shown in Fig. 12.18. Further, a slight hump is observed on the right hand side of the main peak. This indicates the presence of another smaller peak, and hence the presence of a low angle boundary in the specimen crystal. The changes in half widths and shapes of the diffraction curves from different regions of the specimen (Figs. 12.18 and 12.19) suggest that there is a variation in degree of perfection of the specimen from region to region. Also, there is a possibility of low angle boundaries being present in the specimen. For a detailed study, X-ray diffraction traverse topography was combined with diffractometry.

Figure 12.20 shows a typical X-ray diffraction traverse topograph of the BGO specimen of Figs. 12.17–12.19, recorded with (004) diffracting planes in symmetrical Bragg geometry. It is seen that in the top region (marked as R), a part of the crystal is not diffracting. This shows the presence of a low angle boundary. In the lower portion also the intensity is not uniform, which indicates variations in degree of perfection from region to region, broadly similar to the results of diffractometric experiments. The region marked as R in Fig. 12.20, indicating a low angle boundary, has been studied in detail.

To examine the peripheral region of the specimen the height of the exploring X-ray beam perpendicular to the plane of diffraction was reduced to ~9 mm, and its position relative to the crystal was adjusted in such a manner that it irradiated the region R of the specimen (Fig. 12.20). A typical diffraction curve recorded from this region is shown in Fig. 12.21. This curve consists of two well resolved peaks. The angular separation between the two peaks is only ~33 arc sec. The splitting of the diffraction curve into two peaks clearly shows that the specimen contains a low angle boundary. However, the tilt angle between the two subgrains is very small, less than one arc min. Boundaries with such low tilt angles have been termed *very* low angle boundaries [68]. The high sensitivity of the X-ray diffraction technique employed in these experiments enabled direct observation of such *very* low angle boundaries. Subgrains on either side of the boundary, however, give sharp diffraction curves. Indeed, the half width of the larger peak is only ~7.6 arc sec. This peak is even sharper than that obtained from the central region, which was 9 arc sec (Fig. 12.17). High resolution X-ray traverse topographs were also recorded under identical conditions after orienting the specimens at the two peak positions of Fig. 12.21. Figures 12.22 (a) and (b) show topographs recorded respectively with subgrains of the larger and the smaller peaks. Both the topographs are found to be complementary to each other and enabled direct im-

aging of the two subgrains. Further, the intensity in the topographs is not uniform. This is due to small strains present in this region of the specimen. A lower degree of perfection towards the edges is expected because of the high thermal gradient existing between the crystal surface and the surrounding area. However, large central parts of the specimen were nearly perfect. Also, detailed topographic investigation carried out by Lal et al. (1979) on $\alpha\text{-Al}_2\text{O}_3$ crystals grown by the Cz method showed the presence of low angle boundaries with tilt angles of a few arc minute towards the periphery [90].

Bismuth germanate crystals containing *very* low angle boundaries have been investigated in considerable detail [67,69]. Pinning of very low angle boundaries due to decoration by traces of impurities like silicon has been demonstrated [69]. Also, prominent point defect clustering has been observed in the crystals having a yellow tinge [70]. Van Hoof et al. (1985) investigated BGO crystals grown by the Bridgman technique using X-ray diffractometry [58]. They obtained sharp diffraction curves from the central region with half width of ~ 10 arc sec when the irradiated area was $\sim 1.3 \text{ mm}^2$. The half width increased to ~ 20 arc sec when the whole area of about 300 mm^2 was irradiated. Our results are quite similar to these. In the present study,

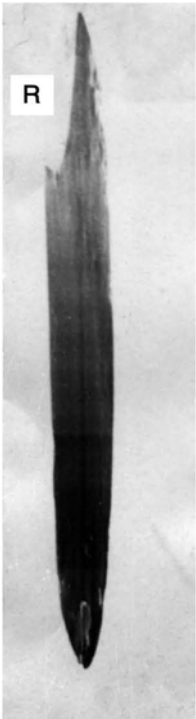


Fig. 12.20. A typical high resolution X-ray traverse topograph of the (001) BGO specimen of Figs. 12.17 to 12.19 recorded with (004) diffracting planes in symmetrical Bragg geometry.

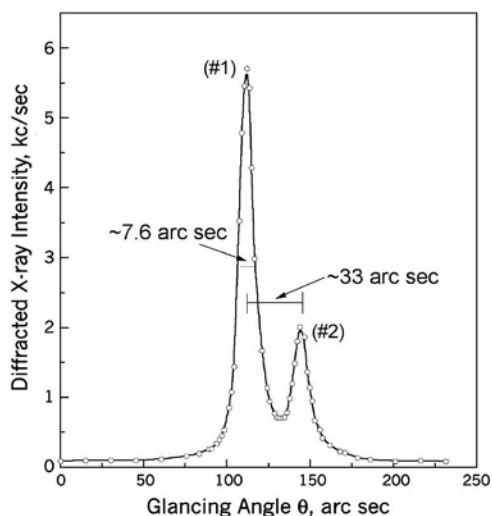


Fig. 12.21. A typical high resolution X-ray diffraction curve of a (001) BGO single crystal recorded from the peripheral region of the specimen. (004) diffracting planes were employed

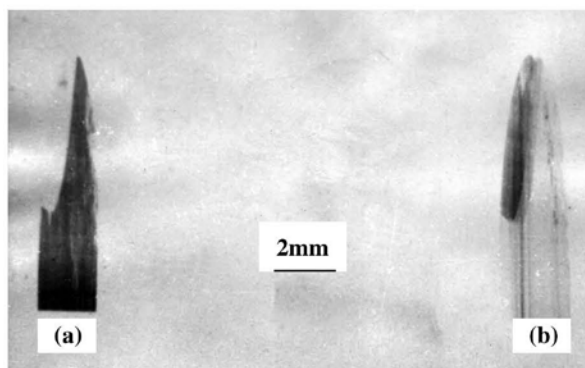


Fig. 12.22. Typical high resolution X-ray traverse topographs of the (001) BGO specimen of Figs. 12.17 to 12.21 recorded with (004) diffracting planes in symmetrical Bragg geometry. (a) and (b) were recorded after orienting the specimen on peak #1 and #2, respectively, of Fig. 12.21.

diffraction curves with half width of ~ 9 arc sec were obtained from the central region. They had reported the presence of dislocations predominantly at the outer edge of the Bridgman grown specimen. The presence of grain boundaries and high dislocation density in the Cz grown specimen was reported. However, we have observed very low angle grain boundaries at the periphery of the specimen. The Cz specimen of Van Hoof et al. had a mosaic structure with a large angular spread

of $\sim 0.15^\circ$. Chemical etching of $\{112\}$ faces of the Bridgman specimens revealed dislocations occurring in rows representing low angle grain boundaries [61].

Brandle and Miller (1974) studied the effect of liquid temperature gradient on the distribution of dislocations in large diameter LiTaO_3 single crystals [75]. Typical radial temperature gradient of their system was minus $3\text{--}5^\circ\text{C}/\text{cm}$ above the crucible and plus $3\text{--}5^\circ\text{C}/\text{cm}$ between the crucible lid and the liquid surface. They suggested that a lower temperature gradient would be required for the growth of good quality single crystals of LiTaO_3 . Takagi et al. (1976) also suggested that a small temperature gradient would be desirable for the growth of gadolinium gallium garnet single crystals [91]. According to their results, when the temperature gradient is small it is easy to grow facet less crystals. All these investigations indicated that improvements in crystalline perfection of oxide single crystals were possible through the maintenance of a small temperature gradient across the melt. The present work has shown that the low thermal gradient Cz technique is quite appropriate to grow nearly perfect single crystals of bismuth germanate. These results are consistent with earlier findings, and also demonstrate that the LTG Cz method can be employed to grow high quality BGO crystals [68] and the degree of their perfection is nearly the same as that reported for Bridgman grown crystals.

12.10 Summary

The recent advances made in the growth and characterization of two technologically important crystals, lithium niobate and bismuth germanate, have been reviewed. Essential features of Cz growth experiments employed for the preparation of mono-domain nearly perfect lithium niobate have been discussed. High resolution X-ray diffraction evaluation gave valuable feedback for the growth of such high quality single crystals.

It has been shown that the LTG Cz method can be employed to grow nearly perfect bismuth germanate crystals. Interesting results concerning direct observation and characterization of *very* low angle boundaries have been described.

Acknowledgments

It is a great pleasure to acknowledge the collaboration of a large number of colleagues particularly K.S. Bartwal (now at CAT, Indore), Lyudmila Kharachenko, V. N. Shlegel, V. Guerasimov (IIC, Novosibirsk), and M. Ravikumar. Partial financial support received from the Department of Science and Technology, New Delhi under ILTP is gratefully acknowledged.

References

1. Rauber A (1978) Current Topics in Materials Science, Vol 1, Kaldis E (ed) North Holland, Amsterdam, pp 481–601
2. Morgan DP (1989) SAWs on lithium niobate: Properties of common orientations. In: Properties of Lithium Niobate. EMIS Datareview, Series No 5, INSPEC, pp 84–93
3. Lal K, Jhans HK (1977) The dielectric constant of gadolinium gallium garnet and α - Al_2O_3 single crystals. *J Phys C: Solid State Phys* 10:1315–1319
4. Takano S, Esashi S, Mori K, Namikata T (1974) Growth of high quality single crystals of lead molybdenate. *J Crystal Growth* 24/25:437–440
5. Feinberg J, Hellworth RW (1980) Phase-conjugating mirror with continuous wave gain. *Opt Lett* 5:519–521
6. White JO, Yariv A (1980) Real time image processing via four wave mixing in a photo-refractive medium. *Appl Phys Lett* 37:5–7
7. Gunter P, Huignard JP (eds) Photorefractive Materials and Their Applications. Top Appl Phys (West Germany) Vol 61 & 62. Springer-Verlag, Berlin (1988)
8. Weber MJ, Monchamp RR (1973) Luminescence of $\text{Bi}_4\text{Ge}_3\text{O}_{12}$: Spectral and decay properties. *J Appl Phys* 44:5495–5499
9. Proceedings of International Workshop on Bismuth Germanate. Department of Physics, Princeton University, November (1982)
10. Drake DM, Nilsson LR, Faucett J (1981) Bismuth germanate scintillators as detectors for high energy gamma radiations. *Nucl Instr and Meth* 188:313–317
11. Nestor OH, Huang CY (1975) Bismuth germanate: A high-Z gamma ray and charged particle detector. *IEEE Trans Nucl Sci NS-22*:68–71
12. Wong W-H, Uribe J, Hicks K, Zambelli M (1994) A 2-dimensional detector decoding study on BGO arrays with quadrant sharing photomultipliers. *IEEE Transactions on Nuclear Science* 41(4):1453–1457
13. Murthy K, Thompson CJ, Weinberg IN, Mako FM (1994) Measurement of the coincidence response of very thin BGO crystals. *IEEE Transactions on Nuclear Science* 41(4):1430–1435
14. Rogers JG, Nutt R, Andreaco M, Williams CW (1994) Testing 144- and 256-crystal BGO block detectors. *IEEE Transactions on Nuclear Science* 41(4):1423–1429
15. Li Zuyu, Jin Genming, Zhang Baoguo, Qiyujin, Wu Heyu, He Zhiyong, Luo Qingzheng, Wen Wan-Xin, Dai Guangxi (1995) BGO detector used to identify charged particles. *Nuclear Techniques* 18(3):151–153
16. Tornai MP, Germano G, Hoffman EJ (1994) Positioning and energy response of PET block detectors with different light sharing schemes. *IEEE Transactions on Nuclear Science* 41(4):1458–1463
17. Moses WW, Derenzo SE (1994) Design studies for a PET detector module using a PIN photodiode to measure depth of interaction. *IEEE Transactions on Nuclear Science* 41(4):1441–1445
18. Thompson CJ, Murthy K, Picard Y, Weinberg IN, Mako R (1995) Positron emission mammography (PEM): A promising technique for detecting breast cancer. *IEEE Transactions on Nuclear Science* 42(4):1012–1017
19. Rapaport MS, Gayer A, Iszak E, Goresnic C, Baran A, Polak E (1995) A dual-mode industrial CT. *Nuclear Instruments and Methods in Phys Research A* 352(3):652–658

20. Liang Z (1994) Detector response restoration in image reconstruction of high resolution positron emission tomography. *IEEE Transactions on Medical Imaging* 13:314–321
21. Kampert KH, Bohne EM, Claussen A, Berger F, Bock D, Glasow R, Heine N, Mau P, Peitzmann T, Purschke M, Samto R, Steffens K, Stuken DJ, Awes TC, Young GR (1994) A high resolution BGO calorimeter with longitudinal segmentation. *Nuclear Instruments and Methods in Physics Research A* 349(1):81–95
22. Schneegans M (1987) Progress of the L3 / BGO Calorimeter. *Nuclear Instruments and Methods in Physics Research A* 257:528–537
23. Melcher CL, Schweitzer JS, Manente RA, Peterson CA (1991) Applications of single crystals in oil well logging. *J Crystal Growth* 109:37–42
24. Takagi K, Oi T, Fukazawa T, Ishi M, Akiyama S (1981) Improvement in the scintillation conversion efficiency of $\text{Bi}_4\text{Ge}_3\text{O}_{12}$ single crystals. *J Crystal Growth* 52:584–587
25. Yin ZW, Fang XQ, Hu GQ (1994) Doping effect and mechanism of radiation damage of bismuth germanate ($\text{Bi}_4\text{Ge}_3\text{O}_{12}$) crystals. *Ferroelectrics* 151(1-4):287–298
26. Bordun OM (1996) Photoluminescence of $\text{Bi}_4\text{Ge}_3\text{O}_{12}$ thin films and ceramics. *J Appl Spectroscopy* 63(1):97–100
27. Lal K (1982) An introduction to the experimental techniques used in X-ray diffraction topography. In: Lal K (ed) *Synthesis, Crystal Growth and Characterization*. North-Holland, Amsterdam, pp 215–241
28. Menzer G (1931) Die Kristallstruktur von eulytin. *Z Krist* 78:136–163
29. International Tables for X-ray Crystallography, Vol I 329 (1952)
30. Durif A, Averbuch-Pouchot MT (1982) Refinement of the crystal structure of $\text{Bi}_4\text{Ge}_3\text{O}_{12}$. *Compt Rend (Paris)* 295:555–556
31. Smet F, Bennema P, Van Der Eerden JP, Van Enckevort WJP (1989) Crystal morphology of bismuth germanate ($\text{Bi}_4\text{Ge}_3\text{O}_{12}$). *J Crystal Growth* 97:430–442
32. Nitsche R (1965) Crystal growth and electro-optic effect of bismuth germanate, $\text{Bi}_4\text{Ge}_3\text{O}_{12}$. *J of Appl Phys* 36(8):2358–2360
33. Reisman A, Holtzburg F (1958) Heterogeneous equilibria in the systems Li_2O -, Ag_2O - Nb_2O_5 and oxide models. *J Am Chem Soc* 80:6503–6507
34. Svaasand LO, Eriksrud M, Grande AP, Mo F (1973) Crystal growth and properties of LiNb_3O_8 . *J Crystal Growth* 18:179–184
35. Lerner P, Legras C, Duman JP (1968) Stochiometric des monocristaux de metaniobate de lithium. *J Crystal Growth* (3/4):231–235
36. Ballman AA (1965) Growth of piezoelectric and ferroelectric materials by the Czochralski technique. *J Am Ceram Soc* 48(2):112–113
37. Polozkov NM, Ivleva LI (1989) Growth of lithium niobate by Stepanov's technique. In: *Properties of Lithium Niobate*. EMIS, Datareview, Series No 5, INSPEC, pp 214–215
38. Ivleva LI, Kuzminov YuS, Osiko VV, Polozkov NM (1987) The growth of multicomponent oxide single crystals by Stepanov's technique. *J Crystal Growth* 82:168–176
39. Nassau K, Levinstein HJ, Loiacono GM (1966) Ferroelectric lithium niobate. I. Growth, domain structure, dislocations and etching. *J Phys Chem Solids* 27:983–988; Ferroelectric lithium niobate. II. Phenomenon of single domain crystals 27:989–996
40. Abrahams SC, Reddy JM, Bernstein JL (1966) Ferroelectric lithium niobate III. Single crystal X-ray diffraction studies at 24°C. *J Phys Chem Solids* 27:997–1010; Abrahams SC, Hamilton WC, Reddy JM (1966) Ferroelectric lithium niobate. IV. Single crystal neutron diffraction study at 24°C 27:1013–1018; Abrahams SC, Leviston HJ, Reddy

- JM (1966) Ferroelectric lithium niobate. V. Polycrystal X-ray diffraction study between 24°C and 1200°C 27:1019–1026
41. Baumann I, Rudolph P, Krabe D, Schalge R (1993) Orthoscopic investigation of the axial optical and compositional homogeneity of Czochralski grown LiNbO₃ crystals. *J Crystal Growth* 128:903–908
 42. Gallagher PK, O'Bryan Jr HM (1985) Characterization of LiNbO₃ by dilatometry and DTA. *J Am Ceram Soc* 68(3):147–150
 43. Bordui PF, Norwood RG, Bird CD, Galvert GD (1991) Compositional uniformity in growth and poling of large-diameter lithium niobate crystals. *J Crystal Growth* 113:61–68
 44. Kushibiki J, Takahashi H, Kobayashi T, Chubachi N (1991) Characterization of LiNbO₃ crystals by line-focus beam acoustic microscopy. *Appl Phys Lett* 58/23:2622–2624
 45. Peterson GE, Lunt SR (1987) Refractive index measurements of lithium niobate integrated optical substrates by total internal reflection. *Ferroelectrics* 75:99–108
 46. Peterson GE, Lunt SR, Holmes RJ, Kim YS (1985) Integrated Optical Circuit Eng II. *Proceedings of SPIE – The International Society for Optical Engineering* 578:31
 47. Silva WJ, Bulmer CH (1985) Integrated Optical Circuit Eng II. *Proceedings of SPIE – The international society for optical engineering* 578:19
 48. Midwinter JE (1967) Assesment of lithium-meta-niobate for nonlinear optics. *Appl Phys Lett* 11:128–130
 49. Byer RL, Young JF, Feigelson RS (1970) Growth of high quality LiNbO₃ crystals from the congruent melt. *J Appl Phys* 41:2320–2325
 50. Reich P, Bohm J, Hermoneit B, Rudolph P, Schalge R, Schultze D (1991) The effect of an electric field on the growth of lithium niobate single crystals. *J Crystal Growth* 108:759–764
 51. Liebertz J (1969) Einkristalizuchtung von wismutgermanant (Bi₄Ge₃O₁₂). *J Crystal Growth* 5:150
 52. Henning Von Philipsborn, Croissance D'Eulytine (1971) C Bi₄Si₃O₁₂ et des composes substitutes Bi₄Ge₃O₁₂ par la methode Czochralski. *J Crystal Growth* 11:348–350
 53. Speransakaya EJ, Arshakuni AA (1964) The bismuth oxide – germanium oxide system. *Russ J Inorg Chem* 9:226–230
 54. Dickinson SK, Hilton RM, Lipson HG (1972) Czochralski synthesis and properties of rare-earth-doped bismuth germanate (Bi₄Ge₃O₁₂). *Mat Res Bull* 7:181–192
 55. Barnes RGL (1984) The influence of impurities on the quality of bismuth germanate (BGO) scintillator crystals. *J Crystal Growth* 69:248–252
 56. Schmid F, Khattak CP, Smith MB (1984) Growth of bismuth germanate crystals by the heat exchanger method. *J Crystal Growth* 70:466–470
 57. Corsmit G, Van Driel MA, Elsenaar RJ, Van De Guchte W, Hoogenboom AM, Sens JC (1986) Thermal analysis of bismuth germanate compounds. *J Crystal Growth* 75:551–560
 58. Van Hoof LAH, Bartels WJ (1985) The perfection of Bridgman-grown Bi₄Ge₃O₁₂ crystals. *Mat Res Bull* 20:79–83
 59. Allergretti F, Borgia B, Riva R, De Notaristenfani F, Pizzni S (1989) Growth of BGO single crystals using a directional solidification technique. *J Crystal Growth* 94:373–380
 60. Smet F, Van Enckevort WJP (1988) On the distribution of point defects in large sized bismuth germanate crystals. *J Crystal Growth* 88:169–179

61. Van Enckevort WJP, Smet F (1990) Optical characterization of crystal dislocations: The case of bismuth germanate. *J Crystal Growth* 102:314–328
62. Takagi K, Fukazawa T (1986) Effect of growth conditions on the shape of $\text{Bi}_4\text{Ge}_3\text{O}_{12}$ single crystals and on melt flow patterns. *J Crystal Growth* 76:328–338
63. Horowitz A, Kramer G (1986) The growth of high quality large $\text{Bi}_4\text{Ge}_3\text{O}_{12}$ (BGO) crystals. *J Crystal Growth* 79:296–302
64. Gopalkrishnan R, Ramaswamy P (1994) Growth of $\text{Bi}_4(\text{Ge,Si})_3\text{O}_{12}$ and $\text{Bi}_{12}(\text{Ge,Si})\text{O}_{20}$ crystals by floating zone technique. *Crystal Research and Technology* 29(8):k107–k111
65. Gopalkrishnan R, Gopinath CS, Ramaswamy P (1996) X-ray photoelectron spectroscopic studies of sellinite and eulytite BGO and BSO crystals. *Crystal Research and Technology* 31(2):249–54
66. Vasiliev YaV, Akhmetshin RR, Barovliev YuA, Grigoriev DN, Gusev VA, Shlegel VN, Smakhtin VP (1996) BGO crystals grown by a low thermal gradient Czochralski technique. *Nuclear Instruments and Methods in Physics Research A* 379:533–535; Barovliev YuA, Ivannikova NV, Shlegel VN, Vasiliev YaV, Gusev VA (2001) Progress in growth of large sized BGO crystals by the low thermal gradient Czochralski technique. *J Crystal Growth* 229:305–311
67. Choubey A (2000) Growth of nearly perfect oxide single crystals like bismuth germanate and their characterization by high resolution X-ray diffraction techniques. PhD thesis, Delhi University, Delhi
68. Anantha Murthy RV, Ravikumar M, Choubey A, Lal K, Kharachenko L, Shlegel VN, Guersimov V (1999) Growth and characterization of large size bismuth germanate single crystals by low thermal gradient Czochralski method. *J Crystal Growth* 197:865–873
69. Choubey A, Shubin YuV, Bhagavannarayana G, Lal K (1999) High resolution X-ray diffractometric and topographic studies of as grown and annealed BGO crystals. *Acta Cryst A* 55 P.05.16.031
70. Bhagavannarayana G, Choubey A, Shubin YuV, Lal K (1999) Diffuse X-ray scattering study of point defect clusters in bismuth germanate single crystals. *Acta Cryst A* 55 P.05.16.029
71. Lal K, Anantha Murthy RV, Ravikumar M, Choubey A, Bhagavannarayana G, Kharachenko L, Shlegel VN, Guerasimov V, Shubin Yu (1999) Growth and characterization of bismuth germanate single crystals. *Acta Cryst A* 55 P.05.16.028
72. Lal K, Anantha Murthy RV, Halder SK, Singh BP, Kumar V (1982) Growth of nearly perfect alkali halide single crystals by Czochralski method and their characterization. *J Crystal Growth* 56:125–131
73. Anantha Murthy RV, Bartwal KS, Lal K (1993) Growth of nearly perfect LiNbO_3 single crystals. *Materials Science and Engineering B* 18:L4–L6
74. Kanter IB, Kolotygina LV, Kuzminov YuS, Kharchenko LYu (1991) Proc Second Soviet – Indian Symposium on Crystal Growth and Characterization (laser and nonlinear crystals). Moscow, p 38
75. Brandle CD, Miller DC (1974) Czochralski growth of large diameter LiTaO_3 crystals. *J Crystal Growth* 24/25:432–436
76. Lal K (1998) Real structure of real crystals. *PINSA* 64/A(5):609–635
77. Lal K (1993) High resolution X-ray diffraction studies of real structure of nearly perfect single crystals. *Bull Mater Sci* 16:617–642

78. Lal K, Kumar V, Evaluation of perfection of silicon single crystal wafers having polysilicon deposits on silicon dioxide films by using a double crystal X-ray diffractometer, NPL report No 85-BN 0051
79. Lal K, Mitra R, Srinivas G, Vankar VD (1996) Study of biaxial stress induced by co-sputtered thin molybdenum silicide films in silicon single-crystal substrates. *J Appl Cryst* 29:222–229
80. Lal K (1991) Structural characterization of single crystals. *Key Eng Materials* 58:205–228
81. Bonse U, Hart M (1965) Tailless X-ray single crystals reflection curves obtained by multiple reflection. *Appl Phys Lett* 7:238–240
82. Lal K, Goswami SNN, Wurfl J, Hartnagel HL (1990) Effect of metallization on crystalline perfection and level of stress in semi-insulating and n-type gallium arsenide single-crystal wafers. *J Appl Phys* 67:4105–4013
83. Batterman BW, Cole H (1964) Dynamical diffraction of X-rays by perfect crystals. *Rev Mod Phys* 36:681–717
84. Pinsker ZG (1978) *Dynamical Scattering of X-rays in Crystals*. Berlin, Springer Verlag
85. Tanner BK (1976) *X-ray Diffraction Topography*. Oxford, Pergamon Press
86. Bowen DK, Tanner BK (1998) *High Resolution X-ray Diffractometry and Topography*. London, Taylor & Francis Ltd, p 233
87. Lal K, Goswami SNN (1987) High resolution X-ray diffraction studies of defect structures produced by high DC electric fields in silicon single crystals. *Mater Sci Eng* 85:147–156
88. Lal K, Niranjana S, Goswami N, Verma AR (1990) A quantitative study of diffracted X-ray intensities from type one natural diamond crystals by high resolution X-ray diffractometry and comparison with nearly perfect silicon single crystals. *Pramana - J Phys* 34:507–523
89. Sugii K, Iwasaki H, Miyazawa S, Niizeki N (1973) An X-ray topographic study on lithium niobate single crystals. *J Crystal Growth* 18:159–166
90. Lal K, Kumar V, Verma AR (1979) A comparative study of perfection of CVD grown and Czochralski grown α - Al_2O_3 single crystals by X-ray diffraction topography. *Ind J Phys* 53A:78–82
91. Takagi K, Fukazawa T, Ishii M (1976) Inversion of the direction of the solid-liquid interface on the Czochralski growth of GGG crystals. *J Crystal Growth* 32:89–94

13 Growth and Development of Nonlinear Optical Borate Crystals for Generation of Visible and UV Light

Takatomo Sasaki, Yusuke Mori, Masashi Yoshimura and Yoke Khin Yap

Department of Electrical Engineering, Osaka University, 2-1 Yamada-oka, Suita, Osaka 565-0871, Japan

13.1 Introduction

13.1.1 Coherent solid-state light source in the visible and UV regions by nonlinear optical crystals

The coherent and monochromatic photon flux of laser light is viewed as a clean energy source for the synthesis and processing of materials. Because of their high photon energies and ability to be tightly focused, radiations at short wavelengths are desired. For instance, photon energy in the UV region is sufficient enough to induce bond-breaking processes in many materials. High-power UV output is currently available only from the rare-gas halide excimer lasers (e.g., XeCl, KrF, and ArF). However, these lasers use corrosive gases, have high voltage gaseous discharges, require regular maintenance, and have bulky dimensions. A compact, maintenance-free, all-solid-state alternative is therefore desired.

An effective technique for UV generation is cascaded sum-frequency generation pumped by the output of near-IR ($\lambda \sim 1 \mu\text{m}$) solid-state lasers by using nonlinear optical (NLO) crystals. For instance, the fundamental wavelength ($\lambda = 1064 \text{ nm}$) of Nd:YAG lasers is first converted to SHG (Second Harmonic Generation) (2ω , $\lambda = 532 \text{ nm}$) and then to UV wavelengths by third, fourth, fifth ... harmonic generations (3ω , 4ω , $5\omega \dots$ at $\lambda = 355 \text{ nm}$, 266 nm , $213 \text{ nm} \dots$, respectively). Thus, NLO crystals that generate visible and UV lights effectively are important for the realization of a high-power, all-solid-state UV light source. For the purpose of reliable laser frequency conversion, NLO crystals need to have properties like: (1) large NLO coefficient, (2) moderate birefringence, (3) small walk-off effect, (4) large angular, spectra and temperature bandwidths, (5) wide transparency range for operating wavelength, (6) high laser-induced damage threshold, (7) ease of growth, (8) low material cost, (9) good chemical stability, and (10) good mechanical stability.

Until 1975, most NLO crystals were based on the P-O, I-O, and Nb-O bonds like those in KDP (KH_2PO_4) [1,2], LiIO_3 [3,4], and LiNbO_3 [5]. KDP meets conditions (5) to (8) and thus is used for frequency conversion in high-power lasers. It is particularly suitable for the purpose of a laser fusion system involving NLO devices with large dimensions of several tens of cm. Likewise, because of properties (1), (2), and (9), crystals like LiNbO_3 and KNbO_3 [6] are frequently used for frequency conversions in semiconductor lasers. The KTP (KTiOPO_4) [7] crystals developed later provide properties that merely combined those of KDP and LiNbO_3 . This makes KTP popular for both high-power and semiconductor laser operations. Comprehensive references on these materials are compiled in the handbook on NLO crystals prepared by Dmitriev et al. (1999) [8].

13.1.2 NLO borate crystals

Borate crystals for UV light generation

NLO crystals with B-O bonds are often employed for high-power UV light generation because of the relatively high resistance against laser-induced damage and higher transparency in the UV region. The first borate crystal described for UV generation was $\text{KB}_3\text{O}_8 \cdot 4\text{H}_2\text{O}$ (KB5) [9]. However, intense research on borate crystals was initiated only after the development of $\beta\text{-BaB}_2\text{O}_7$ (BBO) [10]. After BBO, Chen et al. have developed several other borate crystals like LiB_3O_5 (LBO) [11], $\text{KBe}_2\text{BO}_3\text{F}_2$ (KBBF) [12], and $\text{Sr}_2\text{Be}_2\text{BO}_7$ (SBBO) [13]. The present authors have been involved in the development of several borate crystals like CsB_3O_5 (CBO) [14], $\text{CsLiB}_6\text{O}_{10}$ (CLBO) [15–17], $\text{YCa}_4\text{O}(\text{BO}_3)_3$ (YCOB) [18,19], $\text{Gd}_x\text{Y}_{1-x}\text{Ca}_4\text{O}(\text{BO}_3)_3$ (GdYCOB) [20,21], and $\text{K}_2\text{Al}_2\text{B}_2\text{O}_7$ (KAB) [22,23]. Recently, lithium tetraborate $\text{Li}_2\text{B}_4\text{O}_7$ [24,25] was also reported as a possible NLO crystal for UV light generation. Note that NLO properties of BBO, LBO, as well as KB5 have been described elsewhere [26]. A recent review on borate crystals like BBO, LBO, $\text{Li}_2\text{B}_4\text{O}_7$, $\text{GdCa}_4\text{O}(\text{BO}_3)_3$ (GdCOB) [27,28], and YCOB were prepared by Becker (1998) [29]. Our discussions on borate materials are concentrated on the latest progress with CLBO, GdYCOB, and KAB, which are not well compiled in any review articles available to date. Discussions on other NLO borate crystals are included for comparison. For example, the latest progress on CBO is mentioned in the section on CLBO and new data on GdCOB and YCOB are included in the discussion of GdYCOB. Likewise, properties of KBBF and SBBO are considered together in the section on KAB crystals.

Relation between the anionic borate group and optical properties

The optical properties of borate crystals appeared to be related to their molecular structure. Several borate crystals mentioned earlier are taken as examples and listed in Table 13.1. These crystals are constructed from three basic structural units: $(\text{B}_3\text{O}_6)^{3-}$, $(\text{B}_3\text{O}_7)^{5-}$, and $(\text{BO}_3)^{3-}$ anionic groups. The anionic group is thought

Table 13.1. Properties of some NLO borate crystals

Crystals	Space group	Transparency range [nm]	Nonlinear coefficient [pm/V]	Birefringence Δn	Shortest SHG [nm]	Basic structural unit
β -BaB ₂ O ₄ (BBO)	R 3c	190-3300	$d_{11}= 1.844$	0.12 at 1064 nm	205	B ₃ O ₆
LiB ₃ O ₅ (LBO)	Pna 2 ₁	160-2600	$d_{31}= 0.94$ $d_{32}= 1.13$ $d_{33}= 0.256$	0.04 at 1064 nm	277	B ₃ O ₇
CsB ₃ O ₅ (CBO)	P 2 ₁ 2 ₁ 2 ₁	167-3400	$d_{14}= 0.863$	0.053 at 1064 nm	273	B ₃ O ₇
KBe ₂ BO ₃ F ₂ (KBBF)	R 32	155-3660	$d_{11} = 0.8$	-0.072 at 589 nm	185	BO ₃
Sr ₂ Be ₂ BO ₇ (SBBO)	P 6 ₃	155-3780	$d_{15}= \sim 2$	-0.062 at 589 nm	200	BO ₃
CsLiB ₆ O ₁₀ (CLBO)	I 42 d	180-2750	$d_{36}= 0.95$	0.050 at 1064 nm	237	B ₃ O ₇

to determine the nonlinear optical coefficient of borate crystals according to the anionic group theory [26]. Two fundamental assumptions are considered in the calculation of complete neglect of differential overlap (CNDO) approximations: (1) the macroscopic NLO coefficient of the crystal is the geometrical superposition of the microscopic second order susceptibility tensor ($\chi^{(2)}$) of the relevant anionic groups, and has nothing to do with essentially spherical cations; and (2) the microscopic second order susceptibility can be determined from the localized molecular orbitals of the anionic group using quantum chemical calculation.

Due to the planar hexagonal structure of the (B₃O₆)³⁻ anionic group, borate crystals constructed from this basic unit have larger $\chi^{(2)}$ compared to crystals composed of (B₃O₇)⁵⁻ and (BO₃)³⁻ groups. Thus, in terms of NLO coefficient, the (B₃O₆)³⁻ group is most suitable as the basic structural unit of NLO borate materials, followed by the (B₃O₇)⁵⁻ group and then the (BO₃)³⁻ group. However, the UV absorption edge of some borate crystals containing the (B₃O₆)³⁻ group occurred at a longer wavelength (e.g., BBO) as compared to those constructed from the (B₃O₇)⁵⁻ group (LBO, CBO, and CLBO). Calculations show that π -conjugated orbitals of planar (B₃O₆)³⁻ tend to shift the UV absorption edge toward the red [26]. As one of the boron atoms in (B₃O₆)³⁻ changed from trigonal to tetrahedral coordination, thereby forming nonplanar (B₃O₇)⁵⁻ groups, the π -conjugated orbital system is weakened, as in the case of LBO and CBO, and the UV absorption edge shifts to 160-170 nm. Both CBO and LBO are constructed from a continuous network of nonplanar (B₃O₇)⁵⁻ groups with interstitial cesium and lithium cations, respectively. Based on the absorption edge, therefore, the (B₃O₇)⁵⁻ group is ideal as the basic structural unit of deep UV NLO materials. Likewise, if the dangling bonds of the three terminated oxygen atoms of (BO₃)³⁻ groups are interlinked with

cations, an absorption edge appearing at wavelengths as short as 155 nm is also possible, as is the case with KBBF and SBBO [13].

Crystal growth of some NLO borate crystals

Borate crystals containing the $(\text{BO}_3)^{3-}$ anionic group like KBBF and SBBO tend to grow in a layered structure. To date, KBBF crystals available for laser experiments are still less than 0.5 mm thick [30]. In fact, there is no detailed evaluation of the performance in laser frequency conversion from both KBBF and SBBO, despite their good transparency in the vacuum UV region. Some supplementary discussions on the growth of KBBF and SBBO are included in section 4. Likewise, the BBO crystal has a high temperature phase (α -BBO) that is centrosymmetric. Thus, the melt growth of BBO crystals is relatively difficult because of the phase transition near the melting point. BBO crystals can be grown by flux but suffer from flux inclusions [31,32]. Czochralski (Cz) growth that involved stoichiometric melts avoids flux inclusions but requires a high temperature gradient near the melt surface [33,34]. The Cz grown BBO has a relatively low laser-induced damage threshold. Quality of Cz-BBO crystal can be improved by annealing [35]. On the other hand, LBO crystals do not melt congruently. The LBO is grown by a top-seeded solution growth (TSSG) / top-seeded Kyropoulos method. Both the growth rate and optical quality of LBO seem to be degraded by the high viscosity and low diffusion rate of the flux solution. It takes more than two months for a crystal with a dimension of several cm to grow, and special care is required for thermal homogeneity [11]. Information on growing BBO and LBO was discussed in Ref. [29] and thus is not repeated here.

13.2 CLBO Crystals for High-Power Generation of Deep-UV Light

13.2.1 The search for $\text{CsLiB}_6\text{O}_{10}$ (CLBO)

As discussed, the development of NLO borate crystals is desired for high-power UV light generation like 4ω and 5ω of Nd:YAG lasers. The BBO crystals were widely evaluated for producing 4ω and 5ω of Nd:YAG lasers because of their relatively large nonlinearity. Laser frequency conversion in BBO is limited by the large walk-off angle (due to a large birefringence), as well as the relatively small angular, spectra, and temperature acceptance bandwidths. Its absorption edge at 189 nm also decreased the conversion efficiency because of thermal dephasing initiated by the optical absorption. As mentioned in the previous section, other NLO crystals like the KBBF and SBBO are still not available for practical application. LBO crystals can only generate UV SHG radiation down to 277 nm due to their small birefringence and are thus unable to produce 4ω radiation by SHG of green light. They can generate UV light at shorter wavelengths by SHG, but the effective NLO coefficient is reduced by a factor of $\cos \theta$ or $\cos \phi$ [11,36]. All

these crystals are not easy to grow like the nonborate KDP and KTP crystals. Thus, finding a new borate material for UV light generation is desirable.

The discovery of CLBO is related to CBO and LBO crystals. Properties of LBO crystals are rather well known and have been discussed in many papers since 1989. The first CBO bulk crystal was grown from a stoichiometric melt in Osaka University during 1992 [14]. The CBO crystallizes in an orthorhombic space group $P2_12_12_1$ with unit cell dimensions: $a = 6.213$, $b = 8.521$, $c = 9.170$ Å, and $Z = 4$ [37]. This crystal is constructed of the $(B_3O_7)^{5-}$ group with the Cs^+ cation. Unlike LBO, which is also comprised of the $(B_3O_7)^{5-}$ group, CBO is relatively easy to grow. The CBO crystals melt congruently and thus can be grown from both a stoichiometric melt and a solution. Wu grew CBO from a nearly stoichiometric melt [38]. The starting charges were prepared from a mixture of Cs_2CO_3 and H_3BO_3 by the following chemical reaction:



The mixture was reported to be slightly rich in Cs_2CO_3 , and a crystal as large as $40 \times 25 \times 25$ mm³ was obtained after two weeks of growth. Likewise, Kagebayashi et al. (1999) reported the growth of CBO crystals from a Cs_2O -enriched melt [39]. The starting materials were Cs_2CO_3 and B_2O_3 powders. The melt composition was 26.6 mole % Cs_2O and 73.3 mole % B_2O_3 . The melting temperature was 821.4°C, as compared to 824.7°C of the stoichiometric melt. A colorless, crack-free, and inclusion-free single crystal of CBO as large as $45 \times 41 \times 44$ mm³ can be obtained in 14 days. This crystal is transparent from 170 to 3400 nm.

According to the Sellmeier equation prepared by Kato (1995) [40], the shortest possible SHG wavelength producible from type-1 CBO is 272.8 nm, slightly shorter than that of LBO. The CBO crystal can generate UV light as short as ~ 185 nm, which could not be realized using BBO and LBO crystals [40]. The NLO coefficients of CBO and LBO are almost the same [$d_{14}(\text{CBO}) \sim d_{31}(\text{LBO}) \sim d_{32}(\text{LBO})$] [11]. The marked advantage of CBO over LBO is a larger effective NLO coefficient for UV light generation. The effective NLO coefficients of CBO are given by $d_{\text{eff}} = d_{14}\sin 2\theta$ or $d_{14}\sin 2\phi$ [41] in contrast to that of LBO, which is reduced by a factor of $\cos \theta$ or $\cos \phi$. In particular, d_{eff} of CBO for type-2 third harmonic generation ($1064 \text{ nm} + 532 \text{ nm} \rightarrow 355 \text{ nm}$) or type-1 SHG ($1064 \text{ nm} + 355 \text{ nm} \rightarrow 266 \text{ nm}$) is close to its maximum.

The $(B_3O_7)^{5-}$ network reported so far is connected with one type of cation, that is Li or Cs of LBO and CBO, respectively. We attempted to search for new NLO borate crystals based on the $(B_3O_7)^{5-}$ network. Instead of one, we tried to include two alkali metals into the borate network. Many combinations of various alkali metals were attempted and several of them crystallized [42]. Most of these phases are either not SHG active or weak in SHG. By this method, we found a new phase: $CsLiB_6O_{10}$, from the melted mixtures of Cs_2CO_3 , Li_2CO_3 , and B_2O_3 powders [43].

The relationship between composition and melting temperature in the $(Cs_2O + Li_2O)-(B_2O_3)$ system was investigated. In this case, the ratio of Cs_2O relative to Li_2O was fixed at 1:1 while the proportional ratios of (B_2O_3) to $(Cs_2O + Li_2O)$

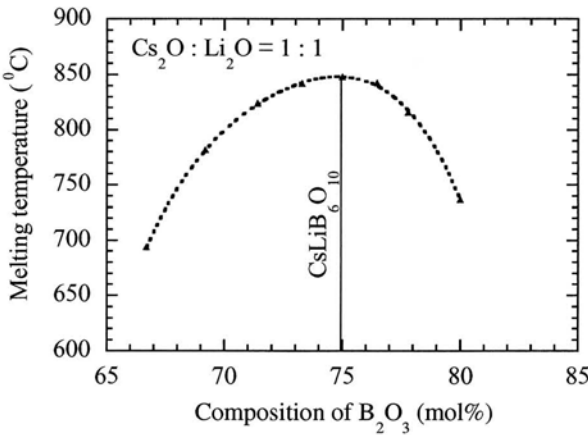


Fig. 13.1. Melting temperatures of the $(\text{Cs}_2\text{O} + \text{Li}_2\text{O})\text{-}(\text{B}_2\text{O}_3)$ system

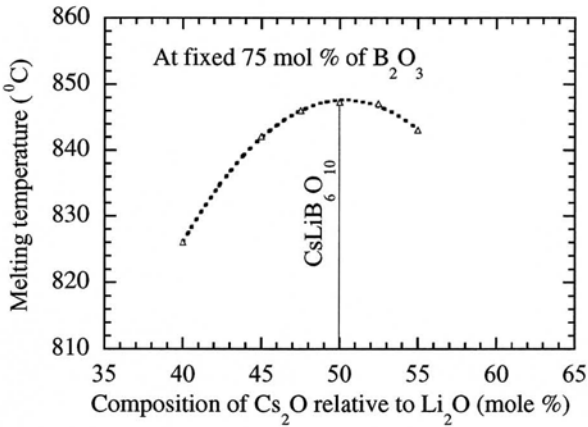


Fig. 13.2. Melting temperatures of the $(\text{Cs}_2\text{O})\text{-}(\text{Li}_2\text{O})$ system at 75 mole % of B_2O_3

were varied from 80.0 to 66.7 mol %. As shown in Fig. 13.1, CLBO was found to melt congruently at 848°C. The recognized phase was CLBO for all indicated data points except at 66.7 mole % of B_2O_3 where CBO coexisted. Next, the system of $(\text{Cs}_2\text{O})\text{-}(\text{Li}_2\text{O})$ was studied by fixing the B_2O_3 content at 75 mole %. In this case, the ratio of Cs_2O to Li_2O was varied from 40.0 to 55.0 mole %. The procedure described for the $(\text{Cs}_2\text{O} + \text{Li}_2\text{O})\text{-}(\text{B}_2\text{O}_3)$ system was repeated. As shown in Fig. 13.2, CLBO was found to melt congruently at 848°C. From these results, the stoichiometric melt must contain $\text{Cs}_2\text{O}:\text{Li}_2\text{O}:\text{B}_2\text{O}_3$ at a ratio of 1:1:6 to grow CLBO at $\sim 848^\circ\text{C}$.

13.2.2 Growth of CLBO

Like the CBO crystals, CLBO crystals are relatively easy to grow. Bulk crystals can be grown from both the stoichiometric melt and a solution by TSSG [44]. A five-zone vertical furnace, as shown in Fig. 13.3 was used due to its high spatial temperature uniformity. The seed rod was rotated at a rate of 15 rpm and inverted to the opposite direction every three minutes. The growth temperature was decreased at a rate of $0.1^{\circ}\text{C}/\text{day}$ during crystal growth. The CLBO crystal with dimensions of $29 \times 20 \times 22 \text{ mm}^3$ was grown from a stoichiometric melt in four days [44]. Solution growth was carried out from a starting mixture of Cs_2CO_3 , Li_2CO_3 , and B_2O_3 at a ratio of 1:1:5.5 (73.3% B_2O_3). The self-fluxed solution poor in B_2O_3

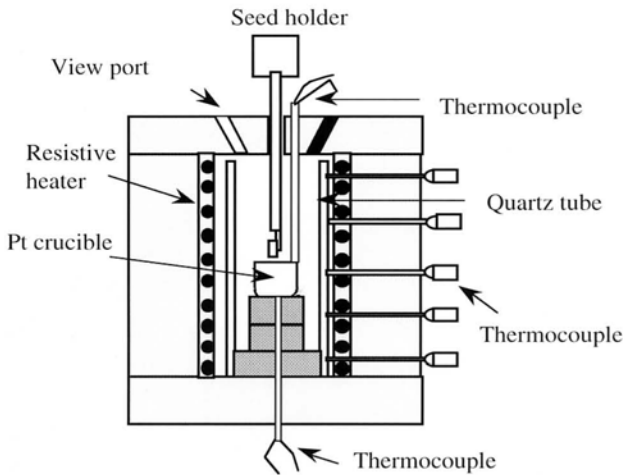


Fig. 13.3. Schematic of a five-zone vertical furnace for top-seeded solution growth of CLBO crystals

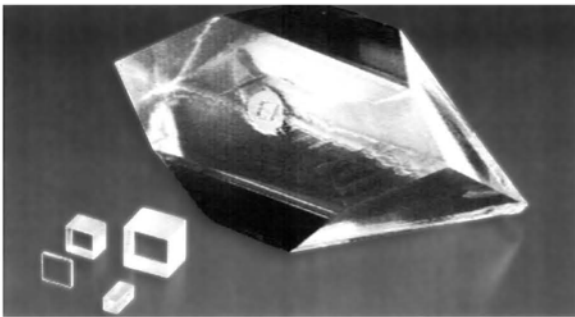


Fig. 13.4. Photograph of a large CLBO crystal with dimensions of $14 \times 11 \times 11 \text{ cm}^3$

was chosen due to its relatively low viscosity. The estimated saturation temperature was 845°C. High-quality CLBO crystal as shown in Fig. 13.4 can be grown this way.

13.2.3 Structural and optical properties of CLBO

The CLBO crystal has a tetragonal structure with a space group of I42d (#122) and cell dimensions of $a = 10.494$, $c = 8.939$ Å, and $Z = 4$, totally different from that of CBO and LBO crystals. The structure is composed of eight-coordinated Cs and four-coordinated Li atoms within the borate network. The basic structural unit of this network is the $(B_3O_7)^{5-}$ anionic. Likewise, the molecular packing of CLBO in a three-dimensional framework is shown in Fig. 13.5. A detailed description of the crystal structure is provided elsewhere [17].

Properties of CLBO that relate to its abilities of high-power laser frequency conversion are listed in Table 13.2. The angular, spectral, and temperature ($\Delta\theta/l$, $\Delta\lambda/l$, $\Delta T/l$, respectively) bandwidths are compared to other frequently used NLO crystals like KD_2PO_4 (DKDP or KD*P), KDP, and BBO. In general, CLBO exhibits a relatively high bulk laser-induced damage threshold [24 GW/cm² and 26 GW/cm² along (001) and (100) directions, respectively] at 1.064 μm with 1.1 ns pulse width. For UV light generation, CLBO has an effective NLO coefficient between BBO and KDP, moderate birefringence between that of LBO and BBO (Table 13.1), and possess a smaller walk-off angle and larger angular, spectral, and temperature bandwidths than KDP and BBO.

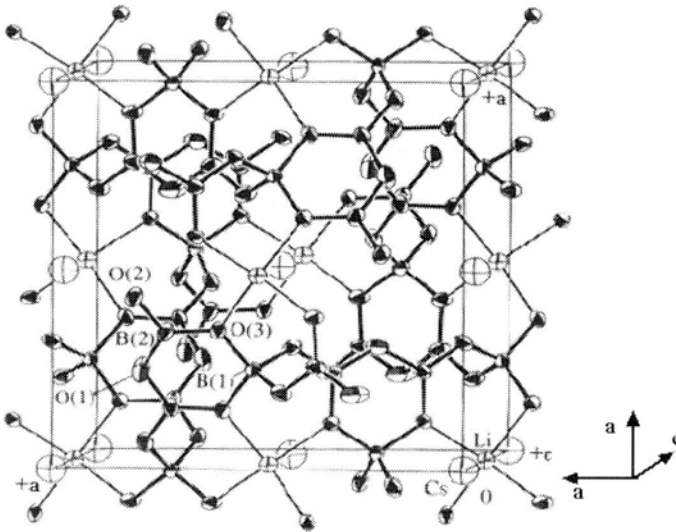


Fig. 13.5. Molecular packing of CLBO in a three-dimensional framework

Table 13.2. Properties of CLBO crystals for harmonic generation of Nd:YAG lasers as compared to other NLO crystals

Wavelength [nm]	NLO crystal	Phase matching angle [θ/deg.]	d _{eff} [pm/V]	Δθ [mrad-cm]	Δλ [nm-cm]	ΔT [°C-cm]	Walk-off angle [deg.]	Damage threshold [GW/cm ²]
1064 + 1064 = 532	CLBO (Type-2)	41.9	0.95	1.7	5.6	43.1	1.78	26
	KDP (Type-2)	59	0.38	3.4	11.5	19.1	-	~20
	KD*P (Type-2)	53.5	0.4	5.0	5.6	6.7	1.38	-
	BBO (Type-1)	22.8	2.06	0.92	2.1	37.1	3.2	13.5
1064 + 532 = 355	CLBO (Type-2)	48.4	0.94	0.82	0.84	21.3	2.1	-
	KDP (Type-2)	58	0.38	1.06	0.95	-	-	-
532 + 532 = 266	CLBO (Type-1)	61.9	0.84	0.49	0.13	8.3	1.83	6.4
	KDP	78	0.51	1.7	0.13	1.2	-	-
	BBO	47.5	1.32	0.27	0.07	4.5	4.8	-
1064 + 266 = 213	CLBO (Type-1)	67.4	0.87	0.42	0.16	4.6	1.69	-
	KDP	51.1	1.26	0.19	0.08	3.1	5.34	-

13.2.4 Degradation of CLBO crystallinity and solution

CLBO possesses good combinations of NLO properties for UV light generation. However, CLBO is hygroscopic and this distorts the refractive index of the CLBO crystal. Many NLO borate crystals are hygroscopic, including CBO and LBO. Hydration of CLBO crystals ($\text{Cs}_2\text{B}_{10}\text{O}_{16} \cdot 8\text{H}_2\text{O}$) was detected with X-ray diffraction (XRD) and occurs at a relatively faster rate at high humidity (>45%), which eventually leads to crystal cracking [45]. Such hydration is eliminated at ~120°C. Basically, one can solve the hydration problem by keeping the crystal dry.

The main problem with CLBO is distortion of the refractive index of the crystal. Such distortions are indicated by the degradation of device performance and are detectable by using a laser transmission interferometer (LTI). Distortion of refractive index is generally induced by mechanical stress arising from various factors. Reduction of distortion rate at low ambient humidity [45] revealed that hydration is one of the origins of stress. However, distortion can still happen if a

device is subjected to dry conditions during use, which indicates that thermal shock introduced during laser operation can also cause crystalline degradation. We have attempted to stabilize the crystallinity of CLBO.

Effect of doping in CLBO

Doping can modify properties of a given material. For borate crystals, systematic investigation of doping has not been reported. We found that various metals can be used to dope CLBO [46]. As shown in Fig. 13.6, the doping efficiency of metal atoms is dependent on ionization number. Doping efficiency is defined as the ratio of dopant concentration in the crystal to that in the growth solution, that is, the ratio between “Metal/Cesium” in the crystal and “M/Cs” in the growth solution, where M = metal. Composition was measured by ICP (inductive coupled plasma) analysis.

For alkali metals, the highest doping efficiency was observed for Rb as compared to K and Na. This is explained by the radii of the Rb⁺ cation closest to that of the Cs⁺ cation. The doping efficiency of Rb atoms increases with increasing dopant concentration in the melt. Almost 100% of the Rb atoms in the melt can be incorporated into CLBO crystals. Single crystals of CLBO:Rb up to a doping concentration as high as 10 mole % can be obtained without inclusions and cracking. Four-circle X-ray diffraction (XRD) analysis revealed that Rb is incorporated by substitution for Cs.

A much lower doping efficiency was observed for alkali earth metals (Mg, Ca, Sr, Ba) compared to that for alkali metals. This might be due to the differences in the ionization number between alkali and alkali earth metals. Despite this, CLBO:Mg crystals with doping concentration as high as 10 mole % can be obtained without inclusions and cracking. On the other hand, it is interesting that Al and Ga can also be used to dope CLBO despite the fact that they are group III elements. The XRD analysis showed that the a-axis expanded while the c-axis contracted as the doping concentration increased. High-quality single CLBO:Al crystals can be obtained up to a doping concentration of about 5 mole %. The doping sites of these elements are not clear.

The effects of doping on various properties of CLBO have been studied [46]. We found that Rb doping could reduce the shortest SHG wavelength that can be phase-matched (λ_c) by CLBO. For example, the λ_c is 2 nm shorter for a CLBO:Rb crystal of 10 mole %. The Rb doping, however, makes CLBO fragile. This was also the case for K and Na doping. On the other hand, Al doping gives rise to an enhancement of mechanical properties of CLBO. Figure 13.7 shows the Vickers hardness as a function of the Al/Cs ratio in the melt. Each data point represents an average value obtained from several indentations. The hardness of undoped CLBO was 270 and 180 for (100) and (001) planes, respectively. The values for 1% Al-doped and 5% Al-doped CLBO were 290 and 310 for (100) and 220 and 230 for (001) surfaces. A similar enhancement of hardness was observed from the doping of Ga. Note that the hygroscopic nature of CLBO is also suppressed by doping with Al. The undoped and 2 mole % Al-doped CLBO crystals were dissolved in a

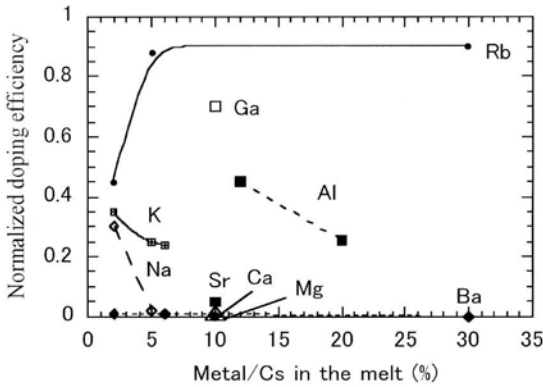


Fig. 13.6. The doping efficiency of various impurities in CLBO crystals as a function of dopant concentration in the melt

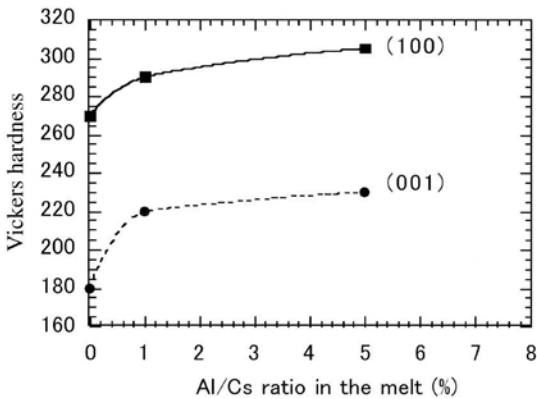


Fig. 13.7. Vickers hardness of Al-doped CLBO (100) and (001) surfaces as a function of Al/Cs ratio in the growth melt

solution of H₂O (20%) and glycerin (80%) for investigation. The samples were dipped in the solution during the experiment. We found that the Al-doped CLBO is less soluble than undoped CLBO [46,47].

Stabilizing CLBO at elevated crystal temperature

Doping with Al improves both mechanical and chemical properties of CLBO. However, these enhancements are insufficient to protect CLBO from crystalline degradation [48]. Thus another attempt was introduced. In fact, it is known that the lattice constants of CLBO crystals are sensitive to changes in the crystal temperature [49]. As shown in Fig. 13.8, an extraordinary behavior of CLBO is ob-

served, where (a) an elongation along the a -axis occurs together with (b) a contraction along the c -axis. A careful interpretation reveals that such changes are relatively larger within the range of room temperature to $\sim 100^\circ\text{C}$ [50]. Note that above 120°C , stress from hydration can be relieved by elimination of CLBO hydrates. Thus, stabilizing a CLBO device at an elevated crystal temperature well above 120°C stabilizes its crystallinity and relieves the crystal distortion from hydration. A detailed investigation was carried out to verify this argument [51–53].

The CLBO crystals were continuously kept at 160°C for long-term observation [52]. The performance of CLBO was examined by measuring the 2ω output of a doubler and 4ω output of a quadrupler. Degradation of crystallinity, if any, was indicated by a decrease in the corresponding harmonic output. As shown in Fig. 13.9, CLBO crystals maintained their crystalline conditions for more than 1 month when exposed to ordinary room humidity. Note that cracking sometimes happened within one week when crystals were continuously exposed to room humidity at room temperature even without being subjected to laser operation [48].

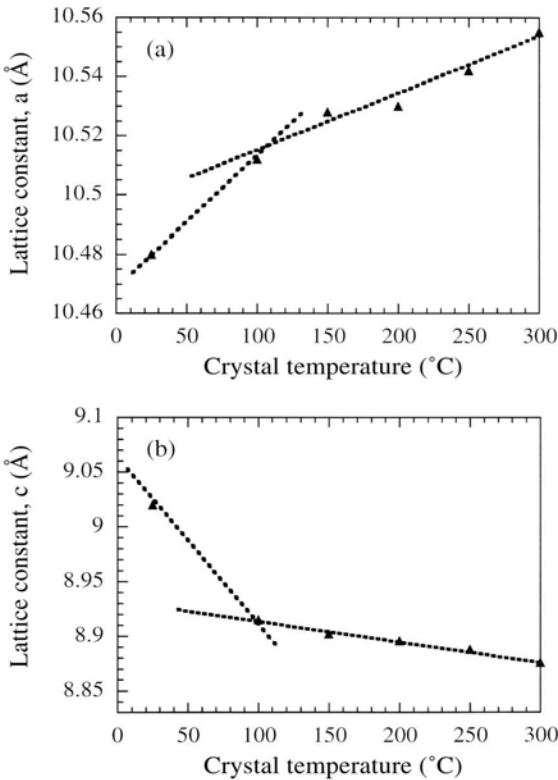


Fig. 13.8. (a) Elongation of CLBO lattice constant along the a -axis and (b) contraction of CLBO lattice constant along the c -axis

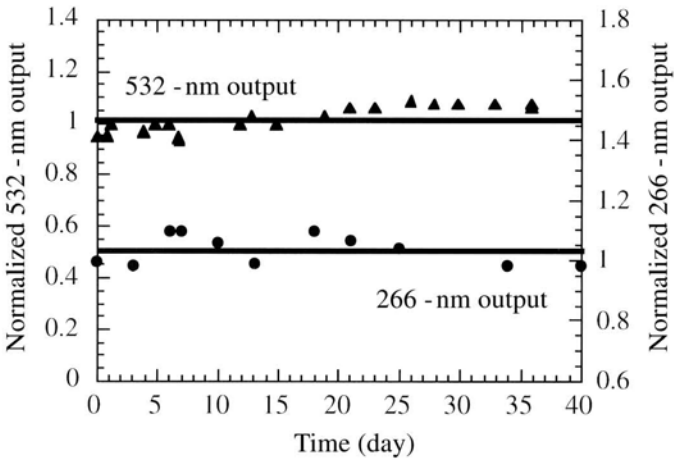


Fig. 13.9. Normalized output energy at 532 and 266 nm from CLBO crystals at 160°C. Stable performance was obtained for more than one month with continuous exposure to ordinary room humidity.

From the point of view of nature, a crystal is most stable in its intrinsic physical structure. For the purpose of applications, NLO crystals are shaped beyond such a stable structure. Thus mechanical stress on a device is always introduced, particularly on the surrounding edges. This effect is very obvious for CLBO crystals due to the existence of large interstitial spaces surrounding the sides of Cs ions [52]. Thus, stress from crystal processing is sufficient to cause crystalline distortions in CLBO. Note that the space is relatively large along the c -axis or $\langle 001 \rangle$ (vertical direction of the figure), and this tends to contract when the neighboring borate network is subjected to thermal vibration. The borate rings joined by the Li ion appeared like a pantograph network. Such a crystalline structure allows active vibration of the Cs ions and their surrounding borate network even at moderate crystal temperatures. This vibration is likely to promote crystal annealing even at temperatures well below the crystal's melting point. At an elevated crystal temperature, such as 160°C, hydration stress on CLBO crystals is prevented. Under this condition, physical stress from crystal processing and thermal shock from laser power absorption can be relieved by activated phonon vibration. Thus, the long-term stability of a CLBO crystal is maintained at an elevated crystal temperature. Note that, as shown in Fig. 13.8, an elevated temperature as low as 80–100°C should be sufficient to obtain long-term operation of CLBO crystals in dry ambient air. In fact, CLBO is currently employed in several commercial solid-state UV laser systems.

13.2.5 Performance of CLBO for generation of deep-UV light

The superior abilities of CLBO crystals for generating UV radiation (4ω and 5ω Nd:YAG laser) were clearly demonstrated at 10 Hz [54], 100 Hz [55], and 1 kHz [56]. For example, the 266 nm output from CLBO is 2.5 times higher than that generated from high-quality BBO (super-BBO/ S-BBO) [56]. An average output of 20.5 W at $\lambda = 266$ nm was recently generated at 10-kHz by means of CLBO crystals [57–59]. The CLBO crystal is no doubt the most effective NLO crystal for deep-UV light generation. This is due to the relatively small walk-off angle of CLBO (related to its moderate birefringence) that produces better spatial overlapping of the mixing beams. Its relatively large angular, spectral, and temperature acceptance bandwidths favor CLBO for stable UV light generation [54]. These properties, in addition to its shorter absorption edge at 180 nm, eventually lead to a high conversion efficiency and stable output of UV radiation. The output-input relation of the 20.5 W UV light ($\lambda = 266$ nm) generation is shown in Fig. 13.10.

Note that CLBO crystals have also been characterized for the operation of continuous-wave [60], picosecond [61,62], femtosecond [63,64], and various schemes of UV lasers [65–72]. High-power UV light at $\lambda = 213$ nm was also used as the pump source for vacuum ultraviolet (VUV) Raman lasers to generate radiation at wavelengths as short as 124.7 nm [73]. It is noteworthy that CLBO was demonstrated to produce deep-UV light at $\lambda = 193$ nm by 8 ω generation of the Er³⁺-doped fiber amplifier [74]. The conversion efficiency from the fundamental wavelength of 1547 nm was 7% by using the CLBO crystal as the eighth harmonic generator ($\omega + 7\omega$). The conversion efficiency was 1.3% when CLBO was replaced by LBO crystal. The schematic layout of this experiment is shown in Fig. 13.11. This is the most effective generation of 193 nm light from an all-solid-state system.

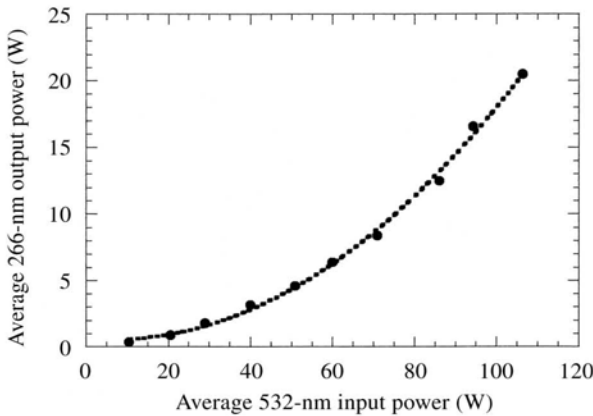


Fig. 13.10. Average UV ($\lambda = 266$ nm) output power as a function of average green input power at 10 kHz. The dotted line is to guide the eyes.

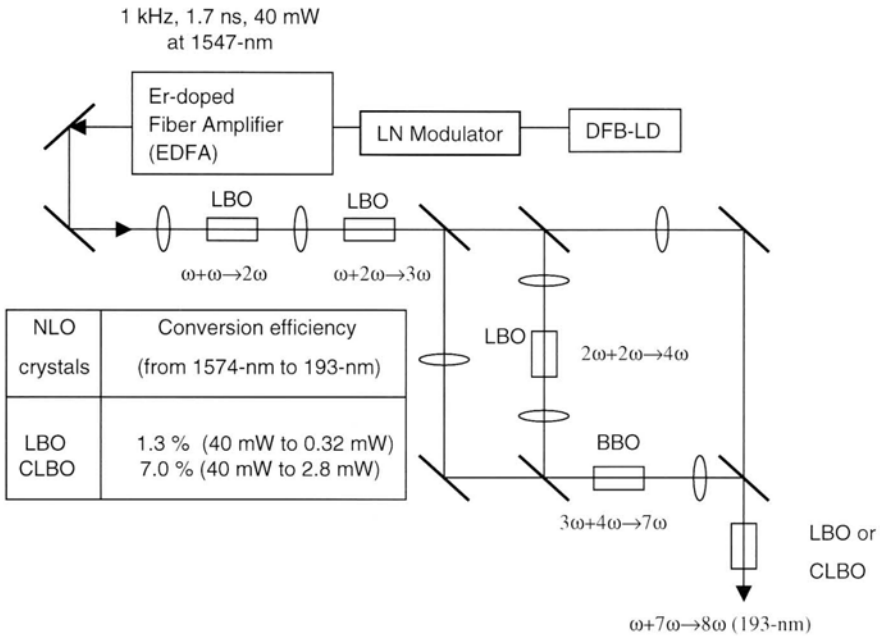


Fig. 13.11. Schematic of experimental set-up for deep-UV light generation at 193 nm

13.2.6 Relation between crystal quality and resistance to bulk laser-induced damage

Laser-induced damages and UV absorption of NLO crystals are among the limitations of the development of solid-state UV radiation by NLO crystals. Microscopic crystal defects inside the NLO devices are the important factors that cause laser-induced damage and UV light absorption. The improvement of bulk quality NLO crystals can effectively reduce the UV absorption, suppress the thermal dephasing, enhance the bulk laser damage threshold, and thus improve the performance of solid-state UV lasers. We have developed a modified crystal growth technique to obtain high-quality CLBO crystals. We found that resistance to bulk laser-induced damage can be enhanced by upgrading crystal quality. This was achieved by the implementation of a stirred solution technique [75]. The bulk laser-induced damage threshold was measured using the 0.75 ns FWHM fourth harmonic generation (266 nm) of a Nd:YAG laser employed in the experiment described previously. The bulk laser-induced damage threshold for CLBO grown by the conventional TSSG method and that grown by the stirred solution technique are shown in Table 13.3. The data from a fused quartz sample was taken as a reference. As shown, the maximum bulk laser-induced damage threshold of CLBO grown by the stirred solution technique increased from 10.4 to 25.4 GW/cm².

Table 13.3. The bulk laser-induced damage threshold of CLBO grown by a conventional TSSG method and by a stirred solution technique. The damage threshold of fused quartz is shown for comparison

	CLBO crystals		Fused quartz
	Stirred solution technique	Conventional TSSG	
Damage threshold (GW/cm ²)	10.4-25.4	8.8-10.4	10.4

The CLBO grown from the stirred solution technique exhibits a bulk laser-induced damage threshold ~2.5 times higher than the conventional CLBO and fused quartz. This result simply implies the improvement of CLBO crystallinity by our stirred solution technique. The details of this technique will be discussed in the future.

13.3 GdYCOB Crystal for Noncritical Phase-Matching (NCPM) of Visible and UV Light

13.3.1 The search for $\text{Gd}_x\text{Y}_{1-x}\text{Ca}_4\text{O}(\text{BO}_3)_3$ (GdYCOB)

The GdYCOB crystal belongs to the so-called rare-earth (Re) calcium oxyborate family, with a general composition of $\text{ReCa}_4\text{O}(\text{BO}_3)_3$. This crystal family is called oxyborate because not all the oxygen atoms are directly bonded to the boron. The first compound in this series, $\text{SmCa}_4\text{O}(\text{BO}_3)_3$ was studied by Khamaganova et al. (1991) [76]. One year later, a series of compounds from this family were examined by Norrestam et al. with $\text{Re} = \text{La}, \text{Nd}, \text{Sm}, \text{Gd}, \text{Er}, \text{and Y}$ [77]. Ilyukhin and Dzhurinskii investigated compounds with $\text{Re} = \text{Gd}, \text{Tb}, \text{and Lu}$ [78]. The space group of this family is monoclinic noncentrosymmetric Cm with $Z = 2$. In 1996, Aka et al. grew a single crystal of $\text{GdCa}_4\text{O}(\text{BO}_3)_3$ (GdCOB) by the conventional Cz method and reported its NLO properties [27,28]. The GdCOB melts congruently at 1480°C. In addition, Y and La were indicated to be alternative rare-earth atoms (Re) for $\text{ReCa}_4\text{O}(\text{BO}_3)_3$ NLO crystals [27]. One year later, Iwai et al. (1997) reported on the growth of GdCOB and YCOB single crystals and investigated their differences in terms of linear and nonlinear optical properties [18]. Furthermore, $\text{ReCa}_4\text{O}(\text{BO}_3)_3$ ($\text{Re} = \text{Gd}, \text{Lu}, \text{Yb}, \text{Tm}, \text{Y}, \text{Sm}, \text{Nd}, \text{La}$) were confirmed to be SHG active [79]. Total substitution of the Ca site by Mg, Sr, and Ba was also attempted, but these compounds did not produce SHG [79].

The detailed linear and NLO properties of GdCOB crystals were reported in 1997 [18,80]. This crystal appeared to be effective for SHG of Nd:YAG lasers. The main advantages of GdCOB compared to other borate crystals are the ease of crystal growth and that they are absolutely nonhygroscopic. This crystal has a

relatively small birefringence ($\Delta n = 0.033$ at $\lambda = 1064$ nm) and has a significant effective NLO coefficient of 1.3 pm/V [18]. The crystal structure of GdCOB is shown in Fig. 13.12 with $a = 8.0937$, $b = 16.013$, $c = 3.5579$ Å and $\beta = 101.27^\circ$ [18].

The properties of the YCOB crystal are significantly different from those of GdCOB [18]. The YCOB melts congruently at 1510°C and was grown by conventional Cz using an Ir crucible in an Ar atmosphere. The YCOB crystal has a slightly smaller NLO coefficient (1.1 pm/V). Note that GdCOB has several absorption lines within 240 to 320 nm that are characteristic of Gd^{3+} . The YCOB has a UV cut-off at 210 nm and is highly transparent up to 2500 nm [20]. The structure of YCOB is identical to that of GdCOB with slightly smaller lattice constants a , b , c and β angle [18]. The most important property of YCOB is the relatively larger birefringence of 0.041 at $\lambda = 1064$ nm. This allows UV generation by YCOB by third harmonic generation (THG) of a Nd:YAG laser (1064 nm + 532 nm \rightarrow 355 nm) that is not possible using GdCOB [18,81]. The shortest type-1 SHG wavelengths phase-matchable along the y -axis of YCOB and GdCOB are estimated at ~ 360 nm and 420 nm [82], respectively, by the Shellmeier equations proposed by Mougél et al. [83]. The difference in birefringence between GdCOB and YCOB is related to the higher lattice constant ratio (a/c) of YCOB (~ 2.288) compared to that of GdCOB (~ 2.275) [82].

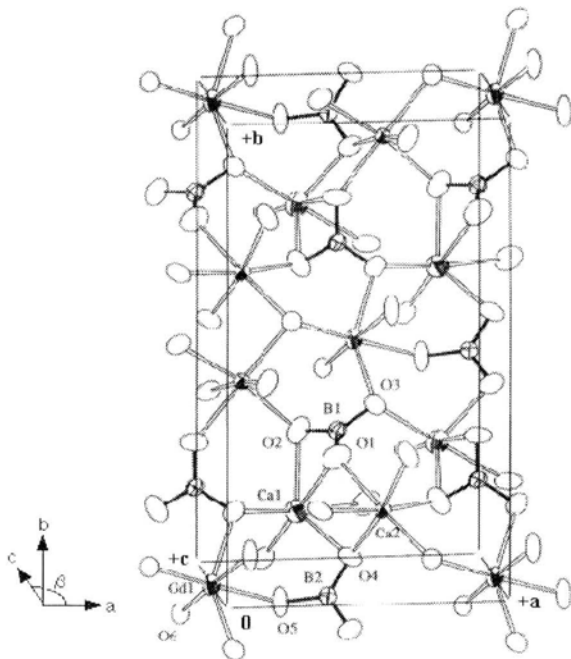


Fig. 13.12. Molecular packing of GdCOB in a three-dimensional framework

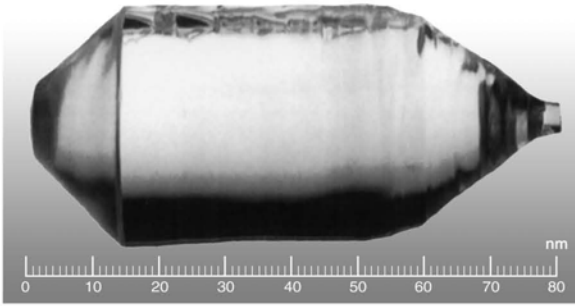


Fig. 13.13. Photograph of the Cz-grown GdYCOB crystal

The total substitution of Gd in GdCOB by Y results in YCOB that is larger in birefringence for producing THG of Nd:YAG lasers. This result simply implies the possibility of modifying crystal birefringence by changing the ratio of Gd:Y in the crystals [81,84]. Single crystals of $Gd_xY_{1-x}Ca_4O(BO_3)_3$ were grown like those of GdCOB and YCOB. The as-grown crystal of $Gd_xY_{1-x}Ca_4O(BO_3)_3$ is shown in Fig. 13.13. The ratios of lattice constants (a/c , a/b) in $Gd_xY_{1-x}Ca_4O(BO_3)_3$ ($x = 0, 0.48, 1$) crystals were measured using a four-circle X-ray diffractometer. The ratios of lattice constants a/c and a/b in GdYCOB were linearly changed with the increase compositional parameter x [20]. This result confirms that GdYCOB is a substitutional solid solution and that it is possible to vary its refractive indices continuously.

13.3.2 Noncritically phase-matched THG for Nd:YAG lasers by GdYCOB

It is known that laser frequency conversion by noncritical phase-matching (NCPM) along the principle axes is advantageous because of a larger angular acceptance and the elimination of the walk-off effect. The phase-matching angles for type-1 THG in YCOB were experimentally determined as $(\theta, \phi) = (90^\circ, 73.2^\circ)$ and $(58.7^\circ, 90^\circ)$ in the xy and yz planes, respectively. In general, as the birefringence of a NLO crystal decreases, the phase-matching angles shift towards a larger value. Partial substitution of Gd for Y in YCOB crystals makes the birefringence small; therefore, we expect to achieve NCPM THG along the y axis by introducing appropriate Gd atoms into the sites of Y atoms of YCOB; i.e. phase-matching of THG in the xy and yz planes should shift toward $(\theta, \phi) = (90^\circ, 90^\circ)$.

We examined the phase-matching angles on the principal planes (xy, yz) for various GdYCOB compounds. The experiments were carried out at room temperature. Type-1 GdYCOB crystals were cut at the y -axis or phase-matching direction for THG. Figure 13.14 represents the phase-matching angles for type-1 THG as a function of the compositional parameter x in $Gd_xY_{1-x}Ca_4O(BO_3)_3$

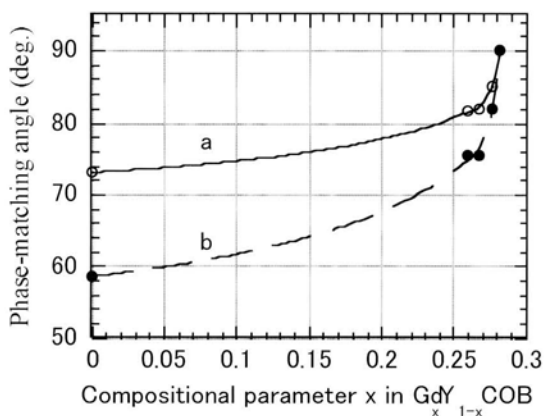


Fig. 13.14. Changes of phase-matching angles for THG as a function of the compositional parameter x

Table 13.4. Properties of GdYCOB for THG of Nd:YAG lasers compared to those of YCOB, LBO, and KDP

	d_{eff} [pm/V]	External angular Acceptance bandwidth [mrad cm]		Temperature bandwidth [°C cm]	Walk-off angle [mrad]
		$\Delta\theta l$	$\Delta\phi l$		
YCOB (type I, xy)	0.52	-	3.2	9.7	8.5
GdYCOB (type I, y)	0.55	114 mrad cm ^{1/2}	65.6 mrad cm ^{1/2}	6.6	0
LBO (type I, xy)	0.68	-	1.71	19.0	18.3
LBO (type II, yz)	0.50	5.02	-	3.7	9.30
KDP (type II)	0.35	1.58	-	5.20	26.5

crystals. For curve a, the wave vector k is in the xy plane and the phase-matching angle is ϕ from the x -axis. Similarly, for curve b the phase-matching angle is θ from the z -axis in the yz plane. The phase-matching angles gradually change to 90° due to increasing of x in $\text{Gd}_x\text{Y}_{1-x}\text{Ca}_4\text{O}(\text{BO}_3)_3$. At $x = 0.28$, the phase-matching angle reaches $(\theta, \phi) = (90^\circ, 90^\circ)$, which is the type-1 noncritical phase-matching at room temperature.

The phase-matching properties for THG of $\text{Gd}_{0.28}\text{Y}_{0.72}\text{Ca}_4\text{O}(\text{BO}_3)_3$ are summarized in Table 13.4 together with those of YCOB, LBO, and KDP. As indicated, we have improved the angular properties of YCOB for THG by the substitution of Gd for Y in YCOB. Furthermore, the zero walk-off effect in $\text{Gd}_{0.28}\text{Y}_{0.72}\text{Ca}_4\text{O}(\text{BO}_3)_3$ allowed perfect spatial overlapping of the mixing beams for THG. These advantages contribute to a THG output from $\text{Gd}_{0.28}\text{Y}_{0.72}\text{Ca}_4\text{O}(\text{BO}_3)_3$ five times higher than that by YCOB [85,86]. These results suggest that $\text{Gd}_{0.28}\text{Y}_{0.72}\text{Ca}_4\text{O}(\text{BO}_3)_3$ is suitable for THG generation and that a longer crystal can be utilized for higher frequency conversion efficiency.

13.3.3 Noncritically phase-matched SHG for Nd:YAG lasers by GdYCOB

We found that the phase-matching angles for type-2 SHG in $\text{Gd}_x\text{Y}_{1-x}\text{Ca}_4\text{O}(\text{BO}_3)_3$ also changed to 90° with an increase in the compositional parameter x , and the angles reached $(\theta, \phi) = (90^\circ, 90^\circ)$ at $x = 0.275$ [87,88]. In addition, $\text{Gd}_{0.28}\text{Y}_{0.72}\text{Ca}_4\text{O}(\text{BO}_3)_3$ was also confirmed to generate SHG along the same direction. That is, the $\text{Gd}_{0.28}\text{Y}_{0.72}\text{Ca}_4\text{O}(\text{BO}_3)_3$ crystal is NCPM for both type-2 SHG and type-1 THG at room temperature.

The phase-matching properties of type-2 SHG in a $\text{Gd}_{0.275}\text{Y}_{0.725}\text{Ca}_4\text{O}(\text{BO}_3)_3$ crystal were measured and are summarized in Table 13.5, together with those of KDP and LBO. We found that d_{eff} of $\text{Gd}_{0.275}\text{Y}_{0.725}\text{Ca}_4\text{O}(\text{BO}_3)_3$ is 0.35 pm/V, smaller than that of LBO and comparable to that of KDP. The angular acceptance bandwidths of $\text{Gd}_{0.275}\text{Y}_{0.725}\text{Ca}_4\text{O}(\text{BO}_3)_3$ are broader than those of the NCPM type-1 LBO [89]. The temperature bandwidth for type-2 SHG in $\text{Gd}_{0.275}\text{Y}_{0.725}\text{Ca}_4\text{O}(\text{BO}_3)_3$ is significantly larger than those of KDP and LBO. A detailed description of these measurements has been presented elsewhere [88].

Table 13.5. Properties of GdYCOB for SHG of Nd:YAG lasers compared to those of YCOB, LBO, and KDP

	d_{eff} [pm/V]	External angular Acceptance bandwidth [deg cm ^{1/2}]		Temperature bandwidth [°C cm]	Walk-off angle [mrad]
		$\Delta\theta l$	$\Delta\phi l$		
GdYCOB (type II, y axis)	0.35	11.5	6.8	32.4@27°C	0
KDP (type II)	0.35	0.2 deg cm	-	18.3@25°C	24.5
LBO (type I, x axis, 148°C)	0.85	4.1	5.7	4.8@149°C	0

13.3.4 Noncritically phase-matched SHG for Ti:sapphire lasers by GdYCOB

Tailoring the atomic ratio of Gd/Y adjusts the birefringence of GdYCOB crystals for NCPM type-2 SHG and type-1 THG of Nd:YAG lasers. We examined the range of NCPM type-1 SHG of Ti:sapphire using GdYCOB. As shown in Fig. 13.15 (a), the type-1 SHG wavelengths phase-matchable along the z -axis for $\text{Gd}_x\text{Y}_{1-x}\text{Ca}_4\text{O}(\text{BO}_3)_3$ at $x = 0$ (i.e., YCOB) and $x = 1$ (i.e., GdCOB) are estimated theoretically as 414 nm and 483 nm, respectively, using the Sellmeier equations proposed by Mougel et al. [83]. Experimentally, the NCPM type-1 SHG wavelengths at $x = 0$ and $x = 0.48$ are 415 nm and 462 nm, respectively. Thus, NCPM of type-1 SHG from ~ 415 to 483 nm can be obtained along the z -axis of GdYCOB.

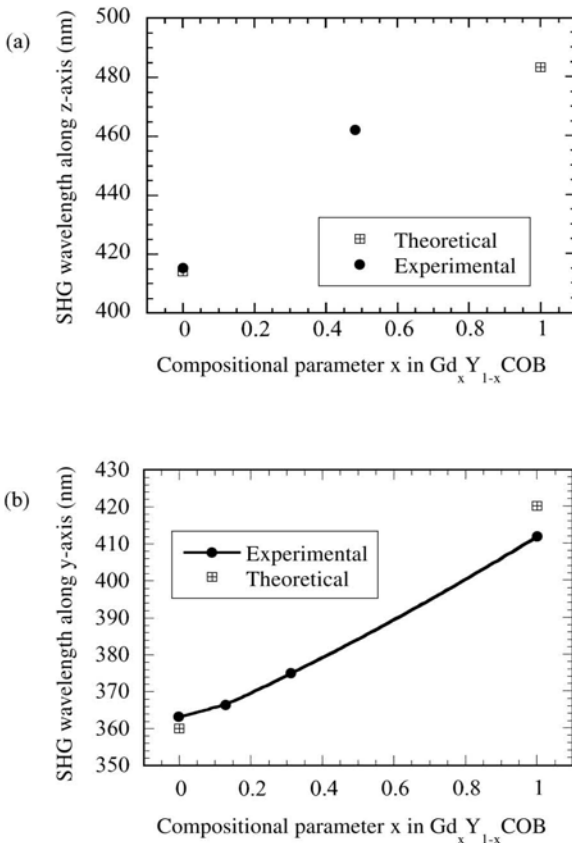


Fig. 13.15. Phase-matched wavelength produced by NCPM type-1 SHG along the (a) z -axis and (b) y -axis of $\text{Gd}_x\text{Y}_{1-x}\text{Ca}_4\text{O}(\text{BO}_3)_3$ as a function of compositional parameter x

Note that shorter SHG wavelengths can be produced by type-1 NCPM along the y -axis with a higher effective NLO coefficient. Several GdYCOB samples with various x compositions were examined using a Ti:sapphire laser. As shown in Fig. 13.15 (b), the NCPM type-1 SHG wavelengths are experimentally estimated to be ~ 363 nm, 366 nm, 375 nm, and 412 nm for cases in which $\text{Gd}_x\text{Y}_{1-x}\text{Ca}_4\text{O}(\text{BO}_3)_3$ at $x = 0$ (i.e., YCOB), 0.13, 0.31, and 1 (i.e., GdCOB), respectively. Thus, type-1 SHG wavelengths from ~ 363 to 412 nm can be obtained along the y -axis of GdYCOB. The effective NLO coefficient for type-1 SHG in this direction is estimated to be 0.55 pm/V.

13.3.5 Optical damage of GdYCOB and its solution

Gray-track and photorefractive damage in GdYCOB

The crystals of GdCOB, YCOB, and GdYCOB have several desired NLO properties for laser frequency conversion. The most interesting features offered by GdYCOB are the ability to generate visible and UV light by means of NCPM. All these crystals appeared to be promising for actual applications in high-power all-solid-state laser systems in the visible and near-UV regions. However, during the high-power THG operation of GdYCOB, optical damages were generated inside the crystals. In fact, two kinds of damages were identified: (1) gray-track and (2) photorefractive damage. Such damages also happened in other $\text{ReCa}_4\text{O}(\text{BO}_3)_3$ crystals like GdCOB and YCOB when irradiated by UV (355 nm) light. Furthermore, we found that these damages can be recovered by annealing at temperatures above 100 to 150°C. The minimum crystal temperature required to avoid gray-track seems to be lower for YCOB and higher for GdCOB. Details of these results were discussed elsewhere [90]. In addition, gray-track in these crystals was investigated by electron paramagnetic resonance (EPR) [91].

Prevention of optical damage in GdYCOB at elevated crystal temperature

We think that it is possible to use GdYCOB for high-power THG operation at elevated temperature without formation of gray-track and photorefractive optical damage. Laser experiments were carried out to verify this idea. As shown in Fig. 13.16, a diode-pumped high repetitive Nd:YVO₄ laser was used for the experiment. The fundamental power was measured before the type-1 LBO doubler, C₁. For frequency tripling, we compared GdYCOB to type-2 LBO. Note that birefringence of GdYCOB decreases with crystal temperature. Thus, GdYCOB crystal with a smaller composition of Gd/Y ($x < 0.28$) was grown for this experiment. The NCPM condition for THG in GdYCOB was fine-tuned by temperature and happened to perform NCPM at 240°C [92]. This crystal was 18 mm in length while the LBO crystal was 12 mm. Note that LBO crystal has AR coating while GdYCOB crystal does not.

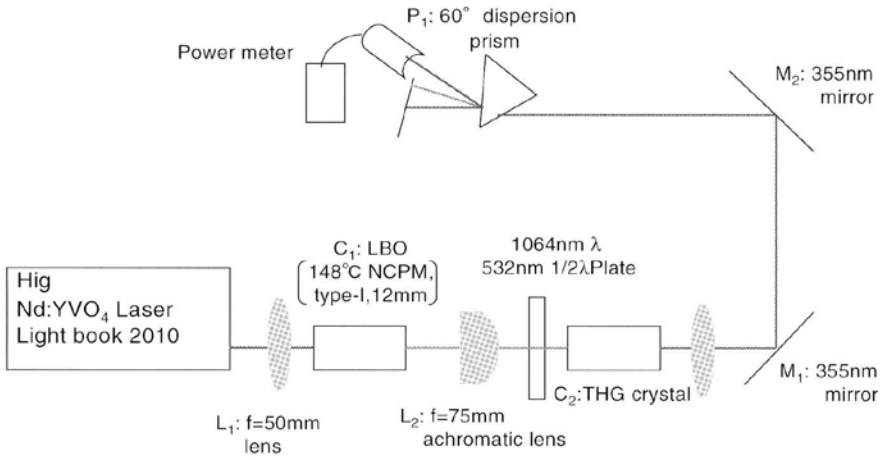


Fig. 13.16. Experimental set-up for high-repetition rate THG measurement

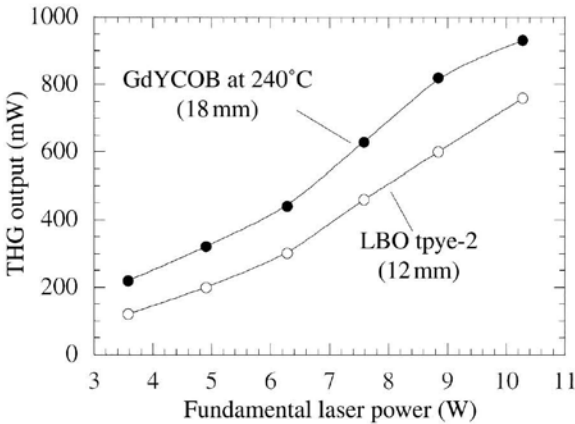


Fig. 13.17. UV output power at 355 nm for two NLO crystals

Figure 13.17 represents the relationship between the output power at 355 nm and the fundamental input power at a repetition rate of 62.5 kHz. For the case of LBO, the third-harmonic power was increased steadily up to 0.74 W. On the other hand, THG output of GdYCOB at 240°C is 0.93 W. Thus, performances of GdYCOB are comparable to that of LBO. Output stability at elevated temperature was excellent (< 1%) with nondistorted beam profile. Both photorefractive damage and gray-track were not formed after experiment. As indicated from this preliminarily result, GdYCOB at elevated temperature is suitable for practical generation of high-average power UV light at 355 nm.

Dependence of gray-track threshold of GdYCOB on the crystal growth atmosphere

Single crystals of GdYCOB were grown by the conventional Czochralski technique. The GdYCOB starting material was prepared by solid-state reaction of Gd_2O_3 , Y_2O_3 , CaCO_3 , and B_2O_3 [20]. In fact, oxygen or oxygen-containing atmosphere is required for the growth of oxyborate crystals like the GdCOB, YCOB, and GdYCOB. Due to the high growth temperatures ($\sim 1500^\circ\text{C}$), an Ir crucible is used instead of a Pt crucible because of its higher melting point (2457°C for Ir, 1772°C for Pt). However, oxygen must be avoided when using an Ir crucible in order to prevent oxidization. Thus, Ar atmosphere was employed when the Ir crucible was used. By this means, oxygen defects can be created in the crystals. We suspect that optical damages discussed so far are related to such crystal defects. Thus, GdYCOB crystals were grown in both Ar and ambient air. The sintered material of GdYCOB was melted in the Ir crucible (in the case of Ar atmosphere) or the Pt crucible (in the case of ambient air) by induction heating. The $\langle 010 \rangle$ -oriented seed crystal was used for crystal growth. For all cases, the pulling rate was 1–4 mm/h and the seed rotation rate was 10–15 rpm.

We examined the threshold of gray-track for GdYCOB grown in Ar and ambient air. Note that all GdYCOB crystals were optically polished without AR coating. Figure 13.18 represents the relationship between the growth atmosphere and gray-track damage threshold. For the case of GdYCOB grown in Ar atmosphere, the damage threshold at 355 nm was 2.3–3.1 MW/cm^2 . On the other hand, in the case of GdYCOB grown in ambient air, the damage threshold was 8.4–10.0 MW/cm^2 , about three-fold larger than that grown in Ar atmosphere.

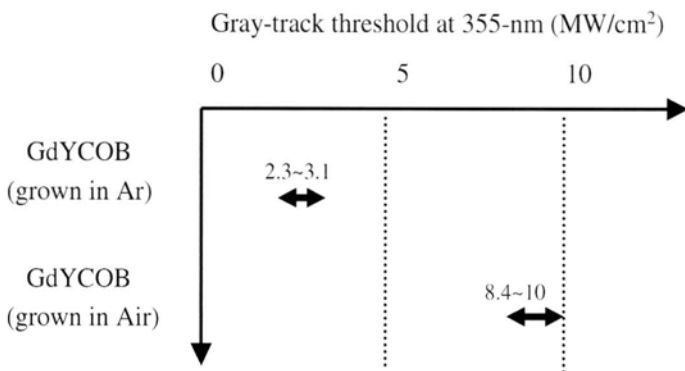


Fig. 13.18. Gray-track threshold of GdYCOB at laser wavelength of 355 nm

13.4 KAB Crystal: Difficulty of Growing Borate Crystal with Layered Structure

13.4.1 The search for $K_2Al_2B_2O_7$ (KAB)

In this section, we describe the search for a new NLO borate crystal: $K_2Al_2B_2O_7$ (KAB). In general, a good NLO crystal that can generate deep-UV light effectively is required to have a birefringence between that of BBO ($\Delta n = 0.12$ at $\lambda = 1064$ nm) [96] and LBO ($\Delta n = 0.04$ at $\lambda = 1064$ nm) [11]. This allows the expansion of the phase-matching range for SHG at a reasonably low walk-off effect and significantly large phase-matching bandwidths. The success of CLBO for high-power deep-UV light conversion is a good example. The CLBO has a birefringence of $\Delta n = 0.052$ at $\lambda = 1064$ nm, slightly larger than that of LBO, and thus can produce the shortest possible SHG wavelength of ~ 237 nm [94,95] as compared to 277 nm for LBO and 205 nm for BBO. Thus, more NLO crystals like CLBO that possesses a birefringence between that of BBO and LBO are desired for effective UV light conversion.

At a wavelength of 589 nm, the KBBF has $\Delta n = 0.072$ while the SBBO has $\Delta n = 0.062$ [96]. However, because of the weak binding between the layered structural units, KBBF is difficult to grow and is mechanically fragile [13]. The SBBO has strong covalent bonds between Be atoms and oxygen atoms in adjacent layers. This makes SBBO mechanically stronger and relatively easy to grow compared to the KBBF. However, Be is toxic, which makes crystal growth inconvenient. Thus, it is important that Be atoms in SBBO be replaced by a nontoxic element. We have attempted to replace $(BeO_4)^{6-}$ with $(AlO_4)^{5-}$ and to replace Sr^{2+} with M^+ ($M^+ = Li^+, Na^+, K^+, Rb^+, \text{ and } Cs^+$) according to the concept of ionic compensation ($Al^{3+} + K^+ \rightarrow Be^{2+} + Sr^{2+}$) [22,23]. In this way, we discovered the potassium aluminum borate crystal: $K_2Al_2B_2O_7$ (KAB), which possesses a spatial arrangement similar to that of SBBO.

The structure of KAB was analyzed by 4-axis X-ray diffraction (Rigaku AFC5R diffractometer). The KAB crystallizes in the trigonal space group P321 (#150) with $a = 8.5657$, $c = 8.463$ Å, $V = 537.7$ Å³, and $Z = 3$ [97]. As illustrated in Fig. 13.19, the basic structural features of the KAB crystal are K^+ cations, $(BO_3)^{3-}$ triangles, and distorted $(AlO_4)^{5-}$ tetrahedra. The triangular and tetrahedral anions form a three-dimensional $Al_2(BO_3)_2O$ framework which houses K^+ cations. This framework is constructed of nearly planar $[BO_3]$ - $[AlO_4]$ units with oxygen connecting the Al atoms between two adjacent layers at an Al-O-Al bond angle of 180° . K^+ cations are arranged in the spaces formed between the layers. Compared to SBBO, the major NLO active group of KAB is also the $(BO_3)^{3-}$ group, with its three terminal oxygen atoms linked to Al atoms. The KAB crystal possesses a spatial arrangement similar to SBBO. The powder of $K_2Al_2B_2O_7$ was previously studied by Kaduk and Sate (1996) [98].

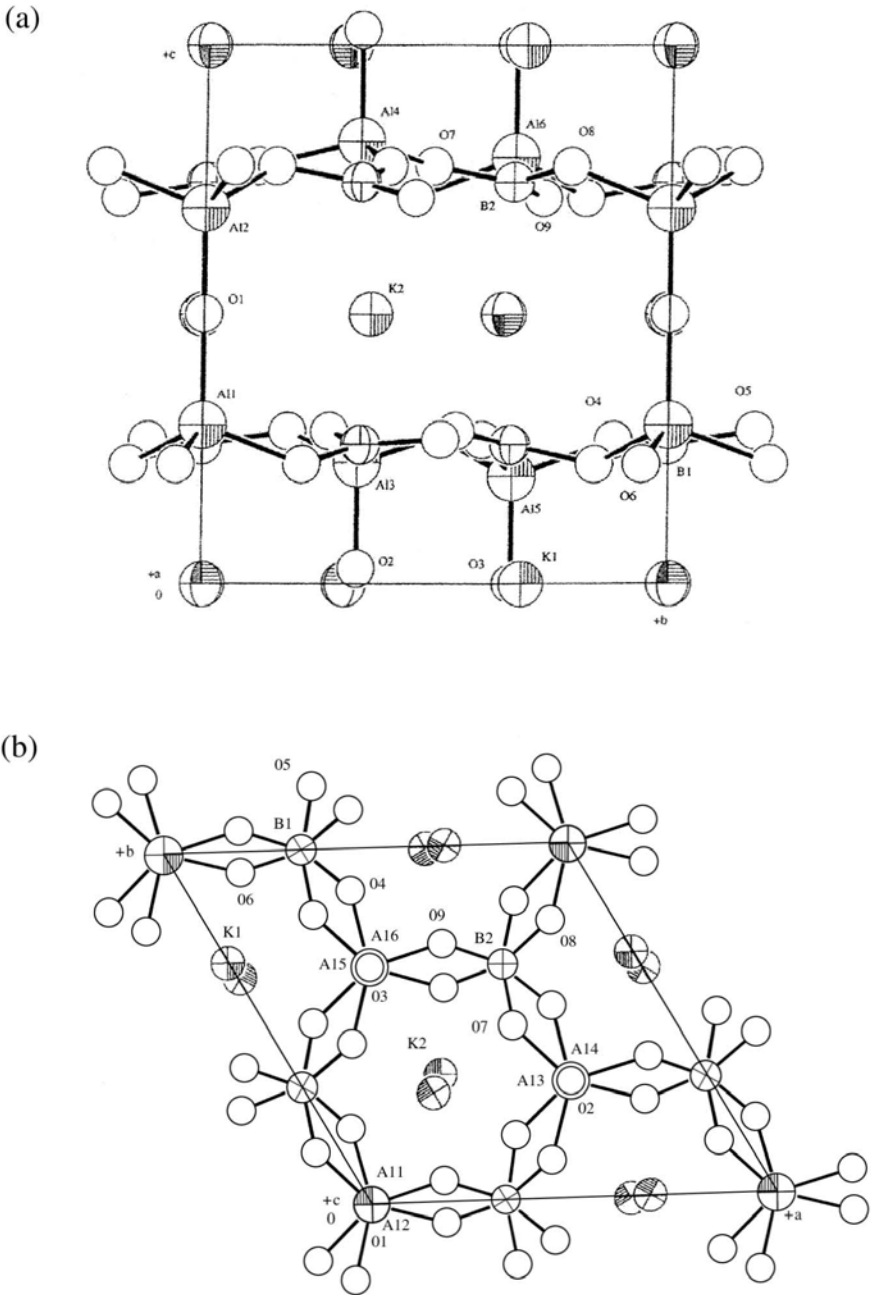


Fig. 13.19. Projection of the KAB crystal along the (a) *a*-axis and (b) *c*-axis

13.4.2 Growth of KAB

The structures of KBBF, SBBO, and KAB consist of layered structures. There are no detailed descriptions of the procedure for growing crystals of KBBF (or more accurately $MBe_2BO_3F_2$ with $M = Na, K$) and SBBO. Crystals of KBBF [96,99,100] and NBBF [101] with dimensions of $10 \times 10 \times 0.3 \text{ mm}^3$ and $0.1 \times 0.4 \times 0.6 \text{ mm}^3$ were reported, respectively. The growth of SBBO is much easier but also not well described, although a crystal with dimensions of $7 \times 7 \times 3 \text{ mm}^3$ was reported to be of good optical quality [13]. In this section, we provide a detailed procedure for the growth of KAB crystals. This may provide some references for the growth of borate crystals with layered crystalline structures.

Growth of KAB crystals by self-flux

The KAB crystals were grown by TSSG in a five-zone vertical furnace like that employed to grow CLBO crystals (Fig. 13.3). The single-phase powders of KAB were prepared from a mixture of a stoichiometric ratio of analytical reagent grade K_2CO_3 , Al_2O_3 , and B_2O_3 . The mixture was first heated at 650°C for one day, followed by further heating at 800°C for two days. The solid-state reaction involved in this case is: $K_2CO_3 + Al_2O_3 + B_2O_3 \rightarrow K_2Al_2B_2O_7 + CO_2$. The powders were ground at room temperature between heating. The final mixtures were ground and compressed into a Pt crucible and melted at 1100°C . The melt was cooled at a constant rate of $5^\circ\text{C}/\text{hour}$ for 50 hours, followed by a cooling rate of $40^\circ\text{C}/\text{hour}$ to room temperature. Many triangular and transparent crystals could be physically selected and used as seed crystals.

An additional flux must be employed for crystal growth because of the high viscosity of the stoichiometric KAB liquid. The B_2O_3 flux alone made the solution very viscous, while using K_2CO_3 alone led to high saturation temperatures and marked volatility of the solution. Thus, a mixture of K_2CO_3 and B_2O_3 was attempted. In short, the increase in B_2O_3 content increased the viscosity and decreased the crystal growth temperature. In such a case, mass transport in the solution is too slow for crystal growth. The condition is reversed for cases with increased K_2CO_3 content. Crystals of KAB with dimensions as large as $18 \times 14 \times 3 \text{ mm}^3$ can be obtained using $K_2CO_3:B_2O_3$ (1:1.8) fluxes. These dimensions are significantly larger than those reported for SBBO and KBBF crystals [13,96,99–101]. The KAB tends to grow in a plate-like structure that seems to relate to its crystalline structure.

Growth of KAB crystals with the addition of alkali metal halides

Crystals of KAB grown from $K_2CO_3:B_2O_3$ (1:1.8) fluxes have many inclusions. Additional solvents that can decrease the viscosity of the solution without significantly increasing the growth temperature and volatility are desired. For cases of B_2O_3 -containing solutions, it is well known that the addition of alkali metals and halide ions can reduce the viscosity of the solution by breaking the $-O-B-O-$

chains in the solution [102,103]. We have investigated the effects of these ions on the viscosity of KAB solutions, as summarized in Fig. 13.20. The viscosity is reduced significantly from 4140 to 1327 cP at 920°C as the ratio of $\text{K}_2\text{CO}_3\text{:B}_2\text{O}_3$ is increased from 1:1.8 (case A) to 1:1.5 (case C). The addition of 0.2 KF in KAB solutions with $\text{K}_2\text{CO}_3\text{:B}_2\text{O}_3$ fluxes at a ratio of 1:1.8 do not obviously change the viscosity of the solution (case B). The addition of 0.2 NaF in KAB solutions with $\text{K}_2\text{CO}_3\text{:B}_2\text{O}_3$ fluxes at a ratio of 1:1.5 decreases the viscosity further as shown in case E. The effect of NaF is stronger than that of LiCl (case D). Note that the reduction of viscosity is more significant in the low temperature range. The NaF appeared to work better because of its higher melting temperature compared to LiCl and KF.

We tried to grow KAB crystals by the procedure described as follows [104]. The starting materials for KAB were prepared using a two-step process. First, a mixture of $\text{Al}(\text{NO}_3)_3 \cdot 9\text{H}_2\text{O}$ and B_2O_3 at a ratio of 2:1 was mixed and ground. The mixture was decomposed at 200°C for 12 hours and sintered at 600°C for 24 hours. K_2CO_3 was then added and the mixture was heated again at 650°C for one day and at 800°C for two days. The KAB raw materials made from this procedure are better for KAB crystal growth. We think that Al_2O_3 can be completely mixed and melted to form a highly homogeneous solution by this method. During crystal growth, we raised the rotation rate of the seed crystals from 20 rpm to 40 rpm to

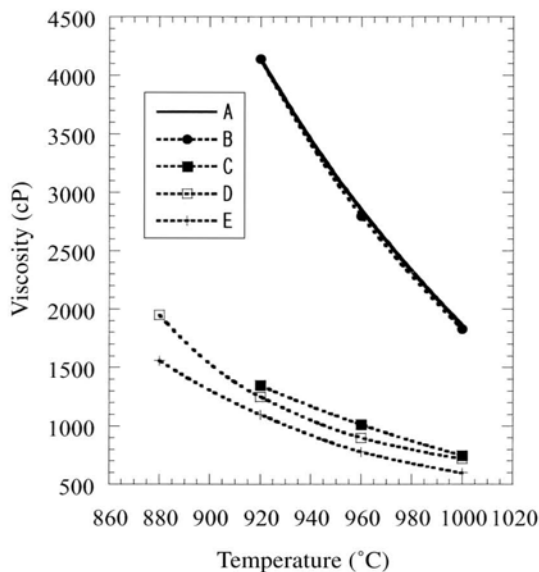


Fig. 13.20. Viscosity of solution for KAB crystal growth as a function of temperature for various fluxes. A = ($\text{K}_2\text{CO}_3\text{:B}_2\text{O}_3 = 1:1.8$), B = ($\text{K}_2\text{CO}_3\text{:B}_2\text{O}_3\text{:KF} = 1:1.8:0.2$), C = ($\text{K}_2\text{CO}_3\text{:B}_2\text{O}_3 = 1:1.5$), D = ($\text{K}_2\text{CO}_3\text{:B}_2\text{O}_3\text{:LiCl} = 1:1.5:0.2$), and E = ($\text{K}_2\text{CO}_3\text{:B}_2\text{O}_3\text{:NaF} = 1:1.5:0.2$)

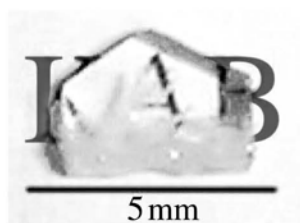


Fig. 13.21. Transparent KAB crystals grown from $K_2CO_3/B_2O_3/NaF$ fluxes

improve the homogeneity of the solution. The flux composition was adjusted to $K_2CO_3:B_2O_3:NaF$ at a 1:1.5:0.2 ratio to decrease the viscosity of solution and thus promote mass transport in the solution. This flux also decreases the supersaturation of the solution and suppresses spontaneous nucleation during growth. In this way, crystal growth can be carried out at relatively lower temperatures with reduced volatility. We further reduced the cooling rate to $\sim 0.2^\circ C/day$. Finally, we have grown transparent KAB crystals as shown in Fig. 13.21.

13.4.3 Optical properties of KAB

It is still difficult to grow transparent KAB to dimensions sufficient for laser experiments. Some optical properties of KAB have been determined. The UV absorption edge of KAB was estimated at a wavelength of 180 nm [22]. The SHG coefficient of KAB was estimated to be comparable to that of KDP ($d_{36} = 0.38$ pm/V) as obtained from powder samples. The refractive indices of the ordinary and extraordinary axes are $n_o = 1.553$ and $n_e = 1.479$ with a birefringence $\Delta n = 0.074$ as determined by the oil immersion technique, as compared to 0.072 and 0.062 for KBBF and SBBO, respectively. The lower effective NLO coefficient of KAB compared to that of SBBO ($= 1.52$ pm/V [105]) is probably due to the lack of identical spatial orientation of the $(BO_3)^{3-}$ groups between adjacent layers. The fact that the UV absorption edge of KAB is longer than that of SBBO is due to the natural absorption of $(AlO_4)^{5-}$.

13.5 Summary and Perspective

We have reviewed the growth and recent development of borate NLO crystals for generation of high-power visible and UV light, especially that of $CsLiB_6O_{10}$ (CLBO), $Gd_xY_{1-x}Ca_4O(BO_3)_3$ (GdYCOB), and $K_2Al_2B_2O_7$ (KAB) crystals. No doubt, development of these new borate materials has stimulated significant progress in the generation of high-power UV light by NLO crystals. Continued efforts to search for new NLO crystals are necessary. The assistance of theoretical approaches to the prediction of crystal structure and properties is still insufficient.

Recently, cluster modeling was used to calculate the electronic structure and NLO properties of LBO, CBO, and CLBO [106]. The nonlinear response of these crystals was considered related to the interaction between the cation and the anionic group, as consistent with that reported earlier for KTP crystals [107]. The usage of such model on structural prediction is still not being demonstrated.

There is no doubt that the development of NLO borate crystals is promoted by the need for a high-power, coherent, all-solid-state UV light source. Under such circumstances, borate crystals of “perfect” quality are needed for minimizing linear and nonlinear optical absorption and thus suppressing the occurrence of laser-induced damage and thermal dephasing. Advances in crystal growth techniques and device processing are important. New approaches for growing crystals like KBBF and SBBO must also be considered for further progress in this area.

References

1. Hagen WF, Magnante PC (1969) *J Appl Phys* 40:219–224
2. Smith WL (1977) *Appl Opt* 16:1798
3. Nath G, Haussuhl S (1969) *Appl Phys Lett* 14:154–156
4. Nash FR, Bergman JG, Boyd GD, Turner EH (1969) *J Appl Phys* 40:5201–5206
5. Boyd GD, Miller RC, Nassau K, Bond WL, Savage A (1964) *Appl Phys Lett* 5:234–236
6. Uematsu Y (1974) *Jpn J Appl Phys* 13:1362–1368
7. Zumsteg FC, Birlein JD, Gier TE (1976) *J Appl Phys* 47:4980–4985
8. Dmitriev VG, Gurzadyan GG, Nikogosyan DN (1999) *Handbook of Nonlinear Optical Crystals*, 3rd ed, Schawlow AL, Siegman AE, Tamir T (eds) Springer
9. Dewey Jr CF, Cook Jr WR, Hodgson RT, Wynne JJ (1975) *Appl Phys Lett* 26:714–716
10. Chen C, Wu B, Jiang A, You G (1985) *Sci Sin Ser B* 28:235–243
11. Chen C, Wu Y, Jiang A, You G, Li R, Lin S (1989) *J Opt Soc Am B* 6:616–621
12. Mei L, Wang Y, Chen C, Wu B (1993) *J Appl Phys* 74:7014–7015
13. Chen C, Wang Y, Wu B, Wu K, Zeng W, Yu L (1995) *Nature (London)* 373:322–324
14. Wu Y, Sasaki T, Nakai S, Yokotani A, Tang H, Chen C (1993) *Appl Phys Lett* 62:2614–2616
15. Sasaki T, Kuroda I, Nakajima S, Yamaguchi K, Watanabe S, Mori Y, Nakai S (1995) in *Advanced Solid-State Lasers*, Vol 24 of OSA Proceeding Series, Fan TY, Chai B (eds) Optical Society of America, Washington, DC, pp 91–95
16. Mori Y, Kuroda I, Nakajima S, Sasaki T, Nakai S (1995) *Appl Phys Lett* 67:1818–1820
17. Sasaki T, Mori Y, Kuroda I, Nakajima S, Yamaguchi K, Watanabe S, Nakai S (1995) *Acta Crystallogr Sect C* 51:2222–2224
18. Iwai M, Kobayashi T, Furuya H, Mori Y, Sasaki T (1997) *Jpn J Appl Phys* 36:L276–L278
19. Kobayashi T, Furuya H, Yoshimura M, Sakai H, Mori Y, Sasaki T, Nakai S, Shimamura K, Fukuda T (1997) *Proc of the Inter Symp on Laser and Nonlinear Optical Ma-*

- terials (Singapore, Nov 3–5, 1997) Sasaki T (ed) Oxford Grap Print, Singapore, pp 317–319
20. Furuya H, Yoshimura M, Kobayashi T, Murase K, Mori Y, Sasaki T (1999) *J Crystal Growth* 198/199:560–563
 21. Yoshimura M, Furuya H, Kobayashi T, Murase K, Mori Y, Sasaki T (1999) *Opt Lett* 24:193–195
 22. Hu Z-G, Higashiyama T, Yoshimura M, Yap YK, Mori Y, Sasaki T (1998) *Jpn J Appl Phys* 37:L1093–L1095
 23. Hu Z-G, Mori Y, Higashiyama T, Yoshimura M, Yap YK, Kagebayashi Y, Sasaki T (1998) Electro-optic and second harmonic generation materials, devices, and application II. Proceedings of SPIE 3556:156–161
 24. Komatsu R, Sugawara T, Sassa K, Sarukura N, Liu Z, Izumida S, Segawa Y, Uda S, Fukuda T, Yamanouchi K (1997) *Appl Phys Lett* 70:3492–3494
 25. Uda S, Komatsu R, Sugawara T, Sarukura N, Fukuda T (1997) Proc of the Inter Symp on Laser and Nonlinear Optical Materials (Singapore, Nov 3-5, 1997) Sasaki T (ed) Oxford Grap Print, Singapore, pp 320–323
 26. Chen C (1993) Development of new nonlinear optical crystals in the borate series. In: *Laser Science and Tech Int Handbook*, Vol 15. Harwood Academic Publishers
 27. Aka G, Kahn-Haradi A, Vivien D, Benitez J-M, Salin F, Godard J (1996) *Eur J Solid State Inorg Chem* 33:727–736
 28. Aka G, Bloch L, Benitez J-M, Crochet P, Kahn-Haradi A, Vivien D, Salin F, Coquelin P, Colin D (1996) OSA Trends in Optics and Photonics, Vol 1, *Advance Solid-State Lasers*, Payne SA, Pollock CR (eds) Optical Society of America, Washington, DC, pp 336–340
 29. Becker P (1998) Borate materials in nonlinear optics. *Adv Mater* 10:979–992
 30. Chen C, Xu Z, Deng D, Zhang J, Wong GKL, Wu B, Ye N, Tang D (1996) *Appl Phys Lett* 68:2930–2932
 31. Jiang A, Cheng F, Liu Q, Cheng Z, Zheng Y (1986) *J Crystal Growth* 79:963–969
 32. Ceng LK, Bosenberg W, Tang CL (1988) *J Crystal Growth* 89:553–559
 33. Itoh K, Maruma F, Kuwano Y (1990) *J Crystal Growth* 106:728–731
 34. Kouta H, Kuwano Y (1991) *J Crystal Growth* 114:676–682
 35. Kouta H, Kuwano Y (1998) OSA Trends in Optics and Photonics, Vol 19, *Advanced Solid-State Lasers*, Bosenberg WR, Fejer MM (eds) Optical Society of America, Washington, DC, pp 28–31
 36. Lin S, Sun Z, Wu B, Chen C (1990) *J Appl Phys* 67:634–638
 37. Krogh-Moe J (1974) *Acta Cryst B* 30:1178–1180
 38. Wu Y (1997) Proc of the Inter Symp on Laser and Nonlinear Optical Materials (Singapore, Nov 3-5, 1997) Sasaki T (ed) Oxford Grap Print, Singapore, pp 120–124
 39. Kagebayashi Y, Mori Y, Sasaki T (1999) *Bull Mater Sci* 22:971–973
 40. Kato K (1995) *IEEE J Quantum Electron* 31:169–171
 41. Wu Y, Fu P, Wang J, Xu Z, Zhang L, Kong Y, Chen C (1997) *Opt Lett* 22:1840–1842
 42. Yamaguchi K. Graduate report, Dept Elect Eng, Osaka University, March 1994 (in Japanese/unpublished)
 43. Mori Y, Sasaki T (1995) *J Jpn Assoc Crystal Growth* 22:310–317 (in Japanese)
 44. Mori Y, Kuroda I, Nakajima S, Taguchi A, Sasaki T, Nakai S (1995) *J Cryst Growth* 156:307–309
 45. Taguchi A, Miyamoto A, Mori Y, Haramura S, Inoue T, Nishijima K, Kagebayashi Y, Sakai H, Yap YK, Sasaki T (1997) OSA Trends in Optics and Photonics, Vol 10, Ad-

- vanced Solid-State Lasers, Pollock CR, Bosenberg WR (eds) Optical Society of America, Washington, DC, pp 19–23
46. Mori Y, Yap YK, Inagaki M, Nakajima S, Taguchi A, Zhou WL, Sasaki T (1996) OSA Trends in Optics and Photonics, Vol 1, Advanced Solid-State Lasers, Payne SA, Pollock CR (eds) Optical Society of America, Washington, DC, pp 341–345
 47. Inagaki M, MEng thesis, Dept Elect Eng, Osaka University, March 1997 (in Japanese/unpublished)
 48. Yap YK, Mori Y, Sasaki T (unpublished)
 49. Takei H, Suzuki T, Mamiya M, Sakai F, Koike M, Mori Y, Sasaki T (1997) Jpn J Appl Phys 36:126–128
 50. Yap YK (1999) PhD thesis, Osaka University, January
 51. Yap YK, Mori Y, Haramura S, Taguchi A, Nishijima K, Inoue T, Miyamoto A, Sakai H, Kagebayashi Y, Sasaki T (1997) Conference on Lasers and Electro-Optics, Vol 11 of 1997 OSA Technical Digest Series. Optical Society of America, Washington, DC, pp 512–513
 52. Yap YK, Inoue T, Sakai H, Kagebayashi Y, Mori Y, Sasaki T, Deki K, Horiguchi M, Opt Lett 23:34–36
 53. Inoue T, Yap YK, Kamimura T, Kagebayashi Y, Sakai H, Mori Y, Sasaki T (1997) Proc of the Inter Symp on Laser and Nonlinear Optical Materials (Singapore, Nov 3-5, 1997) Sasaki T (ed) Oxford Grap Print, Singapore, pp 314–316
 54. Yap YK, Inagaki M, Nakajima S, Mori Y, Sasaki T (1996) Opt Lett 21:1348–1351
 55. Yap YK, Mori Y, Haramura S, Taguchi A, Sasaki T, Deki K, Ohsako Y, Horiguchi M (1997) OSA Trends in Optics and Photonics, Vol 10, Advanced Solid-State Lasers, Pollock CR, Bosenberg WR (eds) Optical Society of America, Washington, DC, pp 10–13
 56. Stamm U, Zschocke W, Schroder T, Deutsch N, Basting D (1997) OSA Trends in Optics and Photonics, Vol 10, Advanced Solid-State Lasers, Pollock CR, Bosenberg WR (eds) Optical Society of America, Washington, DC, pp 7–9
 57. Kojima T, Konno S, Fujikawa S, Yasui K, Yoshizawa K, Mori Y, Sasaki T, Tanaka M, Okada Y (1999) OSA Trends in Optics and Photonics, Vol 26, Advanced Solid-State Lasers, Fejer MM, Injeyan H, Keller U (eds) Optical Society of America, Washington, DC, pp 93–95
 58. Kojima T, Konno S, Fujikawa S, Yasui K, Yoshizawa K, Mori Y, Sasaki T, Tanaka M, Okada Y (1999) Conference on Lasers and Electro-Optics, OSA Technical Digest. Optical Society of America, Washington, DC, p 64
 59. Kojima T, Konno S, Fujikawa S, Yasui K, Yoshizawa K, Mori Y, Sasaki T, Tanaka M, Okada Y (2000) Opt Lett 25:58–60
 60. Zhou W-L, Mori Y, Sasaki T, Nakai S (1996) Opt Commun 123:583–586
 61. Sharma LB, Daido H, Kato Y, Nakai S, Zhang T, Mori Y, Sasaki T (1996) Appl Phys Lett 69:3812–3814
 62. Srinivasan-Rao T, Babzien M, Sakai F, Mori Y, Sasaki T (1997) Appl Phys Lett 71:1927–1929
 63. Zhang T, Yonemura M (1997) Jpn J Appl Phys 36:6353–6352
 64. Tamaki Y, Obara M, Midorikawa K (1998) Jpn J Appl Phys 37:4801–4805
 65. Chandra S, Allik T, Hutchinson JA, Fox J, Swim C (1997) Opt Lett 23:209–211
 66. Trickett RI, Withford MJ, Brown DJW (1998) Opt Lett 23:189–191
 67. Finch A, Ohsako Y, Sakuma J, Deki K, Horiguchi M, Mori Y, Sasaki T, Wall K, Harrison J, Moulton PF, Manni J (1998) OSA Trends in Optics and Photonics, Vol 19,

- Advanced Solid-State Lasers, Bosenberg WR, Fejer MM (eds) Optical Society of America, Washington, DC, pp 16–18
68. Deki K, Kagebayashi Y, Kitatochi N, Ohsako Y, Horiguchi M, Yap YK, Mori Y, Sasaki T, Yoshida K (1998) Conference on Lasers and Electro-Optics, Vol 6 of 1998 OSA Technical Digest Series. Optical Society of America, Washington, DC, pp 521–522
 69. Finch A, Sakuma J, Ohsako Y, Deki K, Horiguchi M, Yokota Y (1999) OSA Trends in Optics and Photonics, Vol 26, Advanced Solid-State Lasers, Fejer MM, Injeyan H, Keller U (eds) Optical Society of America, Washington, DC, pp 70–73
 70. Sakuma J, Finch A, Ohsako Y, Deki K, Yoshino M, Horiguchi M, Yokota Y, Mori Y, Sasaki T (1999) OSA Trends in Optics and Photonics, Vol 26, Advanced Solid-State Lasers, Fejer MM, Injeyan H, Keller U (eds) Optical Society of America, Washington, DC, pp 89–92
 71. Yoshimura M, Murase K, Kamimura T, Nakai K, Yap YK, Mori Y, Sasaki T, Matsumoto Y, Okada Y (1999) OSA Trends in Optics and Photonics, Vol 26, Advanced Solid-State Lasers, Fejer MM, Injeyan H, Keller U (eds) Optical Society of America, Washington, DC, pp 112–114
 72. Deki K, Finch A, Horiguchi M, Kagebayashi Y, Nanzai S, Ohsako Y, Sakuma J, Yokota Y, Yoshino M (1999) Conference on Lasers and Electro-Optics, OSA Technical Digest Optical Society of America, Washington, DC, pp 64–65
 73. Wada S, Tashiro H, Yap YK, Mori Y, Sasaki T (1997) Conference on Lasers and Electro-Optics, Vol 11 of 1997 OSA Technical Digest Series. Optical Society of America, Washington, DC, p 357
 74. Ohtsuki T, Kitano H, Kawai H, Owa S (2000) Conference on Lasers and Electro-Optics, OSA Technical Digest. Optical Society of America, Washington, DC, post-deadline paper CPD9
 75. Nakai K, Kamimura T, Sawada H, Yoshimura M, Mori Y, Sasaki T, Yoshida H, Nakatuka M (1999) The Pacific Rim Conference on Lasers and Electro-Optics 1999. Seoul, Technical digest IEEE catalog # 99TH8464, Vol 3: 967–968
 76. Khamaganova TN, Trunov VK, Dzhurinskii BF (1991) Russ J Inorg Chem 36:484–485
 77. Norrestam R, Nygren M, Bovin J-O (1992) Chem Mater 4:737–743
 78. Ilyukhin AB, Dzhurinskii BF (1993) Russ J Inorg Chem 38:847–850
 79. Iwai M (1997) PhD thesis, Osaka University, January
 80. Aka G, Kahn-Haradi A, Mougél F, Vivien D, Salin F, Coquelin P, Colin P, Pelenc D, Damelet JP (1997) J Opt Soc Am B14:2238–2247
 81. Yoshimura M, Kobayashi T, Furuya H, Murase K, Mori Y, Sasaki T (1998) OSA Trends in Optics and Photonics, Vol 19, Advanced Solid-State Lasers, Bosenberg WR, Fejer MM (eds) Optical Society of America, Washington, DC, pp 561–564
 82. Yoshimura M (1999) PhD thesis, Osaka University, January
 83. Mougél F, Aka G, Salin F, Pelenc D, Ferrand B, Kahn-Haradi A, Vivien D (1999) OSA Trends in Optics and Photonics, Vol 26, Advanced Solid-State Lasers, Fejer MM, Injeyan H, Keller U (eds) Optical Society of America, Washington, DC, pp 709–714
 84. Yoshimura M, Kobayashi T, Furuya H, Mori Y, Sasaki T (1998) Conference on Lasers and Electro-Optics, Vol 6 of 1998 OSA Technical Digest Series. Optical Society of America, Washington, DC, pp 270–271

85. Yoshimura M, Furuya H, Kobayashi T, Murase K, Yamada I, Mori Y, Sasaki T (1999) in 3rd Annual International Conference on Solid-State Lasers for Application to Inertial Confinement Fusion (Monterey, CA, 7-12 June 1998). Proceeding SPIE 3492:825–831
86. Yoshimura M, Furuya H, Yamada I, Murase K, Nakao H, Yamazaki M, Mori Y, Sasaki T (1999) Conference on Lasers and Electro-Optics. OSA Technical Digest Series, Optical Society of America, Washington, DC, pp 529–530
87. Yamada I, Furuya H, Nakao H, Murase K, Yamazaki M, Yoshimura M, Mori Y, Sasaki T (1999) The Pacific Rim Conference on Lasers and Electro-Optics 1999. Seoul, Technical digest IEEE catalog # 99TH8464, Vol 3:969–970
88. Yoshimura M, Furuya H, Yamada I, Murase K, Nakao H, Yamazaki M, Mori Y, Sasaki T (1999) OSA Trends in Optics and Photonics, Vol 26, Advanced Solid-State Lasers, Fejer MM, Injeyan H, Keller U (eds) Optical Society of America, Washington, DC, pp 702–706
89. Ukachi T, Lane RJ, Bosenberg WB, Tang CL (1992) J Opt Soc Am B9:1128–1133
90. Furuya H, Nakao H, Ruan YF, Yap YK, Yoshimura M, Mori Y, Sasaki T (1999) OSA Trends in Optics and Photonics, Vol 34, Advanced Solid-State Lasers, Injeyan H, Keller U, Marshall C (eds) Optical Society of America, Washington, DC, pp 404–408
91. Nakao H, Furuya H, Yamada I, Yap YK, Yoshimura M, Mori Y, Sasaki T, Ruan YF (2000) Conference on Lasers and Electro-Optics, OSA Technical Digest Series. Optical Society of America, Washington, DC, pp 428–429
92. Furuya H, Nakao H, Yamada I, Ruan YF, Yap YK, Yoshimura M, Mori Y, Sasaki T (2000) Opt Lett 25:1588–1590
93. Eimerl D, Davis L, Velsko S, Graham EK, Zalkin A (1987) J Appl Phys 62:1968–1983
94. Umemura N, Kato K (1997) Appl Opt 36:6794–6796
95. Yap YK, Haramura S, Taguchi A, Mori Y, Sasaki T (1998) Opt Commun 145:101–104
96. Chen C, Wang Y, Xia Y, Wu B, Tang D, Wu K, Zheng W, Yu L, Mei L (1995) J Appl Phys 77:2268–2272
97. Hu Z-G, Higashiyama T, Yoshimura M, Mori Y, Sasaki T (1999) Z Kristallogr 214:433–434
98. Kaduk J, Sate L (1994) Powder Diffraction File Set 46:582
99. Mei L, Huang X, Wang Y, Wu Q, Wu B, Chen C (1995) Z Kristallogr 210:93–95
100. Wu B, Tang D, Ye N, Chen C (1996) Opt Mater 5:105–109
101. Mei L, Wang Y, Chen C (1994) Mater Res Bull 29:81–87
102. Elwell D, Sheel HJ (1975) Crystal Growth from High Temperature Solutions. Academic Press, London
103. Barques JS, White WB (1969) J Crystal Growth 6:29–42
104. Hu Z-G, Higashiyama T, Yoshimura M, Mori Y, Sasaki T (2000) J Crystal Growth 212:368–371
105. Chen C, Wu B, Zheng W, Wang Y, Ye N, Yu L (1996) Conference on Lasers and Electro-Optics, Vol 9, 1996 OSA Technical Digest. Optical Society of America, Washington, DC, pp 229–230
106. Cheng W, Chen J, Lin Q, Zhang Q, Lu J (1999) Phys Rev B60:11747–11754
107. Phillips MLF, Harrison WTA, Gier TE, Stucky GD, Kulkarni GV, Burdett JK (1990) Inorg Chem 29:2158–2163

14 Growth of High T_c Crystals

T. Inoue¹, S. Miyashita², Y. Nishimura³, J. Takemoto⁴, Y. Suzuki⁵, S. Hayashi⁶, and H. Komatsu⁷

¹Faculty of Engineering, The University of Tokushima, Tokushima 770-8506, Japan

²Physics, Toyama Medical and Pharmaceutical University, Sugitani 2630, Toyama 930-0194, Japan

³Institute of Low Temperature Science, Hokkaido University, Sapporo 060-0819, Japan

⁴Yamaha Fine Technologies Co., Ltd., 283 Aoya-cho, Hamamatsu, Shizuoka 435-8568, Japan

⁵NTT Network Innovation Laboratories • Network Service Innovation Laboratory, 1-1 Hikarinooka, Yokosuka-City, Kanagawa 239-0847, Japan

⁶Retired from The University of Yamagata under the age limit at 2001

⁷Faculty of Policy Studies, Iwate Prefectural University, Takizawa Vill., Iwate Prefecture 202-0196, Japan

14.1 Introduction

Since the discovery of Ba-La-Cu-O compounds of high T_c superconductors by Bednorz and Muller [1], many papers have been published on the various types of high T_c superconductors containing copper oxides such as $\text{LnBa}_2\text{Cu}_3\text{O}_y$ (123 type), where Ln is a rare earth atom and Y, and Bi-Sr-Ca-Cu-O (BSCCO) compounds. This chapter is made up of the following three parts:

1. Growth of the high T_c phase of BSCCO ($T_c \sim 100$ K)
2. Liquid phase epitaxial growth of the low T_c phase of BSCCO ($T_c \sim 80$ K)
3. Construction of phase diagrams by *in situ* observation and their application to crystal growth of oxide superconductors.

14.2 Growth of the High T_c Phase of BSCCO

Three superconducting phases are known in the Bi-Sr-Ca-Cu-O compounds, which have the formula of $\text{Bi}_2\text{Sr}_2\text{Ca}_{x-1}\text{Cu}_x\text{O}_y$ ($x = 1, 2, 3$). Their structures are similar, differing only in the spacing along the c -axis. The approximate values of c_0 in order of $x = 1, 2$, and 3 are 24, 30, and 36 Å, and their superconducting tran-

sition temperatures T_c are 10, 80, and 105 K, respectively. Hereafter, we call the 30 Å ($x = 2$) and 36 Å ($x = 3$) phases low T_c and high T_c phases, respectively.

Among them, the high T_c phase (2223 phase) is very difficult to grow sizable single crystals. We made the following three experiments for growing the high T_c phase: (1) synthesis by sintering the powder of Bi-Sr-Ca-Cu, (2) annealing the solidified mass of Bi:Sr:Ca:Cu = 4:3:3:4, and (3) conversion of low T_c crystals to high T_c ones by annealing. Most of this part was reported in our papers [2–4].

14.2.1 Synthesis of the high T_c phase by sintering the powder of Bi-Sr-Ca-Cu

Our ultimate purpose is to grow sizable single crystals of the high T_c phase of a BSCCO superconductor. This high T_c phase has a transition above 100 K. It was necessary to obtain fundamental data relating to the thermal stability of this phase before conducting an experiment on single crystal growth. Endo et al. [5] reported an excellent method for preparing sintered samples consisting of about 100% high T_c phase ($T_{c(R=0)} = 107.5$ K). We also tried to synthesize the high T_c phase following their method. Attention was paid to the processes of synthesis and decomposition of this phase.

Powder with a cation ratio of Bi:Pb:Sr:Ca:Cu = 0.8:0.2:0.8:1.0:1.4 was prepared by a coprecipitation method. The powder thus prepared was ground and pressed into pellets 2–3 mm thick. They were heated at 790–880°C for 1–100 hours in a stream of Ar-O₂ gas mixture of about 1 atm with an oxygen partial pressure of 1/13 atm. After heating, they were cooled to 500°C at the rate of about 100°C/h. Their resistivity was measured with a standard four-probe technique. Hereafter, we shall refer to the phase with the lattice parameter $c = 30$ Å as the low T_c phase and that with $c = 36$ Å as the high T_c phase.

Effects of the sintering temperature

Figure 14.1 shows the resistivity R versus temperature T curves for the specimens sintered at various temperatures for 30 h. The following observations were derived from these data.

(a) A single high T_c phase could not be obtained in any case for the sintering time of 30 h. The R - T curves showed a two-step superconducting transition. This suggests a coexistence of the high T_c phase with the low T_c phase in these sintered specimens. This coexistence was confirmed by their X-ray powder diffraction patterns.

(b) The proportion of the high T_c phase increased with sintering temperature in the range of 790–830°C. This increase was significantly greater above 810°C (Fig. 14.1a), whereas the decomposition process of the high T_c phase was dominant at about 870°C (Fig. 14.1b).

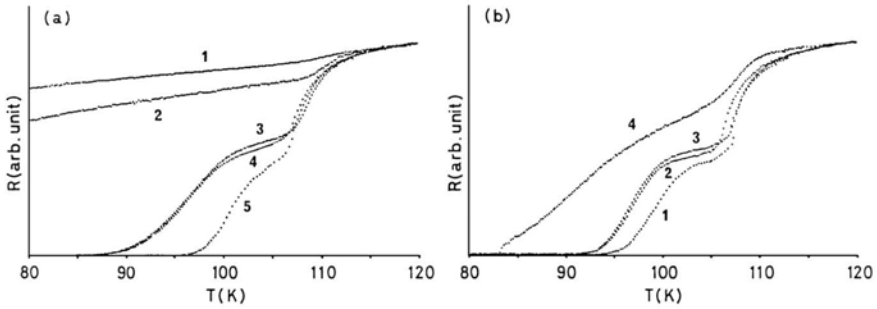


Fig. 14.1. Sintering temperature dependence of the R - T curves for specimens that were sintered at various temperatures for 30 h in a stream of Ar-O₂ gas of about 1 atm with an oxygen partial pressure of 1/13 atm: (a) (1) 790°C, (2) 800°C, (3) 810°C, (4) 820°C, (5) 830°C; (b) (1) 840°C, (2) 855°C, (3) 860°C, (4) 870°C. (From reference 2 by permission of *Jpn. J. Appl. Phys.*)

Effects of sintering time

Figure 14.2 shows the R - T curves for the specimens sintered at 840°C for various periods of time. The content of the high T_c phase increased with the sintering time, and single high T_c phase could be obtained after sintering for 100 h. This was also confirmed by the X-ray diffraction patterns. The $T_{c(R=0)}$ for the low T_c phase gradually increased from 85 to 97 K with the sintering time (Fig. 14.2). Many authors have reported the values of $T_{c(R=0)}$ for the low T_c phase to be 75–85 K [6–11]. But, some authors have reported that the values of $T_{c(R=0)}$ were 87 K [12] and/or 92 K [13]. The reasons for the variety of $T_{c(R=0)}$ values are not clear at present.

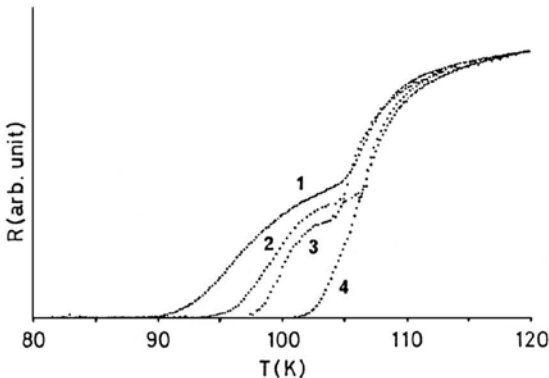


Fig. 14.2. Sintering time dependence of the R - T curves for the specimens that were sintered at 840°C for various periods of time. (1) 1 h, (2) 30 h, (3) 48 h, (4) 100 h. (From reference 2 by permission of *Jpn. J. Appl. Phys.*)

Decomposition of the high T_c phase

The decomposition process of the high T_c phase was studied by heating the single high T_c phase specimen, which had been prepared by the method mentioned above, at various temperatures for 1 h. The results are shown in Fig. 14.3. It was found that the low T_c phase starts to form as soon as the high T_c phase begins to decompose at around 870°C, and that most of the high T_c specimen was transformed into the low T_c phase around 880°C. Figures 14.4a and 14.4b show the grain structure on the surfaces of the sintered specimen of the single high T_c phase and its heat-treated structure at 880°C for 1 h, respectively. The heat-treated specimen was reduced in volume and a number of needlelike crystals were formed in addition to the low T_c phase, as shown in Fig. 14.4b. The composition of the needlelike crystal is shown in Fig. 14.5. This crystal was mainly composed of Ca and Cu. Figures 14.6a and 14.6b show the composition of the high T_c phase (before the heat treatment) and the low T_c phase (after the heat treatment), respectively. The content of Ca and Cu in the low T_c phase (Fig. 14.6b) was slightly poorer than in the high T_c phase (Fig. 14.6a). This shows that the high T_c phase incongruently melted and decomposed into the low T_c phase and liquid, and that the needle-like crystals were crystallized from the liquid in the cooling process.

The above results are summarized as follows. (a) The low T_c phase was dominant at the early stage of the reaction at 840°C. The low T_c phase gradually transformed during sintering through a complicated reaction process [14] into the high T_c phase. These results were nearly the same as those reported by Hatano et al. [15] and Kim et al. [16]. (b) The values of $T_c(0)$ in the low T_c phase varied from 80–97 K depending on the sintering conditions (Figs. 14.1–14.4). (c) The high T_c phase incongruently melted and decomposed into the low T_c phase and liquid around 870–880°C. Needlelike crystals formed from the liquid in the partially melted portion. These are very important results in terms of designing and improving the method of crystal growth.

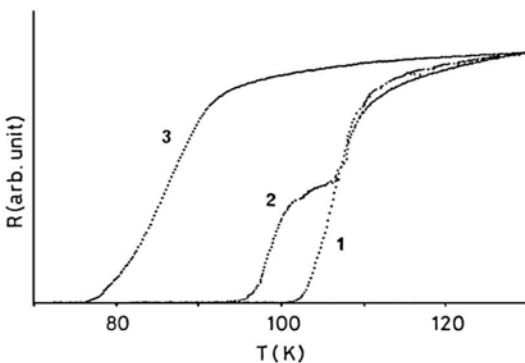


Fig. 14.3. Sintering temperature dependence of the R - T curves for the single high T_c phase specimen. (1) the original high T_c phase specimen before heat treatment, (2) 870°C for 1 h, (3) 880°C for 1 h. (From reference 2 by permission of *Jpn. J. Appl. Phys.*)

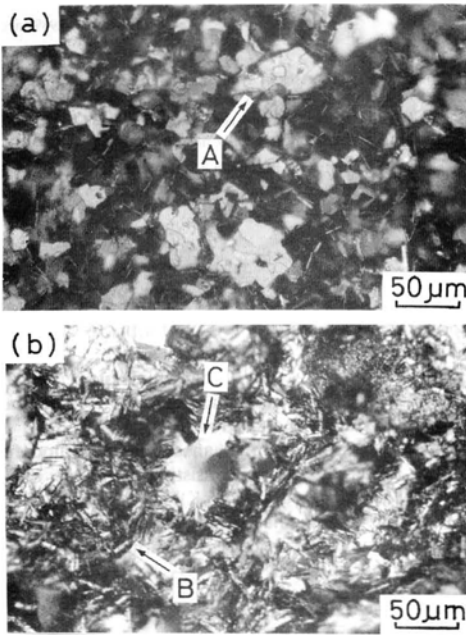


Fig. 14.4. Photographs showing the decomposition of the single high T_c phase specimen by the heat treatment shown in Fig. 14.3 (3). (a) The surface structure of the original specimen of the single high T_c phase [before heat treatment, see Fig. 14.3 (1)]. A: high T_c plate crystals; (b) the surface structure after heat treatment at 880°C for 1 h [see Fig. 14.3 (3)]. B: Needle crystals that were crystallized from the partially melted portion, C: Low T_c plate crystals (optical reflection micrograph). (From reference 2 by permission of *Jpn. J. Appl. Phys.*)

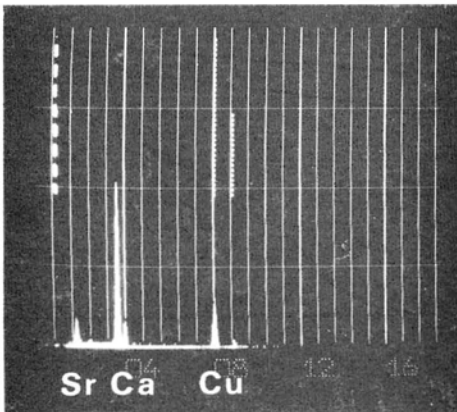


Fig. 14.5. X-ray energy dispersive spectrum of the needle crystals in Fig. 14.4(b) (accelerated voltage: 15 kV). (From reference 2 by permission of *Jpn. J. Appl. Phys.*)

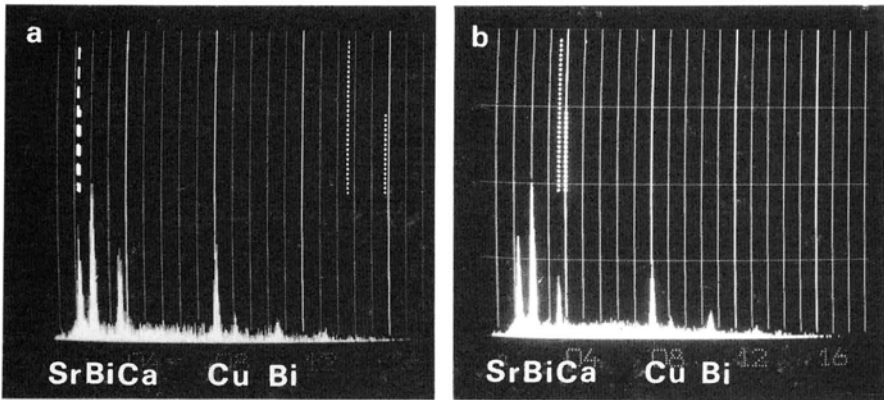


Fig. 14.6. Comparison of the composition of high T_c crystals with that of low T_c crystals using X-ray energy dispersive spectra. The X-ray system used 15 kV. a) High T_c (A in Fig. 14.4a); b) Low T_c (C in Fig. 14.4b). (From reference 2 by permission of *Jpn. J. Appl. Phys.*)

14.2.2 Preparation of single crystals containing the high T_c phase of a Bi-Sr-Ca-Cu-O superconductor

Ono et al. [17] synthesized a single crystal with T_c equal 105 K (0.5 mm \times 0.5 mm) by sintering a pressed pellet with the cation ratio of Bi:Sr:Ca:Cu = 5:4:4:6 at 883°C in air for 24 hours. Strobel et al. [18] synthesized single crystals with T_c = 110 K (0.2~0.8 mm long) by sintering a pressed pellet of 2:1.5:2:3.4 at 846°C for 12 days in a reduced oxygen atmosphere ($P(O_2) = 0.035$ atm).

We grew single crystals with $T_c(0) = 100$ K by annealing solidified samples instead of pressed pellets, which were prepared by slowly cooling the melt of Bi:Sr:Ca:Cu = 4:3:3:4. Sizable single crystals could be more easily obtained by our method than by sintering a pressed pellet. Tarascon et al. [19] first used the composition of 4:3:3:4 for synthesizing the low T_c phase (85 K).

The starting materials were Bi_2O_3 , $CaCO_3$, $SrCO_3$, and $CuO > 99.9\%$. Powder with a cation ratio of Bi:Sr:Ca:Cu = 4:3:3:4 was prepared by grinding the above materials in an alumina mortar. The mixed powder was pressed into a pellet (30 mm ϕ \times 5 mmH) and calcined in air at 800°C for 20~30 hours. The calcined pellet was melted at 1050°C for 2 hours in an alumina crucible, 23 mm ϕ \times 34 mmH. The temperature was then lowered to 500°C at a rate of 10°C/h, and then the sample was furnace cooled to room temperature. The alumina crucible that contained the solidified sample was cut into several pieces by means of a diamond cutter. We will hereafter call the pieces of the solidified sample the bulk sample. The bulk samples were annealed to investigate the effects of annealing upon the formation of the high T_c (>100 K) phase. The annealing conditions were as follows: (1) temperatures: 860~880°C, (2) annealing times: 50~100 h, (3) atmosphere: air.

Platy crystals (~ 1 mm in length), which were embedded in the mother medium, were picked up after breaking the bulk samples. The superconducting properties were determined by both resistivity and magnetization measurements. Resistivity was measured using a standard four-probe technique. The low-field d.c. magnetization measurement was performed using a semiconducting quantum interference device (SQUID) magnetometer. The phases formed were identified using either X-ray powder diffraction measurements or 15° oscillation photographs of single crystals.

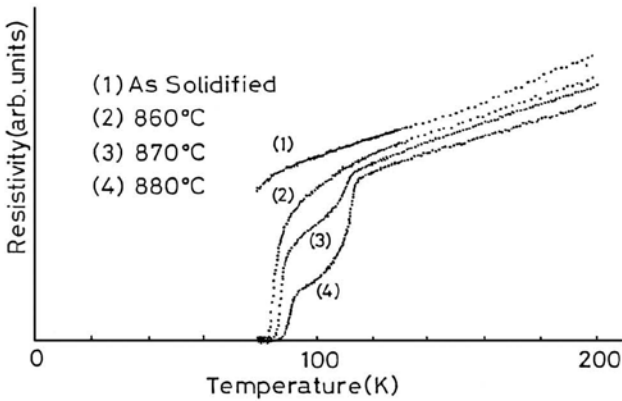


Fig. 14.7. Annealing temperature dependence of the R - T curves for the bulk samples that were prepared by slowly cooling the melt of Bi:Sr:Ca:Cu = 4:3:3:4. The samples were annealed at 860–870°C in air for 50 h. (From reference 3 by permission of *Jpn. J. Appl. Phys.*)

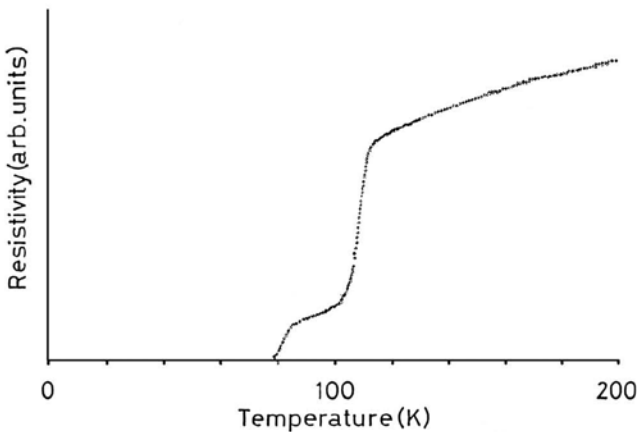


Fig. 14.8. Resistivity-temperature curve in the bulk sample that was annealed at 870°C for 100 h in air. (From reference 3 by permission of *Jpn. J. Appl. Phys.*)

Figure 14.7 shows the resistivity R versus temperature T curves for the bulk samples before [as solidified, (1) in Fig. 14.7] and after [(2)–(4) in Fig. 14.7] annealing at various temperatures for 50 hours. The X-ray powder diffraction measurement on the sample before annealing [(1) in Fig. 14.1] showed the coexistence of the low T_c phase and the 24 \AA ($x = 1$) superconducting phase in equal amounts, but no high T_c phase was found in the sample. The major phase in the annealed samples [(2)–(4) in Fig. 14.7] was the low T_c phase. It was found from Fig. 14.7 that the fraction of high T_c phase ($T_c > 100 \text{ K}$) increased with the annealing temperature, especially above 870°C . The samples annealed above 870°C were partly molten and showed rounded edges. To investigate the effect of the annealing time upon the formation of the high T_c phase, the samples were annealed for a much longer time, 100 hours at 870°C and 880°C in air, respectively. The sample annealed at 880°C for 100 hours was mostly melted, and the high T_c phase could not be detected. A good result was obtained in the sample annealed at 870°C for 100 hours in air, as shown in Fig. 14.8; that is, the fraction of high T_c phase was larger than that in the case for the 50-h annealing time [compare the R - T curve in Fig. 14.8 with (3) in Fig. 14.7].

Resistivities were measured on several single crystals ($0.5 \times 0.7 \times 0.05 \text{ mm}^3$) that were picked up from the broken pieces of the sample annealed at 870°C for 100 h. A few single crystals showed $T_{c(R=0)} = 100 \text{ K}$, although most crystals showed two distinct superconducting transitions at $T_{c1} = 110 \text{ K}$ and $T_{c2} = 85 \text{ K}$, respectively. A typical R - T curve for a high T_c single crystal ($T_{c(R=0)} = 100 \text{ K}$) is shown in Fig. 14.9.

To ensure that the single crystals showing high T_c are bulk superconductors, we measured magnetization with a SQUID magnetometer. The measurements were done on the single crystals used in the resistivity measurement in Fig. 14.9. The result is shown in Fig. 14.10. It was found from the figure that this crystal was

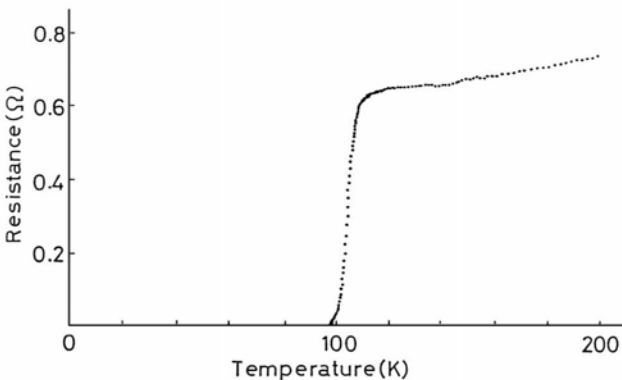


Fig. 14.9. Resistivity-temperature curve in the high T_c single crystal that was found in the bulk sample annealed at 870°C for 100 h in air. (From reference 3 by permission of *Jpn. J. Appl. Phys.*)

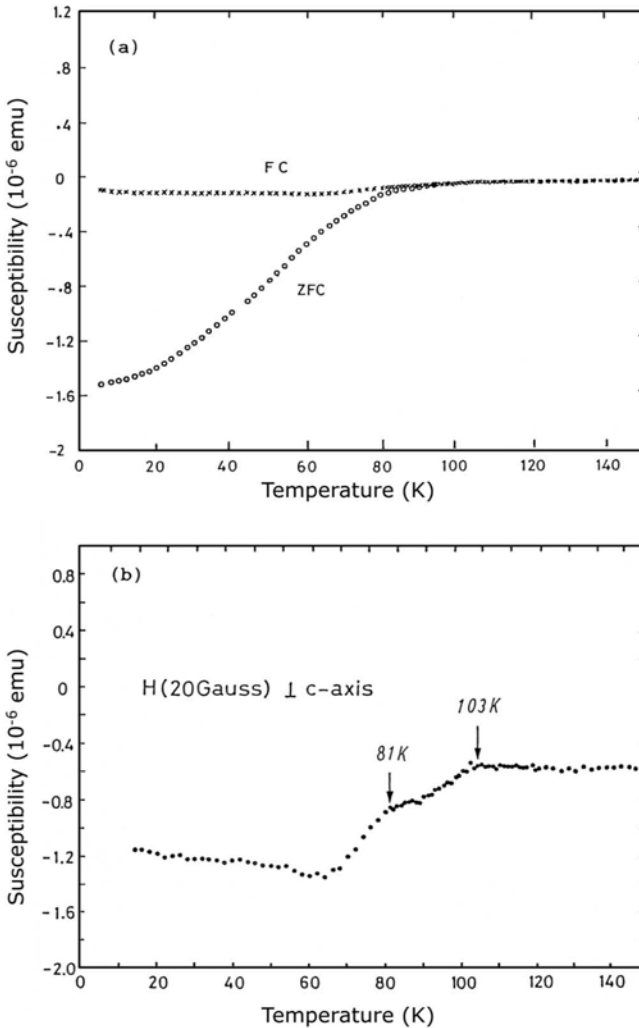


Fig. 14.10. Magnetization as a function of temperature for the high T_c single crystal in Fig. 9. (a) FC: cooling in a field of 20 Gauss, ZFC: cooling in a zero field. (b) This figure shows the same FC data as in (a) except for the units of the vertical axis. The vertical unit is changed from 10^{-6} emu in (a) to 10^{-7} emu in this figure. (From reference 3 by permission of *Jpn. J. Appl. Phys.*)

composed of high T_c (>100 K) and low T_c (~ 80 K) phases with possible intergrowth. Because it was very difficult to estimate quantitatively the volume fraction of superconductive phase only from the magnetization data [20], the fraction of high T_c phase could not be estimated. A 15° oscillation photograph also showed the coexistence of high T_c and low T_c phases.

A surface microtopograph of single crystals showing $T_{c(R=0)} = 100$ K in Fig. 14.9 is shown in Fig. 14.11, which was taken by a differential interference microscope. This photograph indicates that the crystal was grown by the layer-by-layer growth mechanism, which strongly suggests a solution growth mechanism.

The details of the formation mechanism of high T_c crystals are not clear at present. But the following two facts will be important in considering the formation mechanism: (1) the high T_c single crystals were grown in the bulk samples which were annealed at near their melting point and were partially molten, (2) the surface microtopograph of Fig. 14.11 shows a layer-by-layer growth pattern. These facts strongly suggest that the single crystals ($T_{c(R=0)} = 100$ K) were grown from high-temperature solutions which were formed in the partially melted part, and that the composition and temperature ranges of the solution for the high T_c crystal growth were very narrow.

The above results were summarized as follows. High T_c ($T_{c(R=0)} = 100$ K) single crystals were grown by annealing the bulk sample. This sample was prepared by slowly cooling the melt of Bi:Sr:Ca:Cu = 4:3:3:4, at 870°C for 100 hours in air. It was found from the SQUID magnetization measurement that these crystals were composed of a high T_c phase and a low T_c one with possible intergrowth.

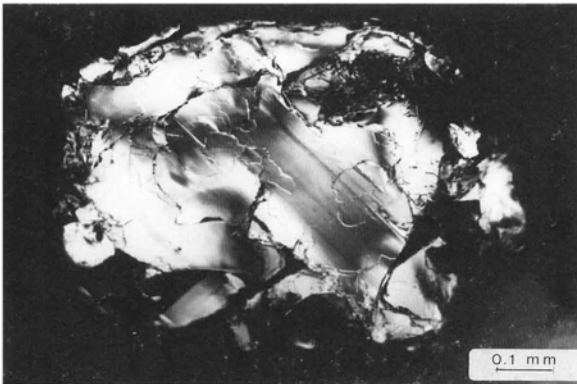


Fig. 14.11. Photograph showing the surface microtopograph of the high T_c single crystal in Fig. 14.9. A differential interference micrograph was used. (From reference 3 by permission of *Jpn. J. Appl. Phys.*)

14.2.3 Conversion of superconducting Bi-system single crystals from 2212 to 2223 by the annealing method

In the previous section [21], we reported the preparation of single crystals ($T_{c(R=0)} = 100$ K) by annealing solidified samples containing 2212 single crystals. However, the fraction of 2223 phase was small in the annealed crystals. The purpose of this study is to re-examine the conversion of flux grown 2212 single crystals to 2223

crystals by the annealing method of Matsubara et al. [22], and thereby obtain a more complete understanding of the following points: (a) the dependency of 2223 formation upon the annealing temperatures, (b) the change of the surface microtopographs of the annealed crystals with increasing annealing temperatures, and (c) the change of the chemical compositions caused by annealing the crystals.

Two series of 2212 single crystals for the annealing experiments were grown from melts A and B as follows. The A series crystals were grown from a melt of Bi:Sr:Ca:Cu = 3.3:2:2:2.7, whereas the B series crystals were grown from a melt of Bi:Sr:Ca:Cu = 2:1:1:2. The chemical compositions of the series A and B crystals were $\text{Bi}_{2.4}\text{Sr}_{2.4}\text{Ca}_{1.6}\text{Cu}_{3.6}$ and $\text{Bi}_{2.4}\text{Sr}_{2.2}\text{Ca}_{1.8}\text{Cu}_{3.6}$, respectively (EDX). The atomic ratio of Ca/Sr for the B crystals was slightly higher than that for the A crystals.

The 2212 single crystals thus obtained (2 mm \times 2–3 mm) were buried in a powder with the composition of $\text{Bi}_2\text{Sr}_2\text{Ca}_{1.6}\text{Cu}_{3.6}$, which had been calcined at 820°C for 20 h. The powder containing the 2212 single crystals was annealed at 841, 843, 845, 847, 850, and 852°C for 150 h in air, respectively. The annealing temperatures were measured by the Pt/Pt-Rh (13%) thermocouple, which was directly put into the powder. The homogeneity of the temperature was within $\pm 0.5^\circ\text{C}$ in the powder.

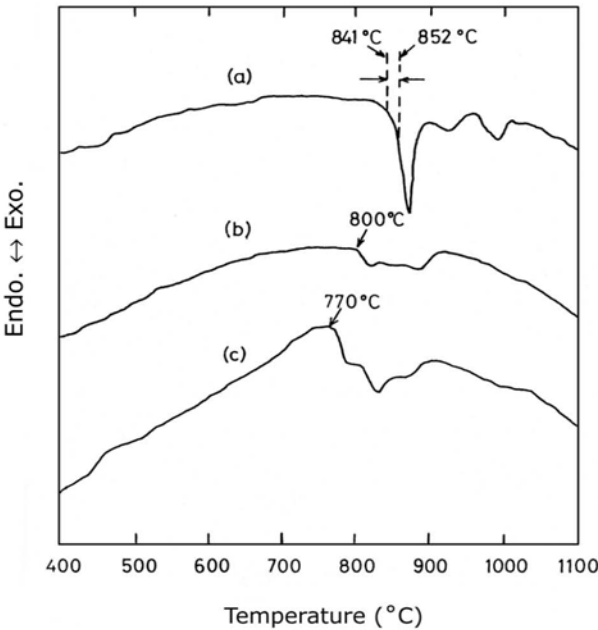


Fig. 14.12. DTA heating curves for (a) the calcined powder of $\text{Bi}_2\text{Sr}_2\text{Ca}_4\text{Cu}_6\text{Pb}_{0.5}\text{O}_y$, (b) the series A crystals, and (c) the series B crystals before annealing experiments (heating rate; $10^\circ\text{C}/\text{min}$). Arrows indicate the range of annealing temperatures used in this study (841–852°C). (From reference 4 by permission of *Jpn. J. Appl. Phys.*)

The following was found from the DTA curves in Fig. 14.12: (1) the partial melting of the calcined powder started around 840°C. (2) Some structural change occurred around 800°C in the series A and 770°C in the series B crystals, respectively. (3) The range of annealing temperatures (841 ~ 852°C) that were employed in this experiment is marked by arrows on the DTA curve for the powder. These annealing temperatures existed in the partial melting range of the powder. The dependency of the phase conversion from 2212 to 2223 upon the annealing temperatures is shown in Fig. 14.13 (series A crystals) and Fig. 14.14 (series B crystals), respectively. These figures indicate the following: (1) The conversion from 2212 to 2223 is very sensitive to the annealing temperature, that is, the temperature range of the formation of 2223 was probably within 2°C. (2) The best temperature for the conversion was 852°C. (3) The fraction of 2223 phase in the series B crystals, which were annealed at 852°C for 150 h, was a little higher than that in the series A crystals. (Compare Fig. 14.13f with Fig. 14.14c.) If the annealing temperature was raised above 852°C, the single crystals could not be separated

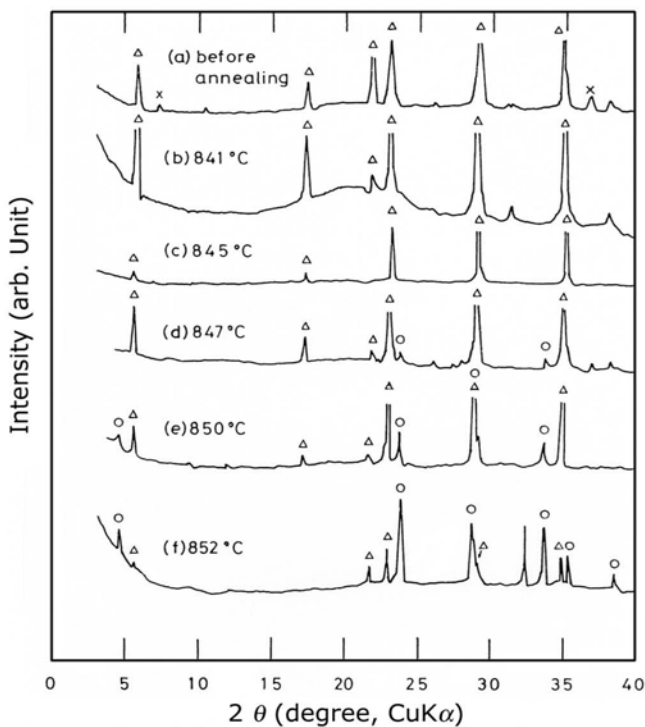


Fig. 14.13. X-ray diffraction patterns for the series A single crystals before (a) and after annealing in the calcined $\text{Bi}_2\text{Sr}_2\text{Ca}_4\text{Cu}_6\text{Pb}_{0.5}\text{O}_y$ powder at (b) 841°C, (c) 845°C, (d) 847°C, (e) 850°C, and (f) 852°C for 150 h in air. (x) 2201; (Δ) 2212; (Υ) 2223. (From reference 4 by permission of *Jpn. J. Appl. Phys.*)

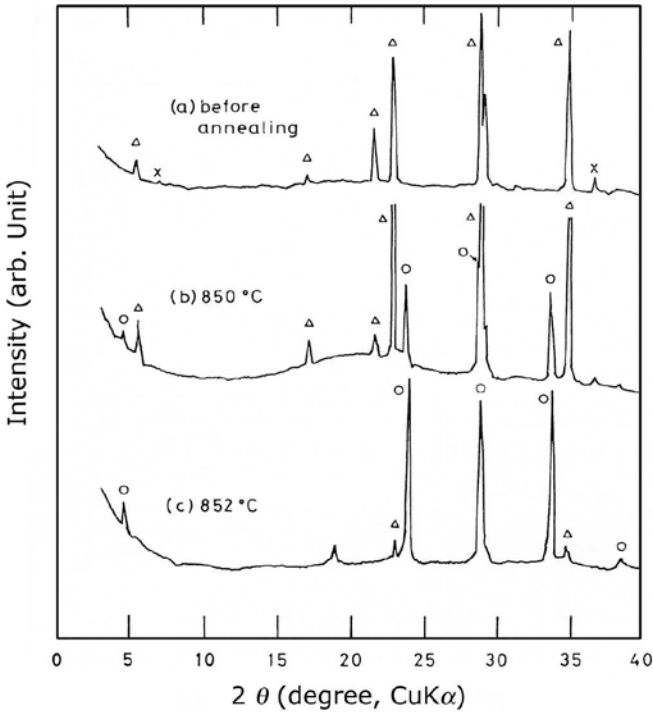


Fig. 14.14. X-ray diffraction patterns for the series B single crystals (a) before and (b, c) after annealing in the calcined powder at (b) 850°C and (c) 852°C for 150 h in air. (×) 2201; (Δ) 2212; (○) 2223. (From reference 4 by permission of *Jpn. J. Appl. Phys.*)

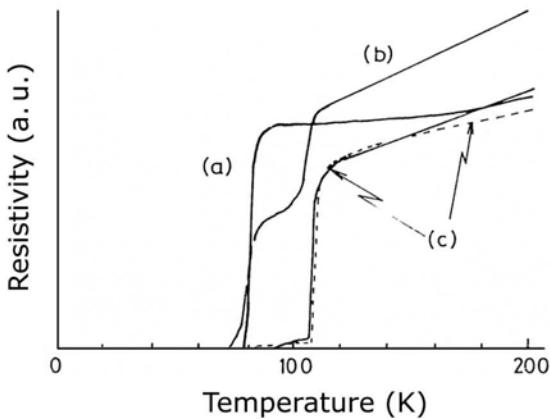


Fig. 14.15. Annealing temperature dependence of the R - T curves for the series A crystals (a) before and (b, c) after annealing at (b) 841°C and (c) 852°C. (From reference 4 by permission of *Jpn. J. Appl. Phys.*)

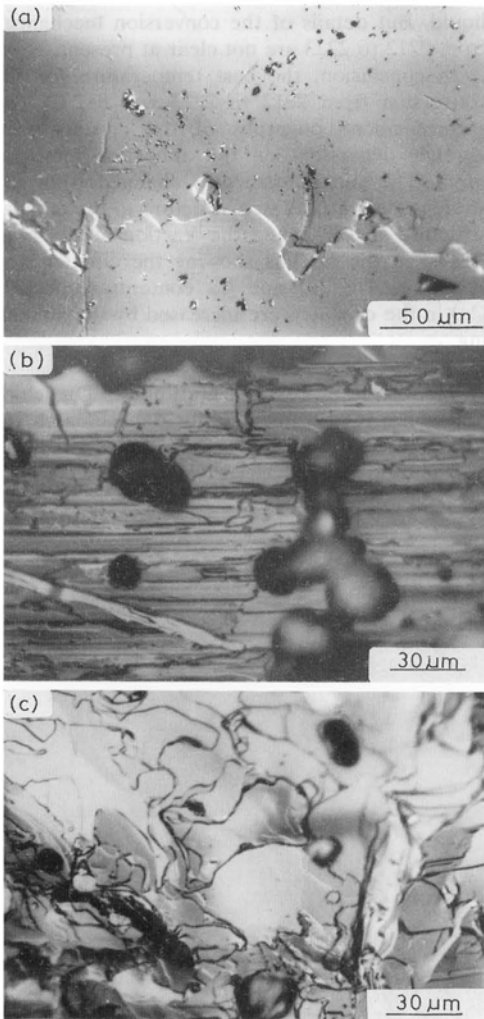


Fig. 14.16. Photographs showing the surface microtopographs of the series B crystals (a) before and (b, c) after annealing at (b) 850°C and (c) 852°C. (From reference 4 by permission of *Jpn. J. Appl. Phys.*)

from the partially melted powder because the molten portion of the powder increased. The resistivity R versus temperature T curves showing the annealing effects for the series A crystals are summarized in fig. 14.15. This figure shows that the major phase converted from 2212 to 2223 in the crystals after annealing at 852°C, although a small amount of 2212 phase was still left, which is consistent with the X-ray diffraction data. The R - T curves for the series B crystals after annealing at 852°C for 150 h were the same as those for the series A crystals.

Figure 14.16 shows the change of the surface microtopographs with increasing annealing temperatures for the series B crystals. The cleaved surface which was flat and smooth became rough and stepwise after annealing above 847°C for 150 h in air. In the temperature range of 847 to 850°C, a structure consisting of straight steps that ran parallel to each other formed (Fig. 14.16b). However, the step structure suddenly changed from the parallel pattern to the circular one at 852°C, as shown in Fig. 14.16c. The same results were obtained in the series A crystals. As already mentioned, the fraction of 2223 was largest in the crystals annealed at this temperature. Thus it was found that there was a strong correlation between the formation of 2223 and the surface microtopograph.

The chemical compositions of the crystals were quantitatively examined by the energy-dispersive X-ray (EDX) analyzer. The compositions (cation ratio) of the series B crystals changed from $\text{Bi}_{2.4}\text{Sr}_{2.2}\text{Ca}_{1.8}\text{Cu}_{3.6}$ to $\text{Bi}_{2.0}\text{Sr}_{2.0}\text{Ca}_{1.9}\text{Cu}_{4.2}$ by annealing at 852°C for 150 h in air. It was found that the contents of Cu and Ca (especially Cu) increased, whereas those of Bi and Sr decreased by the annealing.

The range of the annealing temperatures employed in this experiment was in the partial melting region of the calcined $\text{Bi}_2\text{Sr}_2\text{Ca}_4\text{Cu}_6\text{Pb}_{0.5}\text{O}_y$ powder, as shown in the DTA curve in fig. 14.12. The microtopographs of the annealed crystals strongly suggest the reaction of the 2212 crystals with the liquid. But details of the conversion mechanism from 2212 to 2223 are not clear.

In conclusion, the best temperature for the conversion from 2212 to 2223 was 852°C. The surface microtopographs of the crystals were strongly dependent on the annealing temperatures. The surface structure changed from the straight and parallel step structure to the circular structure at 852°C, and the fraction of 2223 was largest in the crystals showing the circular step structure. The Cu and Ca contents (especially Cu) in the crystals were increased by the annealing.

The above results are summarized as follows. The composition and temperature ranges of the solution for the high T_c crystal growth were very narrow. The formation temperatures of the high T_c crystals were slightly different depending on the chemical compositions. The high T_c crystals were formed by reactions of the low T_c crystals with the liquid, which formed in the partially melted region of calcined Bi-Sr-Ca-Cu-Pb-O.

14.3 Liquid Phase Epitaxial Growth of Low T_c Phase of BSCCO

The epitaxial films of the Bi-based superconductors, $\text{Bi}_2\text{Sr}_2\text{Ca}_2\text{Cu}_3\text{O}_x$: 2223 phase, $\text{Bi}_2\text{Sr}_2\text{CaCu}_2\text{O}_y$: 2212 phase, and $\text{Bi}_2\text{Sr}_2\text{CuO}_z$: 2201 phase, have usually been grown from the vapor phase and sometimes from the liquid phase. Liquid phase epitaxy (LPE), however, seems to be a promising method for growing the films of an atomically flat surface in a wide area because the LPE growth can be done at a considerably lower supersaturation than that from the vapor phase [23]. For example, in the case of the $\text{YBa}_2\text{Cu}_3\text{O}_7$ (or $\text{NdBa}_2\text{Cu}_3\text{O}_7$) superconducting system, extremely flat surfaces of wide area have been grown by the LPE method [23,24].

Table 14.1. Crystallographic data of the Bi-based superconductors and the substrates used in this study. (From reference 29 by permission of *J. Crystal Growth*)

	Lattice spacing ^a [Å]			Crystal system ^b
	a	b	c	
2212 phase	~ 5.4	~ 5.4	~ 30.8	Orthorhombic
2201 phase	~ 5.4	~ 5.4	~ 24.6	Orthorhombic
SrTiO ₃	3.91	–	–	Cubic
LaAlO ₃	3.79	–	–	Cubic
NdGaO ₃	5.43	5.50	7.71	Orthorhombic

^a At room temperature^b At 840°C

So far, many reports have been published on the preparation of Bi-based superconducting films by the LPE method [25–27]. However, most of the reports were limited to a brief description of the characteristics of the films, and almost no attention was paid to the growth mechanism or the flatness of the films. We report here results of the characterization and some growth mechanisms of the Bi-based superconductors grown on three types of substrates by the LPE method using a KC1 flux. Most of this section previously appeared in our papers [28,29].

Well-reacted oxide powder having an atomic ratio of Bi:Sr:Ca:Cu = 2:2:1:2 was prepared from sintering powders of Bi₂O₃, SrCO₃, CaCO₃, and CuO. The final reaction temperature was 850°C, and the total sintering time was 100 h. It was confirmed using the X-ray powder diffraction method that the sintered material was close to the 2212 single phase. This material was used as a nutrient in all experiments reported here.

The nutrient powder (5 g) was placed at the bottom of an alumina crucible (30 ml), and KC1 powder (20 g) was put on it as a flux [30,31]. These materials were heated at 925°C for 2 h. Then, the solution was cooled down to the growth temperature (840°C) in 30 min, and held at this temperature for 2 h. The substrate was fixed horizontally to the end of an alumina shaft, and dipped about 14 mm into the solution and rotated (20 rpm). Many experiments were conducted by varying the growth period and the substrate. At the end of each growth experiment, the substrate was pulled up about 10 mm above the liquid surface, and cooled to room temperature. Throughout the experiments, the upper part of the crucible was kept colder than the lower part to induce the natural convection and increase nutrient transport. SrTiO₃ (100), LaAlO₃ (100), and NdGaO₃ (001) were used as the substrates, whose crystallographic data together with the superconducting phases are shown in Table 14.1. The phase of each LPE-grown film was determined by X-ray diffraction (XRD). Back-reflection Laue photographs were taken to find out the crystallographic orientation of the film relative to the substrate [32]. The macroscopic surface morphology of the films was examined by polarizing light microscopy (PLM) and differential interference microscopy (DIM). The microscopic sur-

face morphology was observed by atomic force microscopy (AFM). Two-beam interferograms (TBI) were taken to measure the film thickness and the three-dimensional morphology of island layers. The temperature dependence of the electric resistivity was measured by an ordinary four-probe method to check the critical transition temperature of superconductivity ($T_{c(R=0)}$), and the transition width (ΔT_c).

14.3.1 SrTiO₃ (100) substrate [28]

The 2212 phase initially grew as island layers and then developed into a continuous single film in due course of time. Figure 14.17a and Fig. 14.17b are PLM photographs showing 2212 phase islands for the growth period of 10 h and a film grown continuously for 22 h, respectively. As is clear from the PLM photographs, the film thus obtained had twin structures. The diameter of the LPE-grown single

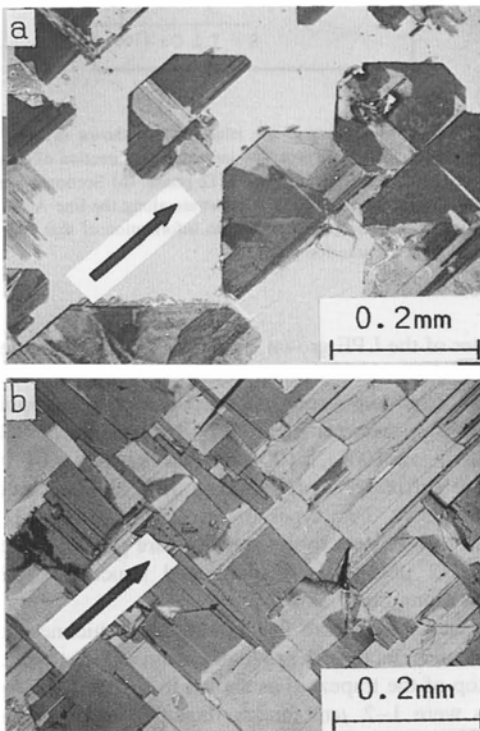


Fig. 14.17. PLM photographs (cross-nicols) of the 2212 phase on the SrTiO₃ (100) substrate. (a) Island layers grown in a period of 10 h, and (b) continuous film grown in a period of 22 h. The arrow indicates $\{011\}$ of SrTiO₃ and $[100]$ or $[010]$ of the 2212 phase. (From reference 29 by permission of *J. Crystal Growth*)

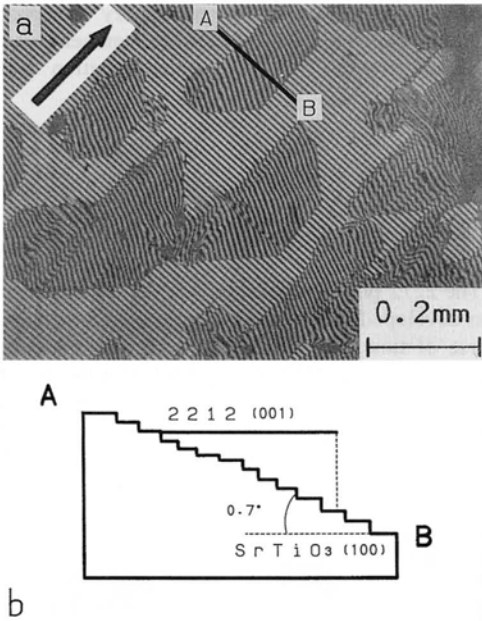


Fig. 14.18. (a) Interferogram of the island layers shown in Fig. 14.1a (wavelength: 5470Å). The arrow indicates the direction of either [100] or [010] with respect to the 2212 phase. (b) Sectional view of an island layer on the SrTiO₃ substrate along the line A-B in (a). The dashed line indicates that no information of that part is obtained from the interferogram. (From reference 29 by permission of *J. Crystal Growth*)

grains was estimated to be about 100 μm, which is larger than those grown from the vapor phase. The crystallographic relationship between the 2212 film and the SrTiO₃ substrate was (001)_F || (100)_s, [100]_F or [010]_F || (011)_s, where suffixes F and S indicate film and substrate, respectively. Two types of orientation of the 2212 phase with respect to the substrate are possible since the 2212 phase has a modulated structure of Bi atoms along the *b*-axis [33]. It was found from the TBI that the thickness of the islands increased gradually from the bottom to the top of the trapezoid as shown in Fig. 14.18a. The topsides were 1–2 μm thicker than the bottom sides. This suggests that the substrate surface is a vicinal face that is inclined at an angle of a few tens of minutes from the exact (100) crystallographic plane. This was confirmed by a back reflection Laue photograph and XRD, which indicated that (001)_F and (100)_s are exactly parallel to each other. The schematic of Fig. 14.18b shows the geometrical relation of the LPE grown 2212 layer and the substrate. For this reason, when the 2212 island layers coalesced to form a continuous layer, a height difference of about 1 μm was formed. Thus the obtained film was not so flat from the microscopic point of view. Figure 14.19 shows a resistance curve as a function of temperature for the film grown for 20 hours. This film showed a superconducting transition with $T_{c(R=0)} = 84$ K and $\Delta T_c = 4$ K.

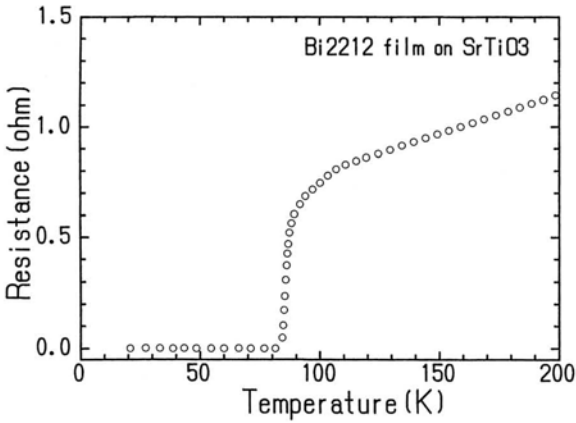


Fig. 14.19. Temperature vs resistance curve of the film grown for 20 hours. (From reference 28 by permission of the *Jpn. J. Appl. Phys.*)

14.3.2 LaAlO₃ (100) substrate

During the growth, numerous microcrystals of the 2212 phase were obtained in the solution. Then some of these microcrystals drifted with convection, and others formed a cloud in the lower part of the solution. When LaAlO₃ was used as a substrate, many microcrystals adhered randomly to the substrate and the film. However, the 2212 continuous film was grown only when the microcrystals coexisted in the solution. We checked this point repeatedly and arrived at a working hypothesis that the components of the 2212 phase were provided via the microcrystals, which might be a transient phase. The 2212 continuous film was composed of two types of domains whose b -axes were perpendicular to each other as in the case of the SrTiO₃ (100) substrate. In addition, this film had a similar morphology to the film grown on the SrTiO₃ (100) substrate. Its $T_{c(R=0)}$ and ΔT_c were 81 and 8 K, respectively.

Aiming at avoiding the adhesion of the microcrystals, we fixed the substrate to the rotating shaft vertically and rotated the substrate eccentrically. As a result, we could avoid the adhesion of the microcrystals, but the film had the 2201 phase. At present, we conjecture that the microcrystals have a significant role to supply solute to the growing film. If the growing film is kept far away from the microcrystals, the Ca atoms will be poorly supplied from the microcrystals because the solubility of Ca atoms in molten KCl is very low. This is one reason why the 2201 phase formed instead of the 2212 phase. A DIM microphotograph of this film is shown in Fig. 14.20.

We also observed the microscopic flatness of this film by AFM, which showed flat terraces expanding up to several μm^2 . This area is two orders of magnitude wider than the flat area of the films produced from the gas phase. The step height difference between the terraces was a few times that of the unit cell height (c-spacing) in the 2201 phase.

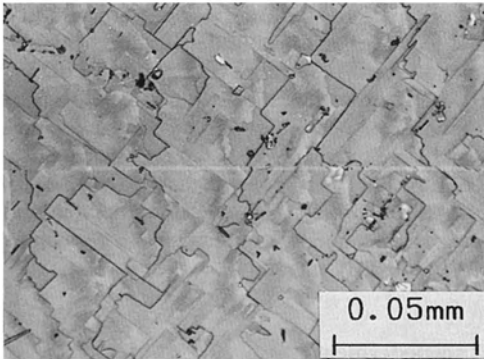


Fig. 14.20. Continuous film of the 2201 phase grown on the (100) face of the LaAlO_3 substrate (DIM micrograph). The film thickness was about $1\ \mu\text{m}$. (From reference 29 by permission of *J. Crystal Growth*)

14.3.3 NdGaO_3 (001) substrate

When NdGaO_3 was used as a substrate, the adhesion of the microcrystals was remarkable as in the case of LaAlO_3 . Figure 14.21 shows the surface of the 2212 phase film, which escaped from the adhesion of microcrystals. In contrast to the film grown on the SrTiO_3 (100) substrate (Fig. 14.17b), this film shows a uniform tint except for a small area as shown in the PLM photograph (Fig. 14.21). This suggests that the film is nearly twin free, and we confirmed by a Laue photograph that the crystallographic a -axis of the film coincided with that of the substrate. The thickness of the film grown for 10 h was about $1.5\ \mu\text{m}$, and there existed about a

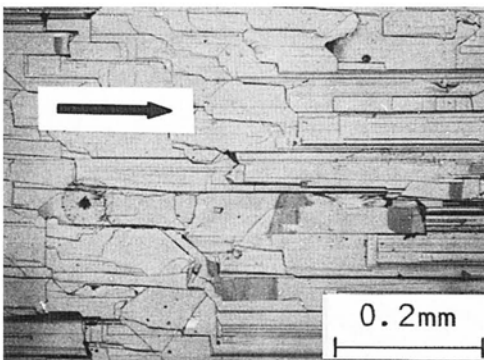


Fig. 14.21. PLM photograph (cross-nicols) of a continuous film of the 2212 phase grown on the NdGaO_3 (001) substrate in a period of 10 h. The arrow indicates [100] of NdGaO_3 and [100] of the 2212 phase. (From reference 29 by permission of *J. Crystal Growth*)

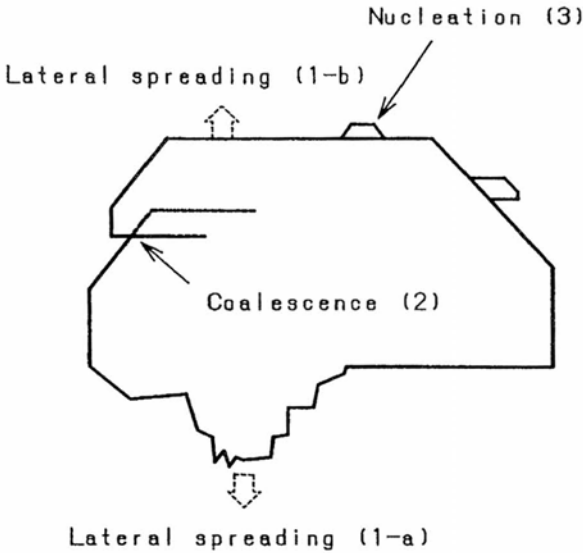


Fig. 14.22. Schematic explanation of the enlarging processes of superconducting layers. (From reference 29 by permission of *J. Crystal Growth*)

0.5 μm height difference among the grains. This film showed a superconducting transition with $T_{c(R=0)} = 79$ K and $\Delta T_c = 6$ K. However the resistivity exhibited an anomalous increase with decreasing temperature near the critical temperature, whereas a monotonous decrease was observed in the case of SrTiO_3 and LaAlO_3 . Furthermore, the resistivity at room temperature was one order of magnitude larger (~ 20 $\text{m}\Omega \cdot \text{cm}$) than that of the 2212 films grown on the other substrates (~ 1 $\text{m}\Omega \cdot \text{cm}$). These differences might be caused by contaminants from the substrate as suggested by Balestrino et al. [27].

From the present observations, we propose three processes that increase the island size as follows. (1) Nucleation of the crystals at the interface between the substrate and the island as seen in Fig. 14.17a. (2a) Lateral spreading toward the A direction in Fig. 14.18b. (2b) Lateral spreading toward the B direction. (3) Coalescence of the islands as a result of spreading. A schematic drawing to explain these processes is shown in Fig. 14.22. In this study, the highest wettability between the substrate and the 2212 phase was observed when NdGaO_3 (001) was used, whereas SrTiO_3 (100) had the lowest wettability. This result is consistent with the misfit ratios of each substrate. There are two barriers that must be overcome to produce a film having a macroscopically flat surface. One is solved by avoiding the random adhesion of the microcrystals to the film. The key to solving this problem will lie in the control of the liquid flow by rotating the substrate as mentioned in the case of the LaAlO_3 (100) substrate. The other problem is solved by changing the growth mode from three-dimensional island growth to the layer-by-layer growth mode. Reducing the supersaturation might solve this problem. This opera-

tion will make the spacing among steps larger and, microscopically as well as macroscopically, a flat surface in a wider area will form [23]. However, we presume that the wettability between the substrate and the solution and/or that between the solution and the film is a more significant factor than the supersaturation, because layer-by-layer growth has been observed in the gas phase system even on the SrTiO_3 (100) substrate, which has the largest misfit ratio ($\sim 2.4\%$) among the substrates used in this study, and the supersaturation in the gas phase system is higher than that in the liquid phase system.

The above results are summarized as follows. LPE growth of Bi-based superconductors was carried out on three types of substrates. Three-dimensional island growth was observed, irrespective of the type of substrate. The enlarging processes of the island layers were suggested. Because a difference in height is created when the islands coalesce to form continuous films on the vicinal surface, macroscopic flatness of the films was not attained in this study. However, reasonably flat surfaces which have an area of about $1 \mu\text{m}^2$, were confirmed to exist in the 2201 film grown on the LaAlO_3 (100) substrate. This shows the possibility of obtaining an atomically flat and large terrace of Bi-based superconductors by the LPE method. It was shown that the NdGaO_3 (001) substrate, which belongs to the orthorhombic crystal system, is effective in suppressing the formation of twins in the 2212 phase.

14.4 Construction of Phase Diagrams by *In Situ* Observation and Their Application to Crystal Growth of Oxide Superconductors

Growing single crystals without a phase diagram is just like making a voyage without a map. In crystallization from multicomponents systems, it is difficult to grow your target crystal as a single phase because there are many byproducts and the crystallization condition is complicated. Precise phase diagrams are therefore indispensable, especially for growing single crystals of incongruent-melt compounds by the traveling solvent floating zone method, the top-seeded solution growth method, the liquid phase epitaxy method, and other methods. The most important information for single crystallization is the condition in which your target crystal can crystallize from solution without any other solid phases. On the phase diagram, this is the liquidus line. From the liquidus line, we can evaluate the solubility and the driving force for crystallization. This driving force is the supersaturation.

Oxide superconductors are composed from many elements and their crystal structures are complicated. They incongruently melt when they are heated. To construct phase diagrams for these materials, it is difficult for us to precisely follow when the liquid-solid reaction process occurs by ordinary thermal analysis such as DTA. This is because such analysis needs a large heating or cooling rate to obtain large enough signals. Thus, techniques suitable for growth at very slow rates are needed. High-temperature microscopy is one such candidate. *In situ* ob-

servations are convincing because seeing is believing. Using high-temperature optical microscopy, we observed crystallization and dissolution processes of oxide superconductor systems to make their phase diagrams. Here, we introduce this method and some results [34]. The main merits of this are that we can slow down the heating or cooling rate to the extent that the system is approximately in equilibrium, which are approximately the same conditions for actual solution growth experiments; furthermore, we can directly observe the processes contributing to crystal growth and dissolution to recognize the order of the phase formation.

14.4.1 Apparatus

The apparatus used was composed of a reflection type optical microscope (Nikon Optiphot) and an infrared heating furnace (Sinkuriko model MS-E1R). Figure 14.23 is a photograph of the apparatus and Fig. 14.24 shows an illustration of the furnace. The latter was composed of a gold-plated mirror housed in the chamber. The mirror shape was ellipsoidal; a halogen lamp was placed on one focus and the sample cell sat on a thermocouple at the other focus. This chamber could be sealed and we could make a vacuum condition or change the gas atmosphere in it. The cup-shaped sample cell was made from alumina with a diameter of 5.5 mm and



Fig. 14.23. Photograph of the observation system

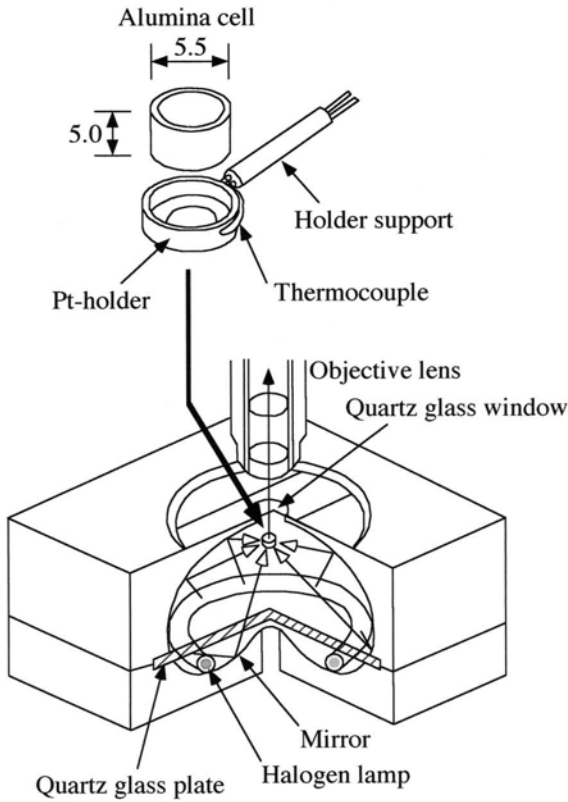


Fig. 14.24. Schematic of the infrared heating furnace and the sample cell (Reprinted from [34(c)], with permission of Elsevier Science)

height of 5 mm. Long working distance objectives (larger than 11 mm, magnification 5 \times , 10 \times , and 20 \times) enabled us to observe the high-temperature growth through a chamber window. The image of the sample was monitored by a CCD camera and recorded by a time-lapse video recorder because crystallization of multicomponent system takes a long time. The time and sample temperature were also recorded on the VTR. In the chamber, the light emitted from the halogen lamp was focused to the sample cell and heated it up to 1200 $^{\circ}$ C. The sample temperature was regulated by a PID controller. The monitored temperature was calibrated by the melting points of standard materials such as Bi₂O₃ (824 $^{\circ}$ C), LiF (848 $^{\circ}$ C), PbO (886 $^{\circ}$ C), silver (961 $^{\circ}$ C), and gold (1064 $^{\circ}$ C). The error in the temperature measurement was estimated to be within about $\pm 1.5^{\circ}$ C.

The volume of the chamber was about 150 cm³, and it had gas inlet and outlet ports. The oxygen partial pressure in the chamber was controlled by adjusting the mixing ratio of oxygen and argon gases by mass-flow meters. The oxygen concentration was measured by an oxygen meter (Iijima model G-101) with a gal-

vanic cell-type sensor that was precise to 0.1%. The total flow rate of the gas mixture was about $100 \text{ cm}^3/\text{min}$. The total pressure was kept at atmospheric pressure (0.1 MPa).

Samples were prepared as follows. The raw materials were prepared by mixing powders of oxides. They were calcined several times in air in the temperature range from 750 to 800°C for one day. A small amount of sample powder was put on a cleaved thin plate of an MgO single crystal, which was put on the bottom of an alumina sample cell in the chamber. The cell was heated by focusing the light of the halogen lamp. This allowed us to heat and cool the cell rapidly between room temperature and 1200°C because the thermal capacity of the cell was small. As temperature increased, the sample powder melted and formed a tiny droplet. For the solution of oxide superconductors, the wettability between the substrate and the sample droplet was poor: the contact angle was less than 90° . Then, the droplet was halted on the substrate. Below 1200°C , no reaction with the substrate and the droplet seemed to occur from the observation of the interface.

The merits of this method to construct phase diagrams are summarized as follows:

1. We can choose heating and cooling rates arbitrarily and observe the sample *in situ*. The time-lapse video recording enables us to visualize very slow changes for a long time period.
2. We can recognize the existence of the new phase in the image even though it is too tiny to be detected by thermal or X-ray analysis.
3. Intermediate phases can be recognized. In the peritectic reaction, as temperature decreases, an intermediate phase tentatively crystallizes by a small amount and dissolves again. We think this method is a unique way to detect such a phase.
4. If there are many phases in the texture, direct observation enables us to recognize the order of crystallization.
5. We can seal the furnace chamber. Then we can study the effect of oxygen partial pressure on crystallization.
6. Only a small amount of sample will suffice for fundamental studies because the process is magnified by optical microscopy.
7. The volume of the sample is small and the solution cannot escape from the droplet. Thus, the composition of the solution is kept constant and homogeneous.

The demerits are as follows: we can only observe the surface process of the droplet. To observe inside, the droplet should be transparent. We can measure the growth rate under various conditions, but we cannot adjust the crystal orientation in the droplet by hand and it is difficult to study growth rates along a required direction. We cannot remove the crystal from the solution.

Here we introduce two examples of the construction of a phase diagram of oxide superconductors [$\text{SmBa}_2\text{Cu}_3\text{O}_{7-\delta}$ and $\text{Bi}_2(\text{Sr,Ca})_{x+1}\text{Cu}_x\text{O}_y$ ($3 > x > 0$)] and their application to real growth experiments.

14.4.2 Phase diagram of $\text{SmBa}_2\text{Cu}_3\text{O}_{7-\delta}$ and its application

Here we describe how to determine the liquidus lines of oxide superconductor phases. The $\text{Sm}_2\text{O}_3\text{-BaO-CuO}$ system is used as an example. $\text{RBa}_2\text{Cu}_3\text{O}_{7-\delta}$ (R is a rare earth element) is well known as a superconductor phase. Hereafter, we call it R123.

Phase diagrams of R123, especially Y123, have been widely made by thermal analysis and X-ray powder diffractometry after quenching, and using element analysis of the solution [35]. However, it was difficult to precisely determine the liquidus temperatures and compositions because only a small amount of R123 crystallizes from the solution. Furthermore, thermal analysis needs a large cooling and heating rate to obtain a clear signal. Meanwhile, *in situ* observation is a powerful technique to determine the phase diagram in such a system.

For the Sm123 system, the phase diagram at 950°C in the $\text{Sm}_2\text{O}_3\text{-BaO-CuO}$ system made by the quenching method was reported, and the Sm123 phase is considered to crystallize in a triangle of Sm123-BaCuO₂-CuO [36]. To determine precise liquidus lines, where primarily the Sm123 phase crystallizes, we made seven pseudo-binary phase diagrams in the region of Sm123-BaCuO₂-CuO [37]. Here, we describe how to construct the phase diagram with this method by using the Sm123-“Ba₇Cu₁₈O₂₅” pseudo-binary system as an example. The quotes are used because no such material exists. The liquidus lines should be, in principle, determined both by the crystallizing temperature and the dissolution temperature obtained by *in situ* observation. However, the liquidus temperature determined by the crystallizing temperature is lower than that by the dissolution temperature because the nucleation needs a large supersaturation. In this study, we observed the dissolution process and determined the liquidus temperature.

The procedure used in this study is as follows. Sample powders of systematically selected compositions were first prepared. The composition was expressed as a molar percentage of Sm123 in Ba₇Cu₁₈O₂₅ as a solvent where BaO:CuO = 7:18 was reported to be a eutectic point of the BaO-CuO system [38], and the dissolution temperature was expected to be lowest near this point. All experiments were carried out in air. The prepared sample was heated up to 950°C – 1000°C and formed a mixture of tiny crystals and high temperature solution. At this temperature, we increased and decreased the temperature several times. In this procedure, the tiny crystals coalesced, and finally only one crystal remained in the solution (Fig. 14.25). We call this the self-seeding method. After only one crystal was formed, we slowly increased the temperature (1°C per 30 minutes) and finally, the crystal was completely dissolved. We measured this temperature and adopted it as the liquidus temperature. This process is shown in Fig. 14.26. To check that no crystals remained in the solution, we decreased the temperature by 5°C – 10°C . If tiny crystals had remained in the solution, they would soon grow to an observable size because the supercooling of 10°C is too small for nucleation. Conversely, a lack of observed crystals indicated that no crystals remained.

As temperature was increased, needle $\text{Sm}_2\text{BaCuO}_5$ crystals [39], hereafter we call Sm211, sometimes crystallized before the Sm123 crystal completely dissolved.

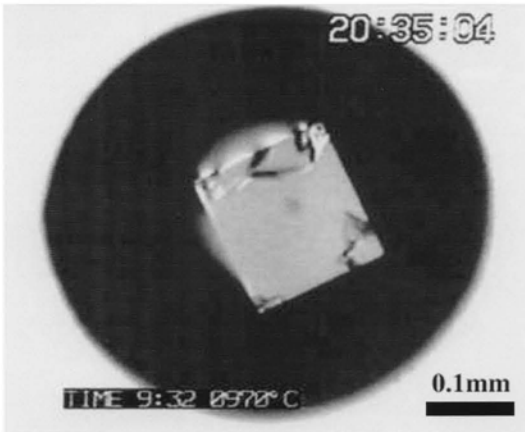


Fig. 14.25. Optical micrograph of the Sm123 crystal coexisting with the liquid in air [37]

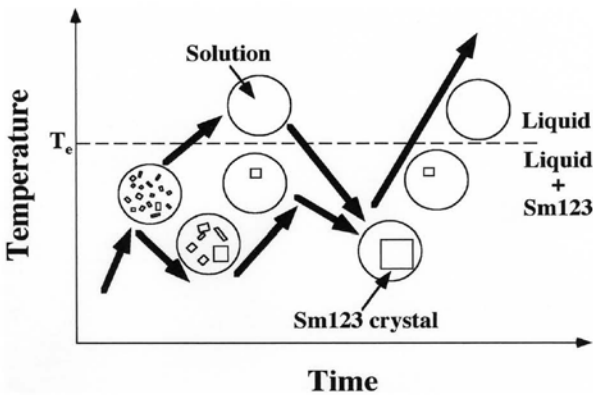


Fig. 14.26. Diagram of the self-seeding technique and determination of the liquidus temperature [37]

When this occurred, a peritectic reaction [29] of $\text{Sm123} \rightarrow \text{Sm211} + \text{liquid}$ occurred at this composition, and from this composition, we could not directly grow the Sm211 crystals. We also determined this partial melting temperature. We measured the temperature at which the Sm211 crystals first appeared four times. The average temperature was adopted as the partial melting temperature for this composition. Figure 14.27 shows a constructed pseudo-binary phase diagram. It shows that the Sm123 phase primarily crystallizes in the composition range from 5 mol% to 40 mol%. Above 45 mol% concentration, the peritectic reaction $\text{Sm123} \rightarrow \text{Sm211} + \text{liquid}$ occurs, and the Sm123 crystals decompose at about 1060°C to form the Sm211 phase. The liquidus line of the Sm211 phase lies above 1080°C .

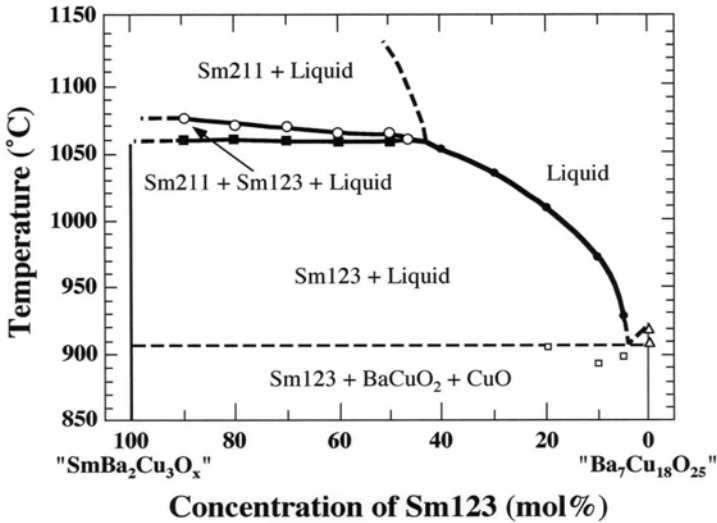


Fig. 14.27. Pseudo-binary phase diagram of the Sm123 system in air [37]

Three phases of Sm123, Sm211, and the liquid coexist in the composition range between 45 mol% and 90 mol%, and in the temperature range between 1060°C and 1080°C. As temperature increases in this region, the Sm123 crystal dissolves but the Sm211 grows. Conversely, as temperature decreases, the Sm211 dissolves and the Sm123 grows. These processes were directly observed.

A precise phase diagram enables us to calculate the supersaturation. Using the obtained phase diagram, we measured the dependence of the growth rate on supersaturation. Supersaturation was determined as follows. First, we let only one crystal remain in the solution in equilibrium; this temperature and solubility are denoted T_e and $C_e(T_e)$, respectively. In this state, the supersaturation is zero. We next increased the temperature to T , and the crystal dissolved by a certain amount. If the crystals remained in the solution after this operation and they were in equilibrium, the solubility of the solution could be expressed as $C_e(T)$. Then, we rapidly reduced the temperature to T_e . In this case, the supersaturation σ could be expressed as $\sigma = [C_e(T) - C_e(T_e)]/C_e(T_e)$. Under the microscope, we could measure the growth rate along the crystallographic a - and c -axis under various supersaturations. In this experiment, the composition of the sample was 35 mol% of Sm123 in the Ba₈Cu₁₇O₂₅ solvent, and the growth temperature was kept constant at $T_e = 1000^\circ\text{C}$. Up to a supersaturation of 0.4, the growth rate along the a -axis gradually increased as the supersaturation increased. At the supersaturation of 0.4, it was about 12 $\mu\text{m}/\text{min}$. Above 0.4, the growth rate rapidly increased with supersaturation. At the supersaturation of 0.7, it was about 70 $\mu\text{m}/\text{min}$. On the other hand, the growth rate along the c -axis was one order of magnitude less than that along the a -axis, although it gradually increased with supersaturation. This growth rate anisotropy is probably caused by the strong anisotropy in crystal structure.

This method was also applied to study the effect of oxygen partial pressure on phase diagrams [41], to construct phase diagrams of other solvent compositions [42], to study the effect of rare earth elements [43], and to construct phase diagrams of other oxide systems [44]. This information was used to grow single crystals by the self-seeding method and by the traveling-solvent floating-zone method.

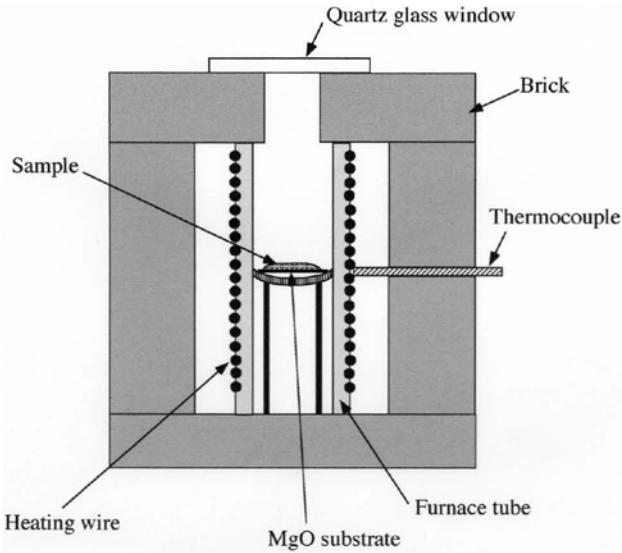


Fig. 14.28. Schematic of the furnace used to scale-up phenomenon under the microscope [37]

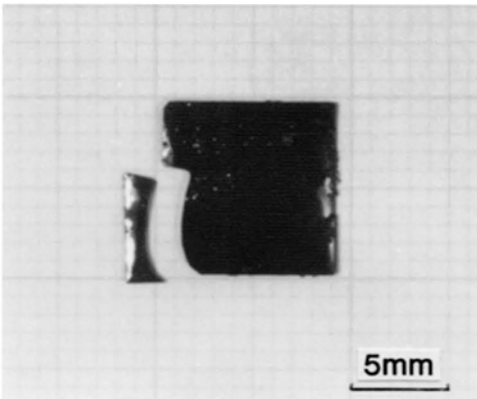


Fig. 14.29. Photograph of the Sm123 crystal grown by the self-seeding technique under the large furnace [37]

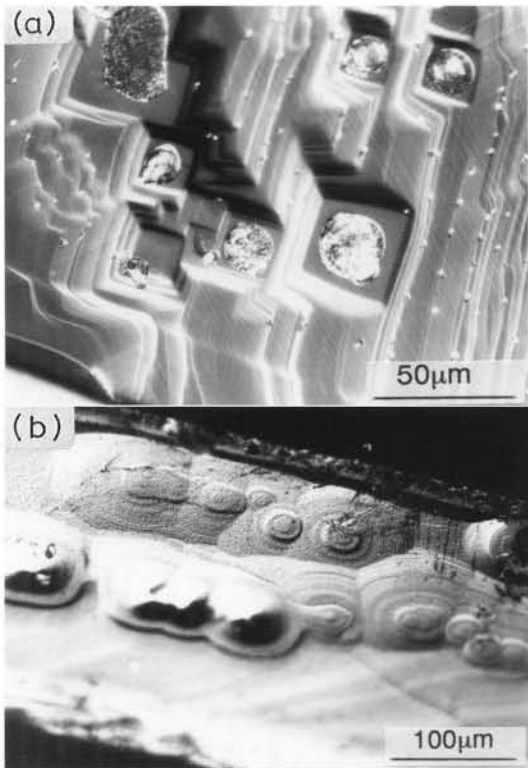


Fig. 14.30. Differential interference contrast optical micrograph of the as-grown Sm123 crystal [37]. (a) *c*-plane, (b) *a*-plane

The self-seeding growth technique mentioned above was achieved under the optical microscope in a droplet with diameter of several millimeters. This method, however, should be scaled up to obtain larger single crystals that are easier to handle. We then made a simple furnace, and tried to grow larger crystals using information obtained under the microscope. Figure 14.28 shows a schematic of this furnace. In principle, this system was similar to the high-temperature optical microscopy system except for the heating method. The size of the cleaved MgO plate was $20 \times 20 \text{ mm}^2$ and the diameter of the sample droplet was about 15 mm. The temperature at the edge of the droplet was higher by 3°C than at the center. The composition of the sample was 40 mol% of Sm123 in the $\text{Ba}_7\text{Cu}_{18}\text{O}_{25}$ solvent.

The procedure of the self-seeding method was just the same as that used under the microscope. When only one crystal remained in the solution, the temperature was decreased at a rate of $1^\circ\text{C}/\text{h}$ to grow the crystal. We succeeded in obtaining a $10 \times 10 \times 0.5 \text{ mm}^3$ -size single crystal, which showed that the phenomenon under the microscope could be scaled up. Figure 14.29 shows a photograph of the obtained crystal. Finally, the residual solution was sucked up into a porous alumina

rod, and then a sole crystal was obtained. The observed crystal surface was the c -plane. It is well known that oxide superconductors have strong anisotropy in growth rate between that in the c -plane and that along the c -axis. Figure 14.30a shows a differential interference contrast micrograph of the as-grown surface of the c -plane on the obtained crystal. Two-dimensional hillocks and many macrosteps were observed. The hillocks are rectangular with edges parallel to the a - and b -axes. Figure 14.30b is that of the a -plane. Round growth hillocks and fine steps are visible. The shapes of the hillocks were elliptic with major axis along the a -axis.

14.4.3 Phase diagram of Bi-based oxide superconductors

Three types of Bi-based oxide superconductors, $\text{Bi}_2\text{Sr}_2\text{CuO}_6$, $\text{Bi}_2\text{Sr}_2\text{CaCu}_2\text{O}_8$ (the low T_c phase), and $\text{Bi}_2\text{Sr}_2\text{Ca}_2\text{Cu}_3\text{O}_{10}$ (the high T_c phase) are known [45]. Their critical temperatures are 20, 80, and 110 K, respectively. Large single crystals of the low T_c phase have been grown from high temperature solutions using either the flux growth method or the traveling-solvent floating-zone method. But on the other hand, it has been difficult to grow the high T_c phase crystals even though this has the highest critical temperature and its application is expected. This phase is composed of five elements and is known as an incongruently melting compound. Therefore, it is difficult to recognize the phase relation at high temperatures. Especially, since it was not known whether this phase coexisted with the liquid phase. This information is essential to grow crystals from solution.

Shigematsu et al. [46] proposed a $\text{Bi}_2(\text{Sr,Ca})\text{O}_4\text{-(Sr,Ca)CuO}_2$ pseudo-binary phase diagram that had no liquidus coexisting with the high T_c phase. However, there were a few reports suggesting the possibility of growth of the high T_c phase from the liquid [47]. Thus, a reliable phase diagram is a key to growing single crystals of the high T_c phase. To determine whether or not the high T_c phase could be grown from solution, we studied the phase relation using high-temperature optical microscopy [34].

Samples were prepared as follows. The raw materials were prepared by mixing powders of Bi_2O_3 , SrCO_3 , CaCO_3 , and CuO . Following the work of Shigematsu et al. [46], we chose their nominal composition $\text{Bi}_2(\text{Sr,Ca})_{x+1}\text{Cu}_x\text{O}_y$ ($3 > x > 0$). The samples were calcined in air in the temperature range from 750°C to 800°C for one day. These samples were then used for high-temperature optical microscopy.

We observed the crystal growth processes of $\text{Bi}_2(\text{Sr,Ca})_{x+1}\text{Cu}_x\text{O}_y$ by slow cooling from high-temperature solutions with respect to the values of x of the starting material. The low T_c phase is $x = 2$, whereas the high T_c phase is $x = 3$. In the case of $3 > x > 1.2$, the first solids that appeared were needle crystals of $(\text{Sr,Ca})\text{CuO}_2$ [48], and as the temperature decreased, thin plate crystals began to grow at 878°C .

In the case of $1.2 > x > 0.9$, the plate crystal of the low T_c phase appeared directly from the liquid. Another type of plate crystals of $\text{Bi}_2(\text{Sr,Ca})_2\text{CuO}_6$ appeared directly from the liquid in the range of $0.9 > x > 0.4$ and below 860°C . We could distinguish this crystal from other plate crystals by its striations. The low T_c crystal shows clear striations after crystallization was complete, whereas the crystal of

$\text{Bi}_2(\text{Sr,Ca})_2\text{CuO}_6$ has no striation. The striations are at an angle of 45° to the edges of the single crystal. The origin of this striation is not known.

In the case of the solution of $x = 1.3$, needle crystals and plate crystals (the first crystal) nucleated at the same time in the earlier stage of cooling. In the mean time, some of the plate crystals dissolved to form new crystals in spite of the cooling of the solution. The details of the processes observed under the microscope were as follows. After the growth of the first crystal (Fig. 14.31a), which kept its facet while dissolving (Fig. 14.31b), new thin plate crystals (the second crystals) formed at the expense of the first crystals at 865°C (Fig. 14.31c). When the furnace temperature reached 850°C , we quenched the sample and measured the electric resistance.

As the temperature decreased, the resistance began to decrease at about 110 K and it dropped to zero at 87–89 K as shown in Fig. 14.32a. We attributed the features of the resistivity curve to the oxygen deficiency [49] of the samples that were a mixture of the high and low T_c phases because of quenching. To supply oxygen, the samples were annealed under an oxygen atmosphere at 800°C for 24 h. We obtained the resistivity curve as shown in Fig. 14.32b. It clearly shows the existence of the high T_c phase. The analysis using an electron probe microanalyzer could not identify the high T_c phase because the thickness of the first crystal lying on other crystals was too small (5–10 μm) to identify the chemical composition.

Thus, growth experiments from high temperature solutions suggested the formation of the high T_c phase as a result of the peritectic reaction of the first crystals with the solution.

The partial melting of the low T_c phase was then examined. As the temperature increased, the low T_c phase single crystal began to decompose into liquid at 865°C . When we kept the sample at 870°C , needle crystals of $(\text{Sr,Ca})\text{CuO}_2$ began to grow. Then, two kinds of solids (the needle and the low T_c phase) and a liquid coexisted for a while. Ten hours later, very thin plate crystals began to grow on the surface of the liquid and grew for 18 h. We quenched this sample and annealed it at 800°C for 24 h under an oxygen atmosphere. The resistivity of this sample is shown in Fig. 14.33, which clearly reveals the existence of the high T_c phase. This suggests that the thin plate crystal would be a crystal of the high T_c phase. But the size of this crystal was too small ($100 \times 100 \times 2 \mu\text{m}^3$) to be identified by normal X-ray diffraction.

Following the results described above and our measurements of differential thermal analysis, we propose a modified phase diagram along the composition line of $\text{Bi}_2(\text{Sr,Ca})_{x+1}\text{Cu}_x\text{O}$ as shown in Fig. 14.34, which indicates the possibility of obtaining high T_c phase single crystals from solution though the coexisting region of the high T_c phase and the liquid is narrow. This would explain why the high T_c phase was not detected by thermal analysis.

In order to confirm this phase diagram, we tried *in situ* observations of the partial melting of the low T_c phase because it was expected to decompose into the high T_c phase and the liquid according to the proposed pseudo-binary phase. The starting material consisted of the low T_c phase crystals obtained by slow cooling of the oxide flux of $\text{Bi}:\text{Sr}:\text{Ca}:\text{Cu} = 1.65:1:1:1.35$. These crystals were heated in air at

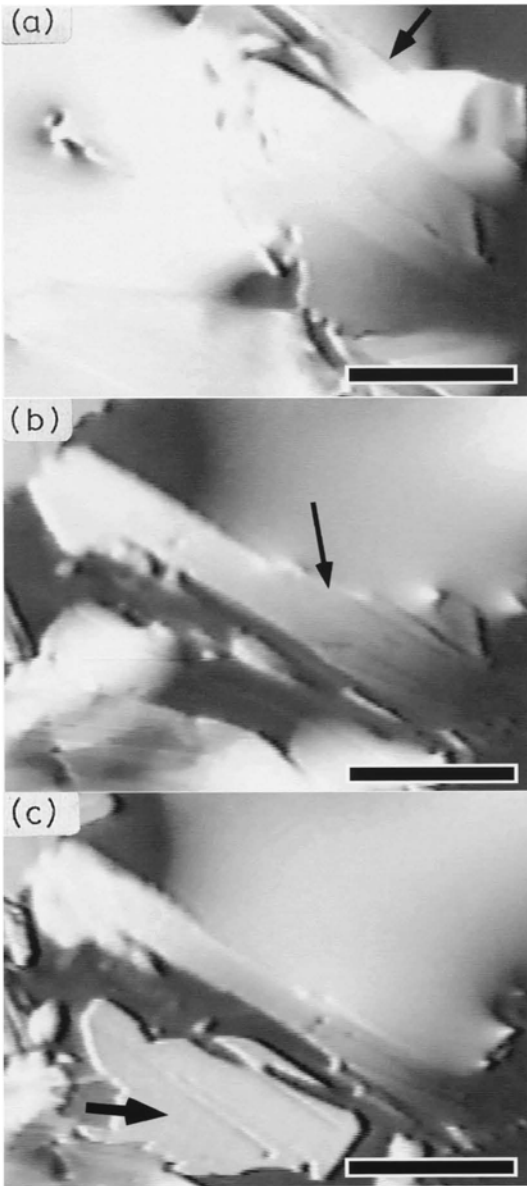


Fig. 14.31. Photographs of the plate crystals that appeared as the temperature decreased. The scale bar indicates $100\ \mu\text{m}$. (a) The first crystals grown on the surface of a liquid (marked by an arrow) at 865°C . (b) The first crystals dissolved at 860°C . The solid-liquid boundary is marked by an arrow. (c) The second crystals (marked by an arrow) grew from the liquid at 845°C . (Reprinted from [34(a)], with permission of Elsevier Science)

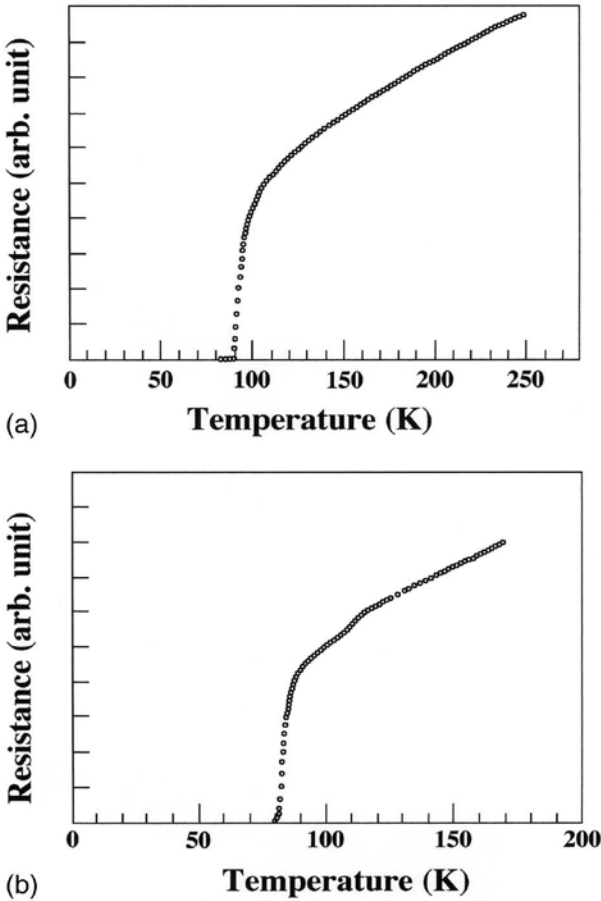


Fig. 14.32. Temperature dependence of the resistance of the sample grown from a high-temperature solution. a) As-grown sample. (b) The sample annealed at 800°C in oxygen atmosphere for one day. (Reprinted from [34(a)], with permission of Elsevier Science)

a rate of 3°C/min to find the partial melting temperature. At 860°C, small droplets began to emerge on the surface of the crystals [50]. These droplets grew large as the temperature increased. The crystals of the low T_c phase began to decompose into a viscous and opaque liquid at 865°C. When we kept the temperature of the sample at 870°C, needle crystals of (Sr,Ca)CuO₂ began to grow (Fig. 14.35a), then needle crystals, low T_c phase crystals, and a liquid coexisted for a while. The temperature was kept at 870°C for 10 h, after which it was noticed that very thin plate crystals began to grow on the liquid surface that grew for 20 h (Fig. 14.35b). The growth rate of these crystals was very small (80 μm/h). After keeping the temperature at 870°C for 50 h, we quenched them at a rate of 100°C/s. The rest of the solution quickly solidified and the surface of the droplet became wavy.

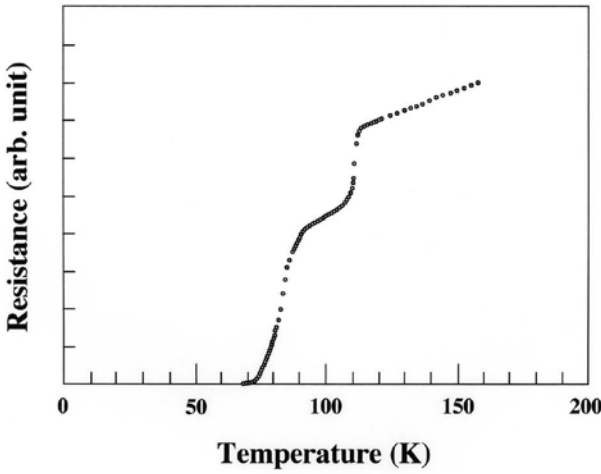


Fig. 14.33. Temperature dependence of the resistance of the sample annealed at 800°C in an oxygen atmosphere (Reprinted from [34(a)], with permission of Elsevier Science)

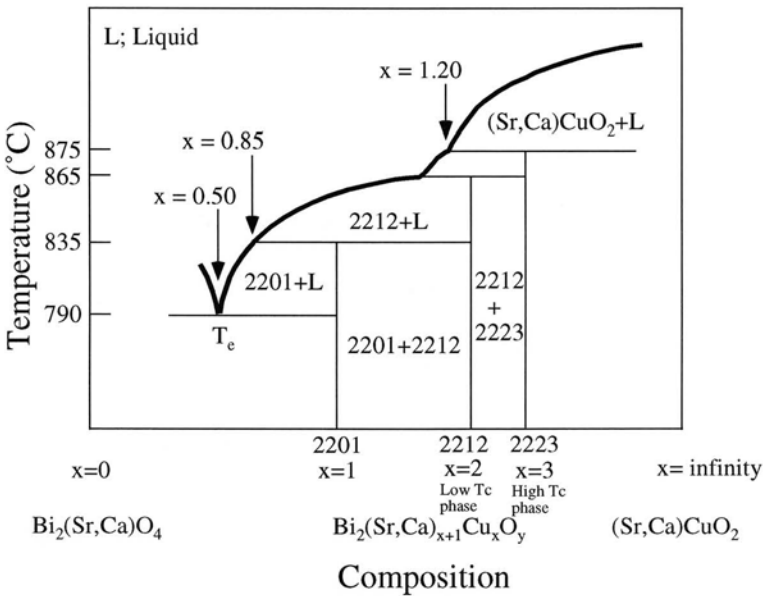


Fig. 14.34. The pseudo-binary phase diagram of $\text{Bi}_2(\text{Sr,Ca})_{x+1}\text{Cu}_x\text{O}_y$ proposed after *in situ* observation. $\text{Bi}_2(\text{Sr,Ca})\text{O}_4$ at $x = 0$ and $(\text{Sr,Ca})\text{CuO}_2$ at $x = \text{infinity}$ (Reprinted from [34(a)], with permission of Elsevier Science)

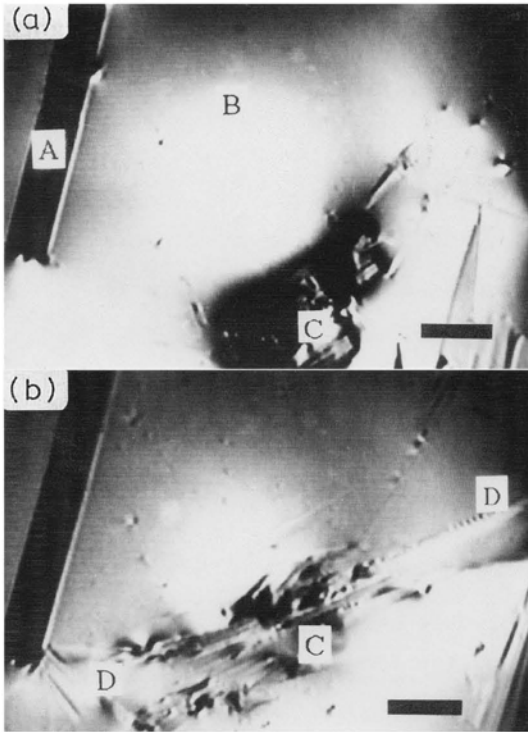


Fig. 14.35. Optical micrographs of the surface of the sample. Scale bars indicate 100 μm . (a) After the temperature of the sample was kept at 870°C for 24 h. A: the needle crystal of (Sr,Ca)CuO₂; B: surface of the liquid; C: crystals of the low T_c phase. (b) 18 h after (a). D: newly grown plate crystals. (Reprinted from [34(b)], with permission of Elsevier Science)

We then annealed them in oxygen flow at 800°C for 24 h to distinguish the high T_c phase from the low T_c phase. The annealing temperature was low enough and no phase change occurred. This sample showed electric resistance drops both at 110 K and 80 K, which clearly revealed the coexistence of the high T_c phase with the low T_c phase. It was assumed that the thin plate crystals grown after the partial melting were the high T_c phase. The size of these plate crystals was so small and thin ($100 \times 100 \times 2 \mu\text{m}^3$) that we could not identify the high T_c phase by normal X-ray diffraction. Then we analyzed this thin crystal by micro-area X-ray diffraction to identify a small area on the surface of the sample. The size of the incident beam was 50 μm in diameter, and it struck the crystal surface at a low glancing angle. This crystal was grown after the partial melting. (See point c in Fig. 14.36, which is a micrograph of the surface of the sample.) The surface of this area was highly oriented and parallel to the c -planes of Bi-based oxide superconductors. The (001) X-ray profile obtained is shown in Fig. 14.37. Peaks attributed to the high T_c phase ($c_0 = 3.7 \text{ nm}$) were found together with those of the other two superconducting phases.

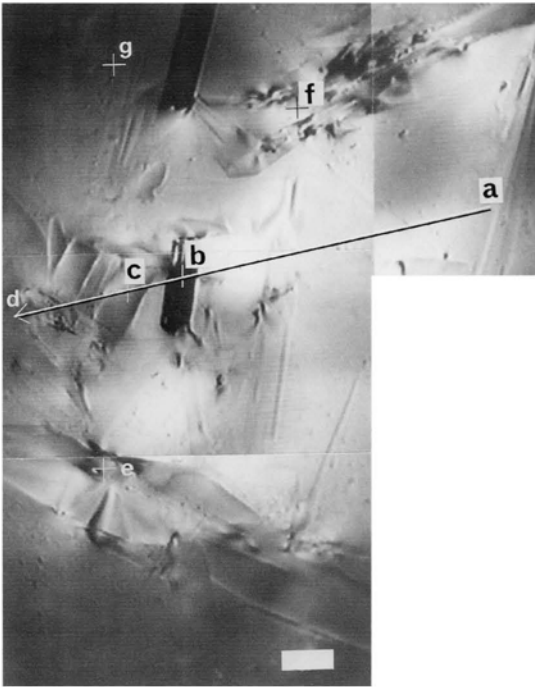


Fig. 14.36. Micrograph of the surface of the sample. The temperature of the sample was 870°C and had been kept constant for 18 h. The scale bar indicates $100\ \mu\text{m}$. This sample was quenched 32 h later. After quenching, micro-area X-ray analysis was done at the point c (see Fig. 14.37). The concentration distribution of the cations measured along the line abcd are shown in Fig. 14.38. The ratios of cations measured at points c, e, f, and g are listed in Table 14.2. (Reprinted from [34(b)], with permission of Elsevier Science)

Thus, the existence of the high T_c phase was proved. EDX measurements with an acceleration voltage of 15 kV were also done to analyze the chemical composition of the sample. Distributions of concentrations of Bi, Sr, Ca, and Cu cations along line a-d in Fig. 14.36 are shown in Fig. 14.38. The sharp change at point b is attributed to the presence of the needle crystal of $(\text{Sr,Ca})\text{CuO}_2$. Bi concentrations varied with position and showed negative correlation with those of Ca and Cu. The concentrations of Ca and Cu at point c, where the high T_c phase was detected by the X-ray measurement, were larger than those in nearby regions. The ratios of cations at the points c, e, f, and g in Fig. 14.36 are listed in Table 14.2. In Fig. 14.36, there exist other thin plate crystals grown after partial melting at point e, and the low T_c phase crystals at point f. The liquid surface is revealed at point g. The ratio of cations at point c showed that this area was composed mainly of the low T_c phase although we found the high T_c phase by X-ray diffraction. Components of Sr, Ca, and Cu at points c and e, where thin crystals have been observed

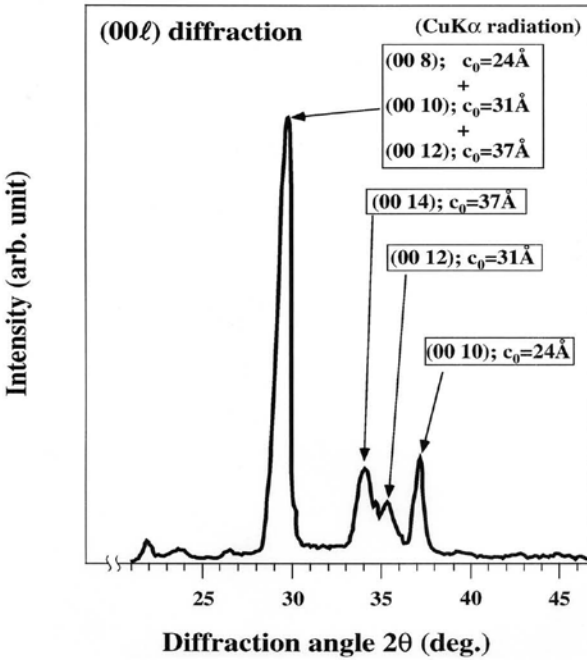


Fig. 14.37. X-ray profile at the point c in Fig. 14.36 obtained by micro-area X-ray diffraction. The size of the incident beam was 50 μm in diameter. (Reprinted from [34(b)], with permission of Elsevier Science)

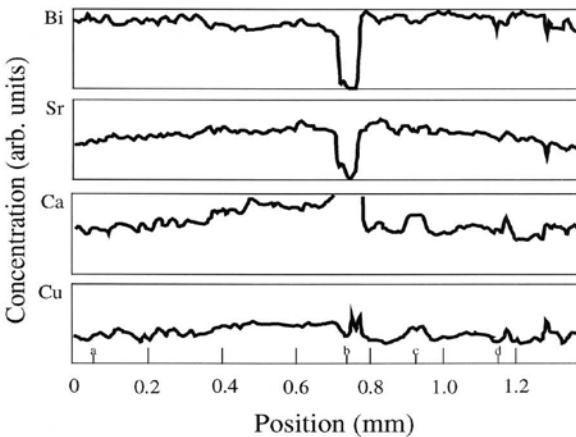


Fig. 14.38. Distributions of concentrations of Bi, Sr, Ca, and Cu cations along the line a-d in Fig. 36. EDX was used to obtain this result. A large variation at point b was attributed to the needle crystal of $(\text{Sr,Ca})\text{CuO}_2$. The high T_c phase was detected at point c by micro-area X-ray diffraction. (Reprinted from [34(b)], with permission of Elsevier Science)

Table 14.2. Cation ratios obtained by EDX. They are normalized for bismuth content equal to 2.0. Points c, e, f, and g are indicated in Fig. 14.36

Points	Bi	Sr	Ca	Cu
c	2.00	1.21	1.37	2.03
e	2.00	1.10	1.67	2.34
f	2.00	0.97	1.01	1.73
g	2.00	0.72	0.71	0.91

to grow, were larger than those at points f and g. The high T_c phase crystals were so thin that the EDX measured contributions from both the high T_c phase and the material beneath it (presumably, the low T_c phase).

We then heated the sample in Fig. 14.35 at a rate of 2°C/h. The high T_c phase crystals completely melted at 875°C. Up to this temperature, crystals of the low T_c phase had already melted, and only needle crystals of (Sr,Ca)CuO₂ and the liquid existed. This result showed that the high T_c phase and the liquid would coexist in the temperature range from 865°C to 875°C. Reprinted from [34(b)], with permission of Elsevier Science.

14.4.4 Primary crystallization field of Bi-based oxide superconductors and its application

The composition in the phase diagram mentioned above represents the one along a line in a tetrahedron whose apices are BiO_{1.5}, SrO, CaO, and CuO. In this tetrahedron, the composition in which primarily the superconductor phases grow (primary crystallization field) should be in regions having certain volumes. It would take, however, a long time to make many pseudo-binary phase diagrams to find the coexisting regions of the destiny phase and the liquid in this 4-dimensional space. In such a case, *in situ* high temperature optical microscopy is a powerful tool to find these regions. Here we introduce how to determine the primary crystallization field (PCF) by *in situ* observations of dissolution and crystallization over a wide composition range. The PCF consists of a part of the phase diagram and corresponds to the liquidus line in the binary phase diagram.

The procedure used here is similar to that for the Sm123 system mentioned above. The sample was heated up just before it changed to a uniform liquid. The remaining crystals were regarded as the primary crystal of that solution. The temperature that crystals of the superconductor phase completely dissolved was measured against the sample composition. Thus, the PCF was determined. In Fig. 14.39, the PCF was illustrated in the case of 10 mol% composition of Ca. Open circles indicate the composition belonging to the PCF of the superconductor phase. The dissolution temperatures are also labeled. Filled circles indicate that

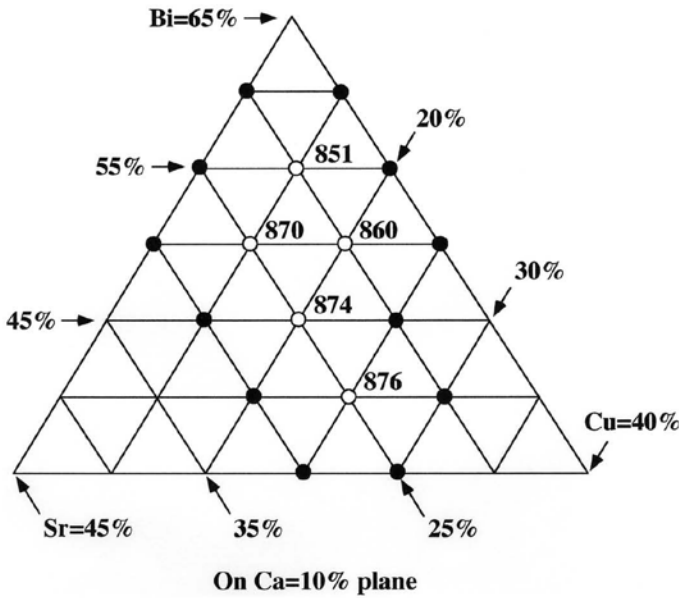


Fig. 14.39. The PCF of the Bi-based oxide superconductors [51]. These crystals had a 10 mol% composition of Ca and were grown in air. Open circles indicate the composition belonging to PCF. The dissolution temperatures were written together. Filled circles indicate other phases remained.

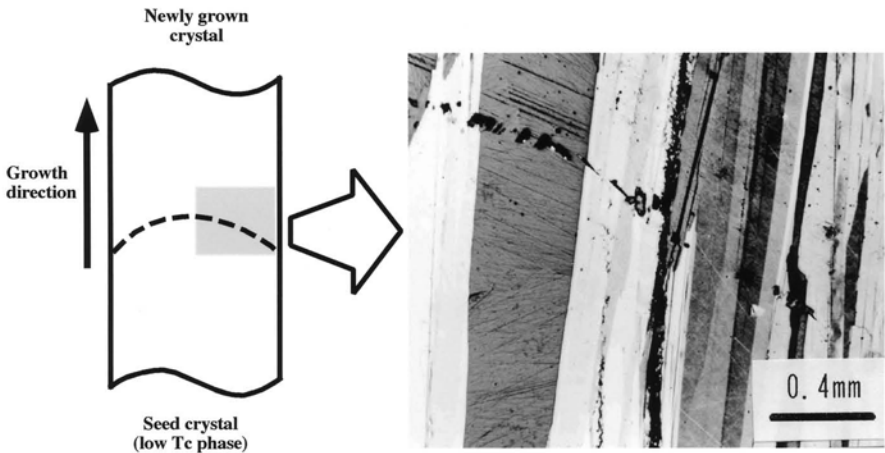


Fig. 14.40. Optical micrograph of the section along the growth direction of the rod grown by the TSFZ method with the seed [51]. New crystals continued to grow from the seed crystals.

other phases remained. Similar results were obtained with 15 mol% of Ca composition. These results suggest that the composition belonging to the PCF of the superconductor phases lay in a long and narrow composition region where the composition of Sr + Ca is between 30 mol% and 35 mol%.

We applied the obtained PCF composition to the traveling-solvent floating-zone (TSFZ) method [52]. We prepared a seed crystal rod of $\text{Bi}_2\text{Sr}_2\text{CaCu}_2\text{O}_8$ by the TSFZ method using a sintered rod as a seed. Although this rod was polycrystalline, large single crystalline regions formed. A sintered rod whose composition belonged to the PCF was made and used as the solution part. These rods were used in the TSFZ growth experiments. As a result, newly grown crystals continued to grow from crystals in the seed keeping their crystallographic orientation without crystallizing other phases. Figure 14.40 shows an optical micrograph of a region near the interface of the seed and the newly crystallized crystals. Thus, the composition in the PCF was shown to be a good solution for the TSFZ method.

Acknowledgments

We wish to express our gratitude to Messrs. M. Shimizu, Y. Kato, Y. Yasuhara, M. Nakayama, Dr. T. Nakada, and Dr. G. Sasaki for their help in conducting this work. This work was done at the Institute for Material Research, Tohoku University, Miyagi, Sendai, Japan.

References

1. Bednorz JG, Muller KA (1986) *Z Phys* B64:189
2. Suzuki Y, Inoue T, Hayashi S, Komatsu H (1989) *Jpn J Appl Phys* 28:L1382
3. Suzuki Y, Inoue T, Hayashi S, Komatsu H (1990) *Jpn J Appl Phys* 29:L1089
4. Inoue T, Hayashi S, Miyashita S, Shimizu M, Nishimura Y, Komatsu H (1992) *J Crystal Growth* 123:615
5. Endo U, Koyama S, Kawai T (1988) *Jpn J Appl Phys* 27:L1476
6. Maeda H, Tanaka Y, Fukutomi M, Asano T (1988) *Jpn J Appl Phys* 27:L209
7. Hidaka Y, Oda M, Suzuki M, Maeda Y, Enomoto Y, Murakami T (1988) *Jpn J Appl Phys* 27:L538
8. Balestrino G, Gambardella U, Liu YL, Marinelli M, Paoletti A, Paroli P, Paterno G (1988) *J Crystal Growth* 92:674
9. Cizek TF, Goral JP, Evans CD, Katayama-Yoshida H (1988) *J Crystal Growth* 91:312
10. Gazit D, Feigelson RS (1988) *J Crystal Growth* 91:318
11. Kawai T (1989) *Solid State Physics (Kotai Butsuri)* 24:102 (in Japanese)
12. Takekawa S, Nozaki H, Umezono A, Kosuda K, Kobayashi M (1988) *J Crystal Growth* 92:687
13. Shishido T, Shindo D, Ukei K, Sasaki T, Toyota N, Fukuda T (1989) *Jpn J Appl Phys* 28:L791
14. Kijima N, Endo H, Tsuchiya J, Sumiyama A, Mizuno M, Oguri Y (1988) *Jpn J Appl Phys* 27:L1852

15. Hatano T, Aota K, Ikeda S, Nakamura K, Ogawa K (1988) *Jpn J Appl Phys* 27:L2055
16. Kim CJ, Rhee CK, Lee HG, Lee CT, Kang SJ-L, Won DY (1989) *Jpn J Appl Phys* 28:L45
17. Ono A, Kosuda K, Sueno S, Ishizawa Y (1988) *Jpn J Appl Phys* 27:L1007
18. Strobel P, Korczak W, Hodeau JL, Tholence JL (1989) *Physica C* 161:155
19. Tarascon JM, Hull GW, Giround M, Hwang DH (1988) *Phys Rev B* 37:9382
20. Kishio K, Hasegawa T, Kitazawa K (1990) *Oyo Buturi* 59:554 (in Japanese)
21. Suzuki Y, Inoue T, Hayashi S, Komatsu H (1990) *Jpn J Appl Phys* 29:L1089
22. Matsubara I, Tanigawa H, Ogura T, Yamashita H, Kinoshita M, Kawai T (1990) *Appl Phys Lett* 57:2490
23. Scheel HJ (1994) *Advances in Superconductivity VI*, 6th Int Symp on Superconductivity (Hiroshima, October 1993), Fujita T, Shiohara Y (eds) Springer, Tokyo, p 29
24. Scheel HJ, Klemenz C, Reinhar F-K (1994) *Appl Phys Lett* 65:901
25. Belt RF, Ings J, Diercks G (1990) *Appl Phys Lett* 56:1805
26. Balestrino G, Marneni M, Malani E, Paoletti A, Paroli P (1990) *J Appl Phys* 68:361
27. Balestrino G, Marinelli M, Paoletti A, Paroli P (1991) *J Appl Phys* 70:6939
28. Takemoto J, Inoue T, Komatsu H, Hayashi S, Miyashita S, Shimizu M (1993) *Jpn J Appl Phys* 32:L403
29. Takemoto J, Miyashita S, Inoue T, Komatsu H (1996) *J Crystal Growth* 163:100
30. Katsui A (1988) *Jpn J Appl Phys* 27:L844
31. Schneemeyer LF, van Dover RB, Glarum SH, Sunshine SA, Fleming RM, Batlogg B, Siegrist T, Marshall JH, Waszczak JV, Rupp LW (1988) *Nature* 332:422
32. Guien Z, Huang SL, Yunbo J, Jiang L, Genda G, Weili C, Yaozhong R, Yuheng Z (1993) *Jpn J Appl Phys* 32:774
33. Matsui Y, Maeda H, Tanaka Y, Takayama-Muromachi E, Takekawa S, Horiuchi S (1988) *Jpn J Appl Phys* 27:L827
34. (a) Komatsu H, Kato Y, Miyashita S, Inoue T, Hayashi S (1991) *Physica C* 190:14
(b) Miyashita S, Kato Y, Komatsu H, Inoue T, Hayashi S, Horiuchi H, Sueno S (1993) *Physica C* 213:283
(c) Nishimura Y, Yasuhara Y, Miyashita S, Komatsu H (1996) *J Crystal Growth* 158:255; Phase diagram of the Nd₁₂₃-Ba₃Cu₁₀₀13 system with use of similar *in situ* observation was reported by other group: Aswal DK, Shinmura M, Hayakawa Y, Kumagawa M (1998) *J Crystal Growth* 193:61
35. Whittler JD, Roth RS (eds) *Phase Diagrams for High-T_c Superconductors*. The American Ceramic Society, Westerville, OH, 1991; Krauns C, Sumida M, Tagami M, Yamada Y, Shiohara Y (1994) *Z Phys B* 96:207; Nakamura M, Kambara M, Umeda T, Shiohara Y (1996) *Physica C* 266:178
36. Czerwonka J, Eick HA (1991) *J Solid State Chem* 90:69
37. Y. Nishimura Y (1996) PhD dissertation, Tohoku University
38. Zhang W, Osamura K, Ochiai S (1990) *J Am Ceram Soc* 74:1958
39. Shigematsu K, Higashi I, Hoshino K, Takahara T, Aono M (1989) *Jpn J Appl Phys* 28:L1442
40. Asaoka H, Takei H, Iye Y, Tamura M, Kinoshita M, Takeya H (1993) *Jpn J Appl Phys* 32:1091; Asaoka H, Takei H, Noda K (1994) *Jpn J Appl Phys* 33:L923
41. Nishimura Y, Miyashita S, Durbin SD, Nakada T, Sazaki G, Komatsu H (1999) *J Crystal Growth* 205:503
42. Nishimura Y, Miyashita S, Komatsu H (1995) *J Jpn Assoc Crystal Growth* 22:228 (in Japanese)

43. Nakayama M, Nishimura Y, Miyashita S, Nakada T, Sazaki G, Komatsu H (1995) *J Jpn Assoc Crystal Growth* 23:275 (in Japanese)
44. Nishimura Y, Miyashita S, Durbin SD, Nakada T, Sazaki G, Komatsu H (1999) *J Crystal Growth* 205:503
45. Michel C, Herieu H, Bolel MM, Grandin A, Deslandes F, Provost J, Raveau B (1987) *Z Phys B* 68:421; Maeda H, Tanaka Y, Fukutomi M, Asano T (1988) *Jpn J Appl Phys* 27:L209
46. Shigematsu K, Takei H, Higashi I, Hoshino K, Takahara H, Aono M (1990) *J Crystal Growth* 100:661
47. Suzuki Y, Inoue T, Hayashi S, Komatsu H (1990) *Jpn J Appl Phys* 29:L1089; Majewski P, Freilinger B, Hettich B, Popp T, Schulze K (1990) *Proc KMC (i.e. 1990) Conf on High-temperature Superconductors Material Aspects. Garmish-Partenkirchen*
48. Shigematsu K, Higashi I, Hoshino K, Takahara T, Aono M (1989) *Jpn J Appl Phys* 28:L1442
49. Tang IM, Eaiprasertsak K, Chitree R, Winotai P (1990) *Physica C* 167:491; Sarkar AK, Maartense I (1990) *Physica C* 168:591; Almond DP, Chapman B, Aaunders GA (1988) *Supercond Sci Technol* 1:153
50. Morgan PE, Housley RM, Porter JR, Ratto JJ (1991) *Physica C* 176:279
51. Takemoto J (1996) PhD dissertation, Tohoku University

15 Growth of Zinc Chalcogenides

Robert Triboulet

Centre National de la Recherche Scientifique (CNRS), Laboratoire de Physique des Solides et de Cristallogenese, 1 Place Aristide Briand, 92195 Meudon Cedex, France

15.1 Introduction

The fairly high ionic character of the II-VI chemical bond governs not only most of the physical properties of these semiconductors but also their crystal growth. Generally, the higher the ionicity, the lower the thermal conductivity will be. The thermal conductivity of II-VIs is then generally lower than that of more covalent compounds, making it difficult to control the growth interface in both melt and vapor growth. The characteristics of the highly ionic chemical bond also cause II-VI melts to remain highly associated at temperatures close to the melting point, leading to the presence of highly organized particles which influence the nucleation process and growth kinetics. Because of a stronger interaction between unlike particles arising from the considerable ionic contribution to the bond energy, the II-VI liquidus curve of the phase diagram shows a hyperbolic shape near the congruent melting point.

It has been shown that the higher the ionicity of the bond, the smaller will be the energy of formation of vacancies, which are the major defects in II-VIs. This accounts for the large II-VI nonstoichiometry, which is an additional complicating factor for their crystal growth.

The higher the ionicity, the smaller will be the energy of creation of dislocations and of stacking faults. This makes the highly ionic II-VI crystal lattice very sensitive to any strain and easily defective. Similarly, the higher the ionicity, the higher is the tendency to form hexagonal structure. As a result, the cubic II-VIs suffer from extensive twinning. Because of their high ionicity, ZnSe and ZnS show a phase transition in the solid state, from the hexagonal structure at high temperature to the zincblende one at lower temperature. This tendency to polymorphism is considered at the origin of twinning when cooling the crystals after melt growth: crossing the transition temperature during the cooling process induces a very high density of twins. All these factors clearly have a major impact on II-VI crystal growth.

Table 15.1. Ionicity λ , melting point M_p , energy gap E_g , enthalpy of formation ΔH_f , thermal conductivity W , hexagonal to cubic transition temperature, lattice parameter of Zn chalcogenides

Material [structure @ RT]	λ	M_p [°C]	E_g @ RT [eV]	ΔH_f @ RT [kJ/mol]	W [Wcm ⁻¹ K ⁻¹]	Hex.-cub. transition temperature	Lattice parameter [nm]
ZnTe (ZB)	0.49	1298	2.26	119	0.18	—	0.61034
ZnSe (ZB)	0.63	1526	2.67	159	0.19	1425	0.56690
ZnS (ZB)	0.77	1718	3.66	201	0.166	1020	0.54094
ZnO (W)	0.8	1880	3.4	350	0.54	—	a = 0.32501 c = 0.52071

RT = Room temperature

Zinc is the smallest atom of the second column of the periodic table of the elements. Among II-VI compounds, zinc chalcogenides thus present stronger bonding, and then higher energy gaps, higher enthalpies of formation, and higher melting points, as displayed in Table 15.1 in which the hexagonal to cubic transformation temperature for both ZnSe [1,2] and ZnS [3] is also given.

15.2 Zn Chalcogenide Growth

Given the difficulties arising from the high ionic character of their chemical bond – low thermal conductivity, associated melts, large nonstoichiometry, tendency to polymorphism – and because of their high melting points, Zn chalcogenides have been submitted to a wide variety of growth techniques: melt growth, solution growth using either homo- or hetero-solvent, growth from the vapor phase in open, semi-closed and closed systems by sublimation or by chemical vapor transport, and hydrothermal growth.

15.2.1 ZnTe

The interest in this compound has been recently renewed: ZnTe showed only *p*-type conductivity, impeding fabrication of *p-n* junctions, but low resistivity *n*-type layers have recently been demonstrated [4]. Moreover, intrinsic *p-n* junctions have been very recently realized by a simple thermal diffusion process, making possible strong pure green light emission [5].

Melt growth is generally preferred for the preparation of large volume single crystals. In spite of the ZnTe melting point lying in the temperature range where silica begins to soften, ZnTe melt growth by sealed ingot zone refining in specially treated silica tubes has been shown to be possible [6]. ZnTe can conveniently be grown by the Bridgman technique under pressure, according to two variants. In

the classical technique proposed by Fischer [7], an inert gas pressure reduces the loss of volatile components. This technique is still used today for the industrial growth of large high purity ZnTe ingots. In the sealed tube technique, sometimes called soft ampoule method, a silica ampoule, which is thermoplastic at the compound melting point, serves as a gas-tight liner. The decomposition pressure forces the silica against a tight-fitting graphite enclosure, which counteracts the mechanical forces. This last technique has been used [8] for the growth of In-doped ZnTe crystals. Excellent large diameter (70 mm) ZnTe crystals with average EPD less than $2000/\text{cm}^2$ have also been grown by the vertical gradient freezing method (VGF) from a melt encapsulated by B_2O_3 under 10 atm nitrogen [5]. More recently, 80-mm diameter single crystals (Fig. 15.1), which is the largest diameter reported so far for ZnTe single crystals, have been grown by the same group using the same VGF technique in a high pressure furnace (Fig. 15.2) under B_2O_3 encapsulation [9]. The crystals are reported to present EPDs of $5000\text{--}10,000 \text{ cm}^{-2}$ with rocking-curve FWHMs around 20 arcsec.

ZnTe solution growth, which allows a lower melting temperature, has been reported by the vertical Bridgman technique (VBT) [6,10–13] and by the traveling solvent method (TSM) according to two variants, the traveling heater method (THM) [6,14] and temperature gradient solution zoning (TGSZ) [15], using Te as the solvent. Crystals grown by THM show hole mobilities as high as $8000 \text{ cm}^2/\text{V s}$ at 35 K (Fig. 15.3) attesting to their high purity level as a result of the low growth temperature, in addition to the efficient purification of solution zone refining [6]. Indium has been used as the solvent for the ZnTe growth by VBT [16] and by THM [17]. The possibility of hetero-seeding, using a (0001) sapphire substrate as a hetero-seed material, has been demonstrated for the first time in the ZnTe solution growth in a vertical Bridgman arrangement [12]. Very pure ZnTe crystals, have been obtained by the cold traveling heater method (CTHM), a modification of the classical THM, in which the source material is constituted of a Zn rod surrounded by Te powder (Fig. 15.4) [14]. The high purity of the crystals is attested to by photon spectroscopy experiments [18] and hole mobilities as large as $7180 \text{ cm}^2/\text{V s}$ measured at 81 K, which is among the highest values reported so



Fig. 15.1. 80-mm diameter ZnTe single crystal (from Reference 9)

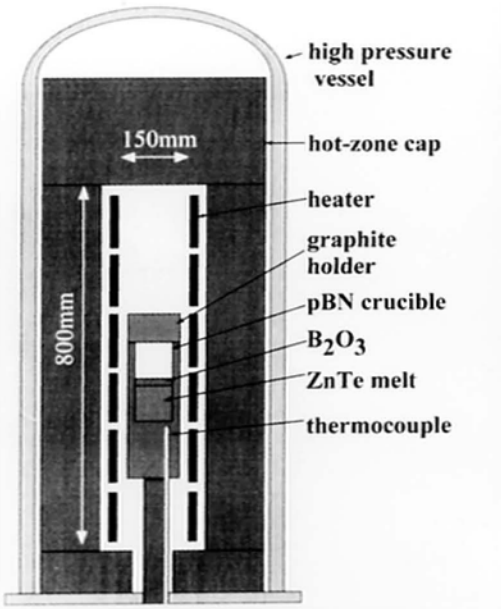


Fig. 15.2. High pressure VGF furnace (from Reference 9)

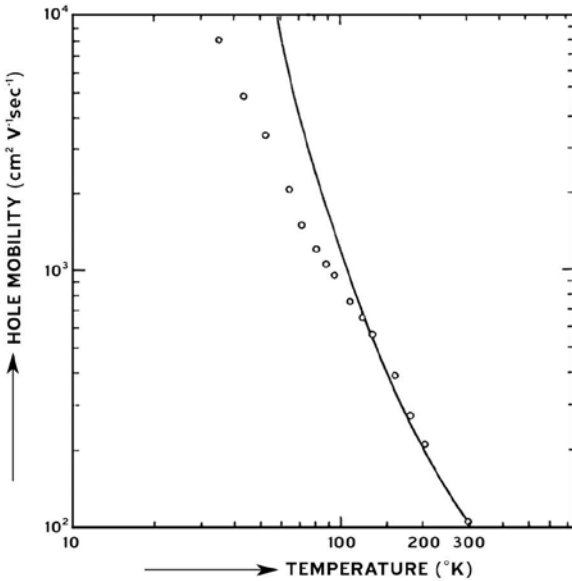


Fig. 15.3. Electron mobility versus temperature for a THM grown ZnTe crystal (from Reference 6)

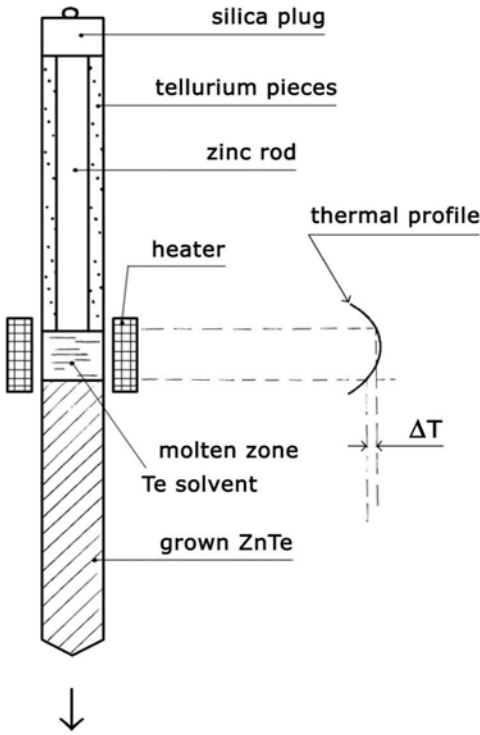


Fig. 15.4. Schematic diagram of “cold THM” principle (from Reference 14)

far. Synthesis, purification, and growth are achieved in the same run, at the moderate temperature of 950°C.

According to the mode of transport used, vapor growth can be subdivided into static and dynamic techniques, or closed tube and open tube methods, respectively. In the closed tube method, the transport of the polycrystalline ZnTe charge occurs either by dissociative sublimation followed by diffusion to lower temperatures or by chemical vapor transport (CVT). In the first method, often called physical vapor transport (PVT), the charge is kept at temperatures ranging from 1050 to 1250°C, with an undercooling ΔT of 10–20°C [19–21]. By CVT, generally carried out with iodine as a chemical agent, the ZnTe charge is kept at 700–800°C, and an undercooling ΔT of 10–20°C is used [22,23]. The Sublimation Traveling Heater Method, with the solvent zone of classical THM replaced by an empty space, has also been used for the growth of ZnTe with the sublimation interface set at 815°C and the crystallization interface temperature at 785–800°C [24]. In order to release the excess volatile component until the total pressure in the ampoule has reached its minimum value, corresponding to congruent sublimation and then maximum growth rate, a new method has been disclosed [25] in which the elements are heated in an ampoule with a pinhole at one end. According to the

same principle, DeMeis and Fischer [26] attached a long capillary to one end of the ampoule, which extended to the room ambient air and acted as a cold trap for the excess vapor.

In the open tube method, the powder is heat-treated at 950–1000°C in a stream of H₂ or of inert gas like Ar, or in a low pressure system, with a difference between saturation temperature and equilibrium growth temperature $\Delta T \sim 10\text{--}30^\circ\text{C}$ [27,28], or in a stream of iodine-hydrogen mixture with the source at 927–1008°C and a substrate temperature of 877°C [29].

Small (0.2 cm³) dark red ZnTe crystals have been obtained under hydrothermal conditions at a temperature of 350°C and a pressure of 150–200 MPa in (OH)⁻ solutions, at a growth rate of 0.3 mm/day [30].

15.2.2 ZnSe

From the announcement in 1991 of the first ZnSe-based blue-green emitting laser diodes, ZnSe bulk growth has been considerably increased for fabricating epitaxial substrates. Like in the case of ZnTe, melt growth, solution growth using either homo- or hetero-solvent, vapor phase growth in open, semi-closed and closed systems by sublimation or by chemical vapor transport, and hydrothermal growth have been used for the growth of ZnSe crystals, as well as solid phase recrystallization.

Since Se is smaller than Te, the main differences between ZnSe and ZnTe lie in the higher melting point and in the ZnSe tendency to polymorphism, due to the higher ionicity of its chemical bond.

A review of the ZnSe melt growth is proposed by Rudolph [31]. After thermodynamic analysis and phase equilibria calculations of the Zn-Se system [(32), the Zn-Se phase diagram, knowledge of which is necessary to achieve melt growth under well-controlled conditions, has been recently reanalyzed [33] and experimentally determined by DTA [34].

In order to grow large crystals at a high growth rate, numerous efforts have been concentrated on the melt growth of ZnSe by the vertical Bridgman technique under inert gas pressure, but this approach has up to now partly failed mainly because of the twinning tendency of ZnSe (Fig. 15.5). The inert gas, either Ar or N₂, counter-pressure, dedicated to retain the volatile species in the melt, ranges usually between 5 to 10 MPa [31,35–42], but can reach up to 20 MPa [43]. With B₂O₃ as the encapsulant, the counter-pressure can be reduced down to 1 MPa using a molybdenum capsule (Fig. 15.6) [2] and down to 0.8 MPa when sealing screwed caps on graphite containers using sealants like B₂O₃ or Ti [31]. The growth rate ranges generally from 30 to 100 mm/day.

By applying the so-called soft ampoule method, either with a tight-fitted silica ampoule [44] or a molybdenum capsule [45,46], the pressure can be lowered down to less than 10⁻⁴ Pa in this last case. A self-sealing technique in which a graphite crucible is sealed by the ZnSe vapors needs an outer pressure of only 0.5–0.7 MPa (Fig. 15.7) [47–49]. Lower pressure has been shown efficient in reducing the



Fig. 15.5. ZnSe crystal grown by high pressure Bridgman method (from Reference 41)

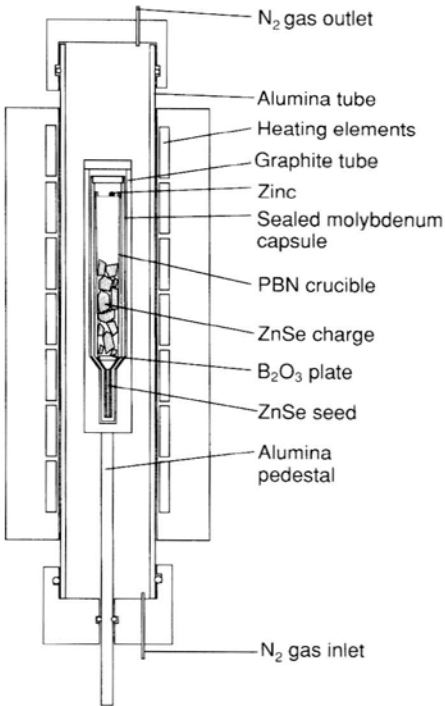


Fig. 15.6. Schematic diagram of the VGF system with the molybdenum Capsule (from Reference 2)

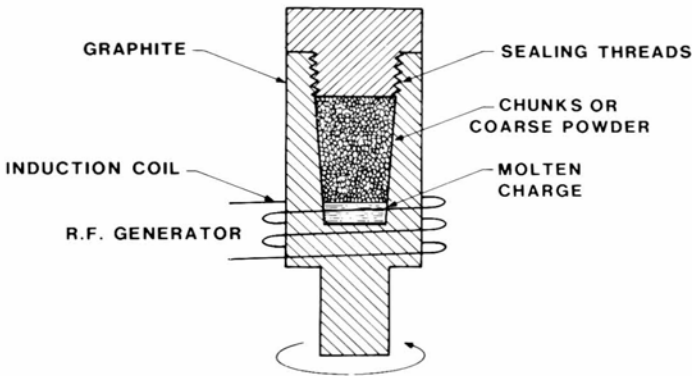


Fig. 15.7. Self-sealing system for the growth of ZnSe crystal (from Reference 48)

density of microvoids in the crystals [39]. The control of the crystal stoichiometry by applying a Zn partial pressure in the high-pressure chamber [50–52] or in the soft ampoule method [46] has also been reported.

The LEC technique, using B_2O_3 as the encapsulant, has been attempted in order to obtain ZnSe crystals [46,53]. Although the growth of big cylindrical boules has been reported, no single crystals have been obtained so far by this technique. By the Kyropoulos technique, large cylindrical blocks with large grains have been obtained, but no structural feature of the crystals is given by the authors [54].

One of the major problems in the melt-grown ZnSe crystals is their high tendency toward twinning, essentially because of the presence of a first-order type phase transition from high temperature wurtzite to low-temperature zincblende structures.

The attempts to reduce this twinning tendency by reducing the supersaturation of the wurtzite phase either using a zincblende seed or grain boundaries in the first to freeze region have not fully succeeded [31]. A significant decrease in the twinning tendency has been observed after Mn doping (10^{18} – 10^{20} Mn/cm³), but not in a reproducible way [49]. Adopting a closed double crucible assembly and suitable growth conditions ($G/R \sim 83$ Kh/cm², with a typical gradient of 30 K/cm, a growth rate of 3.6 mm/h, a superheating temperature of 76°C, and a holding time of 6–8 h in the molten state) Wang et al. [55] have very recently demonstrated the growth of twin-free single crystals 12 mm in diameter and 55 mm in length by a seeded vertical Bridgman method (Fig. 15.8).

The difficulties inherent in the volatility of the constituents, in the microvoids constituted by inert gas inclusions, in the phase transitions, in the plastic deformations, and in the contamination from the environment so far have not allowed large melt-grown crystals exploitable for making epitaxy substrates to be obtained.

Vapor growth presents the frequently stressed drawbacks of low growth rate, crystals of limited thickness – because the initial optimal thermal conditions are progressively lost after about 2–3 cm of growth due to the low thermal conductivity of the material – and variable single crystal yield.

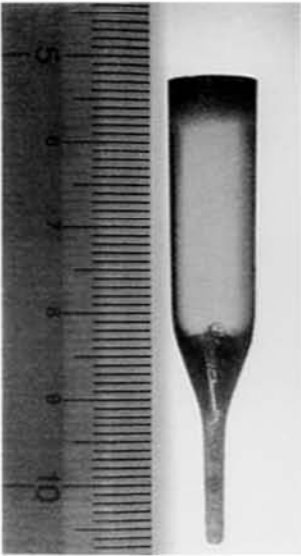


Fig. 15.8. Melt-grown twin-free ZnSe crystal (from Reference 55)

Apart from these drawbacks, crystallization from vapor by physical vapor transport (PVT) or dissociative sublimation presents some advantages over melt growth: 1) the lower processing temperature involved, 2) the purification effect as the result of the differences in the vapor pressures of the native elements and the impurities, and 3) the higher interfacial morphological stability of the solid-vapor interfaces. Sizable crystals of high quality can be obtained by PVT. In the PVT of II-VI compounds, the species found in the vapor phase are group II elements, Zn or Cd, and diatomic molecules of group VI elements, O_2 , S_2 , Se_2 , or Te_2 . The transport rate is controlled by the temperature of the source [56], the partial pressures of the species II and VI_2 in equilibrium with the II-VI compound, which can vary by orders of magnitude as the composition of the compound varies over the homogeneity range, and the enclosed gas nature and pressure [57]. The maximum transport rate occurs under the condition of congruent sublimation [58,59]. The mass fluxes of ZnSe by PVT have been measured in the temperature range 1050–1140°C using an *in situ* dynamic technique and have been found in good agreement with those calculated from a one-dimensional diffusion model [60]. Water has been shown to be an “activator” of ZnSe sublimation [61].

Many PVT closed and semi-open systems have been designed in order to reach the conditions of congruent sublimation. A method, in which a capillary connected to the ampoule is aimed at reaching the stoichiometry of the charge in order to adjust the total pressure to its minimum value corresponding to congruent sublimation, and then maximum growth rate, has been reported [26,62,63]. ZnSe crystals 40–55 mm in diameter have been grown using the Markov-Davydov technique [64] of seeded PVT on (111) seeds [65] and (100) seeds [66] (Fig. 15.9). In

this so-called free-growth method, the polycrystalline source is put in a chamber with perforated walls in the upper part of the ampoule as schematized in Fig. 15.10. A seed is placed below at a definite distance from the chamber on the center of a sapphire or quartz pedestal. The total pressure in the growth ampoule is about 1 atm. H_2 or its mixture with Ar is used as residual atmosphere in sealed ampoules, or He with the cold end of the ampoule connected to a He reservoir for gas refeeding. The presence of a cool end of the ampoule also allows the total pressure to be controlled in order to reach the conditions of congruent sublimation.

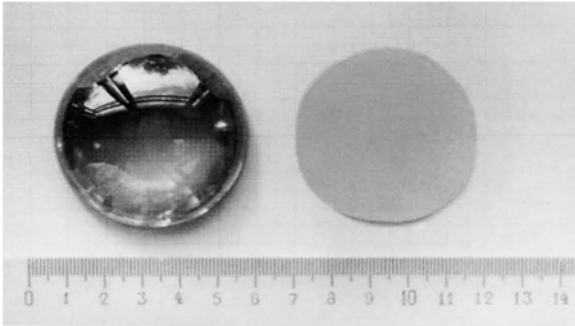


Fig. 15.9. ZnSe single crystal grown by a seeded vapor-phase free method in $\langle 100 \rangle$ direction and (100) substrate cut from such crystal (from Reference 66)

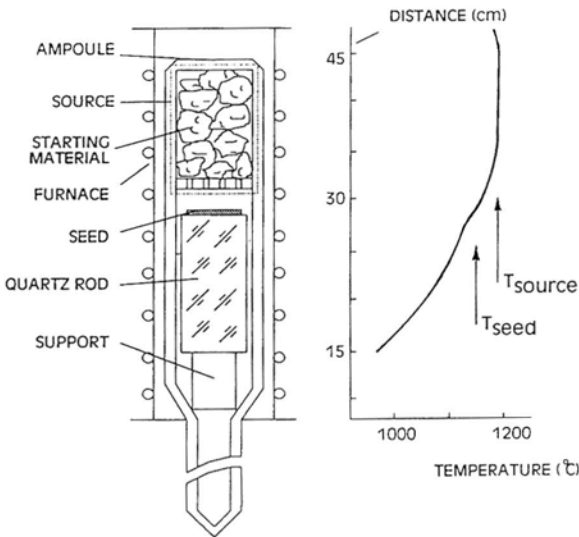


Fig. 15.10. Growth ampoule and temperature profile for the growth of ZnSe crystals by a seeded vapor-phase free growth (from Reference 65)

Another way of controlling the stoichiometry of the charge is the use of a Zn reservoir, either in a horizontal configuration [59,67–69] or in a vertical one [70]. In the classical method of Piper and Polich [71], successfully used for the growth of ZnSe single crystals [72–77], no control of the stoichiometry of the charge is used, but sometimes there is a preliminary treatment of the source [69,78,79]. Either seeding using the (111)B face of ZnSe crystals [80] or the selection of a seed crystal from a needle-shaped cavity in the cold finger attached to the growth end of the ampoule [74] were sometimes used in this simple Piper and Polich configuration. Like in the ZnTe case, ZnSe single crystals with rocking-curve full width half maximum (FWHM) as low as 20 arcsec have been grown by sublimation THM [80–82], at source temperatures ranging from 900 to $\sim 1155^\circ\text{C}$, ΔT of $\sim 5\text{--}35^\circ\text{C}$, and pulling rates ranging from 0.04 to 0.26 mm/h depending on the growth temperature. Using some kind of semi-open system, in which the source is loaded in an ampoule, including a vent hole of 1–2 mm diameter, which is then placed in an outer quartz tube sealed off at one end and connected to a vacuum pump and an Ar supply connected in parallel, as described by Boone et al. [83] for CdTe (Fig. 15.11), excellent ZnSe substrates are industrially produced by Eagle Picher using seeded PVT: 2-in. diameter twin-free ZnSe crystals with lengths up to 25 mm and weighing up to 190 g are obtained under a residual Ar pressure adjusted to a value allowing congruent sublimation [84].

Introduction of Ar gas in a semi-closed horizontal ampoule has been shown to make the leakage of the excess component from the growth zone controllable [85,86]. The growth rate was then determined by the diffusion of component gases Zn and Se₂ in Ar with a constant nonstoichiometry. ZnSe single crystals weighing 25 g have been grown without seeding by a dynamic open system vapor growth technique, in which the flow of saturated vapor species is constricted [87].

Chemical vapor transport (CVT) using iodine as the chemical agent has been widely used, since it allows crystal growth far below melt and transition temperatures even more than PVT. While the crystals grown by CVT are of excellent crystalline quality, they are indeed generally of rather small size (Fig. 15.12). CVT is still used today for the growth of twin-free conductive ZnSe crystals in horizontal [22,88–91] or vertical [92–95] configuration. Growth conditions for preparing large single crystals are given by Fujita et al. [95]. Numerical studies have been carried out to evaluate the influence of typical growth parameters on heat and mass transport. The growth of crystals of good perfection requires the following conditions: a sufficiently high growth temperature ($T_g > 750^\circ\text{C}$) to restrict condensation and source evaporation limitations; $\Delta T < 100\text{ K}$ between source and crystal; $dT/dx < 10\text{ K/cm}$ at the growth interface; a transport regime with the Rayleigh number up to 4000 with the aspect ratio of the ampoule ranging between 9 and 15 [96]; and share of convective transport lower than 20–30% [97]. NH₄Cl has been used as a transport agent as well [98].

Solution growth of ZnSe crystals has been investigated in order to use normal silica tubes. The use of such solvents as Sn and Bi [99], Ga and In [100], Te [101], In-Zn alloys [102], PbCl₂ [92,103], ZnCl₂ [104], PbSe [103], As₂Se₃ and Sb₂Se₃ [105], Se [103,106,107], Se/Te mixed solution [108,109], and SnSe [110] have

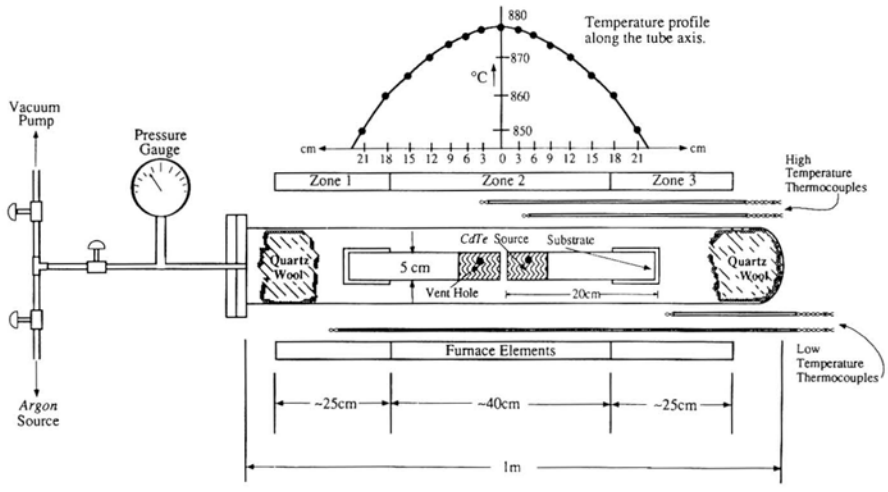


Fig. 15.11. SPVT system used by Eagle Picher for the growth of CdTe and ZnSe (from Reference 83)



Fig. 15.12. ZnSe crystal grown by chemical vapor transport with iodine as chemical agent (from Reference 92) (scale in mm)

been reported. In most cases, a vertical Bridgman configuration is used. Crystals with a minimum deviation from stoichiometry and then improved properties have been grown from a pre-annealed source crystal with an optimum vapor pressure of Zn in Se/Te solvent and of Se in Zn solvent [111]. The liquid encapsulated flux growth has been achieved using Se as the solvent with the evaporation suppressed using a liquid encapsulant and an Ar overpressure [103,106]. By the technique of temperature difference method under controlled vapor pressure (TDMCVP) [107], ZnSe crystals were grown at 1050°C from Se solvent under Zn pressure, and

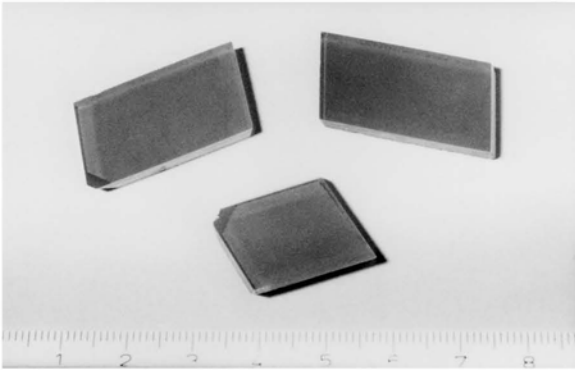


Fig. 15.13. (100) ZnSe substrates grown by solid-state recrystallization (from Reference 114)

p-type crystals were obtained when adding lithium to the solution. THM has been used with PbCl_2 [92,103], PbSe [103], and SnSe [110] as the solvents. Compared to the growth from PbCl_2 solution, a drastically reduced density of inclusions was found in crystals grown with SnSe as the solvent.

Solid-state recrystallization (SSR), long used in the past for the growth of HgCdTe , has been extended to ZnSe [112,113]. Crystals of high crystallographic quality, with rocking curve FWHM ~ 14 arcsec and a dislocation density $\leq 10^2 \text{ cm}^{-2}$ have been grown by long annealing at 1100°C under high Se partial pressure (Fig. 15.13) [114], while low resistive *n*-type samples have been obtained by Al-diffusion from Al-doped molten zinc, with carrier concentrations reaching $5 \times 10^{17} \text{ cm}^{-3}$ [115]. Twinning remains the main concern of this technique.

Good quality ZnSe seeded growth has been achieved under hydrothermal conditions from $(\text{OH})^-$ solutions in the presence and in the absence of Li^+ [116].

15.2.3 ZnS

Because of its highly ionic chemical bond, ZnS is known to crystallize in a large variety of crystallographically different structures (more than 80!), called polytypes, which are observed in natural as well as synthetic crystals grown from the vapor phase at temperatures above 1100°C . The growth of ZnS crystals has stimulated less effort than the growth of ZnSe.

Like for ZnSe, growth from the melt under high pressure by the Bridgman and Tamman (gradient freeze) techniques has been widely developed [117–120].

Growth from the vapor phase, either by PVT, with the charge at a temperature of $1200\text{--}1350^\circ\text{C}$ and an undercooling of $10\text{--}20^\circ\text{C}$ [19,22,65,121–129], or by the flow method in open tubes [130–132], or by chemical vapor transport, with either iodine (charge at $850\text{--}1000^\circ\text{C}$ and ΔT of $7\text{--}20^\circ\text{C}$) [22,95], HCl [133,134], or NH_4Cl [98] as chemical agents, has been widely used.

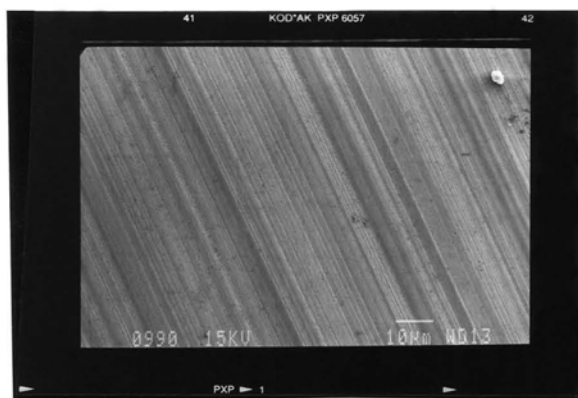


Fig. 15.14. Micro-twins seen on SSR grown ZnS crystals by scanning electron microscopy (from Reference 141)

Solution growth of small ZnS crystals has been reported using KCl [135], ZnF₂ [136], Ga and In [137], or Te [101,138] as the solvents.

Crystals of several grams have been obtained using the hydrothermal method [139].

Tiny ZnS crystals have been even grown by directly interacting the component colloids in silica gels [140].

Large ($\sim 70 \text{ cm}^3$) but highly twinned ZnS crystals (Fig. 15.14) of cubic structure have been obtained very recently by solid phase recrystallization (SPR) at 1100°C under sulfur pressure [141]. Cubic ZnS crystals with monocrystal area of $20 \times 20 \text{ mm}^2$ and thickness of 2 mm have been obtained by SPR as well during hot pressing in the phase transition region [142]. Hot pressing was conducted in vacuum in the temperature range 900–1150°C and at pressures of 200 MPa from several minutes to several hours of In-doped ZnS with a grain size of about 1.5 μm . No indications are given by the authors on the crystallographic properties of the crystals and on their actual twinning state.

15.2.4 ZnO

In spite of its very high melting point and its high reactivity with any surrounding material but platinum, cm-sized ZnO crystals with rocking-curve FWHM of ~ 125 arcsec have been grown from the melt using Cermet's melt growth apparatus with water-cooled crucible (Fig. 15.15) [143].

The hydrothermal method has been shown suitable for the growth of large ZnO crystals from (OH)⁻ solutions at temperatures $< 500^\circ\text{C}$ under high pressure (15 to 50 MPa) with a temperature difference $\Delta T \sim 3\text{--}40 \text{ K}$ and a growth rate in the range 0.05–0.3 mm/day [139,144–146]. More recently, high quality ZnO crystals, as

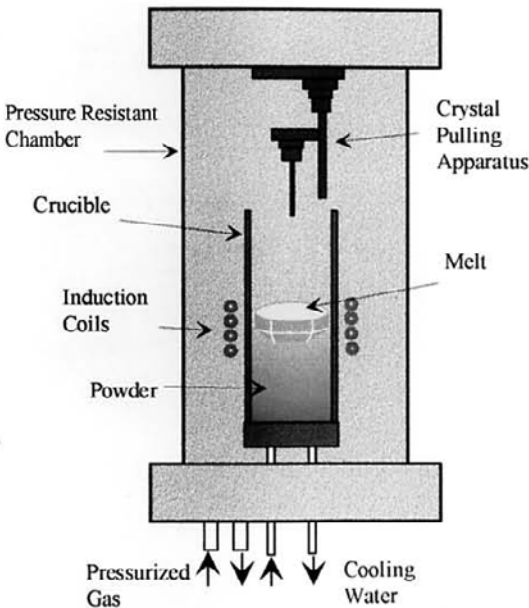


Fig. 15.15. Cermet's melt growth apparatus used for the ZnO growth (from Reference 143)

demonstrated by X-ray rocking curves in the 40 arcsec range and sharp PL peaks, have been grown hydrothermally at 355°C with a ΔT of 10°C from $(\text{OH})^-$ solutions [147].

Large diameter (2-inch diameter) boules have been recently reported to be grown by SPVT in a nearly closed horizontal tube using H_2 as a carrier gas and a small amount of water to maintain the proper stoichiometry [148]. Furthermore, residual water, present in H_2 or Ar, has been shown to act as sublimation activator of the vapor phase transport of ZnO [149]. Cm^3 size single crystals with rocking curve FWHM ~ 28 arcsec have been obtained by chemical vapor transport using C as the transporting agent [150].

Smaller crystals have been obtained by CVT in closed tubes using such chemical transport agents as HCl, Cl_2 , NH_3 , NH_4Cl , HgCl_2 , H_2 , Br_2 , and ZnCl_2 at source temperatures ranging from 800 to 1150°C and ΔT from 20 to 200°C [151–155].

Crystals of small size have been grown as well in open tube systems, either by oxidation of ZnI_2 [156], ZnS , ZnSe [157], ZnBr_2 [158], and Zn [159–161] or by hydrolysis of ZnF_2 [162], ZnCl_2 [163,164], or ZnI_2 [165]. The oxidation or hydrolysis character of the reaction can depend on the temperature range used for a same source. The temperature of the growth region ranges generally in such experiments from 900 to 1350°C.

Such solvents as PbF_2 [166] and $\text{V}_2\text{O}_5/\text{P}_2\text{O}_5$ mixtures [167] have been used for the flux growth of ZnO crystals. Using PbF_2 as the solvent in sealed Pt crucibles, ZnO crystals have been grown by THM [168]. PbCl_2 has been found to be a very

good solvent of ZnO as well, but also shows a great reactivity with any surrounding material but platinum [169]. The same authors have found the Zn-In alloys to be good solvents of ZnO without reactivity with silica.

15.3 Properties and Defects of the Crystals

Sizable high quality crystals have been obtained for both ZnTe and ZnSe. The case of ZnSe, which has been the most studied Zn chalcogenide: very large ingots, up to 100 mm diameter, have been grown from the melt under high inert gas pressure [39] and crystals showing a crystallographic perfection close to the III-V's one have been obtained by SPVT, with an X-ray FWHM of 8.6 arcsec [83] and a dislocation density between 640 and 1300 cm⁻² [170]. Using solid-state recrystallization, a density of dislocations as low as 10² cm⁻² has been reported [171]. Crystalline perfection and size are lower for the other Zn compounds.

The presence of microvoids is reported in the crystals melt-grown under inert gas pressure, likely due to argon gas trapped during the melting process. These voids can completely disappear by reducing the gas pressure [39]. Inclusions and precipitates are frequently reported in the growth from nonstoichiometric melts, and Se or C inclusions are observed as well in the SSR ZnSe crystals [171]. In the ZnTe case, Te precipitates due to the retrograde solidus shape have been shown to act as a source of impurities, which can be released in the crystal by post-growth annealing [172].

As pointed out in the introduction, the highly ionic II-VI crystal lattice is very sensitive to any strain and is easily defective. Dislocations and subgrain boundaries are then frequently observed. Dislocation density generally exceeds 10⁵ cm⁻² in the ZnSe Bridgman crystals and has been shown to depend on the impurity concentration through the effect of solution hardening [38]. ZnSe crystals free from rod-like low angle grain boundaries have been grown from the melt under Ar pressure under a small temperature gradient of 12–22°C/cm [40].

One of the major concerns in the growth of these highly ionic chalcogenides is their high tendency to twinning along the {111} planes. The occurrence of twinning and of both low and high angle grain boundaries appears to be reduced in the ZnSe PVT crystals which have been shown to present rocking curve FWHM as low as 10 arcsec compared with 60–70 arcsec for Bridgman grown material [84].

Zn interstitials and vacancies have been frequently pointed out in Zn chalcogenides. The Zn interstitial in ZnSe was the first isolated native interstitial directly observed in a semiconductor [173]. From theoretical calculation, Laks et al. [174] have concluded that the dominant defect in *p*-type ZnSe is the interstitial Zn_i²⁺. The double charged Zn vacancy has been reported to be the dominant intrinsic defect in ZnSe, the band gap energy position of which should be 0.66 eV above the valence band [175]. Their complexes with residual donors (V_{Zn}²⁻-D⁺) or with interstitials, like (V_{Zn}, Li_i) considered as an acceptor in ZnSe [176], have been frequently reported. Chalcogen vacancies and their complexes with acceptors, acting as deep electron traps, have been pointed out as well in ZnSe and ZnS [177]. Te

antisites acting as donor-like deep states have been considered from theoretical calculations to be prevalent in tellurides [178]. Such deep levels can compensate shallow dopants, resulting in a decrease of conductivity.

15.4 Purity, Contamination and Doping

The crystals grown by the Bridgman method under inert gas pressure are markedly contaminated by residual impurities due to the contact with the crucible over long periods of time at high temperature. There is thus a contamination of the starting charge in the case of the highest melting point compounds like ZnSe and ZnS. Such elements as Na, K, Cu, Al, Si, and Fe are generally found to be the major residual impurities [179]. Depending on the purity of the starting CVD charge, ZnSe crystals of extremely high purity have been obtained by SSR as assessed from photoluminescence measurements [180]. ZnTe crystals of very high purity as shown from two photon spectroscopy experiments [18], have been obtained by solution zone melting using the cold traveling heater method (CTHM) [14].

Zn oxide, sulphide, and selenide are generally *n*-type, and Zn telluride is *p*-type. *P*-type ZnO layers [181] and *n*-type ZnTe layers [4] have been nevertheless obtained using respectively N and Al as the dopants. Very recently, *p*-type ZnO layers showing a carrier concentration in the 10^{19} cm^{-3} range have been obtained by Ga+N co-doping [182], and the surface of ZnTe bulk crystals has been converted to *n*-type by a simple thermal diffusion process [5]. *P*-type ZnSe layers are now commonly grown by MBE and at lower doping level by MOCVD. *P*-type bulk ZnSe crystals have even been obtained using Li as the dopant by controlling the stoichiometry of the crystals either during the growth [183] or during a post-growth annealing process [184].

15.5 Applications and Perspectives

Bulk semiconductor crystals have been long privileged subjects for fundamental studies and applications. Much of the knowledge of the fundamental properties of II-VI semiconductors comes from studies on bulk crystals. Bulk material is now widely replaced by thin layers, even though it keeps some niches, like nuclear detectors or epitaxy substrates, and it is still used for some studies needing sizable samples.

Green emitting diodes have been recently realized on Bridgman grown bulk ZnTe crystals on which *p/n* junctions have been obtained by diffusion of a donor through the vapor phase [5].

In thin film form, ZnSe has been studied since 1991 for its potentialities in blue light emitting devices. Now, not only challenged but also clearly dominated by nitrides and mainly GaN for such blue light emitting devices, ZnSe nevertheless keeps some attractive niches and prospects, even in the domain of light emission.

While some progress can be expected for blue light emitting devices grown from ZnSe homoepitaxial layers, ZnSe-based white LEDs have been demonstrated in which the devices use a phenomenon unique to ZnSe homoepitaxy [185]. A portion of the main greenish-blue emission from the active layer of a p/n junction diode is absorbed by the conductive substrate, which in turn gives an intense broadband yellow emission. Both emission bands combine to give a light, which appears white to the naked eye. Lifetimes of such devices are said to exceed 800 h at room temperature by the authors [185]. This revolutionary new form of high-efficiency lighting opens the way to the fantastic market of compound semiconductor LEDs, which could replace incandescent light bulbs. Another attractive application of bulk ZnSe lies in the realization of tunable mid-infrared sources from alternate ZnSe stack quasi-phase matching overcoming the fact that ZnSe is isotropic, so that no birefringence phase-matching scenarios are available [186]. Such devices will benefit from the high optical nonlinear susceptibility $\chi^{(2)}$ of ZnSe, its high threshold damage power density, its excellent transparency over the 1–15 μm wavelength range, its good mechanical properties, and the possibility of future integration with the pumping source [187].

ZnS is presently used for making alternating-current electroluminescent (ACTFEL) displays. It presents, however, interesting possibilities as well for light emitting and detecting devices, mainly since high conductivity p -type doping has been recently demonstrated [188] which now paves the way to the realization of diodes.

ZnO, due to its unique combination of piezoelectric, conducting, thermal, and optical properties, is used for making piezoelectric transducers, optical wave guides, acoustooptic media, conductive gas sensors (detectors of gas like ammonia), and transparent conductive electrodes for use in efficient solar cells. It could be thought of also as a scintillator. Furthermore, ZnO, with an exciton binding energy (60 meV) well above the thermal energy at room temperature, has been shown to display excitonic stimulated emission up to 550 K, the highest temperature ever reported for any semiconductor [189]. This is a significant indicator for possible stimulated emission and lasing at room temperature with large gain. ZnO substrates are also in great demand for making homoepitaxial ZnO layers and as heterosubstrates of GaN.

The lack of commercial availability of large good quality Zn chalcogenide substrates at low price still limits their possibilities and use. Progress still needs to be made in the Zn chalcogenide growth area.

References

1. Kulakov MP, Kulakovskii VD, Fadeev AV (1976) Twinning in ZnSe crystals grown from the melt under pressure. *Inorg Mater* 12:1536–1538
2. Okada H, Kawanaka T, Ohmoto S (1997) Melt growth of ZnSe single crystals with B_2O_3 encapsulant: The role of solid-solid phase transformation on macro defect generation in ZnSe crystals. *J Crystal Growth* 172:361–369

3. Allen ET, Crenshaw JL (1912) The sulfides of zinc, cadmium and mercury; their crystalline forms and genetic conditions. *Am J Sci* 34:341–396
4. Ogawa H, Irfan GS, Nakayama H, Nishio M, Yoshida A (1994) Growth of low resistivity *n*-type ZnTe by metalorganic vapor phase epitaxy. *Jap J Appl Phys* 33:L980–L982
5. Sato K, Hanafusa M, Noda A, Arakawa A, Uchida M, Asahi T, Oda O (2000) ZnTe Pure Green Light-Emitting Diodes Fabricated by Thermal Diffusion. *J Crystal Growth* 214/215:1080–1084
6. Triboulet R, Didier G (1975) Growth of ZnTe by stoichiometric and off stoichiometric zone refining. *J Crystal Growth* 28:29–35
7. Fischer AG, Carides JN, Dresner J (1964) Preparation and properties of *n*-type ZnTe. *Solid State Comm* 2:157–159
8. Tubota H (1963) Electrical properties of $A^{II}B^{VI}$ compounds CdSe and ZnTe. *Jpn J Appl Phys* 2:259–265
9. Asahi T, Arakawa A, Sato K (2001) Growth of large-diameter ZnTe single crystals by the vertical gradient freeze method. *J Crystal Growth* 229:74–78
10. Title RS, Mandel G, Morehead FF (1964) Self-compensation-limited conductivity in binary semiconductors. II. *n*-ZnTe. *Phys Rev* 136:A300–A302
11. Crowder BL, Hammer WN (1966) Shallow acceptor states in ZnTe and CdTe. *Phys Rev* 150:541–545
12. Seki Y, Sato K, Oda O (1997) Solution growth of ZnTe single crystals by the vertical Bridgman method using a hetero-seeding technique. *J Crystal Growth* 171:32–38
13. Bhunia S, Bose DN (1998) Microwave synthesis, single crystal growth and characterization of ZnTe. *J Crystal Growth* 186:535–542
14. Triboulet R, Pham Van K, Didier G (1990) “Cold traveling heater method,” a novel technique of synthesis, purification and growth of CdTe and ZnTe. *J Crystal Growth* 101:216–220
15. Steininger J, England RE (1968) Growth of single crystals of ZnTe and $ZnTe_{1-x}Se_x$ by temperature gradient solution zoning. *Trans Met Soc AIME* 242:444–448
16. Höschl P, Moravec P, Prosser V, Sakalas A, Jasinskaite R (1981) Electrical characterization of ZnTe crystals grown from in solvent. *Phys Stat Sol* 66:K41–42
17. Wald FV (1976) Self-compensation in CdTe and ZnTe crystals grown from indium solvents. *Phys Stat Sol (a)* 38:253–259
18. Fröhlich D, Kubacki F, Schlierkamp M, Triboulet R (1992) Two photon spectroscopy of excitons in ZnTe under uniaxial stress. *Europhys Lett* 17:237–242
19. Reynolds DC, Czyzak SJ (1950) single synthetic zinc sulfide crystals. *Phys Rev* 79:543–544
20. Aven M, Segall B (1963) Carrier mobility and shallow impurity states in ZnSe and ZnTe. *Phys Rev* 130:81–91
21. Jordan AS, Derick L (1969) Vapor growth of high resistivity ZnTe. *J Electrochem Soc* 116:1424–1430
22. Hartmann H (1977) Studies of the vapor growth of ZnS, ZnSe and ZnTe single crystals. *J Crystal Growth* 42:144–149
23. Kitamura N, Kakehi M, Wada T (1977) Low temperature vapor growth of zinc telluride. *Jap J Appl Phys* 16:1541–1546
24. Taguchi T, Fujita S, Inuishi Y (1978) Growth of high-purity ZnTe single crystals by the sublimation traveling heater method. *J Crystal Growth* 45:204–213

25. Yamanaka Y, Shiraishi T (1965) A new method for growing ZnTe crystals. *Jpn J Appl Phys* 4:826–827
26. DeMeis WM, Fischer AG (1967) Improved method for growing II-VI crystals from the vapor phase. *Mat Res Bull* 2:465–468
27. Reed TB, Lafleur WF (1972) Dependence of growth temperature on carrier gas velocity in open tube transport. *J Crystal Growth* 17:123–127
28. Iida S (1972) Luminescence due to oxygen and self-activated centers in zinc telluride. *J Phys Soc Jap* 32:142–151
29. Ogawa H, Nishio M (1981) Chemical vapor growth of ZnTe by open tube method. *Jap J Appl Phys* 20:2251–2252
30. Hartmann H, Mach R, Selle B (1982) Wide gap II-VI compounds as electronic materials. In: Kaldis E (ed) *Current topics in materials science*, Vol 9, Chapt 1. North Holland
31. Rudolph P, Umetsu K, Koh HJ, Schäfer N, Fukuda T (1995) The state of the art of ZnSe melt growth and new steps towards twin-free bulk crystals. *Mat Chem Phys* 42:237–241
32. Sharma RC, Chang YA (1988) Thermodynamic analysis and phase equilibria calculations for the Zn-Te, Zn-Se and Zn-S systems. *J Crystal Growth* 88:193–204
33. Brebrick RF, Liu H (1996) Analysis of the Zn-Se System. *J Phase Equilibria* 17:495–501
34. Okada H, Kawanaka T, Ohmoto S (1996) Study of the ZnSe phase diagram by differential thermal analysis. *J Crystal Growth* 165:31–36
35. Obreimov J, Shubnikov L (1924) Ein method zur herstellung ein kristalliger metalle. *Z Phys* 25:31–36
36. Kozielski MJ (1975) Polytype single crystals of $Zn_{1-x}Cd_xS$ and $ZnS_{1-x}Se_x$ solid solutions grown from the melt. *J Crystal Growth* 30:86–92
37. Kikuma I, Furukoshi M (1977) Melt growth of ZnSe crystals under argon pressure. *J Crystal Growth* 41:103–108
38. Kulakov MP, Savtchenko IB, Fadeev AV (1981) Some properties of melt-grown zinc selenide crystals. *J Crystal Growth* 52:609–613
39. Kulakov MP, Fadeev AV (1981) Stoichiometry of zinc selenide crystals obtained from the melt. *Inorg Mater* 17(9):1156–1160
40. Kikuma I, Sekine M, Furukoshi M (1986) Growth of ZnSe crystals free from rod-like low angle grain boundaries from the melt under argon pressure. *J Crystal Growth* 75:609–612
41. Triboulet R (1991) The growth of bulk ZnSe crystals. *Semicond Sci Technol* 6:A18–A23
42. Yoshida H, Fujii T, Kamata A, Nakata Y (1992) Undoped ZnSe crystals growth by the vertical Bridgman method. *J Crystal Growth* 117:75–79
43. Kulakov MP, Kulakovskii VD, Savchenko IB, Fadeev AV (1976) Phase transition in zinc selenide crystals. *Sov Phys-Solid State* 18:526–527
44. Holton WC, Watts RK, Stinedurf RD (1969) Synthesis and melt growth of doped ZnSe crystals. *J Crystal Growth* 6:97–100
45. Omino A, Suzuki T (1992) Bridgman growth of ZnSe crystals with a PBN crucible sealed in a molybdenum capsule. *J Crystal Growth* 117:80–84
46. Fischer AG (1970) Techniques for melt-growth of luminescent semiconductor crystals under pressure. *J Electrochem Soc* 117:41c–47c

47. Debska U, Giritat W, Harrison HR, Yoder-Short DR (1984) RF-heated Bridgman growth of $(\text{ZnSe})_{1-x}(\text{MnSe})_x$ in self-sealing graphite crucibles. *J Crystal Growth* 70:399–402
48. Fitzpatrick BJ, McGee III TF, Harnack PM (1986) Self-sealing and self-resealing technique (SSSR) for the crystal growth of II-VI compounds. *J Crystal Growth* 78:242–248
49. Shone M, Greenberg B, Kaczinski M (1988) Vertical zone growth and characterization of undoped and Na, P and Mn doped ZnSe. *J Crystal Growth* 86:132–137
50. Kikuma I, Kikuchi A, Yageta M, Sekine M, Furukoshi M (1989) Growth of ZnSe crystals from the melt under Zn partial pressure. *J Crystal Growth* 98:302–308
51. Kikuma I, Kikuchi A, Furukoshi M (1990) Effect of Zn partial pressure during growth on electrical properties of ZnSe crystals grown from the melt. *Jpn J Appl Phys* 29:L1963–L1965
52. Kikuma I, Matsuo M, Komuro T (1991) Growth and properties of ZnSe crystals by a modified bridgman method. *Jpn J Appl Phys* 30:2718–2722
53. Hruban A, Dalecki W, Nowysz N, Strzelecka S (1997) ZnSe crystals grown by LEC method. *Inst Phys Conf Ser* 155:339–342
54. Hruban A, Dalecki W, Nowysz N, Strzelecka S, Gladki A (1999) Synthesis and crystallization of ZnSe by the liquid encapsulation technique. *J Crystal Growth* 198/199:282–286
55. Wang JF, Omino A, Isshiki M (2000) Melt growth of twin-free ZnSe single crystals. *J Crystal Growth* 214/215:875–879
56. Fujiwara S, Matsumoto K, Shirakawa T (1996) *In situ* transport rate monitor during ZnSe crystal growth by PVT. *J Crystal Growth* 165:169–171
57. Muranoi T, Shiohara T, Sotokawa A, Yoshida H, Isobe S, Kanbe N (1995) Gas effect on transport rates of ZnSe in closed ampoules. *J Crystal Growth* 146:49–52
58. Faktor MM, Heckingbottom R, Garrett I (1970) Growth of crystals from the gas phase. Part I. Diffusional limitations and interfacial stability in crystal growth by dissociative sublimation. *J Chem Soc A* 2657–2664
59. Kiyosawa T, Igaki K, Ohashi N (1972) Vapor phase crystal growth of zinc selenide under controlled partial pressure and its crystal structure. *Trans Jap Inst Metals* 13:248–254
60. Su C-H, Sha Y-G, Mazuruk K, Lehoczyk SL, Liu H-C, Fang R, Brebrick RF (1996) Mass flux and partial pressures of ZnSe by physical vapor transport. *J Crystal Growth* 166:736–744
61. Mimila J, Triboulet R (1995) Sublimation and chemical vapor transport, a new method for the growth of bulk ZnSe crystals. *Mat Lett* 24:221–224
62. Blanconnier P, Hénoç P (1972) Croissance épitaxiale des composés II-VI en phase vapeur. *J Crystal Growth* 17:218–221
63. Papadopoulos AC, Jean-Louis AM, Charil J (1978) Properties of homogeneously doped ZnSe single crystals obtained by a new growth method. *J Crystal Growth* 44:587–592
64. Markov EV, Davydov AA (1975) Growing oriented single crystals of CdS from the vapor phase. *Neorg Mater* 11:1755–1758
65. Korostelin YuV, Kozlovsky VI, Nasibov AS, Shapkin PV (1996) Vapor growth of II-VI solid solution single crystals. *J Crystal Growth* 159:181–185
66. Korostelin YuV, Kozlovsky VI, Nasibov AS, Shapkin PV, Lee SK, Park SS, Han JY, Lee SH (1998) Seeded vapor-phase free growth of ZnSe single crystals in the $\langle 100 \rangle$ direction. *J Crystal Growth* 184/185:1010–1014

67. Igaki K, Satoh S (1979) The electrical properties of zinc selenide heat-treated in controlled partial pressures of constituent elements. *Jpn J Appl Phys* 18:1965–1971
68. Mochizuki K, Masumoto K, Yasuda T, Segawa Y, Kimoto K (1994) Sublimation growth of high-purity ZnSe single crystals and photoluminescence. *J Crystal Growth* 135:318–322
69. Hartmann H, Siche D (1994) ZnSe single crystal growth by the method of dissociative sublimation. *J Crystal Growth* 138:260–265
70. Cutter JR, Woods J (1979) Growth of single crystals of zinc selenide from the vapor phase. *J Crystal Growth* 47:405–413
71. Piper WW, Polich SJ (1961) Vapor-phase growth of single crystals of II-VI compounds. *J Appl Phys* 32:1278–1279
72. Lauer RB, Williams F (1971) Vapor growth of graded composition crystals of (Zn,Cd)S and (Zn,Cd)Te. *J Crystal Growth* 8:333–336
73. Koyama T, Yodo T, Yamashita K (1989) Crystallographic properties of ZnSe grown by sublimation method. *J Crystal Growth* 94:1–5
74. Cheng H-Y, Anderson EE (1989) The growth of ZnSe single crystals by physical vapor transport. *J Crystal Growth* 96:756–762
75. Chen K-T, George MA, Zhang Y, Burger A, Su C-H, Sha Y-G, Gillies DC, Lehoczyk SL (1995) Selenium precipitation in ZnSe crystals grown by physical vapor transport. *J Crystal Growth* 147:292–296
76. Geissler U, Hartmann H, Krause E, Siche D (1996) Investigation of the transition range in seeded vapor grown ZnSe crystals. *J Crystal Growth* 159:175–180
77. Fujiwara S, Morishita H, Kotani T, Matsumoto K, Shirakawa T (1998) Growth of large ZnSe single crystals by CVT method. *J Crystal Growth* 186:60–66
78. Graszka K, Janik E, Mycielski A, Bak-Misiuk J (1995) The optimal temperature profile in crystal growth from the vapor. *J Crystal Growth* 146:75–79
79. Siche D, Hartmann H, Böttcher K, Krause E (1996) Growth of bulk ZnSe crystals—recent developments. *Phys Stat Sol (B)* 194:101–108
80. Taguchi T, Kusao T, Hiraki A (1985) Growth of high-purity ZnSe by sublimation THM and the characteristics of the Y and Z deep-level emission lines. *J Crystal Growth* 72:46–50
81. Lee H, Kim TS, Jeong TS, An HG, Kim JY, Youn CJ, Yu PY, Hong KJ, Lee HJ, Shin YJ (1998) Growth of zinc selenide single crystal by the modified Piper and Polich sublimation method. *J Crystal Growth* 191:59–64
82. Yakimovich VN, Levchenko VI, Yablonski GP, Konstantinov VI, Postnova LI, Kutas AA (1999) Vapor growth of bulk ZnSe single crystals. *J Crystal Growth* 198/199:975–979
83. Boone JL, Cantwell G, Harsch WC, Thomas JE, Foreman BA (1994) Electrical and crystallographic characterization of CdTe grown by the vapor transport method. *J Crystal Growth* 139:27–36
84. Cantwell G, Harsch WC, Cotal HL, Markey BG, McKeever SWS, Thomas JE (1992) Growth and characterization of substrate-quality ZnSe single crystals using seeded physical vapor transport. *J Appl Phys* 71:2931–2936
85. Fujiwara S, Kotani T, Matsumoto K, Shirakawa T (1996) Crystal growth of ZnSe by PVT using a semi-open ampule. *J Crystal Growth* 169:660–664
86. Yoshino K (1995) Photoluminescence of zinc selenide single crystals grown by the sublimation method. *Jpn J Appl Phys* 34:6331–6333

87. Vohl P (1969) A technique for vapor phase growth of zinc selenide. *Mat Res Bull* 4:689–698
88. Nitsche R, Bölsterli HU, Lichtensteiger M (1961) Crystal growth by chemical transport reactions I. Binary, ternary and mixed-crystal chalcogenides. *J Phys Chem Solids* 21:199–205
89. Simanovskii AA (1969) Production of ZnSe single crystals via a transport reaction. In: *Growth of crystals*, Vol 7. Plenum, New York, pp 224–229
90. Recker K, Schoepe R (1971) Zur züchtung von ZnSe-einkristallen durch chemische transportreaktion. *J Crystal Growth* 9:189–192
91. Parker SG (1971) Single crystals and epitaxial films of ZnSe by chemical transport. *J Crystal Growth* 9:177–182
92. Triboulet R, Rabago F, Legros R, Lozykowski H, Didier G (1982) Low-temperature growth of ZnSe crystals. *J Crystal Growth* 59:172–177
93. Kaldis E (1965) Nucleation and growth of single crystals by chemical transport—II zinc selenide. *J Phys Chem Solids* 26:1701–1705
94. Catano A, Kun ZK (1976) Growth and characterization of ZnSe and homogeneous ZnS_xSe_{1-x} crystals. *J Crystal Growth* 33:324–330
95. Fujita S, Mimoto H, Takebe H, Noguchi T (1979) Growth of cubic ZnS, ZnSe and ZnS_xSe_{1-x} single crystals by iodine transport. *J Crystal Growth* 47:326–334
96. Böttcher K, Hartmann H (1995) Zinc selenide single crystal growth by chemical transport reactions. *J Crystal Growth* 146:53–58
97. Böttcher K, Hartmann H, Röstel R (1996) Influence of convection on zinc selenide crystal growth by chemical vapor transport. *J Crystal Growth* 159:161
98. Matsumoto K, Shimaoka G (1986) Crystal growth of ZnS and ZnSe by chemical transport using NH_4Cl as a transport agent. *J Crystal Growth* 79:723–728
99. Rubenstein M (1968) Solution growth of some II-VI compounds using tin as a solvent. *J Crystal Growth* 3:309–312
100. Wagner P, Lorenz M (1966) Solubility of ZnSe and ZnTe in Ga and In. *J Phys Chem Solids* 27:1749–1752
101. Washiyama M, Sato K, Aoki M (1979) Solution growth of ZnS, ZnSe, CdS and their mixed compounds using tellurium as a solvent. *Jpn J Appl Phys* 18:869–872
102. Kikuma I, Furukoshi M (1980) Solution growth of ZnSe crystals using In-Zn solvents. *J Crystal Growth* 50:654–658
103. Weber A-D, Müller M, Hofmann D, Winnacker A (1998) Growth stability of zinc selenide bulk crystals from solutions. *J Crystal Growth* 184/185: 1048–1052
104. Ido T (1981) Liquid phase epitaxy of ZnSe at low temperature. *J Crystal Growth* 51:304–308
105. Bohac P, Gäumann A (1976) New fluxes for crystal growth of chalcogenides. *J Crystal Growth* 26:171–173
106. Unuma H, Higuchi M, Yamakawa Y, Kodaira K, Okano Y, Hoshikawa K, Fukuda T, Koyama T (1992) Liquid encapsulated flux growth of ZnSe single crystals from Se solvent. *Jpn J Appl Phys* 31:L383–L384
107. Nishizawa J, Itoh K, Okuno Y, Sakurai F (1985) Blue light emission from ZnSe *p-n* junctions. *J Appl Phys* 57:2210–2216
108. Okuno Y, Sano M, Kato H, Maruyama T (1992) Growth and characterization of ZnSe crystals grown from the solution growth method. *Appl Phys Lett* 60:3274–3276
109. Okuno Y, Tamura H, Maruyama T (1993) Crystallographic evaluation of ZnSe crystals by X-ray diffraction. *J Electron Mater* 22:685–688

110. Dohnke I, Mühlberg M, Neumann W (1999) ZnSe single-crystal growth with SnSe as solvent. *J Crystal Growth* 198/199:287–291
111. Okuno Y, Kato H, Sano M (1997) Stoichiometry control of ZnSe crystals. *J Crystal Growth* 171:39–44
112. Terashima K, Kawachi M, Takena M (1990) Growth of ZnSe crystals by non-stoichiometric annealing. *J Crystal Growth* 102:387–392
113. Triboulet R, Ndap J-O, Tromson-Carli A, Lemasson P, Morhain C, Neu G (1996) Growth by solid phase recrystallization and assessment of large ZnSe crystals of high purity and structural perfection. *J Crystal Growth* 159:156–160
114. Fusil S, Lemasson P, Ndap J-O, Rivière A, Neu G, Tournié E, Geoffroy G, Zozime A, Triboulet R (1998) New results on the solid phase recrystallization of ZnSe. *J Crystal Growth* 184/185:1021–1025
115. Lemasson P, Rivière A, Didier G, Tromson-Carli A, Triboulet R (1999) Low resistive ZnSe substrates. *J Crystal Growth* 197: 462-465
116. Kolb ED, Laudise RA (1970) Hydrothermal crystallization of zinc selenide. *J Crystal Growth* 7:199–202
117. Addamiano A, Aven M (1960) Some properties of zinc sulfide crystals grown from the melt. *J Appl Phys* 31:36–39
118. Shionoya S, Kobayashi Y, Koda T (1965) Polarization of the green-copper luminescence in hexagonal ZnS single crystals. *J Phys Soc Jpn* 20:2046–2053
119. Demianiuk M, Zmija J (1979) Macroscopic inclusions and defects in zinc sulfide and zinc selenide single crystals grown from a melt under pressure. *Sov Phys-Crystallogr* 24(4):501–503
120. Bulanyi MF, Klimenko VI, Polezhaev BA (1996) EPR and luminescence of plastically deformed ZnS:Mn crystals. *Inorg Mater* 32:19–21
121. Piper WW (1952) Growth of ZnS single crystals. *J Chem Phys* 20:1343
122. Tomlinson TB (1956) Luminescence in ZnS:Cu,Cl single crystals. *J Electronics* 2:293–300
123. Kröger FA (1956) Some optical and electrical measurements on blue fluorescent ZnS-Cl single crystals. *Physica* 22:637–643
124. Hamilton DR (1958) The synthesis of single crystals of the sulphides of Zn, Cd and Hg and of HgSe by vapor phase methods. *Brit J Appl Phys* 9:103–105
125. Greene LC, Reynolds DC, Czyzak SJ, Baker WM (1958) Method for growing large CdS and ZnS single crystals. *J Chem Phys* 29:1375–1380
126. Samelson H (1961) Vapor phase growth and properties of zinc sulfide single crystals. *J Appl Phys* 32:309–317
127. Toyama M, Sekiwa T (1969) Kinetics of the vapor growth of II-VI compound crystals. II. Zinc Selenide. *Jap J Appl Phys* 8:855–859
128. Kaldis E (1969) Crystal growth and growth rates of CdS by sublimation and chemical transport. *J Crystal Growth* 5:376–390
129. Russell GJ, Woods J (1979) Vapor growth and defect characterization of large single crystals of ZnS and Zn (S,Se). *J Crystal Growth* 47:647–653
130. Krumbiegel J (1954) Investigations on ZnS crystals. *Z Naturforsch* 9a:903–904
131. Kremheller A (1960) Growth and heat treatment of ZnS single crystals. *J Electrochem Soc* 107:422–427
132. Steinberger IT, Alexander E, Brada Y, Kalman ZH, Mardix S (1972) Growth and perfection of ZnS crystals grown from the vapor phase. *J Crystal Growth* 13/14:285–291

133. Samelson H (1962) Growth of cubic ZnS single crystals by a chemical transport process. *J Appl Phys* 33:1779–1783
134. Jona F (1962) Kinetics of vapor solvent growth in the system ZnS:HCl. *J Phys Chem Solids* 23:1719–1728
135. Mita Y (1962) Growth of ZnS single crystals from flux. *J Phys Soc Jpn* 17:784–787
136. Linares RC (1963) Phase equilibrium and crystal growth in the system ZnS-ZnF₂. *Met Soc Conf* 19:329–335
137. Harsy M (1968) Synthesis and growth of ZnS, ZnSe, ZnTe, GaS, Ga₂Se₃ and InS crystals in Ga and In melts. *Mat Res Bull* 3:483–488
138. Sato K, Aoki M (1979) Photoluminescent properties of ZnS grown from tellurium solution. *Jpn J Appl Phys* 18:705–706
139. Laudise RA, Ballman A (1960) Hydrothermal synthesis of zinc oxide and zinc sulfide. *J Phys Chem* 64:688–691
140. Abdulkhadar M, Ittyachan MA (1981) Growth of single crystals of ZnS and PbS from interacting colloids in gels. *J Crystal Growth* 55:398–401
141. Lemasson P, Fusil S, Triboulet R, to be published
142. Lott K, Ana'eva G, Gorokhova E (2000) Solid-phase recrystallization of ZnS ceramics in phase transition region. *J Crystal Growth* 214/215:894–898
143. Agarwal G, Nause JE, Hill DN (1998) A new approach to growth of bulk ZnO crystals for wide bandgap applications. *Mat Res Soc Symp Proc* 512:41–46
144. Kolb ED, Laudise RA (1966) Hydrothermally grown ZnO crystals of low and intermediate resistivity. *J Am Ceram Soc* 49:302–305
145. Laudise RA, Kolb ED, Caporaso AJ (1964) Hydrothermal growth of large sound crystals of zinc oxide. *J Am Ceram Soc* 47:9–12
146. Venger EF, Melnichuk AV, Melnichuk LYu, Pasechnik YuA (1995) Anisotropy of the ZnO single crystal reflectivity in the region of residual rays. *Phys Stat Sol (B)* 188:823–831
147. Suscavage M, Harris M, Bliss D, Yip P, Wang S-Q, Schwall D, Bouthillette L, Bailey J, Callahan M, Look DC, Reynolds DC, Jones RL, Litton CW (1999) High quality hydrothermal ZnO crystals. *MRS Internet J Nitride Semicond Res* 4S1:G3.40
148. Look DC, Reynolds DC, Szelove JR, Jones RL, Litton CW, Cantwell G, Harsch WC (1998) Electrical properties of bulk ZnO. *Solid State Comm* 105:399–401
149. Ntep J-M, Barbé M, Cohen-Solal G, Bailly F, Lussou A, Triboulet R (1998) ZnO growth by chemically assisted sublimation. *J Crystal Growth* 184/185:1026–1030
150. Ntep J-M, Said Hassani S, Lussou A, Tromson-Carli A, Ballutaud D, Didier G, Triboulet R (1999) ZnO growth by chemical vapor transport. *J Crystal Growth* 207:30–34
151. Shiloh M, Gutman J (1971) Growth of ZnO single crystals by chemical vapor transport. *J Crystal Growth* 11:105–109
152. Piekarczyk W, Gazda S, Niemyski T (1972) The growth of zinc oxide crystals by chemical transport method. *J Crystal Growth* 12:272–276
153. Matsumoto K, Konemura K, Shimaoka G (1985) Crystal growth of ZnO by vapor transport in a closed tube using Zn and ZnCl₂ as transport agents. *J Crystal Growth* 71:99–103
154. Matsumoto K, Shimaoka G (1988) Crystal growth of ZnO by chemical transport. *J Crystal Growth* 86:410–414
155. Matsumoto K, Noda K (1990) Crystal growth of ZnO by chemical transport using HgCl₂ as a transport agent. *J Crystal Growth* 102:137–140

156. Hirose M, Kubo I (1969) Growth of ZnO single crystals by oxidation of ZnI₂. *Jpn J Appl Phys* 8:402
157. Park YS, Reynolds DC (1967) Growth of ZnO single crystals. *J Appl Phys* 38:756–760
158. Hirose M, Furuya Y, Kubo I (1970) Growth of ZnO single crystal from ZnBr₂. *Jpn J Appl Phys* 9:726–727
159. Scharowsky E (1953) Optical and electrical properties of ZnO single crystals with excess zinc. *Z Phys* 135:318–330
160. Nielsen KF (1968) Growth of ZnO single crystals by the vapor phase reaction method. *J Crystal Growth* 3/4:141–145
161. Fischer KJ (1976) Vapor phase growth of ZnO crystals in an open tube flow system. *J Crystal Growth* 34:139–144
162. Kubo I (1961) Crystal growth of zinc-oxide by chemical reaction of zinc-fluoride with air. *J Phys Soc Jap* 16:2358–2359
163. Takahasi T, Ebina A, Kamigawa A (1966) Vapor reaction growth of ZnO single crystal. *Jpn J Appl Phys* 5:560–561
164. Weaver EA (1967) Vapor phase growth of ZnO single crystals. *J Crystal Growth* 1:320–322
165. Hirose M, Furuya Y (1970) Growth mechanism of ZnO by oxidation of ZnI₂. *Jpn J Appl Phys* 9:423–424
166. Nielsen KF, Dearborn EF (1960) The growth of large single crystals of zinc oxide. *J Phys Chem* 64:1762–1763
167. Wanklyn BM (1970) The growth of ZnO crystals from phosphate and vanadate fluxes. *J Crystal Growth* 7:107–108
168. Wolf GA, LaBelle Jr HE (1965) Growth of ZnO single crystals by a traveling solvent zone technique. *J Am Ceram Soc* 48(8):441–442
169. Ntep J-M, Dichi E, Legendre B, Didier G, Triboulet R, 2000 *Mater Lett*, to be published
170. Black D, Burdette H, Cantwell G (1995) X-ray diffraction imaging of ZnSe. In: *Proc Symp on Nondestructive Wafer Characterization for Compound Semicond (SOTAPOC XXII)*. Reno, NV, pp 13–22
171. Fusil S, Zozime A, Pénelle R, Grillon F, Le Paven C, Rivière A, Triboulet R (1998) Grain growth of ZnSe recrystallized in the solid phase. *Diffus Defect Data B, Solid State Phenom* 64:311–316
172. Pautrat J-L, Francou JM, Magnea N, Molva E, Saminadayar K (1985) Donors and acceptors in tellurium compounds: The problem of doping and self-compensation. *J Crystal Growth* 72:194–198
173. Rong F, Watkins GD (1987) Optically detected magnetic-resonance observation of the isolated zinc interstitial in irradiated ZnSe. *Phys Rev Lett* 58:1486–1489
174. Laks DB, Van de Walle CG, Neumark GF, Blöchl FE, Pantelides ST (1992) Native defects and self-compensation in ZnSe. *Phys Rev B* 45:10,965–10,978
175. Watkins GD (1990) In: Sumino K (ed) *Defect Control in Semiconductors*. North Holland, Amsterdam, p 933
176. Pohl UV, Kudlek GH, Klimakow A, Hoffmann A (1994) Shallow impurity- and defect-related complexes in undoped ZnSe crystals. *J Crystal Growth* 138:385–390
177. Krasnov AN, Bajcar RC, Hofstra PG (1998) Threshold voltage trends in ZnS: Mn-based alternating current thin-film electroluminescent devices: Role of native defects. *J Crystal Growth* 194:53–60

178. Berding MA, van Schillgaarde M, Paxton AT, Sher A (1990) Defects in ZnTe, CdTe and HgTe: Total energy calculations. *J Vac Sci Technol* 8:1103–1107
179. Rudolph P, Schäfer N, Fukuda T (1995) Crystal growth of ZnSe from the melt. *Mat Sci Engin R* 15:85–133
180. Tournié E, Morhain C, Neu G, Faurie J-P, Triboulet R, Ndap J-O (1996) Photoluminescence study of ZnSe single crystals grown by solid-phase recrystallization. *Appl Phys Lett* 68:1356–1358
181. Minegishi K, Koiwai Y, Kikuchi Y, Yano K, Kasuga M, Shimizu A (1997) Growth of p-type zinc oxide films by chemical vapor deposition. *Jpn J Appl Phys* 36:L1453–L1455
182. Yamamoto Y, Katayama-Yoshida H, Unipolarity of ZnO with a Wide-Band Gap and Its Solution Using Codoping Method, presented in the International Conference on II-VI Compounds. Kyoto, November 1999
183. Nishizawa J, Suzuki R, Okuno Y (1986) p-type conduction in ZnSe grown by temperature difference method under controlled vapor pressure. *J Appl Phys* 59:2256–2258
184. Krasnov AN, Vaksman YuF, Purtov YuN, Serdyuk VV (1992) Attainment of p-type conduction in zinc selenide single crystals. *Sov Phys Semicond* 26:645
185. Katayama K, Matsubara H, Kakanishi F, Nakamura T, Doi H, Saegusa A, Mitsui T, Matsuoka T, Irikura M, Takebe T, Nishine S, Shirakawa T (2000) ZnSe-based white LEDs. *J Crystal Growth* 214/215:1064–1070
186. Haïdar R, Mustelier A, Kupecek P, Triboulet R, Lemasson P, Mennerat G, Tunable mid-infrared (8–12 μm) difference frequency generation in isotropic semiconductors. Submitted to *Appl Phys Lett*
187. Rosencher E (2000) Towards integrated semiconductor optical parametric oscillators. *C R Acad Sci Paris, Série IV* 1(5):615–620
188. Svob L, Thiandoume C, Lussion A, Bouanani M, Marfaing Y, Gorochov O (2000) p-type doping with N and Li acceptors of ZnS grown by metalorganic vapor phase epitaxy. *Appl Phys Lett* 76:1695–1697
189. Bagnall DM, Chen YF, Zhu Z, Yao T, Shen MY, Goto T (1998) High temperature excitonic stimulated emission from ZnO epitaxial layers. *Appl Phys Lett* 73:1038–1041

16 Growth of Hydroxyapatite Crystals

Atsuo Ito and Kazuo Onuma

National Institute of Advanced Industrial Science and Technology, Tissue Engineering Research Center (TERC), Central 4 1-1-1 Higa shi, Tsukuba, Ibaraki 305-8562, Japan

16.1 Introduction

Hydroxyapatite is a calcium orthophosphate containing water with a chemical composition of $\text{Ca}_{10}(\text{PO}_4)_6(\text{OH})_2$. The composition and structure of hydroxyapatite closely resembles that of mineral components of vertebrate hard tissues. Body fluid is supersaturated with respect to hydroxyapatite under normal physiological conditions. Therefore, the growth and dissolution of hydroxyapatite has an important contribution to ossification, calculus formation, and the development of caries. However, the mechanism underlying biological apatite formation is still not sufficiently clear. In addition to the normal calcifications in bone and teeth, some of the pathological calcifications are also regulated by various factors including cells and matrix proteins.

In this chapter, we first briefly review the calcium orthophosphate family to which hydroxyapatite belongs, although detailed reviews on this subject have already been published by a number of authors [1–5]. Some calcium orthophosphates are formed as precursors that have chemical and structural similarities to hydroxyapatite, and others are used as raw materials for calcium phosphate cements and hydroxyapatite single crystals.

An important aspect of hydroxyapatite growth in modern technology is that, in many cases, the nucleation and subsequent growth of hydroxyapatite on the surface of biomaterials implanted in body tissues determine the performance and even lifetime of biomaterials. For biomaterials used in the repair of bone tissue, the formation of hydroxyapatite on the surface is a desirable property, leading to direct bonding between bone and biomaterials. On the other hand, the formation of hydroxyapatite must be avoided for biomaterials used in contact with blood, such as artificial blood vessels and artificial heart valves. Investigations of interfaces between bone and bone-bonding biomaterials have led to the development of a variety of techniques to form a bonelike apatite coating on biomaterial surfaces in aqueous solutions. These techniques have been used to modify the surfaces of metals, ceramics, and polymers to improve biocompatibility and bone-bonding ability. In this chapter we also review the mechanism and kinetics of hydroxyapa-

tite growth in solution, in addition to the aspect of hydroxyapatite growth associated with hardening of calcium phosphate cements, and the fabrication of hydroxyapatite ceramics and single crystals.

16.2 Calcium Orthophosphates

Besides hydroxyapatite, many kinds of calcium orthophosphate salts are listed in Table 16.1. The calcium orthophosphates are conventionally classified according to their Ca/P molar ratio, which varies from 0.5 to 2. These salts are insoluble except for $\text{Ca}(\text{HPO}_4)_2$ and $\text{Ca}(\text{HPO}_4)_2 \cdot \text{H}_2\text{O}$. Hydroxyapatite is the most insoluble salt in neutral and alkaline solutions. Therefore, all of the calcium orthophosphate salts in Table 16.1 can be converted into hydroxyapatite at a pH higher than 5 [6]. Except for tricalcium and tetracalcium phosphates, these salts can be formed in aqueous solutions. However, when a small amount of divalent cation with an ionic radius of 0.07 nm, typically magnesium, is present in solution such as body fluid, whitlockite, that has a structure very similar to β -tricalcium phosphate, is precipitated [7].

Dicalcium phosphate dihydrate (DCPD) with the formula $\text{CaHPO}_4 \cdot 2\text{H}_2\text{O}$ and *dicalcium phosphate anhydrous* (DCPA) with the formula CaHPO_4 are stable phases at a pH lower than 4.5–4.3 at 25°C [6]. Dicalcium phosphate anhydrous is 0.680 times less soluble than dicalcium phosphate dihydrate. Dicalcium phosphate dihydrate gradually dehydrated in water at 60–100°C resulting in the formation of dicalcium phosphate anhydrous.

Table 16.1. Calcium Orthophosphate Family

Ca/P molar ratio	Abbreviation	Log (solubility product) at 25°C
0.50 $\text{Ca}(\text{HPO}_4)_2$	MCPA	—
0.50 $\text{Ca}(\text{HPO}_4)_2 \cdot \text{H}_2\text{O}$	MCPM	—
1.00 $\text{CaHPO}_4 \cdot 2\text{H}_2\text{O}$	DCPD	6.55 [8], 6.66* [9]
1.00 CaHPO_4	DCPA	6.90 [10]
1.33 $\text{Ca}_8\text{H}_2(\text{PO}_4)_6 \cdot 5\text{H}_2\text{O}$	OCF	49.6** [11], 48.4***† [12]
1.50 Amorphous calcium phosphate	ACP	24.8‡ [13], 10.6§, 11.5§ [14]
1.50 $\beta\text{-Ca}_3(\text{PO}_4)_2$	β TCP	28.92 [15]
1.50 $\alpha\text{-Ca}_3(\text{PO}_4)_2$	α TCP	25.5 [16]
1.50 $\alpha^1\text{-Ca}_3(\text{PO}_4)_2$	α^1 TCP	—
1.50–1.67 Calcium-deficient apatite	—	—
1.67 $\text{Ca}_5(\text{PO}_4)_3\text{OH}$	HAP	58.5 [17], 57.5 [18]
2.00 $\text{Ca}_4(\text{PO}_4)_2\text{O}$	TeTCP	38 [19]

* 37.5°C

** pKsp on the basis of $(\text{Ca})^4(\text{H})(\text{PO}_4)^3$

† 23.5°C

‡ pKsp on the basis of $(\text{Ca})^3(\text{PO}_4)^{1.87}(\text{HPO}_4)^{0.2}$

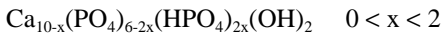
§ pKsp on the basis of $(\text{Ca})(\text{PO}_4)^{0.74}(\text{H})^{0.22}$ at 30–42°C

Octacalcium phosphate (OCP) has the formula $\text{Ca}_8\text{H}_2(\text{PO}_4)_6 \cdot 5\text{H}_2\text{O}$ and often occurs as a transient intermediate in the precipitation of the thermodynamically more stable hydroxyapatite. The crystal structure of octacalcium phosphate consists of two layers parallel to (100), an apatitic layer that corresponds very closely to that of hydroxyapatite and a hydrated layer that contains all the water molecules [20]. Octacalcium phosphate is transformed into calcium-deficient hydroxyapatite by hydrolysis at neutral pH [21].

Tricalcium phosphate (TCP) with the formula $\text{Ca}_3(\text{PO}_4)_2$ has three polymorphs β , α , and super α , with transition temperatures $\beta \rightarrow \alpha$ at 1125°C and $\alpha \rightarrow$ super α at 1430°C [22,23]. The super α phase is unable to survive quenching to room temperature. The crystal structure of the α phase contains an atomic arrangement similar to that of hydroxyapatite [24]. Thus, the hydroxyapatite structure can be derived from that of the α phase. The α phase is transformed by hydrolysis into calcium-deficient hydroxyapatite, octacalcium phosphate, and dicalcium phosphate dihydrate depending on the pH and the temperature [25]. The reactivity toward hydrolysis of the β phase is much lower than that of the α phase.

Amorphous calcium phosphate (ACP) is an amorphous phase with a typical Ca/P molar ratio of 1.50 [26]. Precipitation of calcium orthophosphate from a moderately or highly supersaturated solution at or above neutral pH tends to produce amorphous calcium phosphate as an initial phase. Subsequently, a more stable crystalline phase is formed, such as octacalcium phosphate or hydroxyapatite [27]. The Ca/P molar ratio of amorphous calcium phosphate is reported to be 1.50. However, a detailed study of the composition of amorphous calcium phosphate revealed that the Ca/P molar ratio ranged from 1.18 to 1.50 before washing and 1.50 ± 0.03 after washing. The chemical composition $\text{Ca}_9(\text{HPO}_4)_x(\text{PO}_4)_{6-x}(\text{OH})_x$ is proposed for amorphous calcium phosphate. Chemical compositions of $\text{Ca}_5(\text{HPO}_4)_{0.66}(\text{PO}_4)_{1.56}$ and $\text{Ca}_5(\text{HPO}_4)_{0.2}(\text{PO}_4)_{1.87}$ were reported with defined values of the solubility product [14,28].

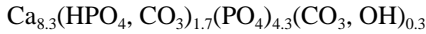
Hydroxyapatite with a Ca/P molar ratio lower than 1.67 is called *calcium-deficient hydroxyapatite*, although stoichiometric hydroxyapatite has a Ca/P ratio of 1.67. Calcium-deficient hydroxyapatite is formed with no difficulty from aqueous reactions between calcium and phosphate ions and/or by conversion from other calcium orthophosphates in water. Several chemical formulas have been proposed for calcium-deficient hydroxyapatite [29]. An example of a proposed formula is [30]:



Any calcium-deficient hydroxyapatite decomposes into hydroxyapatite and tricalcium phosphate at temperatures between 700 and 1200°C .

Bone mineral closely resembles hydroxyapatite in composition and structure. The difference between hydroxyapatite and bone mineral lies in the impurity content and crystallinity. Bone mineral is poorly crystalline apatite and contains sodium (0.5–0.7 wt%), magnesium (0.26–0.55 wt%), water (9.7 wt%), and carbonate (5.8 wt%) as major impurities, and zinc (164–217 ppm), strontium (138–155 ppm), aluminum (60–73 ppm), lead (29–34 ppm), and barium (18–19 ppm) as mi-

nor impurities [31–33]. The metallic ions substitute for calcium sites in the hydroxyapatite structure. Carbonate groups can substitute for both phosphate (so-called Type B substitution) and hydroxyl groups (Type A substitution). Neglecting the metallic impurities, the average composition of bone mineral is indicated by the following chemical formula:



corresponding to calcium-deficient hydroxyapatite with no detectable amount of OH^- ions [34]. The carbonate group substitutes mainly for phosphate groups and minorly for hydroxyl groups in bone mineral. Moreover, bone mineral contains labile carbonate and phosphate and/or hydrogenphosphate groups with a nonapatitic environment [35,36]. These ions may be primarily located on the surface of the crystals.

Tetracalcium phosphate with the formula $\text{Ca}_4(\text{PO}_4)_2\text{O}$ is obtained under anhydrous conditions or under a low water vapor pressure typically at temperatures above 1300°C . Tetracalcium phosphate has a close structural relationship to hydroxyapatite [37].

16.3 *In Vivo* Calcification of Biomaterials

16.3.1 Calcification of biomaterials used in contact with bone

The growth of apatite crystals on the surface of biomaterials determines the characteristics and performance of a number of biomaterials. Because body fluid is highly supersaturated with respect to apatite, with the degree of supersaturation corresponding approximately to 23, apatite deposition may occur on any biomaterial implanted in the body. For biomaterials used in contact with bone, nucleation and growth of apatite on their surfaces are desirable properties, subsequently resulting in the formation of a bond between the bone and the biomaterial. Such a biomaterial is called a bioactive material and is defined as, “a material that elicits a specific biological response at the interface of the material, which results in the formation of a bond between the tissues and the material” [38]. The apatite grown on the surface of a bioactive material is poorly crystallized carbonate-containing hydroxyapatite because body fluid contains a high concentration of carbonate ions. The carbonate groups substitute mainly for phosphate groups in the carbonate-containing hydroxyapatite. The carbonate-containing hydroxyapatite promotes the differentiation of marrow stromal stem cells into osteoblasts that are bone-producing cells [39]. Because the osteoblasts form bone tissue on the bioactive materials, the material finally bonds to the bone.

The promotion of cell differentiation by the carbonate-containing hydroxyapatite is suggested to arise from its nonstoichiometric composition, high specific surface area, and high reactivity. As a result, the carbonate-containing hydroxyapatite can adsorb active proteins such as bFGF (basic fibroblast growth factor) which makes stromal cells differentiate to specific classes of cells [40]. IGFBP-5 (insulin

like growth factor bonding protein-5) that binds to IGF (insulin like growth factor) is well adsorbed to hydroxyapatite [41]. IGF also promotes the differentiation and proliferation of osteoblasts [42]. When the carbonate-containing hydroxyapatite is not formed on the biomaterial surface, no cell differentiation into osteoblasts occurs. Consequently, fibroblastic cells proliferate on the biomaterial surface and produce a fibroblastic membrane around it, which results in nonbonding between the biomaterial and the bone. Therefore, growth of carbonate-containing hydroxyapatite on the surface is an essential requirement for bioactive materials to bond to the bone.

Adsorption of bone matrix proteins (see Section 16.8) to the carbonate-containing hydroxyapatite is suggested to be another important factor in the bonding of bioactive materials to bone tissue [43]. *In vitro* bone cell cultures in association with observation by a field-emission transmission electron analytical microscope suggest that the sequence of bone-bonding starts with the secretion and adsorption of bone matrix proteins onto biomaterials. Because many bone matrix proteins have affinity with hydroxyapatite and, particularly, poorly crystallized carbonate-containing hydroxyapatite, a bond can form between hydroxyapatite and bone. The major proteins adsorbed are osteopontin and bone sialoprotein (see Section 16.8). Mineralization of these matrix proteins occurs by nucleation of nanocrystalline calcium phosphate. The earliest detectable crystallites in this organic matrix are 1–2 nm in size, which corresponds to one or two unit cells of hydroxyapatite. These crystals grow in the organic matrix. At this early stage in the bone-bonding process, no collagen is observed in the organic matrix. Later, an initial collagen fiber assembly is formed on the mineralized organic matrix. Then the collagen is mineralized, producing morphologically identifiable bone matrix.

16.3.2 Calcification of biomaterials used in contact with blood

Apatite formation is an undesirable property for biomaterials or artificial organs used in contact with blood, such as bioprosthetic heart valves, aortic homografts, artificial blood pumps, assist devices, and a total artificial heart. Apatite formation on blood-contacting biomaterials results in thrombosis and/or the loss of flexibility of the biomaterials, thereby causing their mechanical failure and degradation [44–48]. For example, glutaraldehyde-preserved porcine aortic heart valves (bioprosthetic valves), which have been widely used for heart valve replacement, suffered from apatite deposition occurring in 10–20% of the adult recipients within 10 years [49].

A bioprosthetic valve is a collagen-based material. The collagen fibers must be cross-linked to diminish antigenicity and enhance material stability and thus to reduce degradation. The most widely applied cross-linking agent is glutaraldehyde, because it introduces thermally and chemically more stable cross-links into collagen fibers than other aldehydes such as formaldehyde. Many factors are involved in the calcification of glutaraldehyde-treated bioprosthetic valves. First, residual, noncovalently bonded glutaraldehyde encourages calcification, which is demonstrated by the reduction in hydroxyapatite formation by careful removal of nonco-

valently bonded or labile-associated glutaraldehyde by rinsing and neutralization before implantation [50]. Second, glutaraldehyde treatment and other pretreatments cause loss of endothelial cells, loss of interstitial cell viability, loss of inhibitors to calcification, fragmentation of cell membranes, and disruption of the cytoplasm. The cytoplasm, which is an essential part of the cell and is surrounded by a cell membrane, contains a liquid that differs in chemical composition from extra cellular fluid. The cytoplasmic fluid is primarily a phosphate buffer solution containing a very small amount of calcium: normal cells have an approximately ten thousand-fold gradient of calcium from outside to inside (10^{-3} vs. 10^{-7}). Non-viable cells and disrupted cell membranes are unable to maintain such a low intracellular calcium level. Moreover, cell membranes are rich in phospholipids that are known to act as nucleation sites for calcium phosphates. Consequently, nucleation of calcium phosphate occurs at the fragmented cell membranes. Third, alteration of collagen by cross-linking induces calcification although the mechanism is still poorly understood [51]. Fourth, a series of proteins induces calcification. Proteins containing gamma-carboxyglutamic acid (GLA), a calcium-binding amino acid, have been identified in calcified bioprosthetic valves [52]. GLA-containing proteins such as osteocalcin, one of the bone matrix proteins (see Section 16.8), might play a role in the calcification process. Although the source of GLA-containing proteins is unclear, they might be transported by circulating macrophages which are cells involved in the immune system. Fifth, it is known that mechanical stress also stimulates calcification [53,54] although the mechanism is poorly understood. Calcification has been shown to occur in regions of highest stress-strain levels in bioprosthetic valves. In general, all moving parts of the leaflets calcified more than static areas, indicating the importance of stress in the calcification process [55].

Recent evidence suggests that the calcification of bioprosthetic valves is regulated by functional protein molecules similar to those of the bone matrix. The presence and absence of osteopontin have been demonstrated at calcified and non-calcified areas, respectively, on implanted porcine aortic heart valves [56,57]. Osteopontin is a sulfated calcium-binding phosphoprotein rich in sialic acid groups, and is a prominent constituent of the bone matrix and dental cementum. Osteopontin is also associated with diffuse calcification in human coronary atherosclerosis, suggesting an implication of this protein in the onset and progression of calcified atheroma. Although osteopontin is a potent inhibitor of hydroxyapatite formation, osteopontin is considered to be an adhesion molecule between hydroxyapatite crystals and many substrates including valve surfaces, bioactive materials, ligaments, tendons, and dental cementum [58].

The prevention of bioprosthetic valve calcification has been actively attempted although there is still no satisfactory clinical means for preventing the calcification (Table 16.2) [52,59]. The approaches to prevent calcification include extensive extraction of noncovalently bonded glutaraldehyde, extraction of phospholipids, extraction of noncollagenous proteins, nonaldehyde treatments, treatment with inhibitors of calcification, and incorporation of metallic salts.

Table 16.2. Strategies to Prevent Calcification of Bioprosthetic Valves

Removal of glutaraldehyde
Enzymatic removal of noncollagenous proteins
Alternative crosslinking methods
Diphosphonate
Trivalent metal ions
Amino oleic acid
Surfactants
Ethanol

Fresh soft tissue rich in collagen was treated with pepsin, an enzyme that decomposes certain kinds of proteins. Pepsin treatment was carried out under conditions of high ionic strength, which allowed the collagen fibrillar structure to remain intact, while noncollagenous interfibrillar materials, cytoplasmic components, and the antigenic telepeptides of collagen were mostly removed. This pepsin-treated material, subsequently cross-linked with glutaraldehyde using standard procedures, was found to elicit a much reduced calcification response compared to cross-linked pericardium that was not treated by pepsin [50].

Epoxy-cross-linked collagen showed a large reduction in calcification compared with glutaraldehyde-cross-linked materials [60,61]. Dermal sheep collagen was cross-linked by glutaraldehyde, 1,4-butanediol diglycidyl ether (BD), or a combination of 1-ethyl-3-(3-dimethyl aminopropyl) carbodiimide (EDC) and *N*-hydroxysuccinimide (NHS). These cross-linked dermal collagens were implanted subcutaneously in rat up to six weeks. The dermal sheep collagen cross-linked by glutaraldehyde resulted in intensive calcification while that cross-linked by EDC and NHS resulted in moderate calcification at six weeks. No calcification occurred for the collagen cross-linked by BD at 6 weeks. A photooxidative preservation method was also effective to inhibit calcification [62].

Diphosphonate is known to inhibit calcification in bone and pathologic mineral deposition by binding hydroxyapatite and preventing further crystal growth [63]. Diphosphonate compounds are characterized by a P-C-P bond instead of P-O-P bond of pyrophosphate. Local controlled release of ethane hydroxy diphosphonate (EHDP: $\text{PO}(\text{OH})_2\text{-CCH}_3\text{OH-PO}(\text{OH})_2$) in the vicinity of bioprosthetic valves implanted subcutaneously in rats prevented the calcification of bioprosthetic valves for up to 84 days [64]. Amino propane hydroxy diphosphonate (APDP: $\text{PO}(\text{OH})_2\text{-C}(\text{CH}_2\text{CH}_2\text{NH}_3)\text{OH-PO}(\text{OH})_2$) inhibited the calcification of bioprosthetic valves when covalently incorporated in cuspal tissue [65].

Trivalent iron and aluminum ions prevented the calcification of glutaraldehyde-pretreated bioprosthetic valves. These trivalent ions are known to inhibit the activity of alkaline phosphatase, an enzyme that catalyzes the hydrolysis of phosphoesters, thus producing phosphate ions. The presence of alkaline phosphatase has been demonstrated in fresh porcine aortic valves and glutaraldehyde-treated bioprosthetic valves implanted in rats. The alkaline phosphatase in the implanted valves came from the recipient and was found to be adsorbed rapidly following

implantation with maximum enzyme activity at 72 h. Simultaneously with the maximum activity of alkaline phosphatase, bulk calcification was initiated in the bioprosthetic valve. Preincubation of bioprosthetic valves in either FeCl_3 or AlCl_3 solution inhibited calcification and reduced alkaline phosphatase activity significantly [66].

Treatment of glutaraldehyde-treated bioprosthetic valves with 2-amino oleic acid was effective in preventing the calcification of glutaraldehyde cross-linked cusps of aortic valves, but not aortic walls. The mechanism of prevention is considered to be the retardation of the diffusion of calcium ions into the aortic cusps of bioprosthetic valves [67].

Incubation of glutaraldehyde-treated bioprosthetic valves in sodium dodecyl sulfate inhibits calcification. Sodium dodecyl sulfate is an anionic detergent that can hypothetically modify the bioprosthetic tissue in a variety of ways including the extraction of lipids or proteins, protein denaturation, or charge modification. Sodium dodecyl sulfate prevents calcification in the presence of acidic phospholipids and calcium phosphate complexed lipids *in vitro* [68]. The principal effect of sodium dodecyl sulfate is reported to be phospholipid extraction from glutaraldehyde-treated bioprosthetic valves [69].

Pretreatment of glutaraldehyde-cross-linked bioprosthetic valves with 80% ethanol prevented calcification [70,71]. The pretreatment extracts phospholipids, cholesterol, noncovalently bonded glutaraldehyde, and water from the valve and changes the conformation of collagen. Ethanol pretreatment greatly reduces the uptake of cholesterol *in vitro*.

16.4 Apatite Deposition on Biomaterials as Surface Modification

Apatite layers are formed on various substrates in metastable supersaturated solutions to improve biocompatibility of biomaterials. A calcium phosphate layer with a thickness of 7.9 nm was found to be formed on titanium immersed in Hanks' balanced solution (Table 16.3) for 30 days [72]. The Ca/P molar ratio of the calcium phosphate layer was 1.63, indicating the formation of calcium-deficient hydroxyapatite. The apatite layer was formed on a titanium oxide layer on the surface of metallic titanium. A similar calcium phosphate layer is also formed on the surface of titanium implanted in human bone tissue [73]. These calcium phosphate layers are considered to be important for the superior biocompatibility of titanium metal.

It is suggested that Ti-OH groups on the surface of titanium or titanium alloys act as sites for the primary nucleation of calcium titanate in calcium-containing solutions, which subsequently act as secondary nucleation sites for apatite formation [74]. Ti-OH groups can be introduced on the titanium surface by immersing in a NaOH solution at 60°C for 24 hours, followed by heating in air at 600°C for one hour. The titanium thus treated induces apatite formation on its surface in a simulated body fluid (SBF, Table 16.3) or in bone tissue [75]. However, the alkali

Table 16.3. The Ion Concentrations of Supersaturated Fluids (mM)

	Na	Ca	K	Mg	Cl	HPO ₄ ²⁻	SO ₄ ²⁻	HCO ₃ ⁻	pH	Temp. [°C]	Refs.
Hanks	142	1.26	5.81	0.81	145	0.78	0.81	4.17	7.40	37	72
SBF	142	2.5	5.0	1.5	148	1.0	0.50	4.2	7.25– 7.40	37	74
Blood plasma	142	2.5	5.0	1.5	103	1.0	1.0	27.0	7.40	37	

and heat treatment method is ineffective for inducing apatite formation on stainless steel and Co-Cr-Mo alloy. Calcium titanate and/or calcium hydroxide that act as the nucleation site of apatite formation has been directly formed by immersing titanium in a Ca(OH)₂ solution at room temperature, followed by heating at 600°C for 30 minutes at a reduced pressure of 10 MPa [76].

An apatite layer is also known to form on hydrated silica-gel layers on the surface of some silicate-containing glasses and glass ceramics. An amorphous calcium phosphate layer is formed on the silica-gel layer on the surface of Bioglass® with a composition 24.5Na₂O-24.5CaO-45SiO₂-6P₂O₅ followed by crystallization of the amorphous calcium phosphate into apatite by the incorporation of OH⁻, CO₃²⁻, or F⁻ anions from the surrounding solution [77]. Glasses in the system CaO-SiO₂, free from P₂O₅, form the apatite layer in SBF, although a glass in the system CaO-P₂O₅ does not [78,79]. The former glasses form a silica hydrogel layer prior to the nucleation of apatite. Pure silica gel, prepared by the sol-gel method, forms an apatite layer on its surface when soaked in SBF, although neither silica glasses nor crystalline quartz form the apatite layer [80]. The apatite-forming ability of silica gel depends on the heat-treatment temperature. Silica gel prepared from the hydrolysis of tetraethoxysilane followed by heating at a temperature of 800°C or lower formed an apatite layer on its surface, although that heated at 900°C or higher did not [81]. Therefore, hydrated silica gel, or more specifically, silanol groups on the silica gel surface could be responsible for the nucleation and formation of the apatite layer.

It has been suggested that silica dissolved in solution also contributes to apatite formation [82]. Polyether sulfones treated with O₂ plasma were placed in SBF parallel to plates of silica gel and silica glass with various silica solubilities at a distance of 0.5 mm. After four days soaking, the polyether sulfone plates were removed from the SBF and soaked in 1.5SBF that has ionic concentration 1.5 times that of SBF. All of the silica gel plates released silicate ions in the SBF at the first soaking, although the silica glass plates did not. The dissolved silicate ions adsorbed to the polyether sulfone plates. Only polyether sulfone plates with adsorbed silicate formed an apatite layer on their surface during the second soaking. Therefore, silicate ions dissolved from the silica gel and adsorbed to the substrates have apatite-forming ability.

Apatite can also deposit on polymer surfaces with appropriate functional groups. Poly(ethylene oxide) (PEO)/poly(butylene terephthalate) (PBT) copolymer

induces apatite deposition because of the presence of the hydrophilic PEO component [83]. Polar groups such as carboxylic and carbonyl groups introduced on polyether sulfone by glow discharge treatment in O₂ gas effectively induced apatite nucleation on the surface of polyether sulfone in SBF [84]. Methacryloyloxyethylene phosphate (MOEP) with the chemical structure CH₂ = C(CH₃)-CO-OCH₂CH₂O-PO-(OH)₂ was graft-polymerized onto the surface of poly(ethylene terephthalate) (PET). Apatite was rapidly deposited on this polymer substrate with phosphate graft chains in a supersaturated solution. It is considered that the graft chains produced some interfacial bonds with the deposited hydroxyapatite layer [85]. Phosphorylated polymer surfaces also induce hydroxyapatite deposition [86]. Hydroxyapatite was formed on self-assembled monolayers (SAMs) of alkanethiols with CH₃, PO₄H₂, COOH, CONH₂, OH, and NH₂ terminal groups in SBF [87]. The most potent inducer of apatite nucleation was the SAM with PO₄H₂ groups. The SAMs with CONH₂, OH, and NH₂ groups possess much weaker inducing ability, and that with CH₃ possesses the least ability. The growth rate of hydroxyapatite on these SAMs shows a tendency similar to their nucleation ability: the growth rate decreased in the order PO₄H₂ > COOH >> CONH₂ ≅ OH > NH₂ >> CH ≅ 0. Negatively charged groups strongly induced apatite formation although positively charged groups did not.

Hydroxyapatite crystals were precipitated on compressed Langmuir monolayers [88]. Langmuir monolayers of surfactant molecules can be used as molecular templates for the oriented nucleation of either organic or inorganic crystals. The compressed Langmuir monolayer of stearic acids was effective for the nucleation of hydroxyapatite from a subphase solution prepared by mixing a calcium hydrogen-carbonate solution (Ca: 5.0 mM), an ammonium hydrogen phosphate dibasic solution (P: 3.0 mM), and CO₂ gas. As CO₂ gas was liberated from the solution, hydroxyapatite crystals precipitated because of the increase in pH. The nucleation of hydroxyapatite occurred mainly at the air/water interface. The (001) planes of hydroxyapatite were parallel to the interface. It was considered that the hydroxyapatite was nucleated epitaxially because the arrangement of calcium in the hydroxyapatite (001) plane is very similar to that of the stearic acid head groups in the monolayer.

Heterogeneous nucleation of apatite is also affected by the surface charge of substrates. Negatively charged substrates accelerated the nucleation and growth of apatite in 1.5SBF compared with uncharged and positively charged substrates [89]. Hydroxyapatite ceramics (1 mm thick) sintered at 1200°C with a flow of steam were electrically polarized at 120 V/mm for one hour in a dc field at 300°C followed by immersion in 1.5SBF. Apatite was formed within 6 to 12 hours on the negatively charged surface of the hydroxyapatite disk, although no growth occurred on the positively charged surface even after immersion for three days. The growth rate on the negatively charged surface was six times higher than that on the uncharged surface.

A study for comprehensive understanding of the factors that control the heterogeneous nucleation of calcium phosphates has been carried out by analyzing the surface tension components for silicone rubber, poly(methyl methacrylate), poly(tetrafluoroethylene-co-hexafluoropropylene), anatase, and rutile [90]. Al-

though the Lifshitz-van der Waals surface tension components are approximately the same for all these materials, the Lewis acid-base surface tension components vary greatly. Effective nucleation of calcium phosphates was observed only on surfaces with relatively high values of the Lewis acid-base surface tension component. Comparison of the induction time for the heterogeneous nucleation of hydroxyapatite on rutile and anatase surfaces revealed that the induction time on the anatase surface was much shorter than that on the rutile surface under the same supersaturation. The calculated surface tension components showed a very high value of the Lewis base surface tension parameter associated with the anatase surface, 48 mJm^{-2} , in comparison with that associated with the rutile surface, 16 mJm^{-2} [91].

Hydroxyapatite was formed on collagen in the presence of poly-L-aspartate (MW 13700) by mixing a calcium-containing collagen solution and a neutral phosphate solution [92]. It is known that bone mineralization is controlled by so-called noncollagenous proteins containing unusual amounts of anionic amino acids such as aspartate and glutamate (see Section 16.8). For this reason, polyaspartate and polyglutamate have been used as model compounds for the noncollagenous proteins. Indeed, polyaspartate and polyglutamate strongly affect the kinetics of calcium phosphate formation by interacting with calcium. The calcium-containing collagen solution was prepared by adding a calcium chloride solution to a collagen solution. The calcium-containing collagen solution was mixed with a potassium phosphate solution buffered at pH 7.4 containing poly-L-aspartate. The reaction is a combination of collagen fibril formation and calcium phosphate formation. In this way, a homogeneously mineralized collagen gel was obtained with a three-dimensional network of collagen fibrils covered by calcium phosphate, which is probably an intermediate phase between octacalcium phosphate and hydroxyapatite. In the absence of poly-L-aspartate, calcium phosphate microcrystals aggregated spherically and loosely bound to the fibrils. However, in the presence of poly-L-aspartate, the microcrystals located separately on or inside the collagen fibrils. The adsorption of two polyelectrolytes, poly-L-glutamate (25.2 KD) and poly-L-aspartate (28.8 KD), on hydroxyapatite crystals was studied both experimentally and theoretically [93]. Langmuir adsorption isotherms were obtained for both polyelectrolytes, with binding constants of $K = 6 \times 10^6$ and $3 \times 10^6 \text{ M}^{-1}$, respectively, at 37°C , at pH 7.4 and at an ionic strength of 0.15 M. Theoretical analysis indicated the presence of a "train-loop" type of adsorption of the molecules on the surface of hydroxyapatite, where a 42% portion of the molecular chain is attached to hydroxyapatite.

Hydroxyapatite was formed using alkaline phosphatase and calcium β -glycerophosphate solutions at pH 9.0 and 37°C . Alkaline phosphatase is an enzyme that catalyzes the hydrolysis of phosphate monoesters to form inorganic orthophosphate ions. The optimal pH for alkaline phosphatase activity is 10. Alkaline phosphatase is present on the cell membrane of osteoblasts and plays important roles in bone formation. It was demonstrated that apatite grew on a modified collagen tape in solutions containing alkaline phosphatase, calcium β -glycerophosphate, and phosphovitin (a phosphoprotein), through the decomposition of

calcium β -glycerophosphate by alkaline phosphatase [94]. The collagen tape functioned as a template for inducing apatite deposition. Although the mechanism associated with collagen templating remains unknown, this method was applied in the production of apatite-collagen complexes for bone substitutes [95]. Reconstituted type I collagen as well as sheet collagen was cross linked in the presence of alkaline phosphatase and egg-yolk phosphovitin. The cross linked collagens were immersed in daily-renewed calcium β -glycerophosphate solutions for two or four weeks to induce the deposition of apatite on the collagen fibers. The complex showed visible elastic deformation without detachment of apatite crystals, which is never shown by sintered hydroxyapatite ceramics. The complex material resembles bone more closely than any other currently available material.

Supersaturated bicontinuous microemulsions were used to synthesize polycrystalline hydroxyapatite with an organized microstructure. In a typical experiment, freshly prepared supersaturated calcium phosphate solution was added dropwise to a stirred mixture of didodecyldimethylammonium bromide and alkane oils. The mixtures were stored at various temperatures from -25 to $+46^{\circ}\text{C}$ for 3 to 90 days. Nucleation of apatite occurred within the nanometer-size water conduits of the oil/water microemulsions. After extraction of the oils, the polycrystalline hydroxyapatite material exhibited a microskeletal or "reticulated" architecture composed of micron-sized crystals [96,97].

16.5 Calcium Phosphate Cements

Hardening of calcium phosphate cements for dental and orthopedic uses involves hydroxyapatite growth. Calcium phosphate cements are of considerable interest in medicine and dentistry owing to their biocompatibility, bioactivity, ability to form *in situ*, and ability to harden *in vivo*. Calcium phosphate cement paste is used to fill the spaces between prosthetic implants and bone tissue, to fill the defects in dental enamel and dentin, and to fill dental pulp cavities.

Calcium phosphate cements consist of combinations of aqueous solutions and powders of calcium phosphates, except hydroxyapatite. The calcium phosphate powders convert into calcium-deficient hydroxyapatite or octacalcium phosphate in aqueous solutions by hydrolysis because hydroxyapatite is the most stable phase in water at neutral pH. Interwinding and heterogeneous nucleation of micro crystals of calcium-deficient hydroxyapatite cause the hardening of calcium phosphate cements. The hardening of calcium phosphate powder was first reported by Monma for α -tricalcium phosphate in water [98]. However, this cement required two hours at 80°C to harden and was far from satisfying clinical requirements. Many α -tricalcium phosphate cements using organic acid solutions were developed in the 1980s with satisfactory reduction in the hardening time and improved mechanical strength. However, the organic acid solution was less biocompatible, evoking an adverse tissue reaction because of its low pH. To overcome this problem, two α -tricalcium phosphate cements without using organic acids were developed which harden at neutral pH [99]. They are the mixtures of 95–90% α -

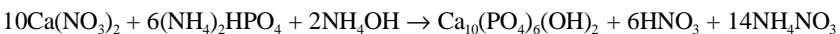
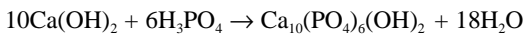
tricalcium phosphate and 5–10% dicalcium phosphate dihydrate heated at 1250°C with a Ca/P ratio of 1.47, accompanied by a solvent containing 10% sodium chondroitin sulfate, 12% sodium succinate, and 78% water.

Another class of calcium phosphate cement uses tetracalcium phosphate and dicalcium phosphate dihydrate or dicalcium phosphate anhydrous as cement powders which harden at or near neutral pH [100,101]. Calcium-deficient hydroxyapatite with a Ca/P molar ratio of 1.5 is formed initially in the hardening of an equimolar mixture of tetracalcium phosphate and dicalcium phosphate anhydrous. The calcium-deficient hydroxyapatite exhibits a gradual increase in Ca/P molar ratio, a process of so-called maturation. An excess amount of dicalcium phosphate anhydrous in the mixture delays the increase in Ca/P molar ratio during hardening. The highest mechanical strength of the set cement is associated with an equimolar mixture of tetracalcium phosphate and dicalcium phosphate anhydrous. The setting reaction and the properties of the set cement are highly dependent on the molar ratio of tetracalcium phosphate to dicalcium phosphate anhydrous [102].

A paste consisting of monocalcium phosphate monohydrate, α -tricalcium phosphate, calcium carbonate, and a sodium phosphate solution has useful rheological characteristics before hardening, and thus can be implanted into fractured sites in bone by the minimally invasive means of injection through the skin to repair the fracture [103]. The paste hardens in minutes, concurrent with the formation of carbonate-containing hydroxyapatite under physiological conditions, with an ultimate compressive strength of 55 MPa.

16.6 Hydroxyapatite Ceramics

The manufacture of hydroxyapatite ceramics involves processes related to crystal growth. Hydroxyapatite ceramics are used as artificial bone to repair bony defects, to augment alveolar ridges, to enhance guided tissue regeneration, and to reconstruct the middle ear in either porous sintered bodies or dense sintered bodies. The preparation of hydroxyapatite ceramics consists of three steps: (1) preparing the apatite powder, (2) compacting it into a desired shape, and (3) sintering it in the temperature range of 900 to 1200°C. For preparing apatite powders, the following two reactions are widely utilized:



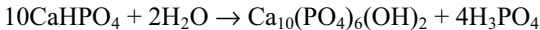
A typical example of the former reaction is the drop wise addition of a 1.8 mol/L solution of H_3PO_4 into a 3 mol/L suspension of $\text{Ca}(\text{OH})_2$ in water with vigorous stirring [104,105]. After the addition of H_3PO_4 , the reaction mixture is aged for 3 to 48 hours to complete the reaction. Because the solubility of $\text{Ca}(\text{OH})_2$ is as low as 0.02 mol/L at the saturation point in water, the mechanism of apatite formation is not likely to be a simple ionic reaction; this remains to be clarified. The reaction product is poorly crystallized apatite with a crystallite size of 30 to 50 nm, as de-

terminated by the Debye-Scherrer method, or that of approximately 15 to 50 nm, as determined by transmission electron microscopy. The poorly crystallized apatite is heated over the temperature range of 700 to 850°C before compaction. During this heat treatment, the apatite particles grow to a size of 50 to 100 nm. By sintering the compacted apatite powder, the particles grow further to a size of 600 nm to 3 μm .

16.7 Hydrothermal Growth of Hydroxyapatite

The most successful method to grow hydroxyapatite single crystals is hydrothermal synthesis (Table 16.4). Using hydrothermal methods, crystals with sizes larger than one millimeter have been grown in the temperature range of 200 to 700°C. A review of earlier works was published by Skinner (1974) [106] and Elliott (1994) [107]. Phase diagrams in the system $\text{CaO-P}_2\text{O}_5\text{-H}_2\text{O}$ were reported in the temperature range of 300 to 600°C at 200 MPa and in the temperature range of 700 to 950°C at 100 MPa [106,108]. Because hydroxyapatite exhibits retrograde solubility, a gradual increase in temperature is an effective way to grow large crystals [109]. Flux-grown single crystals of hydroxyapatite or carbonated apatite were prepared in the temperature range of 745 to 1400°C.

Hydrolysis reactions employed in the hydrothermal growth of hydroxyapatite single crystals lead to the production of phosphoric acid that decreases the pH. For example:



Hydroxyapatite crystals tend to grow larger in acidic hydrothermal solutions than in neutral or alkaline solutions. However, the excess H^+ ions in the solution are readily incorporated into the hydroxyapatite lattice, resulting finally in the formation of calcium-deficient hydroxyapatite crystals with a Ca/P molar ratio lower than the stoichiometric value of 1.67.

Hydrothermal techniques are used to stabilize plasma-sprayed apatite coated on metallic implants. The plasma-sprayed apatite layer contains amorphous calcium phosphate, α -tricalcium phosphate, calcium oxides, and/or tetracalcium phosphate phases, all of which are the decomposition products of hydroxyapatite formed at a high temperature of $\sim 10,000^\circ\text{C}$ associated with the plasma-spraying process. To convert the decomposition products into hydroxyapatite, the coated implants are treated hydrothermally or heated in water vapor after plasma spraying.

Hydroxyapatite whiskers have been prepared by the hydrothermal method to develop new asbestos-substituting materials. Hydroxyapatite whiskers could be the most biocompatible material among the currently available inorganic fibrous materials such as glass, carbon, asbestos, SiC , Al_2O_3 , and ZrO_2 . Moreover, stoichiometric hydroxyapatite has better heat resistance than chrysotile, the main component of asbestos: it has a decomposition temperature of 1200°C which is 600°C higher than that of chrysotile [117]. Although hydrothermally synthetic

Table 16.4. Hydrothermal Growth of Hydroxyapatite

Starting Material	Method	Temp. °C	Pressure MPa	Product	Size mm	Ref.
DCPA	hydrolysis	300	8.6	HAP		110
HAP	recrystallization	430–500	200	HAP	3.5	111
TCP-Ca(OH) ₂	flux growth	900–775	103	HAP	4	112
TCP-Ca(OH) ₂ -H ₂ O	flux growth	900–745	103	HAP	4	112
DCPA, CO ₂	hydrolysis	180–290		A-CHAP*	12.5×0.2	109
DCPA	hydrolysis	170–230		HAP	8.3	113
HAP	recrystallization	390–470	310–412	HAP	7×7×0.2	114
TCP, CaCO ₃	hydrolysis	850	15	A-CHAP		115
TCP, Ca(OH) ₂ , CaCO ₃	hydrolysis	750–900	103	B-CHAP [†]		115
αTCP-CaCO ₃	flux growth	1400	54	AB-CHAP [‡]	0.7	116

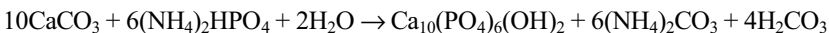
*A-CHAP: A-site (OH site) carbonated hydroxyapatite

[†]B-CHAP: B-site (PO₄ site) carbonated hydroxyapatite

[‡]AB-CHAP: Both A and B-site carbonated hydroxyapatite

whiskers are calcium-deficient hydroxyapatite with lower heat resistance, their Ca/P molar ratio is improved to the stoichiometric value of 1.67 after heating with calcium carbonate at 600°C [118]. The hydrothermally synthetic hydroxyapatite whiskers have diameter, length, and aspect ratio in the range of 1 to 10 μm, 30 to 50 μm, and 5 to 20, respectively. The mechanical properties of hydroxyapatite whiskers were measured by three-point bending and tensile tests. The three-point bending strength is 500 ± 184 MPa in air and 454 ± 204 MPa in water [119]. The tensile strength is 410 ± 13 MPa in air [113].

A porous hydroxyapatite body for use as an implant material is prepared from coral skeletal calcium carbonate by hydrothermal conversion, in addition to the conventional ceramic manufacturing processes [120]. The open pore structure of porous hydroxyapatite bodies is clinically important because vascular formation in the pores promotes bone ingrowth and regeneration. However, it is difficult to manufacture a porous body, by the conventional ceramic processes, with sufficiently open and interconnected pores and with mechanical strength at a level that satisfies clinical requirements. Coral skeletal calcium carbonate has an open and interconnected pore structure and is hydrothermally converted into hydroxyapatite according to the following reaction:



The reaction takes place in a temperature range of 180 to 250°C while maintaining the porous structure of the coral skeleton. A topotactic reaction of aragonite with phosphate would take place in the hydrothermal conversion into hydroxyapatite [121].

16.8 Factors Influencing Apatite Formation in Hard Tissues

Apatite is formed in bone, dentin, and dental enamel in vertebrates. Bone and dentin belong biologically to the same class of tissue originating from the mesoderm, although dental enamel originates from the ectoderm; this means that dental enamel is a completely different tissue from bone and dentin, and is rather close to skin. Therefore, in the mechanism of formation, cells and proteins involved are somewhat similar between bone and dentin, but very different between dental enamel and these two calcified tissues. Bone and dentin consist of cells, matrix protein (approx. 30 wt%), and apatite (approx. 70 wt%). The most important cells in bone are osteoblasts and osteoclasts. Osteoblasts form apatite and matrix proteins, although osteoclasts dissolve them by decreasing the local pH and using various enzymes. Cells involved in the formation of dentin are called odontoblasts. In dentin, there are no cells corresponding to the osteoclasts in bone. Dental enamel consists of 2 to 6 wt% protein and 94 to 98 wt% apatite with no cells. Dental enamel is formed by ameloblasts.

Various factors influence apatite formation in bone, dentin, and dental enamel (Table 16.5). The *in vivo* formation and dissolution of apatite are controlled not only by physicochemical factors such as inhibitors, promoters, and supersaturation but also by other cell-biological factors. The cell-biological factors, which regulate various cells, include matrix proteins, growth factors, growth hormones, and essential trace elements. Several factors show the opposite effect on apatite formation under different conditions.

The matrix proteins of bone and dentin consist of a large amount of collagen (50–90%) and a small amount of noncollagenous proteins [122]. Collagen in bone and dentin are mainly Type I collagen. Noncollagenous proteins include osteopontin, osteocalcin (bone Gla protein), bone sialoprotein, and osteonectin for bone, and dentin phosphophoryn and osteocalcin for dentin (Table 16.5). Many of these noncollagenous proteins show inhibitory effects on hydroxyapatite formation when they are present in solution as free molecules, although some of them show promotive effects when they are immobilized on substrates such as agarose and collagen. These opposite effects are considered to result from the conformational differences in these proteins when they are present as free molecules and as immobilized ones. Moreover, many of the noncollagenous proteins show concentration-dependent promoting and inhibiting effects on hydroxyapatite formation, promoting at low concentrations and inhibiting at high concentrations [123,124].

Type I collagen is the most abundant protein among bone matrix proteins. Type I collagen in bone is produced from the same gene as that in noncalcified tissue. Therefore, Type I collagen in bone is essentially the same molecule as that in noncalcified tissue. The differences between bone Type I collagen and that in noncalcified tissue arise from the so-called posttranslational modification. This modification includes hydroxylation of lysine residues, glycosylation of hydroxylysine, and phosphorylation, and is believed to play an integral role in collagen mineralization [125]. From the viewpoint of hydroxylation, for example, the extent of hy-

droxylation of lysine residues is much higher in bone collagen than in noncalcified tissue. The extent and site of the hydroxylation governs cross-linking patterns, hence, packing of collagen molecules. It is noteworthy that the average gap between collagen molecules in tendons (0.3 nm) is smaller than the diameter of phosphate ion, although that in bone (0.6 nm) is larger than that of phosphate ion which enables the phosphate ions migrate into collagen fibrils [126].

Apatite crystals grow preferentially lengthwise in the direction of the long axis of collagen and in width along channels or grooves that are formed by adjacent hole zones of collagen [127]. However, numerous studies indicate that collagen is not a direct nucleator of apatite deposition. Rather, collagen provides a template for mineral deposition which may be initiated by associated noncollagenous proteins [128].

Osteocalcin is the most abundant protein among the noncollagenous proteins in bone, and is produced by osteoblasts [122,128]. Osteocalcin contains γ -carboxyglutamic acid (Gla) and has affinity with calcium and hydroxyapatite. However, a number of studies have demonstrated the inhibitory effects of osteocalcin on hydroxyapatite formation. In dentin, osteocalcin is a very minor constituent. Osteocalcin appears to be more involved in the regulation of bone turnover, particularly in the inhibition of hypercalcification.

Osteopontin and bone sialoprotein have many similarities in their structures, that is, they contain many sugar chains with sialic acid [122,128]. They both have the Arg-Gly-Asp sequences for cell attachment. However, osteopontin inhibits hydroxyapatite formation whereas bone sialoprotein promotes it. The promotional effects of bone sialoprotein on hydroxyapatite formation are due to the poly(glutamic acid) sequences that are present in bone sialoprotein and absent in osteopontin. Osteopontin is a prominent constituent of bone matrix and dental cementum.

Dentin phosphophoryn is dentin-specific and is also the most abundant non-collagenous protein in dentin [129]. Dentin phosphophoryn contains approximately 40% aspartic acid and 50% serine. Most serine residues are phosphorylated, resulting in a very high negative charge density.

Osteonectin is a glycoprotein that is present in high concentrations in bone. The role of osteonectin in apatite formation is less clear [122,128].

Zinc and magnesium are typical inorganic inhibitors of hydroxyapatite formation [130–132]. The former is 100 to 1000 times more effective in inhibiting hydroxyapatite growth than the latter. The inhibitory effect arises partly from the mismatch of the ionic radius between these elements (Mg: 0.072 nm and Zn: 0.075 nm) and calcium (0.100 nm). These ions are adsorbed on the surface of hydroxyapatite and inhibit the growth. However, trizinc phosphate octahydrate (hopeite) formation on the surface is also involved in the inhibitory mechanism. In contrast, a small amount of zinc stimulates osteoblast activity and suppresses osteoclast activity, resulting in enhancement of bone formation [133–136]. The mechanism of the stimulatory effect of zinc on bone formation is not sufficiently clear because of the presence of many zinc-containing proteins and enzymes in the cells.

Table 16.5. Matrix Proteins and Ions Influencing Hydroxyapatite Growth

	Hydroxyapatite formation	Remarks
Type I collagen	—	serves as a template for mineral deposition
OPN	inhibits formation [137–139]	promotes cell attachment [58] an acidic protein
OC(f)	inhibits formation [140,141]	inhibits hyperactivity of osteoblasts [142]
OC(i)	inhibits seeded growth [143,144] promotes or no effect [145,146]	binds to HAP, but not to ACP [140] affinity for HAP (100) face [147] affinity for collagen [148] an acidic protein
ON(f)	inhibits formation [141]	binds to HAP and Type I collagen [149]
ON(i)	inhibits seeded growth [143,149,150] no effect (on agarose) [145] inhibits and promotes formation (on collagen) [151,152]	affinity for HAP (100) face [147] an acidic protein
DPP(f)	inhibits formation [141] inhibits growth [154] promotes formation at low conc. [123]	affinity for collagen [153] affinity for Ca and PO ₄ ions [155] affinity for HAP (100) face [147]
DPP(i)	promotes nucleation promotes formation [145,146,156,157]	an acidic protein
BSP(f)	promotes nucleation [158]	promotes cell attachment [159] affinity for collagen [148] promotes osteoblast differentiation [160] an acidic protein
EN(f)	inhibits formation [161]	an acidic protein
AM(f)	inhibits formation [161,162]	
Zinc	inhibits formation [163] inhibits seeded growth [130,132]	promotes osteoblast activity [133,164]
Magnesium	inhibits seeded growth [130,132]	
Fluorine	promotes formation	fluorosis in dental enamel at an elevated concentration

OPN: osteopontin; OC: osteocalcin; BSP: bone sialoprotein; ON: osteonectin; DPP: dentin phosphophoryn; EN: Enamelin; AM: Amelogenin. Symbols (f) and (i) indicate free and immobilized proteins, respectively.

16.9 Ectopic Calcifications

Hydroxyapatite growth is often associated with pathological and ectopic calcifications such as arteriosclerotic calcification, dental calculus, and urinary stones.

In human atherosclerotic lesions, cholesterol often coexists with calcium-containing deposits that are most likely hydroxyapatite [165]. Crystallographically, hydroxyapatite and cholesterol monohydrate usually develop (001) faces. A fit of the (001) planes shows close superposition of the hydrogen bonding groups from the two crystal structures [166]. The corresponding superlattice nets have $a = 1.884$, $b = 1.631$ nm, $\gamma = 90^\circ$ for hydroxyapatite and $a = 1.913$, $b = 1.584$ nm, and $\gamma = 90.1^\circ$ for cholesterol monohydrate. Each structure may serve as a nucleus for the growth of the other crystal, utilizing the intervention of a transition layer of hydrogen-bonded water molecules. It is therefore possible that cholesterol monohydrate is implicated in calcification often associated with the later stages in the development of atherosclerotic plaques. *In vitro* nucleation of cholesterol crystals on hydroxyapatite occurred when hydroxyapatite seeds were immersed in an ethanolic solution of cholesterol that was very slightly supersaturated with respect to cholesterol [167].

However, evidence is accumulating that vascular calcification is an active process that has many similarities with ossification. Messenger RNAs (mRNAs) for OP, ON, OC, and bone morphogenetic protein type 2 (BMP-2) were detected in calcified atherosclerotic plaques. This indicated that there were cells producing OP, ON, OC, and BMP-2 in the calcified plaques. All these proteins are commonly associated with normal calcification and remodeling of bone. In particular, OC and BMP-2 are bone-specific proteins produced by osteoblasts. The origins of bone-forming cells and osteoclast-like cells in the artery wall remain unknown. It is considered that calcification in coronary artery disease is not a passive process but an active process closely associated with plaque development, which is regulated in a fashion similar to bone mineralization [168–171].

Dental calculus is mineralized dental plaque formed both above (supragingival) and below (subgingival) the gumline dental enamel [172]. Mineral crystals found in human dental calculus are typically calcium phosphates including dicalcium phosphate dihydrate, octacalcium phosphate, hydroxyapatite, and magnesium-substituted whitlockite [173]. It has been suggested that calculus mineralization begins with the deposition of kinetically favored precursor phases such as dicalcium phosphate dihydrate and octacalcium phosphate, and is followed over time by maturation into hydroxyapatite and whitlockite phases.

The development of human dental calculus invariably involves plaque bacterial calcification. Dental plaque consists of approximately 80% water, 14% microorganisms, and 6% organic materials including a number of proteins. Dental plaque itself adsorbs calcium and phosphate from the surrounding fluids such as saliva for supragingival calculus and crevicular fluid for subgingival calculus, resulting in an increase in supersaturation. Areas adjacent to saliva ducts where fresh saliva is supplied tend to suffer more from calculus formation than any other areas [174]. Supersaturation can also increase by a local increase in pH, which is caused by bacterial ammonium formation [175]. Cell membranes of microorganisms containing phospholipids act as nucleation sites for calcium phosphates. Nonviable microorganisms are unable to maintain cytoplasmic fluid, a phosphate buffer solution inside the microorganisms, and are also unable to block calcium inflow into microorganism from the surrounding fluid. The contribution of the cell membrane

and nonviable microorganisms to calcification is quite similar to the case of the calcification of bioprosthetic valves (see Section 16.3.2). Other factors contributing to calculus mineralization may include salivary ion levels and dietary components such as silicon [176]. On the other hand, natural inhibitory factors may include salivary phosphoproteins and pyrophosphate. Clinical strategies to inhibit dental plaque mineralization include utilization of pyrophosphate, gantrez acid copolymer, and zinc citrate with antimicrobial ingredients as dentifrice components [172].

In urinary stones, hydroxyapatite is not necessarily the major component. However, 56.4 to 62% of urinary stones still contain hydroxyapatite as one of the crystalline components [177]. Other crystalline components include calcium oxalate, dicalcium phosphate dihydrate, magnesium ammonium phosphate, uric acid, and cystine. Most urinary stones are admixtures of two or more components, with the primary admixture being calcium oxalate and hydroxyapatite [177,178]. Hydroxyapatite-containing urinary stones often possess a periodically laminated central structure [177].

16.10 Kinetics of Hydroxyapatite Crystal Growth in Solution

Most information about kinetics of hydroxyapatite crystal growth has been obtained from the constant pH method or the constant composition method [179,180]. Depending on supersaturation, precursors appear such as octacalcium phosphate, dicalcium phosphate dihydrate, or an amorphous phase with a Ca/P molar ratio of 1.45 ± 0.05 [181–183]. In a less supersaturated solution, there is general agreement that the growth rates are too low to be transport-controlled. Many studies have shown the values of the effective reaction order, n , to range from 2.1 to 4.0 in the formula

$$R = k\sigma^n,$$

where R , k , and σ are growth rate, effective rate constant, and thermodynamic driving force, respectively [184]. This indicates the involvement of a polynucleation mechanism. Values of interfacial tension between hydroxyapatite surfaces and the solution phases ranged from 10 to 120 mJm⁻² [184]. Values of interfacial tension obtained from growth data are greater than those obtained from dissolution kinetics. Growth rate measurement for hydroxyapatite at very low supersaturation demonstrated that the linear growth rate as a function of driving force in the pH range of 5.0 to 6.5 was different from that in the pH range of 7.0 to 8.5 [185]. As a result, the growth rate of hydroxyapatite is approximately 2.5 times larger in the pH range of 5.0 to 6.5 than in the pH range of 7.0 to 8.5 even under the same supersaturation. Between these pH ranges, there is the point of zero charge of hydroxyapatite at about pH 7.0, which were verified experimentally [186,187]. An understanding of the apparent change in the kinetics of hydroxyapatite growth at pH above and below this value may require elucidation of the role of surface

charge on crystallization. A similar pH dependence of the growth rate was reported for the growth of dicalcium phosphate dihydrate [185].

Using atomic force microscopy and large single crystals of hydroxyapatite as seeds, *in situ* growth observation was performed in a simulated body fluid [109,188,189]. Under this condition, growth on the *c*-face proceeded by a polynuclear mechanism and no spiral growth was observed. Growth on the *a*-face proceeded by step flow with step heights of 0.8 and 1.6 nm as well as by two-dimensional nucleation. Step velocity on the *a*-face as functions of the step height and interstep distances indicates that none of volume diffusion, surface diffusion, nor dehydration of growth units determines the growth rate. The step kinetic coefficient, β , which is the reciprocal of the relative resistance to incorporation of a growth unit into the bulk crystal, was calculated to be 0.4×10^{-4} cm/s. This value is 100 to 1000 times lower than those of other inorganic crystals, and is comparable to those of protein and virus crystals growing by the unit of a macromolecule which have extremely low probability of incorporation [190]. The value of edge free energy of hydroxyapatite also shows similarities to that of protein and virus crystals [191]. Therefore, it is possible that the growth units of hydroxyapatite are not simple spherical ions but calcium phosphate clusters. The presence of calcium phosphate clusters with a size of approximately 0.8 nm was demonstrated by dynamic light scattering measurements, in a magnesium-carbonate-free simulated body fluid, the simulated body fluid (SBF in Table 16.3), and other calcium phosphate solutions [192–194]. The calcium phosphate clusters were detected even when the solutions were undersaturated with respect to amorphous calcium and octacalcium phosphates and were supersaturated with respect only to hydroxyapatite. On the basis of these findings, a cluster growth model for hydroxyapatite is proposed in which hydroxyapatite grows by hexagonal packing of $\text{Ca}_9(\text{PO}_4)_6$ clusters 0.8 nm in size [192]. Stacking faults of clusters can create a reflection twin crystal, edge dislocations with Burgers vector of $C/2$, and screw dislocations (Figs. 16.1, 16.2 and 16.3). Therefore, spiral dislocations can be introduced even when hydroxyapatite does not grow by the spiral growth mechanism. The same type of $\text{Ca}_9(\text{PO}_4)_6$ cluster exists in the structure of amorphous calcium phosphate and octacalcium phosphate, both of which are the precursors of hydroxyapatite. Theoretically, clusters with a size smaller than that of the critical nucleus can exist stably in solutions when the size dependence of surface tension is taken into account in the theory of homogeneous nucleation [195]. *Ab-initio* calculation revealed a large stabilization energy associated with the clustering of $\text{Ca}_3(\text{PO}_4)_2$ species with a D_{3h} symmetry in vacuum [196].

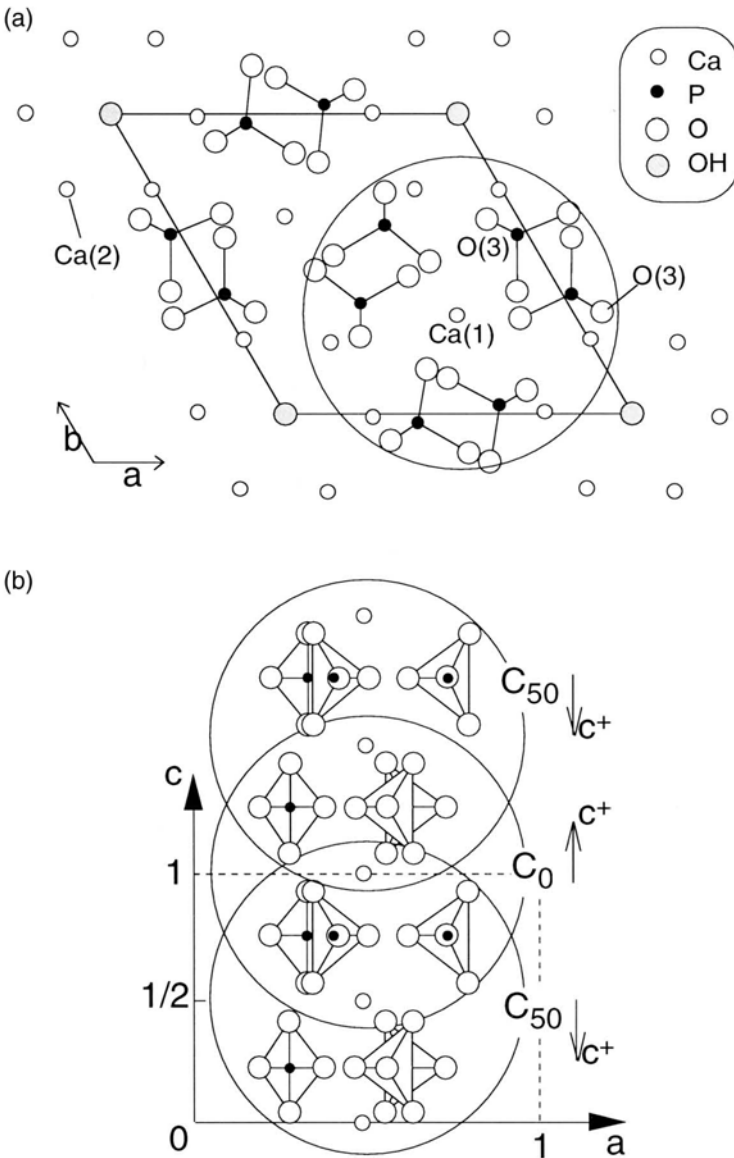


Fig. 16.1. $\text{Ca}_9(\text{PO}_4)_6$ cluster unit, C_0 and C_{50^+} projected on the ab plane (a) and ac plane (b) of the hydroxyapatite. Because both cluster units have only C_3 symmetry (noncentrosymmetric) and are related by mirror planes at $z = 1/4$ and $3/4$, they are chiral. (Reprinted with permission from Onuma, K., Ito, A. *Chemistry of Materials*, 10:3346–3351 (1998). Copyright 1998 American Chemical Society.)

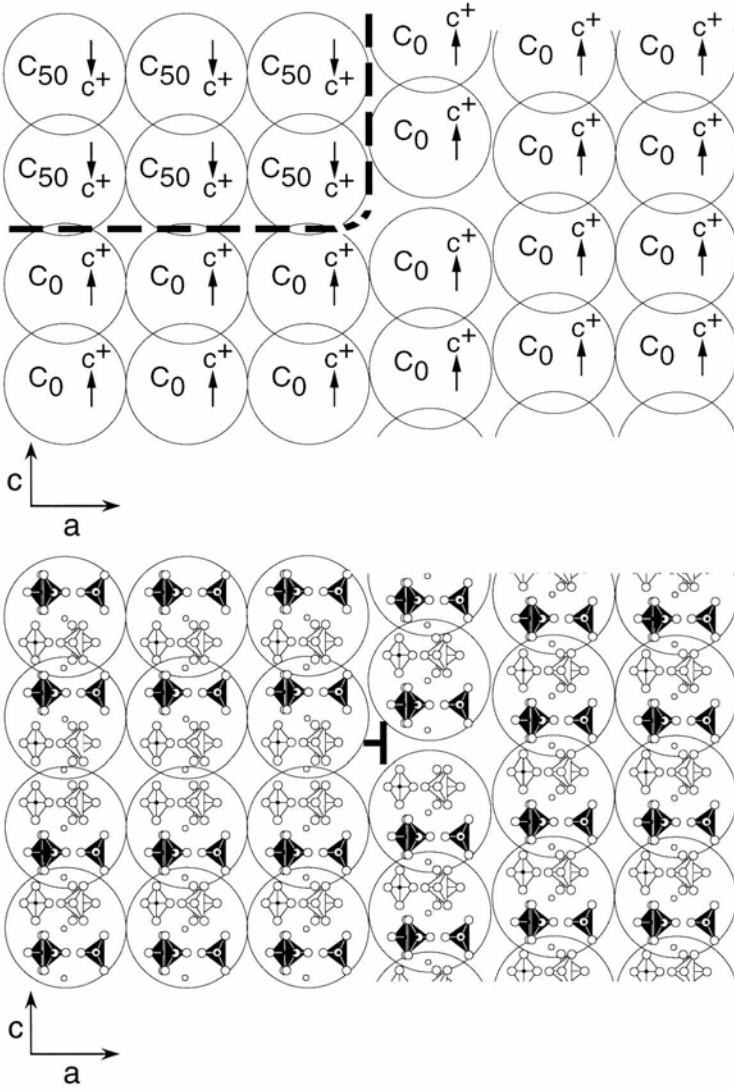


Fig. 16.2. A edge dislocation with Burgers vector of $C/2$ formed by stacking fault of C_0 and C_{50} clusters. The interface between C_0 domain and C_{50} domain is perpendicular to the c -axis, and the C^+ direction of each domain is anti-parallel.

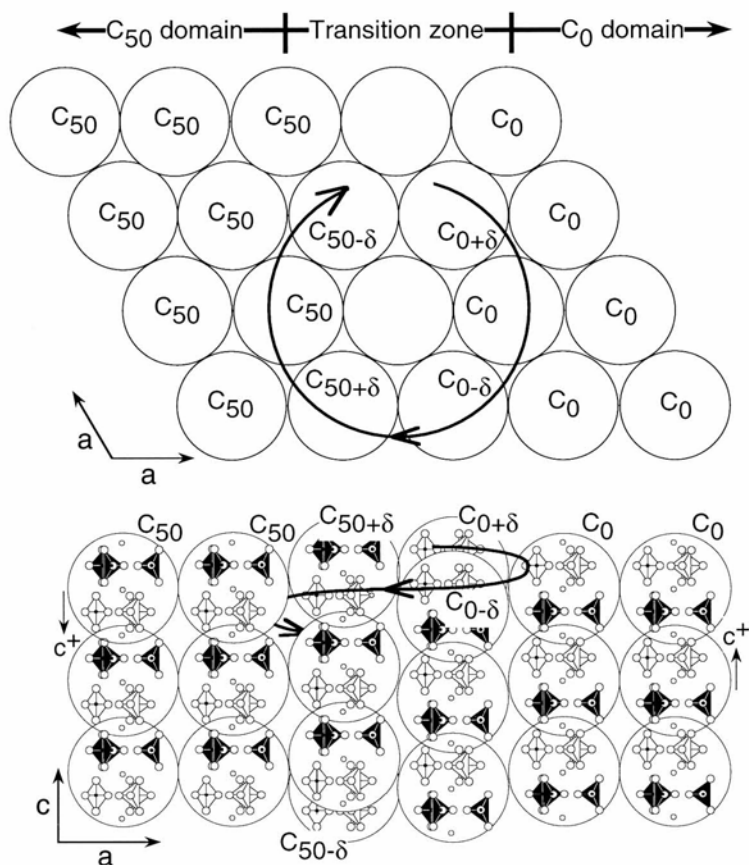


Fig. 16.3. A screw dislocation formed by a stacking fault of C_0 and C_{50} clusters. The interface between the C_0 domain and the C_{50} domain is parallel to the c -axis, and the C^+ direction of each domain is anti-parallel. In the transition zone, clusters slightly shift upward or downward by δ along the c -direction. The positional shift, δ , is expressed as $\delta = 100R/3T$, where R and T are the cluster diameter in ab plane and the width of transition zone, respectively. The figure represents the minimum width of transition zone ($T = 2R$), hence, the largest δ . (Reprinted with permission from Onuma, K.; Ito, A. *Chemistry of Materials*, 10:3346–3351 (1998). Copyright 1998 American Chemical Society.)

References

1. Corbridge DEC (1990) Phosphorus 4th edition, An Outline of its Chemistry, Biochemistry and Technology. Elsevier, Amsterdam, pp 178–185
2. Kanazawa T (ed) (1989) Inorganic Phosphate Materials, Materials Science Monograph 52. Elsevier, Amsterdam

3. Oonishi H, Oomamiuda K (1998) Degradation/resorption in bioactive ceramics in orthopedics. In: Black J, Hastings G (eds) *Handbook of Biomaterials Properties*. Chapman & Hall, London, pp 406–419
4. Mooney RW, Aia M (1961) Alkaline earth phosphates. *Chem Rev* 61:433–462
5. Van Wazer JR (1958) *Phosphorus and Its Compounds*, Vol 1. Interscience Publishers, New York
6. Vereecke G, Lemaître J (1990) Calculation of the solubility diagrams in the system $\text{Ca}(\text{OH})_2\text{-H}_3\text{PO}_4\text{-KOH-HNO}_3\text{-CO}_2\text{-H}_2\text{O}$. *J Crystal Growth* 104:820–832
7. Rowles SL (1968) The precipitation of whitlockite from aqueous solutions. *Bull Soc Chim Fr* 1797–1802
8. Moreno EC, Brown WE, Osborn G (1960) Solubility of dicalcium phosphate dihydrate in aqueous systems. *Soil Sci Soc Pro* 24:94–98
9. Moreno EC, Gregory TM, Brown WE (1966) Solubility of $\text{CaHPO}_4\cdot 2\text{H}_2\text{O}$ and formation of ion pairs in the system $\text{Ca}(\text{OH})_2\text{-H}_3\text{PO}_4\text{-H}_2\text{O}$ at 37.5°C. *J Res Natl Bureau Stand* 70A:545–552
10. McDowell H, Brown WE, Sutter JR (1971) Solubility study of calcium hydrogen phosphate. Ion-pair formation. *Inorg Chem* 10:1638–1643
11. Heughebaert JC, Nancollas GH (1985) Solubility of octacalcium phosphate at 25 and 45°C in the system $\text{Ca}(\text{OH})_2\text{-H}_3\text{PO}_4\text{-KNO}_3\text{-H}_2\text{O}$. *J Chem Eng Data* 30:279–281
12. Tung MS, Eidelman N, Sieck B, Brown WE (1988) Octacalcium phosphate solubility product from 4 to 37°C. *J Res Natl Bur Stands* 93:613–624
13. Meyer JL, Eanes ED (1990) A thermodynamic analysis of the amorphous to crystalline calcium phosphate transformation. *Calcif Tiss Res* 106:349–354
14. Christoffersen MR, Christoffersen J, Kibalczyk W (1990) Apparent solubilities of two amorphous calcium phosphates and octacalcium phosphate in the temperature range 30–42°C. *J Crystal Growth* 106:349–354
15. Gregory TM, Moreno EC, Patel JM, Brown WE (1974) Solubility of $\beta\text{-Ca}_3(\text{PO}_4)_2$ in the system $\text{Ca}(\text{OH})_2\text{-H}_3\text{PO}_4\text{-H}_2\text{O}$ at 5, 15, and 37°C. *J Res Natl Bur Stand* 78A:667–674
16. Fowler BO, Kuroda S (1986) Changes in heated and laser-irradiated human tooth enamel and their probable effects on solubility. *Calcif Tissue Int* 38:197–208
17. McDowell H, Gregory TM, Brown WE (1977) Solubility of $\text{Ca}_5(\text{PO}_4)_3\text{OH}$ in the system $\text{Ca}(\text{OH})_2\text{-H}_3\text{PO}_4\text{-H}_2\text{O}$ at 5, 15, 25 and 37°C. *J Res Natl Bur Stands* 81A:273–281
18. Bell LC, Mike H, Kruger BJ (1978) Synthetic hydroxyapatite-solubility product and stoichiometry of dissolution. *Archs Oral Biol* 23:329–336
19. Chow LC, Brown WE (1975) Singular points in the chemistry of teeth. *J Dent Res* 54(Special Issue A):Abstract 120
20. Mathew M, Brown WE, Schroeder LW, Dickens B (1988) Crystal structure of octacalcium bis(hydrogenphosphate) tetrakis(phosphate)pentahydrate, $\text{Ca}_8(\text{HPO}_4)_2(\text{PO}_3)_5\cdot 5\text{H}_2\text{O}$. *J Cryst Spect Res* 18:235–250
21. Brown WE, Smith JP, Lehr JR, Frazier AW (1962) Crystallographic and chemical relations between octacalcium phosphate and hydroxyapatite. *Nature* 196:1050–1055
22. Welch JH, Gutt W (1961) High-temperature studies of the system calcium oxide-phosphorus pentoxide. *J Chem Soc* 4442–4444
23. Nurse RW, Welch JH, Gutt W (1958) A new form of tricalcium phosphate. *Nature* 182:1230
24. Mathew M, Schroeder LW, Dickens B, Brown WE (1977) The crystal structure of $\alpha\text{-Ca}_3(\text{PO}_4)_2$. *Acta Cryst B* 33:1325–1333

25. Monma H, Nagai M (1989) Calcium orthophosphates. In: Kanazawa T (ed) *Inorganic Phosphate Materials*, Materials Science Monograph 52. Elsevier, Amsterdam, pp 79–104
26. Termine JD, Eanes ED (1972) Comparative chemistry of amorphous and apatitic calcium phosphate preparations. *Calcif Tiss Res* 10:171–197
27. Eanes ED, Termine JD, Nysten MU (1973) An electron microscopic study of the formation of amorphous calcium phosphate and its transformation to crystalline apatite. *Calcif Tiss Res* 12:143–158
28. Meyer JL, Eanes ED (1978) A thermodynamic analysis of the amorphous to crystalline calcium phosphate transformation. *Calcif Tiss Res* 25:59–68
29. Elliott JC (1994) *Structure and chemistry of apatites and other calcium orthophosphates*. Elsevier, Amsterdam, p 149
30. Posner AS, Stutman JM, Lippincott ER (1960) Hydrogen-bonding in calcium-deficient hydroxyapatite. *Nature* 188:486–487
31. LeGeros RZ, LeGeros JP (1993) Dense hydroxyapatite. In: Hench LL, Wilson J (eds) *An Introduction to Bioceramics*. World Scientific, Singapore, pp 139–180
32. Smeyers-Verbeke J, Michotte Y, Pelsmaeckers J, Lowenthal A, Massart DL, Dekegel D, Karcher D (1975) The chemical composition of idiopathic nonarteriosclerotic cerebral calcifications. *Neurology* 25:48–57
33. Hamilton EI, Minski MJ, Cleary JJ (1972/1973) The concentration and distribution of some stable elements in healthy human tissues from the United Kingdom: An environmental study. *The Sci Total Environ* 1:341–374
34. LeGeros RZ, Balmain N, Bonel NG (1986) Structure and composition of the mineral phase of periosteal bone. *J Chem Res Synop* 1:8–9
35. Rey C, Collins B, Shimizu M, Glimcher MJ (1990) Resolution enhanced Fourier transform infrared spectroscopic study of the environment of phosphate ion in the early deposits of a solid phase of calcium phosphate in bone and enamel and their evolution with age: I-investigation in the ν_4 PO_4 domain. *Calcif Tissue Int* 46:384–394
36. Rey C, Kim H-M, Gerstenfeld L, Glimcher MJ (1995) Structural and chemical characteristics and maturation of the calcium-phosphate crystals formed during the calcification of the organic matrix synthesized by chicken osteoblasts in cell culture. *J Bone Miner Res* 10:1577–1588
37. Dickens B, Brown WE, Kruger GJ, Stewart JM (1973) $\text{Ca}_4(\text{PO}_4)_2\text{O}$, Tetracalcium diphosphate monoxide. Crystal structure and relationships to $\text{Ca}_5(\text{PO}_4)_3\text{OH}$ and $\text{K}_3\text{Na}(\text{SO}_4)_2$. *Acta Cryst B* 29:2046–2056
38. Hench LL, Kokubo T (1998) Properties of bioactive glasses and glass-ceramics. In: Black J, Hastings G (eds) *Handbook of Biomaterial Properties*. Chapman & Hall, London, p 355
39. Ohgushi H, Dohi Y, Tamai S, Tabata S (1993) Osteogenic differentiation of marrow stromal stem cells in porous hydroxyapatite ceramics. *J Biomed Mater Res* 27:1401–1407
40. Midy V, Rey C, Bres E, Dard M (1998) Basic fibroblast factor adsorption and release properties of calcium phosphate. *J Biomed Mater Res* 41:405–411
41. Ferry RJ, Cerri RW, Cohen P (1999) Insulin-like growth factor binding proteins: New proteins, new functions. *Horm Res* 51:53–67
42. McCarthy TL, Centrella M, Canalis E (1989) Regulatory effects of insulin-like growth factors I and II on bone collagen synthesis in rat calvarial cultures. *Endocrinology* 124:301–309

43. Davies JE (1996) In vitro modeling of bone/implant interface. *The Anatomical Record* 245:426–445
44. Han DK, Park KD, Jeong SY, Kim YH, Kim UY, Min BG (1993) In vivo biostability and calcification-resistance of surface-modified PU-PEO-SO₃. *J Biomed Mater Res* 27:1063–1073
45. Coleman DL (1981) Mineralization of blood pump bladders. *Trans Am Soc Artif Intern Organs* 27:708–713
46. Schoen FJ, Harasaki H, Kim K, Anderson HC, Levy RJ (1988) Biomaterial-associated calcification: Pathology, mechanisms, and strategies for prevention. *J Biomed Mater Res Appl Biomater* 22(A1):11–36
47. Golomb G (1992) Calcification of polyurethane-based biomaterials implanted subcutaneously in rats: Role of porosity and fluid absorption in the mechanism of mineralization. *J Mater Sci: Mater Med* 3:272–277
48. Srivasta SS, Harrity PJ, Maercklein PB, Kleppe L, Veinot J, Edwards WD, Johnson CM, Fitzpatrick LA (1997) Increased cellular expression of matrix proteins that regulate mineralization is associated with calcification of native human and porcine xenograft. *J Clinical Invest* 99:996–1009
49. Magllion DJ, Lewis JW, Tilley B, Peterson E (1985) The porcine bioprosthetic valve: Twelve years later. *J Thorac Cardiovasc Surg* 89:499–507
50. Nimni ME, Myers D, Ertl D, Han B (1997) Factors which affect the calcification of tissue-derived bioprostheses. *J Biomed Mater Res* 35:531–537
51. Levy R, Schoen FJ, Sherman FS, Nichols J, Hawley MA, Lund SA (1986) Calcification of subcutaneously implanted Type I collagen sponges, Effect of formaldehyde and glutaraldehyde pretreatments. *Am J Pathol* 122:71–82
52. Rao KP, Shanthi C (1999) Reduction of calcification by various treatments in cardiac valves. *J Biomater Appl* 13:238–268
53. Thubrikar MJ, Deck JD, Aouad A, Nolan SP (1983) Role of mechanical stress in calcification of aortic bioprosthetic valve. *J Thorac Cardiovasc Surg* 86:115–125
54. Bernacca GM, Tobasnick G, Wheatley DJ (1994) Dynamic in-vitro calcification of porcine aortic valves. *J Heart Valve Dis* 3:684–687
55. Bernacca GM, Fisher AC, Wilkinson R, Mackay TG, Wheatley DJ (1992) Calcification and stress distribution in bovine pericardial heart valves. *J Biomed Mater Res* 26:959–966
56. Shen M, Marie P, Farge D, Carpentier S, de Pollak C, Hott M, Chen L, Martinet B, Carpentier A (1997) Osteopontin is associated with bioprosthetic heart valve calcification in humans. *C R Acad Sci Paris, Sciences de la vie/Life Sciences* 320:49–57
57. Srivatsa S, Harrity PJ, Maercklein PB, Kleppe L, Veinot J, Edwards WD, Johanson CM, Fitzpatrick LA (1997) Increased cellular expression of matrix proteins that regulate mineralization is associated with calcification of native human and porcine xenograft. *J Clinical Investigation* 99:996–1009
58. McKee MD, Nanci A (1996) Osteopontin at mineralized tissue interfaces in bone, teeth and osseointegrated implants: Ultrastructural distribution and implications for mineralized tissue formation, turnover, and repair. *Microscopy Res and Tech* 33:141–164
59. Schoen FJ, Levy RJ (1999) Tissue heart valves: Current challenges and future research perspectives. *J Biomed Mater Res* 47:439–465

60. van Wachem PB, Zeeman R, Dijkstra PJ, Feijen J, Hendriks M, Cahalan PT, van Luyn MJA (1999) Characterization and biocompatibility of epoxy-cross-linked dermal sheep collagens. *J Biomed Mater Res* 47:270–277
61. van Wachem PB, van Luyn MJA, Olde Damink LHH, Dijkstra PJ, Feijen J, Nieuwenhuis P (1994) Biocompatibility and tissue regenerating capacity of cross-linked dermal sheep collagen. *J Biomed Mater Res* 28:353–363
62. Moore MA, Phillips RE (1997) Biocompatibility and immunologic properties of pericardial tissue stabilized by dye-mediated photooxidation. *J Heart Valve Dis* 6:307–315
63. Fleisch H, Felix R (1979) Diphosphonates. *Calcif Tissue Int* 27:91–94
64. Levy RJ, Wolfrum J, Schoen FJ, Hawley MA, Lund SA, Langer R (1985) Inhibition of calcification of bioprosthetic heart valves by local controlled-release diphosphonate. *Science* 228:190–192
65. Webb CL, Benedict JJ, Schoen FJ, Linden JA, Levy RJ (1988) Inhibition of bioprosthetic heart valve calcification with aminodiphosphonate covalently bound to residual aldehyde groups. *Ann Thorac Surg* 46:309–316
66. Levy RJ, Schoen FJ, Flowers WB, Staelin ST (1991) Inhibition of mineralization in bioprosthetic heart valves: Studies of alkaline phosphatase activity and its inhibition by $AlCl_3$ or $FeCl_3$ preincubations. *J Biomed Mater Res* 25:905–935
67. Chen W, Kim JD, Schoen FJ, Levy RJ (1994) Effect of 2-amino oleic acid exposure conditions on the inhibition of calcification of glutaraldehyde cross-linked porcine aortic valves. *J Biomed Mater Res* 28:1485–1495
68. Boskey AL, Goldberg MR, Posner AS (1979) Effect of diphosphonates on hydroxyapatite formation induced by calcium-phospholipid-phosphate complexes. *Calcif Tissue Int* 27:83–88
69. Hirsch D, Drader J, Thomas TJ, Schoen FJ, Levy JT, Levy RJ (1993) Inhibition of calcification of glutaraldehyde pretreated porcine aortic valve cusps with sodium dodecyl sulfate: preincubation and controlled release studies. *J Biomed Mater Res* 27:1477–1484
70. Vyavahare NR, Hirsch D, Lerner E, Baskin JZ, Schoen FJ, Bianco R, Kruth HS, Zand R, Levy RJ (1997) Prevention of bioprosthetic heart valve calcification by ethanol preincubation: Efficacy and mechanism. *Circulation* 95:479–488
71. Vyavahare NR, Hirsch D, Lerner E, Baskin JZ, Zand R, Schoen FJ, Levy RJ (1998) Prevention of calcification of glutaraldehyde-cross-linked porcine aortic cusps by ethanol preincubation: Mechanistic studies of protein structure and water-biomaterial relationship. *J Biomed Mater Res* 40:577–585
72. Hanawa T, Ota M (1991) Calcium phosphate naturally formed on titanium in electrolyte solution. *Biomaterials* 12:767–774
73. Sundgren JE, Bodö P, Lundström I (1986) Auger electron spectroscopic studies of the interface between human tissue and implants of titanium and stainless steel. *J Colloid Interface Sci* 110:9–20
74. Li P, Ohtsuki C, Kokubo T, Nakanishi K, Soga N, de Groot K (1994) The role of hydrated silica, titania, and alumina in inducing apatite on implants. *J Biomed Mater Res* 28:7–15
75. Kim H-M, Miyaji F, Kokubo T, Nakamura T (1996) Preparation of bioactive Ti and its alloys via simple chemical surface treatment. *J Biomed Mater Res* 32:409–417
76. Hanawa T, Kon M, Ukai H, Murakami K, Miyamoto Y, Asaoka K (1997) Surface modification of titanium in calcium-ion-containing solutions. *J Biomed Mater Res* 34:273–278

77. Hench LL (1991) Bioceramics: From concept to clinic. *J Am Ceram Soc* 74:1487–1510
78. Ohura K, Nakamura T, Yamamuro T, Kokubo T, Ebisawa Y, Kotoura Y, Oka M (1991) Bone-bonding ability of P_2O_5 -free CaO-SiO₂ glasses. *J Biomed Mater Res* 25:357–365
79. Ohtsuki C, Kokubo T, Yamamuro Y (1992) Mechanism of apatite formation on CaO-SiO₂-P₂O₅ glasses in a simulated body fluid. *J Non-Crystal Solids* 143:84–92
80. Li P, Ohtsuki C, Kokubo T, Nakanishi K, Soga N, Nakamura T, Yamamuro T (1992) Apatite formation induced by silica gel in a simulated body fluid. *J Am Ceram Soc* 75:2094–2097
81. Cho SB, Kokubo T, Nakanishi K, Soga N, Ohtsuki C, Nakamura T, Kitsugi T, Yamamuro T (1995) *J Am Ceram Soc* 78:1769–1774
82. Cho SB, Miyaji F, Kokubo T, Nakanishi K, Soga N, Nakamura T (1996) Apatite forming ability of silicate ion dissolved from silica gels. *J Biomed Mater Res* 32:375–381
83. Radder AM, Leenders H, van Blitterswijk CA (1994) Interface reactions to PEO/PBT copolymers (Polyactive TM) after implantaion in cortical bone. *J Biomed Mater Res* 28:141–151
84. Tanahashi M, Tao T, Kokubo T, Minoda M, Miyamoto T, Nakamura T, Yamamuro T (1995) Apatite coated on organic polymers by biomimetic process: Improvement in its adhesion to substrate by glow-discharge treatment. *J Biomed Mater Res* 29:349–357
85. Kato K, Eika Y, Ikada Y (1996) Deposition of a hydroxyapatite thin layer onto a polymer surface carrying grafted phosphate polymer chains. *J Biomed Mater Res* 32:687–691
86. Mucalo MO, Yokogawa Y, Suzuki T, Kawamoto Y, Nagata F, Nishizawa K (1995) Further studies of calcium phosphate growth on phosphorylated cotton fibers. *J Mater Sci: Mater Med* 6:658–669
87. Tanahashi M, Matsuda T (1997) Surface functional group dependence on apatite formation on self-assembled monolayers in a simulated body fluid. *J Biomed Mater Res* 34:305–315
88. Unuma H, Ito K, Oka T, Takahashi M (1996) Precipitation of hydroxyapatite under stearic acid monolayers. *J Am Ceram Soc* 79:2474–2476
89. Yamashita K, Oikawa N, Umegaki T (1996) Acceleration and deceleration of bone-like crystal growth on ceramic hydroxyapatite by electric poling. *Chem Mater* 8:2697–2700
90. Wu W, Nancollas GH (1998) Factors controlling crystallization of calcium phosphates on solid surfaces. In: LeGeros RZ, LeGeros JP (eds) *Bioceramics*, Vol 11, Proc 11th International Sym Ceram in Med. World Scientific, Singapore, pp 469–472
91. Wu W, Nancollas GH (1998) Kinetics of heterogeneous nucleation of calcium phosphates on anatase and rutile surfaces. *J Colloid Inter Sci* 199:206–211
92. Bradt J-H, Mertig M, Teresiak A, Pompe W (1999) *Chem Mater* 11:2694–2701
93. Tsortos A, Nancollas GH (1999) The adsorption of polyelectrolytes on hydroxyapatite crystals. *J Colloid Inter Sci* 209:109–115
94. Banks E, Nakajima S, Shapiro LC, Tilevitz O, Alonzo JR, Chianell RP (1977) Fibrous apatite grown on modified collagen. *Science* 198:1164–1166
95. Doi Y, Horiguchi T, Moriwaki Y, Kitago H, Kajimoto T, Iwayama Y (1996) Formation of apatite-collagen complexes. *J Biomed Mater Res* 31:43–49

96. Walsh D, Hopwood JD, Mann S (1994) Crystal tectonics: Construction of reticulated calcium phosphate frameworks in bicontinuous reverse microemulsions. *Science* 264:1576–1578
97. Walsh D, Mann S (1996) Chemical synthesis of microskeletal calcium phosphate in bicontinuous microemulsions. *Chem Mater* 8:1944–1953
98. Monma H, Kanazawa T (1976) The hydration of α -tricalcium phosphate. *J Ceram Soc Jpn* 84:209–213
99. Yamamoto H, Niwa S, Hori M, Hattori T, Sawai K, Aoki S, Hirano M, Takeuchi H (1998) Mechanical strength of calcium phosphate cement in vivo and in vitro. *Biomaterials* 19:1587–1591
100. Brown WE, Chow LC (1985) US Pat 4518430
101. Chow LC (1991) Development of self-setting calcium phosphate cements. *J Ceram Soc Jpn* 99:954–964
102. Ishikawa K, Takagi S, Chow LC, Suzuki K (1999) Relation of calcium phosphate cements with different amount of tetracalcium phosphate and dicalcium phosphate anhydrous. *J Biomed Mater Res* 46:504–510
103. Constantz BR, Ison IC, Fulmer MT, Poser RD, Smith ST, Van Wagoner M, Ross J, Goldstein SA, Jupiter JB, Rosenthal DI (1995) Skeletal repair by *in situ* formation of the mineral phase of bone. *Science* 267:1796–1799
104. Rathje W (1939) Zur Kenntnis de Phosphate I. Uber Hydroxyapatite. *Bodenk Pflernah* 12:121–128
105. Akao M, Aoki H, Kato K (1981) Mechanical properties of sintered hydroxyapatite for prosthetic application. *J Mater Sci* 16:809–812
106. Skinner HCW (1974) Studies in the basic mineralizing system $\text{CaO-P}_2\text{O}_5\text{-H}_2\text{O}$. *Calcif Tissue Res* 14:3–14
107. Elliott JC (1994) Structure and chemistry of the apatites and other calcium orthophosphates. Elsevier, Amsterdam, pp 137–138
108. Biggar GM (1966) Experimental studies of apatite crystallization in parts of the system $\text{CaO-P}_2\text{O}_5\text{-H}_2\text{O}$ at 1000 bar. *Min Mag* 35:1110–1122
109. Ito A, Nakamura S, Aoki H, Akao M, Teraoka K, Tsutsumi S, Onuma K, Tateishi T (1996) Hydrothermal growth of carbonate-containing hydroxyapatite single crystals. *J Crystal Growth* 163:311–317
110. Perloff A, Posner AS (1956) Preparation of pure hydroxyapatite crystals. *Nature* 124:583–584
111. Arends J, Schuthof J, Van der Linden WH, Bennema P, Van den Berg PJ (1979) Preparation of pure hydroxyapatite single crystals by hydrothermal recrystallization. *J Crystal Growth* 46:213–220
112. Roy DM (1971) Crystal growth of hydroxyapatite. *Mat Res Bull* 6:1337–1340
113. Teraoka K, Ito A, Onuma K, Tateishi T, Tsutusmi S (1999) Hydrothermal growth of hydroxyapatite single crystals under natural convection. *J Mater Res* 14:2655–2661
114. Mengerot M, Harvill ML (1973) Gilliam OR, Hydrothermal growth of calcium hydroxyapatite single crystals. *J Crystal Growth* 19:199–203
115. Roy DM, Eysel W, Dinger D (1974) Hydrothermal synthesis of various carbonate containing calcium hydroxyapatites. *Mat Res Bull* 9:35–40
116. Suetsugu Y, Tanaka J (1999) Crystal growth of cabonated apatite using a CaCO_3 flux. *J Mater Sci, Mater in Med* 10:561–566
117. Brindley GW, Zussman J (1957) A structural study of the thermal transformation of serpentine minerals to forsterite. *Am Miner* 42:461–474

118. Suchanek W, Suda H, Yashima M, Kakihana M, Yoshimura M (1995) Biocompatible whiskers with controlled morphology and stoichiometry. *J Mater Res* 10:521–529
119. Teraoka K, Ito A, Maekawa K, Onuma K, Tateishi T, Tsutsumi S (1998) Mechanical properties of hydroxyapatite and OH-carbonated hydroxyapatite single crystals. *J Dent Res* 77:1560–1568
120. Roy DM, Linnehan SK (1974) Hydroxyapatite formed from coral skeletal carbonate by hydrothermal exchange. *Nature* 247:220–222
121. Eysel W, Roy DM (1975) Topotactic reaction of aragonite to hydroxyapatite. *Z Kristallogr* 141:11–24
122. Fujisawa R, Kuboki Y (1998) Bone matrix proteins. *Nihon-Rinsyo* 56:1425–1429 (in Japanese)
123. Boskey AL, Maresca M, Doty S, Sabsay B, Veis A (1990) Concentration-dependent effects of dentin phosphophoryn in the regulation of in vitro hydroxyapatite formation and growth. *Bone and Miner* 11:55–65
124. Boskey AL (1998) Biomineralization: Conflicts, challenges and opportunities. *J Cell Biochem Suppl* 30/31:83–91
125. Knott L, Bailey AJ (1998) Collagen cross-links in mineralizing tissues: A review of their chemistry, function and clinical relevance. *Bone* 22:181–187
126. Katz EP, Li S-T (1973) Structure and function of bone collagen fibrils. *J Mol Biol* 80:1–15
127. Landis W (1996) Mineral Characterization in calcifying tissue: Atomic, molecular and macromolecular perspectives. *Connective Tissue Res* 34:239–246
128. Robey PG (1996) Vertebrate mineralized matrix proteins: Structure and function. *Connective Tissue Res* 35:131–136
129. Dimuzio MT, Veis A (1978) Major noncollagenous proteins of rat incisor dentin. *Calcif Tissue Res* 25:169–178
130. Fuierer TA, LoRe M, Puckett SA, Nancollas GH (1994) A mineralization adsorption and mobility study of hydroxyapatite surface in the presence of zinc and magnesium ions. *Langmuir* 10:4721–4725
131. LeGeros RZ, Bleiwas CB, Retino M, Rohanizadeh R, LeGeros JP (1999) Zinc effect on the in vitro formation of calcium phosphates: relevance to inhibition of calculus formation. *Am J Dent* 12:65–71
132. Kanzaki N, Onuma K, Treboux G, Tsutsumi S, Ito A (2000) Inhibitory effects of magnesium and zinc on crystallization kinetics of hydroxyapatite (0001) face. *J Phys Chem B* 104:4189–4194
133. Yamaguchi M, Oishi H, Suketa Y (1987) Stimulatory effect of zinc on bone formation in tissue culture. *Biochem Pharmacol* 36:4007–4012
134. Kishi S, Yamaguchi S (1994) Inhibitory effect of zinc compounds on osteoclast-like cell formation in mouse marrow culture. *Biochem Pharmacol* 48:1225–1230
135. Ito A, Ojima K, Naito H, Ichinose N, Tateishi T (2000) Preparation, solubility and cytocompatibility of zinc-releasing calcium phosphate ceramics. *J Biomed Mater Res* 50:178–183
136. Kawamura H, Ito A, Miyakawa S, Layrolle P, Ojima K, Ichinose N, Tateishi T (2000) Stimulatory effect of zinc-releasing calcium phosphate ceramic on bone formation in rabbit femora. *J Biomed Mater Res* 50:184–190
137. Hunter GK, Hauschka PV, Poole AR, Rosenberg LC, Goldberg HA (1996) Nucleation and inhibition of hydroxyapatite formation by mineralized tissue proteins. *Biochem J* 317:59–64

138. Hunter GK, Kyle CL, Goldberg HA (1994) Modulation of crystal formation by phosphoproteins: Structural specificity of the osteopontin-mediated inhibition of hydroxyapatite formation. *Biochem J* 300:723–728
139. Boskey AL, Maresca M, Ullrich W, Doty SB, Butler WT, Prince CW (1993) Osteopontin-hydroxyapatite interactions in vitro: Inhibition of hydroxyapatite formation and growth in a gelatin-gel. *Bone and Miner* 22:147–159
140. Price PA, Otsuka AS, Posner JW, Kristaponis J, Raman N (1976) Characterization of a γ -carboxyglutamic acid-containing protein from bone. *Proc Natl Acad Sci USA* 73:1447–1451
141. Doi Y, Horiguchi T, Kim S-H, Morikawa Y, Wakamatsu N, Adachi M, Ibaraki K, Moriyama K, Sasaki S, Shimokawa H (1992) Effects of non-collagenous proteins on the formation of apatite in calcium β -glycerophosphate solutions. *Arch Oral Biol* 37:15–21
142. Ducy P, Desbois C, Boyce B, Pinero G, Story B, Dunstan C, Smith E, Bonadio J, Goldstein S, Gundberg C, Bradley A, Karsenty G (1996) Increased bone formation in osteocalcin-deficient mice. *Nature* 382:448–452
143. Romberg RW, Werness PG, Riggs BL, Mann KG (1986) Inhibition of hydroxyapatite crystal growth by non-specific and other calcium-binding proteins. *Biochemistry* 25:1176–1180
144. Boskey AL, Wians FH, Hauschka PV (1985) The effect of calcification on in vitro lipid-induced hydroxyapatite formation and seeded hydroxyapatite growth. *Calcif Tissue Int* 37:57–62
145. Doi Y, Horiguchi T, Kim S-H, Morikawa Y, Wakamatsu N, Adachi M, Shigeta H, Sasaki S, Shimokawa H (1993) Immobilized DPP and other proteins modify OCP formation. *Calcif Tissue Int* 52:139–145
146. Linde A, Lussi A, Crenshaw MA (1989) Mineral induction by immobilized polyanionic proteins. *Calcif Tissue Int* 44:286–295
147. Fujisawa R, Kuboki Y (1991) Preferential adsorption of dentin and bone acidic proteins on the (100) face of hydroxyapatite crystals. *Biochem Biophys Acta* 1075:56–60
148. Fujisawa R, Kuboki Y (1992) Affinity of bone sialoprotein and several other bone and dentin acidic proteins to collagen fibrils. *Calcif Tissue Int* 51:438–442
149. Romberg RW, Werness PG, Lollar P, Riggs BL, Mann KG (1985) Isolation and characterization of native adult osteonectin. *J Biol Chem* 260:2728–2736
150. Menanteau J, Neuman WF, Neuman MW (1982) A study of bone proteins which can prevent hydroxyapatite formation. *Metab Bone Dis Rel Res* 4:157–162
151. Doi Y, Okuda R, Takezawa Y, Shibata S, Morikawa Y, Wakamatsu N, Shimizu N, Moriyama K, Shimokawa H (1989) *Calcif Tissue Int* 44:200–208
152. Termine JD, Kleinman HK, Whitson SW, Conn KM, McGarvey ML, Martin GR (1981) Osteonectin, a bone-specific protein linking mineral to collagen. *Cell* 26:99–105
153. Veis A (1993) Mineral-matrix interactions in bone and dentin. *J Bone Min Res* 8:S493–S497
154. Termine JD, Eanes ED, Conn KM (1980) Phosphoprotein modulation of apatite crystallization. *Calcif Tissue Int* 31:247–251
155. Mash ME (1989) Binding of calcium and phosphate ions to dentin phosphophoryn. *Biochemistry* 28:346–352
156. Lussi A, Crenshaw MA, Linde A (1988) Induction and inhibition of hydroxyapatite by rat dentine phosphoprotein in vitro. *Arch Oral Biol* 9:685–691

157. van den Bos T, Steinfort J, Beertsen W (1993) Effect of bound phosphoproteins and other organic phosphates on alkaline phosphate-induced mineralization of collagenous matrices in vitro. *Bone and Miner* 23:81–93
158. Hunter GK, Goldberg HA (1993) Nucleation of hydroxyapatite by bone sialoprotein. *Natl Acad Sci USA* 90:8562–8565
159. Oldberg Å, Franzén A, Heinegård D (1988) The primary structure of a cell-binding bone sialoprotein. *J Biol Chem* 263:19430–19432
160. Zhou H-Y, Takita H, Fujisawa R, Mizuno M, Kuboki Y (1995) Stimulation by bone sialoprotein of calcification in osteoblast-like MC3T3-E1 cells. *Calcif Tissue Int* 56:403–407
161. Doi Y, Eanes ED, Shimokawa H, Termine JD (1984) Inhibition of seed growth of enamel apatite crystal growth by amelogenin and enamelin protein in vitro. *J Dent Res* 63:98–105
162. Aoba T, Fukae M, Tanabe T, Shimizu M, Moreno EC (1987) Selective adsorption of porcine-amelogenins onto hydroxyapatite and their inhibitory activity on hydroxyapatite growth in supersaturated solutions. *Calcif Tissue Int* 41:281–289
163. Bigi A, Foresti E, Gandolfi M, Gazzano A, Roveri N (1995) Inhibiting effect of zinc on hydroxylapatite crystallization. *J Inorg Biochem* 58:49–58
164. Yamaguchi M, Igarashi A (1999) Increase in bone protein components with healing rat fractures: Enhancement by zinc treatment. *Int J Mol Med* 4:615–620
165. Hirsch D, Azoury R, Sarig S, Kruth HS (1993) Colocalization of cholesterol and hydroxyapatite in human atherosclerotic lesions. *Calcif Tissue Int* 52:94–98
166. Craven BM (1976) Crystal structure of cholesterol monohydrate. *Nature* 260:727–729
167. Hirsch D, Azoury R, Sarig S (1990) Co-crystallization of cholesterol and calcium phosphate as related to atherosclerosis. *J Crystal Growth* 104:759–765
168. Rumberger JA, Sheedy PF, Breen AF, Fitzpatrick LA, Schwartz RS (1996) Electron beam computed tomography and coronary artery disease: Scanning for coronary artery calcification. *Mayo Clin Proc* 71:369–377
169. Boström K, Watson KE, Stanford WP, Demer LL (1995) Atherosclerotic calcification: Relation to developmental osteogenesis. *Am J Cardiology* 75:88B–91B
170. Parhami F, Boström K, Watson K, Demer LL (1996) Role of molecular regulation in vascular calcification. *J Atheroscler and Thromb* 3:90–94
171. Severson AR, Ingram RT, Schwartz RS, Fitzpatrick LA (1993) Matrix proteins associated with bone calcification are present in human aortic vascular smooth muscle cells [abstract]. *Circulation* 88(Suppl 1):I-367
172. White DJ (1997) Dental calculus: Recent insights into occurrence, formation, prevention, removal and oral health effects of supragingival and subgingival deposits. *Eur J Oral Sci* 105:508–522
173. Daculsi G, Bouler J-M, Legeros RZ (1997) Adaptive crystal formation in normal and pathological calcifications in synthetic calcium phosphate and related biomaterials. *Internl Review of Cytology* 172:129–191
174. Mandel ID (1974) Biochemical aspects of calculus formation: Comparative studies of plaque in heavy and light calculus formers. *J Periodont Res* 9:10–17
175. Schamschula RG, Pearce EIF, Un PSH, Cooper MH (1985) Immediate and delayed effects of enzyme dependent mineralizing mouthrinse on dental plaque. *J Dent Res* 64:454–456

176. Hidaka S, Okamoto Y, Abe K (1993) Possible regulatory roles of silicic acid, silica and clay minerals in the formation of calcium phosphate precipitates. *Arch Oral Biol* 38:405–413
177. Murphy BT, Pyrah LN (1962) The composition, structure and mechanisms of the formation of urinary calculi. *British J Urology* 34:129–159
178. Mandel N (1996) Mechanism of stone formation. *Semin Nephrol* 16:364–374
179. Zhang J-W, Nancollas GH (1990) Mechanism of growth and dissolution of sparingly soluble salts In: Hochella Jr MF, White AF (eds) *Mineral-Water Interface Geochemistry*. Mineralogical Soc Am, Washington, DC, pp 365–396
180. Thomson MB, Nancollas GH (1978) Mineralization kinetics: A constant composition approach. *Science* 200:1059–1060
181. Koutsoukos P, Amjad Z, Tomson MB, Nancollas GH (1980) Crystallization of calcium phosphates. A constant composition study. *J Am Chem Soc* 102:1553–1557
182. Nancollas GH, Mohan MS (1970) The growth of hydroxyapatite crystals. *Archs Oral Biol* 15:731–745
183. Nancollas GH, Tomazic B (1974) Growth of calcium phosphate on hydroxyapatite crystals. Effect of supersaturation and ionic medium. *J Phys Chem* 78:2218–2225
184. Wu W, Nancollas GH (1999) Determination of interfacial tension from crystallization and dissolution data: A comparison with other methods. *Adv Collid Inter Sci* 79:229–279
185. Hohl H, Koutsoukos PG, Nancollas GH (1982) The crystallization of hydroxyapatite and dicalcium phosphate dihydrate: Representation of growth curves. *J Crystal Growth* 57:325–335
186. Somasundaran P (1968) Zeta potential of apatite in aqueous solutions and its change during equilibration. *J Coll Inter Sci* 27:659–666
187. Saleeb FZ, de Bruyn PL (1972) Surface properties of alkaline earth apatites. *Electroanal Chem Inter Electrochem* 37:99–118
188. Onuma K, Ito A, Tateishi T, Kameyama T (1995) Growth kinetics of hydroxyapatite crystal revealed by atomic force microscopy. *J Crystal Growth* 154:118–125
189. Kanzaki N, Onuma K, Ito A, Teraoka K, Tateishi T, Tsutsumi S (1998) Direct growth rate measurement of hydroxyapatite single crystal by Moire phase shift interferometry. *J Phys Chem B* 34:6471–6476
190. Onuma K, Ito A, Tateishi T (1996) Investigation of a growth unit of hydroxyapatite crystal from the measurements of step kinetics. *J Crystal Growth* 167:773–776
191. Onuma K, Kanzaki N, Ito A, Tateishi T (1998) Growth kinetics of the hydroxyapatite (0001) face revealed by phase shift interferometry and atomic force microscopy. *J Phys Chem B* 40:7833–7838
192. Onuma K, Ito A (1998) Cluster growth model for hydroxyapatite. *Chem Mater* 10:3346–3351
193. Oyane A, Onuma K, Kokubo T, Ito A (1999) Clustering of calcium phosphate in the system $\text{CaCl}_2\text{-H}_3\text{PO}_4\text{-KCl-H}_2\text{O}$. *J Phys Chem B* 39:8230–8235
194. Oyane A, Onuma K, Kokubo T, Ito A (1999) Clustering of calcium phosphate in SBF and in the system $\text{CaCl}_2\text{-H}_3\text{PO}_4\text{-KCl-H}_2\text{O}$. In: Ohnishi H, Hastings GW, Yoshikawa T (eds) *Bioceramics*, Vol 12, Proc 12th International Sym Ceram in Med. World Scientific, Singapore, pp 157–160
195. Söhnle O, Garside J (1988) Solute clustering and nucleation. *J Crystal Growth* 89:202–208

196. Treboux G, Kanzaki N, Onuma K, Ito A (1999) Energy-preeminent isomer of the $\text{Ca}_3(\text{PO}_4)_2$ cluster. *J Phys Chem A* 40:8118–8120

17 Crystal Growth of Gemstones

Shuji Oishi

Department of Environmental Science and Technology, Faculty of Engineering,
Shinshu University, Wakasato, Nagano 380-8553, Japan

17.1 Introduction

Gemstones are usually used for human ornamentation. Diamond (C), ruby ($\text{Al}_2\text{O}_3:\text{Cr}$), and emerald ($\text{Be}_3\text{Al}_2\text{Si}_6\text{O}_{18}:\text{Cr}$) are well-known gemstones. The gemstones are principally natural minerals that are highly valued for their beauty, durability, and rarity. Portability is also required for the use of gem materials. The majority of gemstones are single crystals of minerals. As an example of natural minerals, spessartine garnet crystals found at Wada-toge Pass, Nagano Prefecture, Japan, are shown in Fig. 17.1. The garnet crystals have a beautiful glassy luster, and are black and opaque. They can be used for ornamental purposes without cutting. Other gemstones are not single crystals. Opal is one of the best-known non-crystalline gemstones. Natural minerals of good quality are getting scarce with the passing of time.

The high value placed on gemstones for use in jewelry has led to many attempts to synthesize natural gemstones. The duplication of beautiful gemstones in the laboratory has been one of man's aims. Manmade and natural gemstones have the same chemical composition and crystal structure. Ruby crystals were grown by the flux method in 1837 by Gaudin [1]. He grew ruby crystals of up to 0.187 g from molten potassium alum and potassium chromate. Small emerald crystals were grown from lithium molybdate and lithium vanadate fluxes in 1888 by Hautefeuille and Perrey [2]. The method involving use of flame fusion was developed in 1902 by Verneuil [3]. The method of pulling from the melt was first developed in 1918 by Czochralski [4]. A lot of scientists tried to grow diamond crystals. A reproducible synthesis of diamond was first reported in 1955 by Bundy et al. [5]. Metallic solutions at high pressure and high temperature were used to grow diamond crystals. A listing of major single crystal gemstones used in jewelry, which have been successfully grown as synthetics is given in Table 17.1. Many other gemstones such as spinel (MgAl_2O_4) and rutile (TiO_2) crystals have also been grown. Crystal growth is progressing gradually from an art to a science. Now, synthetic gemstones are marketed on a large scale. Figure 17.2 shows synthetic ruby and sapphire (pure Al_2O_3 or Al_2O_3 doped with transition elements) cut stones. Synthetic star ruby and sapphire stones are shown in Fig. 17.3. Synthetic gem-

stones are also used in electronics devices. Excellent books and reviews that deal with the crystal growth and characterization of gemstones have been published by Elwell and Scheel [6], Elwell [4], Nassau and Nassau [7], and O'Donoghue [8]. A comparison of natural gem materials with synthetic ones has been described by Sunagawa [9] earlier and also in Chapter 1 of this book.

This chapter describes a simple method of growing crystal gemstones. An outline of the growth methods is given. The flux method is mentioned in some detail since the stones produced closely resemble the natural gems. The flux growth of emerald crystals as an example of gemstones is described. Growth of emerald crystals by the flux evaporation technique is introduced to make a collection of man-made gemstones. You can grow beautiful emerald crystals with a minimum of equipment and information.

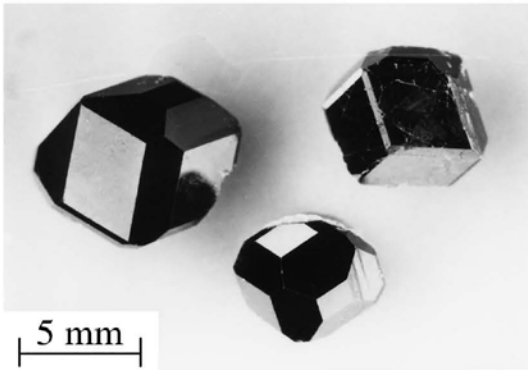


Fig. 17.1. Natural garnet crystals found at Wada-toge Pass, Nagano Prefecture, Japan



Fig. 17.2. Synthetic ruby and sapphire cut stones

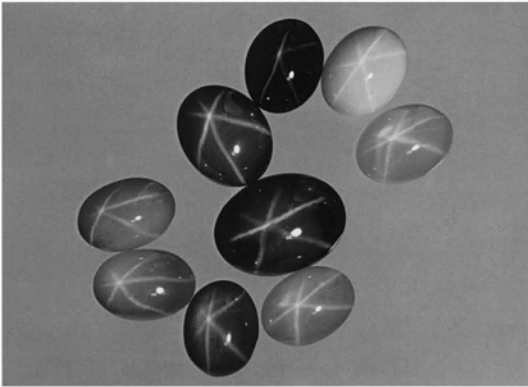


Fig. 17.3. Synthetic star ruby and sapphire stones

Table 17.1. Major Single Crystal Gemstones and the Growth Methods

Gemstone	Mineral	Chemical Formula	Growth Method
Diamond	Diamond	C	High Pressure
Emerald, Aquamarine	Beryl	$\text{Be}_3\text{Al}_2\text{Si}_6\text{O}_{18}$	Hydrothermal, Flux
Quartz	Quartz	SiO_2	Hydrothermal
Ruby, Sapphire	Corundum	Al_2O_3	Verneuil, Czochralski, Hydrothermal, Flux

17.2 Growth Methods of Gemstones

Matter may exist in three states of aggregation — solid, liquid, or gas. Solids have rigidity, fixed shape, and mechanical strength. A crystalline solid is characterized by long-range order extending over many atom diameters. Crystals are by no means grown at equilibrium. Crystal growth of gemstones involves precise control of a phase change. The growth requires that the equilibrium is displaced very slightly in the direction of the intended solid. This is usually accomplished by careful control of the temperature. After a stable nucleus has been formed, it grows at a rate fixed by the conditions of temperature and the degree of supersaturation or supercooling.

Crystal growth processes may be divided into three main categories: (1) growth from the solid (solid \rightarrow crystal), (2) growth from the liquid (liquid \rightarrow crystal), and (3) growth from the vapor (vapor \rightarrow crystal). Solid-state growth (1) requires atomic diffusion in the crystalline solid. Even at high temperatures, the rate of diffusion is usually very low. Therefore, the solid-state growth technique is seldom

employed to grow large crystals. Vapor growth (3) is often the technique by which whiskers or thin film crystals can be formed. Growth from the liquid (2) has been used to advantage in growing large crystals. It is convenient to divide growth from the liquid into two classes according to whether the liquid involved is composed only of the same components as the crystal (a melt) or components in addition to those contained in the crystal (a solution). The rate of growth from the melt is normally much higher than that from the solution. Melt growth can produce large crystals and is commercially the most important method of crystal growth. The principal advantage of growth from solution is that crystal growth occurs at a lower temperature than that required for melt growth. Another advantage of solution growth is that the crystal can grow with well-developed faces. The solubility data of solutes in fluxes are very important to grow crystals. The use of phase diagrams in crystal growth has been mentioned [10]. Excellent books and reviews on various growth methods have been published by Pamplin [11,12], Laudise [13], and Byrappa and Yoshimura [14].

Major techniques for the crystal growth of gemstones from melts are the Verneuil and Czochralski methods. Typical growth techniques from solutions are the hydrothermal and flux methods. These methods are outlined below and a relatively detailed description of flux growth is given.

17.2.1 Verneuil method

The Verneuil technique is a commercial method for growing gemstones. It was developed in 1902 by Verneuil [3]. The principle of the method is schematically shown in Fig. 17.4. The apparatus is basically an oxyhydrogen torch through which powders of the material to be grown are passed. The powders melt in the flame and form a small puddle on a seed crystal. The crystal is grown on the seed crystal, which is lowered as the crystal builds up. The form of the crystal grown by the Verneuil method is cylindrical.

The Verneuil method has the great advantage of being crucible less. In addition, it can grow larger crystals of gemstones at higher temperatures than any other technique. The upper temperature is limited by the oxyhydrogen flame temperature. By regulating the H_2/O_2 ratio in the flame, one can sometimes grow oxide crystals that are difficult to prepare in other methods. Because the method is non-conservative, solid solutions of uniform composition can be grown. A disadvantage is that the growing crystal is exposed to a steep temperature gradient. Some of grown crystals have consequently been broken into pieces.

Shinkosha Co., Ltd., Japan, has produced ruby and sapphire crystals by the Verneuil method. Red and transparent ruby boules grown are shown in Fig. 17.5. The synthetic ruby, sapphire, star ruby, and star sapphire crystals shown in Figs. 17.2 and 17.3 were also grown by this method.

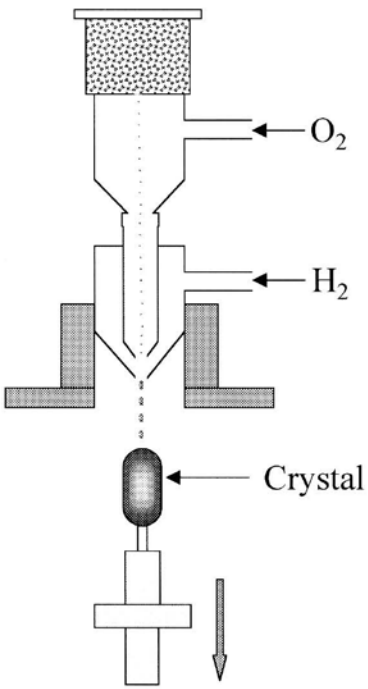


Fig. 17.4. Schematic diagram of Verneuil apparatus

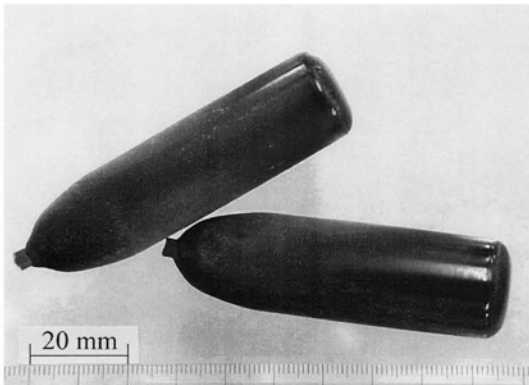


Fig. 17.5. Ruby boules grown by Verneuil method

17.2.2 Czochralski method

The Czochralski technique is a popular method of crystal growth because it can produce large and dislocation-free crystals in a relatively short time. The principle of the method is schematically shown in Fig. 17.6. The material to be grown is molten in a crucible. A seed crystal is then dipped into the melt and slowly withdrawn. The seed is rotated at the same time in order to attain thermal symmetry and also to stir the melt. The crystals grown by the Czochralski method have the form of a cylinder. With semiconductor silicon material, the Czochralski method is a very important process.

The opportunity to grow crystals of many orientations is one of the major advantages of the Czochralski method. Another advantage is that separation of the crystal from the melt is not necessary. Still another advantage is that by pulling small crystals from large melts one can minimize the compositional change in solid solution crystals. However, considerable operator skill is necessary for crystal pulling. The method requires a crucible, so contamination can be a problem, and atmosphere control is complicated. Furthermore, the equipment is usually expensive since it requires very well designed and constructed motors and mechanisms for rotation and withdrawal of the crystals.

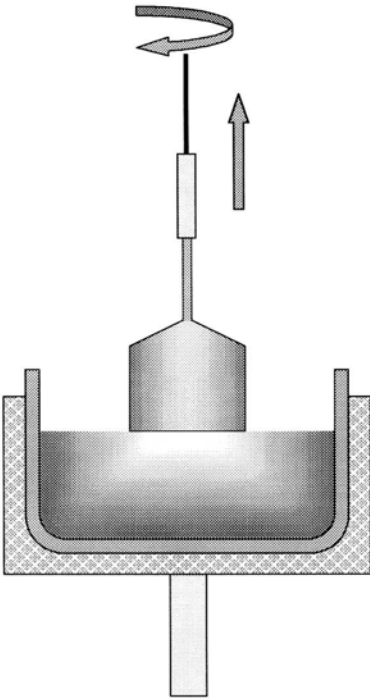


Fig. 17.6. Schematic diagram of Czochralski apparatus

17.2.3 Hydrothermal method

Hydrothermal technique is a method of crystal growth from a solution in water at high temperatures and pressures [13,14,15]. Spezia made the first attempt to produce quartz (SiO_2) crystals on the seed crystals in the system $\text{SiO}_2\text{-H}_2\text{O}$ [14,15]. Since then hydrothermal systems involving quartz have been studied extensively because of the economic importance of piezoelectric quartz devices. The basic hydrothermal process is essentially a solution growth by temperature gradient transfer. Small quartz nutrient is placed in the bottom of the vessel (autoclave) and seed crystals of quartz are suspended in the upper growth region. The vessel is filled to some predetermined fraction of its free volume, typically 0.8 with a dilute basic solution such as 0.5 M NaOH. The vessel is placed in a furnace that has been designed to heat the lower dissolving section isothermally hotter than the upper growth region, which is also maintained isothermal. A typical example of quartz crystal hydrothermally grown on an industrial scale is shown in Fig. 17.7. The colorless and transparent crystal is surrounded by well-developed faces.

There are practical advantages to the technique. The modest temperature required and the large thermal mass of the autoclave permit the use of simple and inexpensive furnaces and controllers. Although autoclaves are expensive, they have a long life if handled carefully. A disadvantage of the method is the possibility of incorporating H_2O or OH^- in the crystals.



Fig. 17.7. Quartz crystal hydrothermally grown

17.2.4 Flux method

Flux growth is a method by which a wide range of gemstones may be obtained with less sophisticated equipment and information. Components of the gem material desired in the single crystal form are dissolved in a flux (solvent). A flux permits the growth to proceed at temperatures well below the melting point of the solute phase. This reduction in temperature is the principal advantage of flux

growth over growth from the pure melt. Excellent books and reviews have been published by Chase [16], Elwell and Scheel [6], Elwell [17,18], and Wanklyn [19].

A reduction in the temperature is desirable for the growth of a wide range of materials, in particular those in the following categories:

- a. Materials which are incongruently melting
- b. Materials which have a very high melting point
- c. Materials which undergo a phase transition
- d. Materials which have a very high vapor pressure at the melting point
- e. Materials which have a very volatile constituent

Other advantages of flux growth are based on the fact that the growing crystal is not exposed to steep temperature gradients and that the crystal can grow free from mechanical or thermal strain into the solution. Therefore, well-formed crystals are grown. The disadvantages of the method are substitutional or interstitial incorporation of flux ions into the crystal, inclusions of flux or impurities, and a slow growth rate.

The choice of flux is difficult because very little work has been done to date concerning the solubility of the solute in flux at high temperatures. From the solubility point, a good flux should be chemically similar concerning the type of bonding to the solute. On the other hand, crystal-chemical differences should exist in order to prevent solid solubility between the solute and flux. There are no fixed rules for choosing a suitable flux. One of the easiest starting points for choosing a flux is to study information contained in phase diagrams [20]. Another useful practice is to survey the literature for fluxes that have been used for similar compounds. In many cases, this approach will yield a suitable flux. In this way, the flux has been normally chosen by trial and error procedures, taking into account previous experiences. On the other hand, a guide to the choice of suitable fluxes for the crystal growth of oxides was proposed [21]. In this guide, the criteria have been formulated using some fundamental information, such as ionic radius, melting point, ionicity of chemical bondings, Dietzel's parameter, and acidity and basicity.

In the flux growth, supersaturation can be obtained by a slow cooling, by flux evaporation or by the temperature gradient technique. The flux growth can be classified into three techniques.

1. *Slow Cooling Technique*: The most common technique for producing supersaturation in flux growth is by slow cooling of the solution. In general, a linear cooling rate of 1 to 10°C/h is applied. The slower the cooling rate is, the better and larger the crystals are. The slow cooling technique is relatively simple for the growth of known and also new crystals up to mm size. The technique is highly suitable for exploratory materials research.
2. *Flux Evaporation Technique*: Flux evaporation could be generally used to grow crystals, which show a low variation of solubility with temperature. Since flux evaporation may be carried out isothermally, this technique offers the advantages connected with growth at constant temperature. As shown in Fig. 17.8,

the temperature program is very simple. An approximately constant concentration of equilibrium defects and homogeneous incorporation of dopants can be expected.

3. *Temperature Gradient Technique*: This technique is suitable for the growth of large crystals. Growth experiments have been performed with the knowledge of the appropriate solubility data. The principle of the temperature gradient technique is similar to that of hydrothermal growth of quartz crystals. Nutrient is held at the bottom (hotter region) in a solution. By natural or forced convection, a flow of solution occurs towards a cooler region where a seed crystal is held, the solution becomes supersaturated and crystal grows on the seed crystal.

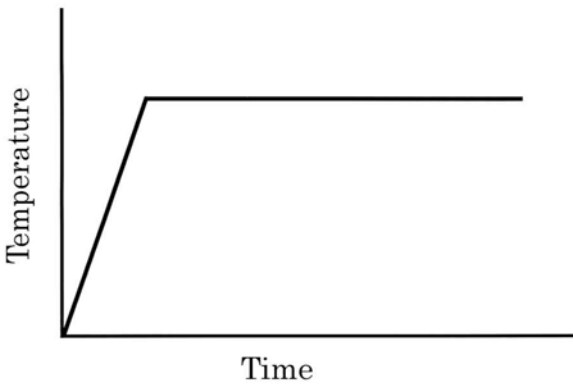


Fig. 17.8. Temperature program of flux evaporation experiment

17.3 Emerald

17.3.1 Growth of emerald crystals

Emerald ($\text{Be}_3\text{Al}_2\text{Si}_6\text{O}_{18}:\text{Cr}$) has been regarded as a beautiful and attractive gemstone from olden times. Emerald is a beryl ($\text{Be}_3\text{Al}_2\text{Si}_6\text{O}_{18}$, beryllium aluminum silicate) doped with chromium. The chromium gives emerald its characteristic green color. The emerald crystals belong to the hexagonal system with space group $P6/mcc$ [22].

Like diamond, emerald has been the object of many attempted syntheses. Synthetic emerald crystals have always been of considerable interest for gemstones. There has been a paper focused only on synthetic emerald crystals [23]. Emerald melts incongruently at high temperature [24]. In spite of this problem, Gentile and his colleagues have grown emerald crystals by the Verneuil method [25]. A boule several inches in length and 0.5 inch in diameter was grown in three to four hours. Crystal growth of emerald has been made by using a high-pressure temperature

technique [26,27]. Emerald crystals have also been produced by the hydrothermal method on a commercial basis [4,8]. By the flux method, the first successful synthesis of emerald crystals was reported in 1888 by Hautefeuille and Perrey [2]. The flux process for emerald crystals was developed by Espig, Zerfass, Nacken, Chatham, and Gilson [4,7,8,23]. The growth of emerald crystals from fluxes is particularly attractive because it readily allows the growth. There have been a number of investigations into the flux growth of emerald crystals. The following fluxes have been used:

MoO₃ [28,29]
Li₂O-MoO₃ [2,29,30,31,32,33,34,35,36]
K₂O-MoO₃ [37,38]
MoO₃-B₂O₃ [39]
PbO-MoO₃ [4,40]
Li₂O-WO₃ [4,30]
PbO-WO₃ [4,40]
PbO-PbF₂ [29]
V₂O₅ [30,31,40,41,42,43,44]
Li₂O-V₂O₅ [2,33]
PbO-V₂O₅ [31,45,46,47]
B₂O₃ [6,29]

In particular, Li₂O-MoO₃ and V₂O₅ fluxes have been successfully used by the slow cooling and temperature gradient techniques, respectively. We have grown emerald crystals from a PbO-V₂O₅ flux by a slow cooling method [46]. Large emerald crystals weighing 150 ct have been grown on seeds from the PbO-V₂O₅ flux by controlled crystallization [47]. However, the flux is too time-consuming to dissolve the solidified flux in hot nitric acid. In addition, Pb and V are toxic to human beings.

Little work has been reported on the growth of emerald crystals by the flux evaporation method. Because flux evaporation may be carried out isothermally, this technique offers the advantages connected with the growth at constant temperature; for example, the temperature control is very easy. Growth of emerald crystals from pure MoO₃ flux has been reported only very briefly with no description of the experimental conditions and results [29]. Pure MoO₃ has not been used as flux due to its volatility and generally speaking is not a suitable flux. However, we have easily grown emerald crystals from MoO₃ [28], Li₂O-MoO₃ [36], K₂O-MoO₃ [38], and MoO₃-B₂O₃ [39] fluxes by the flux evaporation method. A technique of easily growing emerald crystals from MoO₃-based fluxes is described below.

17.3.2 A simple method of growing emerald crystals

Well-formed emerald crystals can be easily grown by the evaporation method of MoO₃, Li₂O-MoO₃, K₂O-MoO₃, and MoO₃-B₂O₃ fluxes. The concentration of emerald constituents in the solution may be slowly increased by evaporation of the

fluxes. The evaporation technique is carried out isothermally. Since the temperature control is easy, a temperature controller is not always needed. Operating skill is not necessary. The basic requirements for the growth of emerald crystals are a crucible, furnace, thermocouple, and chemicals.

Experimental

Reagent grade BeO , Al_2O_3 , SiO_2 , Cr_2O_3 , MoO_3 , Li_2CO_3 , K_2CO_3 , and B_2O_3 were used for the flux growth of emerald crystals. The beryl mixture ($3\text{BeO} + \text{Al}_2\text{O}_3 + 6\text{SiO}_2$) was prepared from BeO , Al_2O_3 , and SiO_2 powders and the oxide dopant (Cr_2O_3) added as 1.0 mass% of the beryl mixture. This mixture was used as a solute for flux growth runs. Pure MoO_3 , $\text{Li}_2\text{O-MoO}_3$, $\text{K}_2\text{O-MoO}_3$, and $\text{MoO}_3\text{-B}_2\text{O}_3$ were used as fluxes. BeO is toxic to humans. Care is required to handle it.

The solute and flux powders were weighed out and mixed together. The mixtures were put into platinum crucibles of 30 cm^3 capacity (36 mm in diameter and 40 mm high). In the case of $\text{K}_2\text{O-MoO}_3$ flux, a 240 cm^3 crucible (60 mm in diameter and 80 mm high) was also used to grow large crystals. After closing the lids, the crucibles were placed in an electric furnace with silicon carbide heating elements. The furnace was heated at about 45°C/h to 1100°C and held at this temperature for 0–240 h. Then the crucible was removed and allowed to cool rapidly to room temperature. The crystal products were then separated from the flux in warm water.

The cost of the apparatus can be relatively low. The most readily available material of crucible is platinum. A 30 cm^3 crucible is enough to grow emerald crystals with a few mm in size. Furnaces to able reach 1300°C can be obtained commercially.

The crystals obtained were examined using an optical microscope and a scanning electron microscope (SEM). The crystal phases were identified by X-ray diffraction (XRD). The length, L (parallel to the c -axis), and width, W (perpendicular to the c -axis), of the emerald crystals grown were measured. The density of the crystals was pycnometrically determined. Infrared (IR) absorption spectra of the crystals were measured. The samples were prepared as KBr disks. An electron probe microanalyzer (EPMA) was used to study variations in the concentration of the major constituents of the grown crystals. The presence of impurities from the fluxes and Pt crucible was also checked. However, these processes of characterizing are not always necessary if you only enjoy yourself by making beautiful emerald crystals.

Flux growth of emerald crystals

A lot of small emerald crystals were easily grown by the MoO_3 flux evaporation method [28]. The obtained emerald crystals were transparent and exhibited the typical emerald-green color. Their form was a twelve-sided prism bounded by well-developed faces. The oxide MoO_3 used as a flux was too volatile to grow large emerald crystals. The high volatility of MoO_3 flux is expected to be greatly lowered when the complex must be stable in the high-temperature solution by the

addition of basic oxide such as Li_2O or K_2O . Addition of Li_2O to MoO_3 flux in fact made the high-temperature solution relatively nonvolatile. Similarly, K_2O added to MoO_3 flux acted to control the amount of flux evaporation. Relatively large emerald crystals were grown from $\text{Li}_2\text{O-MoO}_3$ and $\text{K}_2\text{O-MoO}_3$ fluxes [36,38]. The form of the crystals grown from these fluxes was also a twelve-sided prism. As an example, typical emerald crystals grown from $\text{Li}_2\text{O-MoO}_3$ flux are shown in Fig. 17.9. At first sight, the crystals look just like hexagonal prisms because of six well-developed prismatic faces. On the other hand, an attempt to improve flux properties was performed by adding B_2O_3 to MoO_3 flux. Since B_2O_3 has a high viscosity, it is expected that B_2O_3 generally suppress flux evaporation. Addition of B_2O_3 to MoO_3 actually suppressed evaporation of the flux. Hexagonal thin plate-like emerald crystals as shown in Fig. 17.10 were grown from $\text{MoO}_3\text{-B}_2\text{O}_3$ flux [39].



Fig. 17.9. Emerald crystals grown from $\text{Li}_2\text{O-MoO}_3$ flux

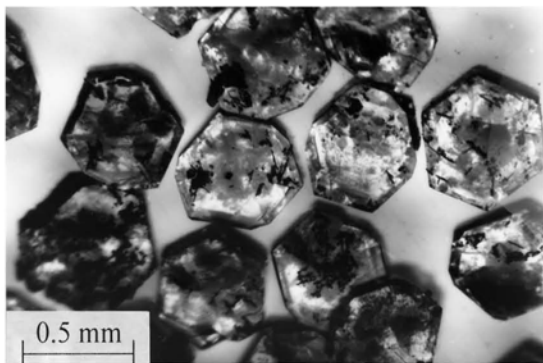


Fig. 17.10. Emerald crystals grown from $\text{MoO}_3\text{-B}_2\text{O}_3$ flux

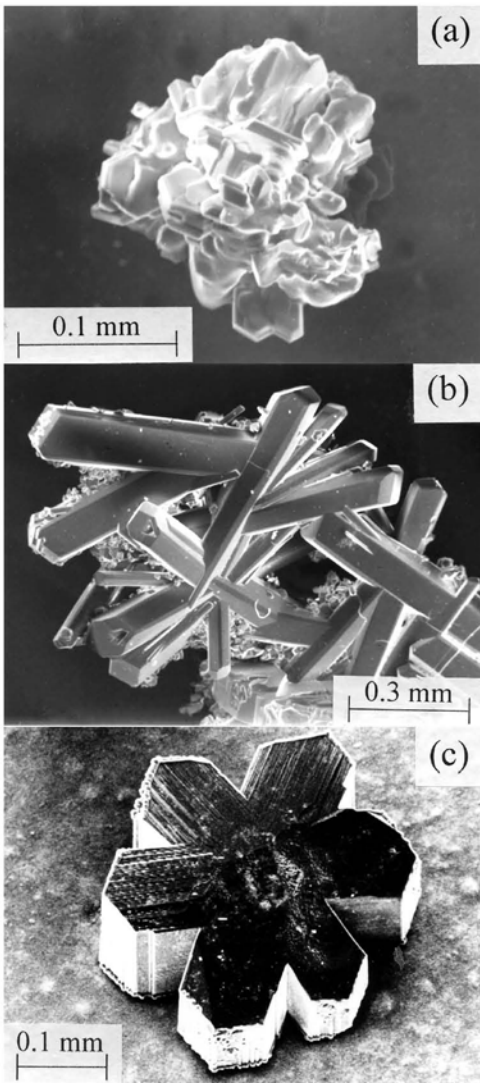


Fig. 17.11. By-product crystals of (a) cristobalite, (b) phenacite, and (c) chrysoberyl

It was found that prismatic and plate-like emerald crystals can be grown by the simple operation of only evaporating MoO_3 -based fluxes at constant temperature. The resulting crystals could be readily separated from the MoO_3 -based fluxes in warm water. The platinum crucibles were found to be undamaged after use with no evidence of attack from the MoO_3 -based fluxes. The fluxes were compatible with platinum at the intended temperature. A disadvantage of the isothermal flux evaporation technique was the difficulty of controlling the evaporation rate. By-

products such as cristobalite (SiO_2) and phenacite (Be_2SiO_4) crystals were formed from MoO_3 , $\text{Li}_2\text{O-MoO}_3$, $\text{K}_2\text{O-MoO}_3$, and $\text{MoO}_3\text{-B}_2\text{O}_3$ fluxes. The former crystals were colorless and transparent. Their form was a thin plate. The latter crystals were also colorless and transparent. Their form was a hexagonal rod. In the small number of the growth experiments, dark green chrysoberyl (BeAl_2O_4) crystals were formed. The grown crystals were always twinned. The twin crystals had pseudo-hexagonal symmetry owing to cyclic twinning. By-product crystals of cristobalite, phenacite, and chrysoberyl are shown in Fig. 17.11. The secondary phases (insoluble in warm water) could be clearly distinguished from emerald crystals because of the differences in color and shape. Owing to the formation of 2 or 3 kinds of by-product crystals, the system used for growing emerald crystals cannot rigorously be reduced to a pseudo-binary system of solute and flux. The crystallization process of emerald crystals from the high-temperature solutions of the MoO_3 -based fluxes is very complex.

MoO₃ flux [28]: The most suitable composition of the high-temperature solution was solute (9.06 g)- MoO_3 (30.0 g) when the holding time was 30 h. The evaporation loss of the MoO_3 flux was about 99 mass%. The approximate rate of evaporation was calculated as 8.8×10^{-4} g/(h mm²). The crystal growth was promoted by the evaporation of flux, which increased with the holding time. A lot of small emerald crystals, up to 0.86 mm *L* and 0.64 mm *W*, were grown from the flux. The crystal sizes were dependent on the evaporation loss of flux. The numbers of obtained crystals were very large. The obtained crystals were twelve-sided prism-shaped and the crystal surfaces were very flat. The aspect ratios (*L/W*) were in the region of 1.2 to 1.5. It was found that MoO_3 flux could produce emerald crystals. However, MoO_3 was insufficient as a flux to grow large emerald crystals due to its very high volatility.

Li₂O-MoO₃ flux [36]: The most suitable composition of the high-temperature solution was solute (7.00 g)- Li_2O (1.50 g)- MoO_3 (30.0 g) when the holding time was 40 h. Evaporation loss of the Li_2O (1.50 g)- MoO_3 (30.0 g) flux was about 7 mass%. The rate of evaporation was calculated as approximately 5.4×10^{-5} g/(h mm²). The evaporation loss of flux decreased gradually with an increase in the amount of Li_2O added to MoO_3 . Addition of Li_2O to MoO_3 made the high-temperature solution relatively less volatile owing to the interaction between Li_2O and MoO_3 . The Li_2O acted to control the amount of flux evaporation. It was considered that the evaporation loss from the $\text{Li}_2\text{O-MoO}_3$ flux consisted mainly of MoO_3 . The evidence for this view came from the precipitation of MoO_3 on the crucible lid and furnace brick. Owing to the preferential evaporation of MoO_3 , the flux composition changes with time. Emerald crystals of up to 3.4 mm *L* and 2.4 mm *W* were readily grown by the $\text{Li}_2\text{O-MoO}_3$ flux evaporation method. The crystal sizes were evidently dependent on the amount of Li_2O present, that is, the evaporation loss of flux. The obtained emerald crystals were twelve-sided prisms bounded by well-developed faces with aspect ratios in the region of 1.2 to 1.9.

K₂O-MoO₃ flux [38]: The most suitable composition of the high-temperature solution was solute (3.80 g)- K_2O (1.50 g)- MoO_3 (28.5 g) when the holding time was 24 h. About 34 mass% of the K_2O (1.50 g)- MoO_3 (28.5 g) flux evaporated. The



Fig. 17.12. Large emerald crystals grown from K_2O - MoO_3 flux

approximate rate of evaporation was calculated to be 4.2×10^{-4} g/(h mm²). The evaporation loss decreased gradually with an increase in the amount of K_2O , which acted to control the amount of flux evaporation in a similar manner as the case of Li_2O . The evaporation loss from K_2O - MoO_3 flux consisted mainly of MoO_3 . Emerald crystals of up to 1.8 mm L and 1.3 mm W were readily grown by the K_2O - MoO_3 flux evaporation method. The form of the obtained crystals was similar to that of crystals grown from MoO_3 and Li_2O - MoO_3 fluxes. The aspect ratios were in the region of 1.2 to 2.3.

An attempt to grow large crystals by scaling up the mass of the mixture by a factor of 6 was investigated. The composition of the mixture was solute (22.8 g)- K_2O (9.00 g)- MoO_3 (171.0 g). The holding time was 240 h. The evaporation loss of the flux was about 58 mass%. Emerald crystals of up to 4.5 mm L and 2.9 mm W were grown. The mass of the largest crystal was about 0.04 g (0.2 carat). Large emerald crystals are shown in Fig. 17.12.

MoO₃-B₂O₃ flux [39]: The suitable composition of the high-temperature solution was solute (9.00 g)- MoO_3 (30.0 g)- B_2O_3 (0.36 g) when the holding time was 30 h. Approximately 60 mass% of the MoO_3 (30.0 g)- B_2O_3 (0.36 g) flux evaporated. The approximate evaporation rate was 5.8×10^{-4} g/(h mm²). The evaporation of flux decreased gradually with an increase in the amount of B_2O_3 added to MoO_3 flux. The B_2O_3 addition remarkably suppressed MoO_3 flux evaporation. The evaporation loss from MoO_3 - B_2O_3 flux consisted mainly of MoO_3 . Hexagonal thin plate-like emerald crystals of up to 1 mm W were readily grown by the MoO_3 - B_2O_3 flux evaporation method. The aspect ratios of the plate-like crystals were approximately 0.2. The flux is found to be a suitable flux for the growth of plate-like thin emerald crystals. The morphology of emerald crystals was controlled by the B_2O_3 addition.

Characteristics of the emerald crystals

Some characteristics of emerald crystals grown from MoO_3 , Li_2O - MoO_3 , K_2O - MoO_3 , and MoO_3 - B_2O_3 fluxes were investigated [28,36,38,39]. The emerald crys-

tals obtained were transparent and with the typical emerald-green color as described above. The sizes of the prismatic emerald crystals were up to 4.5 mm L and 2.9 mm W . The widths of thin plate-like emerald crystals were up to 1 mm. They were identified as emeralds by their powder XRD patterns, using data given in the JCPDS card [48].

Emerald crystals obtained from MoO_3 -based fluxes were classified into two distinct morphological types: prism and plate. The forms were dependent on the fluxes used. The form of the emerald crystals grown from MoO_3 , $\text{Li}_2\text{O-MoO}_3$, and $\text{K}_2\text{O-MoO}_3$ fluxes was a twelve-sided prism. A typical prismatic crystal grown from $\text{Li}_2\text{O-MoO}_3$ flux is shown in Fig. 17.13. On the basis of the XRD data and interfacial angle measurements, it was found that the crystals were bounded by the $c\{0001\}$, $m\{10\bar{1}0\}$, and $a\{11\bar{2}0\}$ faces. The c and m faces were always well-developed. Natural emerald crystals are also prismatic [49]. On the other hand, $\text{MoO}_3\text{-B}_2\text{O}_3$ flux produced the hexagonal thin plate-like emerald crystals of up to 1 mm W . A typical plate-like crystal is shown in Fig. 17.14. The plate-like crystals were bounded mainly by the c and m faces. There were crystals in which some small a faces appeared. The c faces were smooth while m and a faces were rough, forming skeleton crystals in many cases. Only the addition of a slight amount of B_2O_3 to MoO_3 flux suppressed the growth of emerald crystals in the c -axis direction, and crystal habit changed from columnar to thin plate-like crystals as B_2O_3 content increased. The probable causes are that boron atoms from B_2O_3 are selectively adsorbed by the c faces of emerald crystals and crystal components are hardly supplied to the c faces, and that there is an effect of a change in supersaturation by regulating the evaporation rate of flux.

The variations in the concentration of the major constituents in the grown prismatic emerald crystals were investigated by the use of EPMA. Aluminum, silicon, and oxygen were distributed almost homogeneously in the crystals. The distribution of beryllium could not be determined due to the low atomic mass of the element. The EPMA data showed that chromium was incorporated preferentially in the central parts of the crystals. A small amount of chromium existed in the outer parts of the crystals. In addition, there was a preferential incorporation into the prismatic faces compared to the basal ones. The orientation-dependent chromium incorporation is probably due to the difference in adsorption on specific faces or in the crystallographic direction. Molybdenum from the fluxes and platinum from the crucible were not detected. Emerald crystals grown from $\text{K}_2\text{O-MoO}_3$ flux were contaminated by a very small amount of potassium from the flux. The potassium was incorporated in the central parts of the crystals.

The density of the emerald crystals was pycnometrically determined to be 2.65–2.66 g/cm^3 , in good agreement with literature values (2.64 [48] and 2.69 [4] g/cm^3). IR absorption spectra recorded in the range 450–4000/ cm were obtained for the emerald crystals grown. Absorption bands at approximately 493, 523, 590, 650, 681, 740, 806, 961, 1020, and $1204 \pm 3/\text{cm}$ were observed. These values were in good agreement with literature data for emerald crystals grown from V_2O_5 flux [41]. The observed bands were independent of the crystal growth conditions. A broad band at 3450/ cm was also observed, which is believed to be extraneous to

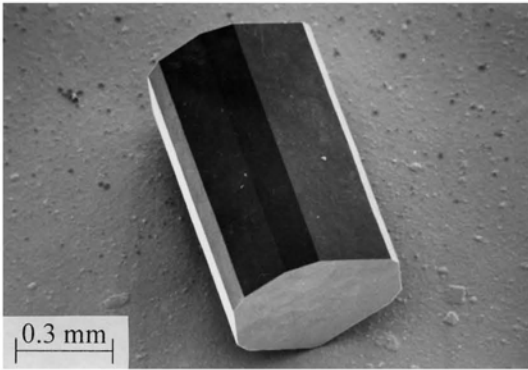


Fig. 17.13. A twelve-sided prismatic emerald crystal

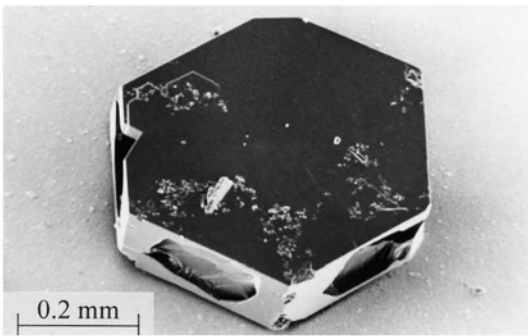


Fig. 17.14. A plate-like emerald crystal

the sample and related to water pick-up by KBr during sample preparation. Of course, sharp OH bands were not observed because the emerald crystals grown from flux contained no water. Natural and synthetic hydrothermal emerald crystals exhibited sharp OH bands [7,9,23,30,31].

Inclusions were rarely found in the emerald crystals grown from $\text{Li}_2\text{O-MoO}_3$ and $\text{K}_2\text{O-MoO}_3$ fluxes. The quality of these crystals was good. On the other hand, various kinds of imperfections were present in the crystals grown from MoO_3 flux although good crystals were also obtained. The crystals generally had flux inclusions in the central parts but the peripheral portion was quite transparent, as shown in Fig. 17.15. It is considered that the growing crystal trapped flux. This is evidence of an internal defect suggesting that some considerable degree of supersaturation is first experienced and a rapid growth stage follows nucleation. Subsequently, higher quality growth occurs on the outer surfaces, but at a slower rate. In addition, emerald crystals having raised corners and edges were also grown and a

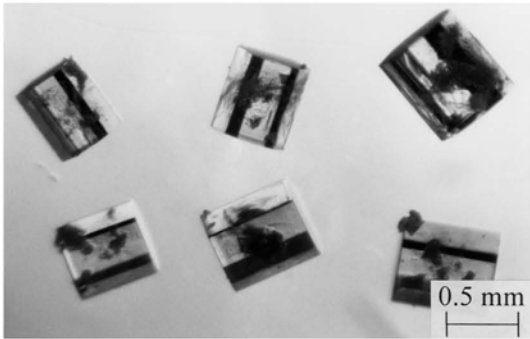


Fig. 17.15. Emerald crystals having inclusions in the central parts

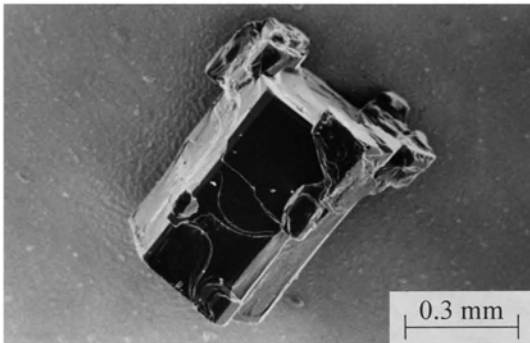


Fig. 17.16. Emerald crystal having raised corners and edges

typical example is shown in Fig. 17.16. The proportion of terraced crystals grown tended to increase as flux evaporation losses increased. The higher supersaturation at the corners and edges of a crystal will lead to an onset of more rapid growth in these regions. A progressive increase in the supersaturation gradient leads first to the formation of raised corners and edges, then to the development of terraced crystals.

17.4 Summary

An outline of the crystal growth of gemstones was given. The flux growth of emerald crystals as an example of gemstones was described. Well-formed and transparent emerald crystals exhibiting emerald-green color could be easily grown by the evaporation of MoO_3 , $\text{Li}_2\text{O-MoO}_3$, $\text{K}_2\text{O-MoO}_3$, and $\text{MoO}_3\text{-B}_2\text{O}_3$ fluxes. The forms of the emerald crystals were prismatic and plate-like. Growing beautiful

emerald crystals is enjoyable and can be done with the minimum of equipment and information.

Acknowledgments

The author is grateful to Mr. K. Mochizuki and Mr. T. Yonezawa, Shinkosha Co. Ltd., for kindly supplying photographs used in Figs. 17.2, 17.3, and 17.5. Particular thanks are due to Emeritus Professor S. Taki, Yamanashi University, for the supply of quartz crystal used in Fig. 17.7 and to Emeritus Professor Y. Sumiyoshi, Gunma University, for his continuing interest and encouragement.

References

1. Gaudin M (1837) *Compt Rend* 4:999
2. Hautefeuille P, Perrey A (1888) *Compt Rend* 106:1800
3. Verneuil A (1902) *Compt Rend* 135:791
4. Elwell D (1979) *Man-Made Gemstones*. Ellis Horwood
5. Bundy FP, Hall HT, Strong HM, Wentorf Jr RH (1955) *Nature* 176:51
6. Elwell D, Scheel HJ (1975) *Crystal Growth from High-Temperature Solutions*. Academic Press
7. Nassau K, Nassau J (1980) *The Growth of Synthetic and Imitation Gems*. In: Freyhardt HC (ed) *Crystals*. Springer-Verlag, pp 1–50
8. O'Donoghue M (1981) *Prog Cryst Growth Charact* 3:193
9. Sunagawa I (1982) *Gem Materials, Natural and Artificial*. In: Kaldis E (ed) *Current Topics in Materials Science, Vol 10*. North-Holland Publishing Company, pp 353–497
10. Nielsen JW, Monchamp RR (1970) *The Use of Phase Diagrams in Crystal Growth*. In: Alper AM (ed) *Phase Diagrams: Materials Science and Technology, Vol 3*. Academic Press, pp 1–52
11. Pamplin BR (ed) (1975) *Crystal Growth*. Pergamon Press
12. Pamplin BR (ed) (1980) *Crystal Growth, 2nd Edition*. Pergamon Press
13. Laudise RA (1970) *The Growth of Single Crystals*. Prentice-Hall
14. Byrappa K, Yoshimura M (2000) *Handbook of Hydrothermal Technology*. William Andrew/Noyes Publications
15. Taki S (1991) *Prog Cryst Growth Charact* 23:313
16. Chase AB (1971) *Exploratory Flux Crystal Growth*. In: Lefever RA (ed) *Preparation and Properties of Solid State Materials, Vol 1*. Marcel Dekker, pp 183–264
17. Elwell D (1975) *Flux Growth*. In: Pamplin BR (ed) *Crystal Growth*. Pergamon, pp 185–216
18. Elwell D (1980) *High-Temperature Solution Growth*. In: Pamplin BR (ed) *Crystal Growth, 2nd Edition*. Pergamon Press, pp 463–483
19. Wanklyn BM (1975) *Practical Aspects of Flux Growth by Spontaneous Nucleation*. In: Pamplin BR (ed) *Crystal Growth*. Pergamon Press, pp 217–288
20. Levin EM, Robbins CR, McMurdie HF (eds) *Phase Diagrams for Ceramists*. The American Ceramic Society (1964)
21. Oishi S, Tate I, Hirano S, Naka S (1984) *Nippon Kagaku Kaishi* 685 (in Japanese)

22. Artioli G, Rinaldi R, Stahl K, Zanazzi PF (1993) *Am Mineral* 78:762
23. Nassau K (1976) *J Crystal Growth* 35:211
24. Miller RP, Mercer RA (1965) *Mineral Mag* 35:250
25. Gentile AL, Cripe DM, Andres FH (1963) *Am Mineral* 48:940
26. Wilson W (1965) *J Appl Phys* 36:268
27. Takubo H, Maki J, Shimada M, Kume S, Koizumi M (1967) *Mem Inst Sci & Ind Res, Osaka Univ* 24:129
28. Oishi S, Mochizuki K (1993) *Brit Ceram Trans* 92:214
29. Lefever RA, Chase AB, Sobon LE (1962) *Am Mineral* 47:1450
30. Flanigen EM, Breck DW, Mumbach NR, Taylor AM (1967) *Am Mineral* 52:744
31. Kojima H (1968) *Ceramics Japan* 3:497 (in Japanese)
32. Ashida S (1968) *Kobutsugaku Zasshi* 8:407 (in Japanese)
33. Inoue M, Morishita T, Narita E, Okabe T (1979) *Nippon Kagaku Kaishi* 1489 (in Japanese)
34. Flamini A, Gastaldi L, Viticoli S (1986) *Mater Res Bull* 21:1
35. Miyata T, Kawabata Y, Takeda I, Kojima H (1990) *J Crystal Growth* 99:869
36. Oishi S, Mochizuki K (1995) *J Mater Chem* 5:1257
37. Sakamoto C (1973) *Jpn Pat* 23278 (in Japanese)
38. Oishi S, Yamamoto H (1996) *J Mater Chem* 6:1687
39. Oishi S, Mochizuki K, Hirano S (1994) *J Ceram Soc Jpn, International Edition* 102:503
40. Linares RC, Ballman AA, Van Uitert LG (1962) *J Appl Phys* 33:3209
41. Ushio M, Sumiyoshi Y (1972) *Nippon Kagaku Kaishi* 1648 (in Japanese)
42. Ushio M, Sumiyoshi Y (1973) *Nippon Kagaku Kaishi* 506 (in Japanese)
43. Ushio M, Sumiyoshi Y (1973) *Nippon Kagaku Kaishi* 941 (in Japanese)
44. Ushio M (1976) *Nippon Kagaku Kaishi* 748 (in Japanese)
45. Linares RC (1967) *Am Mineral* 52:1554
46. Oishi S, Hirao M (1991) *J Mater Sci* 26:6401
47. Barilo SN, Bychkov GL, Kurnevich LA, Leonuk NI, Mikhailov VP, Shiryaev SV, Koyava VT, Smirnova TV (1999) *J Crystal Growth* 198/199:716
48. JCPDS (Joint Committee for Powder Diffraction Standard) card 9-430
49. Dana ES, Ford WE (1972) *A Textbook of Mineralogy*. Wiley, pp 579–581

Index

% fill, 351

15R SiC, 224

2D nuclei, 70

2D-nucleation growth mode, 61

2D-nuclei, 57

2D-SROES, 125

II-VI compounds, 498

III-V epitaxy, 55

4H SiC, 190

6H SiC, 190

abrasive tool coating, 98

absolute solubility, 343

absorption, 421

absorption coefficient, 361

absorption measurements, 361

absorption spectra, 362

acetate, 305

acetylene, 118

Acheson method, 186

acidity and basicity, 568

activation energy, 100, 257, 318

activity, 246

adatom concentration, 59

adsorption, 576

AlGaAs, 72

alkali, 309

alkali metal hydrides, 445

alkali metals, 423

alkaline, 324

ammonia (NH₃), 325

amorphous carbon, 103

anatase, 318

angular acceptance bandwidth, 438

anionic group, 420

antiphase domain-free, 84

apparent activation energies, 318

aquamarine, 563

Arrhenius equation, 317

Arrhenius plot, 344

Arrhenius-type, 257

arsenic oxide, 73

as-grown surfaces, 355

associated melt, 498

atomic force microscope, 105

atomic hydrogen, 94

autoclave, 567

automatic weight controller, 404

back-reflection synchrotron white beam

 X-ray topography (BR-SWBXT), 213

back-reflection topography, 205

basal plane dislocations, 204, 221

BaSnO₃, 301

(Ba,Sr)TiO₃, 301

(Ba,Sr)(Ti,Zr)O₃, 301

BaTiO₃, 301

Ba(Ti,Sn)O₃, 301

Ba(Ti,Zr)O₃, 301

BaZrO₃, 301

Be₃Al₂Si₆O₁₈:Cr, 561

beauty, 561

beryl, 569

beryllium aluminum silicate, 569

Bi₂Sr₂Ca₂Cu₃O₁₀, 483

Bi₂Sr₂CaCu₂O₈, 483

Bi₂Sr₂CuO₆, 483

bias-enhanced nucleation, 104

birefringence, 389, 419

bismuth germanate, 387

bismuth vanadate, 342

- Bi-Sr-Ca-Cu-O superconductor, 458
block structures, 356
borate, 420
boule, 564
Bridgman technique, 498
BR-SWBXT, 213
Burgers vector, 204
buffer layer, 104
bulk diamond, 98
bulk growth, 193
buoyancy flow, 238
buoyancy force, 237
by-product, 573
- C/H ratio, 118
carbide, 95
carbon mole fraction, 117
carbon phase, 102
carbonate, 308
carbon-containing species, 95
catalyzer, 93
CaTiO₃, 301
CaZrO₃, 301
CdTiO₃, 301
characteristics, 575
chemical reaction, 239
chemical vapor deposition (CVD), 93, 191
chemical vapor transport (CVT), 501
choice of flux, 568
chromium, 569
chrysoberyl, 574
closed core screw dislocations, 204
coil, 236
cold THM (CTHM), 499
color centers, 335
combustion flame CVD, 97
complexation process, 344
compositional homogeneity, 389
computational domain, 251
concentration, 307
conduction and radiation, 235
congruent melt, 389
conoscopic interferogram, 402
container-free epitaxial growth, 194
contamination, 513, 566
contrast formation mechanism, 208
cooling, 237
copper coil, 236
coprecipitation, 299
corundum, 563
cristobalite, 574
critical supersaturation, 63
critical temperature, 61
critical thickness, 82
critical width, 89
crucible, 236
crucible assembly, 392
crystal cross-section controller, 403
crystal defects, 395
crystal growth, 185, 347, 561
crystal growth rate, 403
crystal habit, 576
crystal pulling, 566
crystal surface, 574
crystalline perfection, 395
crystallization, 300
CsB₃O₅ (CBO), 420
CsLiB₆O₁₀ (CLBO), 422
cubic, 311
Curie temperature, 300
current density, 241
curvilinear grid, 243
cutting tool coating, 98
CVD, 93
CW characteristics, 361
Czochralski (Cz) growth, 422
Czochralski method, 566
Czochralski (Cz) technique, 340, 389
- damage threshold, 433
dangling bond, 107
DC arc plasma jet CVD, 97
decomposing reaction, 97
decomposition, 300
defect, 102
degradation, 427
degree of supersaturation, 351
dendritic, 321
density, 571
denuded zone, 75
deposition, 239
desorption, 95
device structure, 214
diamond, 93, 561
diamond film, 93
diamond film quality, 123
diamond growth, 93
diamond ID cutter, 401
diamond synthesis, 93
diamond-like carbon, 102
Dietzel's parameter, 568

- diffraction/rocking curves, 397
 diffusion, 95, 316
 diffusion coefficient, 239
 diffusion length, 59
 diode-laser pumped, 335, 359
 dipole, 300
 discrete exchange factor (DEF), 244
 dislocation, 204, 263
 dislocation free, 86
 dislocation image, 209
 dislocation nucleation, 213
 dislocation pair, 217
 displacement, 264
 dissolution, 312
 dissolution-precipitation, 312
 dopant, 569
 doping, 200, 428, 513
 double crystal X-ray diffractometer, 395
 DTA curves, 399
 durability, 561
- Eddy currents, 241
 effective conductivity, 236
 effective heat capacity, 243
 effective heat transfer coefficient, 243
 effective nonlinear optical coefficient, 419
 eighth harmonic generation, 8ω , 432
 elastic material constant, 264
 electric furnace, 571
 electrical conductivity, 236
 electrochemical-hydrothermal, 318
 electromagnetic field, 241
 electron bombardment, 106
 electron cyclotron resonance microwave plasma-assisted CVD, 97
 electron paramagnetic resonance (EPR), 440
 electron probe microanalyzer (EPMA), 571
 electron temperature, 128
 electron trap, 73
 electronic, 300
 electronic device, 97
 emerald, 569
 emerald-green, 571
 emission cross-sections, 336
 emission intensity, 124
 emissivity, 240
 energy barrier for migration, 75
 energy transport, 242
- environmental, 299
 epilayer, 214
 epitaxial films, 200
 epitaxial growth, 200
 epitaxial relationship, 109
 equilibrium, 563
 equilibrium constant, 245
 equilibrium partial pressure, 247
 Er³⁺-doped fiber, 432
 etch pits, 212
 ethylene diamine tetra acetic acid (EDTA), 305
 eutectic reaction, 478
 evaporation diffusion length, 66
 excimer laser, 419
 exothermic and endothermic, 239
- face centered cubic, 300
 feed back control system, 403
 ferroelectric domains, 401
 ferroelectric, 299
 field-electron emission, 101
 fifth harmonic generation, 5ω , 419
 fine focus X-ray source, 396
 finite element, 249
 finite volume, 249
 five crystal X-ray diffractometer, 397
 flame fusion, 561
 flat-panel display, 101
 fluorescent lifetime, 336
 flux, 561
 flux agents, 342
 flux evaporation, 568
 flux growth, 341
 flux impurities, 342
 flux method, 567
 fourth harmonic generation, 4ω , 433
 Frank's theory, 204
 frequency conversion, 419
- GaAs, 58
 garnet, 561
 gas phase reaction, 131
 gas temperature, 114
 gas-phase chemistry, 120
 gas-phase species, 113
 GdCa₄O(BO₃)₃ (GdCOB), 420
 Gd_xY_{1-x}Ca₄O(BO₃)₃ (GdYCOB), 420
 gel, 309
 gem material, 561

- gemstone, 561
- Gibbs free energy, 114
- Gibbs function, 114
- Gibbs-function, 245
- graphite insulation, 236
- graphite susceptor, 241
- graphitization, 203
- Grashof number, 238
- gray-track, 440
- gray-track threshold, 442
- grazing incidence reflection topograph, 215
- green light emission, 498
- growth, 181, 235
- growth atmosphere, 442
- growth kinetics, 197, 248
- growth layers, 356
- growth mechanism, 103, 336
- growth method, 563
- growth of vanadates, 343
- growth process, 94, 197
- growth rate, 93, 197, 257, 351
- growth spirals, 201, 205
- growth system, 195, 235

- halide ions, 445
- Hancock and Sharp, 315
- heat power, 235
- heat resistance, 240
- heat sink, 97
- Henry's law, 246
- heteroepitaxy, 103
- hexagonal voids, 204, 222
- HFCVD, 94
- high melting point, 362
- high pressure, 561
- high pressure and high temperature, 93
- high pressure Bridgman, 503
- high resolution transmission electron microscopy, 106
- high resolution X-ray diffractometry, 404
- high resolution X-ray topography, 404
- high temperature, 561
- high temperature CVD, 192
- high temperature growth technique, 343
- high temperature optical microscopy, 491
- high temperature solution growth, 193, 341
- highly-mismatched heteroepitaxy, 84

- high-oriented diamond film, 95
- high- T_c crystal, 467
- hollow core, 204
- homoepitaxy, 102
- homogeneity, 310, 422
- hot-filament CVD, 94
- hot-wall CVD, 192
- HPHT, 93
- HRTEM, 107
- HTCVD, 192
- humidity, 427
- hydrates, 430
- hydrocarbon, 103
- hydrogen, 94
- hydrogen passivation, 75
- hydrothermal, 299
- hydrothermal autoclave, 347
- hydrothermal conditions, 335
- hydrothermal growth, 343
- hydrothermal method, 336, 510, 567
- hydrothermal mineralizers, 343
- hydrothermal process, 343
- hydrous, 309
- hydroxyl, 311
- hygroscopic, 427

- image contrast, 213
- imperfection, 577
- impurities, 513
- impurity, 217
- inclusion, 217, 577
- incongruent melt, 569
- incongruent vanadium oxide vaporization, 342
- incongruent vaporization, 337
- incorporation, 576
- incorporation diffusion length, 66
- incorporation lifetime, 70
- indigenous versatile crystal puller, 392
- induction heating, 195
- inert gas pressure, 259
- in situ diagnostic technique, 116
- in situ fabrication of the morphology, 362
- in situ observation, 474
- in situ transformation, 312
- integral equation for radiative heat transfer, 244
- integrated intensity, 397
- interface, 105
- interface demarcation, 262

- interface supersaturation, 62
interfacial energy (IE), 319
interstitial, 421
intersurface diffusion, 68
ion bombardment, 95
ion exchange, 316
ionic compensation, 443
ionic radius, 568
ionicity, 497, 568
IR absorption, 576
IR studies, 358
iron doped LiNbO_3 , 401
isobaric expansion coefficient, 238
- jewelry, 561
Johnson-Mehl-Avrami (JMA), 314
- $\text{K}_2\text{Al}_2\text{B}_2\text{O}_7$ (KAB), 443
 K_2CO_3 , 308
 $\text{K}_2\text{O-MoO}_3$, 570
 $\text{KB}_5\text{O}_8 \cdot 4\text{H}_2\text{O}$ (KB5), 420
 $\text{KBe}_2\text{BO}_3\text{F}_2$ (KBBF), 420
KBr, 3109
KDP (KH_2PO_4), 420
KF, 446
kinetics, 312
 KNbO_3 , 420
Knudsen cell, 56
Kronecker's delta, 244
KTP (KTiOPO_4), 420
- large area deposition, 95
large effective absorption, 336
laser ablation CVD, 97
laser-induced damage threshold, 419
laser-induced damages, 433
laser-induced fluorescence (LIF), 120
laser spectroscopy, 358
latent heat, 239
lateral flow, 70
lateral sticking probability, 75
lattice, 300
lattice constant, 429
lattice mismatch, 109
layer-by-layer growth, 78
layered structure, 443
Lely method, 187
Lely plate, 197
Lely seed, 253
 $\text{Li}_2\text{B}_4\text{O}_7$ (lithium tetraborate), 420
 $\text{Li}_2\text{O-MoO}_3$, 570
 LiB_3O_5 (LBO), 420
LiCl, 446
LIF, 120
ligand, 321
light emitting devices, 513
 LiIO_3 , 420
 LiNbO_3 , 420
LiOH, 309
liquid, 561
liquid phase epitaxy (LPE), 193
lithium niobate (LiNbO_3), 387
low thermal gradient Czochralski (LTG Cz), 393
low toxicity, 75
LPE growth of low T_c crystal, 467
- magnetic vector potential, 251
man-made gemstone, 561
Markov-Davydov technique, 505
mass transfer, 236
mass transport, 445
mass transport limited regime, 78
MASTRAPP, 249
Maxwell's equation, 241
MBMS, 123
mechanism, 312
melt growth, 498, 564
melting point, 568
metal organic chemical vapor deposition (MOCVD), 55
metastable, 311
metastable condition, 93
methane, 118
methyl radical, 118
microbalance, 395
microchannel epitaxy, 84
micropipes, 201, 204
microprocessor controls of crystal growth, 403
microscope, 571
micro steps, 356
microwave plasma-assisted CVD, 95
mild hydrothermal conditions, 336
mineral, 561
mineralizer, 309, 347
mineralizer solution, 350
minimum reaction temperature, 311
MOCVD, 55
model, 305
modeling and simulation, 235

- modified Lely method, 189, 235
MoK_{α1} X-ray beam, 397
molar ratio, 307
molarity of the mineralizer, 351
molecular beam epitaxy (MBE), 55
molecular beam mass spectroscopy (MBMS), 123
monodispersed, 316
MoO₃, 570
MoO₃-B₂O₃, 570
morphology, 319, 351, 575
morphology control, 336
morphology of rare earth orthovanadates, 351
morphology of rare earth vanadates, 351
MPCVD, 95
multigrid, 249
- NaF, 446
nano, 327
NaOH, 309
native defects, 512
natural gemstone, 561
Nd:GdVO₄, 336
Nd:RVO₄, 335
Nd:YAG, 358
Nd:YAG laser, 419
Nd:YVO₄, 336
Nd:YVO₄ laser, 440
negative electron affinity (NEA), 101
network analysis, 240
Nielsen's equation, 317
nitrogen-containing radical, 127
noncritical phase-matching (NCPM), 434
non-diamond substrate, 103
non-equilibrium thermodynamical process, 114
nonlinear optical (NLO) crystals, 419
nonlinear optics, 434
non-preferential etching, 391
nonradiative center, 73
normal stress, 264
n-type doping, 100
nucleation, 103, 217, 314, 447
nucleation density, 104
nucleation process, 103
nucleation site, 104
nutrient, 567
- OES, 123
- opal, 561
optical damages, 440
optical emission spectroscopy (OES), 123
optical homogeneity, 387
optical lense, 99
optical transparency, 96
optical window, 99
optic-axis picture, 402
optimization of growth parameters, 400
opto-electronic material, 387
order-of-magnitude analysis, 236
ornamentation, 561
Ostwald ripening, 314
output power, 360
oxidation, 300
oxide crystal, 564
oxide single crystals, 387
oxyborate, 434
oxygen defects, 335
oxygen deficiency, 335, 400
oxygen imperfections, 335
oxygen impurity, 73
oxygen partial pressure, 339
oxygen stoichiometry, 335
- p/n junctions, 513
piezoelectric, 300
partial pressure, 245
Pb₂V₂O₇, 342
(Pb,La)(Zr,Ti)O₃, 301
Pb(Sc,Nb)O₃, 301
Pb(Zr,Ti)O₃, 301
Pb(Zr,Ti)O₃ – MnO, 301
Pb(Zr,Ti)O₃ – Nb₂O₃, 301
PbO, 307
PbTiO₃, 301
PbZrO₃, 301
peak absorption cross-section, 361
Péclet number, 238
peritectic reaction, 479
pH, 307
pH of the growth medium, 347
pH of the medium, 351
pH of the mineralizer, 351
phase, 324
phase change, 563
phase diagram, 112, 564
phase diagram – LiNbO₃, 389
phase diagram of high T_c phase, 483
phase equilibrium, 114, 336

- phase purity, 305
 phase transformation, 299
 phase transition, 497
 phase-matching, 434
 phase-matching angle, 436
 phenacite, 574
 photorefractive, 440
 physical vapor deposition, 94
 physical vapor transport, 235
 physics-based mathematical model, 239
 piezoelectric, 300
 piezoelectric material, 387
 plane wave dynamical diffraction
 theory, 405
 plasma, 124
 plastic deformation, 263
 plate-like crystal, 576
 platinum crucible, 571
 poling, 389
 poling by electric field, 401
 polyacrylic acid, 322
 polycrystalline diamond film, 93
 polymorphism, 497
 polynuclear controlled growth, 317
 polytypism, 202
 poly-vinyl-alcohol (PVA), 322
 porosity, 236
 portability, 561
 post-growth cooling, 392
 potassium hydroxide (KOH), 307
 potassium titanate, 316
 powder, 305
 powder charge, 236
 Prandtl number, 238
 precipitation, 300, 314
 precursor, 107, 324
 preheating, 236
 presence of mixed phases, 342
 pretreatment, 104
 primary crystallization field (PCF), 491
 prismatic crystal, 576
 pseudo-binary phase diagram, 478
 p-type doping, 99
 purity, 513
 PVD, 94

 quantum dot, 80
 quantum well wire, 82
 quartz, 567
 quartz tube, 236

 $R_2O_3+V_2O_5+Nd_2O_3$, 349
 radiation, 243
 radiation from particle to particle, 240
 radiative heat flux, 242
 radical, 107
 radio-frequency current, 236
 radius, 309, 318
 radius of curvature measurement, 397
 Raman spectroscopy, 103
 rare earth orthovanadates, 356
 rare earth vanadates, 335
 rarity, 561
 rate, 312
 rate controlling, 312
 rate of evaporation, 574
 rate-limiting, 316
 $RBa_2Cu_3O_{7-\delta}$, 478
 reaction, 311
 reaction time, 311
 reconstruction, 71
 reflection high-energy electron
 diffraction (RHEED), 56
 residual impurity, 74
 residual stress, 82, 388
 resistance heating, 392
 resolved shear stress, 264
 Rf heating, 392
 RF induction, 236
 RHEED oscillation, 57
 rhombohedral structure, 388
 ring element, 243
 role of pH, 336
 ruby, 561
 ruby pull rod, 395
 rutile, 318, 561
 RVO_4 , 338
 $RVO_4 \cdot nH_2O$, 344

 salts, 300
 sapphire, 561
 saturated vapor, 247
 scanning electron microscope (SEM),
 571
 scanning electron microscopy (SEM),
 107
 scanning tunneling microscopy (STM),
 107
 scintillator, 387
 screw dislocation, 201, 205, 319
 second harmonic generation (SHG), 2ω ,
 419

- section topography, 205
seed crystal, 564
seeded physical vapor transit, 507
seeded sublimation, 194
seeded vertical Bridgman, 504
seed holding assembly, 392
seeding, 197
seed-melt interface, 393
seed pulling assembly, 392
seed rotation assembly, 392
segregation of impurity defects, 406
self-flux, 445
self-sealing technique, 502
self-seeding method, 478
self-surfactant effect, 78
SEM, 107
shape, 324
shear stress, 264
Shellmeier equation, 435
short afterglow, 387
Si- monochromator-collimator, 396
SiC, 181
SiC-based devices, 181
silicon, 566
silicon carbide, 235
simulated contrast, 212
single crystal, 561
single domain crystals, 389
sintered nutrient, 351
sintering, 309
size, 324
skeleton crystal, 576
skin depth, 251
slip system, 265
slope efficiency, 358
slow cooling, 568
small angle boundaries, 204, 221
soft ampoule method, 499
sol-gel, 299
solid, 563
solid matrix, 236
solid solution, 564
solid-state growth, 563
solid-state laser host crystals, 335
solid-state recrystallization (SSR), 509
solid/gas interface, 242
solubility, 343, 568
soluble mobile complexes, 343
solute, 564
solution growth, 502, 567
solvent, 567
solvent-solute interaction, 343
 sp^3 bonding, 105
spatial distribution, 115
special crucible cover, 395
spectra acceptance bandwidth, 422
spinel, 561
spiral growth, 108, 341
spontaneous nucleation, 347, 447
 $Sr_2Be_2BO_7$ (SBBO), 420
 $SrTiO_3$, 301
 $SrZrO_3$, 301
Stefan flow, 238
Stefan-Boltzmann constant, 240
step bunching, 80
step flow, 61
step flow mode, 64
step-flow mode, 78
steric, 324
sticking coefficient, 238
stirred solution technique, 433
STM, 107
stoichiometric composition, 389
stoichiometric, 422
strain field, 207
Stranski-Krastanow growth mode, 80
stress, 427
stress-assisted epitaxy, 85
stress-strain relation, 263
striations, 356
structural characterization, 387
sublimation, 238
sublimation sandwich method (SSM),
190
substitution, 436
substrate surface, 94
substrates, 513
sum-frequency generation, 419
supercooling, 563
supersaturation, 197, 253, 312, 447, 568
superscrew dislocation, 205
surface chemical reaction, 115
surface diffusion, 59
surface diffusion coefficient, 61, 75
surface dissolution features, 356
surface energy, 322
surface free energy, 103
surface morphology, 94, 355
surface reaction, 315
susceptibility, 421
SWBXT, 204
synchrotron transmission topograph, 214

- synchrotron white beam X-ray
 topography (SWBXT), 204
 synthesis, 305
 synthesis of vanadates, 336
- teflon liners, 347
 temperature, 307
 temperature acceptance bandwidth, 422
 temperature differential, 189
 temperature distribution, 254
 temperature gradient, 197, 253, 569
 temperature monitoring, 395
 template, 324
 tensile stress, 103
 terraced crystal, 578
 tetragonal, 311
 tetramethylammonium hydroxide
 (TMAH), 309
 textured diamond film, 110
 theoretical half-width of diffraction
 curve, 395
 thermal conductivity, 96, 240
 thermal cycle treatment, 85
 thermal dephasing, 422
 thermal expansion coefficient, 103
 thermal stress, 263
 thermal-elastic anisotropic, 263
 thermodynamic, 305
 thermodynamics, 113
 thermoelastic, 263
 third harmonic generation (THG), 3ω ,
 435
 threading screw dislocations, 215
 three-zone furnace, 395
 threshold pump power, 360
 Ti:sapphire lasers, 439
 titania (TiO_2), 318
 top-seeded Kyropoulos, 422
 top-seeded solution growth (TSSG),
 342, 422
 transmission topography, 205
 transmittance spectra, 360
 transparency, 419
 transport model, 241
 transport rate, 248
 traveling heater method (THM), 499
 traveling-solvent floating zone (TSFZ)
 method, 493
 traverse topographs, 409
 traversing mechanism, 396
 TSSG, 342
- tunable mid-infrared sources, 514
 twinning, 497, 574
 two-dimensional nucleation, 108
 two-dimensional step, 107
 two-step growth, 111
- unsaturated bond, 104
 UV absorption edge, 421
 UV light, 419
- vacuum degassing, 236
 valency of vanadium, 338
 vanadium ions, 338
 vapor growth, 186, 501, 564
 Verneuil method, 564
 vertical circle goniometers (VCG), 397
 vertical gradient freeze technique, 499
 very low angle grain boundaries, 411
 Vickers hardness, 428
 view factor, 244
 viscosity, 445, 572
 Voigt notation, 264
 volatility, 445, 570
- wafer, 184
 walk-off angle, 422
 wavelength, 419
 weighing mechanism (WM), 393
 wet chemical, 299
 white beam synchrotron X-ray
 topography, 204
 white LEDs, 514
 wide band gap, 99
- X-ray diffraction (XRD), 204, 571
 X-ray lithography, 99
 X-ray topography, 204
 XRD studies, 358
- $\text{Y}_2\text{O}_3\text{-V}_2\text{O}_3\text{-Y}_2\text{O}_5$ system, 339
 $\text{Y}_2\text{O}_3\text{-V}_2\text{O}_5$, 336
 $\text{Y}_2\text{O}_3\text{-V}_2\text{O}_5\text{-V}_2\text{O}_3$, 337
 $\text{Y}_2\text{O}_3\text{-V}_2\text{O}_5$, 336
 $\text{Y}_2\text{O}_3\text{-V}_2\text{O}_{5-y}$, 337
 $\text{Y}_8\text{V}_2\text{O}_{17}$, 342
 $\text{YCa}_4\text{O}(\text{BO}_3)_3$ (YCOB), 420
 yield diagram, 307
 YVO_4 , 336
 $\text{YVO}_4 \cdot n\text{H}_2\text{O}$, 344
 YVO_{4-x} ($0 < x \leq 1$) phases, 342

YVO_{4-x} phases, 337

yield diagram, 307

zinc chalcogenides, 497

zirconia (ZrO_2), 316

ZnO, 510

ZnS, 509

ZnSe, 502

ZnTe, 498

zone melting, 339

β - BaB_2O_2 (BBO), 420